Development and Validation of a Biplane Fluoroscopy System to Quantify In-Vivo Knee Kinematics

Thesis submitted in fulfilment of the requirement for the degree of Doctor of Philosophy in Medical Engineering

By

David Elwyn Williams
BEng

School of Engineering - Cardiff University
UK
2018

DECLARATION AND STATEMENTS

DECLARATION

This work has not been submitted in substance for any other degree or award at this or any other university or place of learning, nor is being submitted concurrently in candidature for any degree or other award.

Signed ……..…….. (candidate) Date ……..……..……

STATEMENT 1

This thesis is being submitted in partial fulfilment of the requirements for the degree of PhD

Signed…… (candidate) Date ……..……

STATEMENT 2

This thesis is the result of my own independent work/investigation, except where otherwise stated, and the thesis has not been edited by a third party beyond what is permitted by Cardiff University's Policy on the Use of Third Party Editors by Research Degree Students. Other sources are acknowledged by explicit references. The views expressed are my own.

Signed …… (candidate) Date ……..……

STATEMENT 3

I hereby give consent for my thesis, if accepted, to be available online in the University's Open Access repository and for inter-library loan, and for the title and summary to be made available to outside organisations.

Signed …… (candidate) Date ……

STATEMENT 4: PREVIOUSLY APPROVED BAR ON ACCESS

I hereby give consent for my thesis, if accepted, to be available online in the University's Open Access repository and for inter-library loans **after expiry of a bar on access previously approved by the Academic Standards & Quality Committee.**

Signed …… (candidate) Date ……..……

ABSTRACT

Accurate measurement of in-vivo joint kinematics is important for understanding normal and pathological knee function and evaluating outcome of surgical procedures. Fluoroscopy and model based image registration (MBIR) provides an accurate and minimally-invasive technique for calculating in-vivo kinematics. This study builds upon existing MBIR protocols and looks at quantifying the errors present in the protocols, with the aim of developing a biplane fluoroscopy system to investigate in-vivo kinematics of the knee.

A retrospective single plane fluoroscopy study was performed on a unique TKR patient group with mal-aligned knee replacements to understand the influence of surgical frontal plane alignment and function. Significant interactions between frontal plane alignment and knee joint kinetics and kinematics were detected using marker-based motion capture. While these interactions were not replicated within in-vivo knee kinematics measured during a step-up activity using fluoroscopy and MBIR, results highlighted interactions with other surgical measures of alignment such as posterior tibial slope angle and Hip-Knee-Ankle angle.

A study was undertaken to examine in-vivo kinematics using three dimensional (3D) models generated from magnetic resonance imaging (MRI) combined with fluoroscopy and synchronised motion analysis. These studies, in which the fluoroscopy was performed at Llandough Hospital X-ray Department, highlighted key technical limitations associated with the currently adopted protocol, and two primary sources of error in determining in-vivo kinematics; generation of three dimensional (3D) bone models and MBIR processing to calculate in-vivo kinematics.

A validation protocol was developed to determine the accuracy of magnetic resonance imaging (MRI) derived 3D bone models. This was performed by imaging five ovine hind limbs using MRI and computed tomography (CT) followed by complete dissection and structured light scanning of the femora and tibiae to calculate the true geometry. The results showed that MRI derived 3D bone models had a RMS error of 0.8 mm when compared with the other modalities. This error was deemed acceptable as it was not larger than the 3D voxel dimension.

A validation study was performed to investigate the accuracy of a biplane C-arm system in calculating skeletal kinematics using MBIR. It examined the static and dynamic accuracy associated with using both Sawbones and an ovine hind limb during a simulated step up activity. Three different dynamic velocities were investigated. Errors were shown to increase with higher velocities highlighting the importance of calculating errors during representative dynamic tasks. The results also highlighted important hardware limitations with the C-arm system.

An in-house combined motion analysis and biplane fluoroscopy system was established at Cardiff University. An updated and validated MBIR protocol was performed on 5 healthy volunteers during a step up and down task. 3D models of bone and cartilage were used in combination with biplane fluoroscopy images to calculate in-vivo kinematics and estimate contact point positions. The validation and MBIR protocols in this thesis have contributed to the development and understanding of the limitations associated with a new unique bespoke biplane X-ray system being designed and manufactured currently at Cardiff University.

ACKNOWLEDGEMENTS

I would like to firstly thank both my PhD supervisors. Dr Gemma Whatling for giving me the opportunity to carry out this work and providing important training. Prof. Cathy Holt for providing much needed support from beginning to end and keeping me motivated till completion of this thesis.

I would also like to show my appreciation to the MSKBRF research team, in particular Dr Paul Biggs, Dr Nidal Khatib, Dr Philippa Jones, Dr Aseel Ghazwan, Dr Hassanain Ali Lafta, Jake Bowd and Samuel Woodgate. Without their support and friendship during my time as a PhD student I don't think I would have been as successful or enjoyed the experience as much as I have.

An extra big thank you to Dr Davide Crivelli and Dr Paul Biggs for providing help and guidance as I struggled through using MATLAB.

I would like to acknowledge all the help from undergraduate students that were involved in building of the knee rig.

My appreciation goes to Dr Michael Sobanski for providing help with setting up the X-ray facility and Arnold rust and his team at RPS Cardiff for their help in calculating radiation doses and medical physics advice during this time. In addition Peter Hobden and Joy Curran for assisting in developing and performing the MRI acquisitions at CUBRIC.

Special thanks to Prof. Scott Banks and his team at the University of Florida for providing expertise on how to best utilise their software and advice on biplane calibration.

I want to give my thanks to my friends and family who have supported me throughout even if they have no idea what I have spent the last few years doing. Thanks to Paul, Nidal and Wayne for providing musical distraction over the last few years.

Lastly, an especially big thank you to my wonderful partner Polly. She has made sure that I have remained in the highest of spirits, eaten well and kept me going even in the most trying times.

TABLE OF CONTENTS

LIST OF ABBREVIATIONS

%Bw	Percentage Body Weight
$_1$H	Hydrogen
2D	Two Dimensional
3D	Three Dimensional
ACI	Autologous Chondrocyte Implantation
ACL	Anterior Cruciate Ligament
ACS	Anatomical Coordinate System
AEC	Automatic Exposure Control
AIM	Automatic Identification Model
AP	Anterior-Posterior
ARUK	Arthritis Research UK
ASIR	Adaptive Statistical Iterative Reconstruction
BMI	Body Mass Index
BNC	Bayonet Neill–Concelman Connector
Bw	Body Weight
CAD	Computer Aided Design
CAST	Calibrated Anatomical Systems Technique
CCD	Charged Coupled Device
CHT	Circle Hough Transform
CISS	Constructive Interference Steady State
CMM	Coordinate Measuring Machine
COM	Centre of Mass

COP	Centre of Pressure
COR	Centre of Rotation
CT	Computerised Tomography
CUBRIC	Cardiff University Brain Research Imaging Centre
DC	Direct Current
DESS	Double Echo Steady State
DICOM	Digital Imaging and Communications in Medicine
DJMS	Dynamic Joint Motion Simulator
DMOADS	Disease Modifying Osteoarthritis Drugs
DOF	Degrees of Freedom
EMG	Electromyography
FIESTA-C	Fast Imaging Employing Steady-state Acquisition - C
FOV	Field of View
FPS	Frames per Second
GCS	Global Coordinate System
GRF	Ground Reaction Force
HKA	Hip-Knee-Ankle angle
HS	Heel Strike
HTO	High Tibial Osteotomy
IR	Infrared Radiation
IRMER	Ionising Radiation (Medical Exposure) Regulations 2017
IRR17	Ionising Radiation Regulations 2017
ISB	International Society of Biomechanics
KOOS	Knee injury and Osteoarthritis Outcome Score

KOS	Knee Outcome Score
LCS	Local Coordinate System
LED	Light Emitting Diode
MBRI	Model Based Image Registration
MPRAGE	Magnetism Prepared RAPid Gradient Echo
MR	Magnetic Resonance
MRI	Magnetic Resonance Imaging
MSKBRF	Musculoskeletal Biomechanics Research Facility
OA	Osteoarthritis
OARSI	Osteoarthritis Research Society International
OKS	Oxford Knee Score
ORUK	Orthopaedic Research UK
PD	Proton Density
PD-TSE	Proton-Density Turbo Spin-Echo
QA	Quality Assurance
QTM	Qualisys Track Manager
REC	Research Ethics Committee
RF	Radio Frequency
RMS	Root Mean Squared
ROM	Range of Motion
RPA	Radiation Protection Advisor
RPS	Radiation Protection Supervisor
RSA	Radiostereometric Analysis
SDD	Source Detector Distance

SI	Superior-Inferior
SL	Structured Light
SOP	Standard Operating Procedures
STA	Soft Tissue Artefact
T_1	Longitudinal Relaxation Time
T_2	Transverse Relaxation Time
TE	Echo Time
TIF	Tagged Imaged File
TKR	Total Knee Replacement
TPR	Target Pattern Recognition
TR	Repetition Time
TS	Tibial Slope
TTL	Transistor - Transistor Logic
UTE	Ultrashort Echo Time
UV	Ultraviolet Radiation
WOMAC	Western Ontario and McMaster Universities Osteoarthritis Index
WORMS	Whole Organ Magnetic Resonances Imaging Score
YLD	Years Lived with Disability
ZTE	Zero Echo Time

Chapter 1 Introduction and Literature review

1.1 Osteoarthritis

Osteoarthritis (OA) is the most common form of arthritis and is a progressive disease characterised by major structural changes of the joint. These changes typically involve thinning of the articular cartilage and damage to the bone. These lead to symptoms including joint pain, stiffness and functional impairment (McGonagle et al. 2010; Lane et al. 2011).

An estimated 242 million people live with symptomatic hip/knee OA which is 3.8% of the total global population (GBD 2013). It is ranked as the 10th leading contributor to global years lived with disability (YLD) accounting for 13 million globally (Cross et al. 2014). These figures are expected to increase due to an aging population and a rise in global obesity rates. Both obesity and age are some of the most common risk factors for OA (Loeser 2011; King et al. 2013; March et al. 2016) and can lead or contribute to other comorbidities.

In a study by Kadam et al. (2004) looking at clinical comorbidity in patients with OA in England and Wales they found that 31% of patients had five or more chronic conditions. The main comorbidities related to OA include hypertension (Puenpatom and Victor 2009), cardiovascular disease (Calvet et al. 2016) and diabetes (Tuominen et al. 2007). These are related as OA is found to impact the ability to exercise and lose weight (Piva et al. 2015), which are both risk factors and potential treatments for these diseases. These comorbidities further add to the total burden of the disease on the patient and society.

The Osteoarthritis Research Society International (OARSI) defines OA as “a disorder involving movable joints characterized by cell stress and extracellular matrix degradation initiated by micro- and macro-injury that activates maladaptive repair responses including pro-inflammatory pathways of innate immunity. The disease manifests first as a molecular derangement (abnormal joint tissue metabolism) followed by anatomic, and/or physiologic derangements (characterized by cartilage degradation, bone remodelling, osteophyte formation, joint inflammation and loss of normal joint function), that can culminate in illness” (Kraus et al. 2015). This definition highlights the complexity of the disease and how it can’t be treated as a single disease.

This heterogeneity across OA subjects results in large variations in responses to treatments, clinical symptoms and biochemical characteristics (Driban et al. 2010). These variations can be present within the subject when considering different joints.

There are several potential disease-modifying treatments for osteoarthritis (DMOADs) that have been investigated but none have resulted in a successful clinical trial. These failures could partially be related to the heterogeneity of the disease and suggests that more patient specific treatments might be better in the future (Karsdal et al. 2016). Therefore, currently there is no cure for OA. There are treatments and interventions available that may help alleviate the symptoms or potentially delay progression.

Approximately one in five people over 45 has knee OA in the UK, it is predicted by 2035 that 8.3 million people in the UK over 45 could be seeking treatment for knee OA (Arthritis Research UK 2013). Understanding how these treatments or interventions perform, whether they are performing as intended and identifying which are most suitable for specific patient groups is important for improving patient outcomes.

1.2 Treatments for Knee OA

Treatments for knee OA can be simply defined into two categories, surgical and non-surgical. Non-surgical options include strength training, weight management, exercise and biomechanical interventions (knee brace, lateral wedge insoles) (Buttgereit et al. 2015). These are usually early strategies in dealing with the symptoms of OA and attempt to slow progression. After these treatment options have been exhausted surgical intervention is usually the next course of action.

1.2.1 Surgical Interventions

Surgical interventions can be used to treat the symptoms of OA or address potential risk factors for developing OA. The most commonly accepted surgical

treatments for OA are arthroscopy, cartilage repair, osteotomy and joint reconstruction (Ronn et al. 2011).

Arthroscopy debridement and lavage is a common treatment with the main aim to remove debris and repair tissues (Ogilvie-Harris and Fitsialos 1991). Debris which are removed can consist of damaged cartilage or torn meniscus fragments. There is controversy on how well this surgery performs on treating OA, with studies (Moseley et al. 2002; Siemieniuk et al. 2017) showing that it no works better than placebo treatment despite patients reporting symptomatic relief after treatment. The most current recommendations from National Institute for Health and Clinical Excellence (NICE) is that arthroscopic surgery should only be part of the treatment of a patient with OA if they have a history of mechanical locking (NICE 2014).

Cartilage repair surgery is performed as articular cartilage has limited to no healing capacity. There are several different approaches including bone marrow stimulating techniques via Microfracture (Pridie 1959), reconstruction by osteochondral plugs taken from different parts of the femur (Hangody and Kárpáti 1994; Hangody et al. 2001) or by using cultivated autologous chondrocytes and re-implanting these underneath a periosteal flap (Autologous Chondrocyte Implantation (ACI)) (Brittberg et al. 1994). Each approach has its own advantages and disadvantages, although recent clinical trials have shown the benefit of performing ACI over Microfracture (Basad et al. 2010; Saris et al. 2014).

Osteotomies are often used to target patients with uni-compartmental OA by altering the weight bearing axis of the lower extremity, which results in the unloading of the damaged compartment (Maquet 1976). This type of surgery is explained further in section 3.1.3.

Surgical interventions that target patients with early to moderate knee OA or patients who are younger are important as they offer the potential to delay knee arthroplasty. New treatments and improvements to existing surgeries is an active research area, however objectively quantifying how they improve patient’s symptoms is challenging.

The subsequent introduction focusses on knee arthroplasty, which is considered the gold standard surgical intervention for treatment of end stage OA.

1.2.2 Total Knee Replacement (TKR)

The TKR surgical procedure consists of removing the diseased ends of the bone and replacing them with orthopaedic prosthesis designed to restore functional movement. The primary aim of the procedure is to reduce pain and to improve joint function. In 2017, 102,177 primary knee procedures were performed in the UK (National Joint Registry 2018).

To clinically assess patient joint function and success after TKR patient reported outcome measures (PROMS) are used. They provide useful information about the point of failure and how the patient perceives their function but do not provide objective reasons for failure or poor outcome. It has been suggested that patients with severe OA have difficulty separating pain and functional limitation when self-assessing their ability to perform activities of daily living (Mizner et al. 2011), with some studies reporting that PROMS cannot determine changes in performance based measures after TKR (Stratford and Kennedy 2006; Jacobs and Christensen 2009; Mizner et al. 2011; Naili et al. 2017).

This highlights the importance of performance-based measures to understand how patients function changes pre and post intervention. One common approach is to perform human motion analysis on patients during activities of daily living.

1.3 Human Motion Analysis

Human Motion Analysis is an objective technique for quantifying biomechanical information of the musculoskeletal system. It can provide kinetic and kinematic information for a range of articulating joints. The most common approach uses motion capture employing optoelectronic stereo photogrammetry (Fernandez et al. 2008; Guan et al. 2016).

1.3.1 Optoelectronic Stereo Photogrammetry

Body segment positions and orientations are tracked in 3D space using markers attached to the segments which are tracked by digital infrared cameras. Kinematics can be calculated by relating the positions and orientations of the two connected segments with each other. The main purpose of this approach is to determine the six degrees of freedom of different joint kinematics during activities of daily living.

Passive optoelectronic stereo photogrammetry has been used at Cardiff University to look at OA subject function (Jones 2004; Whatling 2009; Biggs 2016; Metcalfe et al. 2017) and assess post-surgical intervention (Biggs 2016; Whelton et al. 2017; Van Rossom et al. 2018). Infra-Red (IR) light is emitted from cameras and reflected off retroreflective markers into an IR sensor built into the cameras which capture the reflected light. The positions of the markers can be determined using stereo photogrammetry, which requires a minimum of two cameras to perform this.

Bone position cannot be directly measured in-vivo using body fixed markers so appropriate anatomical markers are placed in specific locations designed to estimate the position and orientation of bone. Retroreflective markers are positioned on anatomical landmarks to define clinically relevant axes for the different body segments and further arrays of markers applied to the segment to act as tracking markers. The tracking markers are required as the markers to define anatomical land marks are highly susceptible to inertial effects, skin movement and contraction of muscles. This means they are moving relative to the bone; known as soft tissue artefact (STA). Tracking markers are positioned onto parts of the segments where less STA is known to occur. A rigid body relationship is assumed between the anatomical and tracking markers and this allows the tracking markers to be used to define position and orientation of different segments.

STA is the primary source of error encountered with marker-based motion capture. The thigh has some of the larger errors with rotational errors larger than 12 degrees (Stagni et al. 2005; Benoit et al. 2006; Tsai et al. 2011). A detailed review (Cappozzo et al. 2005) has been performed looking at all the

errors involved in optoelectronics stereo photogrammetry including instrumental errors (Chiari et al. 2005), STA (Alberto Leardini et al. 2005) and anatomical landmark misplacement (Della Croce et al. 2005). For more information on these errors the reader is directed to read these reviews.

These errors mean that joint translations are ignored from biomechanical analysis using marker-based motion capture. Translations play an important part of how the normal healthy knee functions. Accurate measurement of in-vivo joint kinematics is imperative for understanding normal and pathological human motion and for evaluating the outcome of surgical procedures (Gray et al. 2016). Translational as well as rotational information can provide the six degree of freedom data required to inform design of new prosthesis and surgical techniques.

1.3.2 Calculating In-Vivo Kinematics

There are several different imaging methods employed to calculate in-vivo kinematics of different human and animal joints.

Magnetic resonance imaging (MRI) has been used to measure in-vivo kinematics of the knee during quasi-static activities (Vedi et al. 1999; Patel et al. 2004; Johal et al. 2005; Dragoo et al. 2010) and dynamic activities (Sheehan et al. 1997; Powers et al. 1998; Kaiser et al. 2016; Haug et al. 2017) using dynamic MRI.

Four dimensional computer tomography (4DCT) is a dynamic imaging technique where a three dimensional (3D) computed tomography (CT) volume is imaged over time to create a dynamic 3D dataset (Kwong et al. 2015). It has been used to look at patellofemoral instability (Demehri et al. 2014), femoroacetabular impingement (Wassilew et al. 2013) and wrist motion (Zhao et al. 2015). One of the main limitations for this technique is that the radiation dose supplied with the reported effective dose for femoroacetabular impingement study was 9.8 mSv (Wassilew et al. 2013) equivalent to over three and a half years of background radiation in the UK (Public Health England 2011).

Both these methods allow in-vivo kinematics but are limited by what activities can be performed. This is because the field of view and the ability for volunteers to perform the activity within the confines of the scanner are limiting. In addition both methods would not allow the ability to look at TKR kinematics as TKR would introduce large artefacts (Hargreaves et al. 2011) or both imaging modalities that would make determining accurate in-vivo kinematics challenging.

1.3.3 Fluoroscopy using Model Based Image Registration

1.3.3.1 Single Plane Fluoroscopy

Fluoroscopy combined with Model Based Image Registration (MBIR), provides an accurate and minimally-invasive technique for measuring in-vivo joint kinematics. It is recognised that many different studies have used fluoroscopy to analyse different joints using both MBIR and other methodologies. However, the focus of this literature review will be on fluoroscopy studies that have been applied to study the knee.

The first key study to use this technique was carried out by Banks (1992) to calculate and quantify 6DOF, TKR kinematics using fluoroscopy and 3D surface models. This was performed by projecting a 3D model of an implant onto the 2D X-ray frame and adjusting its position until the projection aligns with the image. Reported accuracy of this method 1mm translations and 0.5° rotations with respect to in plane motions (Banks and Hodge 1996).

This has proven to be an in-valuable measurement technique and numerous groups have developed their own technique based on this approach (You et al. 2001; Mahfouz et al. 2003; Tang et al. 2004; Scarvell et al. 2010).

This technique has been used to assess TKR kinematics (Banks and Hodge 2004; Banks et al. 2005; A. Leardini et al. 2005; Stagni et al. 2010; Harman et al. 2012; Watanabe et al. 2012; Watanabe et al. 2013; Shimmin et al. 2015), intact knees kinematics using CT derived bone models (Komistek and Dennis 2003) and intact knee kinematics MRI derived bone models (Moro-Oka et al. 2008; Hamai et al. 2009; Hamai et al. 2013).

Single plane fluoroscopy has an important associated limitation when measuring out-of-plane translations (Fregly et al. 2005; Hirokawa et al. 2008; Acker et al. 2011). When implants or bone travel out of plane during single plane fluoroscopic examinations they appear subtly larger or smaller making this change difficult to detect manually or via optimisation algorithms. One approach of overcoming this is to use biplane fluoroscopy.

1.3.3.2 Biplane Fluoroscopy

Biplane fluoroscopy seeks to overcome this by using two synchronised fluoroscopes with overlapping imaging views. These set ups are usually consisting of two mobile C-arms, as they are able to be manipulated into overlapping their views (Li et al. 2008; Liu et al. 2010; Barré and Aminian 2018). Using the two view allows more uniform and precise measurements compared with single plane.

Some research groups have developed bespoke biplane X-ray systems that have taken components from clinical fluoroscopes and mounted them within custom housings to maximise positioning capability. They have also replaced some of the components to improve imaging capabilities. This includes replacing the in-built video cameras with high speed cameras to allow recording of dynamic activities with higher frame rates (Brainerd et al. 2010; Torry et al. 2011; Campbell et al. 2016).

Other research groups have taken this one step further and built fully custom biplane X-ray systems. These are typically capable of high-speed video radiography which uses very fast pulsed X-rays of speeds of up to 150 FPS that are time synchronised with high speed cameras (Anderst et al. 2009; Ivester et al. 2015). These are highly accurate systems with precision for tracking bone of less than 1 mm and 1°.

For most biplane X-ray systems, the field of view is smaller than that achieved for single plane fluoroscopy which limits the activities that can be performed or the amount of the activity that can be imaged. For example, when looking at gait, most systems are only capable of imaging the stance phase.

More recently moving fluoroscopy systems have been developed to be able to image more aspects of dynamic systems. List et al. (2017) have adapted a single-plane fluoroscope to track a volunteer during level gait, stairs and downhill walking. The system tracks the volunteer by using a wire sensor and digital goniometer attached to the leg being imaged. Guan et al. (2016) have built the impressive mobile biplane X-ray (MoBiX) system capable of tracking volunteers during over ground gait (Figure 1-1). This system uses a high-speed camera to track a marker on the target joint as well as a learned velocity profile generated from the tracking marker during practice trials. These systems provide the opportunity to further understand in-vivo kinematics during more complex tasks. However, they are more complex compared to the stationary systems and the potential of vibrations during movements could change the positions between image intensifier and X-ray tubes.

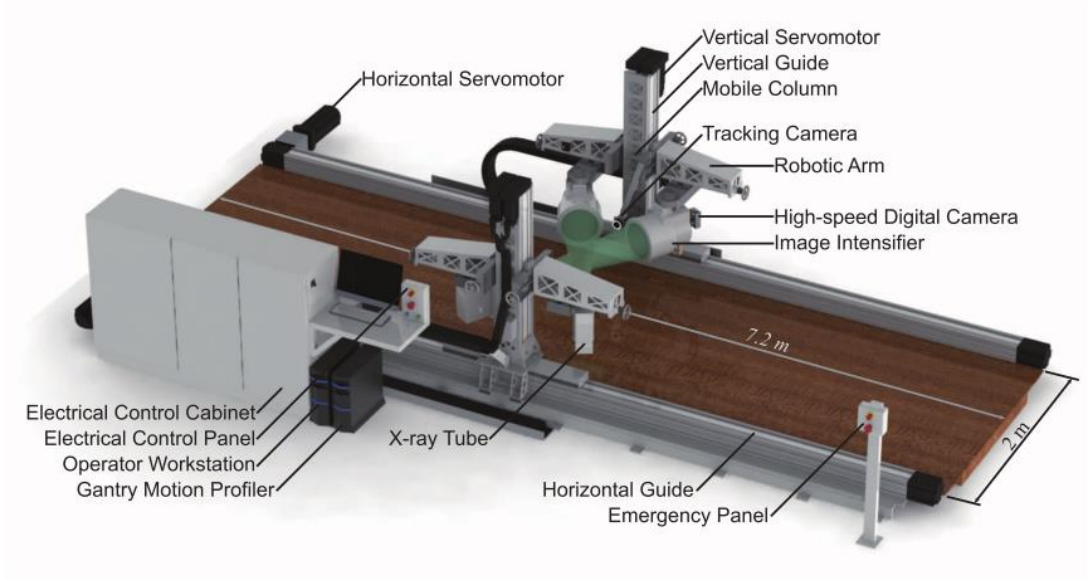

Figure 1-1 Diagram of the mobile biplane X-ray (MoBiX) image reproduced from Guan et al. (2016)

1.3.3.3 Fluoroscopy at Cardiff

Single plane fluoroscopy studies have been performed at Cardiff University looking at differences between image registration and motion analysis kinematics for TKR and intact knee (Whatling 2009) as well as shoulder kinematics (Stroud Larreal 2011). These studies have been limited in terms of

technical capabilities and the errors associated with the MBIR protocol have never been investigated. The next section provides an overview of the different stages of the protocol in terms of the technology used.

1.4 Fluoroscopy and Model Based Image Registration Protocol

There are three main steps involved with carrying out fluoroscopy and model based image registration (MBIR) to investigate in-vivo kinematics.

1. Fluoroscopy Data Collection
2. Generation of a three dimensional (3D) model of the joint of interest
3. Model based Image Registration (MBIR)

1.4.1 Fluoroscopy

1.4.1.1 History

Fluoroscopy provides real-time dynamic viewing of anatomic structures during dynamic activities. Following the discovery of X-rays by William Röntgen in late 1985, the first fluoroscope was invented by Thomas Edison in 1896 (The Edison skiascope) (Mould 1995). The early diagnostic imaging systems suffered from an inability to produce an image with sufficient brightness from the fluorescent screens requiring radiologists to acclimatise their eyes in a darkened room prior to an imaging procedure. The development of image intensifiers in 1953 and subsequent technical advancements years later have allowed the recording of fluoroscopy procedures using digital cameras (B. A. Schueler 2000). Most modern fluoroscopy systems include flat-panel detectors

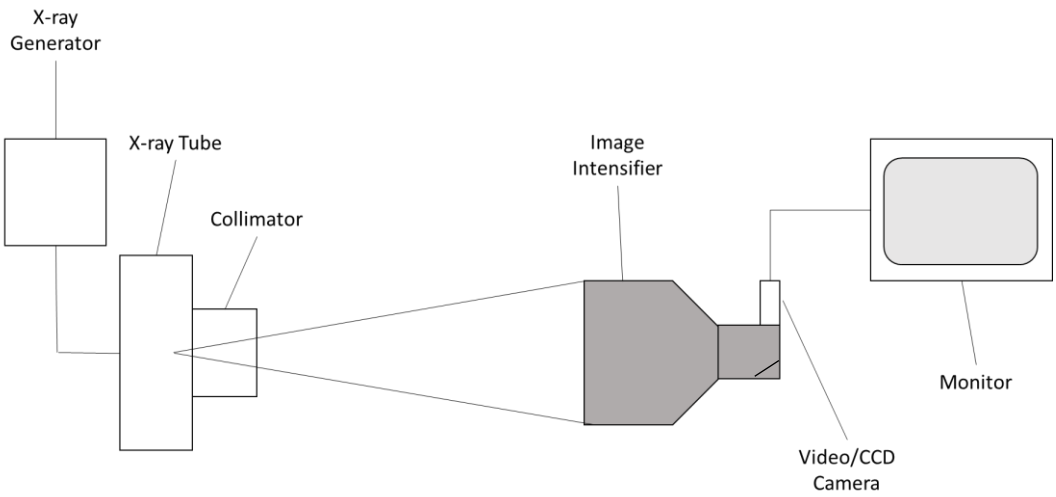

Figure 1-2 Overview of components making up the fluoroscopy imaging chain

which have a large operational dynamic range approximately 60 times greater than image intensifier (Nickoloff 2011). For the application of human motion analysis these are at a disadvantage compared to traditional image intensifiers; they are limited in capture rate due to high data rates, with most clinical systems only capable of speeds up to 30 FPS with significant pixel binning, limiting the spatial resolution. Comparing this with bespoke bi-plane X-ray systems that have image intensifier systems capable of reaching speeds of 1000 FPS using continuous fluoroscopy and 120 FPS using pulsed X-ray (Anderst et al. 2009; Ivester et al. 2015).

1.4.1.2 Fluoroscopy Imaging Chain

The main components in a fluoroscopy system are shown in Figure 1-1. The following briefly describes the function of each component:

- **X-ray Generator**- Is used to select the imaging settings for the X-ray tube. It supplies tube current (mA) and the kilovolt peak (kVp). During continuous fluoroscopy a low continuous tube current is used to keep radiation dose. An automatic exposure control (AEC) is used to maintain a constant brightness of the screen, and changes kVp depending on the thickness of the body part or its attenuation properties (B. a Schueler 2000).

- **X-ray Tube** – converts the supplied electrical energy into an X-ray beam. Electrons are accelerated from a heated filament towards a positively charged rotating tungsten target (McCollough 1997). They are accelerated by applying a high voltage of between 50,000 - 150,000 volts (or 50-150kVp), across the tube. This interaction between the electrons and the target results in X-ray emission. The filament (cathode) and tungsten target (anode) are kept in a vacuum glass tube surrounded by shielding. This increases efficiency of X-ray generation and reduces the heat generated as well as ensuring minimal leakage of X-ray radiation from the tube housing.
- **Collimator –** A series of lead shutter blades that are positioned in front of the X-ray beam. They are used to define the shape and size of the X-ray beam. For most modern fluoroscopy systems, they automatically position the blades such that the X-ray beam is no larger than the image intensifier.
- **Image Intensifier** (Figure 1-3) – Any X-rays that exit the volunteer and hit the input window of the image intensifier tube pass through the vacuum envelope and interact with the input phosphor. Typically this is made from caesium iodide and when X-ray's interact, the energy of the X-ray is converted into light (Balter 1999). A photocathode bonded to the input phosphor emits electrons when illuminated by the phosphor, this is known as photoemission (Bushong 2012). The image intensifier tube has a series of focusing electrodes to direct the electron beam towards the output phosphor. A large potential difference is applied between the photocathode and anode to accelerate the electrons towards the output phosphor. The interaction of these accelerated electrons with the output phosphor produces a bright light signal. X-ray image intensifier's range in size and field of view (FOV) from 230 mm to 400 mm in clinical applications. Output images suffer from distortion due to the process of converting X-ray energy into light. 'Pincushion' distortion is caused by the process of focusing the electrons from the curve photocathode to the flat plane output phosphor (Rudin et al. 1991; Kedgley et al. 2012). The other main type of distortion is 'S-type' which

is due to the Earth's magnetic field. This distortion is greater in larger sized image intensifier and is often combatted by manufacturers by using shielding or a coil creating an opposite magnetic field to counteract Earth's magnetic field (Rudin et al. 1991). How these geometric distortions are overcome is detailed in section 2.2.4.1.

- **Video/CCD camera –** Coupling optics connect the output from the image intensifier to a charge-coupled device (CCD) camera. This converts light into an electronic signal which can be shown on a monitor. Further information on how a CCD operates can be found in section 5.6.3

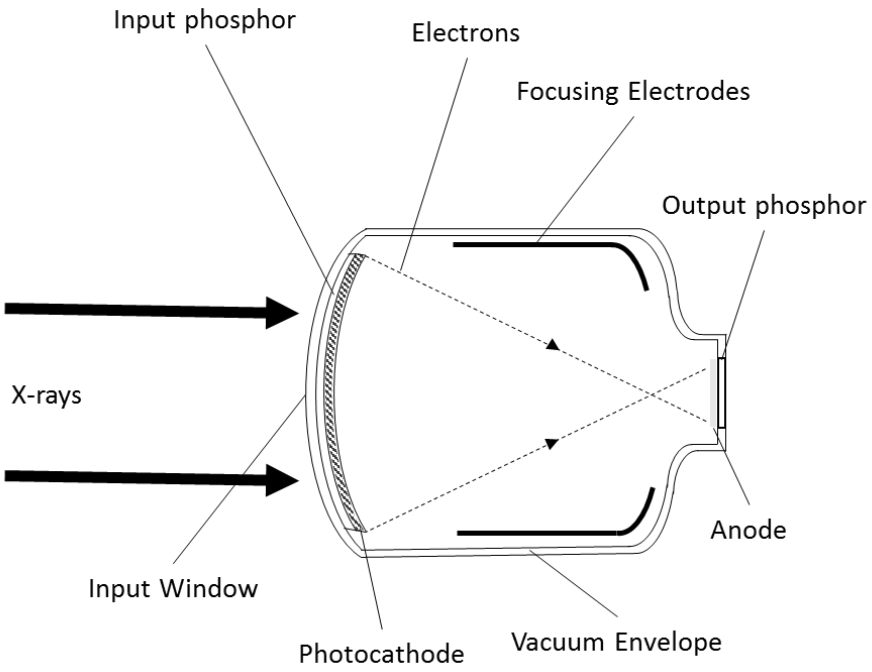

Figure 1-3 Cross-section of X-ray image intensifier tube

1.4.1.3 Fluoroscopy Data Collection

Patient or healthy volunteers asked to perform a particular activity, under instruction and have opportunity to practice the activity of interest several time before actual exposure. The knee of interest is positioned close to the image intensifier to provide good image quality and reduce volunteer exposure (Mitchell and Furey 2011). The fluoroscopy examination is performed by a Radiographer or Approved Operator, and they ensure that the exposures are

kept within the exposure limits set by the Research Protocol. The fluoroscopy examination is either saved as a sequence of image data or as a digital video. Further information for how data collection is performed can be found in section 2.2.4, 3.2.1.2 and 6.2.2.2.3.

1.4.2 Generation of 3D models

For studies involving implanted devices such as TKR components, computer-aided design (CAD) or surface models can be used and are available from the orthopaedic companies who have designed and manufactured them. For intact knee studies subject specific models are usually generated from 3D medical imaging data sets such as Computed Tomography (CT) and MRI. At Cardiff, previous studies (Whatling 2009; Stroud Larreal 2011) have used MRI to generate patient specific bone models and the benefits of using this imaging modality over CT are discussed further in section 4.2.

1.4.2.1 Magnetic Resonance Imaging

MRI is a major diagnostic tool for clinical diagnosis and an important tool for the research community. Magnetic Resonance (MR) can generate 3D image data sets providing detailed visualisation of the anatomy of humans and animals. Unlike CT imaging, which produces a three-dimensional map based on the density of tissue calculated from the attenuation coefficient (the measure of electron density), MR provides information relating to the density of hydrogen atoms (or nuclei). Primarily this is referenced to water and fat and is more commonly known as proton density. MR is also able to provides a lot of other information on the various structure properties in a scanned sample making it one of the most flexible imaging modalities (Doran and Leach 2012).

1.4.2.2 Basic Principles

MRI is based upon the fundamental interaction of a nuclear spin (Figure 1-4) within an external magnetic field. For the majority of medical MRI imaging the focus is on the proton in $_1$H (Hydrogen) and its interaction with external

magnetic field resulting in the precession spin about the direction of the applied field (Figure 1-4). The human body consists of 70% of water so has a large source of $_1H$ protons making it suitable for imaging.

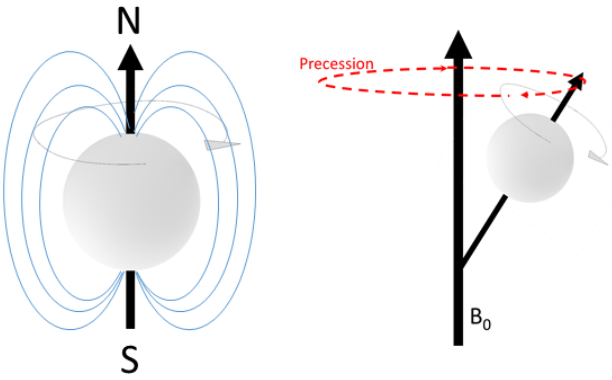

Figure 1-4 The spin of a proton (grey line) is a form of angular momentum, which produces a very small magnetic field (blue lines) that is aligned with the axis of rotation. The black arrow represents the magnetic moment acting through the proton and with it facing upwards this is known as spin up. The spin of the proton can act in the opposite direction causing the magnetic moment to act downwards and this is referred to as spin down (left); When an external magnetic field (B_0) is applied it results in the precession of the proton spin about the field direction (Brown 2014) (Right).

Outside of an external magnetic field the $_1H$ protons spin axis are randomly aligned with the sum of all the magnetic moments creating a net magnetic vector of zero (Figure 1-5). When the body is placed inside the magnetic field of the MR scanner the protons axes are aligned in the direction of the MR scanner field (Figure 1-5).

Some of the protons (spin up) will be aligned parallel and some of the protons will be aligned anti parallel acting in the opposite direction of the applied field (Doran and Leach 2012). The number of protons acting (spin down) anti-parallel is dependent on the strength of the magnetic field applied but is always less than the number acting parallel (Figure 1-6). This creates a net magnetic vector (M_0) acting in the direction of the external field (B_0) (Figure 1-6).

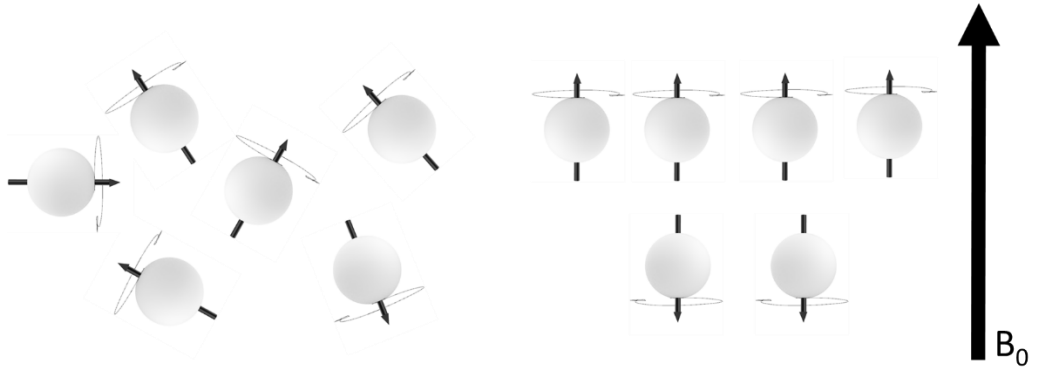

Figure 1-5 Protons in the body outside of a large external magnetic field with randomly aligned spin axis (left); Protons aligned in magnetic field of the magnetic field, with some acting parallel (spin up) and others acting anti-parallel (spin down) (right).

As the spins of the protons precess under the external magnetic field (Figure 1-4), the frequency of this is related to the strength of the field applied and is defined by Larmor's Equation:

$$\boldsymbol{f_o = \frac{\gamma B_0}{2\pi}} \qquad 1\text{-}1$$

Where γ is a constant known as the gyromagnetic ratio which is the ratio of a particle's magnetic moment to its angular momentum in megahertz/tesla (MHz/T) for $_1$H this is 26.7 MHz/T, B_0 is the strength of the external magnetic field in tesla (T) and f_o is the Larmor frequency.

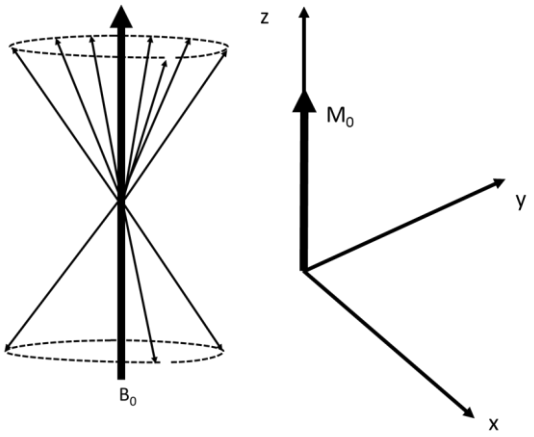

Figure 1-6 The magnetic vectors of the protons precess around the external magnetic field (B_0). The anti-parallel or spin-down magnetic vectors act in the opposite direction but spin at the same angular frequency (known as the Larmor frequency). As there are less spin-down protons the net magnetic vector (M_0) acts in the direction of the applied magnetic field. All the magnetic vectors are out of phase with each other which results in the net magnetic vector to act vertically in positive Z direction (which is the same direction as B_0) (Doran and Leach 2012).

Usually a transmit/receive radiofrequency (RF) coil is placed around the area of interest. If the coil emits a RF pulse of the same frequency as the Larmor frequency (~128.1 MHz at 3T) to the area of interest, the protons absorb the energy from the RF pulse moving to a high energy state and this is known as resonance (Figure 1-7). This causes the magnetic moments precession to be come in phase, shifting the net magnetic vector from a vertical direction to precessing around the external magnetic field (Figure 1-7). Due to the absorption of energy some of the spins acting parallel move to a higher energy orientation and act anti parallel causing the net magnetic vector to be knocked down towards a direction more perpendicular to B_0 (Figure 1-7). The angle which this new orientation occurs for M_0 is known as the flip angle. During this time the precession of the spin induce a voltage on the RF receiver coil providing an MR signal. The intensity of this signal is dependent on the strength of the external field.

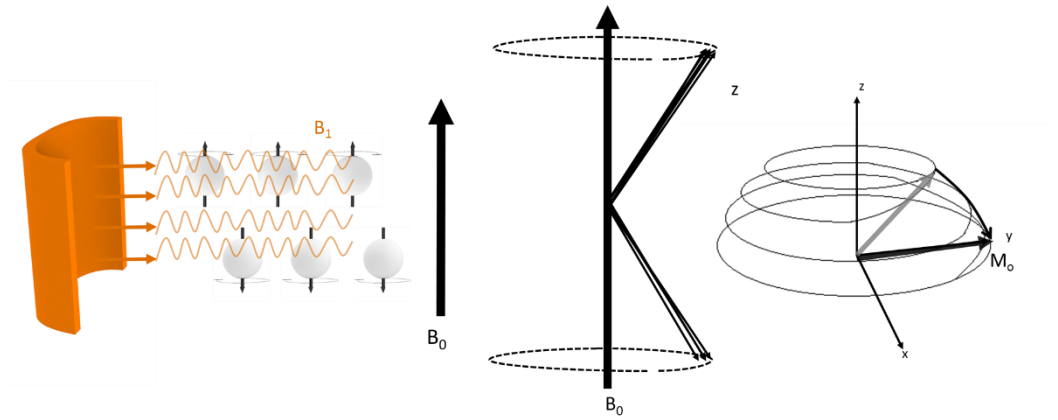

Figure 1-7 The RF coil applies a RF pulse of the Larmor frequency to the protons causing them to absorb the energy and enter into a higher state in a process called resonance. Some of the protons spin flip causing the net magnetic vector to change (left); The magnetic moments of the protons become in phase causing the net magnetic vector to start to precess around the external field and after some of the protons flip eventually to equal numbers forming equal components of the net magnetic vector (middle); This causes the net magnetic vector to be 'knocked down' becoming more perpendicular to the external magnetic field (right).

When the RF pulse is switched off the protons return to their original state, moving from a high energy state to a lower energy state. As the spin of the protons flip back to their original state the net magnetisation vector moves back towards the direction of the external magnetic field, the time it take to recover back to 63% of its original magnitude in the z-direction parallel to B_0, is known as the longitudinal relaxation time (T_1). T_2 relaxation is the process of the magnetic moments of the spin's dephasing causing the net magnetic vector to lose its x and y components and act vertically. The transverse relaxation time (T_2) is a time constant for this dephasing to occur. Both T_1 and T_2 are different values depending on the tissue type (Berger 2002; Doran and Leach 2012).

1.4.2.3 Imaging Parameters

Using the MR signal, the density of the protons can be determined and is referred to as proton density (PD). The contrast of the different tissues that can be visualised is determined from a combination of T_1, T_2 and the PD.

These are manipulated through different imaging sequence parameters such as the repetition time (TR) and the echo time (TE). TE is the time between the RF pulse being delivered and the signal being detected by the coil and TR is the time taken to repeat two consecutive imaging acquisitions. To perform a T_1 weighted image, short repetition times (TR) are used which makes the contrast of the image mainly determined by T_1 values. To perform a T_2 weighted image the echo time (TE) can be adjusted such that the contrast of the image is mainly determined by T_2 values. The other possibility is to determine contrast by the PD of the tissue and such scans are known as PD weighted images where TR is long and TE is short, minimising the influence of T_1 and T_2 (Dale 2015).

1.4.2.4 Segmentation

Image segmentation is the process of separating and defining boundaries for structures of interest on a digital image (Pal and Pal 1993). Medical image segmentation involves performing this separation on medical images such as MRI and CT using a good knowledge of the anatomy of the structures of interest. The advantage of this approach is that using MRI and segmentation allows 3D models to be generated without the need to use ionising radiation and more information on this can be found in section 4.2.

1.4.3 Model Based Image Registration (MBIR)

The MBIR process is based upon the approach developed by Banks and Hodge (1996). Images are thresholded based on image intensity. This is adjusted to obtain suitable contour edges of the subject of interest on the X-ray images using a Canny edge detector. The 3D model is projected onto the individual X-ray image and manually positioned to align with the object edges on the X-ray image. A similarity value is calculated between the model outline and the image outline based on how close the edges are aligned. A simulated annealing optimiser iteratively adjusts the model poses until the model edge is aligned to the edge in the X-ray image. This process is then repeated for subsequent images (Mu 2007). Relative bone or implant poses calculated

during this process can then be used to calculate in-vivo kinematics of the knee during a dynamic activity.

1.5 Aim and objectives of the study

Fluoroscopy and MBIR can be used to determine accurate in-vivo kinematics of implanted and intact knee. It can provide insight into normal and pathological function as well as the effect and efficacy of surgical interventions. The aim of this study was to improve on, and establish a standard MBIR protocol at Cardiff and to develop and validate a Biplane Fluoroscopy System for use in quantifying in-vivo kinematics of the knee.

This aim was split further into five objectives which were addressed through studies presented in this thesis.

Objective 1 (Chapter 2 & 3): *To assess the current single plane protocols performed at Cardiff University and determine essential required improvements.*

Objective 2 (Chapter 2 & 3): *To determine the main potential sources of errors associated with the MBIR protocol.*

Objective 3 (Chapter 4 & 5): *Create a standardised validation protocol for determining the errors and accuracy associated with the MBIR method for use in present and future system and protocol development at Cardiff University.*

Objective 4 (Chapter 5 & 6): *To establish a combined biplane fluoroscopy and motion analysis system in the new Musculoskeletal Biomechanics Research Facility (MSKBRF) at Cardiff University.*

Objective 5 (Chapter 6): *To perform a pilot study using the new MBIR protocol and establish this as a future comparator for future patient studies.*

The application of these objectives contributes to a major focus for research at Cardiff University and across other research centres. It provides a route to enhancing current studies that employ marker-based motion capture to quantify and classify altered kinematics and function for large cohorts of patients who have OA. This study contributes to the strong heritage at Cardiff

in terms of research into the function of patients with OA and who are having subsequent surgery. The major contribution is development of a novel and bespoke biplane fluoroscopy system, the only one of its kind in the UK, along with standardised validation protocols. This provides a much enhanced and validated approach to quantifying knee kinematics, along with a gold standard approach for comparison with either marker based or wearable sensor-based studies. It also establishes an appropriate route to applying the techniques developed to other human and animal joints for related studies into musculoskeletal disease and disorders and their treatments.

Chapter 2 Single Plane Fluoroscopy TKR study: Weston Cohort

2.1 Introduction

Total knee replacements (TKR) are considered to be a successful operation for treating pain and improving function in end stage osteoarthritis. With 94,023 replacements performed in the United Kingdom (excluding Scotland) alone in 2015 (National Joint Registry for England Wales and Northern Ireland 2016). Despite the fact that the recovery of function and the reduction in pain tends to be good in the majority of cases, there is still up to 20% of patients who are dissatisfied with their outcome and suffer symptoms such as chronic pain and poor function (Wylde et al. 2007; Bourne et al. 2010). During TKR surgery, factors including implant position and implant choice are controlled by the surgeon and can greatly influence the outcome for the patient (Czurda et al. 2010; Bonner et al. 2011).

In order for a TKR to function optimally it is widely agreed by orthopaedic surgeons that it should be correctly aligned (Bäthis et al. 2004; Sikorski 2008). The normal range of alignment that is strived for during TKR surgery is considered to be ±3° long leg mechanical alignment in the frontal plane (Jenny et al. 2005; Pang et al. 2009). The idea being that a neutral mechanical alignment produces an even load across the medial and lateral sides of the implant, reducing wear and the potential component loosening (Aglietti and Buzzi 1988; Fang et al. 2009). However, recent studies have suggested that maybe a neutral mechanical alignment does not provide the best outcomes for patients. They suggest an anatomic alignment produces a better outcome for patients (Dossett et al. 2012; Howell et al. 2013). In vitro studies and cadaveric studies have been used to look at the effect of changing frontal plane alignment (D'Lima et al. 2001; Green et al. 2002; Werner et al. 2005; Vandekerckhove et al. 2017a) but no actual patient based studies have investigated the effect on how alignment affects the biomechanics of daily activities. This is due to the infeasibility of getting ethical improvement to purposefully implant TKR's outside the normal ±3° range in the frontal plane.

2.1.1 Weston Cohort

In 2004, as a way of reducing the nearly three year waiting list for TKR surgeries in Wales, the Welsh government introduced the “Second offer Scheme” (Health in Wales 2004; Kempshall et al. 2009). A special NHS treatment centre in Weston Super-Mare (not related to the orthopaedic department of Weston General Hospital) was set up to treat patients on the waiting list. The Cardiff and Vale NHS trust sent 224 patients (258 knees) to be treated at the treatment centre using a Stryker Kinemax total knee replacement prosthesis.

This implant has been shown to have a high survival rate of 96.1% after nine years within normal clinical settings (Back et al. 2001; Wright et al. 2004). Of those 224 patients treated at the Weston Super-Mare NHS treatment centre the survival rate of the implant was found to be 80.6% after five years (Hickey et al. 2012). This was believed to be due to implants being incorrectly sized and maligned during surgery.

2.1.2 Study Overview & Research Questions

The opportunity to study and look at the influence of surgical alignment on biomechanical function in-vivo, is clinically important for orthopaedic surgeons and would provide a rare insight. A cohort of patient volunteers were recruited from the Weston treatment centre. To determine biomechanical function, single plane fluoroscopy was carried out on a step up - step down task and gait analysis was carried out using motion capture. To determine the surgical alignment, long leg scans were carried out to calculate frontal plane alignment and Computed Tomography (CT) scans were carried out to calculate implant rotational alignment. An initial clinical hypothesis was proposed that frontal plane alignment influences loading and function. However, there are some challenges with this data set and some specific research questions that needed to be addressed: -

- Is it possible to generate a useful database of kinematic data using Model Based Image Registration (MBIR) with a library of different sized TKR implants in a retrospective study?

- What other clinically relevant hypothesis can be generated from this data set?

2.2 Methods

2.2.1 Patient Cohort

Ethical approval for the study was obtained from the Cardiff and Vale Research and Ethics Committee. Patients were selected and recruited by two orthopaedic surgeons (A.Metcalfe and P.Kempshall).

Patient data was collected post TKR surgery as part of the service evaluation of this cohort and no pre-TKR data was collected. This was performed prior to this project commencing by colleagues (P.Kempshall, B.Hickey, A.Metcalfe, M.Forster) in 2012.

In 2011 Orthopaedic Research UK (ORUK) funded a 1 year project to collect and analyse this data, and J.Madete was appointed to this project. She worked for 16 months on the project and collected data and started some initial processing, but faced difficulties processing the data. The following chapter documents the full project, with all data processing, analysis being carried out during the project by the author.

2.2.2 Motion Capture

2.2.2.1 Equipment

Figure 2-1 Pro reflex cameras and patient walkway fitted with force platforms in the Cardiff Motion Analysis Laboratory

Motion analysis data was collected using eight Pro-Reflex MCU 120Hz digital cameras (Qualisys, Sweden) capturing at 60 Hz. Each Pro-Reflex camera emits infrared light from an array of LEDs, this light is then reflected from retro-reflective markers placed at specific landmarks on the volunteer. The light re-entering the camera is detected by a sensor allowing the markers to be detected in 2D view. When two or more cameras can see an individual marker the 3D coordinates can be reconstructed from their respective 2D views. The camera location was the same as defined by Whatling (2009) as shown in Figure 2-1.

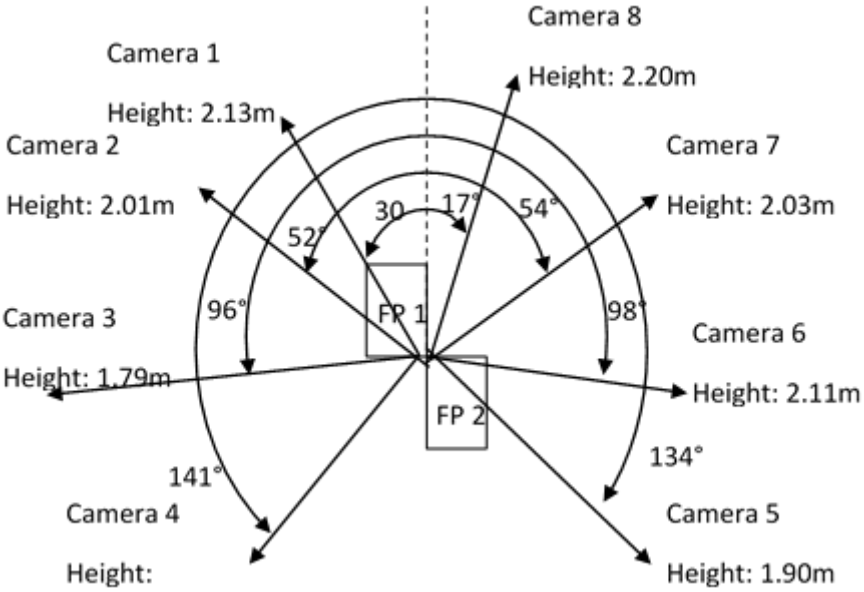

Figure 2-2 Pro-Reflex camera position around the walk way

Force data was captured using two 600mm x 400mm Bertec force plates (Bertec Corporation, Ohio, USA) each with a sample rate of 1080Hz. The position of the force plates can be seen in Figure 2-2.

2.2.2.2 Data Collection

Prior to data collection, the laboratory was calibrated to define a global coordinate system (GCS) and the force platforms were calibrated and defined with respect to the GCS (Figure 2-3)

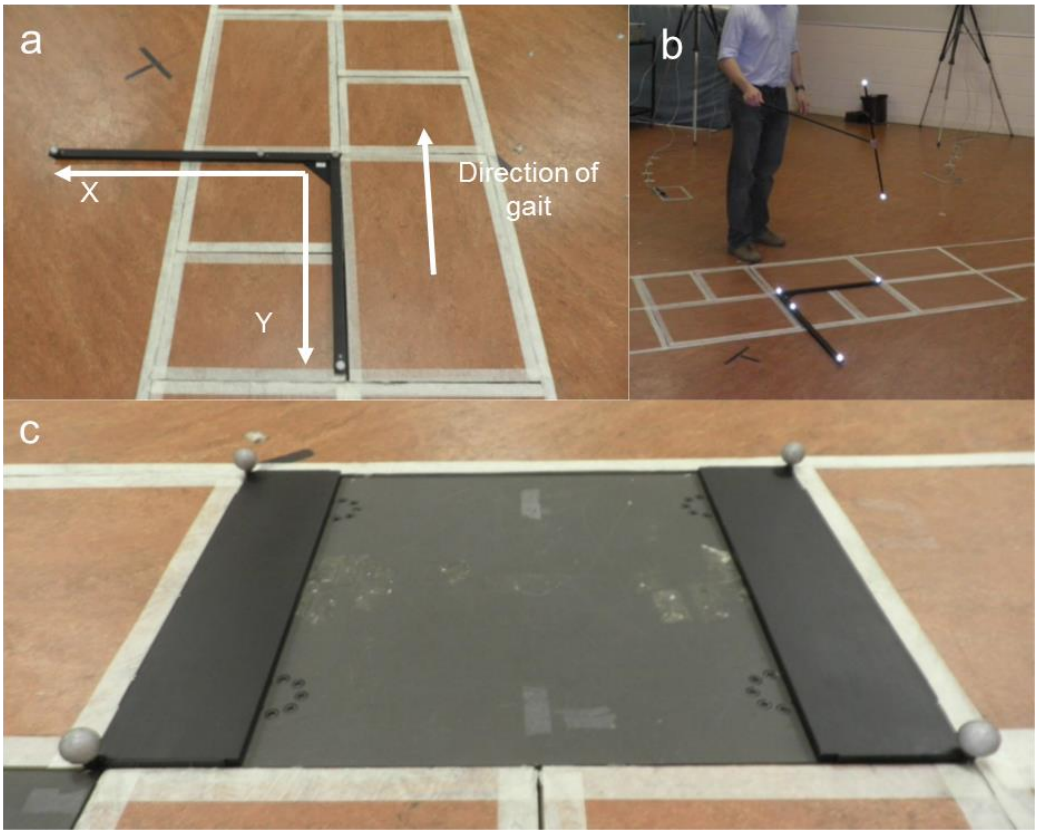

Figure 2-3 **A** To define the GCS for the Qualisys motion capture system a calibration frame was used. The long arm of the frame defined the x-axis and the y-axis was defined by the short arm with the z-axis acting up and out of the floor. For this protocol the negative y-axis was the direction the patient volunteer walked during data collection **B** A calibration wand, with two retroreflective markers placed a known distance apart, is used to calibrate the motion capture system. This is performed by sweeping the wand in the direction of each GCS axis over a 45 second period. The motion capture cameras can use the 2D marker position of the markers for each camera to define the 3D space and subsequently their respective positions from each other **C** Two calibration frames are placed over the ends of the force plate. Each of the four markers are located directly over the corners of the force plate. These provide the X and Y coordinates for the force plates, with the Z-offset defined in Qualisys Track Manager. Photos reproduced from Watling (2014).

All data collection took place at the Cardiff University Motion Analysis Laboratory. Ethical approval for this project was through the umbrella ethical approval for the Arthritis Research UK Biomechanics and Bioengineering Centre (10/MRE09/28), with the fluoroscopy approved as part of an ethical amendment which was approved prior to this project starting.

Volunteers were asked to wear loose fitting clothing and shorts. To standardise the gait data volunteers were asked to remove their footwear and perform the gait analysis barefoot. Before the study began, the trial was explained in detail to the volunteers and they were given the opportunity to ask questions and provide informed consent. Oxford Knee Score (OKS) (Dawson et al. 1998a) and Knee Outcome Survey (KOS) questionnaires (Irrgang et al. 1998) were completed to measure patient-reported outcome measures (Appendices A).

A modified Helen Hayes marker set was used for this study, this is also referred to within literature as the CAST marker protocol (Cappozzo et al. 1996). Twenty-two retro-reflective markers, 20 mm in diameter, were placed on the skin of the volunteer on specific anatomical locations found by palpitation and attached using hypoallergenic double-sided tape. Two rigid based clusters each with four retro-reflective markers were positioned laterally on the thigh and shank for both legs and held on with a self-adhesive Coban tape (3M Ltd.). The complete marker set can be seen in Figure 2-4.

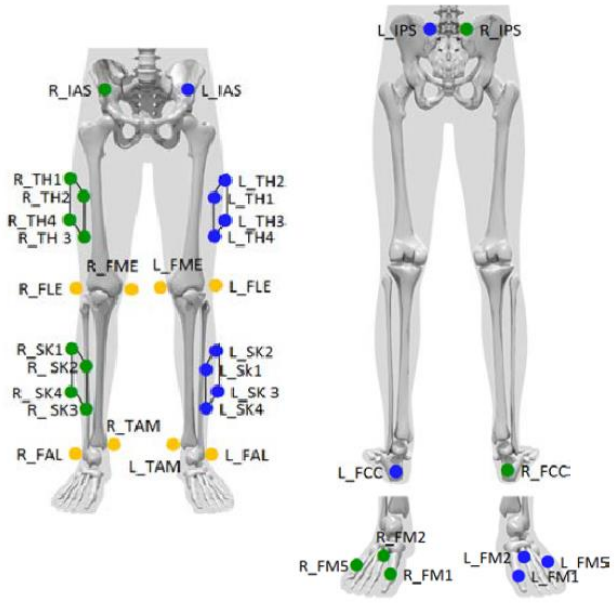

Figure 2-4 Modified Helen Hayes marker set used within the motion capture analysis. Images taken from the Qualisys PAF Package: CAST lower body marker set guide (Qualisys, Sweden)

A series of static calibrations were recorded of the marker positions. The volunteer was asked to remain still with arms by their sides and a one second capture was taken. The volunteer was asked to do these calibrations with individual feet on force plates and a separate calibration with both feet on one force plate. The static calibrations are required for data processing in Visual 3D (C-Motion, Maryland) as described later in section 2.2.2.3.1.

Volunteers were not made aware of where the force plates were located on the walkway so not to alter their natural gait pattern. To ensure they hit the force plates with a full contact of the foot the volunteer was made to adjust their starting position between measurements and were not made aware of the reason for doing this. They were instructed to walk within the outer marks of the walk way (as seen in Figure 2-1) and that the data was only recorded in one direction. The volunteer was asked to walk at a natural and comfortable walking pace. Data collection was complete after six clean force plate strikes had been captured for each leg. For some volunteers who found it difficult to walk the session was shortened.

2.2.2.3 Data Processing

Data processing followed the approach as defined by and has been summarised concisely in Figure 2-5 below.

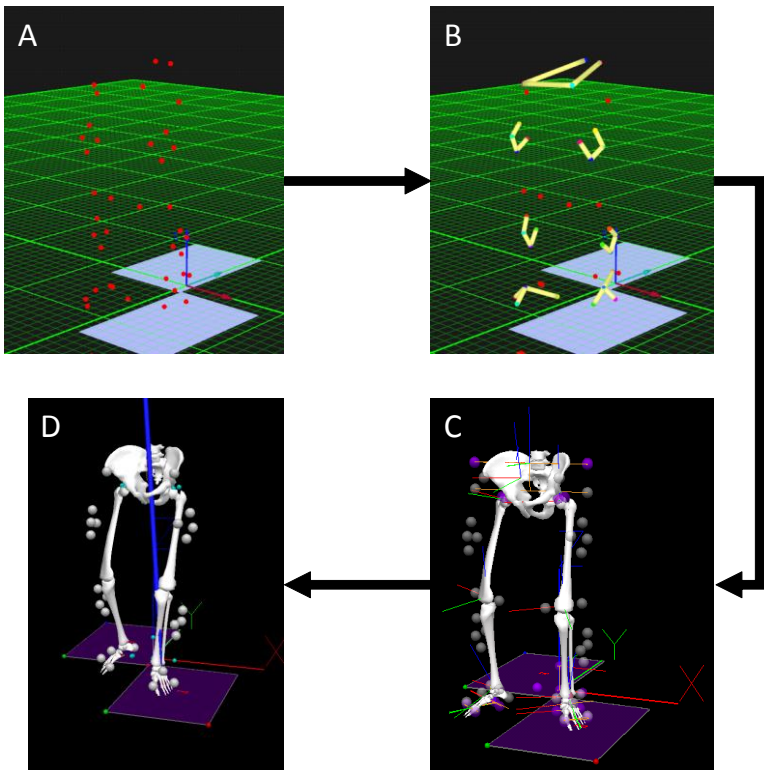

Figure 2-5**A** Marker coordinate data captured during motion analysis in Qualisys Track Manager (QTM) (Qualisys, Sweden). **B** The markers were initially manually tracked and labelled on the first dynamic trial and then used to define an Automatic Identification of Markers (AIM) model which is able to be applied to other trials and statics. Once the QTM files were labelled they are exported as .c3d ready for analysis in Visual3D. **C** Visual3D is used to compute a model-based system where clinically relevant axis are defined using the markers identified in the static trial **D** Kinetics and kinematic data is calculated by applying the model to the dynamic trials

2.2.2.3.1 Visual3D (C-Motion Inc., Maryland, USA)

Joint biomechanics can be calculated in Visual3D by relating the coordinate positions of the skin mounted markers into clinically relevant descriptions. During level gait kinematics and kinetics are defined and calculated between different events. The Visual3D processing was defined following the approach defined by Biggs (2016) and a short overview follows below.

2.2.2.3.2 Calculating Gait Events

A gait cycle is defined between consecutive Heel Strike (HS) of the same leg. To determine the gait cycles as accurately as possible with a dual force plate system the initial heel strike was defined from initial contact with the force plate. Automatic gait events can be defined in Visual3D using a proprietary function which is a gait recognition algorithm that is able to calculate the heel strike based on the axial and anterior posterior position of the proximal end of the foot. This method is called Target Pattern Recognition (TPR) and requires a clean force strike with the foot (Stanhope et al. 1990)

2.2.2.3.3 Kinematics

Kinematics of the hip and ankle are calculated using the Cardan-Euler sequence (X-Y-Z) based on ISB recommendations (Wu et al. 2002) as well as axis definitions. For this study ankle and hip kinematics and kinetics were calculated but not analysed. Knee kinematics were calculated based on Grood and Suntay's joint coordinate system approach (Grood and Suntay 1983)

2.2.2.3.4 Kinetics

Joint kinetics were calculated using the inverse dynamics approach using Visual3D to calculate moments around the joints by using calculated joint forces acting at the foot, the tibia and the femur and resolving the moments about the Centre of Mass (COM) of the segments. The moments were resolved in the local coordinate system of the distal joint. This was performed based on work carried out by Miranda et al. (2013) who used biplane videoradiography

to investigate soft tissue artefact in motion capture. They found that the tibia had the least STA hence knee joint kinetics are resolved in the tibia ACS. Ground reaction forces are normalised to weight and shown as percentage of body weight (%Bw). Moments were normalised for weight and height and expressed as Newton.metres / (Bw.height).

2.2.2.3.5 Motion Analysis metrics

Following recommendations taken from McClelland et al. (2007) the most commonly measured metrics for analysing TKR function were taken from the gait analysis data. A summary for the kinematic metrics can be found in Table 2-1 and for the kinetic metrics can be found in Table **2-2**.

Table 2-1 Kinematics Metrics and Descriptions

Metric	Description
K1	Sagittal Plane Range of Motion
K2	Transverse Plane Range of Motion
K3	Frontal Plane Range of Motion
K4	Angle Flexion at Initial Contact
K5	Flexion Range of Motion during Stance Phase
K6	Maximum angle during Swing
K7	Maximum angle during Stance
K8	Minimum angle during Stance
K9	Maximum Abduction angle (Positive value)
K10	Maximum Adduction angle (Negative value)

Table 2-2 Kinetic Metrics and Descriptions

Metric	Description
GRF F1	Maximum of the first peak in the vertical GRF
GRF F2	Minimum after first peak in the vertical GRF
GRF F3	Maximum of the Second peak in the vertical GRF
GRF F4	Maximum of the Anterior-Posterior GRF
GRF F5	Minimum of the Anterior-Posterior GRF
GRF F6	Maximum Medial GRF
GRF F7	Maximum Lateral GRF
M1	Maximum Flexion Moment
M2	Maximum Extension Moment
M3	Maximum adduction moment
M4	Maximum abduction moment
M5	Maximum Internal Rotation Moment
M6	Maximum External Rotation Moment
M7	Maximum Extension Moment at Initial Contact

2.2.3 Surgical Alignment Clinical Measures

2.2.3.1 Intercomponent Rotations

A limited slice CT scan of the affected knee was performed to calculate femoral and tibial rotation. The protocol was developed specifically for this project by a senior consultant radiologist (Dr K.Lyons) and was approved by REC in an ethical amendment (as described above). A Discovery CT scanner (General Electric, USA) was used to carry out the scans and were carried out in the X-ray department at University Hospital of Wales in Cardiff. To reduce dose an adaptive statistical iterative reconstruction (ASIR) combined with a slice thickness of 4mm was performed (Chauhan et al. 2004). One experienced surgeon (P.Kempshall) carried out radiological measurements using a modified protocol originally defined by Cobb et al. (2008).

Femoral rotation was defined as the angle between the most prominent point of both femoral epicondyles and the femoral implant (measured using the

posterior margin of the anterior flange of the femoral component). Tibial rotation was defined as the angle between the tibial posterior cortical line in the first bony slice under the implant and the tibial pegs.

2.2.3.2 Tibial Slope

Tibial slope was measured from clinical plane X-rays as the intersection of a line drawn across the tibial plateau with a line drawn down the middle of the tibial shaft. The centre was identified at 100 and 200mm down the shaft and a line joining the two was drawn. All measurements were carried out by one experienced surgeon.

2.2.3.3 Frontal Plane Alignment

To calculate frontal plane alignment the volunteer was asked to lay supine on the floor while one full leg-length exposure was capture. One experienced operator, using the approach defined by Cooke et al. (2007), calculated the Hip-Knee-Ankle angle (HKA) from the mechanical axis of the femur and the mechanical axis of the tibia. For this study the following definitions for frontal plane alignment based on HKA angle are as follows:

- Varus alignment – HKA $\theta < -2°$
- Neutral alignment – HKA $-2° \leq \theta \leq 2°$
- Valgus alignment – HKA $\theta > 2°$

This was used to define three distinct groups for statistical analysis in section 2.3.

2.2.4 Dynamic Fluoroscopy

2.2.4.1 Calibration

Before fluoroscopy data collection took place calibration of the fluoroscopy system (Philips Eleva, Philips, Netherlands) was needed to correct images for geometrical distortion. The C-arm was moved into the position shown in Figure 2-6a with the X-ray bed in the vertical position.

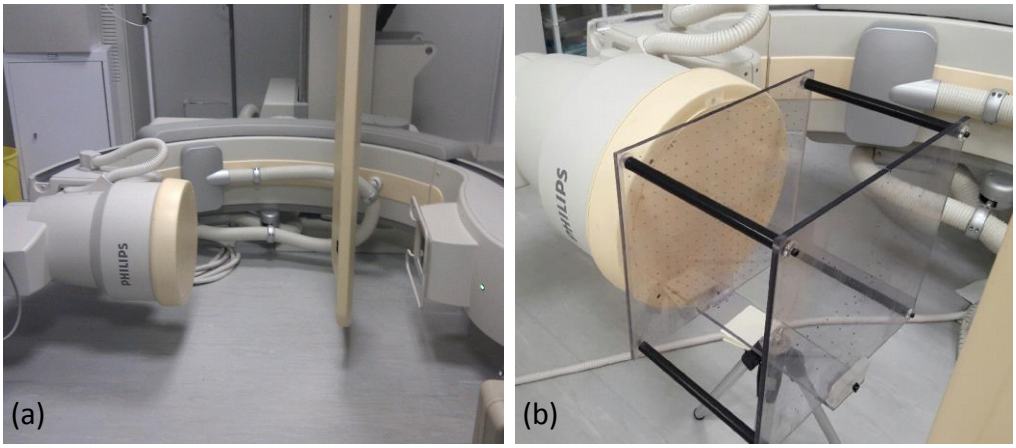

Figure 2-6 **a** C-Arm position during calibration; **b** Calibration frame in position in front of C-arm intensifier

The calibration frame was developed by Whatling (2009) and adapted for ease of data collection for this study. It consists of two Perspex® panels of dimensions 450mm x 450 mm positioned precisely 300 mm apart. The panel positioned closest to the image intensifier (Figure 2-6b) is used for correcting image distortion, consisting of a square array containing 17 x 17, 2mm diameter steel ball bearings with an even spacing of 25 mm. Around the central ball bearing there are an additional four ball bearings forming a square allowing it to be easily identified.

The panel closest to the X-ray source consists of a star shaped array of ball bearing with an even spacing of 25 mm. This panel is used to determine the position of the camera focus. The square array was positioned 40 mm away from the image intensifier due to a safety alarm if the intensifier makes contact during exposure. The centre of the image intensifier was marked with a steel ball bearing fixed to the intensifier and the two panels were aligned such that the centre of both panels lined up with the centre of the intensifier. The data processing for calibration can be seen in Appendix B.

2.2.4.2 Equipment

All exposures took place in the main X-ray department at University Hospital of Wales using a Philips Eleva by a trained radiographer. Ethical approval was given for up to 60 seconds to be undertaken to one knee joint in the lateral

direction. The estimated total fluoroscopy dose was 0.0013mSV which is equivalent to 6 hours background radiation. Patients were asked to perform a step up and step down task three times on a 160mm step (Figure 2-7) with the lateral side facing the image intensifier.

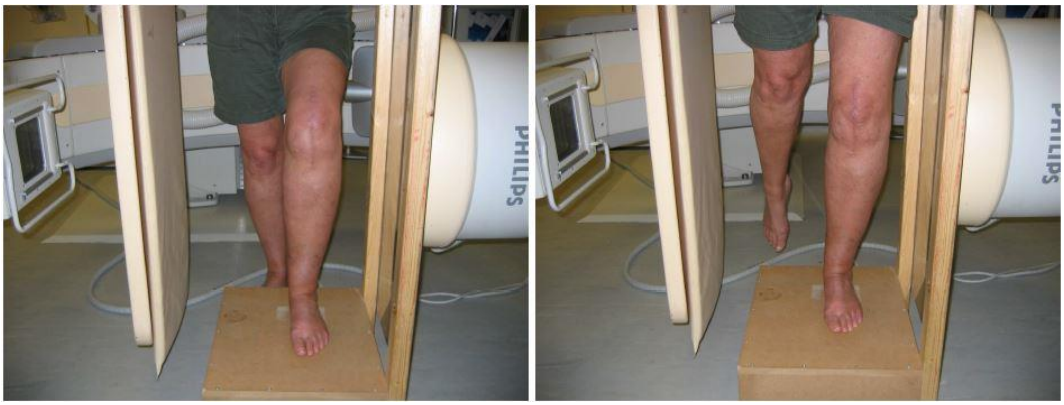

Figure 2-7 Patient performing step up and down activity while being imaged with Philips Eleva C-arm

The fluoroscopy images were saved in a sequence in the Digital Imaging and Communications in Medicine formant (DICOM) and then converted into 8-bit Tagged Image file format (TIF). The images were then undistorted based on the calibration parameters as defined in Appendix B.

2.2.4.3 TKR Model Based Image Registration (MBIR) Processing

2.2.4.3.1 Pre-MBIR Preparation

Before kinematics and contact points can be defined using JointTrack (University of Florida) and JointView (University of Florida) the raw data is processed into suitable format. The overview protocol for this is shown in Figure 2-8 and the protocol followed can be seen in Appendix B.

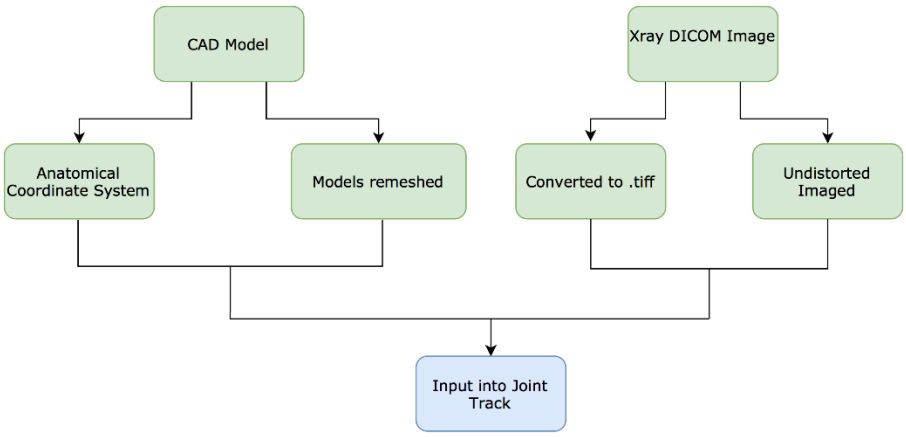

Figure 2-8 Overview of Pre-MBIR TKR protocol as defined in Appendix **B**

2.2.4.3.2 3D CAD Model Preparation

A library of 3D CAD models were provided by Stryker of a range of size of femoral and tibial components. Anatomical coordinate systems for models was defined by using the Banks point which is described in Appendix B.

2.2.4.4 TKR MBIR Protocol Development

2.2.4.4.1 Comparison of Registration Software

Previous MBIR work carried out at Cardiff University (Whatling 2009) was processed using KneeTrack a 2D to 3D image registration software developed by University of Florida (Banks and Hodge 1996). A new version of the software was developed by the same research group (Mu 2010) and a comparison showed the results from the two software were comparable. One noted change was that the z-axis direction was changed between versions changing the polarity of the internal and external rotations in the results. For ease of comparison all results have been converted into the following format:

- Flexion (+ve), Extension (-ve)
- Abduction (+ve), Adduction (-ve)
- Internal Rotation (+ve), External Rotation (-ve)

2.2.4.4.2 Comparison of small and large number of images

Previous work carried out at Cardiff University involved small number of images (approximately 10) to calculate the kinematics. An investigation into what happens if the number of images processed was increased using the MBIR protocol was carried out. This was to look at the difference in kinematics calculated using JointTrack and see if any kinematic information is lost by using a lower number. The comparison was performed using 15 images and then reprocessed using 90 images and performed on three TKR data sets.

Table 2-3 Differences in range of motion between results obtained using large and small number of images

Patient No.	DOF	ROM (degrees) (Large No. of images)	ROM (degrees) (Small No. of images)	Difference in values (percentage)
1	**Flexion**	57.2	58.5	+/-2.2 %
	Abduction	4.2	4.6	+/-0.9 %
	Internal Rotation	21.7	8.5	+/-155.1 %
2	**Flexion**	63.7	58.4	+/-9.1 %
	Abduction	5.4	8.5	+/-36.8 %
	Internal Rotation	10.6	21.4	+/-50.4%
3	**Flexion**	46.2	44.8	+/-3.2 %
	Abduction	4.7	5.4	+/-11.8 %
	Internal Rotation	13.2	11.4	+/-16.0 %

Results shown in Table **2-3** show that the Ranges of Motion (ROM) for the rotations were different between small and large images. With internal rotation showing the largest differences across all three datasets. From the author's experience performing MBIR, processing more images made the entire MBIR easier as the previous positions could be used a reference for subsequent frames. However the issue with increased image numbers is the increased presence of blurred images which causes the potential of an incorrectly

positioned implant. This can be overcome by using the position data from previous and proceeding matched images to help define the implant position within the blurred image.

2.2.4.5 TKR MBIR Protocol

The full TKR updated MBIR protocol can be found in Appendix B.

2.2.4.6 Post-Processing Protocol Development

2.2.4.6.1 Joint View

JointView is software developed by the University of Florida that allows the calculation of kinematics and closest point plots of implants and bones over a series of different movements.

2.2.4.6.2 Kinematics

The 3D poses of each implant are imported into the software for each frame of the movement. Joint rotations are calculated within the software using a 312 Cardan/Euler approach for rigid bodies in 3D space defined by Tupling and Pierrynowski (1987). Joint translations are calculated by measuring the movement of the femoral component origin within the tibial coordinate system. The kinematic calculation methods within JointView are the same approach taken for KneeTrack kinematic calculations (Whatling 2009).

2.2.4.6.3 Closest point calculations

Another feature of the JointView software is the ability to carry out a nearest neighbour algorithm between two models based on regions of interest. The four regions of interest when considering a TKR were defined as follows: -

1. Lateral femoral condyle
2. Medial femoral condyle
3. Lateral section of tibial plateau

4. Medial section of tibial plateau

The four regions of interest were paired with respect to lateral (1 and 3) and medial (2 and 4).

Nearest neighbour

In simplest terms the nearest neighbour algorithm can be defined as when you have two sets of points (F and t) within a global coordinate system (G) find the closest point in F to t, it has also been known as the post-office problem in reference to an application of assigning residences to the nearest post office (Knuth 1998).

The CAD model is a three-dimensional object, the data is converted into a three-dimensional tree to organise the points into a data structure the nearest neighbour can search. After the nearest neighbour algorithm has finished the two vertices with the smallest distance between them are assumed to be the closest points.

This is carried out individually between the two pairs of regions of interests and a lateral and medial closest points are defined as X-Y-Z coordinates. The vector between the medial and lateral closest point points represents the instantaneous flexion/extension axis of the femur at that point in time (Banks and Hodge 2004). The algorithm is subsequently carried out on each individual frame of the data set and the vectors are then projected onto the transverse plane of the tibial plateau to form a closest point plot as shown in Figure 2-9.

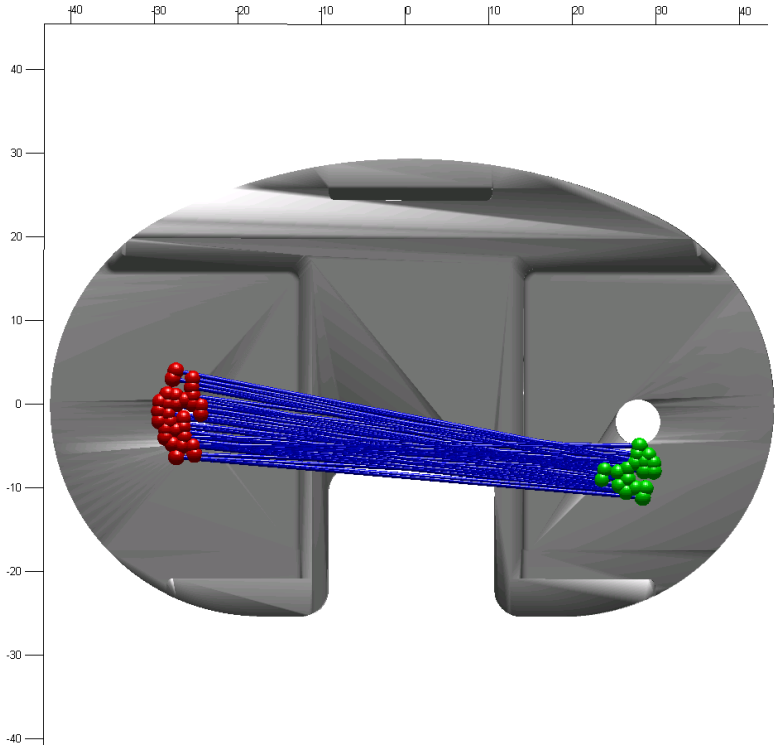

Figure 2-9 A representative closest point plot of the full cycle of step up and step down (No. of frames=100)

2.2.4.6.4 Centre of Rotation

The centre of rotation (COR) is important within implant design as it can help determine whether an implanted knee is functioning the same way a healthy joint functions. In the transverse plane the positon of the COR shows the motion of the condyles of the femoral implant with respect to the tibial plateau (Koo and Andriacchi 2008). Banks and Hodge (2004) devised an approach to calculate the average COR by solving the least-squares of the instantaneous flexion/extension axis of each frame for an activity.

A bespoke MATLAB (The Mathworks, Inc., USA) script was written to take the lines from the closest points plot (flexion/extension axis) and carry out the same approach as above. An overview of how this is calculated is found in the following section.

Calculating the COR

Consider the tibial plateau as an x-y plane, the implant's closest points calculated for the medial section (M_i) and lateral section (L_i) the coordinates for a particular movement would be as follows:

$$\boldsymbol{M_i = \begin{Bmatrix} x_{m,i} \\ y_{m,i} \end{Bmatrix}, L_i = \begin{Bmatrix} x_{l,i} \\ y_{l,i} \end{Bmatrix} \text{ for } i = 1{:}n \text{ where n = number of frames}} \quad (2\text{-}1)$$

For each frame i, the Cartesian equation of the line that passes through the points of M_i and L_i:

$$\boldsymbol{a_i x + b_i y = c_i} \quad (2\text{-}2)$$

With the equation above representing one of the instantaneous flexion/extension axes as shown in Figure 2-9. Therefore the centre of rotation (C) with respect to the tibial plateau is the intersection between all the frames. This is a straightforward calculation when the lines all intersect (Figure 2-10a). If there are more than one intersections, then multiple calculations would need to take place (Figure 2-10b)

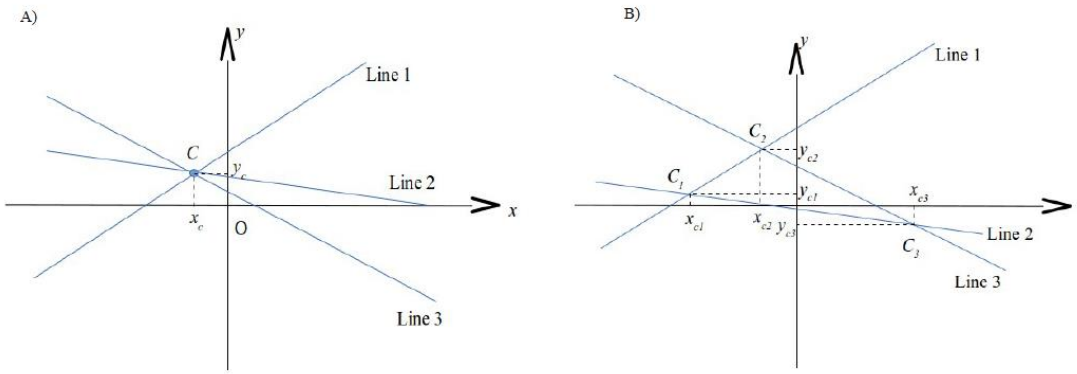

Figure 2-10**a** Simple COR location **b** Multiple COR locations

Applying a least-squares system of equations allows the calculation of the COR by approximation.

If all the Cartesian coefficients are extracted into matrices the equation would be as follows:

$$\boldsymbol{a_i x + b_i y = c_i \text{ for } i = 1{:}n} \rightarrow \begin{pmatrix} \boldsymbol{a_1} & \boldsymbol{b_1} \\ \boldsymbol{a_2} & \boldsymbol{b_2} \\ \cdot & \cdot \\ \cdot & \cdot \\ \boldsymbol{a_n} & \boldsymbol{b_n} \end{pmatrix} \times \begin{pmatrix} \boldsymbol{x} \\ \boldsymbol{y} \end{pmatrix} = \begin{pmatrix} \boldsymbol{c_1} \\ \boldsymbol{c_2} \\ \cdot \\ \cdot \\ \boldsymbol{c_n} \end{pmatrix} (\boldsymbol{x, y} \in \mathbf{IR}) \Leftrightarrow \boldsymbol{AX = C} \qquad (2\text{-}3)$$

This describes the system of equations for the instantaneous flexion-extension axes for frame i=1:n.

Therefore, the average centre of rotation (x_c, y_c) can be defined as:

$$\begin{pmatrix} \boldsymbol{x_c} \\ \boldsymbol{y_c} \end{pmatrix} = \left(\begin{pmatrix} \boldsymbol{a_1} & \boldsymbol{b_1} \\ \boldsymbol{a_2} & \boldsymbol{b_2} \\ \cdot & \cdot \\ \cdot & \cdot \\ \boldsymbol{a_n} & \boldsymbol{b_n} \end{pmatrix}^{\boldsymbol{T}} \times \begin{pmatrix} \boldsymbol{a_1} & \boldsymbol{b_1} \\ \boldsymbol{a_2} & \boldsymbol{b_2} \\ \cdot & \cdot \\ \cdot & \cdot \\ \boldsymbol{a_n} & \boldsymbol{b_n} \end{pmatrix} \right)^{\boldsymbol{-1}} \begin{pmatrix} \boldsymbol{a_1} & \boldsymbol{b_1} \\ \boldsymbol{a_2} & \boldsymbol{b_2} \\ \cdot & \cdot \\ \cdot & \cdot \\ \boldsymbol{a_n} & \boldsymbol{b_n} \end{pmatrix}^{\boldsymbol{T}} \begin{pmatrix} \boldsymbol{c_1} \\ \boldsymbol{c_2} \\ \cdot \\ \cdot \\ \boldsymbol{c_n} \end{pmatrix} \qquad (2\text{-}4)$$

$$\Rightarrow X = (A^t A)^{-1} A^t C \qquad (2\text{-}5)$$

An example average COR calculation plotted on the representative closest point plot can be seen in Figure 2-11. The COR mediolateral and anterior-posterior locations were normalised to the dimensions of each tibial component. The mediolateral position was expressed as a percentage of tibial widths (Banks and Hodge 2004). This was done to allow comparison of COR calculated from different sized tibial implants.

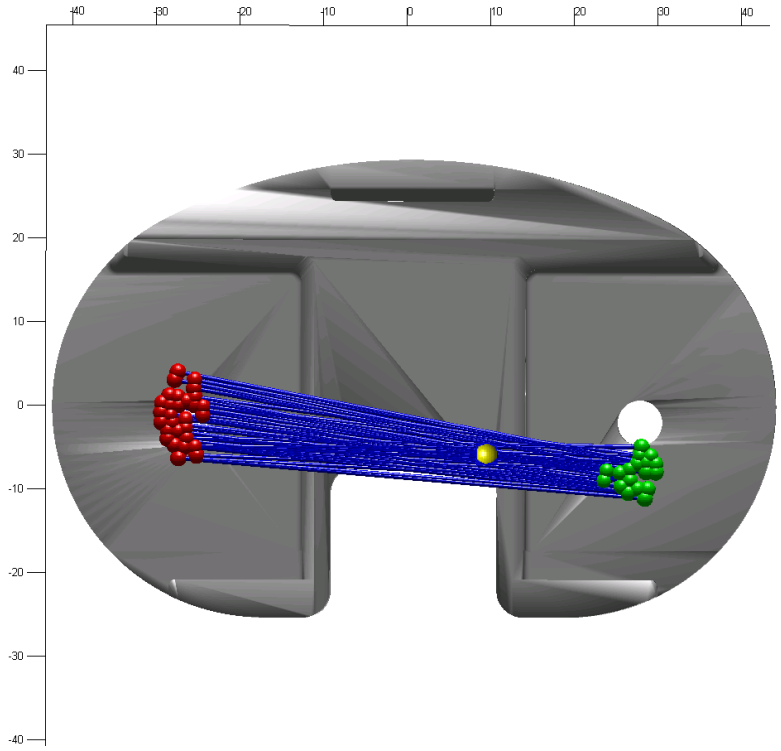

Figure 2-11 Representative closest point plot with the calculated CoR position highlighted in yellow

2.2.4.6.5 Calculating In-Vivo Translation

MBIR provides the ability to calculate the in-vivo translations. Anterior-Posterior (AP) translation was calculated for both medial and lateral movements from the closest point x-axis position for the tibia for each frame. Superior-Inferior (SI) translation (also known as compression/distraction) for medial and lateral side was calculated by taking the y-axis coordinate for the corresponding femur closest point from the y-axis coordinate of the tibia closest point for each frame.

2.2.4.6.6 Looking at different phases of movements

The kinematic and COR data was calculated for the total step up and down movement as well as the individual phases. The step up and down movement was broken into three different phases (Figure 2-12):

1. Step up
2. Loaded
3. Step down

The individual phases start and end points were defined as the change in flexion angle between frames was less than 1°. This provides a large database of kinematic data that can be analysed.

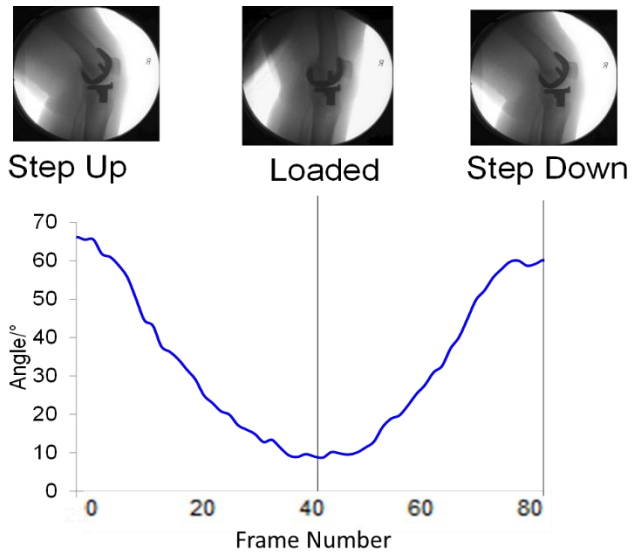

Figure 2-12 Example flexion graph over the full activity with images taken to highlight the different phases

2.2.4.7 Issues faced

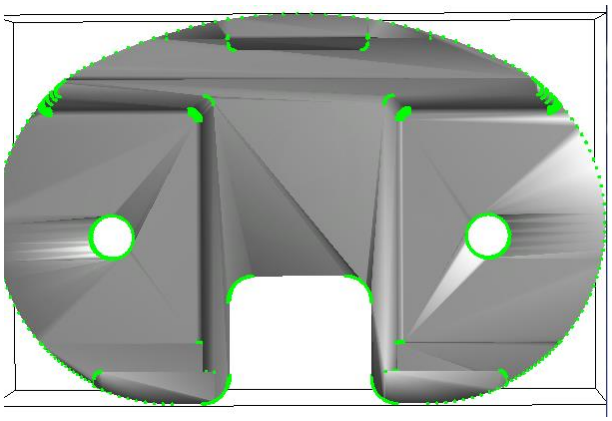

Figure 2-13 Overhead view of tibial component where the green highlighted region showing the limited number of vertices of the models provided.

The total knee replacement CAD models provided by Stryker had a low-quality mesh, meaning that there were a limited number of vertices. These were located on defined edges such as the slot to input the meniscal implant (Figure 2-13). When trying to calculate the contact points of the femoral component in relation to the tibial tray the nearest neighbour approach incorrect locates the closest point to an edge or at the peg insertion slot. To compensate for this problem two different methods were devised. The methods and challenges faced will be summarised in the next section.

2.2.4.7.1 Initial method using Rhino CAD software

The 3D CAD models were imported into Rhinoceros 4 (McNeel, Seattle, USA). The medial and lateral tray were sketched out using lines and curves. A 2D surface was defined by using a series of lines to create an outline which is the same size as the area of interest (Figure 2-14a). The mesh density is then increased within the software creating more vertices on the surface (Figure 2-14b). This surface is then positioned in the same location as the bottom of the tibial tray. This approach increases the density of vertices allowing the nearest neighbour algorithm to be able to calculate the true positions of the closest point between tibia and femur.

However, the mesh that was created using this method was found to be non-uniform and difficult to reproduce consistently. It was also found to be computationally expensive with processing time for the nearest neighbour algorithm increasing significantly to 24 hours to process one side of the implant.

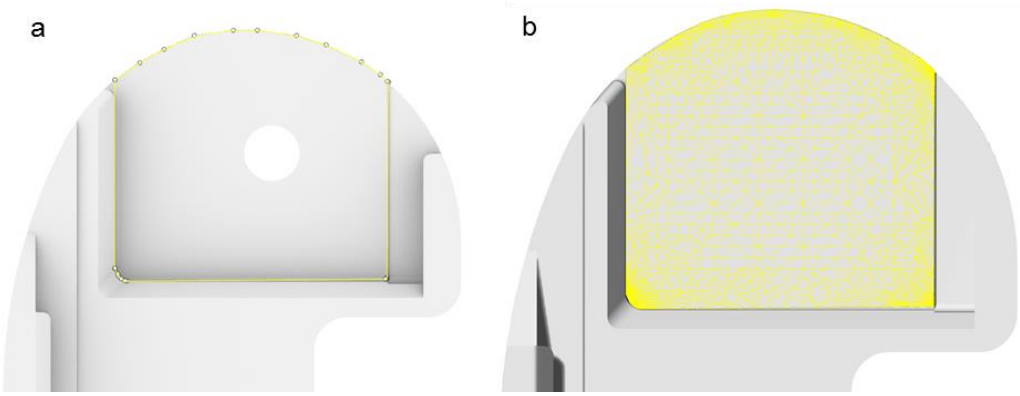

Figure 2-14**a** Tibia tray outlined by defining points and lines (highlighted in yellow) in Rhinoceros 4 (McNeel, Seattle, USA) **b** Mesh created using the same software (highlighted in yellow) found to produce more vertices towards the edges and corners.

2.2.4.7.2 Final Method Using ScanIP

The initial method worked well for increasing the number of vertices in the mesh but was non-uniform and significantly increased processing time.

Scan IP 2016.09 (Synopsys,Inc., USA) has a robust meshing module that allows specification of the size and uniformity of the mesh. The creation of the 2D surface was carried out using the same approach as above and was extruded by 2mm to create a 3D model. This was imported into Scan IP and a uniform mesh was applied (Figure 2-15).

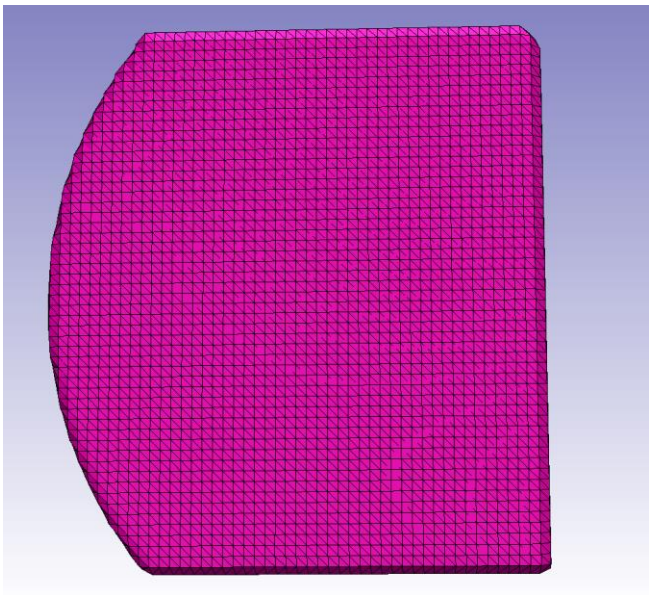

Figure 2-15 Medial tibia tray trace with uniform mesh applied using functions built into ScanIP (Synopsys,Inc., USA).

2.2.4.7.3 Optimising the protocol

A series of optimisation tests were carried out to help best define the size of the mesh grid terms of accuracy and processing speed. A fluoroscopy trial was chosen at random and the appropriate sized femoral and tibial model selected. The mesh sizes that were tested were from 0.1 mm to 0.5 mm in 0.05mm intervals. The first measurement that was looked at was the length of time taken to process the nearest neighbour algorithm. The second measurement that was looked at was the XZ position of the COR for the movement and how it changed for the different sized meshes.

2.2.4.7.4 Optimising Results

Table 2-4 Time taken for nearest neighbour algorithm to run

Mesh spacing Size /mm		
Tibia	**Femur**	**Time Taken /Hrs**
0.10	0.10	N/A
0.15	0.15	N/A
0.20	0.20	N/A
0.25	0.25	30.00
0.30	0.30	16.00
0.35	0.35	9.00
0.40	0.40	7.50
0.45	0.45	4.50
0.50	0.50	3.75

Table 2-5 Difference in COR position calculation against mesh size

Mesh Size/mm	**X COR Position**	**Z COR Position**	**X Difference**	**Z Difference**
0.25	-9.17	24.94	-	-
0.30	-9.09	24.56	-0.08	0.38
0.35	-9.31	25.49	0.13	-0.55
0.40	-9.04	24.24	-0.13	0.70
0.45	-9.26	25.24	0.09	-0.31
0.50	-9.08	24.58	-0.09	0.35

2.2.4.7.5 Discussion of Methods

Mesh Approach

The new ScanIP method provided a more consistent and uniform mesh compared with the original method. As shown in Table 2-4 the time taken for the nearest neighbour greatly reduces to run the code and therefore creates less errors in processing.

The optimisation experiments showed that the benefit of a uniform mesh allows the mesh density to reduce without changing the COR position. This is highlighted in Table 2-5 where the COR result generated by the test with the mesh size of 0.5 mm is very similar to the COR results generated by the 0.25 mm. The value changes by only 1% in both x- and z-coordinate. Considering the time taken to perform the nearest neighbour algorithm being less than 4 hours, further confirms the recommendation for using a 0.5mm mesh size.

Fluoroscopy Output Database

Following the protocols defined above a large database of output information from the fluoroscopy was generated. This combined with the motion analysis metrics can be used to test and generate clinically relevant hypothesis from this unique dataset.

Clinical Hypothesis

Based on literature and the data provided a number of hypotheses were generated to be tested from the outputs of the data.

- Hypothesis 1 - Frontal plane knee alignment influences function and loading when looking at motion analysis.
- Hypothesis 2 – Frontal plane knee alignment influences the in-vivo kinematics during a step up and step down activity.
- Hypothesis 3 – There are other clinical surgical measures that influence in-vivo kinematics and Centre of Rotation calculations

2.3 Results

2.3.1 Patient Demographic

29 patients (34 knees) were recruited from the Cardiff and Vale Orthopaedic Centre. Of those patients, due to issues elaborated later in section 2.4.4, only 25 patients (27 knees) had the full gait analysis, in-vivo fluoroscopy and clinical surgical measures. The subject demographics are described in Table 2-6.

Table 2-6 Overall Subject Demographic and Subgroup Demographics

Group	Number of Knees	Male	Female	Mean Age/ years (Range)	Mean BMI (SD)	Mean HKA Angle/° (Range)	OKS/48 (SD)	KOS/% (SD)
Total	27	12	15	75 (60 to 89)	32.1 (7.4)	1.1 (-9.5 to 10)	34.8 (10.1)	56 (16.4)
Valgus Group	7	2	5	75 (65 to 85)	33.4 (4.4)	-4.9 (-2 to -9.5)	29 (11.9)	46 (18.7)
Neutral Group	9	3	6	73 (60 to 89)	28.1 (6.9)	1.2 (-0.3 to 1.9)	38 (7.9)	68 (13.5)
Varus Group	11	7	4	76 (64 to 83)	33.0 (5.1)	5.2 (2 to 10)	35 (8.9)	58.4 (13.8)

Hypothesis 1

The data was split into three groups (Varus, Neutral and Valgus) as defined in section 2.2.3.3 and the metrics as defined in section 2.2.2.3.5 were calculated for each volunteer. Subsequently the three groups were compared using a one-way ANOVA. Levene's test for equality of variance and Shapiro-Wilks test was carried out to test the variables for normal distribution. A Bonferroni correction was used during the analysis and all *p*-values are shown with this. All statistics were performed using SPSS Statistics V23 (IBM Corporation).

Table 2-7 Kinematic metrics used to compare valgus, neutral and varus alignment.

Variables (°)	Valgus (*n*=7)	Neutral (*n=9)*	Varus (*n*=11)	*p*-Value
K1	41.8 ± 5.1	51.5 ± 7.3	47.1 ± 8.0	0.040[a]
K2	13.1 ± 5.2	13.0 ± 2.0	13.5 ± 4.1	0.763
K3	7.4 ± 4.8	8.8 ± 2.3	7.6 ± 3.2	0.457
K4	3.8 ± 4.9	8.3 ± 5.6	6.5 ± 3.1	0.116
K5	2.4 ± 1.8	7.4 ± 7.4	5.9 ± 4.3	0.107
K6	44.7 ± 7.8	56.0 ± 3.6	51.1 ± 5.4	0.002[a]
K7	8.0 ± 4.6	16.8 ± 5.4	14.1 ± 3.8	0.003[a]
K8	5.5 ± 3.6	9.4 ± 7.2	8.2 ± 5.2	0.217
K9	11.9 ± 5.3	5.9 ± 4.8	2.5 ± 3.9	0.001[b]
K10	4.5 ± 3.1	-2.9 ± 5.5	-5.0 ± 4.0	<0.001[b]

Mean ± Standard deviation; [a] Significant differences (P<0.05) between Valgus and Neutral groups

[b] Significant differences (P<0.05) between Valgus and Varus groups

Table 2-8 Ground Reaction Force metrics used to compare valgus, neutral and varus alignment.

Variables (%BW)	Valgus (*n*=7)	Neutral (*n=9)*	Varus (*n*=11)	*p-Value*
GRF F1	0.98 ± 0.06	1.01 ± 0.08	0.99 ± 0.04	1.000
GRF F2	0.94 ± 0.05	0.86 ± 0.09	0.91 ± 0.03	0.059
GRF F3	1.03 ± 0.03	1.05 ± 0.06	1.03 ± 0.02	1.000
GRF F4	0.07 ± 0.02	0.11 ± 0.04	0.10 ± 0.03	0.063
GRF F5	-0.08 ± 0.03	-1.21 ± 0.05	-0.12 ± 0.05	0.306
GRF F6	0.09 ± 0.02	0.08 ± 0.02	0.074 ± 0.03	0.281
GRF F7	-0.01 ± 0.01	-0.18 ± 0.01	-0.017 ± 0.01	0.092

Mean ± Standard deviation; [a] Significant differences (P<0.05) between Valgus and Neutral groups

[b] Significant differences (P<0.05) between Valgus and Varus groups

Table 2-9 Moment metrics used to compare valgus, neutral and varus alignment.

Variables (Nm/Kg)	Valgus (*n*=7)	Neutral (*n=9)*	Varus (*n*=11)	*p-Value*
M1	0.94 ± 0.92	2.50 ± 1.60	1.53 ± 1.16	0.071
M2	-1.39 ± 1.15	-1.17 ± 0.54	-1.63 ± 0.94	0.804
M3	-0.42 ± 0.61	-2.01 ± 0.78	-2.17 ± 0.91	<0.001[b]
M4	0.74 ± 0.67	0.39 ± 0.17	0.35 ± 0.48	0.270
M5	-0.25 ± 0.23	-0.66 ± 0.33	-0.71 ± 0.48	0.057
M6	0.23 ± 0.18	0.12 ± 0.09	0.13 ± 0.20	0.612
M7	-0.65 ± 0.43	-0.84 ± 0.25	-0.81 ± 0.35	0.483

Mean ± Standard deviation; [a] Significant differences (P<0.05) between Valgus and Neutral groups

[b] Significant differences (P<0.05) between Valgus and Varus groups

Additional analysis was carried out on the Kinetic metrics to see if HKA angle was linearly correlated. A Pearson correlation coefficient and Shapiro-Wilks test was performed to test for correlation and normality.

Table 2-10 Summary of linear correlation between frontal plane alignment as defined by HKA angle and kinetic metrics

Variables	Pearson Correlation	Sig. (2-tailed)	N
GRF F1	-0.037	0.853	27
GRF F2	-0.249	0.210	27
GRF F3	0.071	0.725	27
GRF F4	0.294	0.137	27
GRF F5	-0.323	0.101	27
GRF F6	-0.290	0.143	27
GRF F7	-0.535**	0.004	27
M1	0.137	0.494	27
M2	-0.159	0.429	27
M3	-0.667**	<0.001	27
M4	0.265	0.182	27
M5	-0.505**	0.007	27
M6	-0.129	0.522	27
M7	-0.329	0.093	27

**Significant correlation of P<0.01

Hypothesis 2

The data was split into three groups (Varus, Neutral and Valgus) as defined in section 2.2.3.3 and the fluoroscopy outputs including COR position, kinematic data (Table 2-11), A-P translation (Table 2-12) and S-I Translation (Table 2-13) were calculated for each volunteer. Subsequently the three groups were compared using a one-way ANOVA. Levene's test for equality of variance and Shapiro-Wilks test was carried out to test the variables for normal distribution. A Bonferroni correction was used during the analysis and all p-values were calculated with this. All statistics were performed using SPSS Statistics V23 (IBM Corporation). The results showed that there was no significant differences between the groups.

Table 2-11 Fluoroscopy kinematic metrics comparisons for valgus, neutral and varus defined groups

Metrics	Valgus Mean ± sd	Neutral Mean ± sd	Varus Mean ± sd	Valgus vs Neutral *p*-Value	Varus vs Neutral *p*-Value	Valgus vs Varus *p*-Value
Fluoroscopy Kinematics [°]						
Maximum Flexion	54.7 ± 13.6	61.4 ± 10.6	55.2 ± 8.8	0.679	0.647	1.000
Maximum Extension	2.0 ± 7.6	7.7 ± 14.0	3.1 ± 10.2	0.960	1.000	1.000
Sagittal Plane ROM	52.6 ± 15.6	53.7 ± 14.1	52.1 ± 9.8	1.000	1.000	1.000
Transverse Plane ROM	9.8 ± 2.5	11.1 ± 5.8	9.3 ± 2.9	1.000	0.937	1.000
Frontal Plane ROM	4.9 ± 1.4	4.6 ± 0.9	4.8 ± 1.2	1.000	1.000	1.000
CoR Medial-Lateral Position [%]						
Step Up	5.0 ± 32.2	-36.6 ± 23.7	-11.2 ± 32.9	0.033	0.212	0.823
Loaded	-3.0 ± 12.1	11.6 ± 27.8	-1.1 ± 23.5	0.653	0.685	1.000
Step Down	-6.7 ± 49.6	-14.7 ± 54.9	-14.9 ± 39.5	1.000	1.000	1.000

Table 2-12 Anterior-posterior Translations comparisons for valgus, neutral and varus defined groups

Metrics	Valgus Mean ± sd	Neutral Mean ± sd	Varus Mean ± sd	Valgus vs Neutral *p*-Value	Varus vs Neutral *p*-Value	Valgus vs Varus *p*-Value
Anterior-Posterior Translation for Lateral side [mm]						
Step Up Max	4.9 ± 6.6	7.3 ± 7.6	3.2 ± 5.7	1.000	0.521	1.000
Step Up Min	-0.5 ± 6.7	2.1 ± 7.1	-1.5 ± 6.23	1.000	0.723	1.000
Step Up ROM	5.4 ± 2.4	5.2 ± 1.9	4.7 ± 1.9	1.000	1.000	1.000
Loaded Max	3.4 ± 7.0	7.3 ± 6.8	2.6 ± 6.3	0.794	0.396	1.000
Loaded Min	0.3 ± 7.3	3.5 ± 7.5	-0.2 ± 6.3	1.000	0.735	1.000
Loaded ROM	3.1 ± 1.4	3.8 ± 1.6	2.8 ± 1.56	1.000	0.548	1.000
Step Down Max	5.1 ± 7.7	8.6 ± 6.2	3.8 ± 6.8	1.000	0.415	1.000
Step Down Min	-0.8 ± 7.6	2.4 ± 7.4	-1.1 ± 6.6	1.000	0.886	1.000
Step Down ROM	5.9 ± 2.0	6.2 ± 2.4	4.9 ± 2.3	1.000	0.645	1.000
Anterior- Posterior Translation for Medial side [mm]						
Step Up Max	2.5 ± 9.2	7.5 ± 4.59	2.8 ± 6.2	0.446	0.380	1.000
Step Up Min	-3.3 ± 7.5	-1.3 ± 5.7	-3.1 ± 5.9	1.000	1.000	1.000
Step Up ROM	5.8 ± 2.8	8.8 ± 2.7	5.9 ± 1.8	0.062	0.051	1.000
Loaded Max	2.1 ± 9.7	5.5 ± 7.2	1.8 ± 7.8	1.000	0.973	1.000
Loaded Min	-1.2 ± 9.4	2.8 ± 7.8	-0.9 ± 7.7	1.000	0.976	1.000
Loaded ROM	3.4 ± 1.3	2.7 ± 1.1	2.7 ± 1.6	0.949	1.000	0.921
Step Down Max	2.0 ± 10.1	6.4 ± 4.67	3.0 ± 6.9	0.723	0.925	1.000
Step Down Min	-3.5 ± 8.3	-1.4 ± 4.7	-3.2 ± 6.2	1.000	1.000	1.000
Step Down ROM	5.5 ± 3.5	7.8 ± 2.8	6.2 ± 2.0	0.322	0.604	1.000

Table 2-13 Superior-Inferior Translations comparisons for valgus, neutral and varus defined groups

Metrics	Valgus Mean ± sd	Neutral Mean ± sd	Varus Mean ± sd	Valgus vs Neutral *p*-Value	Varus vs Neutral *p*-Value	Valgus vs Varus *p*-Value
Superior-Inferior Translation						
Step Up Max	-20.6 ± 3.7	-18.9 ± 3.8	-20.9 ± 2.8	0.985	0.605	1.000
Step Up Min	-28.5 ± 2.5	-29.1 ± 2.2	-28.3 ± 1.7	1.000	1.000	1.000
Step Up ROM	8.0 ± 3.2	10.2 ± 3.8	7.4 ± 3.5	0.618	0.255	1.000
Loaded Max	-28.7 ± 2.5	-29.1 ± 2.2	-28.0 ± 1.7	1.000	0.786	1.000
Loaded Min	-28.7 ± 2.5	-29.6 ± 1.6	-28.4 ± 1.7	1.000	0.526	1.000
Loaded ROM	0.3 ± 0.1	0.5 ± 0.7	0.4 ± 0.3	0.781	1.000	1.000
Step Down Max	-20.0 ± 4.3	-19.1 ± 3.8	-19.7 ± 2.3	1.000	1.000	1.000
Step Down Min	-28.4 ± 2.6	-28.9 ± 1.9	-27.9 ± 1.4	1.000	0.852	1.000
Step Down ROM	8.4 ± 4.2	9.7 ± 3.5	8.2 ± 2.2	1.000	0.923	1.000

Hypothesis 3

To investigate the influence other clinical surgical measures have on in vivo kinematic outputs Pearson's product moment correlation was used to compare Tibial rotation, femur rotation, intercomponent rotation and tibial slope against fluoroscopy outputs. A Shapiro-Wilks test was carried out to test the variables for normality. All statistics were performed using SPSS Statistics V23 (IBM Corporation). The results showed that intercomponent rotation, femur component rotation and tibial rotation had no influence on the in-vivo kinematics and so were not included in Table 2-14.

Table 2-14 Summary of linear correlations between tibial slope against fluoroscopy outputs. Statistical significances below p<0.05 are shown in light grey, and p<0.01 in dark grey

		Tibial Slope		
		Corr.	*Sig.*	*N*
% Centre Of Rotation	Step Up	-0.090	.654	27
	Loaded	0.098	.627	27
	Step Down	-0.449*	.019	27
Kinematics	Max Flexion	-0.546**	.003	27
	Min Flex/Max Ext	-0.065	.748	27
	Flexion ROM	-.0417*	.031	27
	Int/External ROM	-0.084	.676	27
	Abd/Add ROM	-0.356	.068	27
AP Translation Lateral	Step Up Max	-0.005	.981	27
	Step Up Min	-0.008	.967	27
	Step Up ROM	0.012	.954	27
	Loaded Max	0.016	.938	27
	Loaded Min	0.032	.873	27
	Loaded ROM	-0.075	.710	27
	Step Down Max	-0.118	.558	27
	Step Down Min	0.004	.982	27
	Step Down ROM	-0.374	.055	27
AP Translation Medial	Step Up Max	0.167	.406	27
	Step Up Min	0.319	.105	27
	Step Up ROM	-0.298	.131	27
	Loaded Max	0.248	.213	27
	Loaded Min	0.276	.163	27
	Loaded ROM	-0.190	.342	27
	Step Down Max	0.224	.261	27
	Step Down Min	0.236	.235	27
	Step Down ROM	0.058	.773	27
Superior Inferior Translation	Step Up Max	-0.542**	.004	27
	Step Up Min	0.176	.381	27
	Step Up ROM	-0.610**	.001	27
	Loaded Max	0.194	.332	27
	Loaded Min	0.244	.220	27
	Loaded ROM	-0.126	.530	27
	Step Down Max	-0.353	.071	27
	Step Down Min	0.265	.182	27
	Step Down ROM	-0.516**	.006	27

2.4 Discussion

2.4.1 Hypothesis 1

2.4.1.1 Valgus Alignment

The results in Table 2-7 taken from the one-way ANOVA show that when comparing the kinematic metrics from gait analysis with the three groups defined by the HKA angle (Valgus, Neutral and Varus) the flexion ROM during gait is significantly reduced for valgus aligned (41.8° ± 5.1°) compared to neutral aligned (51.5° ± 7.3°) patients. This is due to the maximum flexion angle being significantly lower for both swing (44.7° ± 7.8°) and stance phases (8.0° ± 4.6°) for the valgus patients compared with the much higher peaks (and therefore ROM) for the neutral group (56.0° ± 3.6°,16.8° ± 5.4° respectively). This shows that during gait a valgus aligned TKR could potentially be limiting the movement in the sagittal plane and thus reducing overall function.
The significant difference between valgus (11.9° ± 5.3°) and neutral (5.9° ± 4.8°) patients, for maximum abduction angle is not surprising as the abduction angle is directly linked to the frontal plane alignment. This is further confirmed when the significant differences between valgus (4.5° ± 3.1°) and neutral (-2.9° ± 5.5°) are considered, as the highest adduction angle is negative meaning that the valgus aligned knee stays in a valgus position during the whole of the gait cycle.

No other study has been carried out to look at the effect of valgus alignment during gait analysis. One study carried out by Fang et al. (2009) based on 6070 TKR surgeries suggests that the highest survival rates of implants occurs with alignments of 2.4°-7.2° valgus. Several other studies also come to the same conclusion (Ritter et al. 1994; Kim et al. 2014) however as alluded to in a recent review paper (Vandekerckhove et al. 2016) the previous studies have limitations in respect to reliance on short film radiographs and no other analysis. Based on the gait analysis results no recommendation can be made to suggest that valgus alignment is a suitable TKR alignment.

2.4.1.2 Varus Alignment

As shown in Table 2-7 the one-way ANOVA showed that the differences between the three groups with respect to the kinematic there is no difference when focusing on varus alignment when compared to valgus and neutral. When looking at moment metrics (Table 2-9) a significant difference was found between varus (-2.17 Nm/Kg ± 0.911 Nm/Kg) and valgus (-0.42 Nm/Kg ± 0.61 Nm/Kg) aligned patients when looking at adduction moment, where peak adduction and abduction moments are defined as being negative and positive respectively.

A Pearson's product moment correlation was used (Table 2-10) to assess the relationship of frontal plane alignment on kinetic metrics. An increase in HKA angle (i.e. more varus aligned) was found to have a highly significant strong correlation with peak adduction moment, $r(27) = -0.667$, $p<0.001$. A large varus HKA angle was found to have a significant strong correlation with peak lateral GRF, $r(27) = -.535$, $p=0.004$. A significant moderate correlation was found between HKA and Maximum Internal Rotation moment, $r(27) = -.505$, $p=0.007$.

The results show that a varus aligned knee replacement produces higher loading in the joint. Varus alignment causes the knee joint centre to be positioned more laterally during gait. Therefore, the ground reaction force passes through the medial side of the knee replacement increasing the adduction moment. It has been shown that gait speed is related to knee adduction moment (Robbins and Maly 2009; Khan et al. 2017; Telfer et al. 2017) so an additional Pearson's product moment correlation was carried out between peak knee adduction moment and gait speed. A highly significant and strong correlation was found between the two, $r(27) = -.573$, $p =0.002$. The greater speed creates a larger force during the GRF increasing the joint loading at the knee. Several studies have looked at frontal plane alignment and loading during gait analysis and have suggested using the external knee adduction moment as a dynamic measure of knee joint loading (Andriacchi 1994; Hunt et al. 2006). Although this doesn't take into other factors such as muscle contraction and the soft-tissue stability (Miller et al. 2014), it can be

considered to suggest that more loading is taking place with higher peak adduction moments.

One of the potential consequences of a high peak knee adduction moment in an implanted knee is increased wear. Several studies carried out wear analysis on implants with a varus alignment compared with neutral alignment and found increased wear on the medial side (Matsuda et al. 1999; D'Lima et al. 2001; Werner et al. 2005; Collier et al. 2007). Vandekerckhove et al (2017) retrieved 95 polyethylene inserts and analysed the wear and damage patterns. They found that progressive wear occurred as the varus angle increased but compared with the other studies they found increased wear on the lateral side. The authors concluded that this may be due to lateral condylar lift-off.

Based on this study the recommendation is to continue the current practice of neutral frontal plane alignment as it has the least influence on loading compared with varus alignment.

2.4.2 Hypothesis 2

None of the fluoroscopy kinematic metrics within the analysis were found to be significantly different between the groups. This suggests that frontal plane alignment may not influence the in-vivo kinematics during step up and step down. This could be due to the activity being relatively static and therefore less frontal plane movement taking place compared to gait.

2.4.3 Hypothesis 3

2.4.3.1 Tibial Slope (TS)

The effect of TS angle on fluoroscopy metrics was investigated and several relationships were found. Increasing TS angle was found to correlate with the decrease of both maximum flexion angle ($r(27) = -0.546$, $p=0.003$) and ROM ($r(27) = -0.417$, $p=0.031$) and the position of the COR tending towards the lateral side during step down ($r(27) = -0.449$, $p=0.003$). In addition increasing TS angle was found to correlate with decreasing superior-inferior translation

both maximum value for step up ($r(27) = -0.542$, $p=0.004$) and total ROM ($r(27) = -0.610$, $p=0.001$) and total range for step down ($r(27) = -0.516$, $p=0.006$). Superior-inferior translation is the distance between the femoral and tibial components.

Very few studies have investigated the role of sagittal component positioning especially posterior tibial slope on outcome and survival rate for posterior-cruciate retaining implants (In et al. 2009; Okazaki et al. 2014; Chambers et al. 2016). They have found that a small posterior TS angle leads to a tighter flexion gap, where flexion gap is the measurement of the gap using a spacer block when the knee is placed in flexion during surgery. Although it should be noted that these studies were either carried out on cadavers or measurements just carried out during surgery. One contrasting study carried out by Kansara and Markel (2006) on two groups, one with a mean postoperative tibial slope of 1.8° (n=31) and one with a mean slope of 5.5° found no increase in ROM or patient reported outcome measures, which suggests that it is not related to ROM.

The results presented in this study showed that as posterior TS angle increases the flexion ROM, during step up and down decreases. This is most likely related to the height of the patient, as the step was kept at a fixed height. For a taller patient the flexion ROM would decrease.

The results also showed that as posterior TS angle increases distance between the implants decreases, suggesting a smaller flexion gap. These results are converse to what has been reported in the literature. A more lateral COR during step down would mean that the femur is moving forward with flexion rather than rolling back and has been linked to the lack of AP constraint (Banks and Hodge 2004). So the increase of posterior angle is potentially stopping normal TKR function.

In comparison to the literature the data collected in this study has been captured in-vivo and provides an insight to how the knee replacement is performing within a more realistic activity. However the patients here potentially have more than just one type of malalignment and the influence of that will have to be investigated further. The effect of muscle forces on all these

different measures has not been investigated and should be examined going forward. The general consensus for current practice is to use a larger tibial slope angle to increase flexion gap. In the context of this study this may need to be reassessed, where most likely there is an optimum range of posterior tibial slope angle for best TKR function. Overall the results from this hypothesis show that TS plays an important part in optimising function and outcome and should continue to be investigated further.

2.4.4 Limitations

From the 244 patient cohort (254 knees), 29 patients with 34 affected knees were recruited for this study. Three patients with 5 affected knees had to be excluded due to motion capture equipment problems and two more knees were excluded due to fluoroscopic image problems. This meant that the final patient number was 25 (27 knees) who had fluoroscopy, motion analysis and clinical measurements.

This was a retrospective study therefore any pre-surgery clinical measurements were not available for comparison. This includes pre-knee arthroplasty patient reported outcome measures, to understand if any patients has improved in terms of self-assessed pain and function.

In addition due to the legal dispute between two trusts (Toft 2011) no surgical notes were provided. This meant no information was given on soft-tissue balance, which may have played an important influence on certain parameters. As discussed previously the size of tibial and femoral components was not provided and had to be calculated through a combination of CT measurements and trial and error during the MBIR protocol.

The shape of the meniscal bearing had to be discounted during closest point calculations, as the amount of wear that takes place can’t be measured normally until the point of retrieval. The movement of the bearing has been discounted as no metallic beads were implanted in it to allow for tracking.

2.4.4.1 Motion Capture

This data was collected prior to the author's involvement; a number of problems were faced with four knees, which had to be excluded due to difficulty with force plate data collection. One knee had to be excluded due to a marker cluster not being rigidly attached to the thigh. Three patients had less than four gait trials due to difficulties completing six successful gait trials but were still included in the data set.

2.4.4.2 Fluoroscopy

Two knees were excluded due to errors in saving the DICOM images in a correct sequence. There were difficulties determining axial rotation of tibial tray for certain patients, due to the symmetric nature of the tibia implant. The out of plane translation was difficult to calculate due to it only being single plane X-ray, hence medial/lateral shift was not calculated. Out of plane inaccuracy has been calculated using the same image registration software to be as much as 4.5mm for medial-lateral translation (Acker et al. 2011). If an additional frontal fluoroscopy view had been used patella tracking could have been investigated. Patellofemoral pain has been reported as a common symptom post TKR surgery (Board and Javed 2003). The influence of surgical alignment on patellofemoral pain and patella mal-tracking would be an interesting research area to investigate.

2.5 Summary

The study shows that frontal plane alignment does influence biomechanical function and loading during gait. Patients with a valgus knee alignment have reduced range of motion in the sagittal plane during gait. Patients with varus knee alignment have shown increased medial loading. The hypothesis that frontal plane alignment will influence in-vivo kinematics has been shown to be correct. Based on this study, the recommendation is to continue the current practice of going for a neutral frontal plane alignment.

Overall the results from this hypothesis show that Tibial slope may play an important part in optimising function and outcome and should continue to be investigated further.

Despite the limitations described above this patient cohort has provided a rare insight to investigate the effect of TKR malalignment that is clinically important for orthopaedic surgeons. Some of the limitations with the fluoroscopy have the potential to be addressed by using biplane fluoroscopy. These limitations will be further explored using intact knees in the following chapter.

Chapter 3 Assessment and Improvement of Existing Single Plane Intact Knee Fluoroscopy Protocol at Cardiff: Challenges and Recommendations

3.1 Introduction and Background

Measuring three dimensional tibiofemoral kinematics (three rotations and three translations) is essential for understanding and evaluating normal and pathological knee function (Ramsey and Wretenberg 1999). Quantifying how Osteoarthritic and healthy function differs can inform the following; new implant design, understanding disease progression, and quantifiable intervention efficacy.

The most common analysis used to quantify this, is skin based motion analysis. However, due to the errors introduced by soft tissue artefact when measuring skeletal biomechanics in the knee the translations have to be disregarded (Cappozzo et al. 1996; Cappozzo et al. 2005). The translations present in the knee are such a small magnitude that the soft tissue artefact induces a large error and as such invalidates the data collected.

Single plane fluoroscopy has been used for the last two decades to analyse tibiofemoral joint movement for both intact and implanted knees (Banks and Hodge 1996; Moro-Oka et al. 2008; Grieco et al. 2017). Using a three dimensional model based image registration technique, translations and rotations can be determined during activities of daily living. In addition, using the bone position data, in-vivo translations for both the medial and lateral side of the knee can be calculated (Banks and Hodge 1996; Kanisawa et al. 2003). A limitation to this approach is the small field of view which restricts the activities that can be performed.

3.1.1 Combined Fluoroscopy and Motion Capture

Although the two techniques have advantages and limitations combining them provides a detailed and more clinically meaningful analysis of a specific pathology or investigate the efficacy of certain treatments. For example, linking abnormal in-vivo kinematics at the knee calculated with fluoroscopy with what is happening at the other joints using motion capture to provide a more detailed understanding of a pathology (Fantozzi et al. 2003).

Another application and benefit of using the two techniques in combination is the capacity to use the resulting data to perform musculoskeletal modelling (Fernandez et al. 2008). This is especially useful when using MRI derived bone models as it allows the incorporation of soft tissue such as articular cartilage and the ability to locate the positions other structures that cannot be seen on CT such as ligaments, tendons and muscles.

A number of studies (Cappozzo et al. 1996; Garling et al. 2007; Lu et al. 2008; Tsai et al. 2011; Lin et al. 2016) have investigated quantifying soft tissue artefact from motion capture, using fluoroscopy as the gold standard, by performing combined motion capture and fluoroscopy.

The original motivation for carrying out fluoroscopy research at Cardiff University was to enable assessment of the errors associated with motion capture to allow the weighting of the contribution of specific inputs used within the Cardiff Dempster Schafer Theory (DST) classifier (Jones 2004; Biggs 2016). This would enable the classifier to make a more informed decision on whether a patient has a higher belief in healthy or osteoarthritic function.

3.1.2 Previous Fluoroscopy and MBIR studies at Cardiff University

The pilot study described in this chapter follows on from the work carried out by Whatling (2009). The main aim of this study was to assess errors using motion capture systems and model-based image registration (MBIR) by comparing kinematics from both. The main issue highlighted was that the measurements were not taken simultaneously and could not be used as a true comparison between the two approaches. Following this work an Arthritis Research UK (ARUK) Centre of Excellence was awarded to Cardiff University. The Biomechanics and Bioengineering Centre was set up and one of the deliverables of the first five years of funding was to set up a synchronised MBIR and motion capture using MRI derived bone models.

The segmentation and defining coordinate systems from MRI derived bones protocol was developed further by Watling (2014). Some of the improvements from this was also applied to this pilot study.

The work presented in this chapter was performed after the experience of processing the implant study in Chapter 2, therefore some of the updates to the registration protocol have been applied. This was the first opportunity for the author to gain expertise in quantifying in-vivo kinematics for the intact knee using MRI and MBIR for both healthy and pathological volunteers. The existing protocol for image registration processing provided the foundation of this protocol, but new software and techniques meant an update was required and resulted in an improved protocol. The data presented here is the first attempt at carrying out synchronised motion capture and fluoroscopy at Cardiff University.

3.1.3 Patient Cohort Background

Knee malalignment is known to be a risk factor for OA initiation, with a varus malalignment in the frontal plane causing an increased risk of joint space narrowing and causing a higher prevalence of medial compartment OA (Sharma et al. 2001). Malalignment can also be caused by, and further increased by, the presence of knee OA due to the degradation of soft tissues and the loss of bone height (Tanamas et al. 2009).

The patient volunteers included in this pilot study were recruited from a larger study as part of the Arthritis Research UK Biomechanics and Bioengineering centre. This patient cohort consisted of volunteers who had OA only in the medial compartment of their affected knee and some form of frontal plane malalignment. Due to the age and activity of these patients they were deemed suitable for referral for high tibial osteotomy (HTO) surgery.

The patients were due to have a medial opening wedge HTO, which is designed to adjust the weight bearing axis of the knee to off load the medial affected compartment to the relatively undamaged lateral compartment (Seo et al. 2016). This is done by making an incision into the tibia below the tibial plateau and using wedges to gradually open the osteotomy. The new alignment is then kept in position using a locking plate. The main goal of this surgery is to delay the need for a total knee replacement (Kim et al. 2017). One study has found that certain patients have had reversal of the

degenerative processes and shown indications of regeneration of cartilage (Koshino et al. 2003).

For this pilot study the volunteers were recruited prior to their HTO surgery with the original aim to then recruit them post plate removal a year after surgery. Although this didn't take place during the pilot study, this data has the potential to act as comparator for future imaging studies.

3.1.4 Aims

The objectives of the study described in this Chapter were to:

- Develop a new MBIR protocol using Joint Track and Joint View software for tibiofemoral kinematics. This is a continuation of the method defined by Banks and Hodge (1996).
- Improve the existing protocol, defined by Whatling (2009), using magnetic resonance imaging (MRI) to produce subject-specific bone models for image registration. To compare the resulting tibiofemoral kinematics with other studies to assess its clinical viability for future work

- To take advantage of newer and better processing techniques and image sequences.

- Process and compare results of simultaneous motion analysis with MBIR calculated kinematics of the tibiofemoral joint. To try and understand the errors associated with marker-based motion capture

- Carry out an assessment of how the current protocol works and identify any technical errors that are associated with it.

3.2 Methods

3.2.1 Data Collection

There were two main data collection protocols that volunteers attended; a combined fluoroscopy and motion capture session and Magnetic Resonance Imaging (MRI) session. MRI and Fluoroscopy were approved by the Research Ethics Committee for Wales and Cardiff and Vale University Health Board.

All data collection was carried out by colleagues in the research team prior to the author's involvement in the project. The author's contribution to this study is to have developed a new protocol for MBIR, improving the segmentation protocol and processing all the data captured. A short summary of the data collection follows.

3.2.1.1 Motion Analysis

Motion analysis data was undertaken using eight ProReflex MCU 120Hz digital cameras (Qualisys, Sweden) capturing at 120 Hz. The cameras were positioned around the fluoroscopy system (Philips Multi Diagnostic Eleva) (Figure 3-1a) and 3D motion capture data was collected using Qualisys Track Manager (QTM) Software (Figure 3-1b).

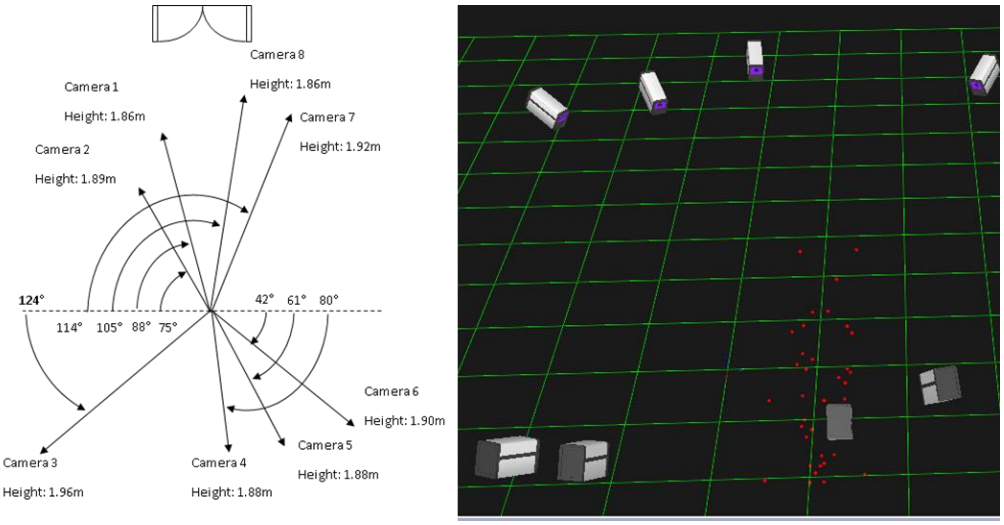

Figure 3-1**a**: Positions and heights of the Motion Analysis cameras **b**: Screenshot taken from QTM showing the camera positions and markers of a volunteer

Force data was captured using a portable 600mmx400mm Kistler force plate (Kistler Systems, Switzerland) with a sample rate of 600Hz. The force plate was positioned underneath a 160mm step used during the activity. The data was captured using Kistler BioWare (Kistler Systems, Switzerland) software on a separate computer to the motion capture data. The method of synchronisation between the motion capture and force platform is highlighted below (section 3.2.1.3).

The global coordinate system (GCS) was defined using an L-Frame, consisting of four markers of a known distance apart, positioned on top of the image intensifier. The GCS axes were defined to the same convention as the fluoroscopy coordinate system with the Z-Axis directed towards the X-ray Source. The position of the corner of the force plate was captured using markers prior to data collection.

Volunteers were asked to wear loose fitting clothing and shorts during the data collection. A modified Helen Hayes marker set was applied using twenty-two retro-reflective markers and two rigid based clusters each with four retro-reflective markers. The positions of these markers are the same as defined in section 2.2.2(Figure 2-4).

3.2.1.2 Fluoroscopy

Continuous fluoroscopy data collection was carried out using the same method as described in section 2.2.4 following the approach of Whatling (2009). Calibration was carried out prior data collection to correct for geometric distortion and to calculate intrinsic and extrinsic camera parameters (section 2.2.4.1).

All exposures took place in the X-ray department at Llandough Hospital using a Philips Eleva RF by a trained radiographer. Ethical approval was given for up to 60 seconds to be undertaken to one knee joint in the lateral direction. The estimated total fluoroscopy dose was 0.0013mSV which is equivalent to 6 hours background radiation. Volunteers were asked to perform a step up and down task three times on a 16cm step with the lateral side facing the image intensifier. Images from the fluoroscopy examination were saved as a sequence of individual DICOM files.

3.2.1.3 Synchronised Fluoroscopy and Motion Analysis

One of the main aims for this study was to capture simultaneous motion capture and fluoroscopy. A custom trigger was used to synchronise the start of data collection, such that when fluoroscopy exposure started the motion capture system started simultaneously.

The trigger used was an X-ray monitor diode (F50-MCS, First Sensor, Germany) that was customised (Figure 3-1a) to output a TTL pulse via a BNC connection to trigger a Qualisys motion capture system and portable force platform (Kistler, Switzerland). An outline of the triggering set up can be seen in Figure 3-2b. The trigger works using a silicon photodiode that is sensitive to within the X-Ray wavelength (between 0.1-1 nm). When the photodiode is struck by a photon an output current is generated by the diode and then amplified and converted to a 5V TTL pulse. The detector was designed to detect backscatter and therefore is very sensitive to low dose rates. A filter is used on the transmission window to block wavelengths greater than 100nm (UV, visible and IR light).

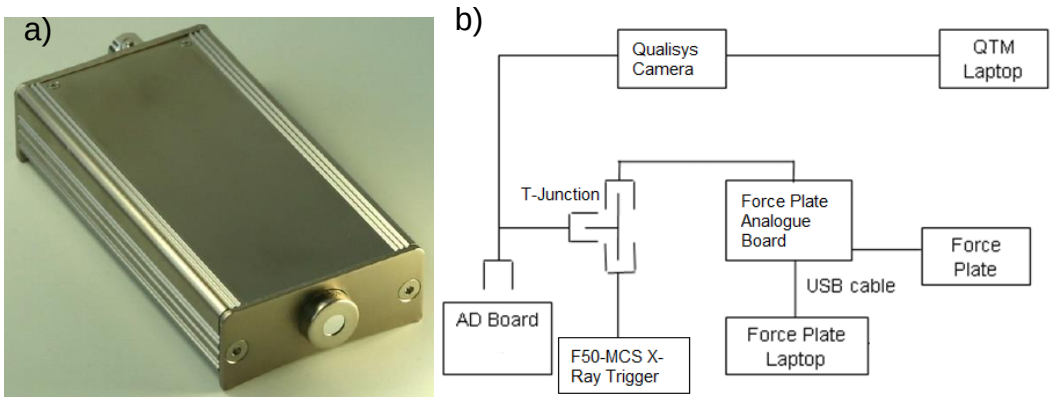

Figure 3-2 **a**: F50-MCS X-Ray Monitor diode **b**: Outline of how the synchronisation of the different systems was set up

3.2.1.4 Magnetic Resonance Imaging

The Magnetic Resonance (MR) Imaging protocol is based upon a combination of methods defined by Watling (2014) and Whatling (2009). A brief overview of the method follows.

All MR Imaging was performed using the Signa HD-xt 3.0T MRI scanner (GE Medical Systems, USA) at Cardiff University Brain Research Imaging Centre (CUBRIC), with one experienced radiographer performing all the scans. During the visit two different set of scans were taken. A high-resolution scan of the tibiofemoral joint, specifically the distal femur and proximal tibia, were needed to create models for the image registration process. Whole-leg scans were required to define and embed anatomical coordinate systems within the models. For all the scans volunteers were positioned such that the leg being imaged was in a neutral straight position.

An initial scout scan, lasting 10-15 seconds, was used to provide the location of the knee within the bore of the scanner. The radiographer then aligned the imaging volume to the centre of the knee joint to capture both tibial and femoral articulating surfaces. Before each sequence the volunteer was informed of the purpose of the scan and approximate duration.

Whole leg scans were carried out first, using the body radio frequency (RF) coil. The sequence used was an Incoherent Gradient Echo, known on the GE

scanner as a (SPGR), which provided a slice thickness of 2.5mm. For this scan the axial plane had the highest in-plane resolution of 1.48 x 1.48 mm and the total imaging volume was 0.053 m^3. Therefore several scans were required to image the whole leg. Typically, this consisted of three or four scans to cover full leg length from above the femoral head to below the malleolus.

High-resolution scans were carried out next and a Flexi-Coil was wrapped around the volunteer's knee which improves the signal to noise ratio. High density foam was used to support the lower limbs, with additional strapping around the knee to reduce movement and help maintain position. A Fast Imaging Employing Steady State Acquisition (FIESTA-C) was used to capture a high-resolution 3D image of the knee. This was chosen due to its high signal to noise ratio and ability to create high resolution scans in a short period of time (Li et al. 2009). This scan is a T2 weighted image tissues meaning high water content and fat appear brightest. The sagittal plane orientation was chosen to have the highest in-plane resolution (0.5 x 0.5 mm) as segmentation of the femur and tibia bone is easiest in this plane. Imaging parameters for both sequences used can be seen in Table 3-1 below.

Table 3-1 Magnetic Resonance Imaging Sequence Parameters

Scan Type	**High Resolution**	**Long Leg Scan**
Sequence	FIESTA-C	3D SPGR
Repetition Time (TR)	4.971 ms	9.664 ms
Echo Time (TE)	2.376 ms	4.248 ms
Orientation	Oblique-sagittal	Oblique-coronal
In-Plane Resolution	0.625 x 0.625 mm	0.7301 x 0.7301 mm
Slice Thickness	0.8 mm	10 mm

3.2.2 Data Processing

There are two different data processing protocols required to analyse the data collected. The MBIR protocol and a motion analysis protocol. The following sections detail the different approaches which were developed and used to process the data.

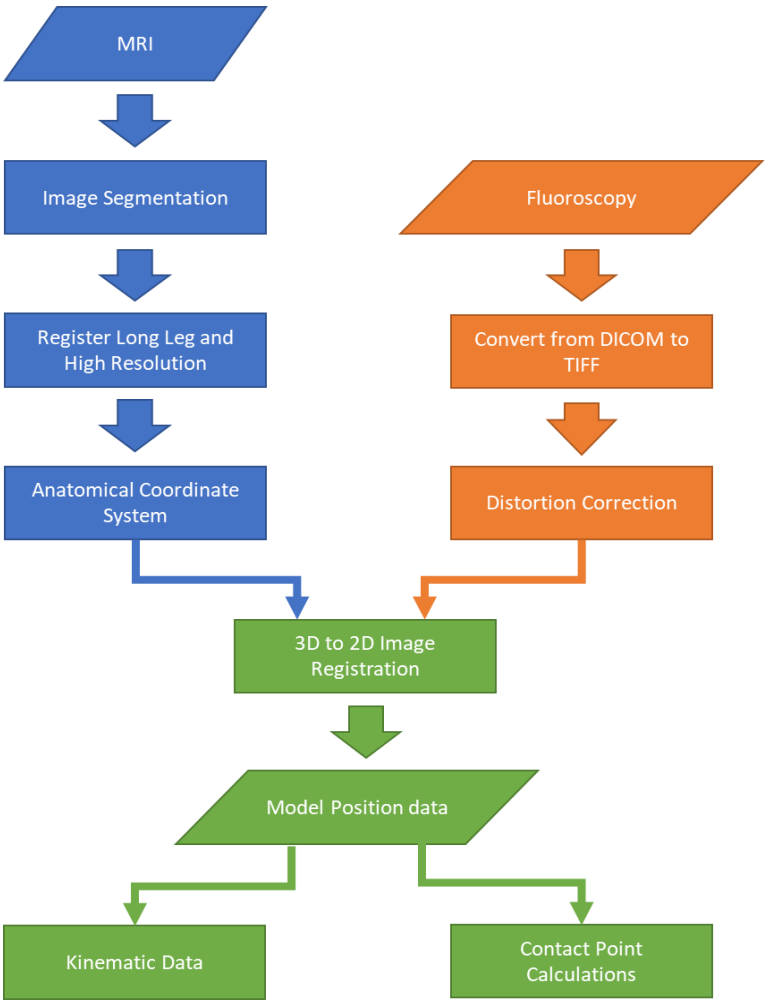

Figure 3-3: Flow diagram of Intact knee Fluoroscopy processing. Blue blocks are the steps to create 3D models from MRI, the orange blocks highlight the steps to process the fluoroscopy image data, with the green blocks showing the image registration and outputs.

3.2.2.1 Model Based Image Registration Protocol

There are several steps required to output kinematic data from intact knee fluoroscopy. A summary of this is shown in Figure 3-3.

3.2.2.1.1 Model Generation and Preparation

The image segmentation process is based upon the protocol defined by Watling (2014) and briefly summarised below.

Image Segmentation

DICOM images outputted from the MR scanner were imported into ScanIP (Synopsys, USA). The image contrast values can be adjusted such that all the structure of interest is easily seen. The DICOM MR images from the high-resolution scan consist of a series of 2D slices (approximately 120 slices per knee) that cover the captured 3D image volume of the knee. The sagittal viewing plane was used as the main plane for segmentation as this was the direction with the highest resolution. The transverse and frontal plane view was used for data checking and clarification on structure boundaries. The software allows the user to highlight a structure of interest by drawing a mask around the structure of interest on an individual slice. A semi-automated threshold function limits the pixels that can by selected based on the greyscale value, allowing certain structures such as cartilage to be selected or ignored. This was performed on each slice with the contours defined by the masks. The slices where then used to form a 3D model. The structures that were segmented from the scan were the femur, tibia, fibula and patella.

Following segmentation and creation of the model, a dilation function was performed, this adds one pixel in all directions to the model; a recursive Gaussian filter to smooth the model. The dilation is performed as the recursive Gaussian filter erodes the 3D model to produce a smooth end result. However this has the potential to remove part of the model that may be needed and could, therefore, lead to an inaccurate model. Using this approach, the recursive Gaussian filter removes the dilated pixels and leaves an accurate representation of the structure of interest.

The whole leg scans were segmented following a similar approach as above with the main difference being that the transverse plane was used for segmentation as it had the highest resolution.

Following smoothing, the models were rendered and exported as binary Stereolithography (.stl) CAD files.

Anatomical Coordinate System

To form a clinically relevant anatomical coordinate systems for the fluoroscopy analysis three anatomical landmarks are required for each bone model. These are defined by Moro-oka et al. (2007) and a protocol, developed by Whatling (2009), which can be used to register whole leg to high resolution models, and defines the anatomical landmarks, was used as the basis of the protocol utilised for this study. An updated protocol was developed to take advantage of improvements in software since the original protocol; the steps involved can be found in detail in Appendix C.

3.2.2.1.2 Model Based Image Registration

The distortion correction and image conversion process was performed using the same approach as defined in Appendix B. The undistorted fluoroscopy images and the subject specific MR derived CAD models were imported into JointTrack (University of Florida). Due to the lack of landmarks on the tibia, the fibula was also imported to aid in calculating the tibial axial rotation. It is assumed that the fibula acted as a rigid body with the tibia.

The position of each bone was initially manually determined with the femur registered first, followed by the tibia and fibula model (Figure 3-4). The software then optimises the bone position using a Canny edge detection algorithm and a direct linear transform function applying a simulated annealing algorithm. It was found that the optimiser was reliant on good initial bone positions and if the image data was blurred, it would not be able to converge on the correct solution which subsequently required manual input of edges to correct the bone positions.

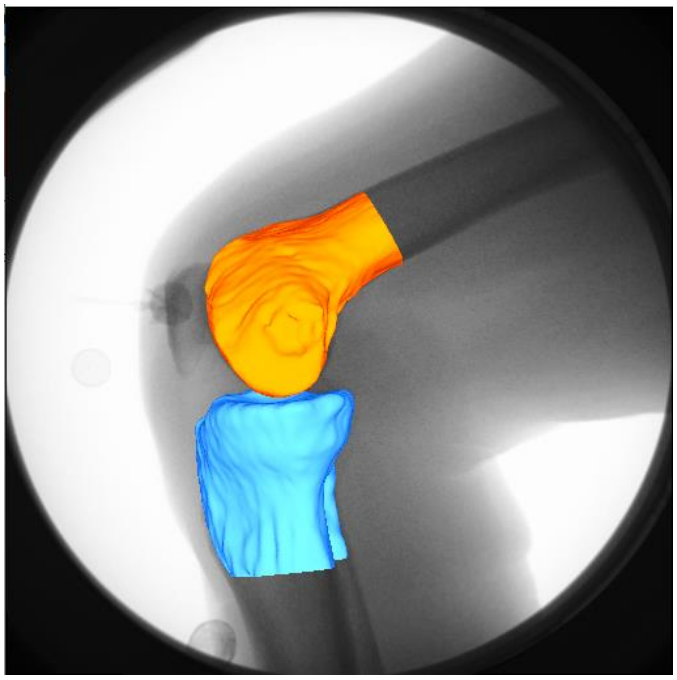

Figure 3-4 Example registered Femur, tibia and fibula models to a single frame of fluoroscopy within Joint Track software.

3.2.2.1.3 Kinematic and Closest Points Calculations

The same kinematic calculations were performed on the tibia and femur model as in section 2.2.4.6.2 to calculate the rotation and translations.

To examine the inter-articular interaction between the femur and tibia a closest point calculation was performed between the bone models of the femur and tibia. The interaction between the femoral condyle and tibial plateau for both lateral and medial side were examined for each fluoroscopy image. This is the same approach as was described in section 2.2.4.6.3.

The kinematic and closest point data were split up into three separate step up and down movements. A MATLAB script provided by Prof. Scott Banks used a spline interpolation with 5° flexion intervals to reanalyse all other translations and rotations as a function of flexion angle (Hamai et al. 2009). From this data average and standard deviation curves for the three step up and down activities were calculated for each volunteer.

3.2.2.2 Motion Capture Processing

The data collected from the Pro-reflex cameras was tracked and exported using QTM following the same process described in section 2.2.2.3. A biomechanical model was applied to the static calibration file and then to the movement file to calculate clinically relevant kinematic and kinetics utilising the same approach as defined in Chapter 2. However, differences in how the motion capture and force data are combined in Visual3D (C-motion, USA) are discussed briefly below.

The raw analogue force plate data was captured synchronously to the motion capture data but was captured on a different computer and using different software. The following steps were performed to get both the force plate data and the motion capture data into Visual3D.

The raw analogue data recorded during the step up and down activity was exported from Kistler BioWare software as a .c3d file and were imported into the step up and down data file within Visual3D. The location of the four corners of the force plate was recorded prior to volunteer data capture and were also imported into Visual3D. The locations were defined with respect to the GCS calibration and allowed the force plate location to be defined within Visual3D. The force platform parameters were selected within Visual 3D; these define how the raw analogue signals stored in the data file are transformed into the ground reaction force, centre of pressure and moments acting around the plate.

Visual3D requires the position of the foot with respect to the force plate to calculate moments. An offset (160mm) was applied to the force platform to account for the step used during the step up and down activity (Figure 3-5). This allowed the software to calculate moments around the hip, knee and ankle using the same inverse dynamics approach as described in section 2.2.2.3.4.

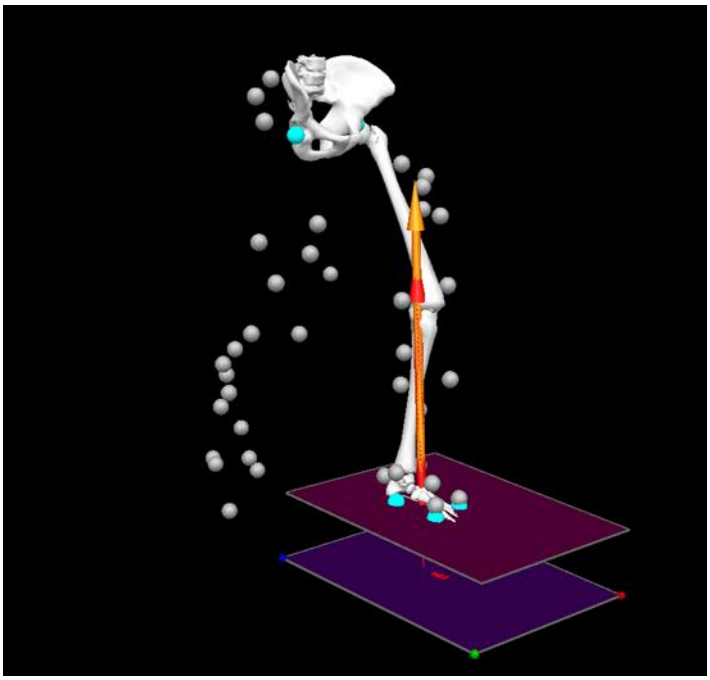

Figure 3-5 Screenshot taken from Visual3D (C-Motion, USA) showing the offset force structure (Purple) and the redefined force vector during the stair activity (Orange)

3.2.2.3 Combining Motion Capture & Fluoroscopy

To directly compare Motion Capture and Fluoroscopy the datasets need to be aligned within the time domain. This can be achieved if the sampling frequency of the two datasets is known. As defined earlier the sampling frequency of the motion capture was 120 Hz. However, the fluoroscopy data capture rate was not known and from similar clinical C-arm systems was thought to be either 25 or 30 Hz. The Signal Processing toolbox within MATLAB (The Mathworks, Inc., USA) was used to visualise the data to determine if there was a time offset (Figure 3-6). Sagittal plane knee angles were used to compare between motion capture and fluoroscopy as the step up and down movement occurs within this plane. The Signal Analyzer application within the toolbox allowed the visualisation of data with different sampling frequencies without the need to resample the data; to visualise the fluoroscopy data a frequency of 30Hz was selected.

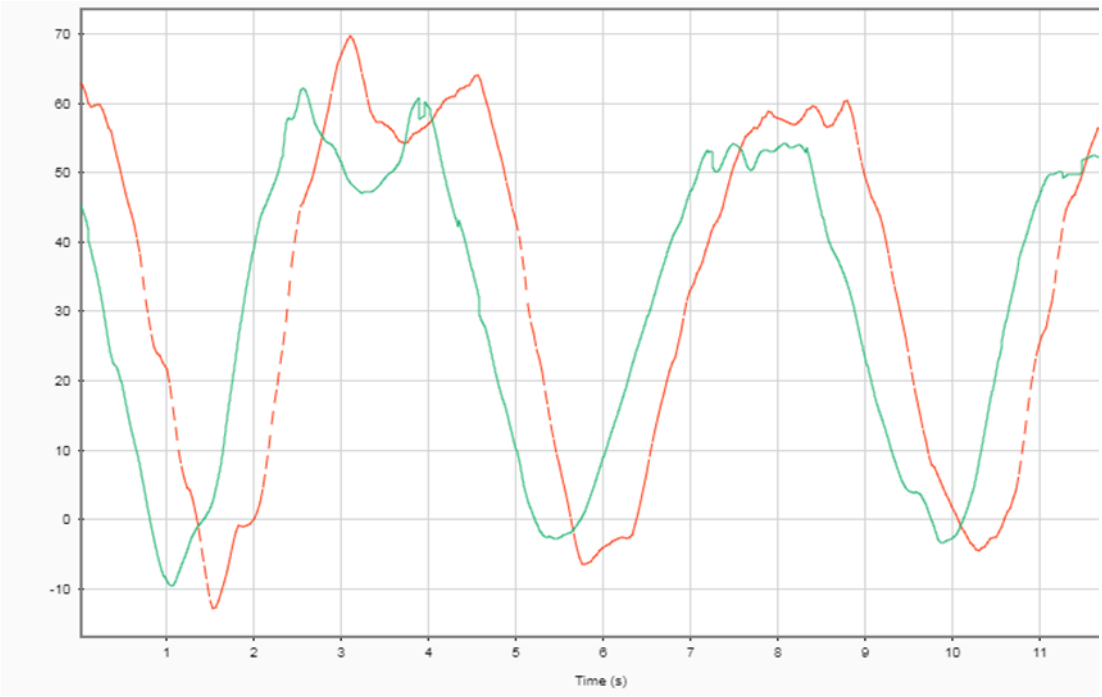

Figure 3-6 Example plot of Knee Flexion angle for Fluoroscopy (Red dashed) and Motion Capture (Green) in MATLAB Signal Analyzer. The graph shows there is a time offset between the two data streams.

As shown in Figure 3-6 there was a time offset between the fluoroscopy data and the motion capture data. Both the true frequency of the fluoroscopy data and the time offset between the data needed to be calculated. To determine this, a bespoke MATLAB script was written, and the steps involved are described below.

The motion capture and fluoroscopy data were imported into MATLAB, and the analysis was performed on the sagittal plane data (Knee Flexion). To find the fluoroscopy frequency the Find Peak Function in MATLAB was used on inverted knee flexion data. This found the local minimums for both data sets (Figure 3-7).

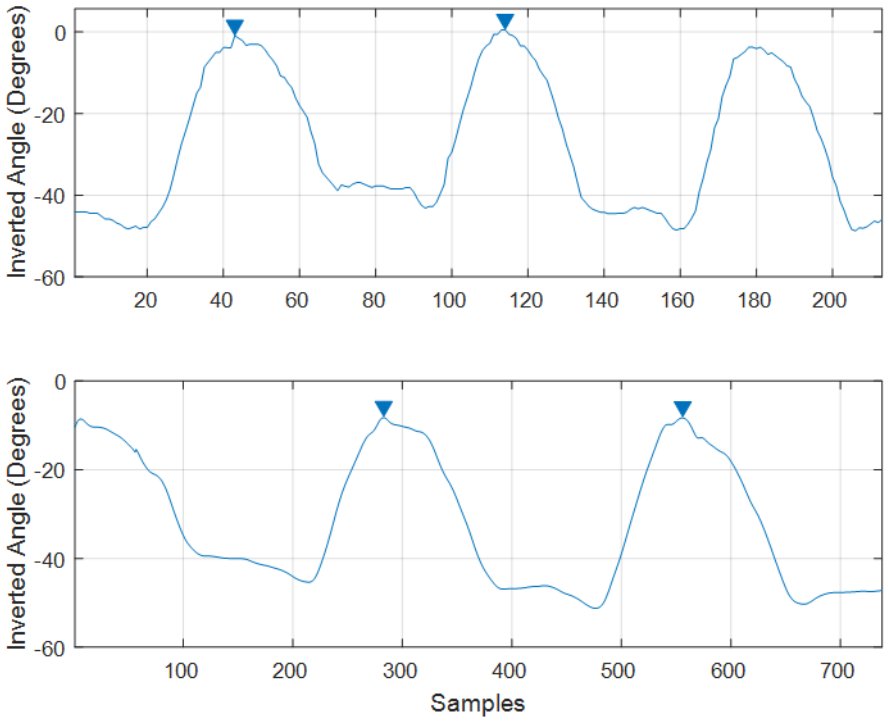

Figure 3-7 Example inverted data where peaks have been detected. Top graph is fluoroscopy data knee flexion and bottom graph motion capture knee flexion.

The sample differences between the peaks were calculated for both datasets. The motion capture sample difference was converted into time difference using its frequency, which was known. Using the time difference calculated for the motion capture and dividing this by the sample difference for fluoroscopy, the sample time calculated. The fluoroscopy frequency was then calculated as the inverse of sample time.

To calculate the time offset between the datasets the fluoroscopy data was resampled into the motion capture data frequency. A cross-correlation function was performed between the two datasets. Cross-correlations are known to be effective at calculating time delay between two signals (Rhudy et al. 2009).

Cross-correlation superimposes the data and moves one of the datasets along the x-axis using a range of offsets, known as lags. For each offset the integral of the product is taken. The offset with the highest integral shows that the peaks and troughs of the two signals are aligned. A plot of the cross-correlation

against the lags was used to visualise where the delay was occurring (Figure 3-8).

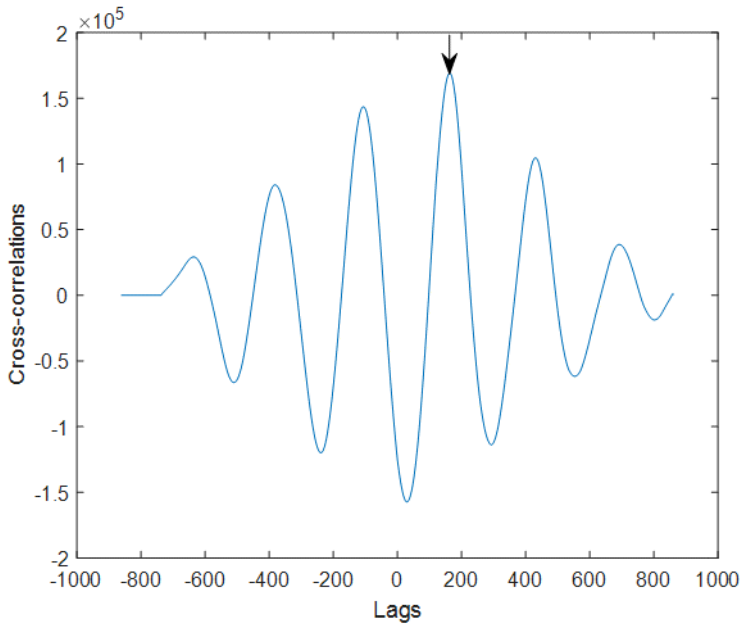

Figure 3-8 Example plot of cross-correlation against the lags used on data for motion capture and fluoroscopy. The arrow indicates the highest cross-correlation and can be used to calculate the time delay between the two datasets.

The highest peak in the cross-correlation plot (Figure 3-8) and the corresponding lag value was then used to determine the time offset. Here the lag refers to the number of sample offsets used. Dividing the lag by the motion capture frequency the time offset was calculated.

This offset was then applied to the motion capture data and the fluoroscopy and motion capture time synchronised rotation data was plotted. The offsets and the frequency calculated for each volunteer can be seen in Table 3-3.

3.3 Results

3.3.1 Volunteers

For this pilot study two patient volunteers were recruited from the patient cohort described in section 3.1.3. An older healthy volunteer was recruited to act as

a direct comparison for both patient volunteers. The individual subject metrics can be seen below in Table 3-2.

Table 3-2 Subject metrics for volunteers undergoing Fluoroscopy and MRI

Volunteer ID	Imaged Knee	Gender	Age/Sex	Height/m	Weight/kg	BMI	KL Grade
PV1	L	M	38/M	1.74	67	22.1	2
PV2	R	M	56/M	1.81	108	32.7	3
HV1	L	M	46/M	1.83	96	28.5	-

KL grade, Kellgren-Lawrence grade

3.3.2 Kinematics from Model-based Image Registration

Tibiofemoral joint kinematics during an individual step up and down were calculated for all volunteers. Average rotation and translation over three consecutive step up movements plotted as a function of flexion angle for HV1, PV1, and PV2 are seen in Figure 3-9, Figure 3-10 and Figure 3-11 respectively and step down movement in Figure 3-12, Figure 3-13 and Figure 3-14 respectively. Medial and lateral X, Y and Z translations during step up as a function of flexion for HV1, PV1, and PV2 are seen in Figure 3-15, Figure 3-16 and Figure 3-17. Standard deviation (±1) for step up graphs is shown by the blue shaded region; the mean curve is plotted as a bold blue curve and the raw individual data curves that made up the mean are plotted in black. Standard deviation (±1) for step down graphs is shown by the red shaded region, the mean curve is plotted as a bold red curve and the raw individual data curves that made up the mean are plotted in black. The reason why the in-vivo kinematics are plotted as a function of flexion angle is it allows the ability to compare directly with other studies and other activities

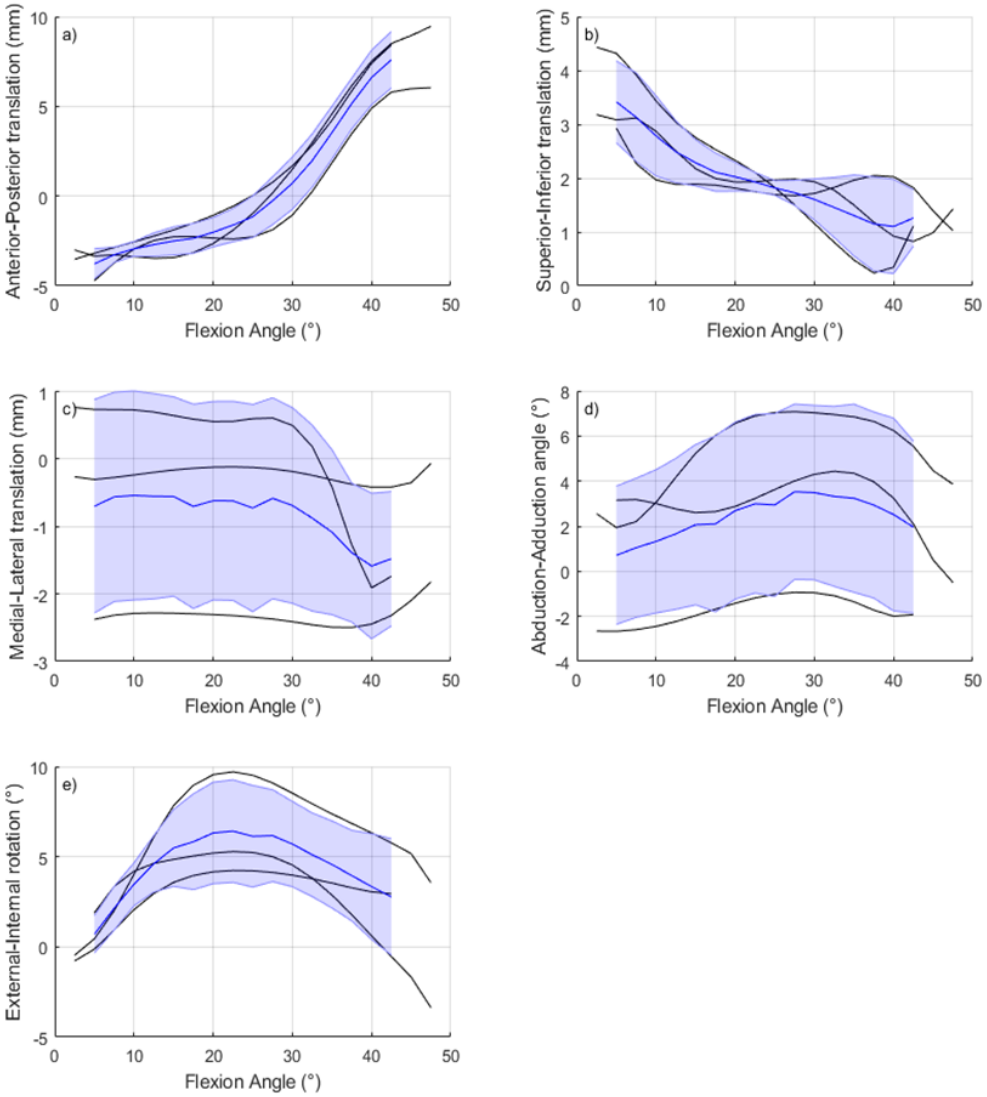

Figure 3-9 Tibiofemoral kinematics during step up as a function of Flexion (+) for HV1 **a**) Anterior(+)-Posterior(-) translation **b**) Superior(+)-Inferior(-) Translation **c**) Medial(+)-Lateral(-) Translation **d**) Abduction(+)-Adduction(-) Angle **e**) External(+)-Internal(-) rotation

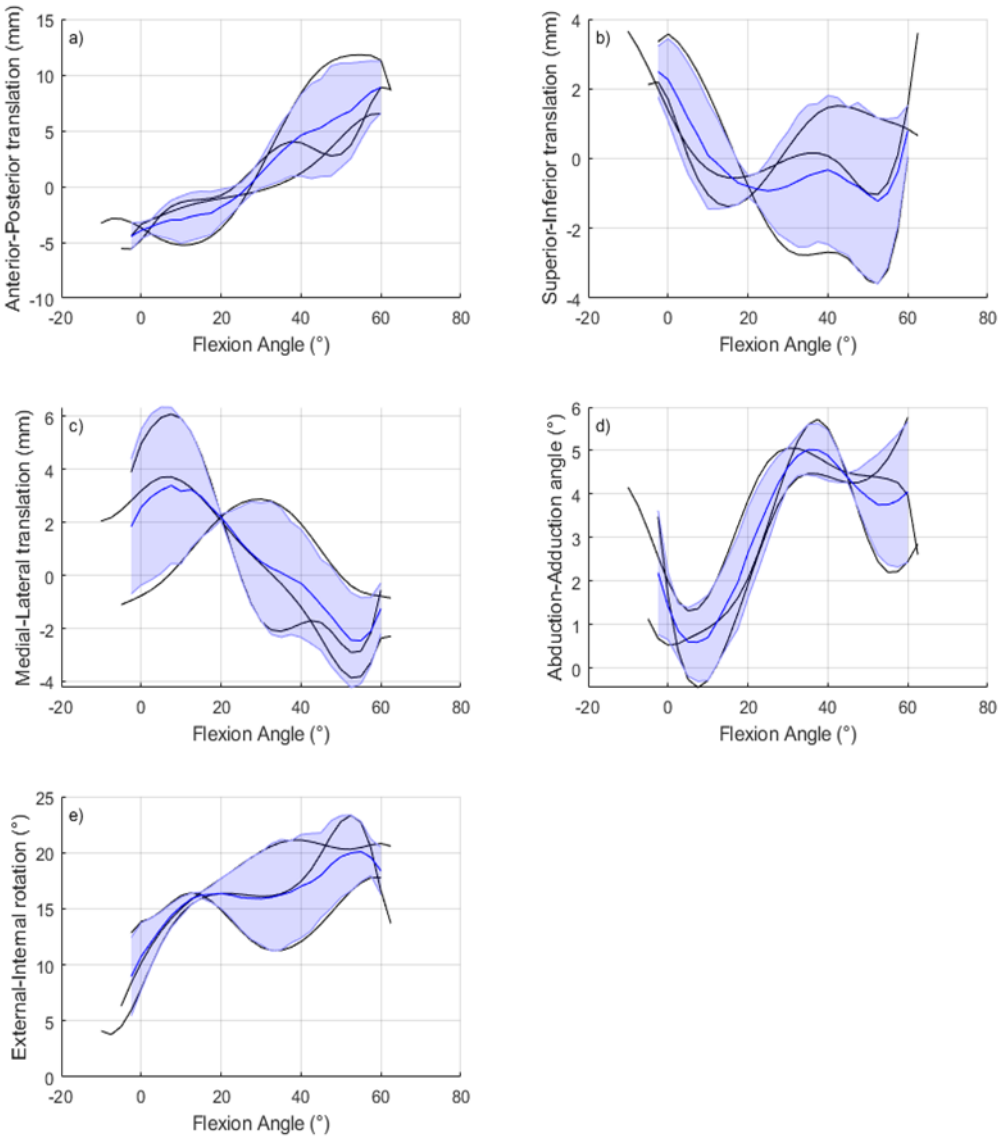

Figure 3-10 Tibiofemoral kinematics during step up as a function of Flexion (+) for PV1 **a**) Anterior(+)-Posterior(-) translation **b**) Superior(+)-Inferior(-) Translation **c**) Medial(+)-Lateral(-) Translation **d**) Abduction(+)-Adduction(-) Angle **e**) External(+)-Internal(-) rotation

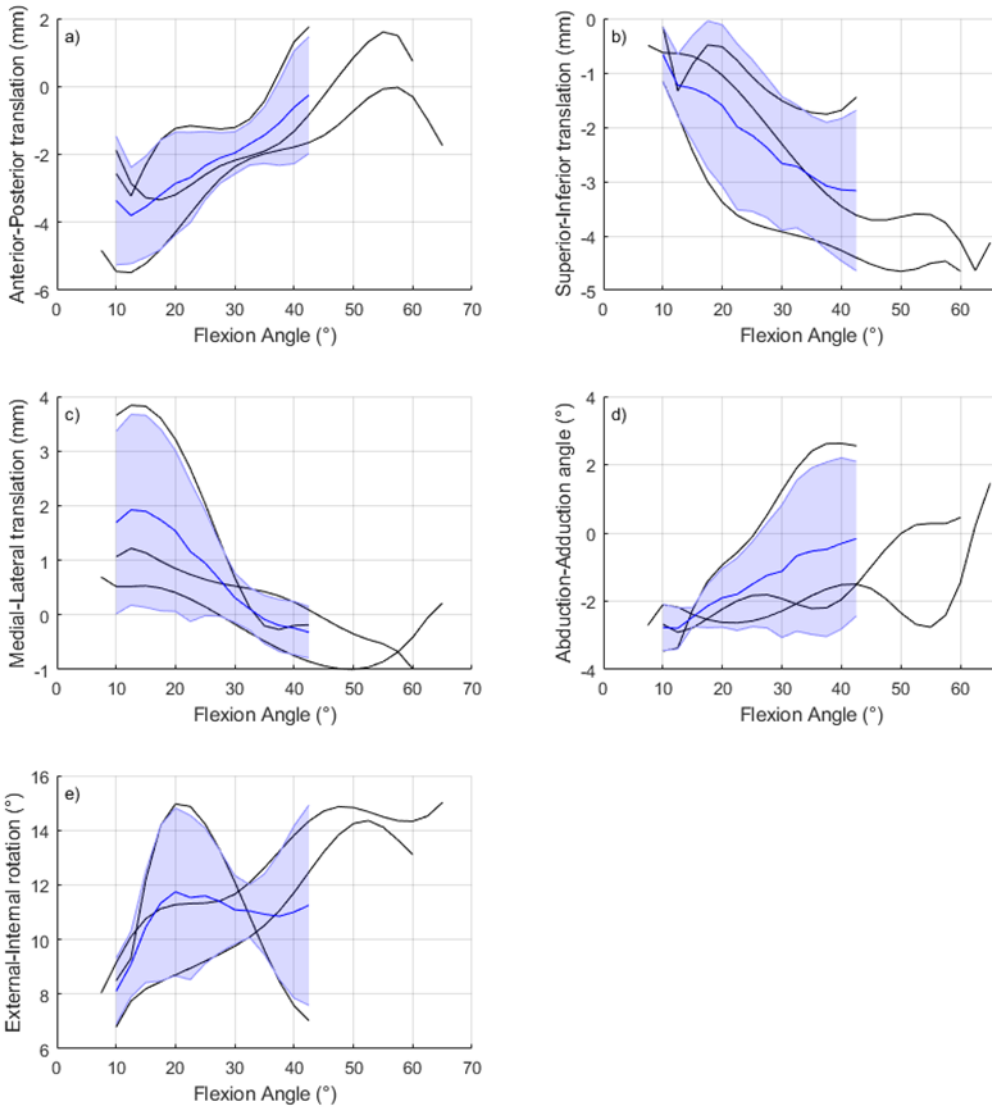

Figure 3-11 Tibiofemoral kinematics during step up as a function of Flexion (+) for PV2 **a**) Anterior(+)-Posterior(-) translation **b**) Superior(+)-Inferior(-) Translation **c**) Medial(+)-Lateral(-) Translation **d**) Abduction(+)-Adduction(-) Angle **e**) External(+)-Internal(-) rotation

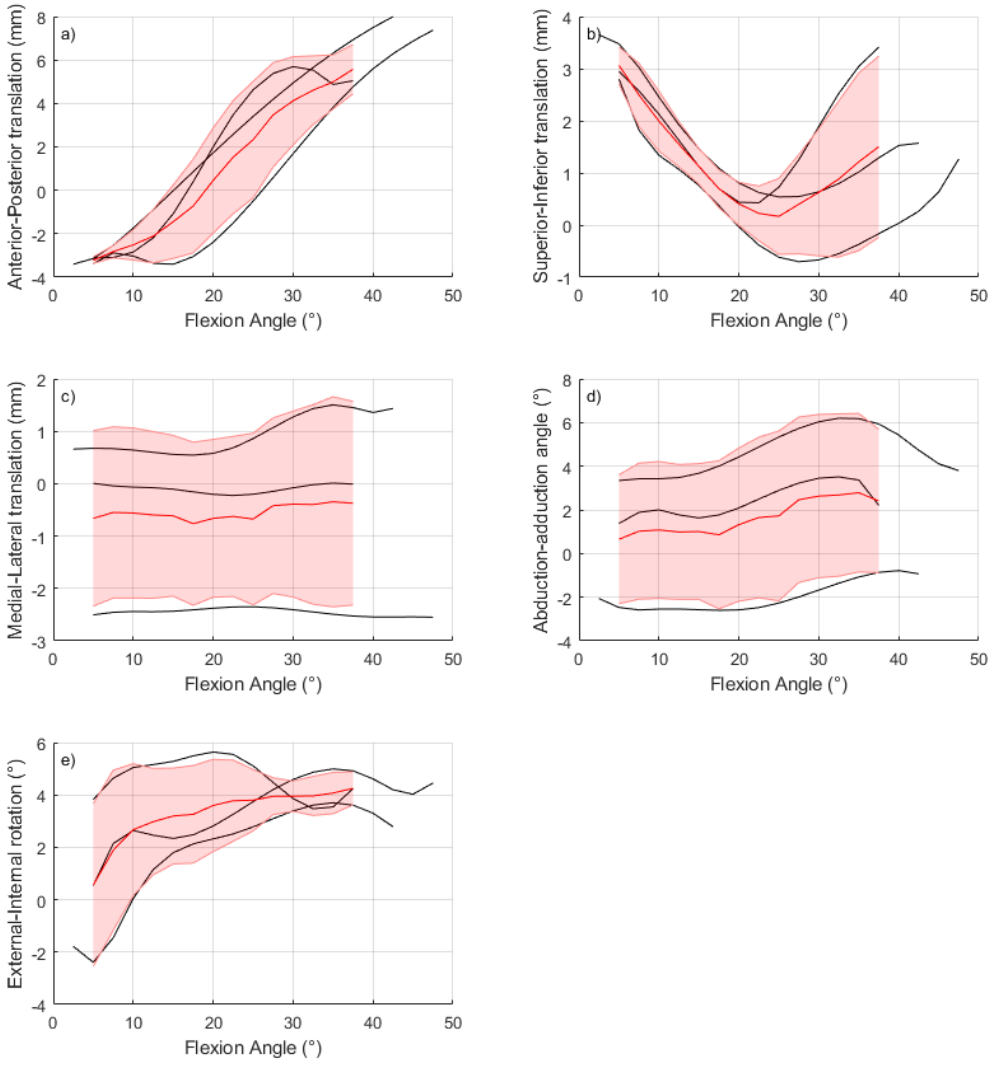

Figure 3-12 Tibiofemoral kinematics during step down as a function of Flexion (+) for HV1 **a**) Anterior(+)-Posterior(-) translation **b**) Superior(+)-Inferior(-) Translation **c**) Medial(+)-Lateral(-) Translation **d**) Abduction(+)-Adduction(-) Angle **e**) External(+)-Internal(-) rotation

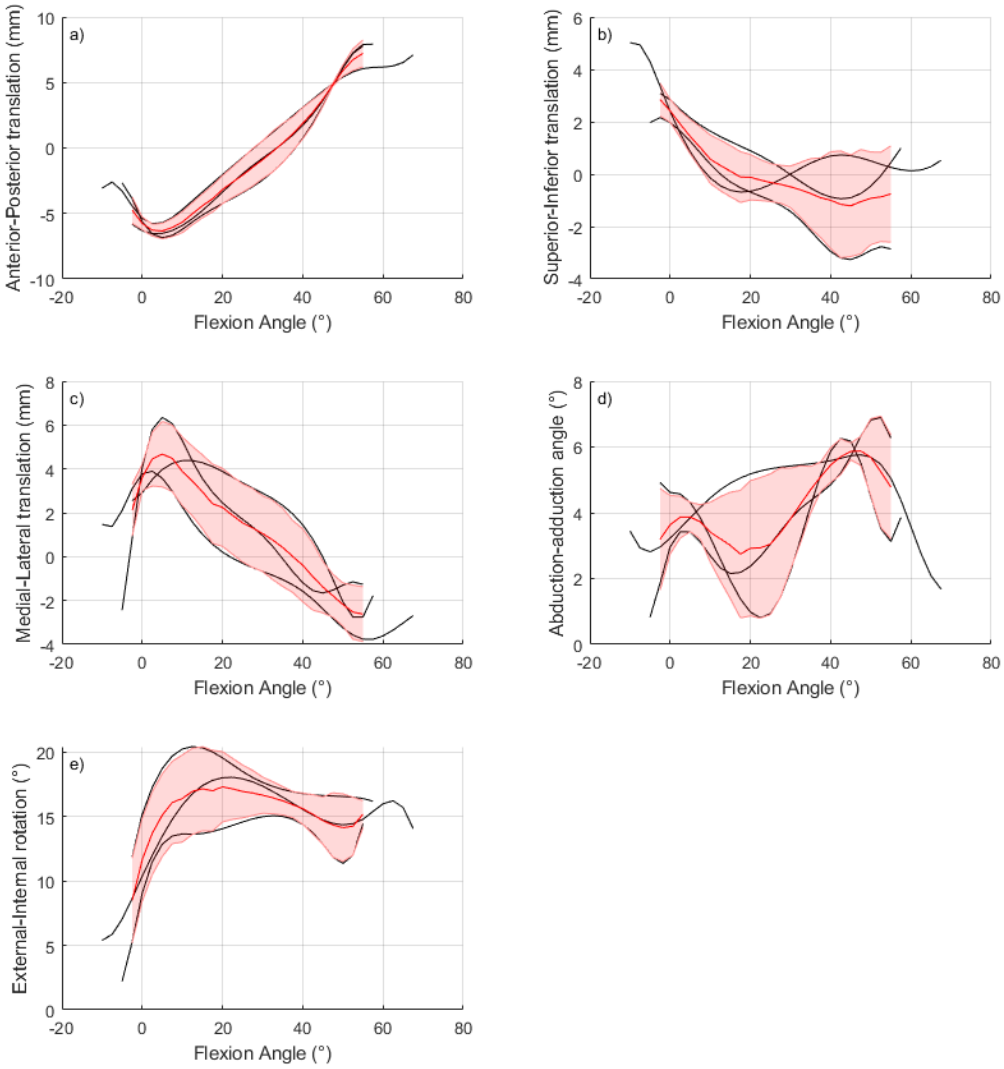

Figure 3-13 Tibiofemoral kinematics during step down as a function of Flexion (+) for PV1 **a**) Anterior(+)-Posterior(-) translation **b**) Superior(+)-Inferior(-) Translation **c**) Medial(+)-Lateral(-) Translation **d**) Abduction(+)-Adduction(-) Angle **e**) External(+)-Internal(-) rotation

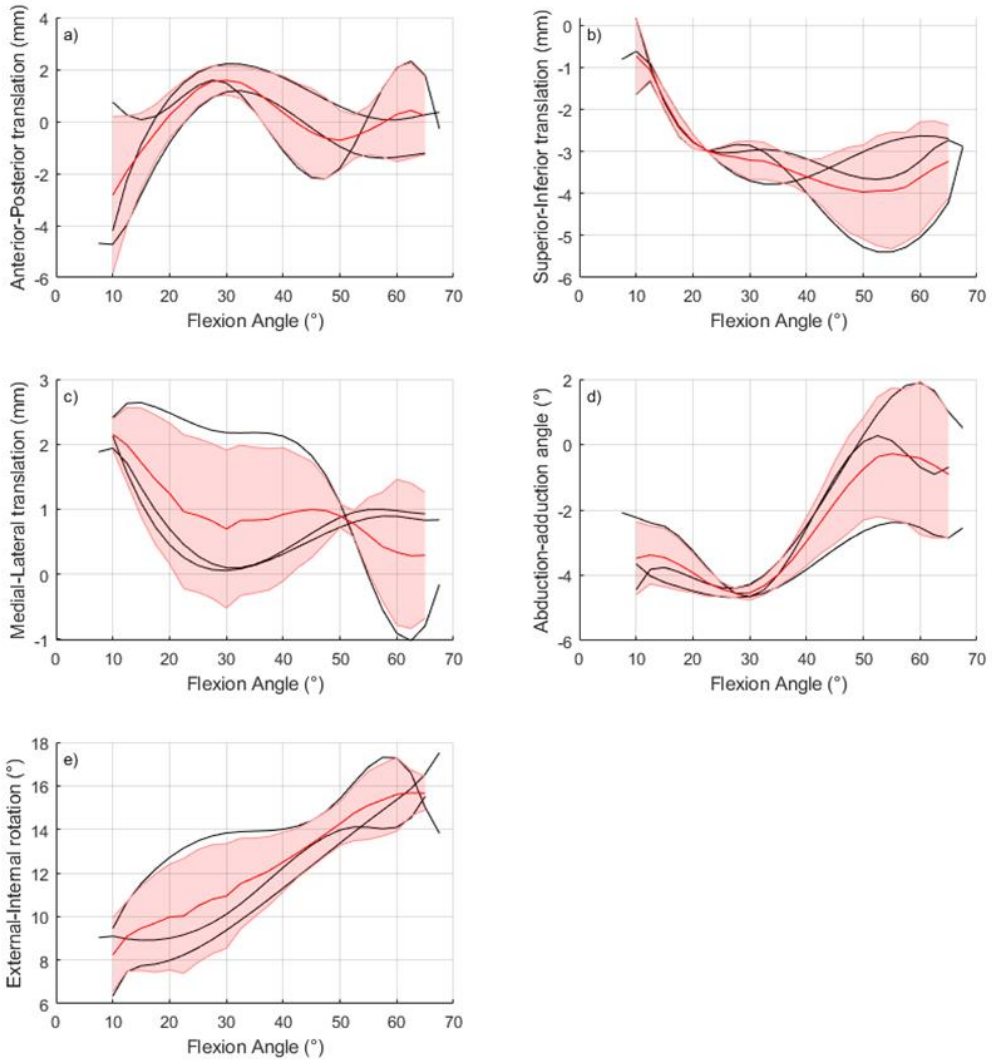

Figure 3-14 Tibiofemoral kinematics during step down as a function of Flexion (+) for PV2 **a**) Anterior(+)-Posterior(-) translation **b**) Superior(+)-Inferior(-) Translation **c**) Medial(+)-Lateral(-) Translation **d**) Abduction(+)-Adduction(-) Angle **e**) External(+)-Internal(-) rotation

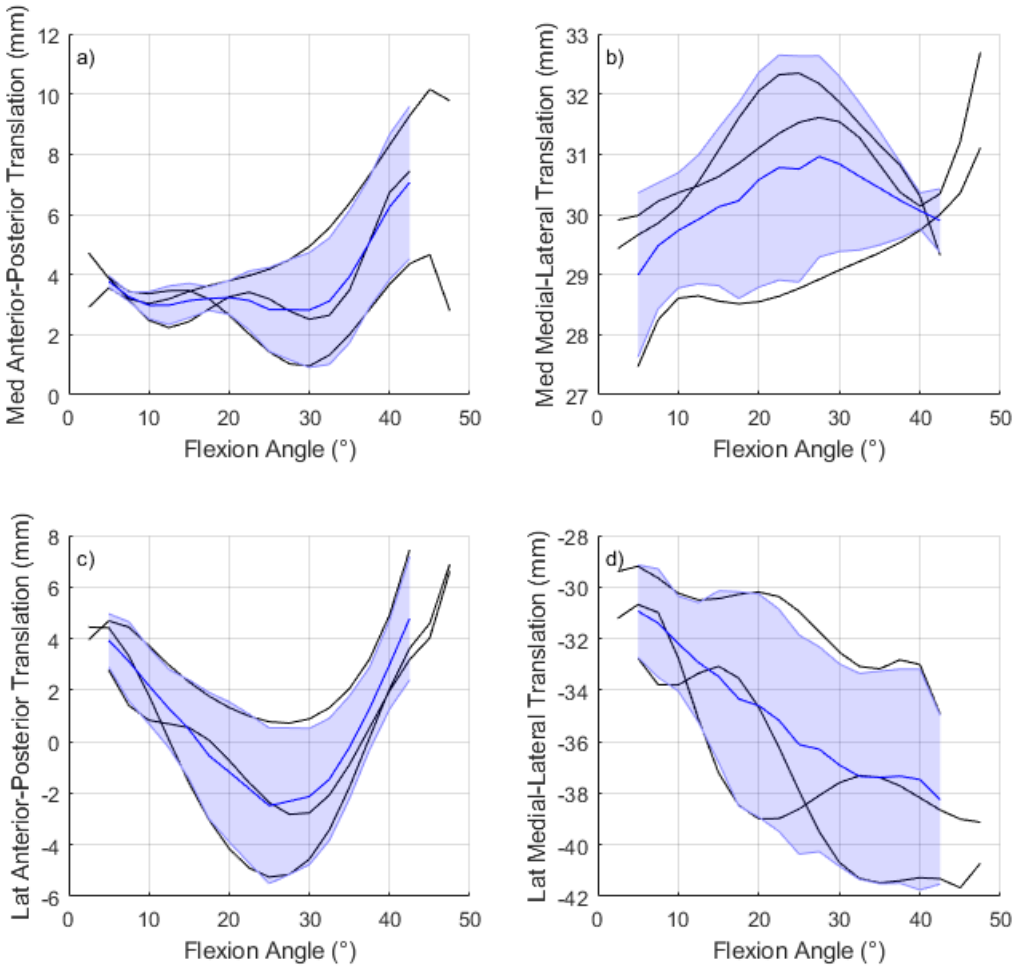

Figure 3-15 Medial and Lateral tibia compartment translations during step up as a function of Flexion for HV1 **a**) Medial compartment Anterior-Posterior translation **b**) Medial compartment Medial-Lateral Translation **c**) Lateral compartment Anterior-posterior translation **d**) Lateral compartment Medial-Lateral Translation

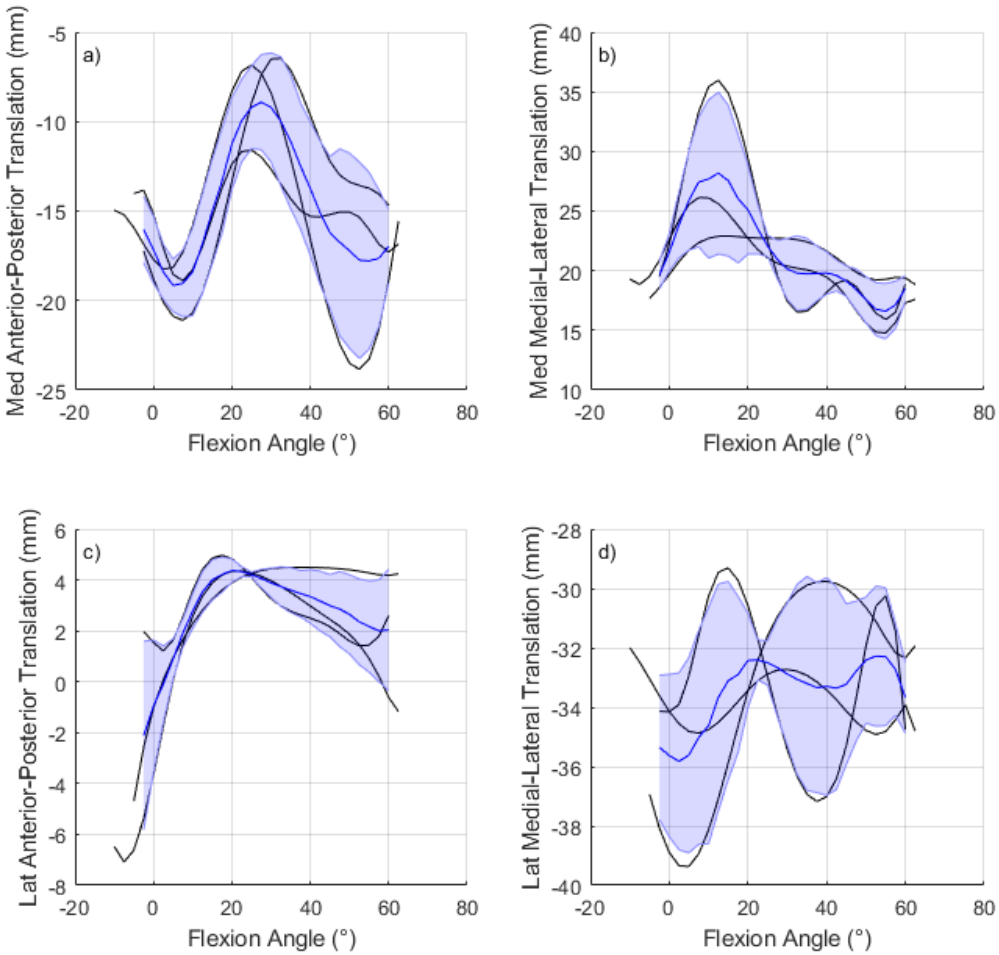

Figure 3-16 Medial and Lateral tibia compartment translations during step up as a function of Flexion for PV1 **a**) Medial compartment Anterior-Posterior translation **b**) Medial compartment Medial-Lateral Translation **c**) Lateral compartment Anterior-posterior translation **d**) Lateral compartment Medial-Lateral Translation

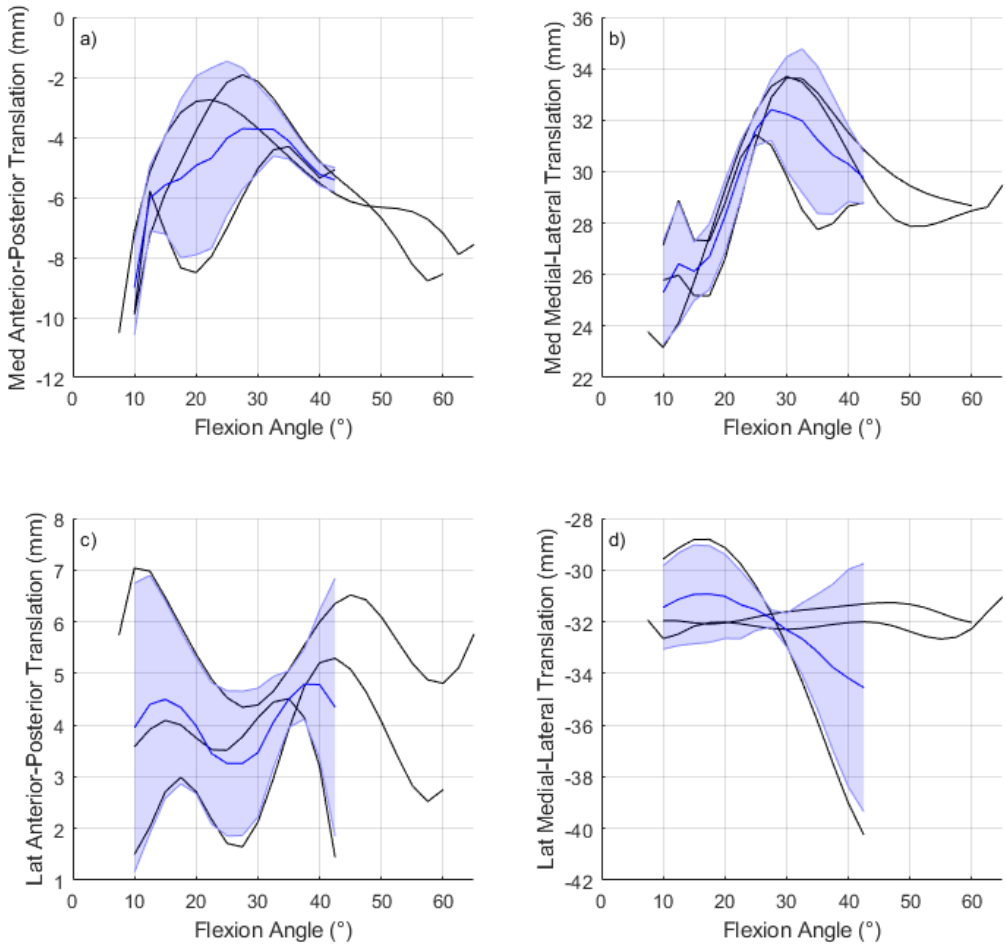

Figure 3-17 Medial and Lateral tibia compartment translations during step up as a function of Flexion for PV2 **a**) Medial compartment Anterior-Posterior translation **b**) Medial compartment Medial-Lateral Translation **c**) Lateral compartment Anterior-posterior translation **d**) Lateral compartment Medial-Lateral Translation

3.3.3 Comparison of Motion Analysis measurements and Model-based Image Registration

Differences between Motion Analysis and MBIR are compared for the Tibiofemoral joint kinematics across the whole step up and down activities for HV1, PV1, and PV2 can be seen in Figure 3-18, Figure 3-19 and Figure 3-20 respectively. The motion analysis is highlighted with the red curve and the MBIR in the blue curve. The offset and fluoroscopy frequency calculations for each volunteer can be seen in Table 3-3.

Table 3-3 Calculated time offset and fluoroscopy frame rate for each volunteer using the methods defined in section 3.2.2.3

Volunteer ID	Calculated Offset Time (Seconds)	Calculated Frame Rate (Hz)
HV1	1.30	30.40
PV1	0.46	30.08
PV2	0.51	29.78

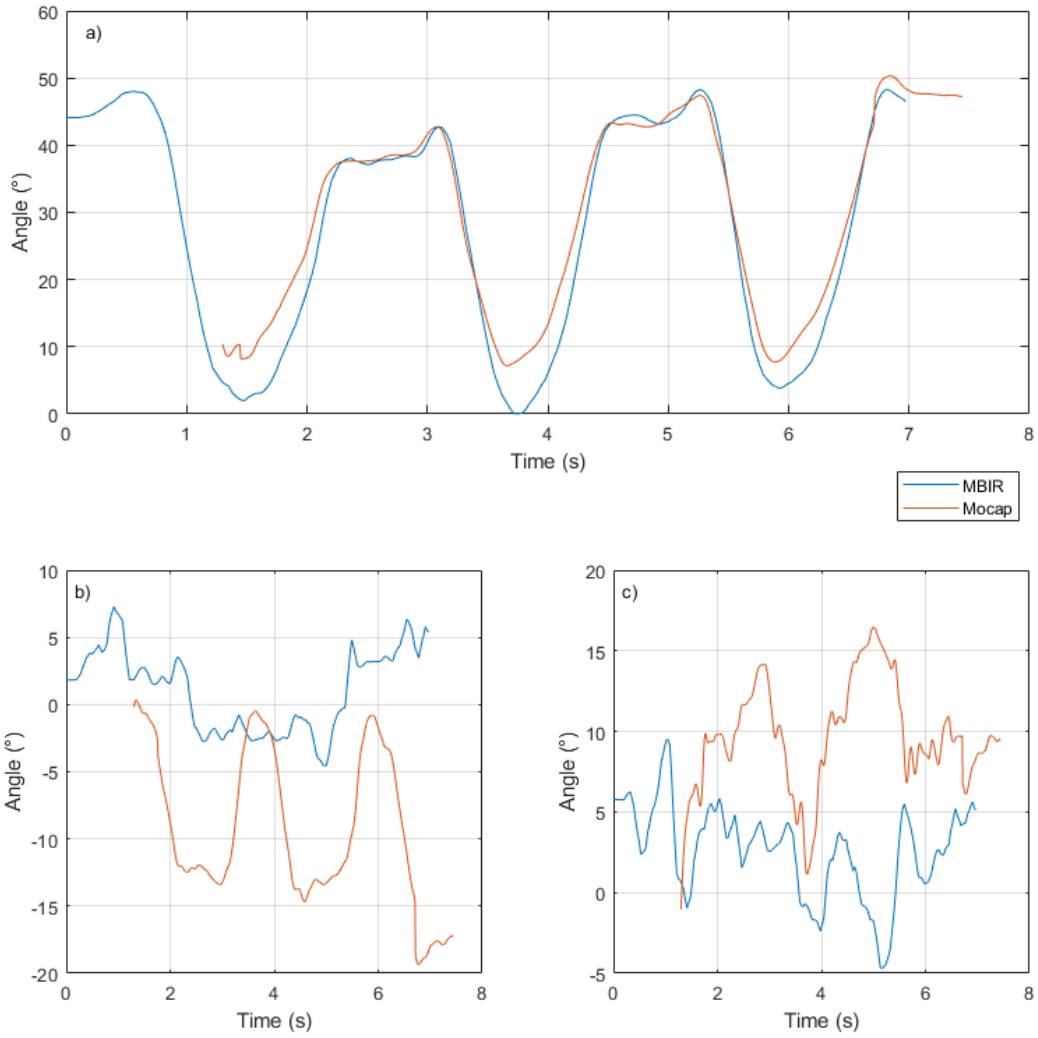

Figure 3-18 Time synchronised Tibiofemoral kinematics from Model Based Image Registration (blue) and Motion Capture (Red) for HV1 during three consecutive step up and down activities a) Flexion-External angle b) Abduction-Adduction angle c) Internal -External Rotation

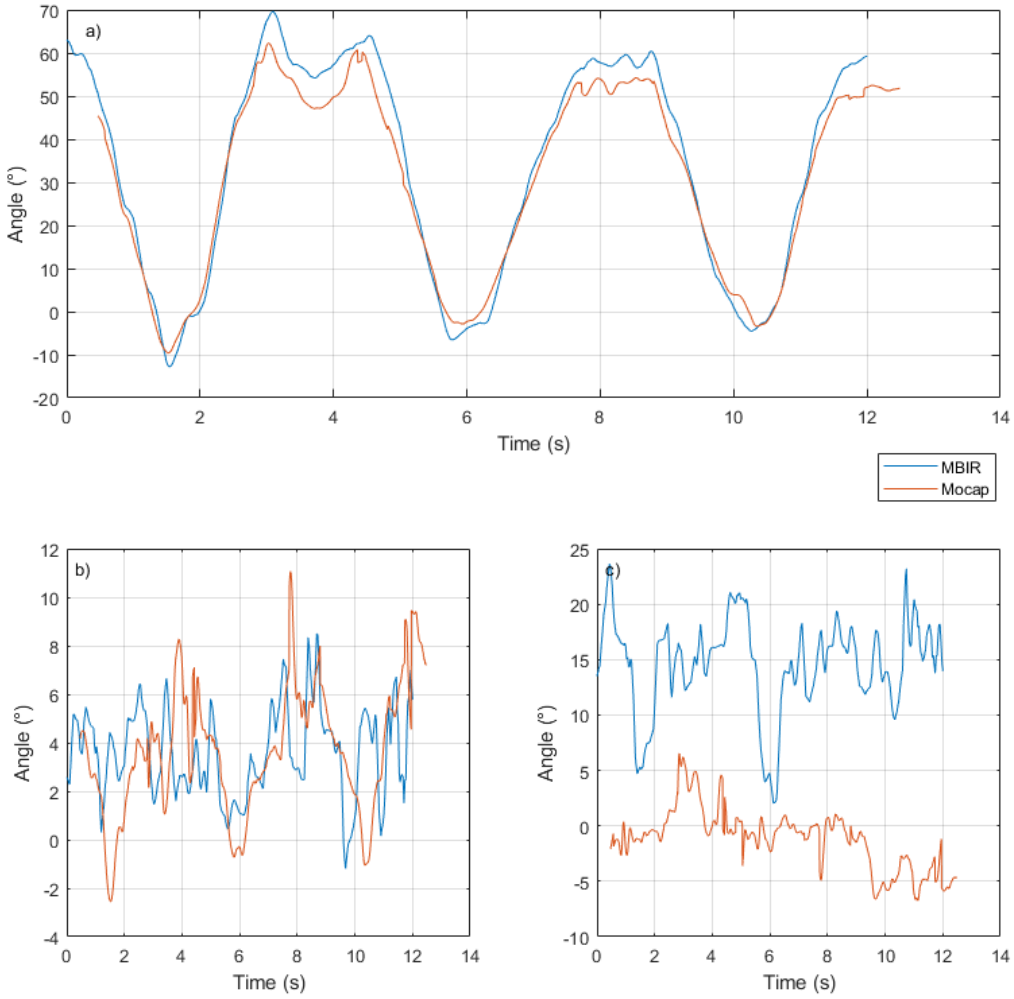

Figure 3-19 Time synchronised Tibiofemoral kinematics from Model Based Image Registration (blue) and Motion Capture (Red) for PV1 during three consecutive step up and down activities a) Flexion-External angle b) Abduction-Adduction angle c) Internal -External Rotation

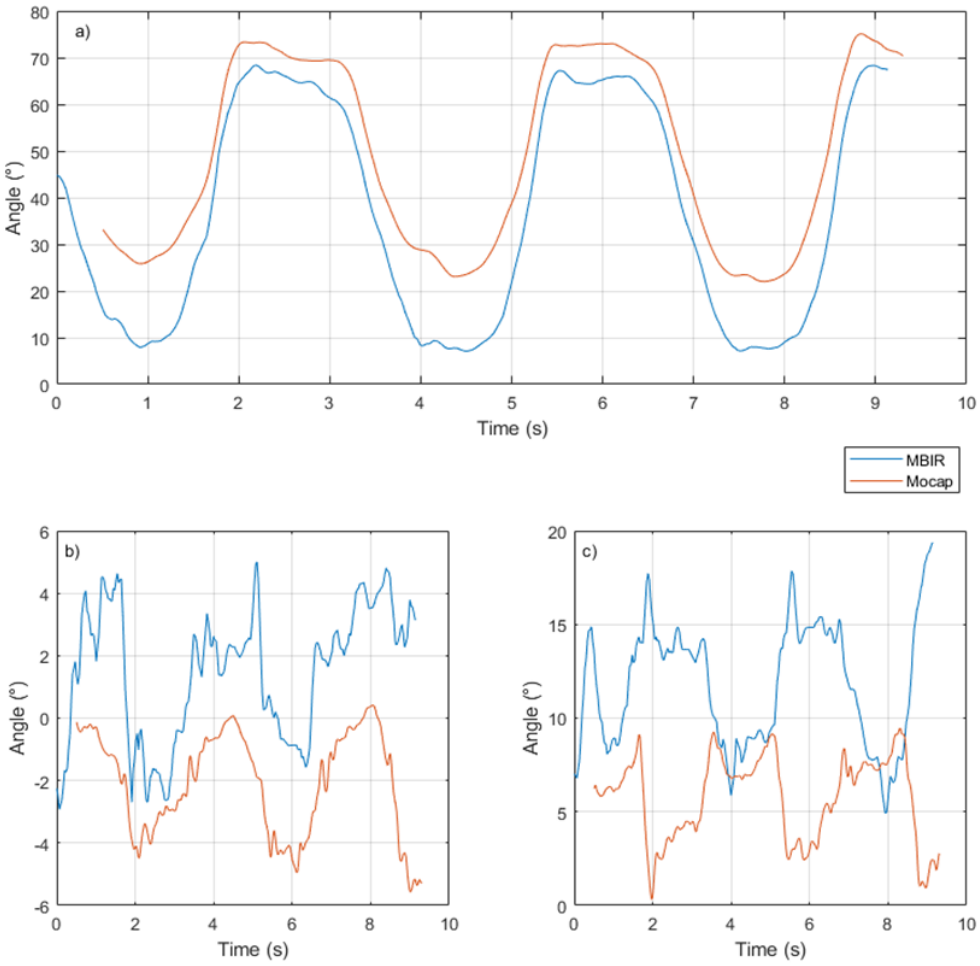

Figure 3-20 Time synchronised Tibiofemoral kinematics from Model Based Image Registration (blue) and Motion Capture (Red) for PV2 during three consecutive step up and down activities a) Flexion-External angle b) Abduction-Adduction angle c) Internal -External Rotation

3.4 Discussion

The main achievement of this study was the development of an improved MBIR processing protocol for single plane fluoroscopy using MRI derived 3D models. This allows the processing of existing data collected at Cardiff and will form the foundation of future fluoroscopy protocols. It is the first time that the combination of motion analysis and MBIR has been completed at Cardiff University. Motion analysis data of the other lower limb joints was also collected but has not been reported, this is due to issues with data quality that will be explained in depth in section 3.4.3.

3.4.1 Kinematics from Model-based Image Registration

3.4.1.1 Step Up Activity

All volunteers during step up posteriorly translated their femur relative to the tibia. When comparing HV1 (Figure 3-9a) and PV2 (Figure 3-11a), PV2 has less ROM during complete AP translation (4mm) over the entire step up movement compared with HV1 (10mm). It has been suggested that the reduction in AP translation for volunteers with medial OA could be related to cartilage-bone erosion specifically on the medial compartment and soft tissue contractures due to the presence of osteophytes (Hamai et al. 2009; Fiacchi et al. 2014). When inspecting PV2, it was found that the 3D bone surface and MR images showed that there was an approximately 5mm focal cartilage defect on the posterior surface of the medial condyle of the femur (Figure 3-21). The reduced overall AP translation seen during step up could be due partially to cartilage-bone erosion.

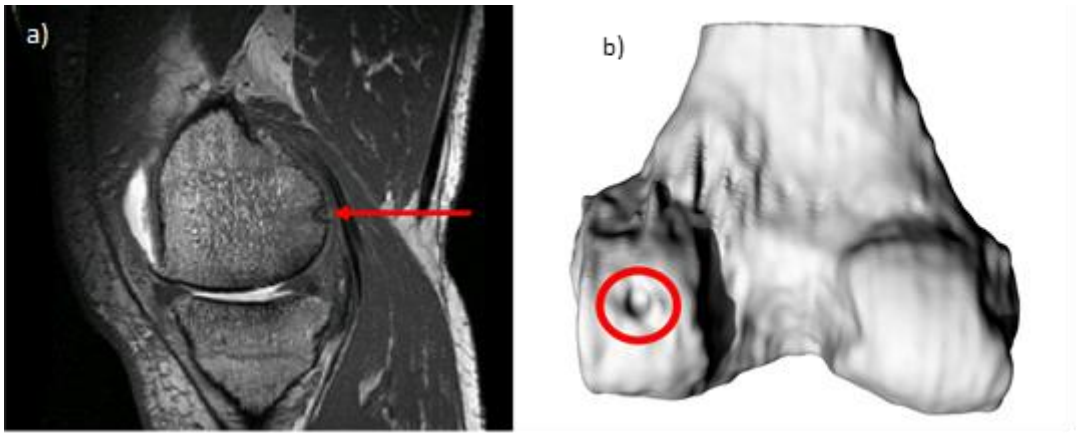

Figure 3-21**a**) Sagittal view of PV2 high res MRI, the red arrow highlights a suspected focal cartilage defect on the posterior side of the medial condyle **b**) Shows the 3D rendered model of the segmented scan with a red circle highlighting the position of the defect. The defect was measured on the MRI and measured approximately 5mm in diameter.

When comparing HV1 and PV1 (Figure 3-9a and Figure 3-10a) total AP translation, PV1 (14mm) ROM is greater than that of HV1 (10mm). This seems to contradict what was said previously, however on investigation of the history provided by PV1 it became apparent that they are anterior cruciate ligament (ACL) deficient. Research using biplane fluoroscopy on ACL cohorts looking at different activities has found that there is an increase in AP translation with patients who are ACL deficient (Yang et al. 2018). This could explain the large ROM of seen for PV1 compared with HV1.

Examining the individual AP translation of the medial and lateral condyles during step up showed a greater ROM for AP translation in the medial compartment for both PV1 and PV2 compared with HV1. Comparing this to what has been described in the literature, a normal healthy knee has typically small AP translation in the medial compartment during step up activity (Komistek et al. 2003; Moro-Oka et al. 2008). The increased medial AP translation of the OA patients could further cause degeneration as it has been shown that these small increases can cause detrimental changes to the loading of the cartilage.

The individual lateral and medial compartment translations were calculated using the closest point method defined in section 2.2.4.6.3. This is a common

approach for fluoroscopy studies, with most studies generating 3D subject specific bone models from Computed Tomography data. However, these studies do not consider the influence of soft tissue on the closest points. Defrate et al. (2004) looked at the differences between using bone models alone and combined cartilage and bone model. They found that at low flexion angles, the estimated closest points using bone models alone overestimated the movement of the contact points on the tibia surface (Figure 3-22).

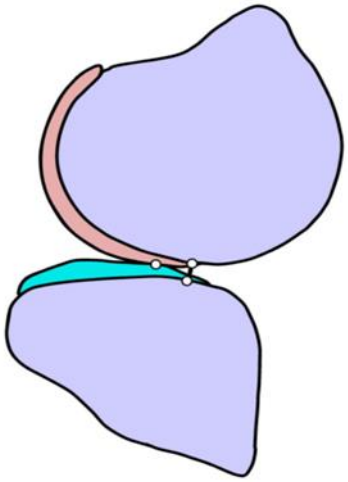

Figure 3-22 Sagittal view of the femur, tibia and respective cartilage surfaces. The difference between closest point between femur and tibia and the cartilage contact point is shown, with the cartilage contact point being more posterior compared with the bone closest point (reproduced from Defrate et al. (2004))

In the context of this study, femoral and tibial cartilage were not segmented due to the in-plane resolution of the MRI scans not being sufficiently high to delineate cartilage from subchondral bone. Additionally, this approach may not be suitable for single plane fluoroscopy studies due to the medial lateral translation errors which lead to inaccurate closest point position calculations.

The overall medial-lateral translations, although reported (Figure 3-9, Figure 3-10 and Figure 3-11), are considerably smaller compared to AP translations and show wide variability. Fluoroscopy imaging takes place in the sagittal plane as this has the greatest benefit when imaging the knee during the stair activity. This causes the out of plane translations to take place in the medio-lateral direction which makes the translational changes appear as a change in

magnification as opposed to a translation (Kanisawa et al. 2003). These small changes and the inaccuracies reported range between 1mm to 4mm for high contrast implant studies (Banks and Hodge 1996; Komistek et al. 2003; Acker et al. 2011), and are even greater in intact knee studies and are not discussed within this intact knee single-plane study.

Knee axial rotation varied between the volunteers. HV1 starts, prior to step up, at approximately 0° axial rotation. During 40-20° of knee extension the tibia externally rotates and finally between 20° and 0° of knee extension the tibia internally rotates back towards 0° axial rotation. This sharp external rotation towards the end is known as the 'screw-home' mechanism and is essential for knee stability (Hallén and Lindahl 1966).

Over the three movement PV1 and PV2 started externally rotated and during step up internally rotate. This initial external rotation of tibia starting point could be related to the varus deformity that is present due to OA or could be the cause of the medial OA present in both patient volunteers. A CT scan based study by Matsui et al. (2005) found that where volunteers with severe OA had a varus deformity, this tended to be related to an external femur rotational deformity. When comparing these results to other single plane fluoroscopy medial OA studies (Hamai et al. 2009; Fiacchi et al. 2014) looked at femoral-tibial kinematics volunteers were unable to reach full extension. In the current study both patient volunteers were able to reach full extension and demonstrate the 'screw home' mechanism. This could be due to the selection criteria of the volunteers who had been referred for high tibial osteotomy, which is suited more for patients who have medial OA but still have a good range of motion (Lee and Byun 2012). So they may have better overall function compared with the severe OA patient studies (Hamai et al. 2009; Fiacchi et al. 2014).

Knee frontal plane angles for PV1 and PV2 changed from abduction to adduction as the knee extends during step-up. PV1 on average remained varus aligned over the entire step up activity while PV2 remained more valgus aligned. One biplane study (Defrate et al. 2006) looked at volunteers with ACL deficiency performing a weight bearing lunge activity and found that they remained in a valgus position during the entire movement. No other studies

have reported on the frontal plane angles during single plane fluoroscopy of medial OA volunteers during a stair activity. This could be due to the activity mainly occurring in the sagittal plane with the volunteers already having a frontal plane deformity, and the main research interests being to investigate what affect this has on the other rotations and translations.

3.4.1.2 Step Down

Step down kinematic data was processed (Figure 3-12, Figure 3-13 and Figure 3-14) but due to the lack of literature on intact knee kinematics during step down and the small sample size it was not investigated further. The lack of literature is most likely due to the step-up activity being seen more suitable for detailed analysis as it is weight bearing and represents an activity of daily living (Banks 1992). However, in-vivo kinematics for step down may be worth investigating in the future with a larger cohort as the activity involves transitioning from a stable to unstable situation.

An example of this can be seen when comparing AP translation during step down for all subjects. PV1 has a greater AP translation ROM (12°) than compared with PV2 (4°) and HV1 AP ROM (8°). This is most likely due to PV1 being ACL deficient and allowing greater posterior translation during step down compared with HV1 and PV2. PV2 could have a reduced ROM due to the focal cartilage defect seen in Figure 3-21.

Although the in-vivo kinematic data presented in this study is from a very small cohort, it shows the additional benefit of measuring this information. This is highlighted with the inclusion of the AP translation as this study has shown that it can be used to provide information on patient specific pathologies.

3.4.2 Comparison of Motion Analysis measurements and Model-based Image Registration

The comparison between MBIR and Motion Analysis calculated knee flexion can be seen in Figure 3-18, Figure 3-19 and Figure 3-20. For HV1 (Figure 3-18a) the rate of extension and peak flexion appears to be the same for both

methods. However, between 10 ° of flexion to peak extension motion capture is found to underestimate the amount of extension for all three cycles, with a maximum of 8° difference between the two methods.

For PV2 (Figure 3-20a) there was an overall offset which was greatest during extension with a maximum difference of 15°. For PV1 (Figure 3-19a) the two flexion curves are similar during both the step up and down movements. However, the flexion angle was determined by MBIR to be greater when the knee flexion went past 70° in between the step up and down movement.

For HV1 the abduction angle during the stair activity varies between the two methods (Figure 3-18b). For motion capture it oscillates between 0° and -15° while for MBIR the oscillation is between 5° and -5°. For PV2 the differences between motion analysis and MBIR aren't as great as HV1, there is a general offset ranging between 2-4°. For PV1 over the entire movement the adduction angle for both systems follows a similar kinematic profile. However, the motion analysis has some high peaks with a difference of 4° or higher in several places (Figure 3-19).

Considering differences in axial rotation for HV1 there is an initial offset during the first step up of approximately 5° between motion capture and MBIR (Figure 3-18). During the second step the motion analysis system detects a large external rotation while the MBIR technique detects an internal rotation. For PV2 the two systems show opposing patterns, for example, during the first step down the MBIR detected a change in external rotation from 9° to 17° while the motion capture for the same movement outputted an internal rotation from 9° to 0° (Figure 3-20). This was investigated further to check for sign or calculation errors, none were observed. For the PV1 the axial rotation angle overall was offset by approximately 15°, with a change in angle of about 10° for MBIR during step up.

For all volunteers the main differences between motion analysis and MBIR occur within frontal and axial rotations. There are several confounding explanations that could help understand these differences for the knee angles.

One of the main explanations of differences would be soft tissue artefact in motion capture. Soft tissue artefact has been investigated in other studies with

fluoroscopy, (biplane and single-plane), being used as the gold standard comparison (Garling et al. 2007; Tsai et al. 2011; Miranda et al. 2013; Fiorentino et al. 2017). The investigation of this comparison was one of the primary reasons why this study was carried out, with the aim being a way of quantifying these errors.

Soft tissue artefacts can introduce significant errors and these errors can propagate if the volunteer has a large BMI, as bony landmarks get more challenging to palpate. This not only influences the movement of markers during dynamic activities but can also have a serious influence on the placement of markers on anatomical landmarks. The landmarks most likely to be affected are used to define the pelvis and the proximal femur as discussed in section 2.2.2.2. This could explain why HV1 and PV2 have greater differences compared with PV1 as they both have a larger BMI when compared with PV1. Considering the abduction and axial angles for HV1 and PV2 there is evidence of the 'cross-talk' effect with the motion analysis data which is known to overestimate the abduction and axial rotation angles (Reinschmidt et al. 1997; Freeman and Pinskerova 2005; Baudet et al. 2014). This error causes angular motion around one axis to be calculated as being part of another axis. This is most evident in the abduction angle for HV1 (Figure 3-18b). This could be due to incorrect marker placement or errors with STA causing the axis to be incorrectly defined.

Another explanation to consider is that the CAST marker set used for motion analysis uses different landmarks to define segments compared with the approach used in MBIR. The approach used for MBIR (Moro-oka et al. 2007) defines the origin of the femur and tibia to be the midpoint between the femoral epicondyles while the motion analysis uses the midpoint between the medial and lateral epicondylar gap. The same landmarks for MBIR are used to define the medio-lateral axis and the centre of the femoral head as defined fitting spheres onto MR derived long leg bone models. For motion analysis the hip joint centre is defined using the approach defined by Harrington et al. (2007) and is the current approach using this marker set at Cardiff University recommend by previous studies (Biggs 2016). The approach uses regressive equations that rely on relationships defined by anatomical landmarks on the

pelvis. Comparing different coordinate systems is challenging as even subtle changes in position of landmarks can introduce different rotations and translations between systems (Zatsiorsky and Zaciorskij 2002).

The global coordinate systems between the two measurements systems during data collection were aligned by the placement of the L-frame on top of the image intensifier in line with the fluoroscopy axis defined using the image intensifier. This, in theory, would align the two systems, however as it relies on human placement it may be firstly inconsistent per volunteer and secondly if not positioned perfectly introduce deviations between the fluoroscopy and the motion analysis. This means that looking at individual marker movement to quantify soft tissue artefact cannot be performed. This has been done in a number of studies (Tsai et al. 2011; Miranda et al. 2013) to quantify the errors encountered during motion analysis and requires use of a transformation matrix to convert motion analysis marker positions into the fluoroscopy global coordinate system.

The challenge with using single-plane fluoroscopy as the gold standard in this study is that the accuracy and precision of the technique and the fluoroscopy system is not known. Within the literature there is reference to the accuracy of the model based image registration technique defined in the landmark paper by Banks and Hodge (1996) as an accuracy of better than 1° and 0.5 mm. This paper relied on computer simulated images of X-rays and looked at a single knee implant component to validate the technique. In a later paper the true accuracy of the technique's ability to calculate knee rotations was determined to be 2.11°, 0.31°, and 1.11° in flexion, abduction, and axial rotation respectively (Acker et al. 2011). Both studies were considering implanted knees within ideal conditions, the registration accuracy is expected to drop even further with intact knees due to the decreased contrast between bones compared with implants. With all this considered it is it is difficult to determine if it is due to errors in this study are present from the motion analysis technique or from the MBIR technique.

The results in Table 3-3 show that the trigger used did not produce a consistent recording delay between volunteers for fluoroscopy and motion capture synchronicity. Although these were later synchronised using the method

described in section 3.2.2.3 it shows the method of triggering from the fluoroscopy using an X-ray Monitor Diode may not be the best approach.

3.4.3 Limitations and Challenges

3.4.3.1 Synchronisation

This 'reactive' trigger relies upon the detection of X-ray backscatter after the X-ray exposure. The time when a backscatter of X-ray is detected is not predictable nor a consistent time. This is due to how X-ray photons are generated in the X-ray tube and how scatter occurs.

X-ray photon generation occurs when a stream of electrons hits a spinning tungsten target, which it may turn into an X-ray photon. The probability of generating a photon is dependent on the current, the voltage across and the quality of manufacture of the X-ray tube. The X-ray photons are then directed towards the volunteer, with approximately 90% absorption. These absorbed photons may generate scatter photons which travel in all direction (Faulkner 2012).

The Monitor Diode works by detecting these scatter photons, therefore it is influenced by where it is positioned relative to the volunteer and the size of the volunteer being exposed. Subsequently there is no repeatable position that can guarantee a consistent offset between volunteers or between separate exposures within the same exposure. The problem with this delay is that motion capture data can miss part or all the initial step up during the activity. Therefore less data is collected as re-exposing the subject is limited because there is a fixed exposure time for a volunteer during any specific research trial.

For future studies it is recommended that a different trigger is used that works in conjunction with the trigger used to generate X-rays. If this is not possible the method described in section 3.2.2.3 is an appropriate method for determining these delays.

The calculated fluoroscopy frequency for each volunteer in Table 3-3 shows that the frequency of the fluoroscopy data grabber is approximately 30Hz. The

peak to peak method is dependent on the accuracy of the input data but the results shown here suggest it is an acceptable approach to approximate the sampling frequency.

3.4.3.2 Motion analysis

There were clear issues with inconsistent data quality regarding the motion capture. There was significant motion analysis marker drop out for all volunteers, which meant that certain motion segments had to be ignored completely with only two or less tracking markers being present during the trial. Other errors included incorrect 3D positioning of markers by motion capture cameras, with the markers being positioned an unrealistic distance away from the volunteer (Figure 3-23).

These errors can be reduced in QTM by segmenting the incorrect marker trajectories and applying a gap fill on the incorrect position using polynomial curves. This can only be applied for a certain number of frames (less than 20) and as it uses a prediction algorithm that can introduce errors. This caused errors within the moment calculations which in turn caused erroneous peaks based on motion segments dropping in and out.

The pelvis anatomical markers were especially prone to drop out which would cause problems with the definition of the hip joint centre. This could explain some of the major deviations for in all three rotation calculations.

One of the main reasons for marker drop out is due to the challenge viewing a single marker by using two separate motion analysis cameras during the recorded movement when other equipment such as the fluoroscopy systems are occluding one or both fields of view. To improve this, the camera locations must be optimised which requires a great amount of time, this was not possible in the hospital X-ray department setting. Once defined the cameras must be retained in these positions; this was challenging within the context of this study as the fluoroscopy equipment used was part of the fluoroscopy suite at Llandough NHS hospital and it was difficult to gain access for the time required due to normal clinical demands. This also caused problems with recruitment

of volunteers to this study as it was difficult to book the time required to set up cameras and all the other equipment, in a consistent way.

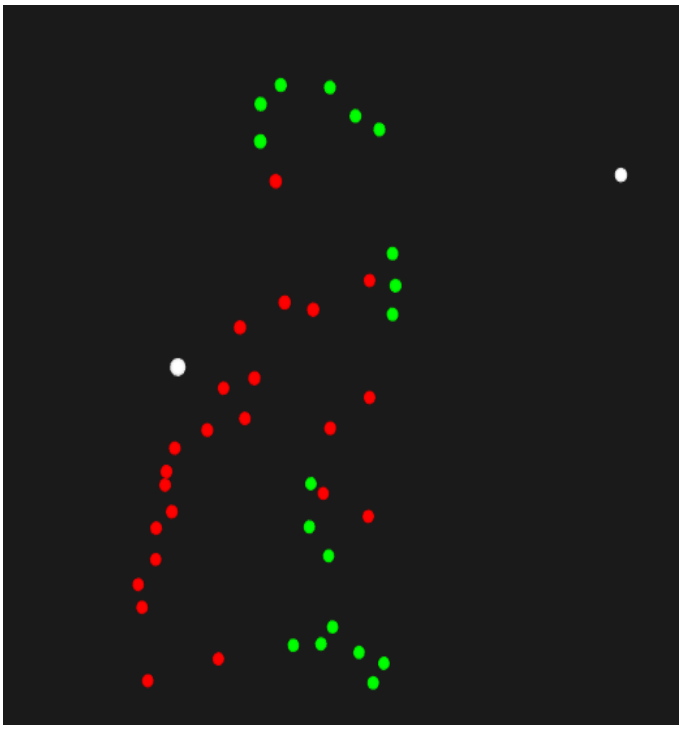

Figure 3-23 Screenshot from Qualisys Track Manager showing a volunteer performing a step-up activity. The green highlighted markers are the tracked markers, the red untracked and the white highlighted markers show the incorrect positioning of markers by the detection of the motion capture cameras.

3.4.3.3 Fluoroscopy

The fluoroscopy image quality varied between volunteers and this could be due to a hardware limitation or inconsistent imaging parameters between volunteers (Figure 3-24). During one of the step-up sequences PV1's knee moved outside the field of view making the image registration much more challenging.

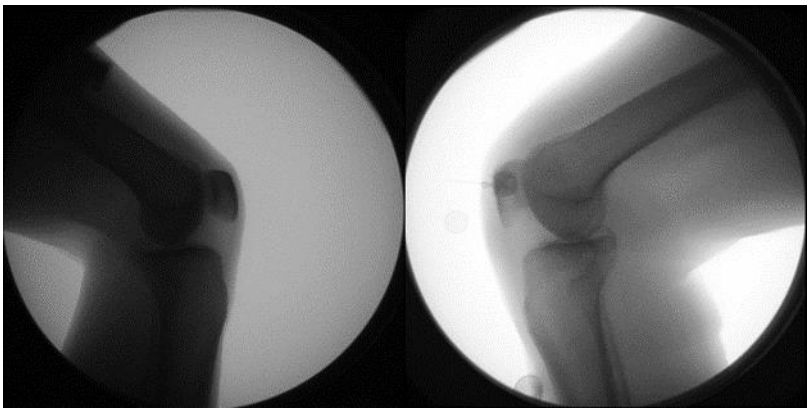

Figure 3-24 Two images from separate volunteers highlighting the difference imaging parameters have on the contrast of the tibiofemoral joint.

Registering the tibia bone models axial rotation is particularly challenging using the sagittal plane alone. This is due to contrast between the different bone features such as the intercondylar tubercles meant that any changes were challenging to see. Compared with the TKR components used in Chapter 2, bone appearance is more subtle as it is not highly contrasted with the other structures in the knee. Other single plane studies (Moro-oka et al. 2007; Hamai et al. 2009; Fiacchi et al. 2014) investigating kinematics of intact knees have used a flat panel based system. Although this typically had a lower sampling rate (8-10Hz compared to 30Hz) the contrast between structures and image quality is superior. These studies tended to use pulsed X-ray instead of continuous. Using pulsed X-rays potentially decreases blurring that occurs during dynamic movement. This is due to short X-ray pulse widths used during pulsed X-Ray of between 2-10ms per frame which has been shown to improve accuracy of image registration (Ellingson et al. 2017). Comparing with continuous X-ray which has a consistent X-Ray beam the amount of exposure per frame is 33ms for a 30Hz sequence. The longer the exposure per frame, the more the subject moves within the field of view, increasing the likelihood of blurred images.

3.4.3.4 MRI

Some problems were faced with MR segmentation for PV2 as part of the high-resolution scan of the knee joint was missing on the lateral side. This meant a complete tibia or fibula 3D model could not be segmented. This introduced potential errors with defining the anatomical coordinate system using registered long leg models. Additionally, this influenced the accuracy of the MBIR approach for PV2 as tibia axial rotation position may have been compromised.

Image segmentation of MRI is a greater challenge as compared with CT image registration and introduces its own inaccuracies. These inaccuracies were not quantified for this study, this makes the single plane MBIR techniques prone to error.

The registration of long leg bones was found to be inconsistent as it relied on the ability to line up separate parts of the long leg bone models with no obvious anatomical landmarks. Taking the femur as an example the two halves of the femur were segmented, one half with the femoral head and one with the femoral condyles. They were registered together in the middle of the femur using only the cylindrical shaft as there are no obvious anatomical bony landmarks that could be used to register them. This has an influence on the determination of the anatomical coordinate systems as incorrect registering of these bones introduces errors in defining these coordinate systems.

3.4.4 Recommendations for combined MBIR and motion analysis study

The single plane fluoroscopy study using MRI derived models shown here has insight into pathological function when looking at intact knee patient cohorts. This is particularly apparent when looking at anterior-posterior translation. Combining this information with motion capture derived kinematics will provide further insight of the biomechanics at other joints. However, from this study it has also shown there are some significant technical challenges that need to be addressed and considered. The following section provides

recommendations for addressing these challenges or suggests what to consider when research groups want to carry out combined motion capture and fluoroscopy.

1. If possible use an X-ray system not in clinical use or in a clinical setting. This would allow more time to improve data collection quality and the ability to set up motion capture cameras in a highly optimised position to maximise the field of view. This does introduce its own challenges as the documentation and governance required to use an X-ray system outside of a clinical environment is considerable and at times challenging.

   If a clinical X-ray system is being used then establishing a good working relationship with the X-ray department is vital to the success of the study. Engaging them with the study will allow them to provide insights into best approaches with imaging and will ensure consistent imaging quality. If possible approach the X-ray department with a predetermined protocol so that they can understand what your research requirements are.
2. The synchronisation of motion capture and fluoroscopy method shown in this study is inconsistent meaning that direct comparison of data is challenging and the method to detect the time lag is prone to error from the noise in the signal. The recommendation would be to not use the method described in this study but to use a trigger which sends out a pulse to all the equipment simultaneously. This could be done by using the X-ray trigger to send a pulse to all the other systems.
3. Either find out from the manufacturers the sampling frequency or carry out tests to determine the frequency. One such approach would be to use metal beads of known positions and size and cover these with retro-reflective tape. These could then be moved in a controlled manner while simultaneously capturing with motion analysis and fluoroscopy. This would eliminate any noise that could be introduced from soft tissue artefact by performing the tests in-vivo.
4. If the research question is related to investigating soft tissue artefacts with fluoroscopy being used as the gold standard to compare

optoelectronic motion capture or any other motion system, then an understanding of the inaccuracies of this protocol at its various stages are needed. This includes understanding segmentation errors as well as errors that take place due to image registration. A combined validation looking at these errors would be the best approach but is challenging.

5. To do a direct comparison of motion capture and fluoroscopy a transformation matrix between the two is needed. It is recommended that an object with markers of known positions is used to be able to calculate this. Knowing the marker locations of three or more non collinear markers within the two systems allows the ability to calculate a transformation matrix between the two systems (Stagni et al. 2005). This can be then used to transform the motion capture data into the fluoroscopy coordinate system allowing a more accurate comparison between the two.
6. When defining anatomical coordinate systems within bone models ensure the approach is repeatable. One approach would be to do a series of lower resolution scans and have the MR scanner composite the scans into a single scan. This would eliminate the need to register the different low resolution scans and would be more accurate as the scanner internal coordinates would be used to composite the scan. However, it may be prone to error as it is reliant on the volunteer not moving and introducing scanning artefacts. There have been a few different studies that have looked at alternative approaches, not using long leg scans. One study defined the femur and tibia ACS only using the high resolution scans (Shefelbine et al. 2006). Another study (Miranda et al. 2010) developed an algorithm to automatically determine ACS for tibiofemoral joint. This was shown to be repeatable, consistent and very quick. The approach defined in Appendix C is time intensive and can be prone to error. However, this algorithm was only investigated on CT derived bones, so a comparison between the different approaches would be recommended to make an informed decision.

7. The final recommendation would be to have MR sequences that allow the ability to segment out soft tissue structures such as cartilage. This would allow the ability to look at articular cartilage interactions using the closest point method defined in Chapter 2.

3.4.5 Recommendations for Future Studies at Cardiff

Following this study and the work carried out in Chapter 2 a number of key points on how to improve the combined MBIR and motion capture protocol at Cardiff have become apparent.

- Single-plane fluoroscopy has limitations with certain parameters such as medial lateral translation having to be ignored. To provide the accurate and detailed biomechanical analysis needed, the only option is to develop a biplane fluoroscopy system. This becomes acutely apparent when performing intact knee studies; due to the lack of contrast between structures compared with implanted knees. Simultaneous biplane imaging would allow more accurate positioning of the tibia and femur. It could also provide the ability to track other structures such as the patella, which could provide further detailed information for understanding a pathology or surgical intervention.
- The accuracy of the MBIR protocol needs to be assessed to fully quantify the errors that may be present. This includes segmentation and image registration.
- A better synchronisation of motion capture and fluoroscopy is needed, the photodiode approach described in this chapter is too inconsistent.
- Optimising the position of the motion capture cameras to ensure full coverage of the capture volume and no marker dropout.

The work following on from Chapter 2 & 3 looks at setting up an in house biplane fluoroscopy system that is synchronised with motion capture and potential approaches for validation of MRI and image registration. It was decided based on the work in Chapter 2 & 3 that in-vivo kinematics of intact knees would be the focus for all future chapters. This is because the source of

error is greater with intact knees as models are generated from segmentation. It is expected that the validation and biplane MBIR protocols generated could be adapted and applied on implanted knee studies in the future.

Chapter 4 Development of an MRI segmentation validation protocol

4.1 Introduction

As shown in the previous chapter, model-based image registration (MBIR) techniques can be used to calculate in-vivo kinematics of an intact knee and can provide clinically relevant insight into both normal and abnormal kinematics. Geometrically accurate three-dimensional (3D) models of the bones are essential for this image registration technique for accurately shape matching to the fluoroscopic images (Komistek et al. 2003; Moro-oka et al. 2007; Fiacchi et al. 2014).

There are several steps involved in generating geometrically accurate 3D models including image data acquisition, segmentation and 3D surface reconstruction. These are all equally important steps in producing these types of models.

Computed Tomography (CT) is considered the gold standard imaging modality for generating geometric 3D bone models (Moro-oka et al. 2007; Lee et al. 2008; Rathnayaka et al. 2012). This is due to CT producing images with high contrast between bone and soft tissue boundaries and the ability to obtain images within a very short acquisition time. Section 4.2.1 covers the principles, advantages and disadvantages of using this modality.

Magnetic Resonance Imaging (MRI) is an alternative to using traditional CT approaches for generating bone models, with the benefit of no associated ionising radiation. MRI is capable of imaging other structures such as articular cartilage which are not visible with CT imaging unless a contrast agent is used. A brief overview of the advantages and challenges of using MRI to generate bone models is discussed in section 4.2.3.

Musculoskeletal MR imaging has been developed, in collaboration with Cardiff University Brain Imaging Centre (CUBRIC), for a number of MBIR studies at Cardiff (Whatling 2009; Stroud Larreal 2011; Watling 2014). In addition, image segmentation and 3D surface reconstruction protocols for tibiofemoral joints have been developed utilising ScanIP (Synopsis, USA) software (section 3.2.2.1.1). However, the accuracy of this protocol to generate 3D bone models has never been investigated so the errors are unknown.

In this chapter, a combination of CT and structured light 3D scans was used to quantify the accuracy of MRI based ovine femora and tibiae 3D models.

4.2 Background

4.2.1 Computed Tomography Imaging

Computed Tomography (CT) imaging was developed in the 1970's and was the first imaging modality developed capable of tomography imaging. The invention is attributed to two physicists Dr G.N Hounsfield and Dr A. M. Cormack, who both independently developed the mathematical theories behind the technique. The first clinical CT scanner system was developed by Dr G.N. Hounsfield and his team in 1971. The first documented clinical use of the system (also in 1971) revealed the presence and location of a cerebral cyst in a patient at Atkinson Morley Hospital (Isherwood 2005).

4.2.1.1 Basic Principles of CT

The fundamental principle for CT is that the attenuation coefficient, calculated after an X-ray beam passes through the body, can be used to measure the density of tissue.

In CT the X-ray beam is emitted from an X-ray tube and passes through an object and an image is generated by a detector. This tube and detector system are rotated around the object taking a series of images which are combined forming a series of projection. The final CT image of an object is reconstructed by combining a significant number of these projections. Early CT scanners imaged patients slice by slice, moving the patient a set distance in between each slice. This was a slow approach which could take up to 9 hours to complete a single scan.

More advance helical CT scanners can perform continuous imaging by moving a patient on a gantry while simultaneously rotating the source and detector (Figure 4-1). This allows the ability to reconstruct the images captured into anatomical planes with a much shorter acquisition time.

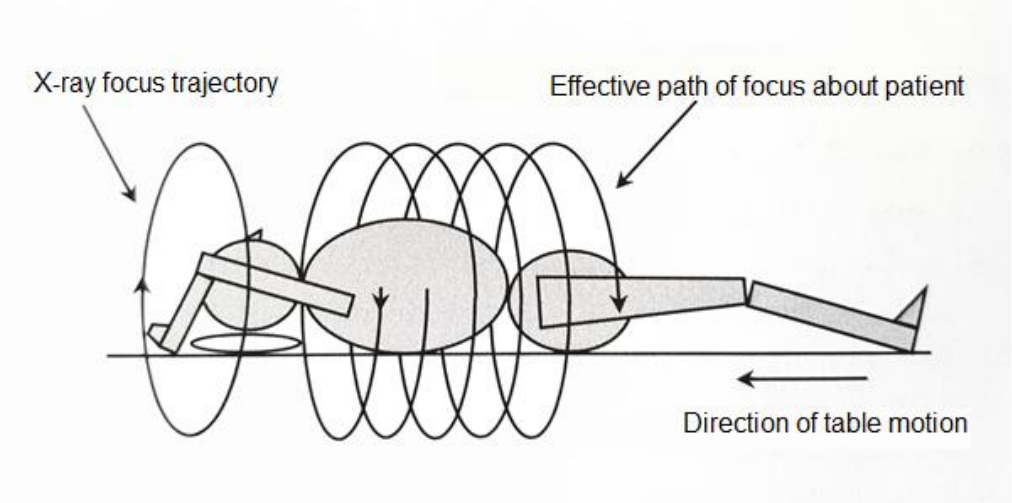

Figure 4-1 Principle of helical CT scanning, image reproduced from Castellano and Webb (2012)

4.2.1.2 CT Applications

CT imaging has been used in a broad range of both clinical and research applications. They are commonly used to create 3D bone models for applications including patients specific surgical guides for osteotomies (Victor and Premanathan 2013), anatomical models (Barker et al. 1994) and biplane fluoroscopy imaging (Tashman and Anderst 2003b; Myers et al. 2012; Miranda et al. 2013; Campbell et al. 2016). With CT pixel intensities directly relating to the attenuation of the tissue or tissues density; tissues with high density, such as cortical bone, are easier to delineate and segment (Bücking et al. 2017).

4.2.1.3 Radiation dose

The major limiting factor with CT scans, is the high radiation dose to the patient or healthy volunteer from a single scan. In the UK, CT scans are not typically allowed to image human volunteers for research purposes due to the high amount of radiation associated with them. This has led to an increase in both clinicians and researchers using alternative imaging modalities such as Magnetic Resonance Imaging (MR) (Semelka et al. 2007). Research is being carried to develop low radiation dose CT sequences and scanners that are capable of providing high geometrically accurate scans for developing patient-

specific bone models (Sint Jan et al. 2006). However MRI has advantages that could justify never needing to use CT imaging.

4.2.2 Structured Light Scanning

Surface reconstruction is a very important technique used in a wide range of applications including inspection of machined parts, 3D mapping of buildings and reverse engineering (Salvi et al. 2004). There are several different approaches for scanning surface geometry including using a coordinate measuring machine (CMM), laser scanner, or industrial computed tomography.

One of the approaches to surface reconstruction is structured light scanning which has specific advantages in that the systems are typically non-contact, lightweight, portable and have high levels of accuracy. It works by the projection of a 2D structured illumination or pattern via a digital light projector or light source onto an object of interest. An imaging sensor, typically a video camera, then acquires a 2D view of the object with the illumination projected on it. If the illumination is projected on a flat surface, then the structured pattern seen by the sensor is similar to the projection. If the illumination is projected on an object, the surface distorts this pattern (Figure 4-2). Based on these distortions, accurate profiles can be computed using the geometric position and relationship between the projection and imaging sensor (Rocchini et al. 2001; Geng 2011).

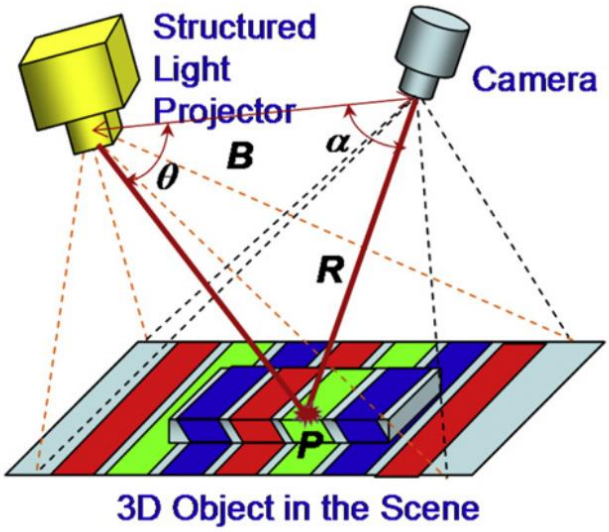

Figure 4-2 Illustration of how structured light works taken from (Geng 2011)

Modern systems use two imaging sensors and stereotriangulation to increase the accuracy of this technique. For this study the technique was used to scan ovine bones, and act as a gold standard for comparing with other imaging modalities

4.2.3 Musculoskeletal Magnetic Resonance Imaging

.An overview of the basic principles of MRI can be found in section 1.4.2.

MRI is used to scan soft tissue using the spin of the Hydrogen nuclei present in the tissue primarily as the signal source. A combination of longitudinal relaxation time, transverse relaxation time and proton density can be used to calculate the signal intensity of different soft tissues.

Certain structures including cortical bone, ligaments and menisci have very short transverse relaxation times which can only be imaged using specialist research imaging sequences. These sequences including ultrashort echo time (UTE) imaging has been used to image meniscus (Sneag et al. 2015) and tendons (Koff et al. 2014; Chang et al. 2015) and more recently zero echo time (ZET) sequences the ability to provide enhanced bone contrast in MR (Breighner et al. 2018). However these image pulse sequences are not present in most clinical MR scanners or even most research MR scanners.

Mammalian bones are surrounded by a significant amount of muscles and soft tissue which have a high signal intensity in MRI. This produces defined boundaries around the bone which can be used to identify the cortical bone on normal clinical MR sequences (Figure 4-3), required for generating 3D bone models.

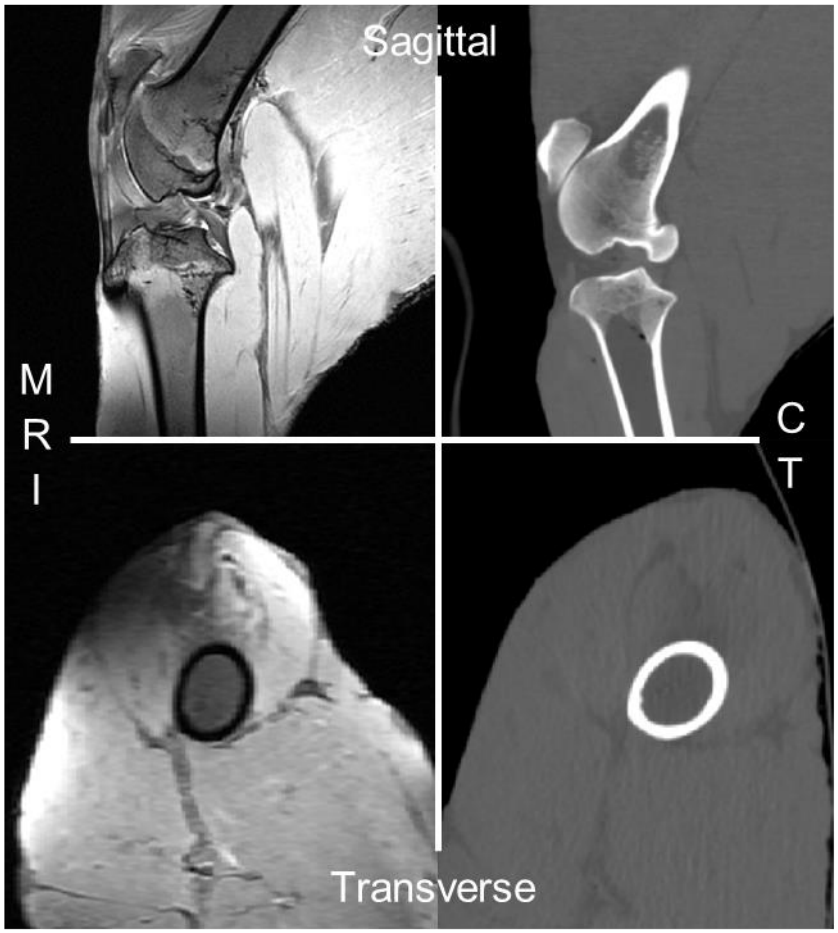

Figure 4-3 MR (left) and CT (right) comparisons from the same anatomical region of a specimen. In the CT Images the cortical bone can be clearly identified from the surrounding muscle and soft tissue. In the MR image cortical bone appears as black as the FIESTA-C sequence used cannot visualise the bone as not enough signal is emitted to be detected. Despite this the cortical bone can clearly by defined using the surrounding tissue and the cancellous bone.

4.2.4 MR kinematics studies

One of the earliest examples of MRI derived bone models being used in combination with MBIR was carried out in a study by Defrate et al. (2004). A combination of cartilage and bone models were segmented from MRI to investigate the differences between tibiofemoral contact points when looking at bone models alone and when incorporating cartilage and bone models. This research group has continued to use MRI bone models for a number of kinematic studies (Li et al. 2005; Li et al. 2008; Kozanek et al. 2009; Varadarajan et al. 2010) but has never investigated or reported on the accuracy of the MRI derived bone models to the authors knowledge.

It is anticipated that more research groups will be incorporating MR imaging into their kinematic studies due to the advantages of non-ionising radiation involved and the ability to image and create 3D models of soft tissue such as cartilage (Ackland et al. 2011). Therefore a standardised protocol for validation at individual sites would be valuable for multi-site studies or comparing results across groups.

4.2.5 MRI Segmentation Validation

There have been a small number of studies which have investigated the accuracy of models generated from MRI compared to CT.

Moro-oka et al. (2007) have investigated whether in-vivo kinematic measurements from MBIR were altered if using MR bone models compared to CT bone models. Three human volunteers were recruited and scanned using CT (0.35 mm x 0.35 mm x 1.00 mm) and MRI (0.39 mm x 0.39 mm x 1.00 mm) scanners. The 3D models were segmented using commercial software and the surface models from the two modalities compared. They reported a difference of -0.11 ± 0.81 mm, -0.23 ± 0.48 mm and -0.12 ± 0.60 mm for the three femora when comparing between CT and MRI. For the three tibiae a difference of -0.14 ± 0.67 mm, -0.13 ± 0.48 mm and -0.15 ± 0.77 mm.

Lee et al. (2008) combined both CT and MRI derived porcine bone models. They wanted to generate a model which used CT for bones and MRI for soft

tissue. Five porcine femora CT (0.4 mm x 0.4 mm x 0.625mm) and MRI scanned (0.3 mm x 0.3 mm x 1.2mm) and then manually segmented to reconstruct the 3D models. A surface matching accuracy of 0.7 ± 0.1 mm was found between the two modalities.

Neubert et al. (2017) investigated the influence that different high resolution 3T MR sequences had on the accuracy of reconstructing 3D bone models. The left knee joint of a fresh-frozen cadaver was CT (0.49 mm x 0.49 mm x 2 mm) scanned and MR imaged using three different sequences: SPACE (0.625 mm x 0.625 mm x 0.7 mm), TrueFisp (0.625 mm x 0.625 mm x 0.7 mm) and VIBE (0.3125 mm x 0.3125 mm x 0.7 mm). The bones were manually segmented and compared to the CT models with the average distance for all bones to be under 1mm. The VIBE sequence was found to provide the best agreement with CT.

These studies show that MRI overall has a sub millimetre accuracy for generating 3D bone models. The main limitation for all the above studies is that they have not used a true reference to compare MRI. CT derived bone models may, for example, be prone to segmentation error or other systematic errors. A ‘ground truth’ is needed for a true validation of MR bone models.

Rathnayaka et al. (2012) compared five ovine femurs with both CT and MRI based 3D models to measurements performed on the dissected bone using a mechanical contact scanner. MRI-based models were found to underestimate the volume and have average error of 0.23 mm, while CT-based models overestimated the volume and found to have an absolute accuracy of 0.15mm.

Van den Broeck et al. (2014) found similar results, when looking at 9 cadaveric legs, with CT (0.41 mm absolute error) over estimating and MRI under estimating (0.51mm absolute error). Van de Broeck found removing the tissue from the cadavers challenging and resorted to use a boiling procedure to remove some of ligament attachments. The boiling procedure was found to reduce the size of the bone influencing the accuracy of the reference standard (Gelaude et al. 2008).

Both these studies used clinical 1.5T MRI scanners and different sequences which could explain the observed variations, however the author has found no

other studies that have investigated accuracy using models derived from a 3T scanner compared to a true reference.

4.2.6 Overview and Aims

There have been a small number of studies that have investigated accuracy of generating 3D bone models from musculoskeletal MR imaging. Several studies have highlighted that a reference standard other than CT is required for a true comparison. One recent study showed that different MR sequences produce different results. This highlights the importance of calculating the accuracy of MR derived bone models whenever a different scanner or sequence is used. None of the studies discussed in detail how all the steps were performed, making it challenging for other research groups to replicate.

At Cardiff University an imaging and segmentation protocol for reconstructing 3D bone models using a 3T MRI scanner has been developed in the past. The accuracy of this approach has not been previously investigated. No other study was found in the past literature that has performed a full validation of 3T MRI derived models using a true reference. Therefore the main aims for this chapter are:-

- To develop a repeatable full validation protocol for MR derive bone models to carry out assessment of existing and future segmentation techniques and imaging sequences at Cardiff
- Compare the accuracy of current MRI segmentation and imaging methods developed at Cardiff against research gold standard (CT) and a true reference (structured light scan).
- Provide insights and recommendations for other research groups who want to quantify the accuracy of using MR bone models with their imaging and segmentation protocols

4.3 Methods

This section details the development processes which were used while creating a process to validate the segmentation methods developed at Cardiff

University. The first section covers the rationale behind the animal model used. This is followed by a pilot study highlighting the development process for defining the final validation protocol.

4.3.1 Suitable Human Equivalent

At Cardiff University there is no protocol or facilities to store cadaveric specimens at the School of Engineering. So cadavers could not be used to develop the pilot for validating MRI bone model accuracy. This meant an anatomically similar animal substitute was required.

Several studies have investigated the use of animal models looking at OA. The commonly suggested animals specimens are bovine, ovine, canine, porcine and leporine (Proffen et al. 2012; McCoy 2015). Ovine was chosen best as there are similar anatomical structures compared to human (Allen et al. 1998; Vandeweerd et al. 2013). Although smaller than a human tibiofemoral joint it can still provide important data to understand and quantify the accuracy of MRI derived bone models.

The stifle joint of the hind leg of an ovine specimen is the anatomical equivalent to the human tibiofemoral joint (Figure 4-4). Both the femur and tibia of the ovine stifle joint will be investigated for this study.

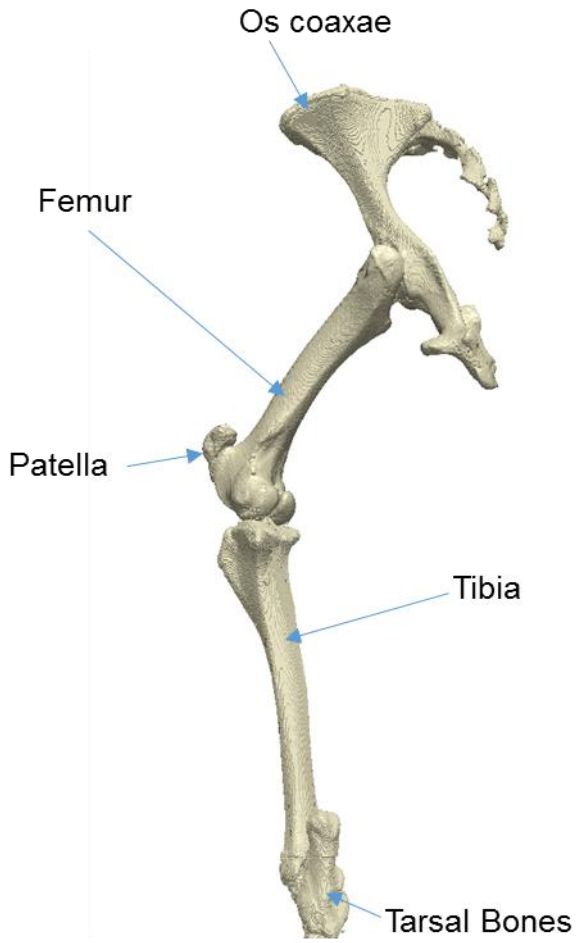

Figure 4-4 Skeletal anatomy of Ovine hind limb

4.3.2 Assessment of Imaging Ovine Stifle Joint

The main purpose of this experiment was to investigate if an ovine stifle joint could be imaged using a MR scanner and what structures are visible in the image. An ovine stifle joint was acquired from a local butcher, with most of the muscular tissue removed prior to acquisition with the stifle joint still intact. The joint was vacuum packed so not to contaminate the MRI scanner during the scan (Figure 4-5a). The scan was carried out using a modified FIESTA-C sequence with a resolution of 0.234 mm x 0.234 m x 0.5mm. As can be seen from Figure 4-5b articular cartilage and bone structure can be delineated clearly. This shows that the ovine stifle joint can be suitably imaged within the existing 3T MR scanner at Cardiff University.

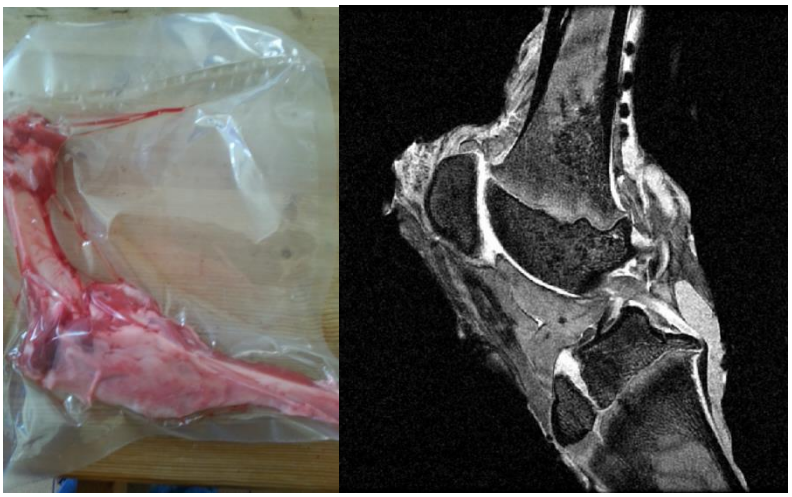

Figure 4-5 **a** Ovine Stifle joint vacuum-packed **b** - MR image of ovine stifle joint

4.3.3 Pilot investigation

Due to the number of technical steps needed to carry out a validation comparison an initial pilot investigation was carried out first. The preliminary aim was to carry out the experiment and discover what was required to improve the process, and if there were any methodological challenges to be addressed. The pilot experiment was carried out within a short time frame due to the limited availability of the structured light scanner. A short summary of the methods, processing and what was learnt during the process follows

4.3.3.1Specimen

A left ovine hind limb (Figure 4-6) with most of the muscular tissue intact was sourced from a local butcher. The approximate age of the sheep was between 9-12 months before slaughter. The specimen was vacuum packed to preserve the specimen and the top end of the femur was removed due to limitations of the maximum capacity of the chamber in the vacuum pack machine. The specimen was stored at a temperature of 3°C and kept chilled in an air tight container when transported.

Figure 4-6- Ovine specimen vacuum packed

4.3.3.2Imaging

CT images of the entire specimen were obtained with a GE Lightspeed VCT scanner using kVp=80, mAs=119, pixel size of 0.488mmx0.488mm and a slice thickness of 0.625mm (Figure 4-7). The scan time was approximately 12 seconds and was carried out at Velindre Cancer Centre by an experienced superintendent radiographer.

Figure 4-7 Ovine specimen being CT scanned by a GE Lightspeed VCT scanner

MR images were taken at Cardiff University Brain Research and Imaging Centre (CUBRIC) using a GE Signa HdX 3.0T scanner. A 3D scan was taken of the hind limb using the Fast Imaging Employing Steady State Acquisition (FIESTA-C) sequence and a flexible knee coil; scan parameters can be seen

in Table 4-1. During all scanning procedures, the long axis of the femur was visually aligned with the long axis of the CT scanner or the static magnetic field of the MRI magnet using location scans. Both CT and MRI were exported in the DICOM image format to allow further processing.

Table 4-1 FIESTA-C Scan Sequence Parameters

Parameters	Values
Repetition Time (TR)	5.1 ms
Echo Time (TE)	2.5 ms
Pixel Spacing	0.3125x0.3125 mm
Slice Thickness	0.8mm
No. of Averages	2
Orientation	Oblique-sagittal
Acquisition time	5 mins

4.3.3.3 Dissection

Dissection was carried out at Cardiff School of Bioscience under the supervision of Dr Emma Blain. Due to the limited timeframe to carry out the preliminary investigation, only three hours was available for dissection in the Bioscience laboratories. It was decided to focus on dissecting the distal Femur of soft tissue and muscle. The surrounding muscle and soft tissue was removed (Figure 4-8) with the articular cartilage being kept intact as no suitable method had been defined to remove it completely without damaging the bone underneath within the time frame of the investigation

Figure 4-8 – Dissected Distal Femur

A standard operating protocol for dissection was followed as defined in Appendix D and the samples were placed backed into cold storage once dissection had been completed.

4.3.3.4 Structured Light Scanning

After completion of the dissection the samples were transported to 3T RPD, a 3D printing company building plastic and metal additive manufacturing parts. Structured light (SL) scans were carried out using a Comet 5 Structured light scanner (Steinbichler, Germany) by a trained operator. The system has a reported accuracy of 50 microns when detecting surfaces by the manufacturer.

First the bone was sprayed with chalk to remove reflection from surfaces thus improving capture quality (Figure 4-9a). The bone was scanned in several stages generating several surfaces depending on the complexity of the bone geometry (Figure 4-9b). These surfaces were aligned with each other and reconstructed into a final 3D model using the capture software Colin3D (Steinbichler, Germany) (Figure 4-9c). The files were exported in the Stereolithography (.STL) format.

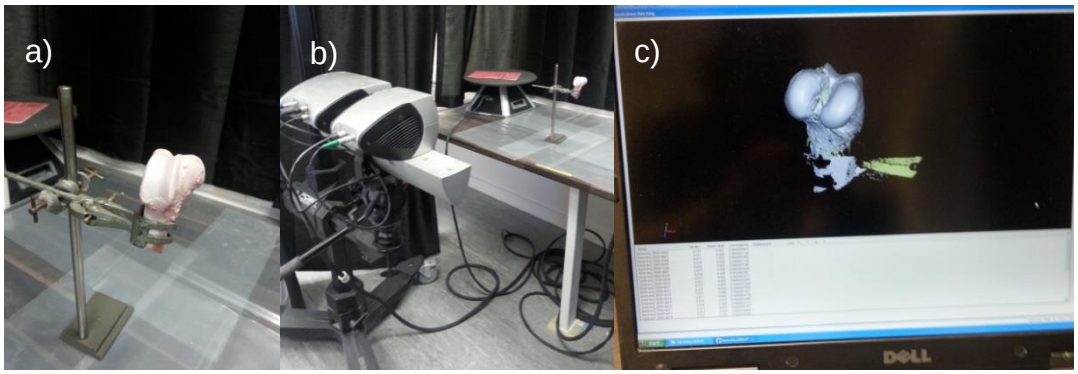

Figure 4-9 **a** - Femur placed in clamp stand and sprayed with chalk **b** - Femur being structured light scanned **c** - Screenshot of surface capture of Femora

4.3.3.5 Segmentation of Ovine Stifle joint

4.3.3.5.1 MRI – Cartilage and Bone

The DICOM files were imported into Scan IP (Synopsis, USA) the image sequence was thresholded using the histogram tool to select the grey scale values that best delineated cartilage and bone clearly (Figure 4-10a). Once imported there are several anatomical views to visualise the data, for the FIESTA-C sequences the best view for the image data is in the sagittal view (Figure 4-10b).

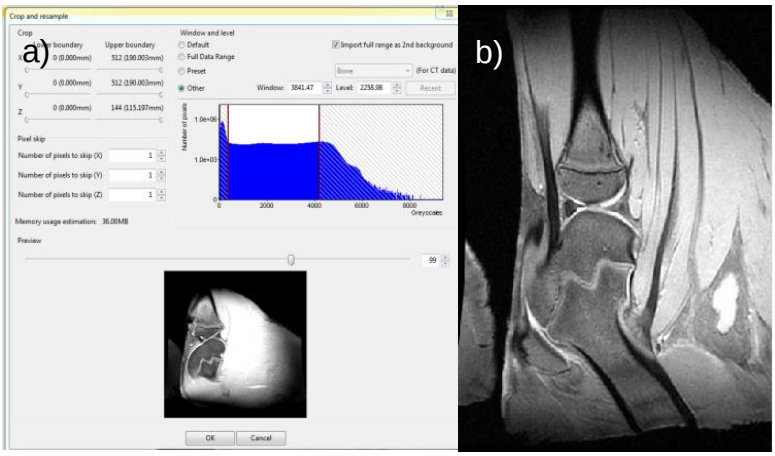

Figure 4-10**a**- Screenshot taken from ScanIP showing the histogram upper and lower boundaries selected to delineate bone and cartilage structures. With the x-axis relating to the intensity values and the y-axis the frequency
b - Sagittal slice of ovine stifle joint using Fiesta-C image sequence.

Using the sagittal imaging plane, a mask was applied to the structures within the ovine stifle joint. Firstly, using a semi-automated method involving paint threshold, the cortical bone is segmented to create an outline of the bone. After the cortical bone was segmented a manual paint tool was used to complete the outline and the flood fill tool can be used to fill in the outline (Figure 4-11a). This is carried out on all the slices to create the bone model. Once complete the bone mask is duplicated and using the semi-automated method again the cartilage is segmented as well as the bone. This creates a combined bone and articular cartilage model (Figure 4-11b). Using Boolean functions within Scan

IP the bone model is taken away from the bone and articular cartilage model just leaving the cartilage mask behind (Figure 4-11c).

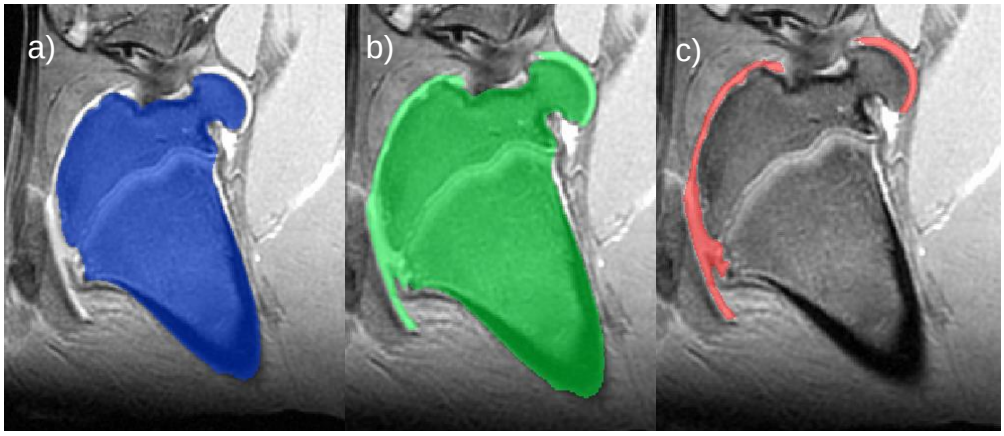

Figure 4-11-**a** Segmented Femur Bone mask **b** – Segmented Bone and Cartilage mask **c** - Cartilage mask

4.3.3.5.2 CT – Bone

The CT scan data was imported as per the MR scan data with the upper and lower bounds of greyscale set by using the histogram. Pre-set values for the histogram were chosen that allow bone to be seen clearly. Segmenting bone from CT data is much more straightforward compared with MRI. As the CT scan only shows the detail of the bone (Figure 4-12) and no soft tissue, using a semi-automated paint threshold technique the bone can be segmented fairly quickly and accurately. With the CT data it was found to take approximately 30 minutes to segment compared to approximately 2 hours for MRI image datasets. The best imaging plane to view when segmenting CT data was found to be the transverse view (Figure 4-12).

Figure 4-12- Ct scan of entire hind limb **b** - Segmented tibia in transverse view

4.3.3.5.3 Generating bone models

There are several smoothing algorithms that can be used within ScanIP including median filtering which assigns a median value to a pixel based on the surrounding pixels and recursive Gaussian which can be used to reduce the noise of the mask. CT scan derived models do not require as much smoothing compared with the MRI derived models.

The final MR bone model smoothing was carried out using the approach recommended and performed in section 3.2.2.1.1. The masks were converted into a surface model using ScanIP and exported as a binary Stereolithography file (STL).

4.3.3.6 Analysis

4.3.3.6.1 Model Comparison

Geomagic studio (3D Systems, USA) is a reverse engineering software primarily designed for analysing and editing 3D scanned data and is often used to compare a scanned printed part with the original CAD model. When a model is first imported the program checks for an intact mesh; if not, there are many options to repair it including removing spikes, filling in holes etc.

4.3.3.6.2 Alignment

Once the two models are successfully imported they need to be aligned to one another before comparison analysis can be undertaken. A Detect Sphere Targets function in the software was used to locate suitable targets on individual models which are then used in the alignment process. A best fit alignment algorithm was used to automatically match the two models together using the sphere targets as reference positions. Tolerance and sample size can be set and affect how long the algorithm takes to complete (Figure 4-13a). For this study the sample size was set at 2000 and tolerance at 0.05mm (Figure 4-13b).

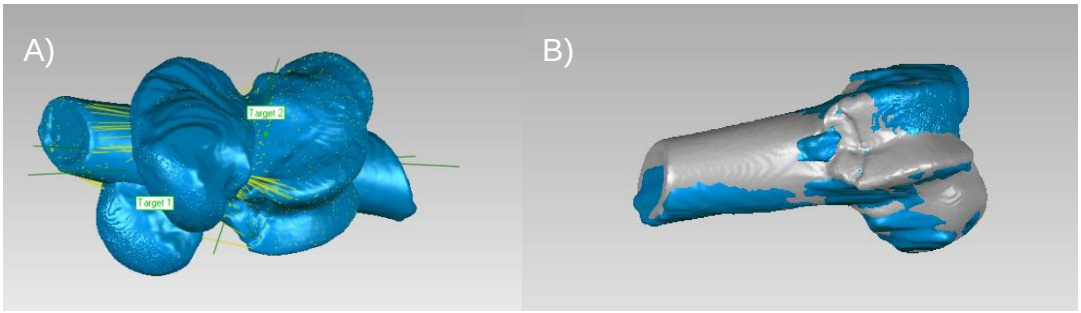

Figure 4-13**a** Geomagic aligning two femur bone models using the Best Fit Alignment algorithm having defined targets as reference points **b** - Aligned bones within Geomagic software

4.3.3.6.3 Surface Deviation Mapping

The surface deviation function built within Geomagic Studio is able to generate a three dimensional, colour-coded mapping of deviations between a reference and a test object. For example, the SL scan model was used as a reference and MRI derived bone model as the test object. Deviations in this context are the minimum distance from a test object point to any point on the reference model. This calculates what the overall accuracy of the test model compared to the reference model and outputs the Root Mean Squared (RMS) error of the test model compared with the reference model.

4.3.3.7 Pilot Results

Due to limitations discussed in Section 4.3.3.3 the dissected distal femur scanned using the SL scanner included articular cartilage. Therefore, the CT scanned derived model was excluded from direct comparison with the SL model as cartilage can't be segmented from CT. The SL model was compared with the MRI generated bone model with the combined cartilage model (Figure 4-14).

A separate comparison was performed to compare the CT derived bone model of the femur with the MRI derived bone model. This was performed to calculate the deviation between CT and MRI bone models (Figure 4-15). Overall deviation statistics were calculated for both deviation comparisons and can be found in Table 4-2.

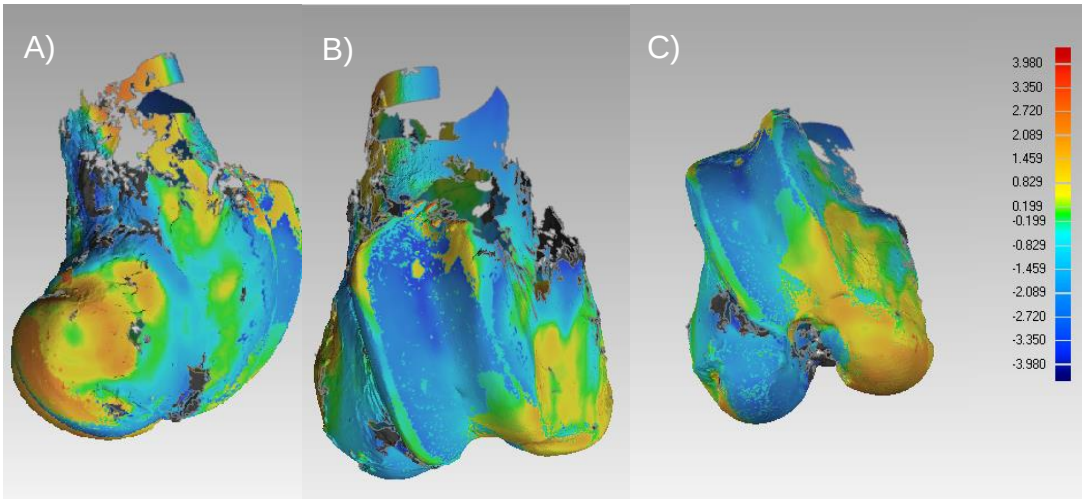

Figure 4-14 3D deviation map of SL cartilage and bone against **a** –Sagittal View **b**- Coronal View **c**- Transverse View

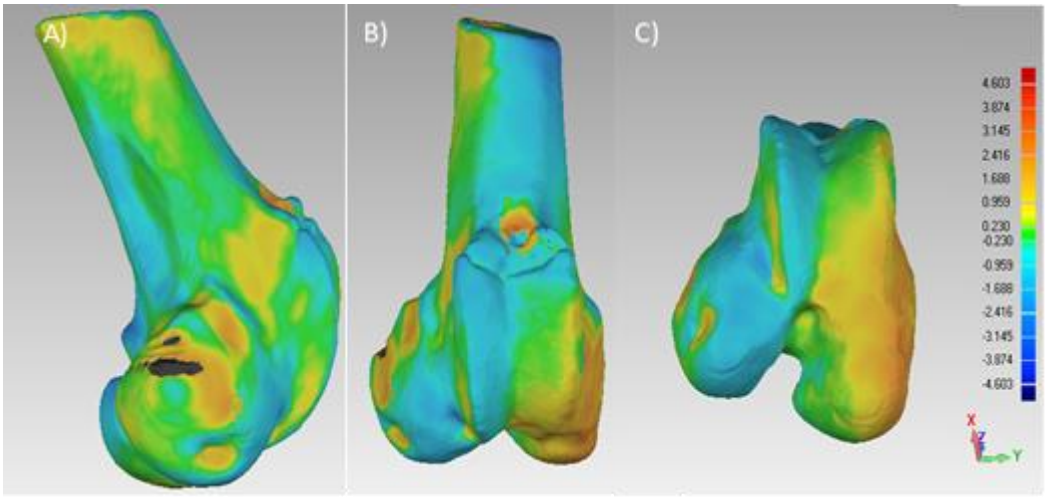

Figure 4-15 3D deviation map of CT bone against MRI **a**- Sagittal view **b**- Coronal View and **c** - Transverse View

Table 4-2 Statistics of 3D Deviation Maps

Statistics	**Structured Light scan Vs MRI (Bone & Cartilage)**	**CT Vs MRI (Bone)**
RMS error (mm)	1.04	0.77

4.3.3.8 Discussion of Pilot study

The results from Table 4-2 show that when comparing CT generated bones and MRI generated bones the RMS error was 0.77mm. An explanation of the high maximum and minimum distance of deviation is due to difficulties with segmenting tendon insertion sites in MRI. There are differences in the anatomy between human and ovine bones with the addition of tendons such as the Common Calcaneal Tendon which starts from the ankle joint and has an insertion point at the femur. This insertion point is difficult to segment due to its similarity in greyscale representation to cortical bone in the FIESTA-C sequence. This would explain the dark patch and high level of deviation in Figure 4-15 as this is where the insertion point of the tendon occurs. The benefit of CT is that tendons and other soft tissue do not appear on the scan data so segmentation of the tendon bone interface is easier. An additional effect that was noticed during segmentation of the MR a warping artefact present on the scans. On consultation with the MR radiographer it was suspected that this was most likely due to the vacuum packing causing the liquid to pool around the specimen. This potentially influences the accuracy of the segmentation.

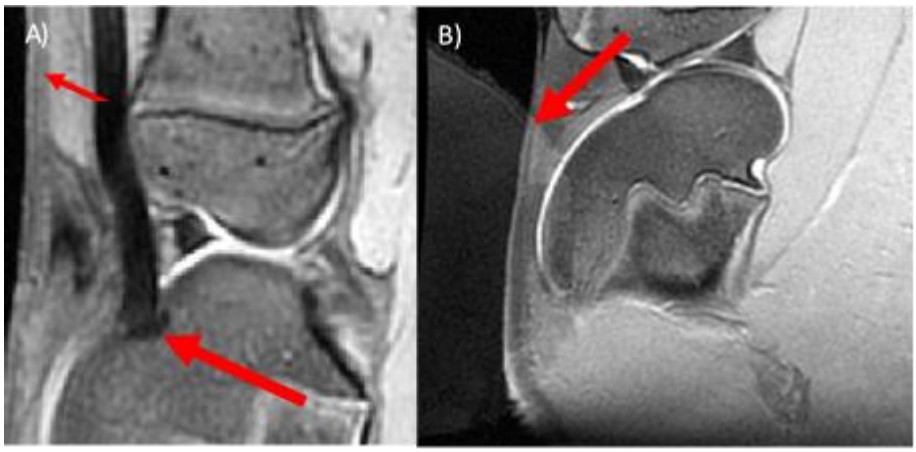

Figure 4-16 – **A** Tendon insertion point on femur **B** - Visible warping on the scan data

The results from Table 4-2 also show that when using SL scan generated bone and cartilage model as the reference model compared with a combined MRI derived articular cartilage and bone model produced an RMS error of 1.036mm. Figure 4-14 shows that on average the MRI derived model underestimated the reference model. This may be due to the SL scan model having holes within its mesh. The reason for this is due to soft tissue such as parts of tendons and other soft tissue not being removed completely during the dissection and causing the SL scanner to scatter. This shows the importance of being able to remove all the soft tissue as it has a direct influence on the quality of the SL scan. In addition the inclusion of cartilage in the final dissected distal femur end does not allow the ability to compare the 'ground truth' with the bone models derived from CT or MRI.

Overall the pilot study highlighted series of methodological challenges that must be addressed during the full validation study. These are summarised below: -

1. This pilot study used Geomagic Software to carry out the model comparison, however access to the software is limited and additional licenses are very expensive. An alternative software will be used for the full validation study.
2. Although the SL scanning is highly accurate, when carried out by a commercial company the price and distance involved prohibits the use of it during the full validation study.

3. Shrink wrapping introduced errors in the MR scan
4. Improve dissection methods to help with gross dissection
5. A method of removal of articular cartilage
6. Carrying out the full validation with the tibia bone as well
7. The ovine sample was relatively immature (9-12 months old) and had a very pronounced growth plate. This is not present in adult human tibiofemoral joints and therefore not a suitable analogous anatomy. Recommendation is to source older ovine specimens where this growth plate is not present.

The following sections covers all the methodological changes that were made to address the challenges found during the pilot study.

4.3.4 Final Validation Protocol

4.3.4.1 Specimens

Five intact cadaver ovine hind limbs were sourced from a local butcher. Compared with the pilot study the ovine hind legs were sourced from more mature sheep with all sheep being 24 months or older. The limbs were amputated prior to being sourced for the study at the pelvis maintaining all soft tissue and to ensure not to expose the femur and tibia to air.

The specimens were not vacuum packed as done in the pilot study but kept in sealed high strength plastic bags. The specimens were MR scanned within 24 hours of being sourced and were then kept frozen between procedures. With each specimen allowed to defrost at room temperature for a minimum of 24 hours before any additional scanning or dissection procedures.

Rathnayaka (2011) performed a statistical analysis of the sample size required for 80% power to detect a 0.06mm difference for ovine legs and found 28 samples were needed. Due to the great amount of time required to process the samples the author used a sample size of 5 and calculated a difference that can be detected is 0.108mm. It was decided to use a sample size of 5 for this study based on the above calculations.

Average dimensions and details for the specimens can be found in Table 4-3.

Table 4-3 Dimensions of Ovine specimens

	Leg	Total Length of Femur (mm)	Total Length of Tibia (mm)	Diameter of Femoral Shaft (mm)	Diameter of Tibial Shaft (mm)	Width of Femoral Condyles (mm)	Width of Tibial Plateau (mm)
OV1	Right	171	210	24	16	46	51
OV2	Left	173	210	25	19	47	54
OV3	Right	170	207	24	20	43	49
OV4	Left	169	206	23	20	45	49
OV5	Right	155	187	23	18	42	43

4.3.4.2 Imaging

CT and MR imaging was performed on all five ovine legs following the parameters defined in section 4.3.3.2 and Table 4-1. The only methodological difference to the previous pilot study was that ovine legs were not vacuum packed as done previously. This was to eliminate the image artefact seen in the MR scan previously (Figure 4-16).

4.3.4.3 Dissection

The dissection protocol was adapted from the pilot study to accommodate some of the problems faced. The following steps were followed: -

- Gross dissection of the muscle and soft tissue was performed following the standard operating protocol (Appendix D) (Figure 4-17a)
- The specimens were left in cold water with a biological enzyme for 48-72 hours, which encourages tissue breakdown (Figure 4-17b). This method is known as cold water maceration and helps with the breakdown of tendon and ligament connection points on the ovine specimens (Sullivan and Romney 1999).
- The tibia and femur are separated, and fine dissection is performed until only articular cartilage remains (Figure 4-17c)

- The distal femur and proximal tibia are place into a beaker containing a 6% sodium hypochlorite solution for 24 hours (Figure 4-17d). This removes the articular cartilage from the joint surface without damaging the bone underneath (DeVries et al. 2008; Koo et al. 2009; Mann and Berryman 2012)
- The specimens were cleaned in soapy water and air dried ready for the next stage (Figure 4-17e).

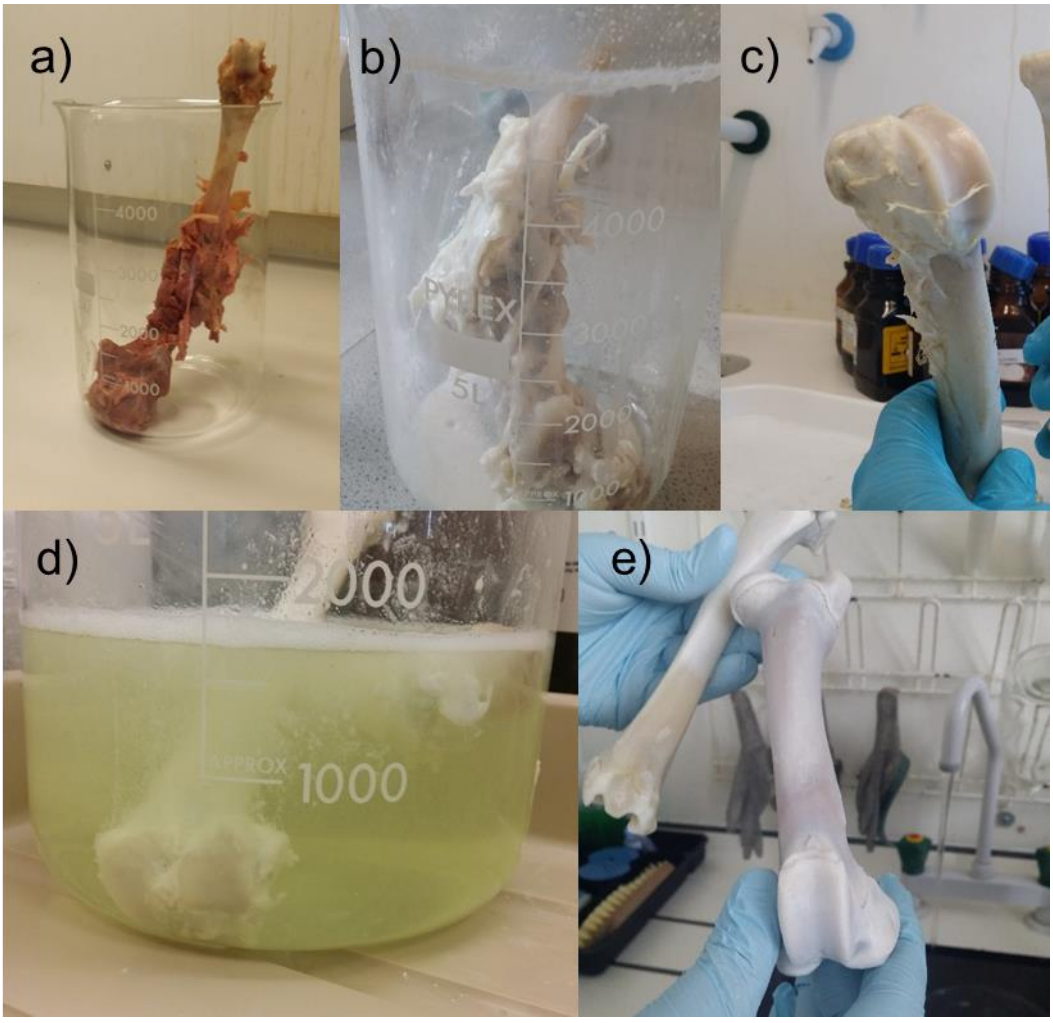

Figure 4-17 **a** Gross dissection of stifle joint **b** Stifle joint post cold water maceration **c** Femur post fine dissection **d** Proximal tibia soaking in 6% sodium hypochlorite **e** Articular cartilage removed from femur

4.3.4.4 Structured light scanning

Following dissection, the femur and tibia of the specimens were scanned using an Artec Space Spider (Artec 3D, Luxembourg) purchased for this study. This system is a different structured light scanner to the one used in the pilot study. The Space Spider (Artec 3D, Luxembourg) is a small lightweight system with a 3D point accuracy of 0.05mm and a resolution accuracy of 0.1mm. The scans were captured and processed in Artec Studio 12 (Artec 3D, Luxembourg). The bones were positioned over coordinate paper which acted as a base for the software and scanner to use as a reference (Figure 4-18).

Figure 4-18 Dissected femur positioned on coordinate paper prior to scanning

Due to the complex geometry several scans had to be carried out to capture all the surface geometry to be able to create a full 3D representation. After each scan was performed the following processing steps were performed in Artec Studio 12: -

1. Base Removal
2. Removal of unwanted elements
3. Alignment with previous scans

At the start of each scan the Artec Space Spider is pointed towards the coordinate paper, this defines the reference base in the software. Following the completion of the scan (Figure 4-19a) the software has an automatic base

removal algorithm which removes the reference base from the scan data (Figure 4-19b).

The next stage is to remove some of the noise that is present in the raw scan. This is due to parts of the bone being semi translucent, the structured light pattern can be reflected causing unwanted elements. Artec Studio 12 has a lasso eraser tool which was used to select all the unwanted elements and remove them from the scan (Figure 4-19c).

Once the scan has all the unwanted elements removed it is ready to be aligned with the other scans. Three corresponding points between the first scan and the second scan are selected to provide a rough registration (Figure 4-19d) and the software performs a fine registration using a rigid registration algorithm (Figure 4-19e). Following this step, the scans are locked in position ready to align with other scans. On average five scans were aligned together to form the final model of each bone.

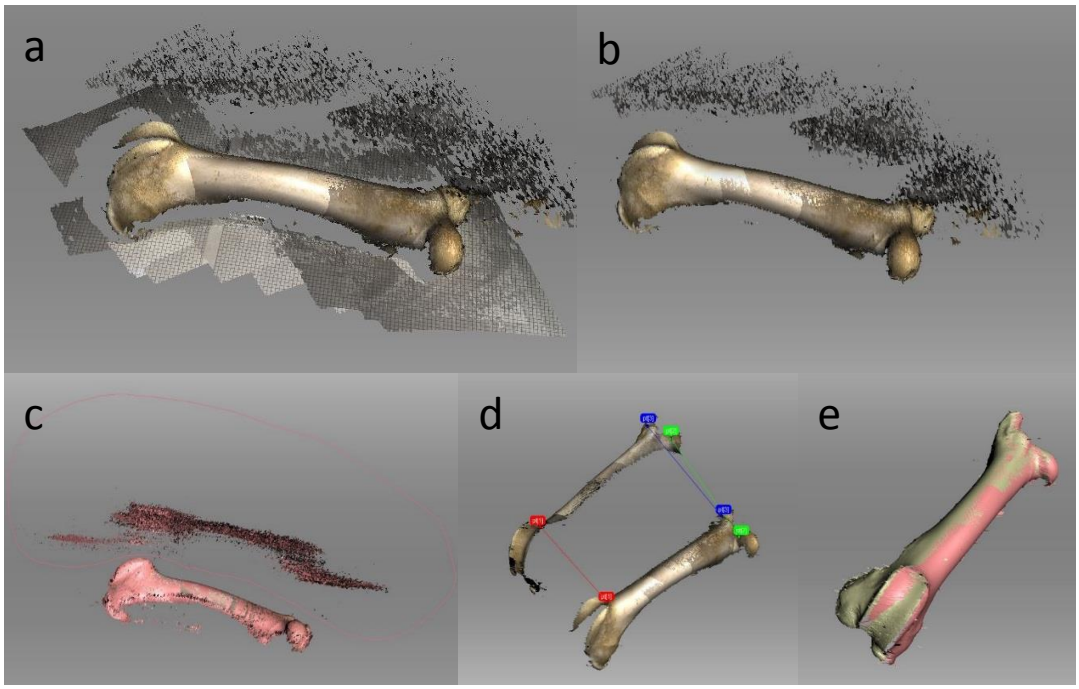

Figure 4-19a Raw scan of femur captured using the Artec Space Spider (Artec 3D, Luxembourg) b Scan data post automatic base removal c Lasso eraser tool selecting all the unwanted elements in the scan data d Three corresponding points selected on first and second scan to perform rough alignment e Two scans post fine alignment. The two different scans are highlighted using different colours.

After all the scans have been registered together, a global registration is performed to bring each individual scan into the same reference frame. To further eliminate 3D noise an outlier removal algorithm removed any elements that were missed during step 2. Using the sharp fusion function the software uses all the point cloud data to provide the most accurate model of the bone the software can generate (Figure 4-20). Scanning and the post-processing was carried out on both femur and tibia bones.

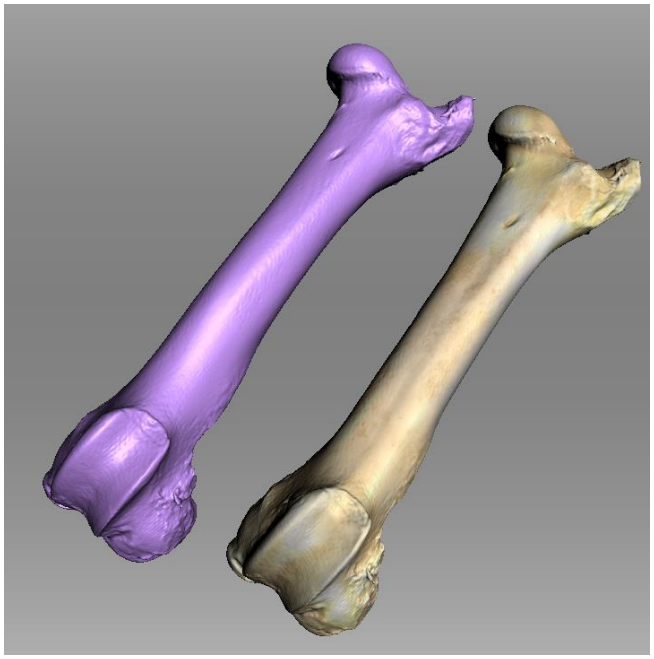

Figure 4-20 Final models generated of ovine femora using sharp fusion function in Artec Studio 12 (Artec 3D, Luxembourg). Purple model is the meshed model and the model on the right has a texture map generated for visualisation to highlight its similarity to the original scanned bone.

4.3.4.5 Segmentation

The primary aim of the study focused on calculating the accuracy of the MR derived bone models. Therefore the CT and MR segmentation was carried out following a similar process to that defined in section 4.3.3.5. The only difference between the full validation and the pilot study was that the bone geometry and not the cartilage was segmented.

4.3.4.6 Surface Deviation

The following section details the steps taken to perform comparisons between the SL, MR and CT generated 3D models.

Alignment

The 3D models for each modality were individually imported into the same workspace within Artec Studio 12. Using the alignment algorithm described in section 4.3.4.4 the three models are aligned together (Figure 4-19d). The SL

model was primarily used as the reference model or if not available the CT model. After alignment the models are exported with the post alignment defined position and rotation.

Sectioning

Both the SL and CT generated bone models are of the entire femur and tibia, however due to the limitation of the field of view of the MR scanner only the distal end of the femur and the proximal end of the tibia. To perform an accurate and robust comparison both the SL and CT models need to be sectioned to match the same proximal or distal bone as the MR generated model.

This was performed by importing the post alignment 3D models into Rhino 6 (McNeel, USA). A 2d planar surface was defined by selecting vertices at the end of the MR bone model (Figure 4-21). This was used to define the cutting plane to section the CT and SL models. A Boolean difference algorithm was used to section the CT and SL models to match the models with the MR model. The volumes of each of the sectioned models were calculated. The sectioned models were imported back into Artec Studio 12 ready for comparison.

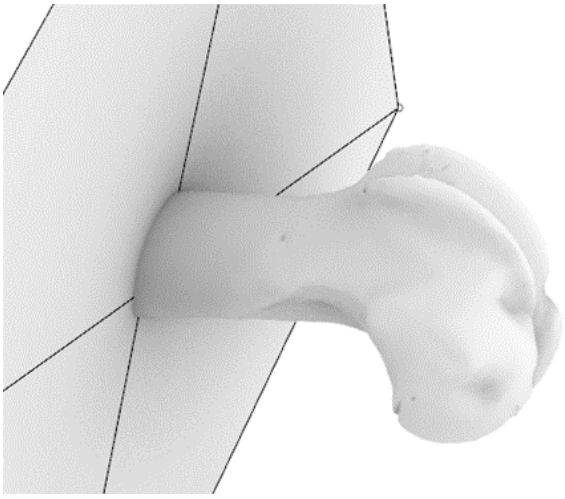

Figure 4-21 A 2D cutting plane defined by using vertices at the end of the MR generated femur bone model

Surface Deviation Calculation

The models were compared using the built in surface distance map function within Artec Studio 12. A search distance of 10mm was used to ensure that all

deviations were considered. The following comparisons were made, with the reference model being defined as the first model:-

1. Structured light vs. Computed Tomography
2. Structured light vs. Magnetic Resonance
3. Computed tomography vs. Magnetic Resonance

Artec studio calculates the root mean square (RMS) difference which is the square root of the mean of the squared distances between the reference and test model. A distance map is also produced highlighting the corresponding distance values with its position on the surface model (Figure 4-22).

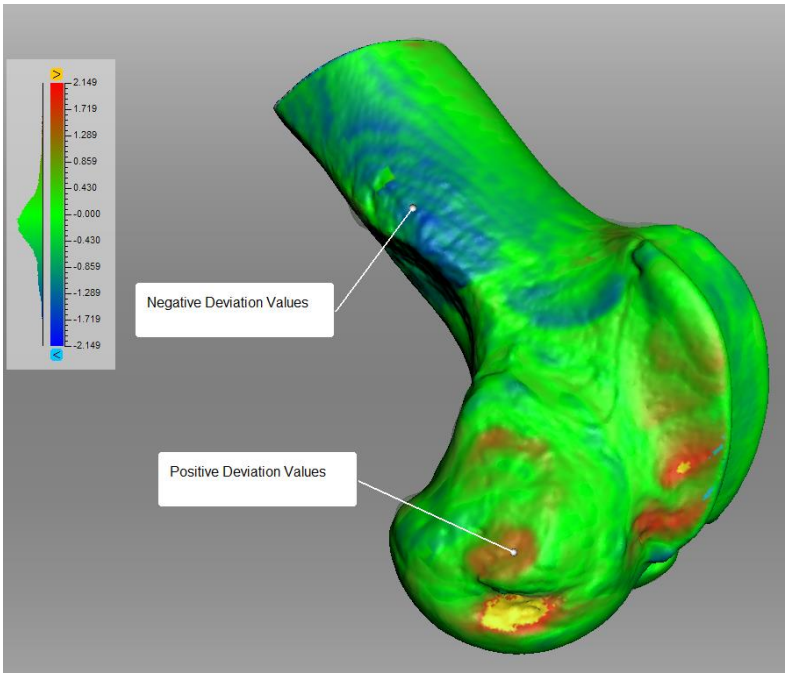

Figure 4-22 Example surface deviation map of structured light scan against magnetic resonance generated model. Annotations on the diagram describe the colour representations.

4.4 Results

Prior to dissection three of the specimens were prematurely disposed of by events beyond the author's control. This means that only two of the ovine specimens performed the full analysis including dissected, structured light scanned and subsequent surface comparison (Table 4-5). Surface deviation

comparisons were performed between CT and MRI generated bone models performed for all specimens on both femur and tibia models (Table 4-6).

A volumetric comparison between structured light, CT and MRI derived models was calculated for OV1 and OV2. Structured light model was defined as the reference with both total volume and % volume difference reported for CT and MRI (Table 4-7). A separate volumetric comparison was performed on all samples, where CT was defined as the reference and the total volume and % volume difference shown for MRI (Table 4-8).

Table 4-4 Surface deviation comparisons between Structured Light Scans and 3D bone models generated from Computed Tomography and Magnetic Resonance Imaging data. For both tibia and femur bones of specimens OV1 and OV2.

	Femur		**Tibia**	
	Structured vs. CT RMS (mm)	**Structured vs. MRI RMS(mm)**	**Structured vs. CT RMS (mm)**	**Structured vs. MRI RMS (mm)**
OV 1	0.26	0.63	0.24	0.58
OV 2	0.34	0.69	0.47	0.65

Table 4-5 Surface deviation comparison between 3D bone models generated from Computed Tomography and Magnetic Resonance Imaging data for Femur and Tibia bones.

	Femur	**Tibia**
	RMS (mm)	**RMS (mm)**
OV1	0.89	0.81
OV2	0.68	0.72
OV3	0.79	0.92
OV4	0.84	0.90
OV5	0.65	0.68

Table 4-6 Volumetric comparison between Structured Light, CT and MRI derived bone models

	Femur Volume (mm^2)			Tibia Volume (mm^2)		
	Structured Light	**CT**	**MRI**	**Structured Light**	**CT**	**MRI**
OV 1	61200	66700 (109%)	59800 (97%)	51700	56700 (109%)	51000 (98%)
OV 2	70700	78500 (111%)	64700 (91%)	51400	59000 (115%)	50100 (97%)

Table 4-7 Volumetric comparisons between CT derived bone models and MR derived bone models

	Femur Volume (mm^2)		Tibia Volume (mm^2)	
	CT	**MRI**	**CT**	**MRI**
OV 1	66700	59800 (89%)	56700	51000 (89%)
OV 2	78500	64700 (82%)	59000	50100 (84%)
OV 3	58000	52100 (89%)	51900	46300 (89%)
OV 4	65800	61000 (92%)	45500	41700 (91%)
OV 5	51200	45600 (89%)	42100	36500 (86%)

4.5 Discussion

Creating highly geometrically accurate bone models is a very important part of the MBIR protocol for calculating in-vivo kinematics. The current gold standard is to have models generated from CT scan data, however, due to large amount of ionising radiation it is not deemed ethical, to use CT scans on healthy volunteers. MRI generated bone models are becoming more prevalent but the standard clinical imaging sequences cannot directly visualise the cortical bone. As long bones are typically surrounded by muscle and soft tissue, which have a high signal intensity in MRI, they can still be segmented and reconstructed into 3D models. There has been very few studies which have investigated the

accuracy of this process especially studies which have compared against the true geometry. The study presented in this chapter shows a comprehensive and robust protocol of how to carry out this type of validation for MRI derived bones.

The study investigates the accuracy of the manual segmentation protocol using the FIESTA-C imaging sequence originally developed by Watling (2014) with improvements on the segmentation protocol made by the author (described in section 3.2.2.1.1). Due to not having the facilities to support working with cadaveric specimens in order to develop a protocol to calculate the accuracy of MR derived bone models, ovine specimens were used due to the anatomical similarity of the hind limb stifle joint. This is the first study to have investigated the accuracy of both femur and tibia derived bone models for ovine specimens imaged using a 3T MR scanner.

4.5.1 Comparison against True Reference

The results showed that when comparing CT derived models against the SL scan for the femur both OV1 (RMS error 0.26 mm) and OV2 (RMS error 0.34 mm) had a sub-voxel level of accuracy. There was similar results when considering the tibia models for OV1 (RMS error 0.24 mm) and OV2 (RMS error 0.47 mm). MRI bone models of the femur were found to have a slightly higher RMS error for OV1 (0.63 mm) and OV2 (0.69mm). MRI bone models of the tibia were found to have a slight lower RMS error for OV1 (0.58 mm) and OV2 (0.65 mm).

Although MR derived models have a higher RMS error compared with CT derived models the RMS error is still submillimetre and below the slice thickness of the MR scan sequence (0.8mm). Similar RMS errors were found in Van den Broeck et al. (2014) study who looked at the accuracy of cadaveric tibiofemoral joints.

When considering the difference in percentage volume from the structured light scan it was found that for CT bone models both OV1 (109%) and OV2 (111%) overestimated the volume by approximately 10%. When comparing the

MR derived models for OV1 (98%) and OV2 (92%) they were found to underestimate the volume when compared to the structured light scan.

4.5.2 MRI comparison against CT

When using CT as the reference standard, the average RMS error for the five femora was calculated as 0.80 ±0.10 mm (mean±stdev). For the five tibiae the RMS error was 0.81±0.11 mm (mean±stdev). Considering the volume difference the mean percentage difference for the femora models was 88%±3% (mean±stdev) and for the tibiae models 88%±3% (mean±stdev).

The results show that the RMS error of the MRI models compared with the CT is higher than when looking at the reference model. Although they are still either below or the same size as the slice thickness of the FIESTA-C imaging sequence. The results can be compared to previous studies that have investigated the difference between CT bone models and MRI bone models. A study performed by White et al. (2008) looked at the difference between MRI and CT scanners for 10 ovine knees to quantify the accuracy for designing patient-specific instrumentation. An average accuracy of 2.15 mm using MRI was found and 0.61 mm for CT. The method of determining the accuracy was by creating physical models and measuring specific landmarks using a calliper. This methodology is prone to error due to the variability of identifying the landmarks on the physical models.

Neubert et al. (2017) looked at three different MR sequences against a CT reference for a single cadaveric knee. All sequences showed an average deviation of under 1 mm when compared against CT. They also investigated the difference in volumes and found that the femur on average was 94.23% and tibia 94.40% across all three MR sequences. They investigated the difference in volume for the Fibula and found it to be on average 86.77%. The results of this study are closet to the study presented here with differences between the average deviation most likely being accounted to the differences in scanning equipment and sequences. The most interesting comparison is the Fibula difference in volume being very similar to the results reported here. This could be down to the diameter of the fibula, approximately 18.4 mm (Ide et al.

2015), being closer in size to the diameter of the femur and tibia of the ovine specimens (Table 4-3) that compared with the human femur diameter of approximately 46.8 mm (Pick et al. 1941).

The overall volume difference when comparing MRI against CT is greater and the RMS error higher than when compared with the structured light scans. This could be due to the overestimation of volume by CT and underestimation by MRI seen in section 4.5.1. These results were also found by other validation studies (Rathnayaka et al. 2012; Van den Broeck et al. 2014). This suggests that future studies that compare just using MRI and CT need to be aware of this as the perceived accuracy could be reduced due to these differences in volume between modalities. However the difference in RMS error seen between the two comparisons is minimal as both are still under or approximately 0.8 mm.

4.5.3 Summary

The image segmentation and MR imaging protocols developed at Cardiff University are highly accurate for segmenting bone models. This is the first study to have investigated the accuracy of a 3T MR scanner and the results are similar to those reported previously. A detailed and comprehensive validation protocol has been described that can be repeated for future changes with sequences or improvements with segmentation techniques.

It is recommended that a validation study is performed when significant changes are made to the imaging protocol. Whether this is with new imaging sequences or if different MR equipment is used. It is preferable for the validation study to be performed with a reference standard of the bone geometry. However if this is not achievable then a comparison with CT imaging is sufficient but anticipate that the accuracy of the MRI bone models to be lower than they actually are.

Chapter 5 Development of MBIR Validation Protocols

5.1 Introduction

The errors associated with measuring 3D joint position using MBIR are related to the X-ray system as well as the activity under investigation. For an observed activity, the joint being imaged and the speed at which the activity is being performed also will also influence the magnitude of the errors (Gray et al. 2016). To effectively assess and quantify these errors a comparison with a reference method or 'gold standard' is required.

Two clinical mobile C-arms acquired previously at Cardiff University were adapted so that they could work together to collect biplane fluoroscopy. The following Chapter focuses on developing a validation protocol to investigate and quantify the errors associated with 3D joint position outputs during a step activity using the biplane system and the MBIR protocols developed in Chapter 3. This Chapter also covers the adaptations that were required to make the MBIR system work effectively to provide biplane fluoroscopy data.

5.2 Background & Literature Review

5.2.1 Radiostereometric Analysis (RSA)

RSA is a stereo X-ray technique developed by Selvik (1989), and has been used in numerous implant studies, including total hip, knee and ankle arthroplasties, to determine the 3D motion or wear of an implant in-vivo (Hilding et al. 1996; Bragdon et al. 2002; Fong et al. 2011). It works by using two 2D X-rays, typically orthogonal, to define the location of a metal bead in 3D space. To achieve this the system is calibrated using a calibration cage where fiducial makers define the positions of the X-ray source between the two X-ray systems. An overview of how this works can be seen in section 5.4.2.2.3.

Three or more implanted non-collinear beads can be used to determine the position of a bone on the assumption that it is a rigid body. The beads are typically made from tantalum and range between 0.6 and 1.0mm in diameter (Karrholm et al. 2006). The rigid body assumption is that there is no deformation occurring within the bone such that, during motion, the relative

position of the beads remains constant. Using these three beads the exact position of the rigid body can be described in 3D space using three rotations and three translations (6 degrees of freedom).

Validation studies performed to examine the errors associated with RSA and have found that the accuracy ranges between 10 µm-100 µm (Ryd et al. 2000; Bragdon et al. 2002; Valstar et al. 2005; Karrholm et al. 2006). One of the most common techniques for validating clinical RSA precision is to perform double examinations. This is where two separate stereo X-rays are performed with a 15 min interval between them. During the interval the patient will be re-positioned to replicate movements encountered during two separate clinical analyses (pre and post). The bead positons are recalculated and the difference between the two measurements provides the precision (Valstar et al. 2005). Accuracy can be calculated using a phantom implanted with beads which is translated/rotated using high precision linear stages, typically of an order of magnitude greater in terms of accuracy; ideally around 1-2 µm accuracy (Önsten et al. 2001; Bragdon et al. 2004; Solomon et al. 2010).

5.2.2 Validation of MBIR Measurement Accuracy

The accepted ideal method to validate the accuracy of MBIR or other X-ray kinematic techniques is to use in-vivo RSA as the reference standard (Anderst et al. 2009; Anderst et al. 2011; Gray et al. 2016; Pitcairn et al. 2018). This method involves implanting tantalum beads (or similar) into volunteers for each of the bones of interest and collection of biplane fluoroscopy/X-ray images during an activity of interest. The bead locations are then processed using the RSA method described previously and the bone kinematics calculated separately and compared. The main challenge with this approach is the invasive nature of implanting beads into volunteers. Therefore alternative approaches have to be adopted for studies where this is deemed unethical.

In-vitro RSA comparison studies are common and use of animal, human or artificial substitutes. They can be typically defined into two categories; studies which investigate the static accuracy of a MBIR technique and studies which also consider the dynamic accuracy.

Static accuracy studies typically consists of an object of interest being placed into different positions to simulate an activity or movement of interest (Banks and Hodge 1996; Mahfouz et al. 2003; Lin et al. 2013). The major limiting factor when considering static errors alone is that the corresponding dynamic error is much greater with studies finding up to a factor of 5 or more difference when compared to in-vivo dynamic studies (Tashman 2008).

Dynamic accuracy studies move an object of interest to simulate an activity during a fluoroscopy session. The majority of studies have performed manual movement of the object of interest (Acker et al. 2011; Tersi et al. 2013; Ellingson et al. 2017; Barré and Aminian 2018). Acker et al. (2011) looked at the accuracy of estimating single plane kinematics for TKR components. Femoral and tibial components of a TKR were implanted into femur and tibia bone models respectively (Sawbones, Pacific Research Laboratories, Inc., USA). Active motion capture marker clusters were embedded into the Sawbones and they were manually moved during simultaneous dynamic data capture. The results from the MBIR TKR kinematics were compared with those calculated using motion capture (Optrack Certus, Northern Digital Inc., Canada) using a Bland-Altman analysis. A similar study (Ellingson et al. 2017) was performed to investigate the influence of pulse width and angular velocity on kinematic accuracy using the same methodology as the previous study but applied to TKR components implanted into a human cadaver. The velocity was varied for each of the differing pulse widths (1 ms, 8 ms and 16 ms). This approach was limited to the velocities they were able to produce manually. Both studies used a similar approach to compare the two methods, and as both methods were independent there was no influential bias with processing the data.

In vitro studies using automated methods to move objects of interest are becoming more common. The benefit of using an automated approach, whether involving actuators or robotic arms, is that the movement should be more repeatable. However this approach is more complex and typically the movement has been rather simplistic and relatively slow compared to the actual activity of interest (Li et al. 2008; Varadarajan et al. 2008). Guan et al. (2016) constructed the Dynamic Joint Motion Simulator (DJMS) to evaluate

the accuracy of their MoBIX system during simulated overground walking. It comprises two carriages allowing horizontal movement overhead and vertical and horizontal on the bottom carriage. This allows three degrees of freedom at the knee joint to be controlled by three servomotors. The DJMS was programmed to simulate stance phase of gait and tested the accuracy when tracking bone position for both Sawbones and cadaveric specimens at 0.7 m/s.

Most studies that have reported accuracy using measures bias and precision for either the position of the bones or kinematics. With bias and precision representing the mean and standard deviation of the difference between two methods respectively with one of the methods used as the reference standard (Ioppolo et al. 2007; Anderst et al. 2009; Brainerd et al. 2010; Fong et al. 2011; Giphart et al. 2012; Lin et al. 2014; Cross et al. 2017). Tersi et al. (2013) critiqued the presentation of errors as bias and precision highlighting that there were definition inconsistencies with groups using mean and standard deviation, or root mean squared error, or absolute errors. They also criticised the small sample size used by some groups and recommended the use of larger sample sizes and a Bland-Altman analysis which is considered to be a more comprehensive statistical approach when comparing methods that are measuring and quantifying the same variable (Bland and Altman 2007; Acker et al. 2011; Tersi et al. 2013; Giavarina 2015; Ellingson et al. 2017).

5.3 Overview and Aims

It is important for every new system, activity, joint of interest or image registration technique, that the errors associated with calculating bone kinematics are investigated. At Cardiff University there were no previous validation protocols for the MBIR and X-ray equipment. Therefore to compare the accuracy of our new protocols a series of experiments were developed.

Based on the literature a comparison of RSA, motion capture and MBIR kinematics were performed under static and dynamic conditions using a Sawbones phantom. Because the C-arms are only able to perform continuous fluoroscopy there was concern that blur may influence the ability to use RSA as the reference standard therefore motion capture was performed using a combination of methods in a similar way to previous studies (Acker et al. 2011; Tersi et al. 2013; Ellingson et al. 2017).

Accuracy tests should, if possible, resemble realistic testing conditions to replicate image conditions and other factors which could introduce errors. To attempt to fully simulate the MBIR protocol at Cardiff University an ovine static and dynamic experiment was carried out using the MRI derived models of the ovine specimen to define bone kinematics.

The main aims of this study are therefore:-

- Develop protocols to perform MBIR using the clinical C-arm scanners
- Develop protocols to quantify the accuracy of MBIR defined kinematics.
- Investigate how the errors change as complexity of the experiment increases from static to dynamic to incorporating soft tissue.
- Understand the capabilities and limitations of dynamic fluoroscopic imaging to calculate bone kinematics using the clinical mobile C-arm scanners combined with the MBIR protocols developed at Cardiff University.

A series of experiments were designed and undertaken to achieve these aims each with their own objectives: -

- **Experiment 1** - determine the measurement accuracy associated with RSA using the C-arms.
- **Experiment 2** –calculate the measurement accuracy of MBIR derived kinematics using a knee phantom in different static positions with RSA as the main reference standard and motion capture investigated as a reference standard.
- **Experiment 3** - Employ the same approach as Experiment 2 but simulate a step activity using a phantom under dynamic conditions. Different dynamic velocities applied to investigate the hypothesis that the errors using MBIR increase as the velocity increases.
- **Experiment 4 & 5** - Perform static and dynamic tasks using an ovine specimen and MRI model to determine the errors introduced by the soft tissue.

5.4 Methods

The first part of this section describes the new equipment used as part of a project to develop a bespoke biplane fluoroscopy facility at Cardiff University. This is followed by the development of all of the new protocols that were required for MBIR using the new equipment. Finally there is a description of methods employed for the validation experiments and the developmental process that occurred to perform them.

5.4.1 Equipment

Two Siremobil 2000 C-arms (Siemens, Germany) were purchased as part of an EPSRC small equipment grant 2012 (awarded to G. Whatling). These machines, which had been used previously within a clinical setting, were refurbished prior to purchase and critically examined on installation at Cardiff University (Figure 5-1). Each system has a 250 mm diameter image intensifier and a source-detector distance (SDD) of 870 mm. Compared with the fixed C-arm system based in Llandough University Hospital, used and described in Chapter 2 and 3, they have a smaller Field of View and shorter SDD but are mobile allowing biplane configurations.

Figure 5-1 Two Siremobil 2000 C-arms with monitor trolleys

Both systems have no built in method of recording the fluoroscopic exposures so an external video recorder was used. The system used was a MediCap USB2000 (Medicapture, USA) which takes in the composite video input from the live monitor of the C-arm and records fluoroscopic examination as an MPEG-4 video file at 25FPS with a frame width of 720 pixels and height of 576 pixels. This video can then be saved onto an external USB drive.

5.4.1.1 Configuration

The mobile C-arms made a number of configurations possible therefore a series of different configurations were investigated and scored based on the following criteria:-

- Proximity of the object/subject to the image intensifier
- Maximising overlapping field of view of both systems
- Allowed position of the object or volunteer in the field of view

The final configuration (Figure 5-2) was chosen as it allowed the ability to place a platform or experimental rig at the base of the field of view, while maximising the overlapping field of view of both C-arms.

Figure 5-2 Final configuration of the two C-arms that was used for all experiments in Chapter 5 and Chapter 6. The angle between the two imaging fields was approximately 90°. The C-arms were rotated axially to 60° and 120° respectively to allow overlapping field of views. The cameras inside the C-arms were rotated to correct for the axial rotation applied to each C-arm.

5.4.1.2 Synchronisation

A custom trigger was developed to synchronise the two C-arms with the Qualisys motion capture system. A two-stage operator presence control switch (Figure 5-3) was connected to a custom circuit consisting of two relay switches with several outputs.

Figure 5-3 Two Stage operate presence control switch

A two stage switch was used because both C-arm systems take approximately 1 second to stabilise to the current at the start of fluoroscopic exposures. This was performed on the first stage and all data capture with the second stage. The operator presence control switch means that the operator has to hold down the button for the entire fluoroscopy examination. This limits the potential for accidental exposures to any volunteers. The MediCap USB200 system, used to digitise the images, accepts a foot switch trigger input to start and stop collecting videos. This input was used on both systems as part of the triggering mechanism. The Qualisys motion capture system and all the other equipment connected with it can be triggered using a 5V TTL pulse. An overview of what each stage of the trigger does can be seen in Figure 5-4.

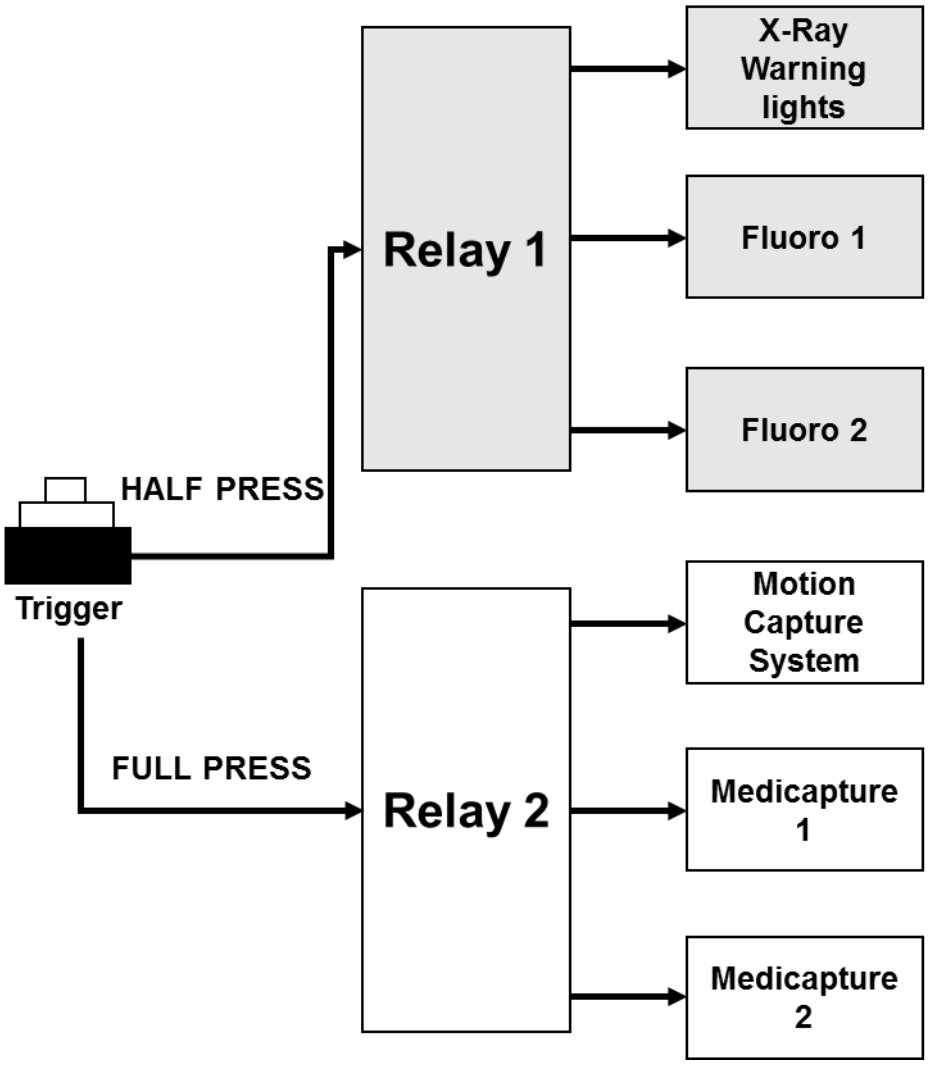

Figure 5-4 A simplified diagrammatic overview of the custom two stage trigger. When the first stage of the trigger is used (Half Press) it engages relay switch 1 which simultaneously sends a signal to both c-arm systems to generate a fluoroscopic exposure and to turn on the X-ray warning light. Once the systems have ramped up to the current voltage the second stage is ready to be triggered (Full Press), this engages relay switch 2. Relay switch 2 sends a simultaneous signal to trigger both Medicapture systems to start collecting video and a 5V TTL pulse to trigger the motion capture system.

5.4.1.3 Motion Capture

Motion analysis data was collected using 11 Qualisys Oqus cameras (10 Oqus 700+ and 1 Oqus 210) positioned around the two C-arms (Figure 5-5). The motion capture cameras were upgraded from the cameras used in Chapter 3 with an increase in the size of the imaging sensor from 3MP to 12MP. The position of the cameras produced a calibration with residual errors less than 0.4mm for each camera.

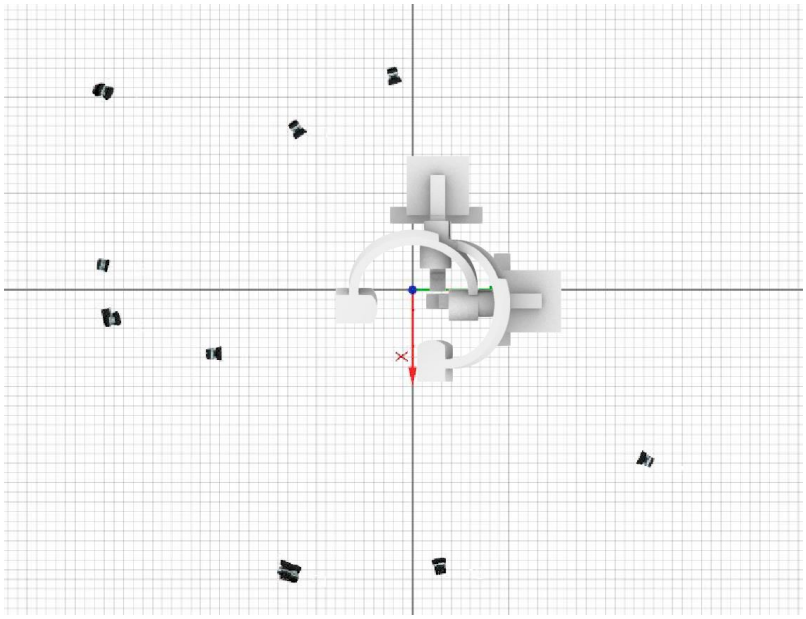

Figure 5-5 Overhead view of the position of the motion captures relative to the two Siremobil C-arms

5.4.2 Development of Calibration Protocols

The following section details the process and development of the protocol to calibrate any two X-ray systems ready to carry out MBIR using biplane imaging.

5.4.2.1 Distortion Calibration

Prior to a fluoroscopic data collection the image must be corrected for geometric distortion. The calibration frame is imaged using both C-arm systems separately following the method described in section 2.2.4.1.

Fluoroscopic examinations are saved and exported as MPEG-4 using the MediCap system. A custom MATLAB code splits the videos into individual frames and saves them in the Tagged Image File Format (.tiff). Using built in functions within ImageJ, an open source image processing software (Schneider et al. 2012), the images are horizontally flipped and converted into 8-bit greyscale. The images of the calibration frame are then processed following the protocol defined in Appendix B.

5.4.2.2 Biplane Calibration

To perform biplane calibration of two X-ray systems the following measurements are required:-

- Internal orientation parameters to define the geometry of the X-ray source relative to the detector
- External orientation parameters to define the orientation of the X-ray equipment relative to a lab coordinate system

Software and advice on how to accomplish this was provided by Prof. Scott Banks. The following section describes how this was set up at Cardiff University.

5.4.2.2.1 Building of Calibration Cube

To define the internal and external parameters a 3D object of known geometry is needed. It has been shown that a calibration object consisting of a cube with embedded steel beads of known position can produce a suitable calibration (Brainerd et al. 2010).

A 100 mm x 100 mm x 100 mm acrylic cube was used to act as the structure of the calibration object (Figure 5-6) and 2mm stainless steel ball bearings to act as the beads.

Figure 5-6 Acrylic cube used to form the basis of the calibration object

To optimise calibration, the position of the beads must be randomly distributed over a uniform coverage of the space. As the beads are positioned on each of the four vetical faces of the cube, overlapping bead positions on opposing sides must be avoided so that calibration errors are avoided during the X-ray, ie, if the beads overlap they appear merged into one bead.

A custom MATLAB script was used to generate the position of each of the beads for the four vertical faces of the cube. Each of the faces was divided into a 10 x 10 grid, and positions of the beads were randomaly generated. To optimise this only one bead position was allowed per row and column. Four position maps were generated with 9 beads per map and the opposing vertical faces were overlaid to check that there was no overlap (Figure 5-7).

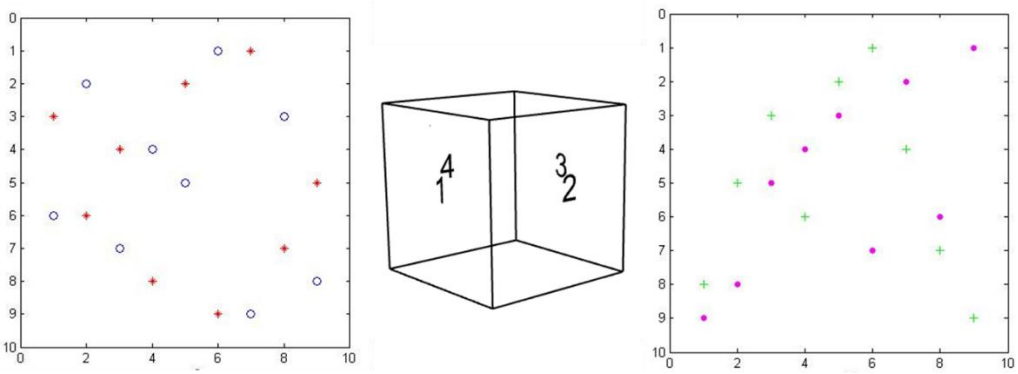

Figure 5-7 Plots exported from the MATLAB script showing the randomly generated positions of the beads. The plot on the left shows the position of the beads for the 1st vertical face (Red stars) over layered with the position of the beads for the 3rd face (Blue circles). The plot of the right shows the position of the beads for the 2nd vertical face (Green crosses) and the 4th vertical face (Pink stars). The plots show that none of the positions of the beads overlap.

These positions were then marked on the acrylic cube for each face and the 2mm stainless steel ball bearings were fixed into place using an adhesive (Figure 5-8).

Figure 5-8 Photo on the left shows the acrylic cube with beads fixed in position. Photo on the right shows biplane X-rays of the cube showing the position of the beads.

5.4.2.2.2 Defining Bead location

To define the fiducial coordinates for each of the beads attached to the calibration cube the following steps were performed.

CT imaging and Segmentation

The calibration cube was CT scanned with a GE LightSpeed VCT scanner using a kVp = 120, mAs = 119, pixel size of 0.48 mm x 0.48 mm and a slice thickness of 0.625 mm. The scans were performed by an experienced superintendent radiographer at Velindre Cancer Centre.

The calibration cube and beads were segmented from the CT data using ScanIP (Synopsys, USA) and exported as 3D models in the .STL format (Figure 5-9).

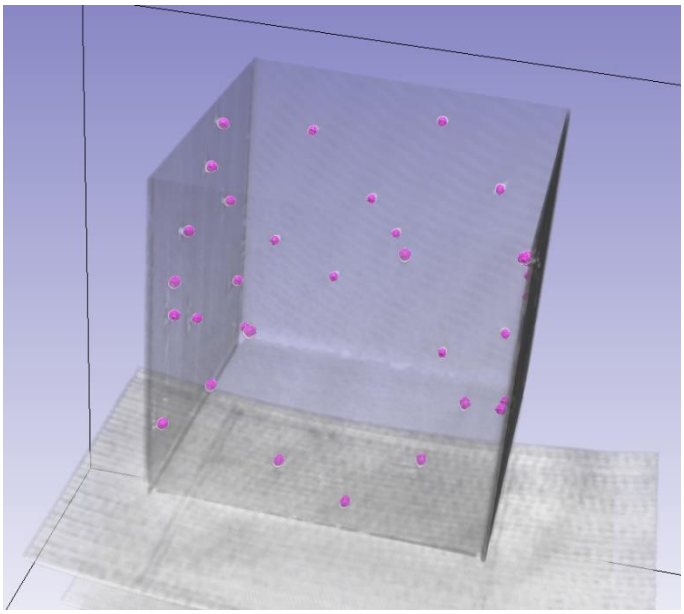

Figure 5-9 Screen shot of segmented metal beads overlaid on a visualisation of the CT scan

Alignment

The 3D models of the calibration cube were imported into Rhinoceros 6 (McNeel, USA) to apply a global coordinate system (GCS) in order to define the bead location. The centroid of the cube was defined as the origin, the z-axis directed towards the centre of the 1st vertical face, the x-axis directed towards the centre of the 2nd vertical face and y-axis acting vertically upwards. This was done to mirror the coordinate systems used in the JointTrack software.

Calculation of individual bead position

After the GCS was applied, the individual fiducial coordinates of each of the beads could be calculated. The segmented 3D model of the beads with the applied GCS were imported into Artec Studio 12 (Artec 3D, Luxembourg). An ideal 2mm sphere was created within Rhinoceros 6 CAD software and fitted to each of the segmented beads using a rigid registration algorithm in Artec Studio 12. The centroid of each of the registered ideal 2mm spheres was calculated and the X, Y, Z centroid coordinate used to define the position of the beads. A total of 35 markers were used in the final calibration cube.

5.4.2.2.3 Software biplane calibration

The MATLAB script (Biplane_Manual.m) provided by Professor Scott Banks (University of Florida) was adapted to work with the calibration object and data collected using the C-arms. The following describes how the software performs the calculations and the associated theory.

An X-ray system can be modelled as an ideal pinhole camera with the X-ray source acting as the camera and the detector (image intensifier) as the imaging plane. Although a point X-ray source cannot be physically created it is assumed that the size of the X-ray source (less than $1mm^2$) is small enough for this to be considered. Using the internal orientation parameters of this 'camera system' and perspective projection geometry, the coordinates of a 3D object can be determined from its position on the 2D imaging plane. The internal orientation parameters used are the principal point and the principle distance. The principal point is the location on the imaging plane where the z-axis of the X-ray system intersects. The principle distance is the length of the distance between the X-ray source and the principle point (Banks 1992; Banks and Hodge 1996).

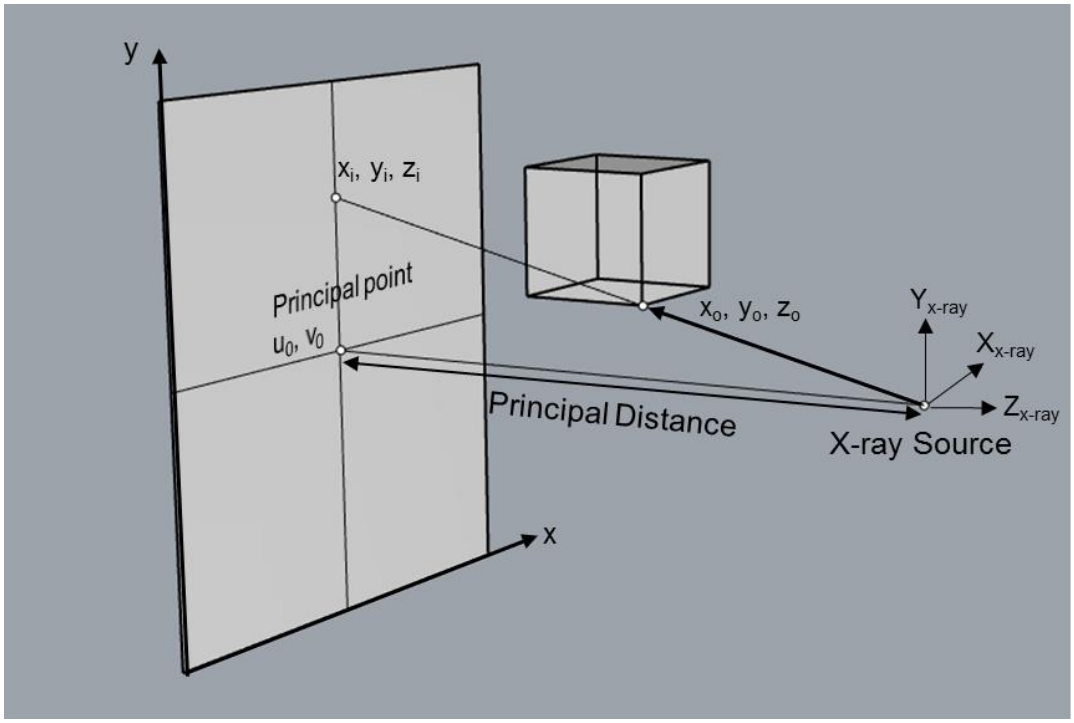

Figure 5-10 A simplified diagram of the X-ray system modelled as a pin-hole camera to describe how a position on an object can be converted into a position on the imaging plane.

Considering a point on the calibration cube situated between the X-ray source and the imaging plane; when the X-ray hits this point its projection on the imaging plane can be calculated. In Figure 5-10 the following geometric relationships, using similar triangles because the corresponding angles are all equal, can be used to calculate the x- position on the imaging plane:-

$$\frac{x_i}{x_o} = \frac{z_i}{z_o} \qquad 5\text{-}1$$

$$x_i = x_o \frac{z_i}{z_o} \qquad 5\text{-}2$$

$$x_i = x_o \frac{Principal\ Distance}{z_o} \qquad 5\text{-}3$$

The same relationship can then be used to calculate the y-position:-

$$\frac{y_i}{y_o} = \frac{z_i}{z_o} \qquad 5\text{-}4$$

$$y_i = y_o \frac{z_i}{z_o} \quad 5\text{-}5$$

$$y = y_o \frac{Principal\ Distance}{z_o} \quad 5\text{-}6$$

To calculate the pixel coordinates on the imaging plane requires a scale factor which converts from millimetres to pixels based on the number of pixels per millimetre in the image. The following equations convert the physical location of the projected point into pixel coordinates.

$$u_i = u_o + x_i \times Scale \quad \textbf{5-7}$$

$$v_i = v_o + y_i \times Scale \quad \textbf{5-8}$$

Using these relationships and the calibration cube created in section 5.4.2.2.1 the software can perform the X-ray system calibration.

The following ten parameters are needed to model the X-ray projection within the MATLAB software:-

- x_0, y_0 ,z_0 – Location coordinates of the origin of the calibration cube with respect to the X-ray focus
- alpha, beta, gamma – Rotations of the calibration cube with respect to the x-, y- and z-axes of the X-rays system respectively.
- u_0,v_0 – Pixel coordinates of the principal point on the imaging plane.
- Principal distance - Length of the line connecting the X-ray focus and the principle point. As the origin is defined to act at the X-ray focus and the principle distance acts along the negative z-axis then the distance is always considered negative.
- Scale – Number of pixels per millimetre in the image, typically defined as the reciprocal of the pixel dimension (typical DICOM value), however for the two C-arms this value was not provided.

An image of the calibration cube is loaded into the MATLAB software along with the fiducial coordinates of the beads calculated in section 5.4.2.2.2. Using a Circle Hough Transform (CHT) function, the position of the beads on the image are automatically located. The CHT is a feature extraction technique

used in image processing to detect circles in an image and works well even when the image is considered to be noisy (Duda and Hart 1972; Rizon et al. 2005). An initial guess is used for the parameters to align a projection of the location of the beads against the location of the beads on the 2D image. Using a nonlinear least squares minimisation function the 10 parameters are optimised, based on limits set in the script, to best match the projection to the locations defined on the 2D image (Figure 5-11).

The calibration file exported after optimisation includes the same internal orientation parameters as calculated using the method described by Whatling (2009) and described in section 2.2.4.1. Those being the principal distance (in mm), the x and y offset for the principal point and the pixel size per mm. The file also exports the external orientation parameters as a 3x3 matrix with each row being a vector. The first row is a vector which describes the position of the X-ray source in the calibration cube's coordinate system (defined in section 5.4.2.2.2), second row is a vector which describes the direction of the principal point to the X-ray source and the third row describes the direction of the vertical axis of the X-ray source.

Therefore, a simultaneous X-ray exposure can be performed on the calibration cube using both C-arms in any configuration (as long as the cube can be seen by both). Using the calibration software described above for both images, the JointTrack software is able to define the position of both X-ray systems relative to each other. This is a different software version of JointTrack used in Chapter 2 and Chapter 3 as it supports the option of using biplane imaging (the version used previously only supported single plane).

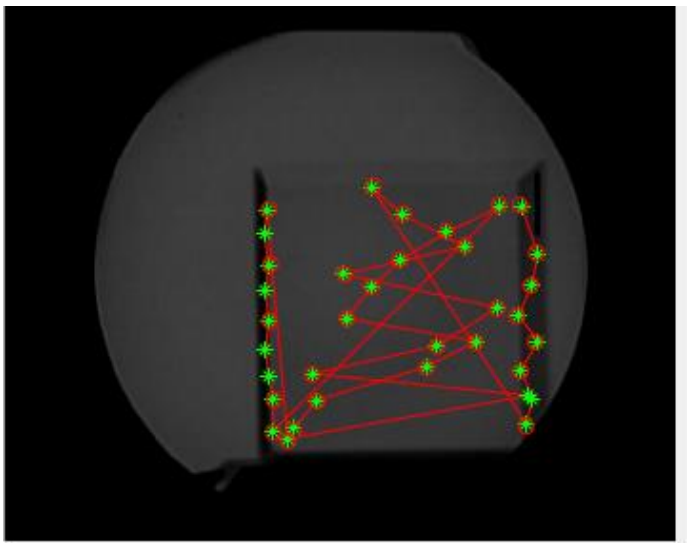

Figure 5-11 Projected 3D points (green stars) of the calibration cube lined up with bead locations detected using a CHT function on the 2D image (red circles) after an optimised calibration

5.4.3 Comparing between Motion capture and Fluoroscopy

To compare motion capture data with fluoroscopy data directly requires a transformation matrix relating the two coordinate systems. This approach was recommended in section 3.4.4, by using three or more non collinear markers that can be detected in both the motion capture and fluoroscopy systems.

Five 14mm retro reflective marker were fixed on to the calibration cube. Four of the markers were attached to the outside of the four vertical faces of the cube and the final marker attached to the inside bottom face. The retroreflective markers are checked for overlap, occlusion of the metal beads on the calibration cube and for collinearity. Five markers were used instead of three markers to ensure marker visibility in either system (Figure 5-12).

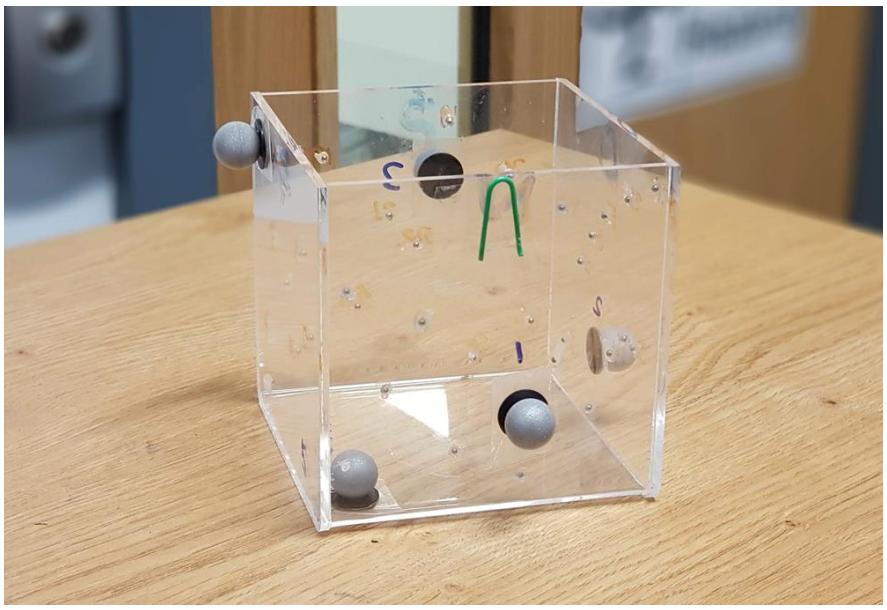

Figure 5-12 Calibration cube with five retroreflective markers attached and labelled

5.4.3.1 Defining motion capture marker positions

The calibration cube was imaged simultaneously using both C-arms and the Qualisys motion capture system. The following stages were performed to locate the positions in both systems:-

1. Using Qualisys Track Manager software, beads were identified and labelled according to the numbering convention highlighted in Figure 5-12.
2. x, y, z coordinates of the five markers within the motion capture global coordinate system were exported.
3. Fluoroscopy images of the calibration cube were processed and calibrated using the methods described in section 5.4.2.
4. Calibration images were imported into joint track and five 14 mm spheres (3D models created in Rhinoceros 6) matched to the markers appearing on the X-ray image (Figure 5-13).
5. x, y, z coordinates of the five markers within the fluoroscopy global coordinate system were exported.

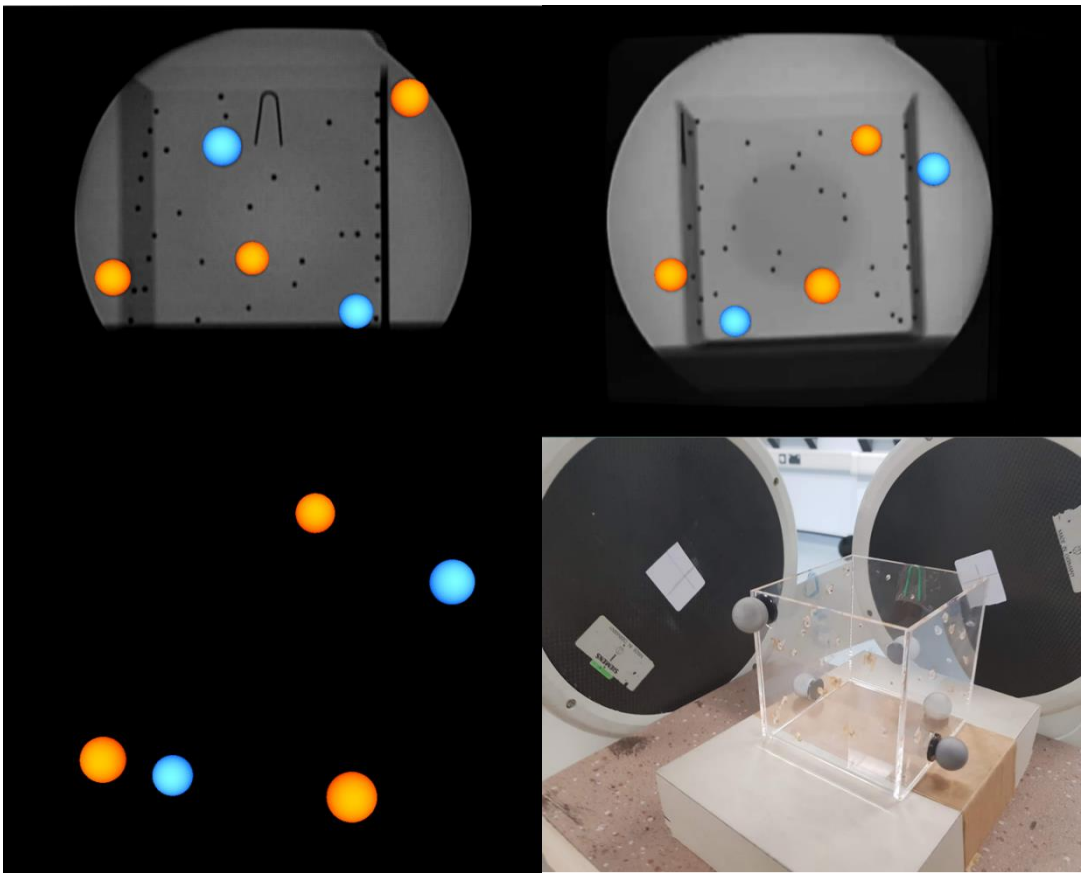

Figure 5-13 Images highlighting the MBIR process for locating the five motion capture markers. **Top:** The two different views of the C-arm systems with registered markers **Bottom Left:** 3D view of the 5 markers within joint track **Bottom Right:** Image of the calibration cube position during the X-ray exposure

5.4.3.2 Generation of transformation matrix

Now the five markers positions have been defined in both the motion capture and the fluoroscopy coordinate systems a transformation matrix can be used to convert motion capture marker data into the fluoroscopy coordinate system. A transformation matrix is a 4x4 matrix consisting of a 3x3 rotation matrix which dictates the rotation changes between axis and a 1x3 location vector which defines the translational change between the coordinate systems. A custom MATLAB script was written to perform the calculations with steps defined below:-

1. Using three of the markers locations defined in the motion capture system, two unit vectors are defined (v_1 and v_2).
2. The cross product between the two unit vectors is calculated (v_3) and a second cross product (v_4) is performed with the new vector and v_1.
3. v_1, v_3 and v_4 are arranged into a direction cosine matrix and define the x-, y- and z-axis respectively. This forms the rotation matrix of the marker cluster LCS.
4. One of the marker locations was defined as the origin and used to form the location vector in the transformation matrix for the marker cluster LCS.
5. These are combined to form the transformation matrix (Figure 5-14) converting the motion capture GCS into the marker cluster LCS (T_{MC}).

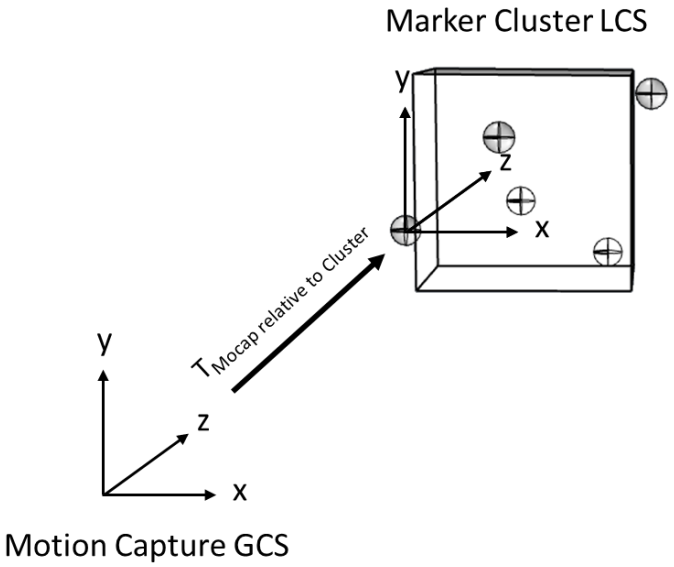

Figure 5-14 Diagrammatic overview of the transformation matrix of the marker cluster local coordinate system relative to the motion capture global coordinate system

6. Steps 1-5 are performed with the marker positions in the fluoroscopy coordinate system.

7. The transformation matrix (Figure 5-15) formed converts position data from the fluoroscopy global coordinate system into the marker cluster LCS (T_{FC}).

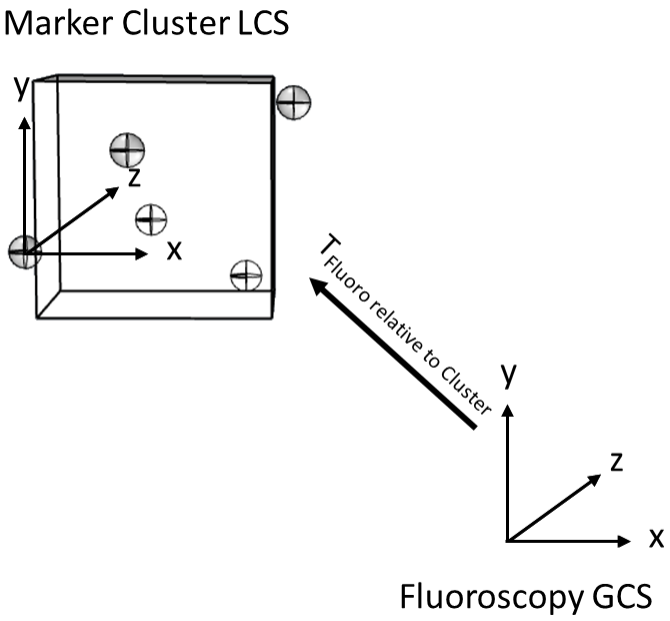

Figure 5-15 Diagrammatic overview of the transformation matrix of the marker cluster local coordinate system relative to the fluoroscopy global coordinate system

8. The inverse of the T_{FC} is performed to calculate T_{CF}.
9. The final transformation matrix (Figure 5-16) converting motion capture to fluoroscopy global coordinate system is defined by the following equation:-

$$T_{MF} = T_{CF} \times T_{MC} \qquad 5\text{-}9$$

This transformation matrix can be used to convert motion capture marker data into the fluoroscopy global coordinate system to allow direct comparisons between motion capture marker data and data calculated using MBIR.

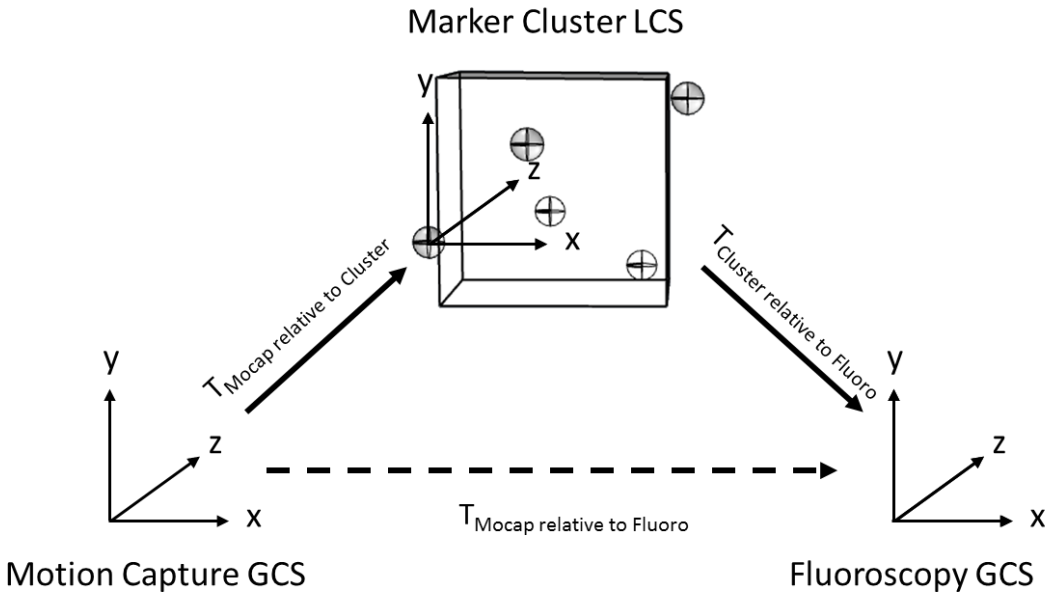

Figure 5-16 Diagrammatic overview of the transformation matrix of the motion capture global coordinate system relative to the fluoroscopy global coordinate system.

5.4.4 Experiment 1 - Metal Bead Validation

To validate the MBIR protocols developed at Cardiff University a reference method is required. It was decided to use metal beads in a similar approach to RSA as a good comparator. The RSA approach developed matches models of the beads to the outline in the image; referred to here with as bead MBIR. The accuracy associated with calculating translations using the beads must therefore be determined.

5.4.4.1 Bead object

To determine the accuracy of locating three beads a validation object was required. Three 6mm stainless steel beads were fixed into an acrylic block to maintain their fixed distance apart. To determine this fixed distance, the acrylic block and beads were scanned using a Skyscan 1272 microCT scanner (Bruker, USA) with a pixel size of 20μm (Filter = Al 0.5mm, Source Voltage = 70 kV, Source Current = 142 μA and Rotation step = 0.6°). Due to the large

size of the acrylic block compared with the field of view of the scanner three horizontal offset scans were used to ensure full capture (Figure 5-17).

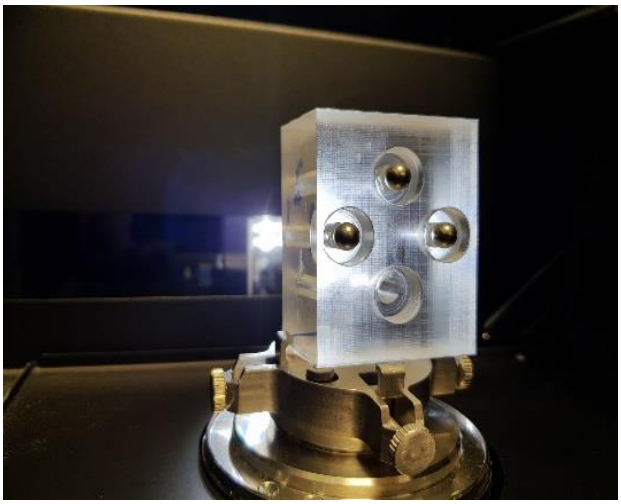

Figure 5-17 Validation object consisting of three stainless steel beads mounted in an acrylic block positioned on the positioning stage in the Skyscan 1272 (Bruker, USA) microCT scanner.

The image data from the microCT scanner was imported into ScanIP (Synopsys, USA) and the steel beads were segmented (Figure 5-18a) and exported as 3D models into Rhino 6. Their volume centroids were calculated and vectors drawn between them. Where the vector from the top bead bisects the vector joining the bottom beads was defined as the the origin of the 3D models with the coordinate axes system of the model aligning with the vectors (Figure 5-18b).

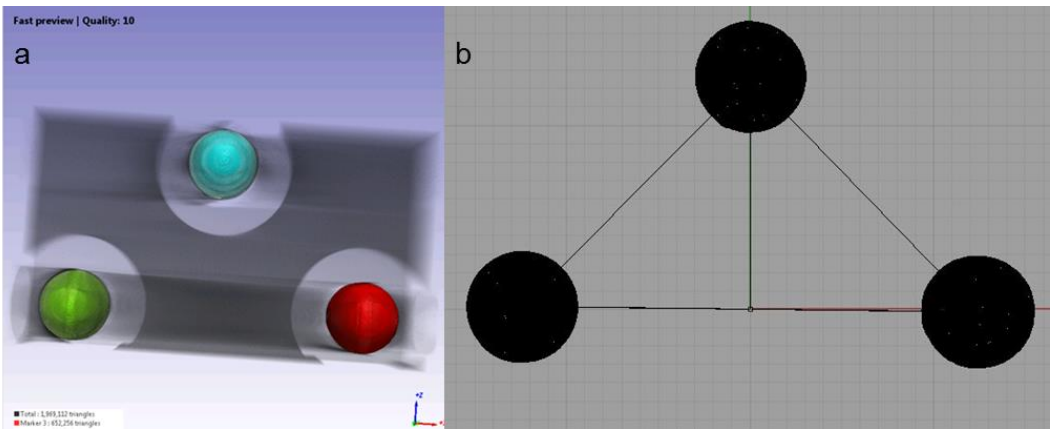

Figure 5-18**a** Segmented stainless steel beads overlaying a visualisation of the microCT data **b** Three beads imported into Rhino 6 and vectors drawn between their volume centroids.

5.4.4.2 Validation

To provide the ground truth data for both translations of the validation bead object a precision manual two-axis linear stage and combined rotation stage (part of a toolmakers microscope), was used as the reference (OMT, UK). The two axis linear stage translates in imperial units and has an accuracy of ±0.0001 inch (0.00254mm).

The validation bead object was mounted on top of the rotation stage with the centre of the validation bead object aligned with the centre of the rotation stage (Figure 5-19). The two axes of the linear stage were aligned with the coordinate system of the calibration cube.

A series of static translations were applied to the validation bead object and static biplane fluoroscopy images were captured. A neutral position image was captured first and a series of ten displacements, with each displacement decreasing in size, applied (Table 5-1). Static translations were applied to both the z-axis and x-axis separately to examine the error in both directions.

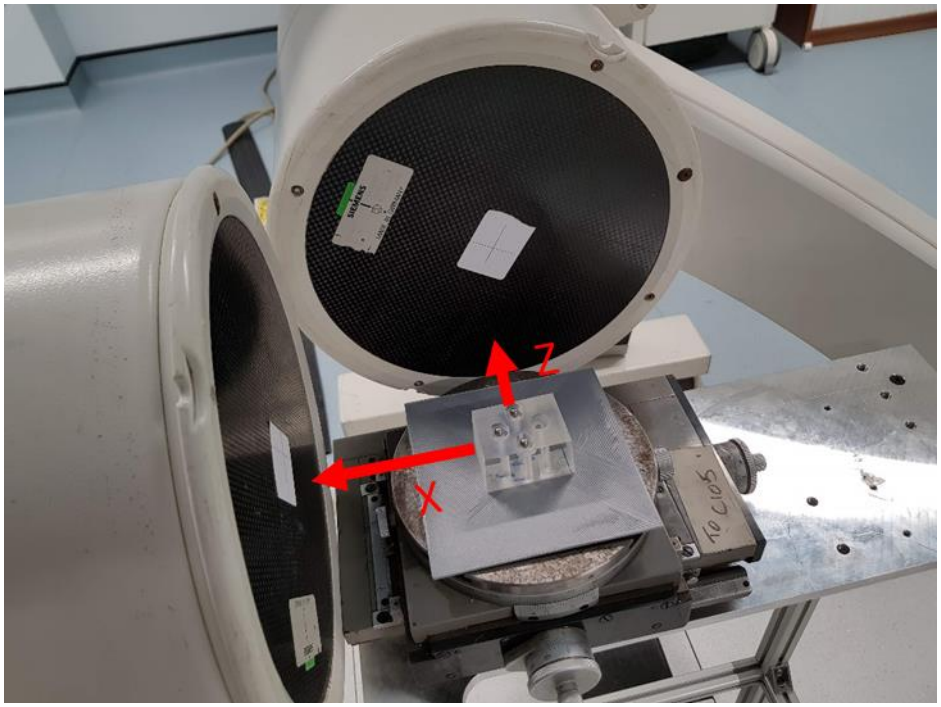

Figure 5-19 Validation bead object mounted on top of the two axis linear stage and combined rotation stage. With the direction of the x- and z-axis highlighted.

Prior to MBIR each pair of biplane images were randomised to remove bias. The 3D model of the beads were imported into JointTrack software and the model matched to all the image pairs. To compare the translations, the neutral position coordinates were taken from each of the positions coordinates output from JointTrack.

Table 5-1 Displacements applied to validation bead object using the positioning stage for each static fluoroscopy capture

	Displacement	
Position	**Inches**	**mm**
0	Neutral	
1	0.5	12.7
2	-0.2	-5.08
3	-0.1	-2.54
4	-0.05	-1.27
5	-0.02	-0.51
6	-0.01	-0.25
7	-0.005	-0.13
8	-0.002	-0.05
9	-0.001	-0.02
10	-0.0005	-0.01

5.4.5 Experiment 2 - Static Validation (Phantom)

5.4.5.1 Experimental method

To investigate the static accuracy of the MBIR protocol using the biplane C-arm system at Cardiff University, a static pose validation experiment was developed and performed. Femur and tibia Sawbones (Pacific Research Laboratories, Inc., USA) were attached together using elastic bands to simulate the anterior and posterior cruciate and medial and lateral collateral ligaments. These were not positioned in a physiologically accurate way but serve the purpose to ensure that two models move relative to each other. This model was used as an imaging phantom to investigate the accuracy of static poses using MBIR with the Siremobil C-arms.

To generate the 3D model required for MBIR the Sawbones were imaged using a CT scanner and segmented following a similar approach as has been described previously in sections 4.3.3.2 and 5.4.2.2.2.

A custom marker cluster was designed and manufactured to support three stainless steel balls. The balls were 6mm diameter with a M3 female thread and were mounted on 12 mm nylon cheese head machine screws (Figure 5-20). The stainless steel balls were enclosed in retroreflective tape to make them visible to the motion capture system. The marker cluster was manufactured from a low density plastic; designed to have reduced visibility when imaged using fluoroscopy to minimise the influence of the marker cluster when registering the models.

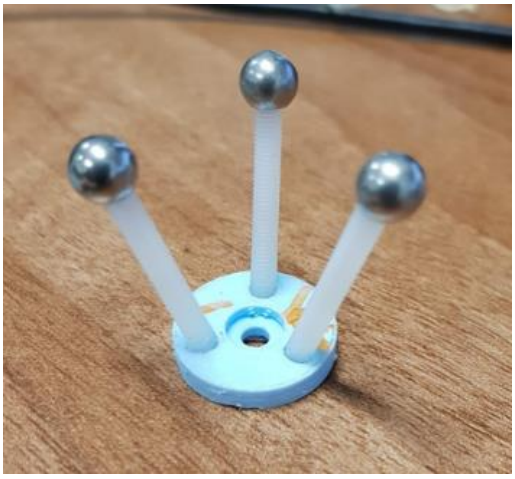

Figure 5-20 Custom marker cluster holding three 6mm stainless steel balls

The marker clusters were rigidly attached to the femur and tibia using a 2.5mm drill to create a pilot hole with a female thread applied using a M3 Tap into each of the bones. They were fixed in place using nylon machine screws (Figure 5-21).

Figure 5-21 Custom marker clusters rigidly attached to Femur and Tibia Sawbones imaging phantom. The stainless steel ball bearings are covered in retro reflective tape for visibility in the motion capture system.

The Sawbones were fixed into a custom knee rig (Figure 5-22a) designed to simulate different flexion angles during step up and down (Fletcher 2016). Each static flexion position related to approximately 5° change in flexion.

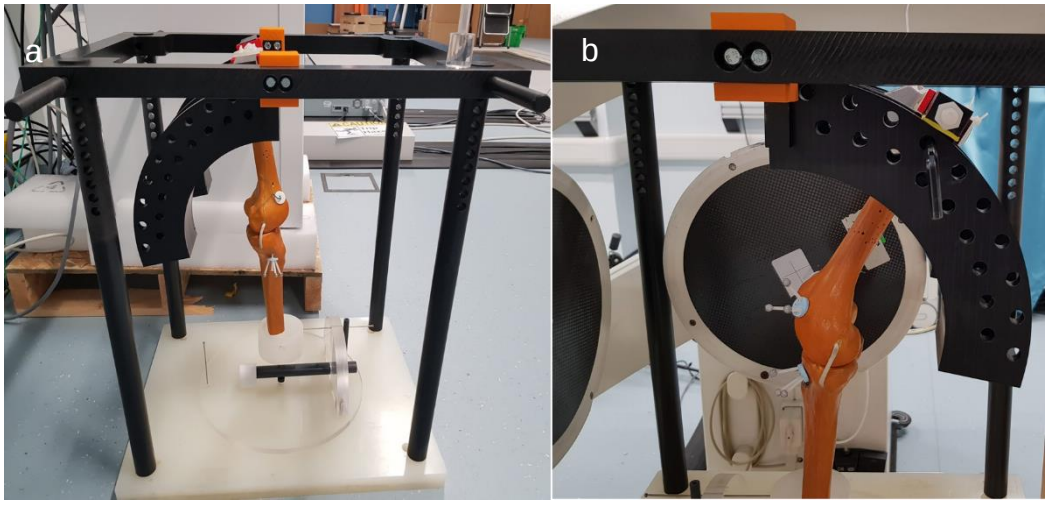

Figure 5-22 **a** Custom knee rig to simulate step up and down **b** Knee rig positioned between the two C-arms in the first static position

The knee rig was positioned into the field of view of the two C-arms with one X-ray system imaging in the frontal plane and the other in the sagittal plane. Five static positions were recorded with synchronised motion capture and biplane fluoroscopy (Figure 5-22b). Each of the static positions chosen

changed the flexion by approximately 10° and the five static positions were repeated three times.

5.4.5.2 Processing Method

5.4.5.2.1 MBIR Processing

To calculate kinematic data from the phantom an anatomical coordinate system (ACS) was applied to the individual bones. The method used previously at Cardiff University and described in section 3.2.2.1.1 works only for full bone models (femoral head to malleolus). The Sawbone phantom only consisted of the proximal tibia and the distal femur so a different approach was used.

Miranda et al. (2010) developed an algorithm that determines the ACS for the knee automatically. It uses a combination of the cross-sectional area, centre of mass, principal axis of inertia and cylindrical fitting to the condyle to construct the ACS. The algorithm was applied to define the ACS for the Sawbone phantom.

Phantom MBIR

The Sawbone phantom models were imported into JointTrack Biplane and each static image pair randomised. The position and rotation data for each of the image pairs was calculated using the MBIR protocol defined in (6.3.2.1). The advantage of using JointTrack Biplane software is the ability to position the model using the two different X-ray views simultaneously. The x-y-z positon of the origin of both models and the Euler rotations (Z-X-Y) applied at each frame were exported out of JointTrack.

Bead MBIR

The x-y-z position for the three individual beads of both marker clusters for each of the fluoroscopy frames were calculated using JointTrack Biplane. 3D models of the beads were imported into the software and matched to the image pairs. The beads positions were located using a separate independent MBIR process to remove bias between the two approaches.

Motion Analysis Processing

The beads on the marker cluster were identified and labelled in Qualisys Track Manager (Qualisys, Sweden) using the raw marker data and the same method as described in section 2.2.2.3. The coordinates for each bead were exported into the motion capture GCS and converted into the fluoroscopy GCS using the transformation matrix T_{MF} (defined in section 5.4.3.2).

5.4.5.2.2 Kinematic Calculation

A custom MATLAB script was used to calculate the tibiofemoral kinematics from the bead data for both the MBIR and motion capture approaches. The following steps were performed in the software code:-

1. The first frame for each of the repeats was used to define a static relationship between the marker cluster and the bone models
2. A LCS was applied to the marker cluster using the three non-collinear beads and a transformation matrix between the marker cluster LCS and the fluoroscopy GCS.
3. An ACS was defined for each of the segments using the X-Y-Z position and Euler rotations exported from Join Track.
4. A transformation matrix between the marker cluster LCS and the ACS of its respective segment was defined. This defines a fixed relationship between the marker cluster and the bone.
5. The LCS for the marker cluster was calculated for each frame and transformed to calculate the ACS for each frame.
6. The kinematics from the marker cluster were calculated using the same approach as the MBIR protocol.

These steps were performed on both motion capture and MBIR defined bead locations to allow kinematic comparison against the MBIR defined phantom position.

5.4.5.3 Kinematic comparison

To compare the differences between the MBIR defined phantom kinematics and the two bead approaches a Bland-Altman analysis was performed using a similar approach as defined by (Acker et al. 2011; Tersi et al. 2013; Ellingson et al. 2017).

A Bland-Altman plot examines the agreement between two quantitative measurements calculating the same parameter and calculates the limit of agreement (Bland and Altman 1986). With the limit of agreement being defined as ±1.96SD of the mean difference between the two measurements (Giavarina 2015). It is expected that 95% of the data should fall between the two limits of agreement (Bland and Altman 2007).

The x-axis of the plot consists of the mean values between the two methods and the y-axis the difference between the two methods. An example plot can be seen in Figure 5-23. It is commonly used to investigate the accuracy of a new method against a gold standard and assumes that even the gold standard has some form of error (Bland and Altman 1991).

Three separate comparisons were performed:-

1. MBIR kinematics vs. Bead MBIR kinematics
2. MBIR kinematics vs. Motion capture kinematics
3. Motion capture kinematics vs. Bead MBIR kinematics

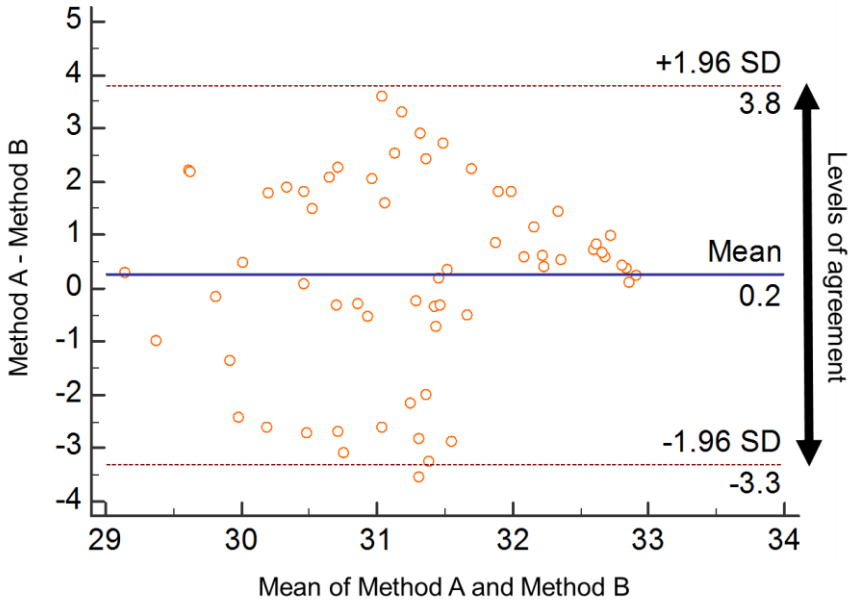

Figure 5-23 Example Bland-Altman plot with the x-axis being the mean of the two methods and the y-axis the difference between the two methods. The bold and dashed lines representing the mean difference and levels of agreement respectively.

5.4.6 Experiment 3 - Dynamic Validation (Phantom)

5.4.6.1 Equipment

To investigate the errors during dynamic activities the custom rig (Figure 5-22) used in the static experiment was adapted to use a linear actuator to move the phantom dynamically.

The linear actuator (Model Number: FA-RA-22, Firgelli Automations, USA) was fixed to the top of the rig and connected to the end of the Sawbone femur phantom (Figure 5-24). A power supply was used to supply a current to drive the femur from a near extension to approximately 80° of flexion, simulating a step down activity.

The top speed of the linear actuator was 300 mm/s with a dynamic force of 10Kg. The speed was deemed appropriate for simulating the step up-down activity based on an analysis of the velocity from motion capture data of the

femur markers performed for step up and down activity (from section 3.2.2.2). It was found that the average peak velocity ranged between 200mm/s – 320 mm/s. To vary the speed of the linear actuator the current supplied to the actuator by the power supply was adjusted.

Figure 5-24 Linear actor mounted to the top of the custom knee rig connected to the proximal end of the femur in the middle of the C-arms field of view. The c-shape runners were used to direct the travel of the linear actuator and the distal end of the tibia was clamped to the base of the rig to ensure the phantom remained in the field of view of the X-ray equipment.

5.4.6.2 Experimental Method

To investigate the errors of MBIR during dynamic activities three different velocities were investigated (Table 5-2). For each of the dynamic tests the linear actuator started fully retracted with the Sawbones phantom at approximately 10° flexion. Simultaneous biplane fluoroscopy and motion capture was recorded during each of the dynamic tests and three repeats were performed for each of the three different velocities.

Table 5-2 The three different velocities investigated using the linear actuator and Sawbones phantom with the corresponding supplied current and peak velocity of the motion capture markers.

	Current Supplied to Linear Actuator (A)	**Peak velocity of Femur Markers (mm/s)**
Slow Dynamic	1.5	100
Medium Dynamic	2.5	150
Fast Dynamic	5.0	240

5.4.6.3 Processing methods

All processing and analysis was performed using the same protocols as defined in section 5.4.5.2.

5.4.7 Experiment 4 & 5– Static and Dynamic Validation (Ovine)

5.4.7.1 Specimen Preparation

The ideal approach to investigate the errors of MBIR during static and dynamic activities using MRI would be to use a cadaveric specimen. As discussed in section 4.3.1 Cardiff University has no protocol in place to use human cadaver samples outside of designated areas. So one of the ovine specimens used in Chapter 4 was used to provide an animal substitute.

During the MR validation study in Chapter 4, one of the ovine specimens (OV1) was selected to perform a part of the MBIR study. The femur and tibia ends were dissected to expose the bone ends, making sure to keep the stifle joint intact. Two small areas, one either side of the stifle joint were dissected to allow room for the attachment of the marker clusters. Using the same protocol as defined in section 5.4.5.1 the marker clusters were rigidly attached to the femur and tibia of the ovine specimen (Figure 5-25a).

To maintain the integrity of the joint capsule surrounding the stifle joint the markers had to be placed further down the bone than when using the phantom. Due to the small field of view of the C-arm system this meant that the beads were not visible in the fluoroscopy images. Therefore, only motion capture and MBIR could be recorded during the static and dynamic tests.

Due to the large size of the femoral head and the shorter length of the femur compared to the ovine tibia the specimen was mounted upside down in the custom knee rig (Figure 5-25b). The tibia was articulated relative to the fixed femur during static and dynamic tests. The ovine specimen was wrapped in polyethylene to ensure no contamination on the X-ray equipment.

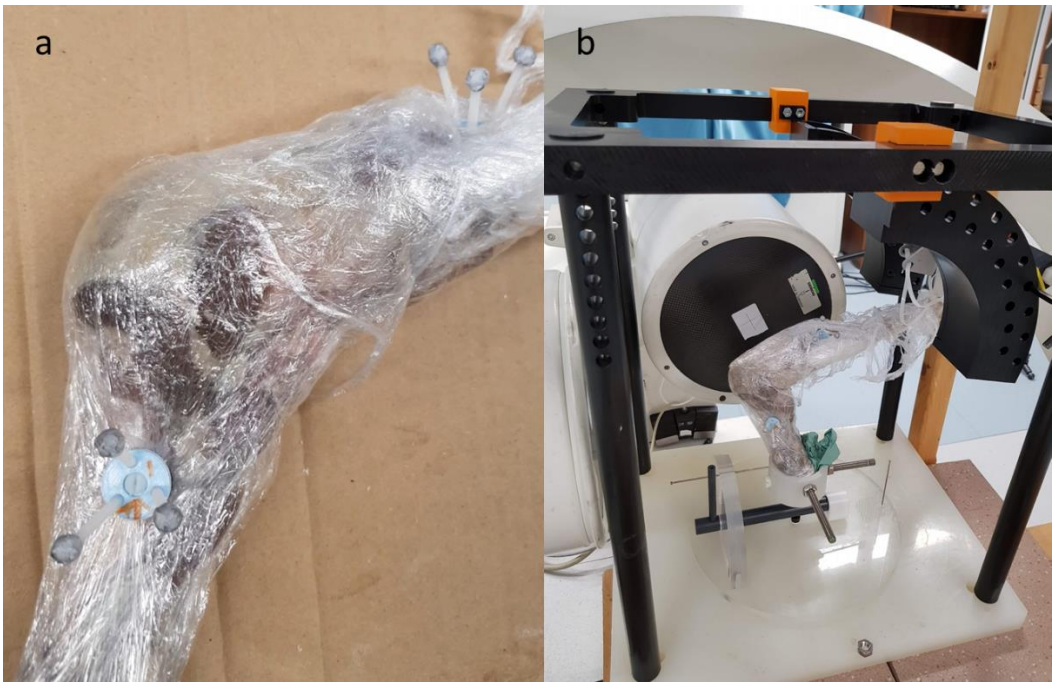

Figure 5-25 **a** Ovine specimen with marker clusters implanted into tibia and femur; **b** Ovine specimen fixed into the custom knee rig in a static position.

5.4.7.2 Experimental Method

The same five static positions used for the static phantom validation were used with the ovine specimen. Synchronised biplane fluoroscopy and motion capture was performed during static and dynamic experiments (Figure 5-26).

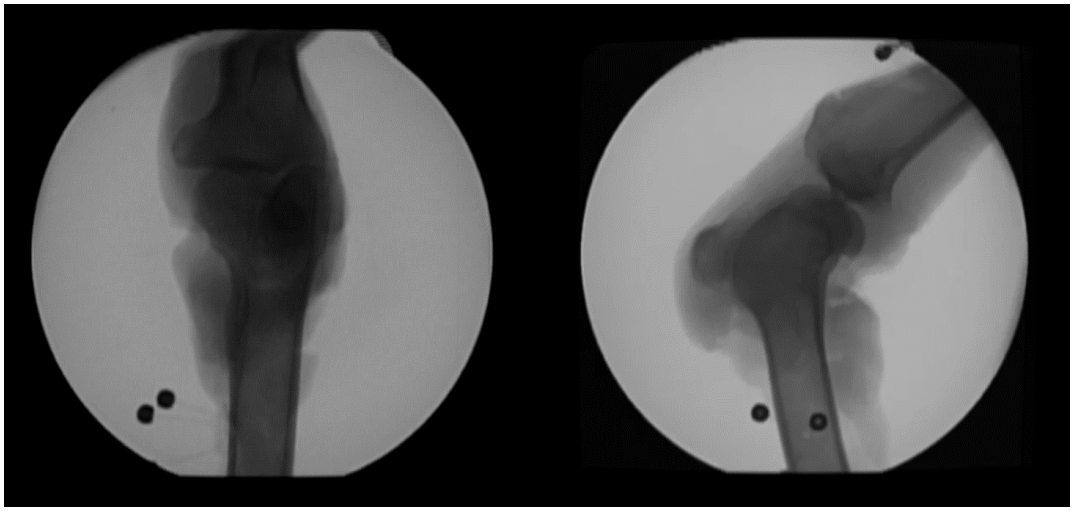

Figure 5-26 Example biplane fluoroscopy image of ovine specimen.

For the dynamic validation experiment only one speed was investigated with three repeats performed. This was because the laxity of the joint increased significantly during the dynamic experiments, compromising the ability to perform the flexion activity. This also compromised the number of repeats that could be performed for the static tests, therefore only two were performed.

5.4.7.3 Processing Method

The method described in section 5.4.5.2 was adapted to process and analyse the static and dynamic ovine data.

The MRI derived 3D model of the ovine specimen was used to perform the MBIR processing described previously in Chapter 4. The MRI scan of the ovine joint imaged the distal femur and proximal tibia only therefore the same automatic ACS algorithm developed by Miranda et al. (2010) was applied to the stifle joint.

Because the beads were not present in the fluoroscopy images, they were not processed using the MBIR method. Comparisons were performed between motion capture data recorded for the bead kinematics and MBIR kinematic data.

5.5 Results

5.5.1 Experiment 1 Bead Validation

Bland-Altman analysis was performed to compare translations computed for the Bead MBIR with the translations applied to the validation object using the 2 axis linear stage. The x-axis (Figure 5-27) and z-axis (Figure 5-28) were analysed separately with the mean difference and the mean absolute difference as output from the analysis (Table 5-3).

Table 5-3 Mean and absolute differences between the Bead MBIR and 2 axis linear stage looking at defined x and z translations.

	X - Translation	**Z-translation**
Mean Difference (Levels of Agreement) (mm)	**0.05** (-0.30 to 0.41)	**0.06** (-0.13 to 0.24)
Mean Absolute Difference ±STD (mm)	**0.16±0.102**	**0.09±0.07**

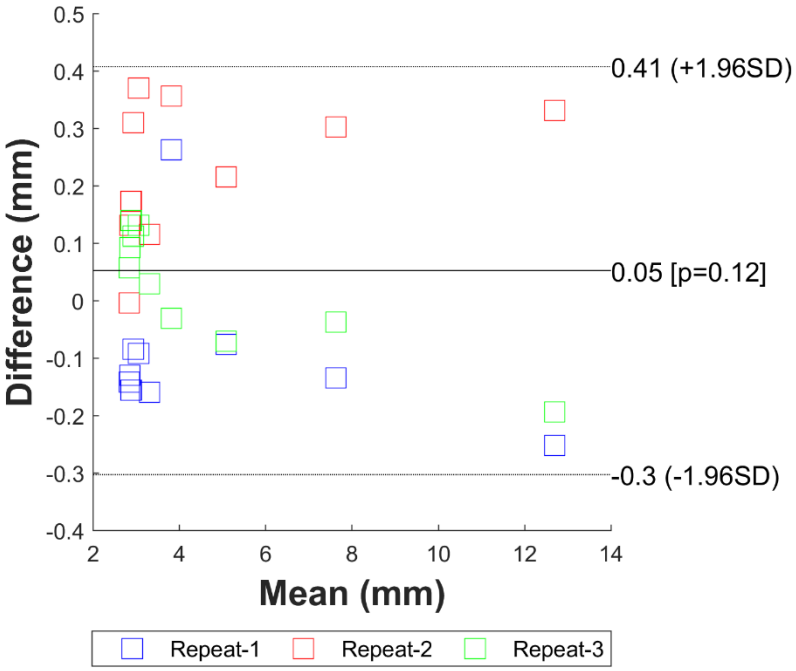

Figure 5-27 Bland-Altman plot comparing Bead MBIR x-axis translation with linear stage translation. With the bold line representing the mean difference and the dotted lines the levels of agreement.

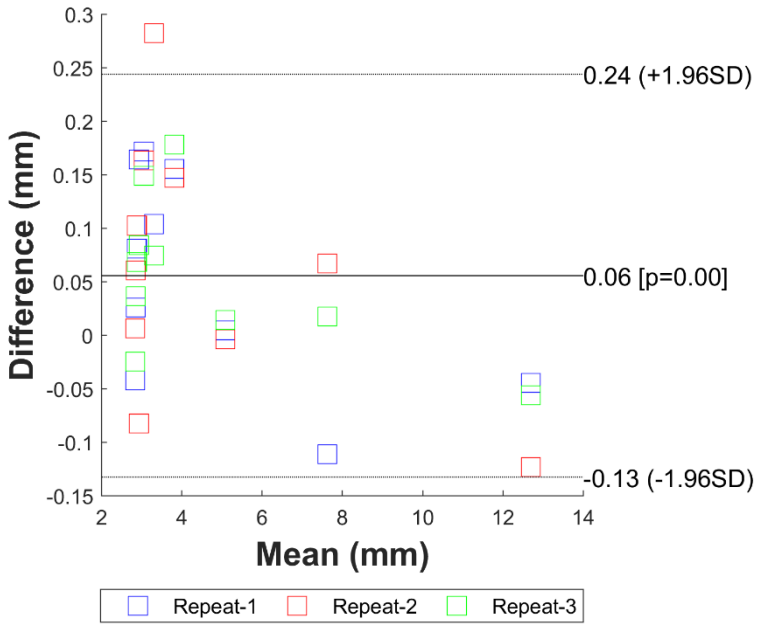

Figure 5-28 Bland-Altman plot comparing Bead MBIR z-axis translation with linear stage translation. With the bold line representing the mean difference and the dotted lines the levels of agreement.

5.5.2 Experiment 2 Static Leg Phantom

Bland-Altman analysis was performed to compare the bone derived kinematics between MBIR, Bead MBIR and Motion capture. The individual Bland-Altman plots can be found in Appendix E. Mean and absolute differences found between the three methods were calculated and are shown in Table 5-4.

Table 5-4 Mean difference between methods in bold, absolute mean difference ± STD bold in brackets and levels of agreement in parentheses for the phantom under static conditions.

	Bead v MBIR	**Mocap v MBIR**	**Bead v Mocap**
Flexion-Extension Angle (°)	**0.05 [1.65±1.31]** (-4.2 to 4.3)	**0.07 [1.08±0.97]** (-3.2 to 3.4)	**-0.01 [0.98±0.82]** (-2.6 to 2.5)
Abduction-Adduction Angle (°)	**1.76 [1.80±1.58]** (-4.8 to 2.3)	**3.13 [3.13±2.20]** (-1.2 to 7.4)	**-1.36 [1.54±1.45]** (-4.4 to 1.2)
Internal-External Rotation (°)	**-1.27 [1.34±1.76]** (-1.4 to 4.9)	**0.29 [0.91±0.85]** (-2.1 to 2.7)	**-1.56 [1.56±1.43]** (-4.5 to 1.8)
Anterior-Posterior Translation (mm)	**1.99 [2.92±2.74]** (-4.9 to 8.9)	**1.19 [1.75±1.94]** (-3.4 to 5.8)	**0.80 [1.28±1.03]** (-2.1 to 3.7)
Superior-Inferior Translation (mm)	**-0.63 [0.95±0.75]** (-2.7 to 1.4)	**-1.18 [1.20±0.91]** (-3.0 to 0.65)	**0.55 [0.77±0.92]** (-1.5 to 2.6)
Medial-Lateral Translation (mm)	**0.78 [1.58±1.72]** (-3.6 to 5.2)	**-0.06 [1.41±1.16]** (-3.7 to 3.6)	**0.84 [1.08±0.98]** (-1.5 to 3.2)

5.5.3 Experiment 3 Dynamic Leg Phantom

Bland-Altman analysis and plots were performed to compare kinematic outputs from all three methods at the three different velocities. The individual dynamic

Bland-Altman Plots can be found in Appendix E. Table 5-5 summarises the mean difference and levels of agreement for Bland-Altman analysis.

A one-way repeated measures ANOVA was conducted (IBM SPSS Statistics v25, USA) this was used to determine if there were significant differences in the absolute differences between the three methods for calculating the 6DOF kinematics over the three different dynamic velocities. There were no outliers and the data was normally distributed, as assessed by the Shapiro-Wilk test (p>0.05). The assumption of sphericity was violated on fourteen of the eighteen comparisons tested, as assessed by Mauchly's test of sphericity. Therefore, a Greenhouse-Geisser correction was applied to all comparisons (Table 5-6). The different dynamic velocity tasks were found to produce significant differences in fifteen of the comparison tests (Table 5-6). Post hoc analysis with a Bonferroni adjustment was used to reveal within comparison differences (Table 5-7).

To summarise the Bland-Altman analysis and the results from the one-way repeated ANOVA a box plot was used for each of the 6DOF kinematics (Figure 5-29 to Figure 5-34) using a similar approach to Ellingson et al. (2017). The three method comparisons were grouped together at each of the dynamic velocities, with the mean difference being represented by a red line and the limits of agreement of each method comparison shown as the top and bottom of the box. The statistical differences revealed from the one-way repeated ANOVA and Bonferroni post hoc test are also labelled on the graph with each comparison represented by a different line type.

Table 5-5 Mean differences between the three different methods under the three different dynamic conditions. Levels of agreement in parentheses, which indicate the lower and upper limits to which 95% of the differences are expected to fall.

	100 mm/s (Slow Dynamic)			**150 mm/s (Medium Dynamic)**			**240 mm/s (Fast Dynamic)**		
	Bead v MBIR	**Mocap v MBIR**	**Bead v Mocap**	**Bead v MBIR**	**Mocap v MBIR**	**Bead v Mocap**	**Bead v MBIR**	**Mocap v MBIR**	**Bead v Mocap**
Flexion-Extension Angle (°)	-3.85 (-9.1 to 1.4)	-1.63 (-5.3 to 2.0)	-2.21 (-7.2 to 2.8)	-3.62 (-7.6 to 0.39)	-1.34 (-4.8 to 2.1)	-2.28 (-6.3 to 1.7)	-6.42 (-14 to 1.6)	-4.66 (-12 to 2.8)	-1.76 (-4.3 to 0.8)
Abduction-Adduction Angle (°)	0.43 (-2.3 to 3.1)	2.87 (-3.0 to 8.7)	2.13 (-2.3 to 3.1)	-0.35 (-2.0 to 1.3)	1.80 (-0.74 to 4.3)	-2.15 (-4.4 to 0.09)	1.38 (-3.2 to 5.9)	3.55 (-2.1 to 9.2)	-2.17 (-5.4 to 1.1)
Internal-External Rotation (°)	-0.81 (-3.7 to 2.0)	1.19 (-4.2 to 6.5)	-2.00 (-6.4 to 2.4)	1.14 (-3.1 to 5.4)	-0.27 (-3.3 to 2.8)	1.41 (-1.5 to 4.3)	1.49 (-5.5 to 8.5)	2.50 (-3.3 to 8.3)	-1.00 (-3.3 to 1.3)
Anterior-Posterior Translation (mm)	-0.53 (-4.4 to 3.3)	-2.66 (-6.6 to 1.2)	2.13 (-2.6 to 6.9)	-1.39 (-5.4 to 2.7)	0.29 (-3.0 to 3.6)	-1.68 (-4.6 to 1.3)	-0.91 (-8.7 to 6.9)	-1.20 (-8.1 to 5.7)	0.29 (-3.4 to 4.0)
Superior-Inferior Translation (mm)	0.25 (-1.3 to 2.5)	-0.34 (-5.3 to 2.0)	0.59 (-1.3 to 2.5)	0.33 (-1.1 to 1.7)	0.65 (-0.22 to 1.5)	-0.31 (-1.6 to 0.93)	0.81 (-1.8 to 3.5)	1.02 (-0.8 to 2.8)	-0.21 (-2.4 to 2.0)
Medial-Lateral Translation (mm)	-1.37 (-3.6 to 0.8)	-0.95 (-2.7 to 0.84)	-0.42 (-2.3 to 1.5)	0.25 (-3.0 to 3.5)	-1.05 (-2.5 to 0.42)	1.30 (-1.5 to 4.1)	-2.40 (-2.0 to 1.8)	-1.76 (-5.2 to 1.6)	-0.64 (-3.4 to 2.1)

Table 5-6 Results from the one-way repeated measures ANOVA showing the absolute differences found between the different methods across three different dynamic velocities. As the assumption of sphericity was violated on the majority of the results it was decided to report all results using the Greenhouse-Geisser correction. All statistically significant differences are highlighted in grey.

Kinematic output (Absolute difference between methods)	Greenhouse-Geiser Test results
Flexion (Bead MBIR vs MBIR)	$F(1.597, 79.857) = 11.934$, $p < .001$
Adduction (Bead MBIR vs MBIR)	$F(1.175, 58.738) = 20.191$, $p < .001$
Internal Rot (Bead MBIR vs MBIR)	$F(1.348, 67.384) = 23.165$, $p < .001$
Anterior Trans (Bead MBIR vs MBIR)	$F(1.920, 95.976) = 7.127$, $p = .002$
Superior Trans (Bead MBIR vs MBIR)	$F(1.986, 99.318) = 11.014$, $p < .001$
Medial Trans (Bead MBIR vs MBIR)	$F(1.552, 77.617) = 11.440$, $p < .001$
Flexion (Motion capture vs MBIR)	$F(1.286, 64.303) = 33.078$, $p < .001$
Adduction (Motion capture vs MBIR)	$F(1.364, 68.222) = 8.952$, $p = .002$
Internal Rot (Motion capture vs MBIR)	$F(1.754, 87.702) = 1.455$, $p = .239$
Anterior Trans (Motion capture vs MBIR)	$F(1.937, 96.871) = 27.619$, $p < .001$
Superior Trans (Motion capture vs MBIR)	$F(1.294, 64.686) = 4.317$, $p = .032$
Medial Trans (Motion capture vs MBIR)	$F(1.493, 74.672) = 12.243$, $p < .001$
Flexion (Bead MBIR vs Motion Capture)	$F(1.351, 67.526) = 6.107$, $p = .009$
Adduction (Bead MBIR vs Motion Capture)	$F(1.765, 88.251) = 0.289$, $p = .722$
Internal Rot (Bead MBIR vs Motion Capture)	$F(1.277, 63.847) = 13.205$, $p < .001$
Anterior Trans (Bead MBIR vs Motion Capture)	$F(1.996, 99.792) = 16.004$, $p < .001$
Superior Trans (Bead MBIR vs Motion Capture)	$F(1.716, 85.796) = 4.829$, $p = .014$
Medial Trans (Bead MBIR vs Motion Capture)	$F(1.832, 91.600) = 0.982$, $p = .372$

Table 5-7 Results from Post hoc tests of the one-way repeated ANOVA with Bonferroni correction. Absolute mean difference ± Standard deviation. All significant differences with a *p*-Value <0.05 are highlighted in grey and all values with a *p*-Value <0.01 are highlighted in grey and bold.

Absolute Difference between methods for derived kinematics	100 mm/s Mean ± sd	150 mm/s Mean ± sd	240 mm/s Mean ± sd	100 vs 150 mm/s *p*-Value	150 vs 240 mm/s *p*-Value	100 vs 240 mm/s *p*-Value
Bead MBIR vs MBIR						
Flexion Angle (°)	4.38 ± 2.95	3.33 ± 1.99	6.43 ± 4.07	0.173	**<0.001**	0.038
Adduction Angle (°)	1.08 ± 0.70	0.69 ± 0.46	2.02 ± 1.79	<0.001	**<0.001**	**0.002**
Internal Rotation Angle (°)	1.33 ± 0.83	1.36 ± 0.99	3.12 ± 2.24	1.000	**<0.001**	**<0.001**
Anterior- Posterior Translation (mm)	1.79 ± 1.44	2.21 ± 1.45	3.14 ± 2.54	0.611	0.060	**0.003**
Superior-Inferior Translation (mm)	0.92 ± 0.80	0.69 ± 0.45	1.29 ± 0.88	0.247	**<0.001**	0.023
Medial-Lateral Translation (mm)	1.56 ± 1.14	1.14 ± 0.93	2.43 ± 2.10	0.147	**0.001**	**0.006**
Motion capture vs MBIR						
Flexion Angle (°)	1.62 ± 1.48	0.89 ± 0.97	4.82 ± 3.60	0.041	**<0.001**	**<0.001**
Adduction Angle (°)	2.67 ± 2.81	1.47 ± 0.99	3.56 ± 2.87	0.022	**<0.001**	0.521
Internal Rotation Angle (°)	0.93 ± 0.62	1.22 ± 0.76	1.12 ± 1.08	0.119	1.000	0.900
Anterior- Posterior Translation (mm)	1.94 ± 1.31	0.97 ± 1.01	3.20 ± 1.83	0.003	**<0.001**	**0.001**
Superior-Inferior Translation (mm)	1.00 ± 0.66	0.70 ± 0.43	1.11 ± 0.81	0.014	**0.008**	1.000
Medial-Lateral Translation (mm)	1.20 ± 0.87	1.23 ± 0.56	1.99 ± 1.46	1.000	**0.004**	**<0.001**
Bead MBIR vs Motion Capture						
Flexion Angle (°)	2.96 ± 2.11	2.86 ± 1.59	1.88 ± 1.09	1.000	**<0.001**	0.020
Adduction Angle (°)	2.31 ± 2.06	2.07 ± 1.20	2.22 ± 1.61	1.000	1.000	1.000
Internal Rotation Angle (°)	1.25 ± 1.19	1.53 ± 1.14	2.82 ± 2.67	0.395	0.255	**<0.001**
Anterior- Posterior Translation (mm)	0.95 ± 0.86	1.96 ± 1.26	1.49 ± 1.17	**<0.001**	0.010	0.039
Superior-Inferior Translation (mm)	1.02 ± 0.83	0.57 ± 0.51	0.88 ± 0.72	**0.007**	0.053	1.000
Medial-Lateral Translation (mm)	0.96 ± 0.72	1.16 ± 1.23	1.20 ± 0.98	0.708	1.000	0.490

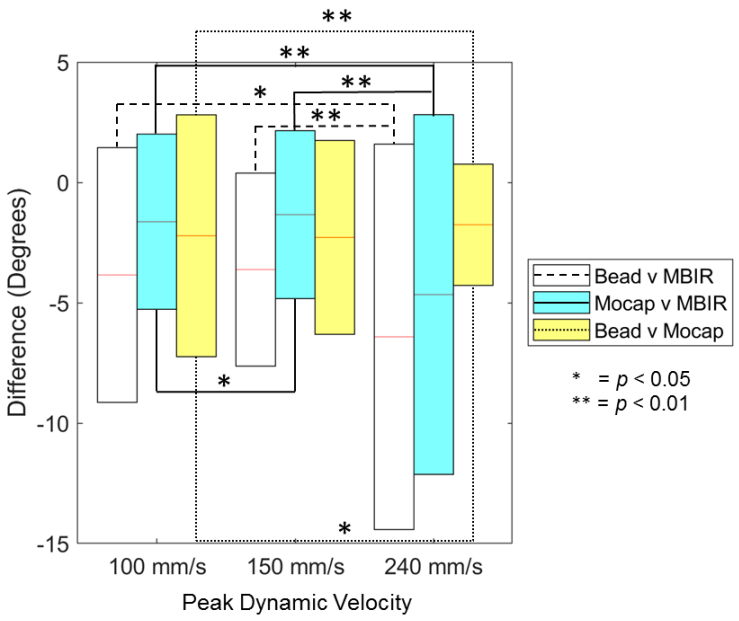

Figure 5-29 Box plots showing the mean difference (red line) and limits of agreement (box) between the three approaches for Flexion-Extension derived kinematics at the three different dynamic velocities tested. Statistical differences between velocities highlighted for the absolute differences between the methods.

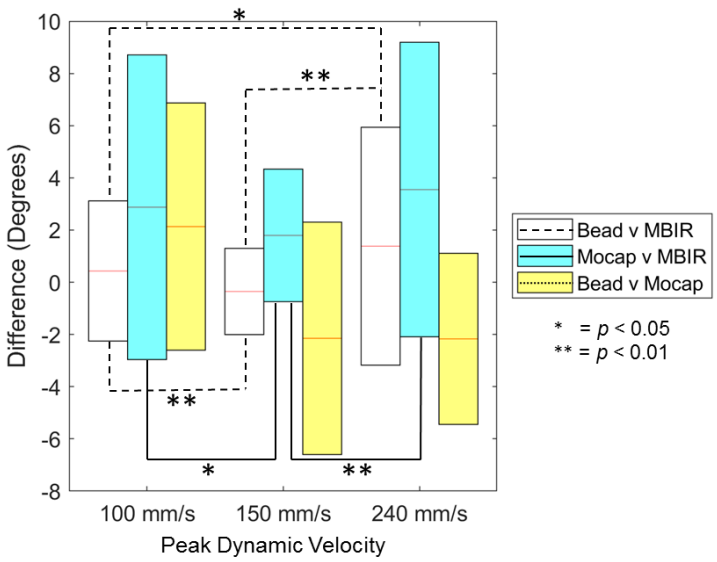

Figure 5-30 Box plots showing the mean difference (red line) and limits of agreement (box) between the three approaches for Abduction-Adduction derived kinematics at the three different dynamic velocities tested. Statistical differences between velocities highlighted for the absolute differences between the methods.

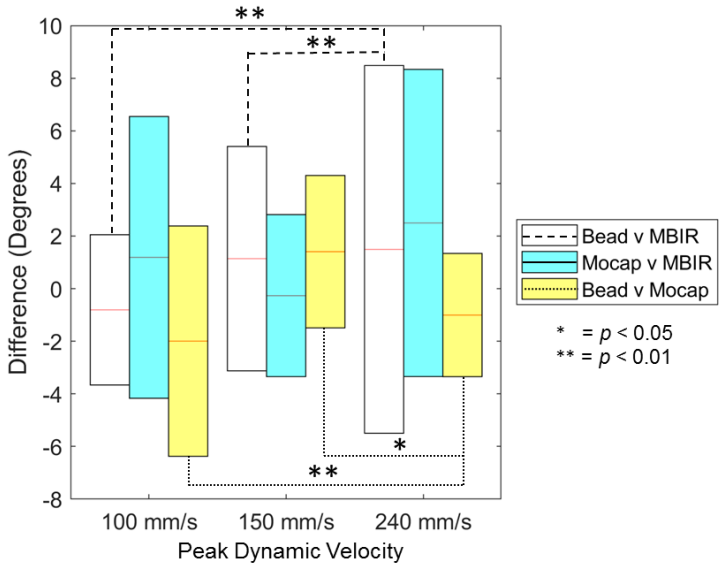

Figure 5-31 Box plots showing the mean difference (red line) and limits of agreement (box) between the three approaches for Internal-External rotation derived kinematics at the three different dynamic velocities tested. Statistical differences between velocities highlighted for the absolute differences between the methods.

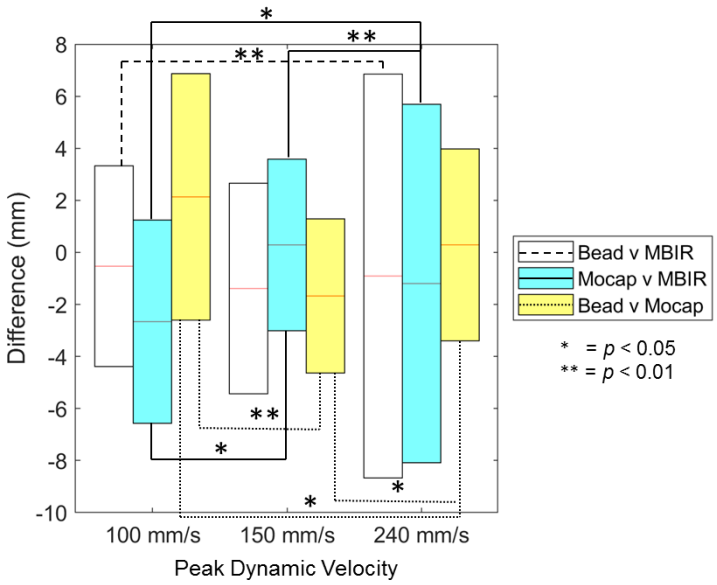

Figure 5-32 Box plots showing the mean difference (red line) and limits of agreement (box) between the three approaches for Anterior-Posterior translation derived kinematics at the three different dynamic velocities tested. Statistical differences between velocities highlighted for the absolute differences between the methods.

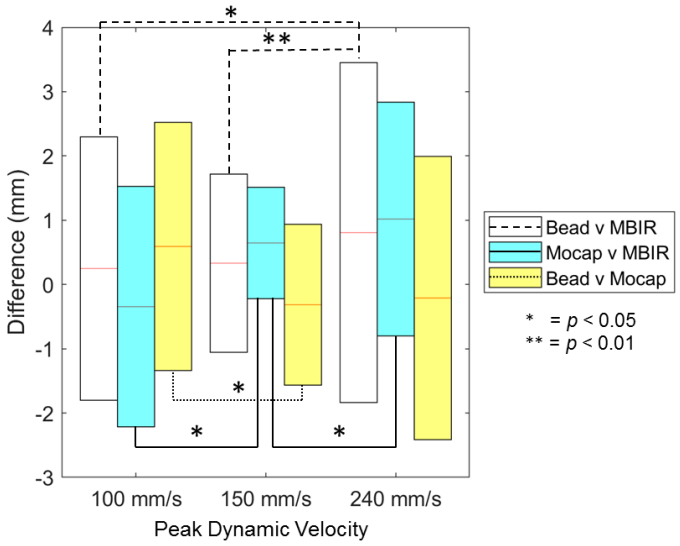

Figure 5-33 Box plots showing the mean difference (red line) and limits of agreement (box) between the three approaches for Superior-Inferior translation derived kinematics at the three different dynamic velocities tested. Statistical differences between velocities highlighted for the absolute differences between the methods.

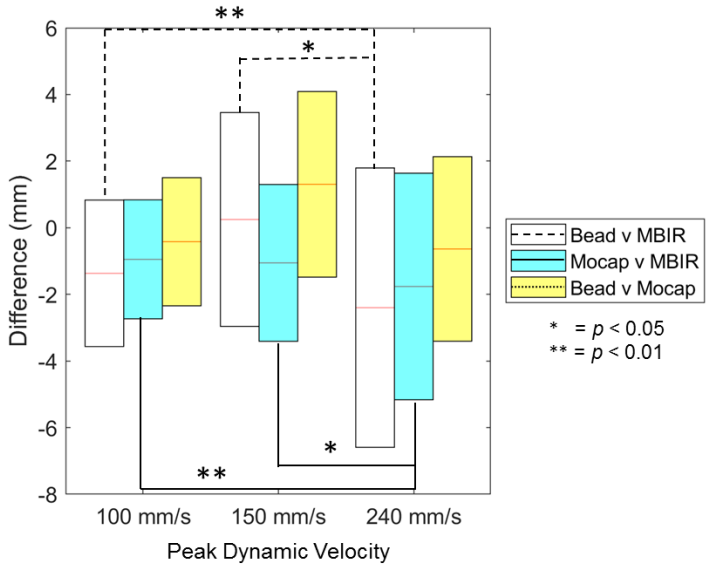

Figure 5-34 Box plots showing the mean difference (red line) and limits of agreement (box) between the three approaches for Medial-Lateral Translation derived kinematics at the three different dynamic velocities tested. Statistical differences between velocities highlighted for each method comparison.

5.5.4 Experiment 4 & 5 Static and Dynamic Ovine

Bland-Altman analysis was performed to compare the bone derived kinematics between MBIR and Motion capture during a dynamic and static activity. The peak velocity for the dynamic activity was calculated to be on average 220mm/s, within the range calculated from volunteer motion capture data (section 5.4.6.2). Mean and absolute differences between ovine MBIR and motion capture were calculated and are shown in with the summarised levels of agreement in Table 5-8. The individual Bland-Altman plots can be found in Appendix E.

Table 5-8 Comparing Motion capture and MBIR for ovine kinematics during static and dynamic conditions. Mean difference between methods in bold, absolute mean difference and standard deviation in bold and brackets and levels of agreement in parentheses.

	Static	Dynamic
Flexion-Extension Angle (°)	**-0.40 [2.45±1.71]** (-6.4 to 5.6)	**0.45 [2.52±2.03]** (-5.9 to 6.8)
Abduction-Adduction Angle (°)	**0.13 [3.81±2.84]** (-9.5 to 9.8)	**2.98 [2.99±1.70]** (-0.4 to 6.3)
Internal-External Rotation (°)	**2.72 [4.33±3.93]** (-7.7 to 13.1)	**2.05 [3.68±4.23]** (-8.2 to 12.3)
Anterior-Posterior Translation (mm)	**3.33 [3.33±2.35]** (-1.2 to 7.9)	**-1.11 [1.73±1.63]** (-5.2 to 3.0)
Superior-Inferior Translation (mm)	**0.48 [3.68±2.27]** (-8.7 to 9.2)	**-0.25 [1.48±1.05]** (-3.8 to 0.65)
Medial-Lateral Translation (mm)	**-4.95 [4.95±3.47]** (-11.7 to 1.8)	**-0.56 [1.38±1.07]** (-3.8 to 2.7)

5.6 Discussion

The main aims of this study were to develop protocols to carry out biplane fluoroscopy and to investigate the errors associated with measurement of knee kinematics during a step activity using MBIR. During this study new protocols were developed at Cardiff University to calibrate two clinical C-arm systems and to combine image data to define the position of objects of interest during

dynamic activities. Additional protocols were also developed to allow a direct comparison between motion capture and biplane fluoroscopy.

This is the first time that biplane fluoroscopy has been performed at Cardiff University and, to the authors knowledge, the first time it has been performed to investigate errors for bone kinematics for the knee in the UK.

Understanding the errors associated with this type of measurement technique has been investigated previously at Cardiff University for single plane fluoroscopy and MBIR to attempt to validate marker based motion analysis accuracy (Whatling 2009). However, the accuracy of MBIR has never been investigated. In this study validation protocols were investigated and developed using two different methods used to quantify the errors associated with MBIR and the new biplane fluoroscopy protocol.

5.6.1 Experiment 1 – Bead MBIR errors

The main objective of this experiment was to determine the errors associated with bead MBIR (a similar method to RSA) when compared to a reference standard or 'ground truth'.

The results (Table 5-3) from the first experiment show that in static conditions both x- and z-axis bead translations can be tracked to sub-millimetre bias and precision (Table 5-3). The x-axis (0.157 ± 0.102 mm) was found to have an increased absolute mean difference compared with the z-axis (0.088 ± 0.066 mm).

When recording images using the two C-arms, the X-ray systems are orthogonal and the translations are acting along the x- and z-axes. One of the C-arms is imaging the validation object moving out of plane and the other moving horizontally across the screen. Therefore, one of the X-ray systems is more reliant on positioning of the 3D model during MBIR processing. The results show that one of the X-ray systems has a larger associated measurement bias.

The two C-arms were purchased with the expectation that they were identical. However during routine quality assurance tests and yearly inspections the

systems was found to differ in terms of limiting spatial resolution. This is most likely due to differing clinical use prior to refurbishment. The results from this experiment have thus highlighted the differences in accuracy that can be encountered for different C-arms. In this case, because the magnitude of the difference was found to be under 0.2 mm it was not considered to be a issue.

Other studies that have used a model based RSA approach have reported accuracy of between 10-100µm (Ryd et al. 2000; Bragdon et al. 2002; Bragdon et al. 2004; Valstar et al. 2005; Karrholm et al. 2006). These are comparable to the accuracy presented in the current study and the bead MBIR approach is therefore accepted as a valid ground truth comparison for static conditions.

5.6.2 Experiment 2 – Phantom Static

To determine the measurement accuracy for MBIR using a phantom under static conditions, both bead MBIR and motion capture were used to compare kinematics derived from each method. Each of the rotations and translations of the knee joint were compared using the three methods at five different static positions, each representing a different stage of the step activity.

When comparing bead MBIR against MBIR kinematics the bias and precision was found to be no more than 1.80 ± 1.58 ° for rotations and 2.92 ± 2.74 mm for translations. Anterior-posterior translation had the highest associated error for translations with the largest translational range of motion in the knee.

When using motion capture as the reference standard, all the kinematics errors were reduced with the exception of the abduction angle (3.13 ± 2.20°) and superior-inferior translation (1.20 ± 0.91 mm) which both increased. For both of these comparisons all MBIR images were randomised, and therefore not processed in chronological order, and other validation studies have reported higher static inaccuracies compared with dynamic studies. Acker et al. (2011) hypothesised that as the dynamic images are processed in order, with established positions from the previous and proceeding images, positioning accuracy is improved.

When comparing bead MBIR against motion capture the largest bias and precision seen for rotations was 1.56 ± 1.43 ° and 1.28 ± 1.03 mm for translations. These represent small differences which can be explained potentially as errors within the measurement systems between the calibration and the transformations. These results suggest that motion capture can also be used as a suitable comparator for MBIR when using fixed clusters.

Overall errors were found to be higher compared with other biplane studies that have investigated static accuracy. Defrate et al. (2006) reported an average error in displacement for each static position of 0.04 ± 0.06 mm and a rotational standard deviation of 0.3°. It is important to note that these were only reported as errors for displacement and rotation of the bones; they did not report kinematic error. Kinematic error can possibly be larger as it is influenced by a combination of both displacement and rotational error for each bone.

Anderst et al. (2009) report kinematic RMS errors of below 0.26 mm and 0.85° for rotations and translations of the knee respectively for a bespoke biplane X-ray system using two 30 cm image intensifiers coupled with high-speed cameras. The results would be expected to be improved noticeably compared to the C-arms used in the current study.

5.6.3 Experiment 3 – Phantom Dynamic

Combining the linear actuator with the custom knee rig allowed successful investigations into the effect of different dynamic velocities during a simulated step down activity on the errors associated with the calculated kinematics.

The results from the one-way repeated measure ANOVA support the original hypothesis; an increase in the errors was found for all kinematic measures when compared to MBIR. These differences occurred when comparing the 100 mm/s and 150 mm/s to the 240 mm/s. Fewer differences were found when comparing 100 mm/s with 150 mm/s. With some of the kinematics (Table 5-7) the errors decreased at the 150mm/s velocity. This suggests that a difference of 50 mm/s is too small to differentiate between the errors calculated at 100mm/s. As an explanation of why the errors improved; with respect to data processing, the 150 mm/s tests were processed subsequently to the 100 mm/s

tests. As MBIR relies on manual matching of images, it is expected that the author improved their matching skills over time. This highlights the importance of performing and inter and intra operator repeatability studies, and this is recommended to be performed in conjunction with future validation studies.

When comparing bead MBIR and MBIR, the bias and precision for the flexion angle increased significantly between 100 mm/s (4.38 ± 2.95°) and 240 mm/s (6.43 ± 4.07°). This is an increase of nearly 50% in terms of measurement bias. From the individual Bland-Altman plots it was found that for the 100mm/s velocity (slow dynamic speed) and 240mm/s (fast dynamic velocity), flexion also had the widest limits of agreement (Figure 5-29). The limits of agreement and mean difference also highlighted a measurement bias for calculating flexion extension for both bead MBIR comparison and motion capture at both velocities. As the dynamic experiment flexed the saw bone models from approximately 10-60°, the MBIR kinematics underestimated flexion when compared with the reference methods. Anterior-posterior translation was also found to have wide levels of agreement as velocity increased (Figure 5-32). This is most likely due to the blur and lag visualised in the images which was present at all three velocities. During imaging there is an initial delay before the image intensifier registers the first movement. The proceeding dynamic frames appear blurred, with the blur increasing as the velocity increases (Figure 5-35). These artefacts are potentially due to a combination of hardware limitations.

The lag observed during data processing most likely occurs due to slow decaying phosphor in the image intensifier. For older fluoroscopic systems the phosphor decay time for the image intensifiers is estimated to be as high as 30-40ms. For more modern systems it is typically of the order of 1ms (B. a Schueler 2000). If the phosphor decay time is high, then the image will take longer to refresh on the image intensifier. The dynamic images (Figure 5-35) suggest that the image intensifiers in the C-arms used in this study have a high phosphor decay time.

In addition to the slow phosphor decay the CCD camera used in the system is a limiting factor and is most likely contributing to image blur. The CCD camera coupled to the image intensifier in the C-arms runs at a 50Hz refresh rate to

generate an image for the viewing screen. The CCD sensor inside the camera operates using the frame-transfer principle where half of the sensor is used for image pixels to detect the photons emitted from the image intensifier and the other half are used to store the image. This other half is typically covered in aluminium to prevent exposure to any more light (Holst 1998). The image is then read out via three readout registers.

At 50Hz during continuous fluoroscopy the 25 frames per second are displayed on the viewing screen (Bushong 2012). The exposure time can be calculated as 40 ms, which is the duration per frame for each image acquisition. The exposure time is important as it can directly influence how a dynamic movement is captured. As any movement during the exposure time causes blur in an image so the exposure time should match the activity.

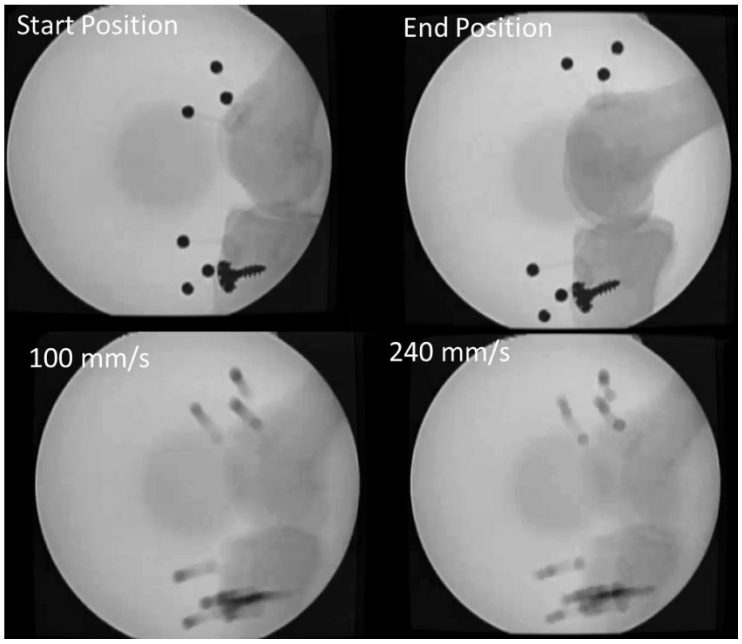

Figure 5-35 Images taken from dynamic phantom trials.

Top Left shows the positon of the saw bone phantom and the implanted marker cluster with beads at the start of the dynamic activity in one of the X-ray views. **Top Right** shows the position at the end of the dynamic task. Both images show clear and easy to distinguish edges of the phantom and beads. **Bottom left** shows the phantom during a slow dynamic movement (100 mm/s), even at this velocity blur is present and the borders of the phantom and beads become challenging to decipher. **Bottom Right** shows the phantom and beads during a fast dynamic speed (240 mm/s) approximately at the same angle as the slow dynamic speed. Visually the blur is considerably greater which explains the wider levels of agreement seen at the higher dynamic speeds

Another biplane study using clinical C-arms used pulsed fluoroscopy rather than continuous X-rays (Li et al. 2008), with pulse widths of 8ms synchronised with the acquisition of the CCD sensor. Tashman (2008) questioned the X-ray settings for dynamic activities such as gait since they calculated that for a volunteer moving at a velocity of 1m/s (the activity under investigation), the volunteer could move as much as 2-8mm, which would blur the image.

When considering the system used in the current study, the experimental velocities, and the exposure time calculated previously, during continuous

fluoroscopy the phantom could potentially move 4 mm during the 100 mm/s velocity and 9.6 mm during the 240mm/s within a single frame. This would explain the blur observed at both velocities and the increase in errors. In addition, as flexion–extension rotation and anterior-posterior translation act in the same plane as the dynamic activity during the experiment, this would explain the wide levels of agreement in the kinematics for these movements.

This may also bring into question the efficacy of using bead MBIR as a reference standard as the beads are also prone to blur, as seen in Figure 5-35. Although the only statistically significant difference found between absolute differences for bead MBIR and motion capture, where errors increased due to increased velocity, was for internal-external rotation. The absolute errors and levels of agreement associated with flexion-extension angle decreased as the velocity increased. Overall the errors were found to be larger (Table 5-5 & Table 5-7), when comparing results found for bead MBIR than those found for motion capture in relation to the kinematics found for the phantom MBIR. This suggests that bead MBIR may overestimate the errors during dynamic experiments involving older clinical C-arms and it is important that other research groups consider this for future studies.

Anterior-posterior translation was also found to have wide levels of agreement in kinematics as the experimental velocity increased (Figure 5-32). The fact that this translation occurs in the same plane as flexion-extension and where the dynamic activity was occurring explains this. Therefore the lag and blur discussed earlier would influence the errors.

A similar in-vitro study was performed to quantify errors associated with single and bi-planar fluoroscopy when calculating 3D kinematics of the knee (Tersi et al. 2013). Tantalum beads were implanted into Sawbones models and a walking task was manually simulated to a peak of 400°/s. The Sawbones were imaged using two synchronised BV Pulsera 300 (Philips Medical System, The Netherlands) at 30 FPS with an exposure time of 8 ms. The biplane results found errors of below 0.7 mm for translations and lower than 1° for flexion extension and ab-adduction. They found a biased error for internal-external rotation, which they summated to be due to longitudinal cylindrical symmetries of the long bones. In comparison the internal-external rotation errors found in

this study was found to produce the second largest rotational errors in terms of levels of agreement which agrees with this statement. The RSA approach used in the similar in-vitro study was not validated as the accuracy was assumed to be of in an order of 10-100 µm. However, this accuracy was based off other studies and was not determined by the research group with their own experiments and equipment.

It is important to consider that these dynamic experiments can be considered to be ideal conditions as no soft tissue is present which is known to influence errors further (Acker et al. 2011; Tersi et al. 2013).

5.6.4 Experiment 4 & 5 – Ovine Static & Dynamic

This is the first time, to the author's knowledge, that a biplane fluoroscopy study has looked at joint and bone kinematic accuracy of MBIR for an ovine specimen. This is also the first study that has investigated accuracy of MRI segmentation and the errors associated with using the constructed model for MBIR during dynamic activities.

It was found that errors associated with the static measurement conditions were greater than those found during dynamic conditions in terms of both absolute accuracy and levels of agreement (Table 5-8). This could be due to the same reason as described in the phantom static study, where manual matching of randomised images for each frame may introduce inaccuracies. Compared with the phantom static study the errors were greater which is due to the inclusion of soft tissue and the use of models segmented from MRI compared to CT derived models. Additionally, the ovine specimen became compromised during the experiment (explained in section 5.4.7.2), so that only two static repeats were performed which could introduce a bias that may be eliminated with more repeats of the experiment (using more ovine specimens).

The anatomy and kinematics of the ovine joint could also contribute to the greater errors. An ovine stifle joint has a larger range of flexion during dynamic activities as compared to the human knee joint and is cannot extend below 40 degrees of flexion (Proffen et al. 2012). This is shown by Tapper et al. (2004) who performed a bone pin study to look at the in-vivo kinematics of five ovine

specimen. The results shows that during gait the ovine stifle joint ROM was between 40° and 70° of flexion, consistently more flexed than a human knee with a ROM of approximately 0° and approximately 70° during gait (Lafortune et al. 1992). Therefore, during the step down activity the ovine stifle joint flexion angle was greater than that for the human phantom with the tibia occluding the view of the femur in the frontal view for some of the static positions. This made matching the bone more challenging as the image was considerably darker compared with the frontal view of the phantom (Figure 5-36).

Figure 5-36 Frontal view images recorded from static ovine and phantom validations. **Top images** show the phantom start (left) and end (right) positions. **Bottom images** show the ovine start (left) and end (right) positions. Comparing the end positions for the two static experiments; the ovine distal femur and proximal tibia are almost impossible to visualise as the tibia overlaps the femur preventing X-ray penetration and worsened by the presence of soft tissue in the ovine joint.

The results from the dynamic ovine experiments were found to have lower calculated errors compared to the 240mm/s dynamic phantom experiments for flexion-extension, anterior-posterior translation and medial lateral translation. For flexion-extension this is likely because ovine specimens have reduced ROM around this axis as discussed previously. The reduced errors seen for

the translations are likely because of the increased constraint in the ovine joint compared with the knee phantom. As the ovine had an intact joint capsule with undamaged ligaments and menisci it would be considered as more constrained compared to the phantom which used elastic cords to simulate ligaments. Although the femur and tibia are considered incongruent surfaces, the large meniscus increases the overall congruency of the stifle joint (Allen et al. 1998). These could explain the lower translational errors as the movement was more constrained compared to the knee phantom.

Errors for the internal-external rotation, abduction-adduction and superior translation were both found to greater when compared to those calculated for the phantom dynamic trials. This can be explained by the quality of the images obtained during the static trials in the frontal view (Figure 5-36). Occlusion of the joint and also the presence of the soft tissue make it difficult to match the bones to the edges of the X-ray, in particular during dynamic movement which affects the superior translation and abduction.

The use of ovine stifles provides an alternative to research groups who can't access cadaveric specimens when they are attempting to quantify the accuracy of dynamic activities during biplane fluoroscopy.

5.6.5 Limitations of the reference standards

Bead MBIR was found to produce small errors in static accuracy for translations in idealised conditions where fixed beads are translated in a single direction, with associated no rotations or other translations applied. The accuracy resulting from more complex orientations or dynamic activities will be limited fundamentally by the resolution of the image and the accuracy of the biplane calibration.

5.6.5.1 Spatial Resolution

The C-arms receive regular quality assurance examinations and one of the tests performed is to measure the resolution limit by imaging a TOR 18FG fluoroscopy phantom (Leeds Test Objects, UK) and examining the resolution

of the test pattern under standardised test conditions. The resolution limit is determined by the number of line pairs (lp) that can be distinguished per mm. With a line pair consisting of a dark and a white line (Figure 5-37); the higher the value the smaller the features that can be discerned by the X-ray system. Therefore, considering a resolution of 5 lp/mm, each line pair would be 0.2 mm wide and each individual line 0.1mm wide.

The C-arms used in the current study were found to have a limiting spatial resolution of 1.2 lp/mm. This is a lower than what is found in modern C-arms with 23 cm image intensifiers having a typical value of 2.2 lp/mm. This spatial resolution was found to be further reduced as the Medicapture down samples/compresses the raw analogue video to a digital format. This is demonstrated in Figure 5-37 showing a photograph of the raw analogue video from one of the Siremobil C-arms alongside an individual frame of the video output from the Medicapture system for the same phantom. In a magnified view of both images, that the Medicapture system image has a considerably reduced spatial resolution compared with the analogue output. It is important to note that this is not the method of determining the limiting spatial resolution following QA protocols, this example is provided only to show the difference visible difference as a qualitative comparison.

Thus for determining the position of beads or bone models the images collected from the C-arms used during MBIR in this study are typically lower in resolution as compared to other C-arm studies. This may potentially contribute to the higher errors found for the experimental results in this chapter compared with other studies.

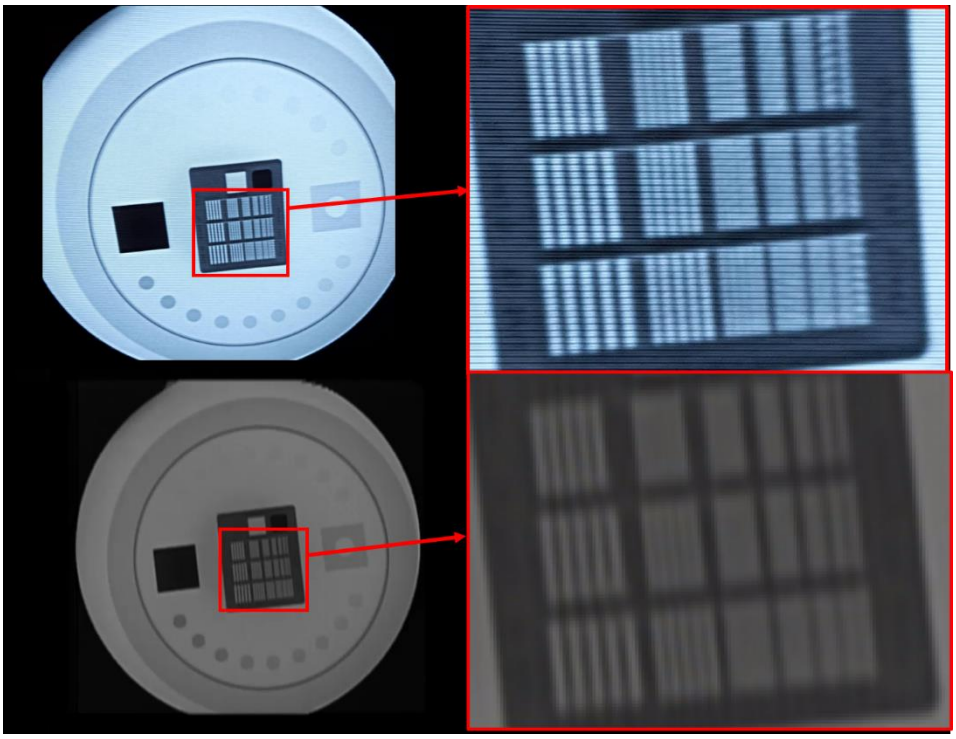

Figure 5-37 **Top image** is a photo taken of the Siremobil viewing screen imaging a TOR 18FG fluoroscopy phantom (Leeds Test Objects, UK). **Bottom image** is a video still captured by the Medicapture system. To the right of each image a magnified view of the resolution test pattern is shown. The top image shows clear separation of the lines for a larger number of line pairs compared with the bottom image.

5.6.5.2 Biplane Calibration Errors

The locations of the beads in the calibration cube were defined using CT scan sequences with a slice thickness and 0.625 mm, segmented using the methods described in section 5.4.2.2. This method was considered appropriate for the first iteration of the calibration cube design and was used to successfully calibrate both X-ray systems. For the next iteration of the calibration cube or object at Cardiff University the fiducial location of the beads must be defined with a higher accuracy. A study (Kaptein et al. 2011) looking at six different method of calibration for biplane fluoroscopy recommended using a foam cube with 8 markers where the fiducial positions of the bead were defined with a different RSA system. This approach relies on the availability of another X-ray system which may not be possible for other research groups.

They looked at the accuracy of calibration for two markers attached to a digital calliper to determine which method was the most accurate. An alternative approach is to use a milling machine to define location of beads. One study manufactured a calibration cube using a 10 cm acrylic cube with twelve 3mm brass spheres machined into known location using a milling machine with an accuracy of ±0.025mm (Tashman and Anderst 2003a). This once again relies on the access to high precision machining equipment which may not be available to research groups, in a clinical setting for example. Knörlein et al. (2016) designed and provided instructions on how to construct a calibration cube from Lego blocks (Lego Group, Denmark) and 5 mm spherical steel beads. The study found that the precision of the Lego phantom was approximately 0.05 mm which suggests that this might be viable alternative for research groups unable to access precision measurement or machining equipment. For future validation studies at Cardiff University an assessment must be performed for future calibration methodologies to fully understand the errors associated with the protocol.

5.6.5.3 Motion Capture Limitations

Due to the limited size of the overlapping field of view of the C-arms, the markers on the custom marker cluster were a short distance apart. As the LCS was calculated from these three markers, any small error occurring either during matching for MBIR or tracking for motion capture could introduce large changes in model orientation. Future validation studies should increase both the distance between adjacent markers and the number of markers.

The motion capture was also assumed to have a good dynamic accuracy due to the small residual errors in calibration (under 0.4 mm). However, if it is used as a reference method the accuracy should be assessed. Therefore it is recommended for that a true dynamic assessment of errors be carried out by moving three markers of a known separation distance and quantifying the variation in distance between them in order to quantify the associated errors.

5.6.6 Dynamic experiment

As the linear actuator only moved the object in one plane of motion, the experimental set up, as it stands, is only able to simulate simple activities such as step down. In addition, for this study the actuator was controlled by a power supply with the amount of input DC current controlling the speed. A control circuit was designed and manufactured to work with the linear actuator that could control the actuator using a 5V digital signal however it was not used for this study as a simple dynamic movement was investigated first.

For future dynamic validation studies, increased complexity of the dynamic movement is recommended by combining multiple actuators or servomotors to simulate more degrees of freedom. An example of a more complex dynamic movement simulator is the dynamic joint motion simulator (DJMS) discussed in section 5.2.2. which allowed the accuracy of a mobile biplane X-ray imaging system to be determined when tracking cadaveric and Sawbones models (Guan et al. 2016). However, the complexity of dynamic activity that could be simulated using the system described in the current study is limited by the small field of view (FOV) of the C-arms small, therefore a larger FOV is recommended in the design of future equipment.

5.6.7 Assessment of C-arm system

Overall the errors associated with the biplane system used in this study are higher than those reported in other studies. This is most likely due to hardware limitations rather than errors within the MBIR protocol.

The C-arms were found to be susceptible to blur for movements involving higher velocity, as shown by the dynamic phantom results. The conversion from analogue to digital images when using the Medicapture system lead to a deterioration of image quality as explained in section 5.6.5.1. Image intensifiers have a limited life and as the C-arms use in the current study are twenty years old, they are potentially coming to the end of their usable life.

However, these C-arms or similar systems can offer the potential for a cheaper alternative approach to undertaking biplane fluoroscopy when compared to

other much more expensive systems. They also have a considerably smaller radiation dose compared to a high-speed biplane X-ray system (Li 2008),

For other research groups who are considering developing a system using two clinical C-arms the following recommendations are suggested:-

- Do not use a video recording system such as the Medicapture system used here; replace the CCD camera in the intensifier with a high speed camera. It is a relatively straightforward approach and would improve image quality allowing control of how the data is captured and processed. For most high-speed cameras some form of synchronisation options is usually offered allowing a relatively simple approach to capture synchronised biplane fluoroscopy images.
- Assess the spatial resolution of the system to ensure that it is capable of performing to the task it is intended for.
- Maximise the FOV by choosing a system with a larger image intensifier. The 23 cm image intensifier used in this study was found to have a very limiting FOV, with the test objects positioned in very limited poses to ensure overlapping FOV of both systems.

5.6.8 Summary

The errors reported in this study have highlighted the limitations of the C-arm system. They demonstrate that this biplane C-arm system is not suitable to act as a gold standard for quantifying the errors associated with traditional optoelectronic motion capture. However, it is important to note that this system can still be used to quantify bone kinematics for both translations and rotations to an acceptable clinical accuracy. It can still provide important biomechanical information when compared to traditional motion analysis which does not allow accurate calculation of joint the translations and bone-on-bone contact locations in the joint.

This study has developed and demonstrated the foundation for a standard validation protocol at Cardiff University to assess and quantify at the errors associated with MBIR and any future techniques that are developed.

The next chapter looks at the development of protocols required to use this system in combination with marker based, optoelectronic motion capture to perform a pilot study with healthy volunteers. It will focus on updating the existing intact knee MBIR protocol described in Chapter 3 to allow biplane fluoroscopy and perform a comprehensive biomechanical analysis to act as comparative data for future patient studies.

Chapter 6 Biplane Fluoroscopy and MBIR: Pilot Study of Healthy Volunteers

6.1 Introduction and Aims

Since the single plane, intact knee study described in Chapter 3 was performed, there have been significant equipment changes, including:-

- The Cardiff University Brain Imaging Centre, where all previous MR scans took place, was moved into a new facility where two new 3T scanners were installed.
- Two C-arms were purchased and installed in a new fluoroscopy facility at the School of Engineering as part of the new Musculoskeletal Biomechanics Research Facility (MSKBRF).

To use the new MR scanner (Siemens, 3T), a suit of new imaging sequences were developed as the existing sequences, developed for the GE 3T scanner, were not compatible.

The two second hand, clinical C-arms (Siremobil) were intended to enable biplane fluoroscopy that could be synchronised with motion capture (with the associated errors assessed in Chapter 5).

This chapter focuses on (i) commissioning the new Fluoroscopy Laboratory equipment to perform ionising radiation studies at the School of Engineering and (ii) updating the MBIR protocol for use when imaging intact knees and to work with the new equipment. This updated MBIR protocol was then applied to a healthy cohort to provide pilot data for future studies. The activity investigated during the pilot study was a step up and down. It was chosen to replicate the work that had been performed previously at Cardiff.

The main aims of this study therefore include:-

- Commission the Fluoroscopy Laboratory to perform ionising radiation studies at Cardiff University
- Define new MR sequences that allow generation of subject specific bone models
- Perform a pilot study with healthy volunteers employing synchronised Biplane Fluoroscopy and motion analysis

- Update the MBIR protocol to analyse Biplane Fluoroscopic images obtained for healthy volunteers
- Assess whether the refurbished clinical C-arms are suitable for future patient studies

6.2 Methods: Improvements and Data Collection

This section covers improvements to the MBIR protocol based on the recommendations made in section 3.4.4 and the requirement to integrate new hardware. In addition, it describes the data collection procedure performed during the pilot study involving healthy volunteers.

6.2.1 Set up of Motion Analysis Equipment

One of the major challenges faced during the single plane fluoroscopy, intact knee protocol described in Chapter 3 was the setup of the motion analysis system in the X-ray department at Llandough Hospital. It led to poor coverage in terms of the capture of the volume and associated marker drop out.

For the new Fluoroscopy Laboratory, a camera based new motion analysis system (Oqus, Qualisys Sweden), was purchased and integrated into the facility. The following work describes design, setup and integration of this equipment to work with the new Biplane Fluoroscopy equipment.

6.2.1.1 Force Plate

To perform a step up and down activity using the two C-arms (fluoroscopy), the subject must be visible in the overlapping field of view of the motion capture cameras. The configuration defined in section 5.4.1.1 along with the surrounding equipment required the use of a platform to position the knee in the mutual field of view of two C-arm fluoroscopy units.

An existing set of stairs (Whatling 2009) was adapted by reducing the height of the top platform and altering the handrail to allow positioning of the C-arms (Figure 6-1). The volunteer was then positioned so that the leg (knee) of interest was on the top platform with a step up performed from the third step.

To capture kinetic data during the stair activity a portable 600 mm x 400 mm

Figure 6-1 Adapted stair set with two C-arms positioned to allow investigation of tibiofemoral kinematics during a stair activity.

force plate (FP4060-05-PT, Bertec, USA), was positioned on the top platform. The advantage of this force plate over the system used previously in section 33.2.1.1 was the direct integration of the force plate data collection with the motion capture software, Qualisys Track Manager (QTM, Qualisys, Sweden). This allowed storage of force plate data in the same data file as the 3D marker position data for the motion capture, thus streamlining data processing.

Force plate manufacturers advise that force plates are installed on rigid surfaces because vibrations can introduce potential errors (Bertec Corporation 2012). An additional validation study was performed to assess the associated errors when the force platform was positioned on top of the platform.

6.2.1.2 Force Plate Validation Study

To assess the errors associated with placing the force plates in two different locations on the top platform a MTD-2 CalTester Rod (Motion Lab Systems, Inc, USA) was used in combination with CalTester software (C-Motion, USA). The CalTester Rod is a rigid, metal rod with tips at each end. Five motion capture tracking markers are attached to the rod and simultaneous recordings of force data and motion capture data are obtained. The location of the end of the rod placed on the force plate, i.e. the Centre of Pressure (COP), can be determined in two ways: (i) using the recorded force plate data and (ii) from the locations of the markers using the motion capture (Goldberg et al. 2009). For more information on how this is calculated the reader is directed to read the CalTester Technical paper (Holden et al. 2003). The deviations in COP calculated the force plate and motion capture data can be used to determine the suitably of the force plate set up. Recommendations within the CalTester software are that deviations under 5 mm are normally acceptable and anything higher than 10 mm must be investigated further.

Tests were performed with the force plate positioned in two different locations: (i) on top of a level concrete floor to act as a reference and (ii) on the top platform of the stairs where the foot is placed during a step up activity. All tests were performed in the Clinical Gait Laboratory using a 14 camera motion capture system (Oqus 700+, Qualisys). A description of how the testing procedure is shown in Figure 6-2. For each force plate location, five different CalTester Rod positions were tested; four corners and the centre of the plate, as recommended by the manufacturer.

For both force plate locations, the mean absolute error for the 5 CalTester Rod positions was under 3 mm, as shown by the displacement vector coordinates (Table 6-1). Both force plate locations produced similar results for all COP coordinates suggesting that positioning the force plate on the top stair platform introduces no additional measurement errors.

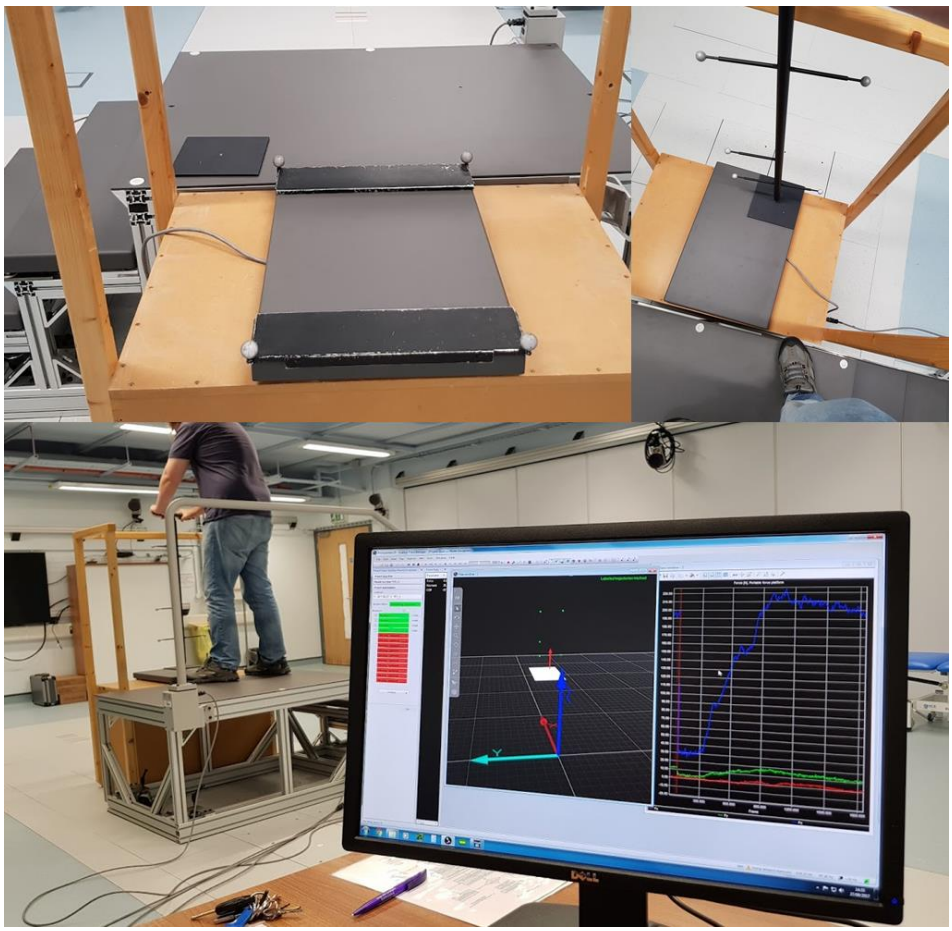

Figure 6-2 Test procedure recording data using the MTD-2 CalTester Rod. **Top Left:** Portable force plate positioned on top of the stairs; location defined using four markers. **Top Right:** Base plate positioned at a corner with a centre-depression to place the tip of the CalTester Rod. **Bottom:** Prior to testing the force plate is zeroed to discount the base plate load. Simultaneous motion and force data is captured while the CalTester Rod is pivoted at a 30 degree angle with a minimum applied load of 200N.

Table 6-1, X, Y, and Z components of the displacement vector between the Centre of Pressure determined using the force and the motion capture data (mean absolute error and standard deviation in bold).

		Tip Coordinates [m]		X [mm]		Y [mm]		Z [mm]	
Location	Position	X	Y	Mean	SD	Mean	SD	Mean	SD
Level Ground	1	0.71	0.11	-1.20	2.12	-0.80	1.39	-2.30	0.24
	2	0.71	0.3	-1.00	2.11	2.00	1.49	-2.10	0.21
	3	1.1	0.3	-0.10	2.17	-1.50	1.61	-1.60	0.28
	4	1.1	0.1	0.10	2.04	-2.60	1.58	-1.80	0.28
	5	0.89	0.2	-0.50	1.92	-0.70	1.58	-1.70	0.27
	Mean Absolute Error			**0.56**	**2.07**	**1.54**	**1.49**	**1.90**	**0.26**
Platform	1	0.68	-0.12	-2.20	2.03	2.30	1.33	-3.10	0.22
	2	0.69	0.07	2.80	2.14	-0.30	1.51	-2.60	0.45
	3	1.08	0.07	1.10	1.88	-3.10	1.47	-2.70	0.23
	4	1.08	-0.13	-0.90	1.87	-2.70	1.64	-3.10	0.23
	5	0.87	-0.03	0.60	1.91	-0.80	1.52	-3.00	0.43
	Mean Absolute Error			**1.50**	**1.97**	**1.86**	**1.49**	**2.89**	**0.31**

6.2.1.3 Motion Capture cameras

With the addition of two C-arm fluoroscopes, positioning of motion capture cameras was very important to ensure consistent tracking of markers during the stair activity. A total of 13 motion capture cameras (12 Oqus 700+ and 1 Oqus 210, Qualisys, Sweden) were used during the study. The layout differs from the previous study in Chapter 3 with a combination of tripods and wall fixtures to mount the cameras. Differing heights were used to overcome disrupted camera line of sight due to the location of the fluoroscopy equipment and the adjusted stairs (Figure 6-3). To optimise the positioning of the cameras a combination of the QTM software “View Cones” feature and using the L-Frame to ensure correct focussing of the cameras.

Due to the variety of the heights and layout, several of the cameras infrared (IR) strobe lights could be visualised in opposing cameras. To overcome this interference, exposure delays were used to group cameras into separate exposure times thus slight delays in exposure between groups of cameras minimised interference.

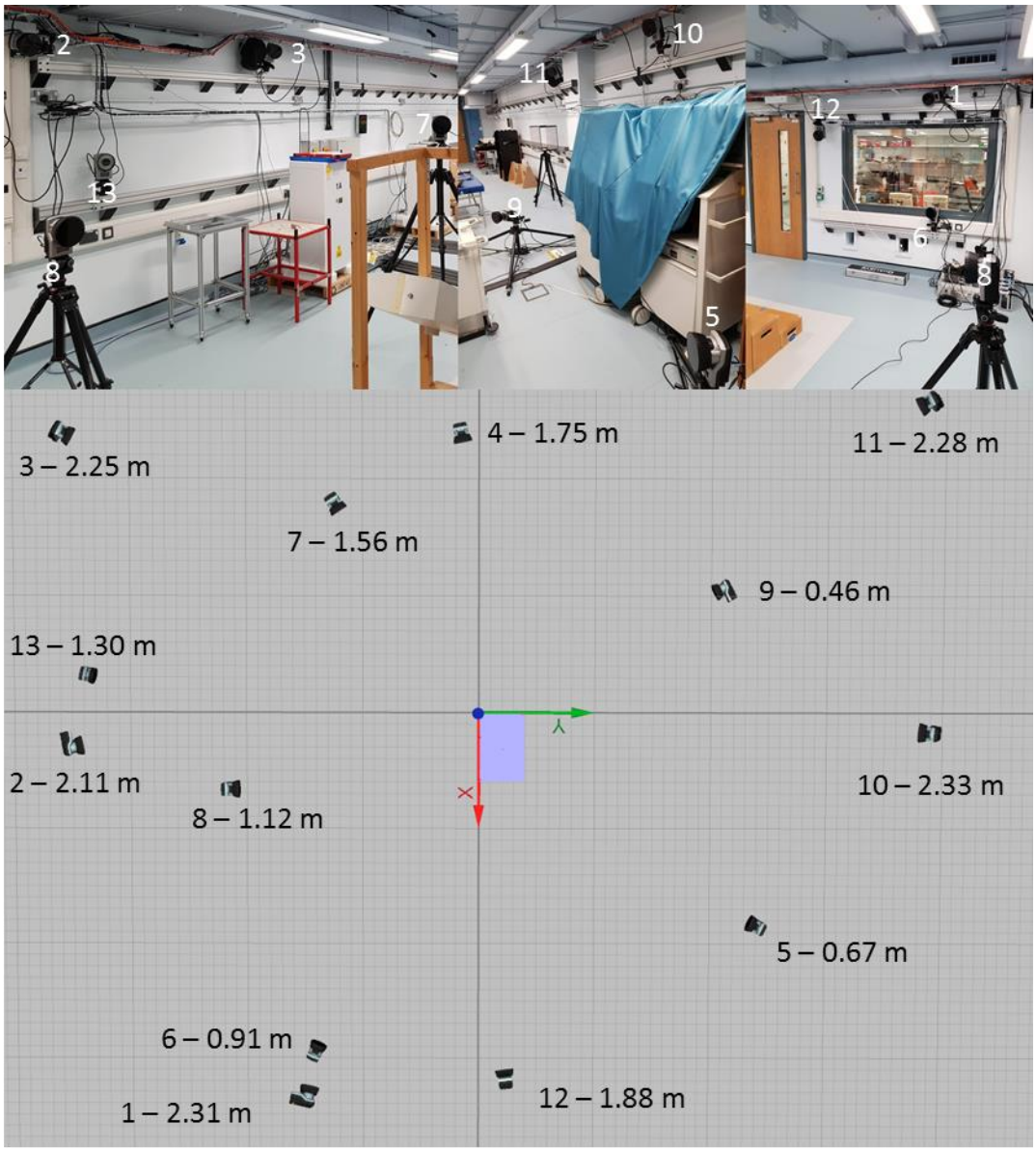

Figure 6-3 Camera positions and heights, with the L-Frame and force plate (blue rectangle) in the centre **Below:** Overhead view within QTM software showing the position and height of each camera. **Above:** Photos highlighting the different mounting and heights of the cameras used to ensure complete coverage.

Compared to the previous study described in Chapter 3, using combined motion capture and fluoroscopy, it was found that during dynamic trials there was no marker drop out or occlusion. This can be attributed to the improved camera positioning as well as the improvement in the imaging sensor of more modern motion analysis cameras.

6.2.2 Biplane Fluoroscopy

6.2.2.1 Commissioning of Biplane Fluoroscopy Facility

To establish an X-ray facility and perform ionising radiation research within a University or clinical environment, requires strict adherence to UK regulations. The two main regulations are (i) the Ionising Radiation Regulations 2017 (IRR17) (Health and Safety, 2017) which covers protection of workers and (ii) the Public and Ionising Radiation (Medical Exposure) Regulations 2017 (IRMER) which covers safety of patients (Health and Safety, 2017). A simplified overview of the steps that were taken to fulfil these regulations are summarised briefly below and shown in Figure 6-4:

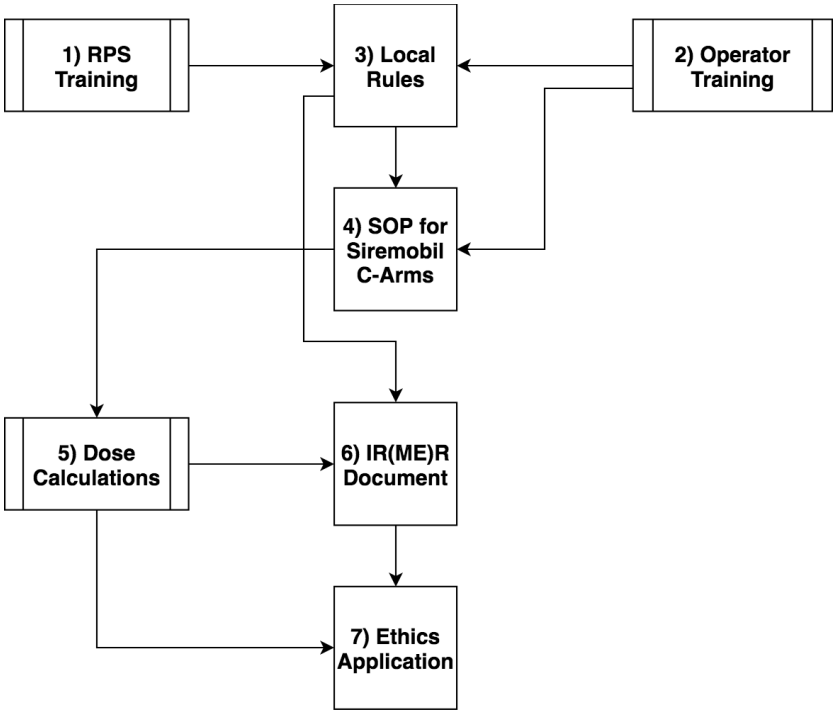

Figure 6-4 Overview of the steps to setting up the fluoroscopy facility and complying with UK regulations

1. **RPS Training** - Radiation protection supervisor (RPS) training was carried out to allow the author act in this role. The role is appointed to ensure compliance with the IRR2017. Example of duties include; carry out risk assessments for work involving ionising radiation, assist in writing local rules, training staff and provide information on safe working

with ionising radiation equipment and make sure that contingency plans exist in the event of an accident or incident.

2. **Operator Training** - How to use the Siremobil C-arms safely and setting up imaging protocols with the equipment. This was provided by Rebecca Vaughan-Roberts, Quality, Health and Safety lead and radiation protection supervisor at University Hospital of Wales.
3. **Local Rules** – To summarise the protocols and instructions intended to restrict exposure in radiation areas. It is a requirement of IRR17 that Local Rules are in place for any X-ray work. The document covers equipment operational procedures, defines the role of the RPS, systems of work and safety measures for all staff and members of public to ensure minimal or no radiation dose, defines radiation controlled areas and emergency arrangements.
4. **SOP for Siremobil C-Arms** – This document covers the protocol for setting up and operating the C-arms during the healthy volunteer pilot study. This was written based on the operator training and the Local Rules. The SOP for using the C-arms during the healthy volunteer pilot study can be seen in Appendix F
5. **Dose calculations** – To carry out ionising radiation studies, specific radiation dose calculations are needed to be known to apply for ethics for a study. These were carried out by local medical physics experts based on recording taken from imaging a phantom. Dose calculations need to be recalculated when equipment changes, activity changes or joint of interest changes. The radiation dose report for this pilot study can be seen in Appendix G
6. **IR(ME)R Document** – Sets out the responsibilities of the radiation employer and the entitlement process. The entitlement process defines the duty holder roles and tasks that individuals are allowed to undertake. The IR(ME)R document also defines the procedures for training records of staff, justification, optimisation, quality assurance of documentation and equipment, volunteer identification and different medical ionising radiation exposures to patients.

7. **Ethics Application –** This is required for every study involving ionising radiation with the dose calculations used to define dose constraints for each research trial.

6.2.2.2 Data Collection

6.2.2.2.1 Volunteers

Five healthy, male volunteers were recruited as part of this pilot study (Table 6-2). To limit the radiation dose, focus was on the right knee only for the imaging and biomechanical analysis. For the required MRI imaging, the volunteers were recruited as part of the Arthritis Research UK umbrella Ethical Approval (10/MRE09/28). For combined Fluoroscopy and motion capture they were recruited as part of a local School of Engineering Ethically Approved Study based on the fluoroscopy protocol defined in the Arthritis Research UK Ethical Approval.

Volunteers were asked to attend a session at the Musculoskeletal Biomechanics Research Facility (MSKBRF), School of Engineering, to record combined biplane fluoroscopy and motion analysis (lasting approximately 1 hour). They were also asked to attend a session at Cardiff University Brain Research Imaging Centre (CUBRIC) to obtain MRI scans of their knee and long leg scans (lasting approximately 2 hours). An information pack was given to the volunteers and written informed consent was obtained for both sessions (Appendix H). The volunteers were asked to complete questionnaires (Table 6-2) including the: Knee Outcome Survey (KOS) (Irrgang et al. 1998), Oxford Knee Score (OKS) (Dawson et al. 1998b), Knee injury and Osteoarthritis Outcome Score (KOOS) (Roos et al. 1998) and the Western Ontario and McMaster Universities Osteoarthritis Index (WOMAC) (Bellamy et al. 1988) (Appendix I).

Table 6-2 Volunteer demographics and Questionnaire scores

ID	Age/ Years	Height/ m	Weight/ kg	KOS /85	KOOS/ %	OKS/ 48	WOMAC/ %
HV1	28	1.75	70.2	85	100	48	100
HV2	26	1.94	111	85	100	48	100
HV3	25	1.82	77.2	85	100	48	100
HV4	42	1.95	83.2	85	100	48	100
HV5	44	1.89	80.7	85	100	48	100

6.2.2.2.2 Motion Analysis

Motion analysis data was undertaken using 12 Oqus 700+ and 1 Oqus 210 (Qualisys, Sweden) capturing at 200 Hz. The cameras were positioned around the C-arm fluoroscopy units as described in section 6.2.1.3. Force data was captured using a portable 600 x 400 mm Bertec portable force plate (Bertec, USA) with a sample rate of 2000 Hz. 3D motion capture data and force plate data was collected using Qualisys Track Manager (QTM) software (Qualisys, Sweden). The global coordinate system (GCS) was defined using an L-Frame, with the origin of the L-Frame located at the corner of the force plate, with the x-axis acting posteriorly and the y-axis medially (Figure 6-5).

Figure 6-5 Location of L-frame on top of force plate and showing the configuration of the two C-arms during data collection.

A modified Cleveland Clinic marker placement was applied (Figure 6-6), with anatomical markers positioned on the left and right acromion, the left and right anterior superior iliac spines, the sacrum (defined as the centre of the posterior superior iliac spines), upper border of the left and right greater trochanter, lateral and medial epicondyles and malleoli, and the 1st and 5th metatarsal heads. Additional markers were used such that at least three tracking markers were visible per segment. These were positioned on the heel, lateral and superior aspect of the foot, at C7, T9 and a cluster of three markers on each thigh and shank.

This full body marker set was chosen over the lower limb only modified Helen Hayes marker set used previously in the work undertaken as described Chapter 2 and 3. This is because it allows the potential for the combined fluoroscopy and motion capture data to be used for musculoskeletal modelling in future studies (Kinney et al. 2013). In addition, it is the same marker set used for assessment of pre and post HTO biomechanics which is a major study at Cardiff (as part of the ARUKBBC) involving an intact knee patient cohort (described in section 3.1.3). This study may be extended and enhanced to include the same biplane fluoroscopy and MBIR protocol in the future.

The motion analysis equipment was synchronised to start capturing data at the same time as the fluoroscopy using the custom trigger described in section 5.4.1.2.

Figure 6-6 Modified Cleveland marker set applied to healthy volunteers

6.2.2.2.3 Biplane Fluoroscopy

Prior to data collection, distortion calibration was carried out on both C-arm systems individually (Figure 6-7).The two C-arms were then positioned into the configuration described in section 5.4.1.1 around the adjusted stair set (Figure 6-5). Biplane calibration was performed to calculate the internal and external orientation parameters using the calibration cube and software described in section 5.4.2.2 (Figure 6-7).

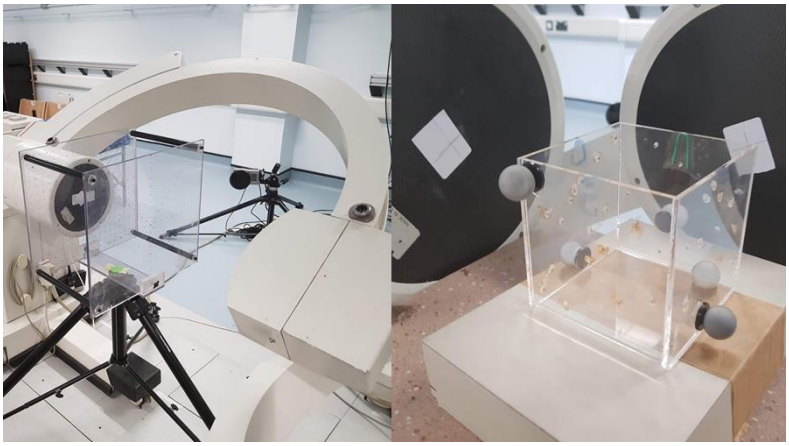

Figure 6-7 Calibration of C-arm systems **Left:** Distortion calibration performed on one of the fluoroscopy C-arms **Right:** Biplane calibration performed on both C-arms

All exposures took place in the Fluoroscopy Laboratory at the School of Engineering using two biplane C-arms by a trained IR(ME)R defined operator.

Ethical approval was granted to allow up to 300 seconds to be recorded. The estimated combined total radiation dose was calculated to be a maximum of 0.013 mSv (Appendix F). The risk from exposure to ionising radiation for such individuals participating in this is 1 in 1.5 million which is equivalent to 48 hours of background radiation. Volunteers were asked to perform a step up and down task on to the wooden platform with a step height of 17 cm. For all volunteers the right knee was imaged, and the volunteer was asked to repeat this activity three times. Volunteers were asked to take care to avoid the contralateral limb passing in the beam of the X-ray and to use the supports if needed.

Biplane fluoroscopy data was recorded using the Medicapture system and exported as MPEG-4.

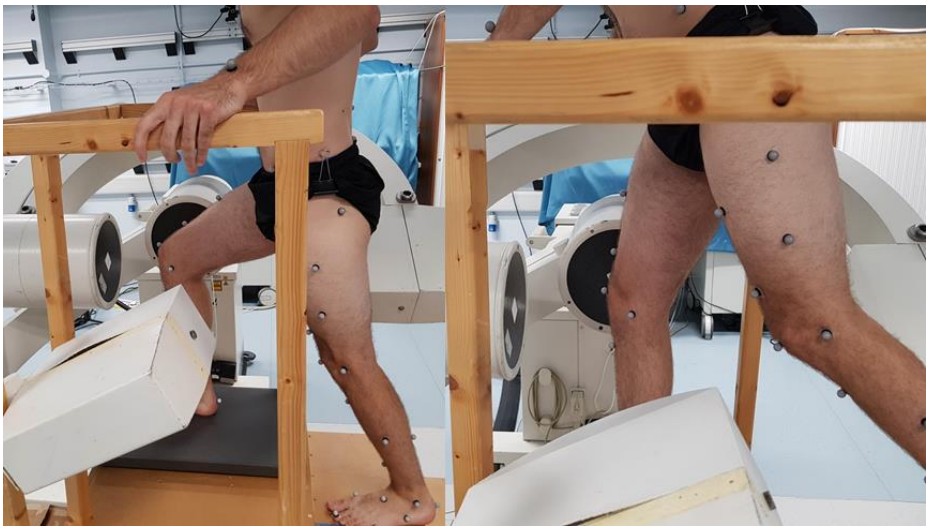

Figure 6-8 Healthy volunteer performed stair activity. **Left:** Starting position of volunteer **Right:** During knee extension after step up

6.2.3 Magnetic Resonance Imaging

For previous studies at Cardiff (Whatling 2009; Stroud Larreal 2011; Watling 2014) and the studies described in Chapter 3 and 4, all MRI scans were performed using the Signa HD-xt 3.0T MR scanner (GE Medical Systems, USA) at Cardiff University Brain Research Imaging Centre (CUBRIC). Since these studies were undertaken CUBRIC was moved to a new £44 million

facility. The original MR scanner was decommissioned and replaced with a 3T Magnetom Prisma MR scanner (Siemens, Germany). As the new MR scanner was manufactured by a different company to the previous scanner the existing imaging protocols could not be transferred, thus new protocols were required.

6.2.3.1 Pilot Studies

A series of pilot studies were performed to optimise MR image protocols working with Peter Hobden, Chief MR Research Radiographer, CUBRIC, and Nidal Khatib, a PhD student in the School of Engineering.

A suite of high resolution image protocols were developed as part of these pilot studies, with each protocol highlighting different structures of interest. An overview of a selection of these sequences can be seen in Figure 6-9.

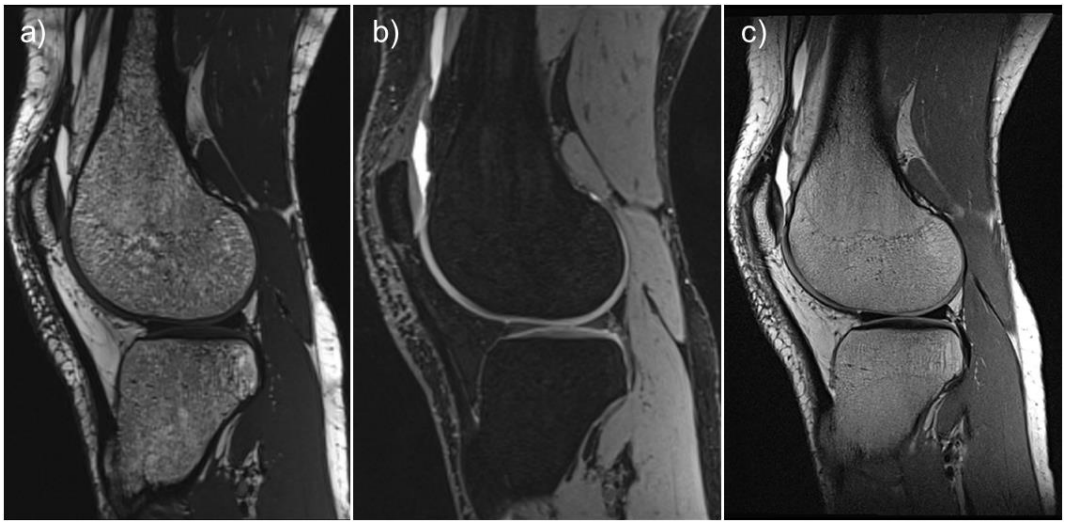

Figure 6-9 Single slice taken from one volunteers MR scans at CUBRIC during the imaging pilot studies **a) Constructive Interference Steady State (CISS)** is the equivalent Siemens sequence as the previously used FIESTA-C sequence in Chapter 3 & 4 showing clear delineation of bone structure and other soft tissues (Van Dyck et al. 2015); **b) Double Echo Steady State (DESS)** is a 3D scan sequence recommended to visualise articular cartilage (Eckstein et al. 2006) where cartilage appears as white to light grey and can be easily distinguished from bone; **c) Proton-Density Turbo Spin-Echo (PD-TSE)** is a 2D scan sequence in the sagittal plane with a high signal-to-noise ratio but a large slice thickness, making it unsuitable for segmentation but suitable for clinical image scoring systems such as Whole-Organ Magnetic Resonance Imaging Score (WORMS) (Peterfy et al. 2004).

6.2.3.2 Long-Leg scan sequence

One of the recommendations made in section 3.4.4 was to improve the quality of the long-leg MRI images based on the potential inconsistencies associated with previous approach to defining the anatomical coordinate systems. This approach involved obtaining a series of lower-leg resolution scans and then to register the resulting bone models post segmentation. Due to the lack of identifiable bony landmarks on the shaft of long bones it was found to be

challenging to register them together. To overcome this a new approach was developed using the 3T Magnetom Prisma

MRI scanner and software

A T1-weighted Magnetisation Prepared RAPid Gradient Echo (MPRAGE) sequence was used with 64 slices per segment (Figure 6-10). Images were acquired in the axial slice orientation and repeated for five or six segments to image bilaterally from the top of the femoral head to below the ankle joint. To enhance the signal to noise ratio, a Peripheral Angio 36 channel coil (Siemens, Germany), covered the leg from the foot to the lower thigh and a flexible body 13 channel coil (Siemens, Gemany), covered the leg from the upper thigh to top of pelvis, combined with a spine matrix coil placed under the volunteer (Figure 6-10). The segments were concatenated together to produce a single MR image sequence of the lower limb (Figure 6-10).

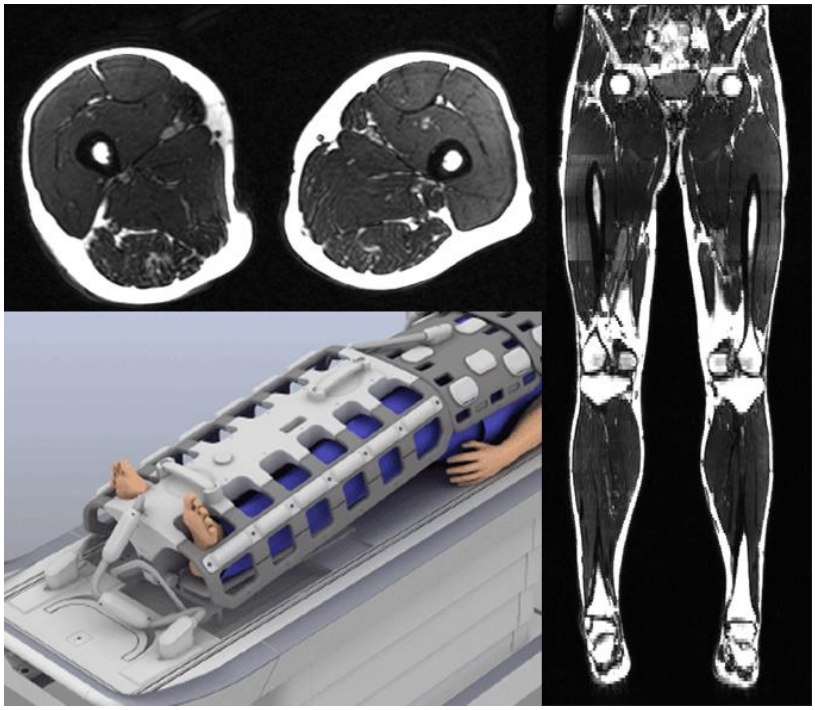

Figure 6-10 **Top Left:** Example slice of T1-MPRAGE sequence of bilateral limbs; femur cortical boundary visually delineated from surrounding muscle. **Bottom Left:** Positioning of Peripheral Angio coil and flexible body coil over volunteer to provide coverage of lower limb. **Right:** Frontal plane view of concatenated segments to produce a single scan of the lower limb.

6.2.3.3 MRI Markers

Custom MR markers were developed to assist with registering the high resolution scans and long leg scans. Cod liver oil tablets have been used as MRI markers to indicate where painful regions were on MRI location scans (Gilbert et al. 2011). These can be used as a cost effective means of creating custom MR markers. Two custom marker holders were designed and modelled in Rhino 6 (McNeel, USA). One was designed to be small, positioned around the knee to fit two 1300mg cod liver oil tablets. The main purpose was to provide additional reference points when registering high resolution scans together and long leg scans. The other holder design was longer in design and acting down the tibia and femur holding five 1300 mg cod liver oil tablets (Figure 6-11). The main purpose was to offer a secondary mechanism for aligning the long leg scans in case the compositing failed or was incorrect. The holders were 3D printed (Ultimaker 2, Ultimaker B.V., The Netherlands) using a 0.8 mm PLA polymer filament.

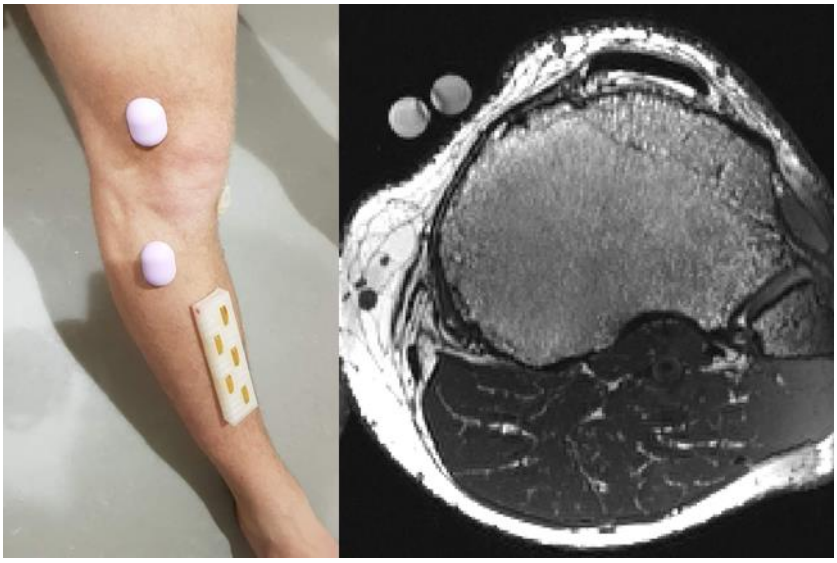

Figure 6-11 **Left:** 3D printed marker holders attached to healthy volunteer using double sided adhesive tape. The smaller marker holders are positioned above and below the joint leg. With the larger marker holder attached to the tibial tuberosity. **Right:** Shows the visibility of the small marker holder in a CISS 3D scan sequence.

6.2.3.4 Data Collection

All MR Imaging was performed using a 3T Magnetom Prisma MRI scanner (Siemens, Germany) at Cardiff University Brain Research Imaging Centre (CUBRIC). All scans were performed by Joy Curran, Research Radiographer based at MSKBRF and CUBRIC.

The volunteers were positioned such that the leg being imaged was in a neutral, extended position and MR markers were positioned on the leg as shown in Figure 6-11. An initial scout scan lasting approximately 10-15 seconds was used to provide the location of the knee within the bore of the scanner. The radiographer then aligned the imaging volume to the centre of the knee joint to capture both tibial and femoral articulating surfaces. Before each sequence the volunteer was informed of the purpose and approximate length of time for the scan.

During the high-resolution scans a dedicated 15-channel phased array knee coil (Siemens, Germany) was used to enhance the signal to noise ratio. High density foam was used to support the lower limbs, with additional strapping around the knee to reduce movement and maintain position. DESS 3D and CISS 3D, two isometric 3D scan sequences were performed consecutively and are described in Figure 6-9. Imaging parameters for both isometric sequences used can be seen in Table 6-3 below.

Table 6-3 MRI Sequence parameters

Sequence	CISS-3D	DESS-3D	MPRAGE
Repetition Time (TR, ms)	5.84	14.84	2200
Echo Time (TE, ms)	2.92	5.04	2.2
Flip Angle (degrees)	50	25	8
Number of Averages	1	1	1
Pixel Spacing (mm)	0.64 x 0.64	0.63 x 0.63	0.78 x 0.78
Slice Thickness (mm)	0.64	0.63	5
Total Acquisition Time (minutes)	12	10	6

Long leg scans were imaged using a MPRAGE sequence (Table 6-3) following the protocol described in section 6.2.3.2. Images were acquired in the axial slice orientation and repeated for a total to five six segments with a total acquisition time of 36 minutes to image the entire lower limb.

6.3 Methods: Data Processing

6.3.1 MRI

6.3.1.1 Image Dataset Registration

DICOM images obtained as output from the MR scanner were imported into ScanIP N-2018.03 SP1 (Synopsys, USA). The CISS-3D and DESS-3D were imported into separate projects within ScanIP. Using the Register Background function within the software, the two image datasets were registered together using corresponding points and additional greyscale-based registration. This allows both image sets to be used in the same project and assists with segmentation of different structures. An overview of the registration steps can be seen in Figure 6-12.

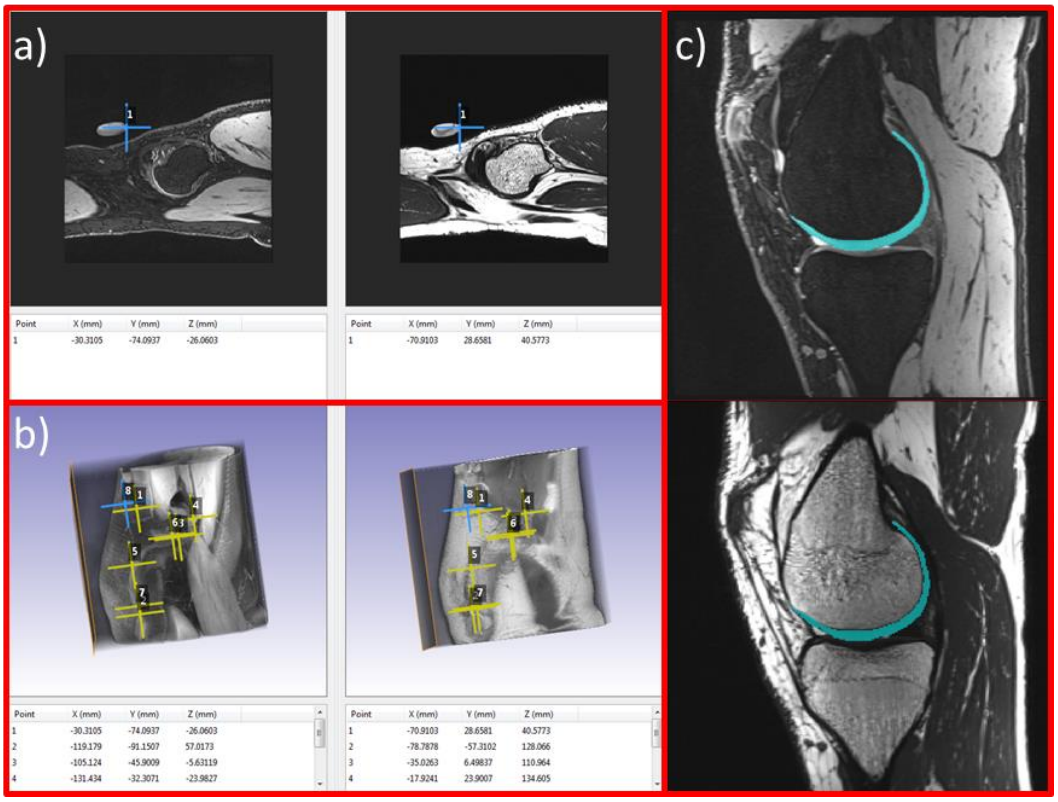

Figure 6-12 Steps performed to register MR scans anticlockwise from **a)** The DESS 3D images were used as the fixed background and the CISS 3D images imported as the moving background. Corresponding points are defined manually in each image set, with the example here being the end of one of MRI marker in the sagittal plane. **b)** A total of 8-10 corresponding points were used per subject to register the image datasets. Points were defined using bony landmarks and MRI markers. All three imaging planes were used to define the corresponding points. The 3D view was used to visualise the points on both data sets to check for any errors with positioning. Once all points were selected registration is performed. **c)** Following registration the two image datasets are in the same project file. This allows masks to be defined using greyscale values in one dataset and being able to be visualised in the other. The example shown here is femoral cartilage being segmented using the DESS-3D (top) and shown in the CISS-3D dataset (below). This allows different structures to be segmented from the two different image datasets and can be rendered into the same model at the end.

6.3.1.2 Image Segmentation

6.3.1.2.1 Bone

A similar segmentation method to that described in section 3.2.2.1.1 was applied to segment bone. The CISS-3D data set was used during the segmentation which is the equivalent to the previously used FIESTA-C sequence. The main advantage with the new sequence was that the image data set is isotropic allowing any of the imaging planes to be used during segmentation. Previously only the sagittal viewing plane was used with the transverse and frontal plane only used for data checking.

Slice interpolation was used to make the segmentation of bone structures more time efficient. A series of slices were segmented with a gap of approximately 5 slices in between. Using the interpolation toolbox built into ScanIP the slice interpolation fills between the slice pairs using the greyscale values between them. This was mainly applied when segmenting the shaft of the femur or tibia in the transverse plane (Figure 6-13).

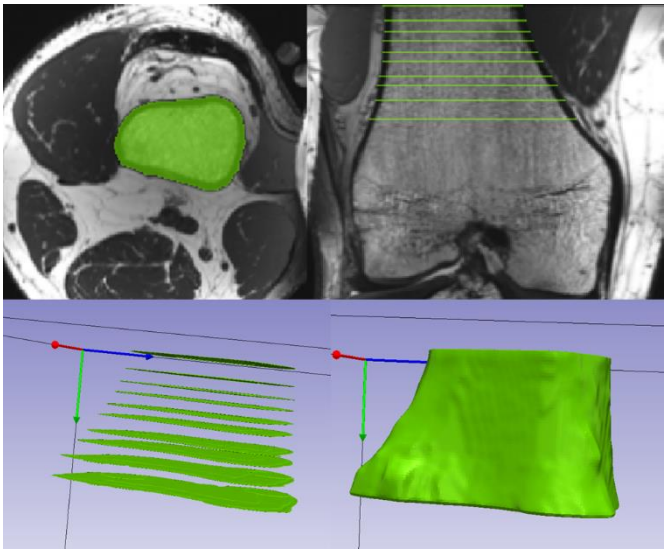

Figure 6-13 Example of slice interpolation on the distal femur shaft **Top Left:** A single segmented femur slice in transverse view **Top Right:** A series of segmented femur slices viewed in the frontal plane. **Bottom Left:** 3D rendering of segmented slices **Bottom Right:** 3D rendering after slice interpolation has been applied

6.3.1.2.2 Cartilage

To segment femoral and tibial cartilage the DESS-3D image dataset was used. Cartilage displays high signal intensity on the DESS-3D image, so that it appears brighter on the image. Bone has very low signal intensity so that it appears dark on the image. This provides clear cartilage and bone boundaries and makes cartilage segmentation simpler compared to FIESTA-C/CISS-3D sequences. A semi-automated threshold function was used to select the corresponding greyscale values for cartilage and each slice was individually segmented.

6.3.1.2.3 Long Leg

Compared with the method described in Chapter 3 the long leg sequence involved one continuous scan thus allowing complete segmentation of long bones (Figure 6-14). Interpolation was used on the long bone shafts to make the segmentation processing more efficient.

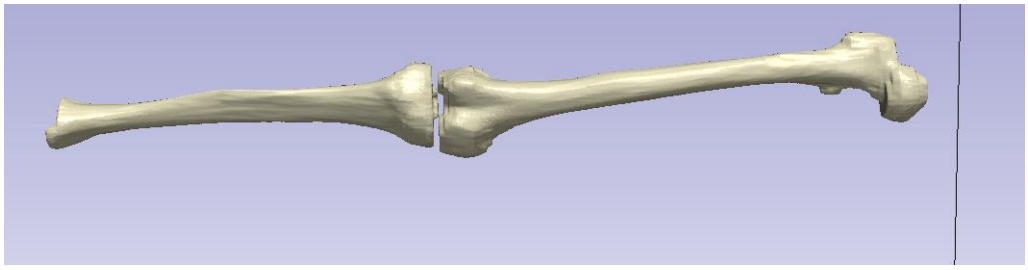

Figure 6-14 Complete segmentation of femur and tibia from concatenated MR image datasets

6.3.1.2.4 Anatomical Coordinate Systems (ACS)

Artec studio 12 (Artec 3D, Luxembourg) was used to register the long leg 3D models to the high resolution 3D knee models. Approximately 10 corresponding points were selected between the long leg models and the respective high resolution model (Figure 6-15). A rough registration was used based on these points followed by a fine registration using a rigid registration algorithm. An ACS was applied to both the femur and tibia cartilage and bone models following the approach defined in Appendix C.

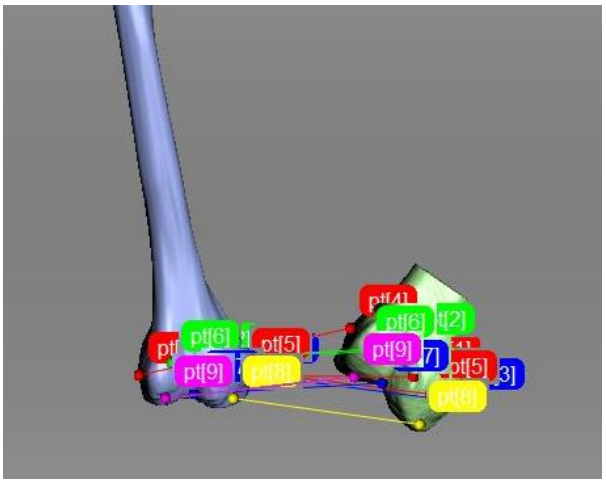

Figure 6-15 Example of corresponding points selected between long leg femur and high resolution femur models

6.3.2 Biplane Fluoroscopy

6.3.2.1 Image registration

The MPEG-4 videos exported from the MediCap systems were converted into individual Tagged Image File Format as described previously in Section 5.4.2 using custom MATLAB code. The images were corrected for distortion using the approach defined in Appendix B. The volunteer specific, biplane calibration intrinsic and extrinsic parameters were calculated using the calibration cube and software (section 5.4.2.2.3).

The calibration file for each of the C-arms, the corresponding image data sets and volunteer specific bone models were imported into JointTrack Biplane (University of Florida). Unlike the previous single plane version of JointTrack, two X-ray views are supported with the ability to visualise models in both simultaneously. For example, applying an out of plane translation to a model in one of the X-ray views would apply the same translation horizontally in the second view.

Individual intensity values for both of the X-ray views were optimised using upper and lower greyscale bounds to ensure that the edges of the bones could be visualised (Figure 6-16). The first step was to align the femur in the sagittal view using a transparent edge rendering on the model. This was carried out

such that the lines of the models could be aligned with the boundaries of the bone on the X-ray. Then the frontal view was used to position the model on the medial lateral axis and frontal plane rotation (Figure 6-16). These steps were repeated to align the tibia model. The models were manually positioned using a combination of keyboard controls and mouse controls which are defined in Appendix B.

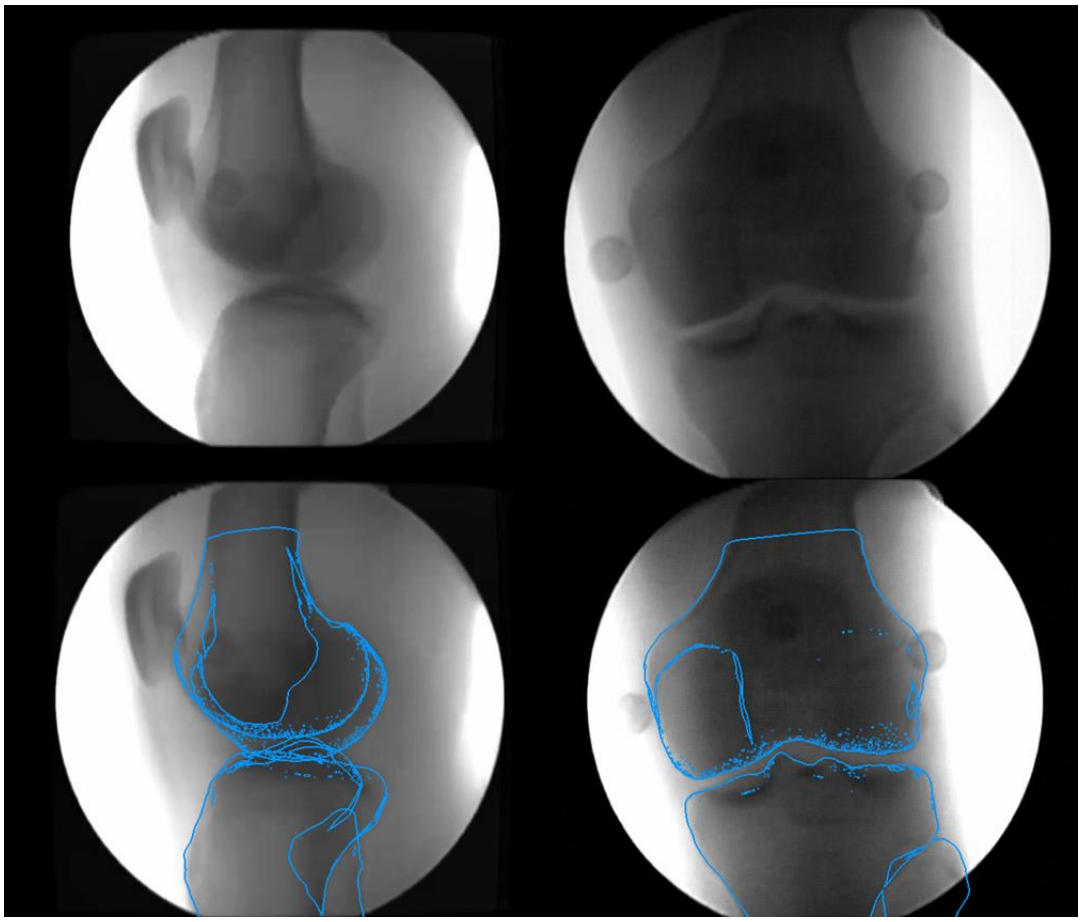

Figure 6-16 **Top:** Show the intensity optimised image pair of a healthy volunteer during extension. With the left image being from the sagittal view and the right image frontal. **Below:** Show the volunteer specific bone models manually aligned with the boundaries of the bone. A transparent rendering is used to visualise the edges of the model.

Due to the limiting spatial resolution (as discussed in section 5.6.5.1) the Canny edge detection built into the software did not work. This was due to the inferior image quality. This meant that the images could not be further optimised using the optimisation functions in the software.

A suspected operating system compatibility issue meant that the software was only capable of processing between 5-10 image pairs at a time. Therefore, images were processed in small 5-10 batches and the output positions of the models for each of these segments exported. The software was then restarted, and the next set of image pairs were loaded. Approximately 500 image pairs were processed for each healthy volunteer. Once all images had been processed the separated output positions of both femur and tibia were concatenated into an individual file for each model using MATLAB code.

6.3.2.2 Kinematic Calculations

The 3D poses of each bone are imported into JointView (University of Florida) and kinematics for each image pair calculated. Joint rotations are calculated using a 312 Cardan/Euler sequence (Tupling and Pierrynowski 1987). Joint translations are calculated by measuring the movement of the femoral origin within the tibial models coordinate system.

6.3.2.3 Contact point calculations

The 3D models of the femoral and tibial cartilage are imported into JointView and applied with the kinematics calculated from the image registration. Using the same approach as section 2.2.4.6.3 regions of interest were defined. These regions of interest included the medial and lateral sides of the femoral and tibial cartilage (Figure 6-17). A nearest neighbour algorithm was used to calculate the closest points explained further in section 2.2.4.6.3. Unlike the previous studies in Chapter 2 and 3, the two articular cartilage surfaces are present allowing the contact point locations to be calculated. The contact points for the medial and lateral condyles are calculated as the centre of the geometric region where the vertices between the models are less than 6 mm apart (Moro-Oka et al. 2008; Hamai et al. 2013) (Figure 6-17). Separate medial and lateral compartment translations were calculated using the contact point locations

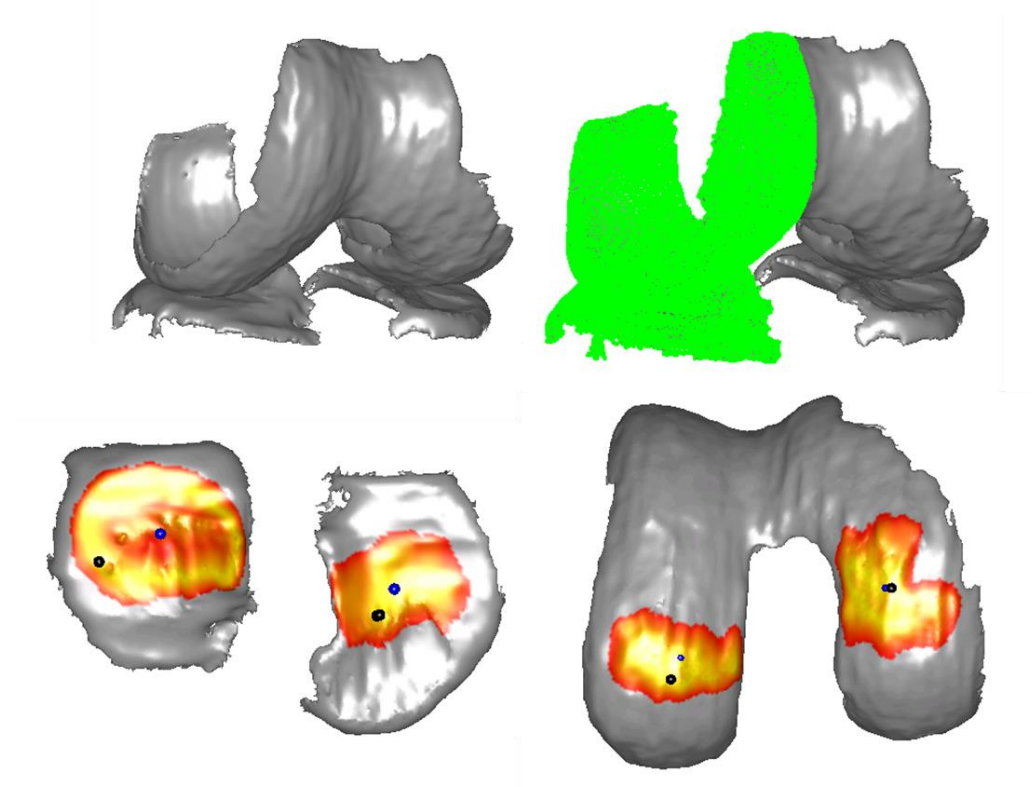

Figure 6-17 Overview of Joint View Contact point calculations **Top Left:** Femur and Tibia cartilage models imported into software with position data calculated from MBIR **Top Right:** Lateral regions of interest (Green) femur and tibia cartilage defined **Bottom Left:** Example contact point plots on tibial cartilage for one frame where the blue sphere represent the position of the contact points and the black sphere the closest point. The closest point is in a different position as it represents the point where the shortest distance between the models exists. **Bottom Right:** Example contact point plot for one frame on femoral cartilage. The red and yellow map represents the vertices that contribute to defining the contact point.

The kinematic data and closest point data were split up into three separate step up and down sections for each volunteer based on the events defined in the motion capture analysis (section 6.3.2.4). A MATLAB script provided by Prof. Scott Banks used spline interpolation with 5° flexion intervals to reanalyse all the translations and rotations as a function of flexion angle (Hamai et al. 2009). From this data the average and standard deviation curves for all healthy volunteers was calculated for step up and step down.

6.3.2.4 Motion Analysis

Data processing was performed using the same methodology as described previously in section 2.2.2.3 and Figure 2-4. With marker data labelled in QTM and imported into Visual 3D v6 (C-Motion, USA) to apply a biomechanical model.

To define the start and end of the step up and down task the velocity of the right knee was calculated. A threshold was set within Visual 3D v6 such that when the velocity increases above or below 0 m/s an event is labelled. When the step-up activity starts, the knee velocity increases from 0 and eventually stops at full extension. The same occurs during step down, allowing a subjective method of defining the start and end of the activities.

Kinematics were calculated using the same ISB recommendations described in section 2.2.2.3.3.

The moments were resolved in the local coordinate system of the distal joint. This was performed based on work carried out by Miranda et al. (2013) who used biplane videoradiography to investigate soft tissue artefact (STA) in motion capture. They found that the tibia had the least STA hence knee joint kinetics are resolved in the tibia ACS. The moments were normalised for weight and height and expressed as a percentage of body weight multiplied by height.

6.4 Results

All kinematic and kinetic motion analysis data was normalised across step up and down at all joints. For each subject the three step activities were averaged, and a group mean and standard deviation was calculated for all five subjects and plotted. It was decided for this study to present knee rotation only for the motion analysis results. All other joint kinematics and kinetics waveforms can be found in Appendix I. For visual comparison of the two methods, the three knee kinematic rotations calculated using the MBIR protocol were normalised to % task based on the same events defined in the motion analysis. Subject average and overall group average and standard deviation were also

calculated. Figure 6-18 and Figure 6-19 show comparisons of the knee rotations calculated using the two methods.

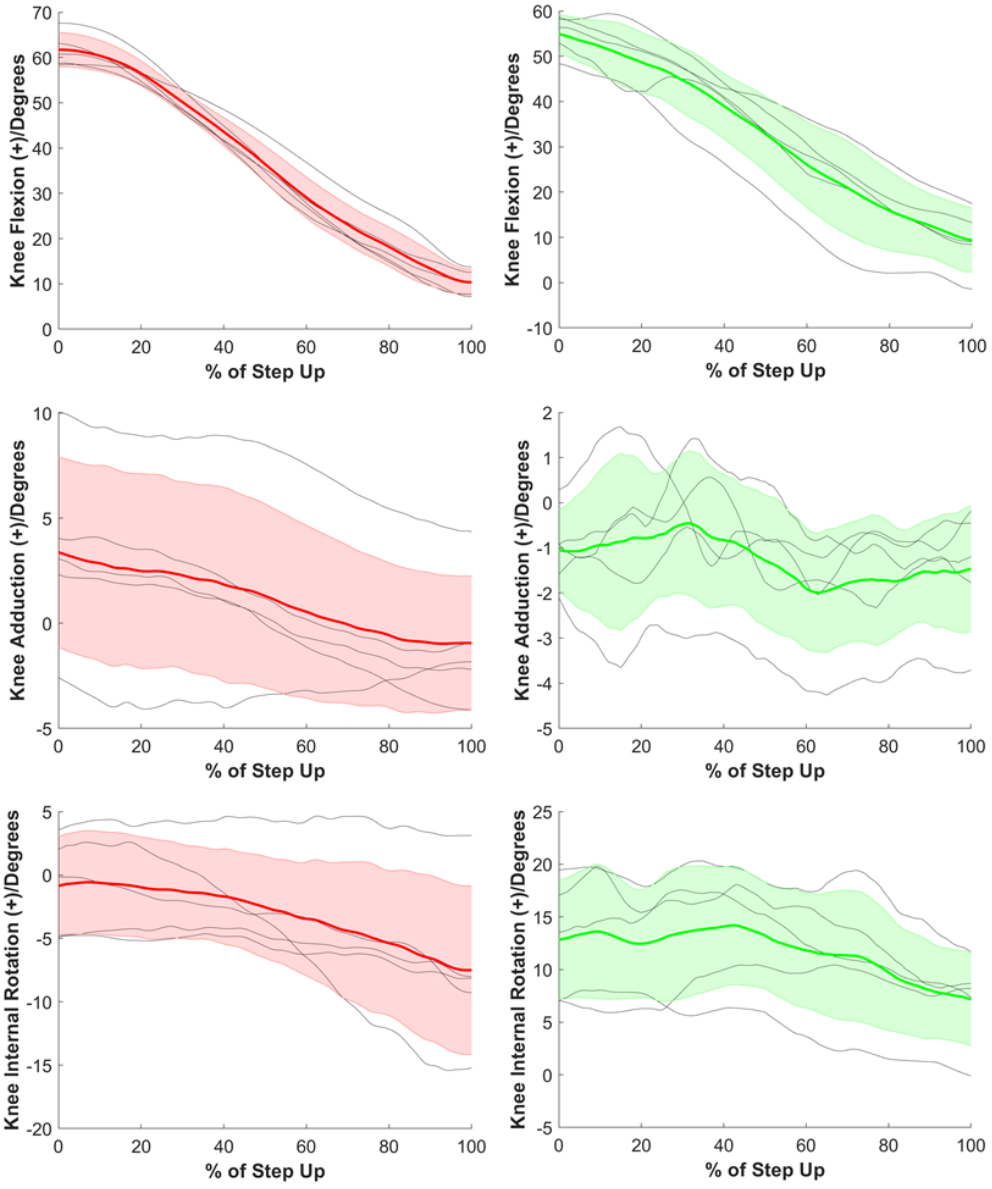

Figure 6-18 Kinematic rotations occurring at the knee during step up as calculated from **motion analysis (red)** and **MBIR (green).** Individual subject means are shown as light grey lines with overall group mean and standard deviation shown as bold line and shaded area respectively.

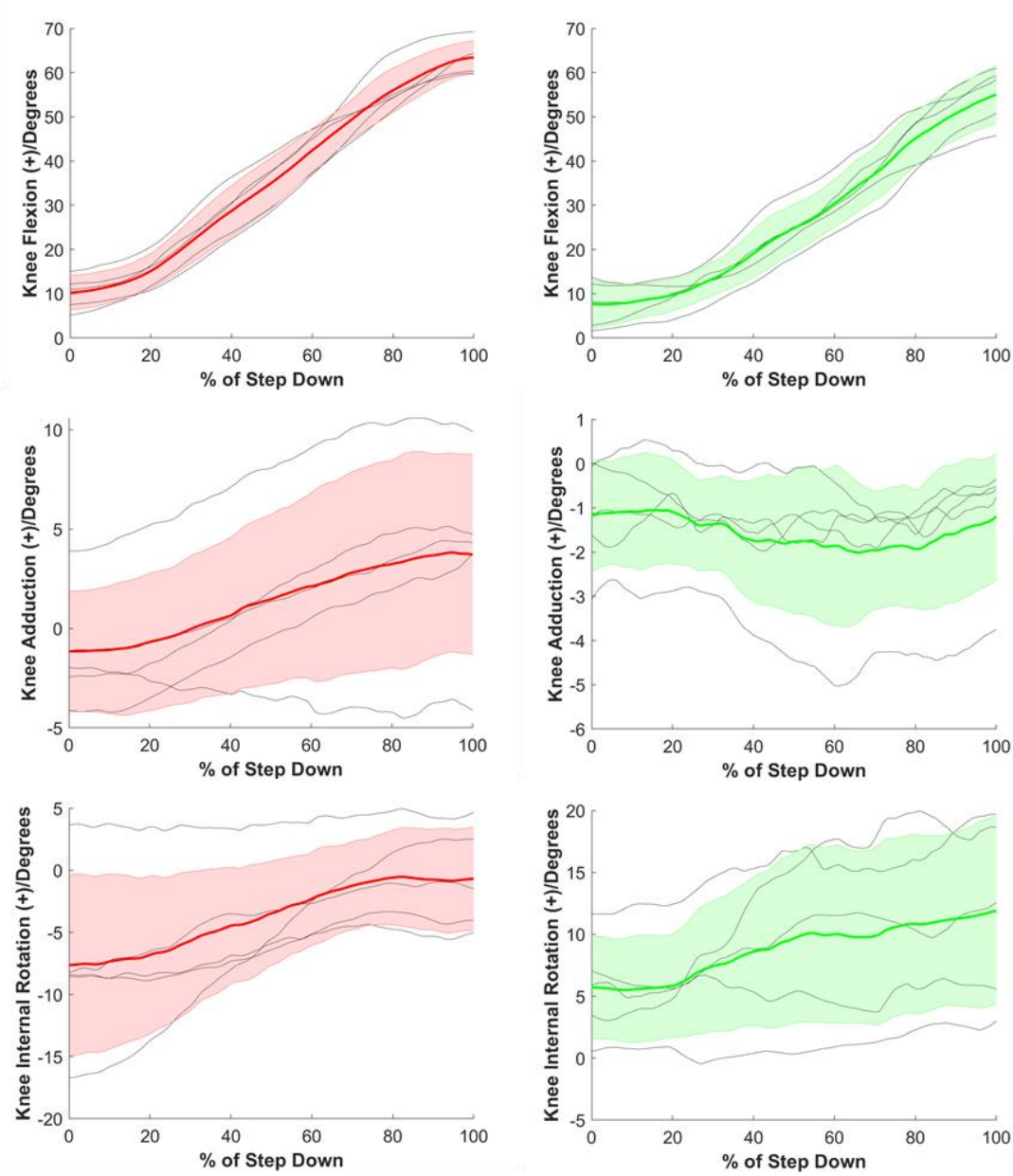

Figure 6-19 Kinematic rotations occurring at the knee during step down as calculated from **motion analysis (red)** and **MBIR (green).** Individual subject means are shown as light grey lines with overall group mean and standard deviation shown as bold line and shaded area respectively.

MBIR calculated kinematics were analysed as a function of flexion angle for both step up and down activities. Tibiofemoral rotations and translations during step up can be seen in Figure 6-20 and separate medial and lateral compartment translation based on contact points can be seen in Figure 6-21. Tibiofemoral kinematics during step down can be seen in Figure 6-22 and medial and lateral compartment translations in Figure 6-23.

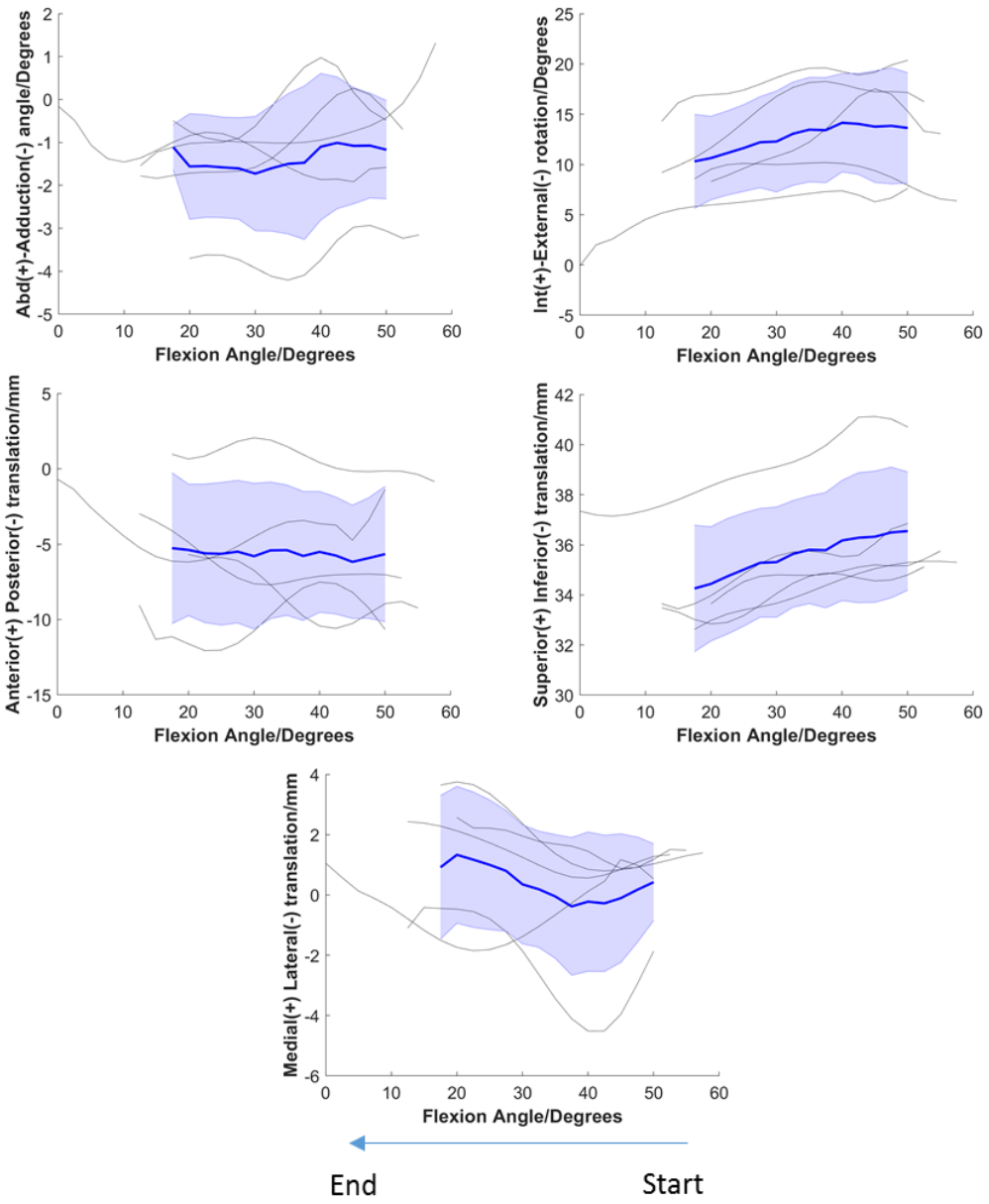

Figure 6-20 Tibiofemoral kinematics during step up. Grey lines represent individual volunteer mean over three step ups with group mean and standard deviation represented by the blue bold line and blue shading. Arrow indicating direction of start and end of step up activity.

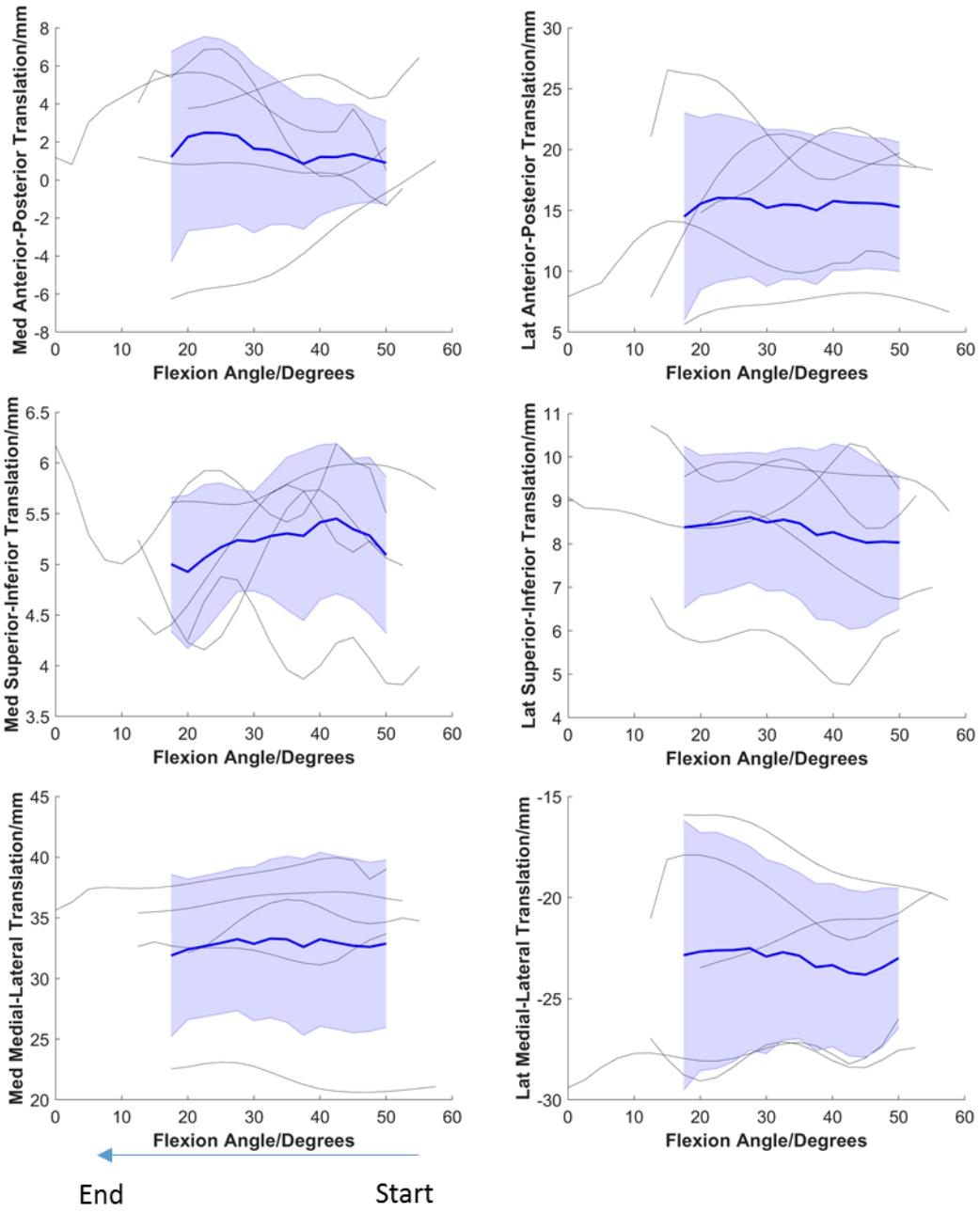

Figure 6-21 Medial and lateral contact point translations. Grey lines represent individual volunteer mean over three step ups with group mean and standard deviation represented by the blue bold line and blue shading. Arrow indicating direction of start and end of step up activity.

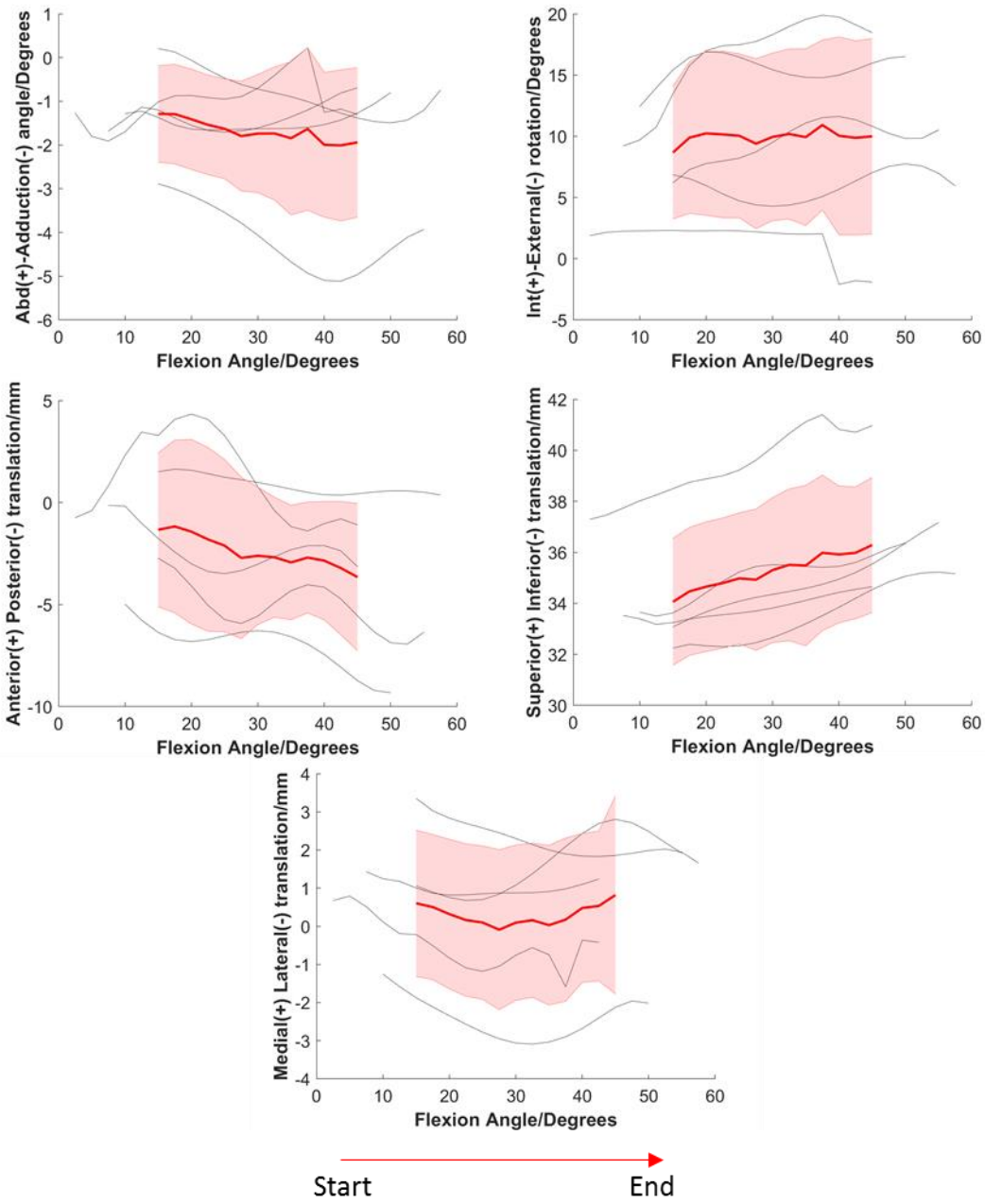

Figure 6-22 Tibiofemoral kinematics during step down. Grey lines represent individual volunteer mean over three step ups with group mean and standard deviation represented by the red bold line and red shading. Arrow indicating direction of start and end of step down activity.

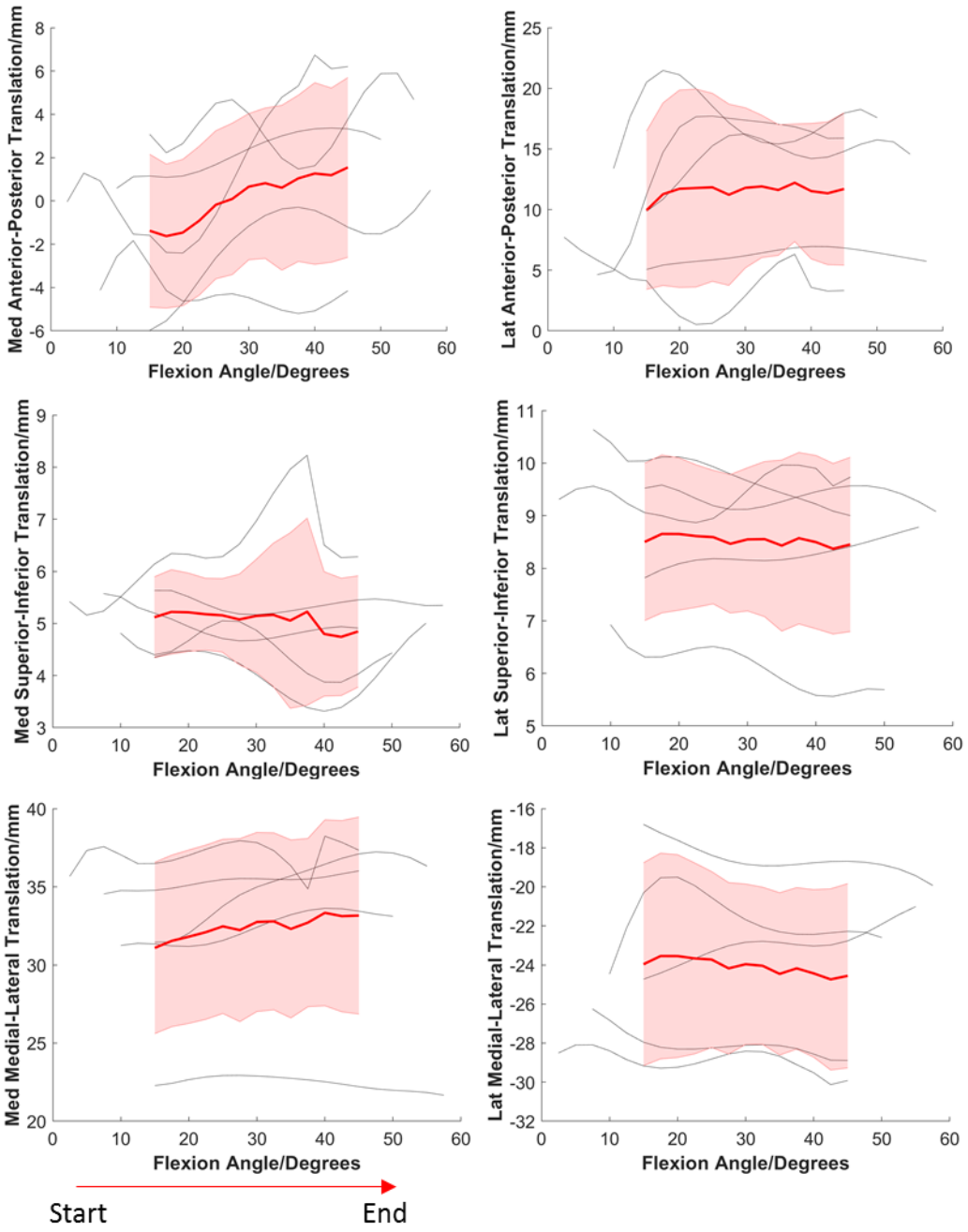

Figure 6-23 Medial and lateral contact point translations. Grey lines represent individual volunteer mean over three step ups with group mean and standard deviation represented by the red bold line and red shading. Arrow indicating direction of start and end of step down activity.

6.5 Discussion

This study demonstrates the processes involved in setting up a Fluoroscopy Laboratory in a non-clinical environment and all the steps that must be undertaken to adhere to UK regulations. This is the first time a facility of this kind has been set up at Cardiff University and the protocols that have been defined will form the foundation for future projects and technological developments.

This pilot study is the first time that biplane fluoroscopy has been performed on a healthy population at Cardiff University. To the authors knowledge this is also the first time it has been carried out to investigate knee biomechanics in the UK.

Several improvements have been made to the MBIR protocol including more advanced imaging protocols and efficient image segmentation methods. These improvements have allowed the incorporation of cartilage models to look at estimated contact locations. The improvements to the MBIR protocol have allowed successful data collection of both motion capture and biplane fluoroscopy.

Comparing motion capture kinematics and fluoroscopy kinematics it can be seen that flexion angle for both step up and down shows a similar pattern and magnitude (Figure 6-18 & Figure 6-19). This is expected as STA investigations have found that flexion-extension angles have the least associated errors (Stagni et al. 2005; Benoit et al. 2006; Tsai et al. 2011). There is a difference in peak flexion of approximately 5 degrees which could be due to differences in the anatomical coordinate systems or inaccuracies in the measurement systems. The method described in section 5.4.3 allows a direct comparison between motion capture and fluoroscopy outputs to calculate the errors. However, this was not performed because the kinematic errors calculated as part of that study were found to be large due to the limitations of the C-arm equipment, thus it was decided that a validation comparison was not appropriate.

For abduction and internal rotation angle, it is recognised that motion analysis has higher associated errors. MBIR kinematics for abduction resulted in a smaller range of motion across the group of mean and individual subject means compared with motion capture (Figure 6-18 & Figure 6-19). While internal rotation there was noted to be an offset of as large as 15 degrees between the group means of the motion analysis and MBIR during step up (Figure 6-18).

When considering the tibiofemoral kinematics, as flexion angle changes during step up and down (Figure 6-20 to Figure 6-23), there was found to be a lot of variability between subject means. This was particularly apparent when looking at the anterior posterior translation and abduction angle during both step up and down. This was assumed to be linked not only to natural variation between subjects but also to other external factors.

One of these external factors is due to the biplane C-arms having a very small imaging volume due to limitations in the size of the image intensifiers and the small source to detector distance. This can be demonstrated by Figure 6-24 where the calibration cube was found to have limited visibility when imaged in both C-arms. The total volume of the cube was 0.001 m^3; the same volume as 1 litre of water. In contrast a bespoke dynamic RSA system with 300 mm image intensifiers looking at treadmill gait had a total imaging volume of 0.038 m^3 (Tashman et al. 2004). This was achieved using a larger image intensifier combined with a large source to detector distance.

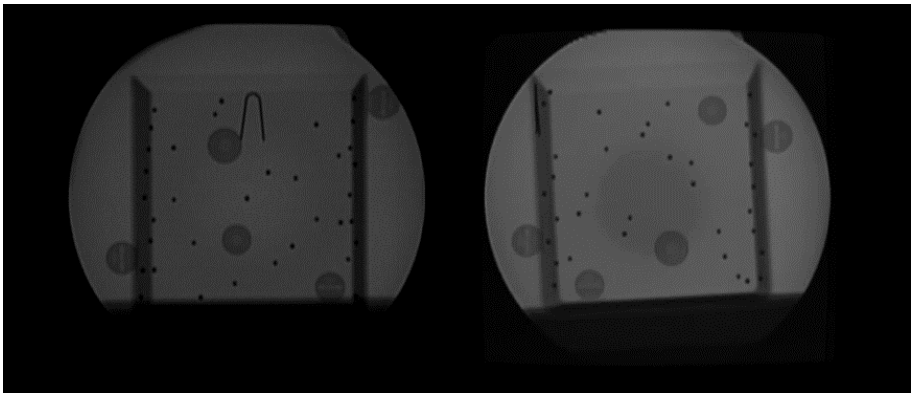

Figure 6-24 The calibration cube with a total volume of 0.001 m^3 was found to only just fit in both views of the C-arms.

This limited the allowable knee movement during the step up activity and volunteers were asked to keep the knee fixed in position. In addition, volunteers were asked to take care to not allow the contralateral limb to pass into the X-ray beam. This caused the volunteers to perform the activity using unnatural movements. This can be seen when looking at the Visual3D avatar (Figure 6-25) where the trunk position between volunteers differed significantly. This has the potential of significantly influencing the in-vivo kinematics occurring at the knee and thus the resulting conclusion drawn regarding range of motion.

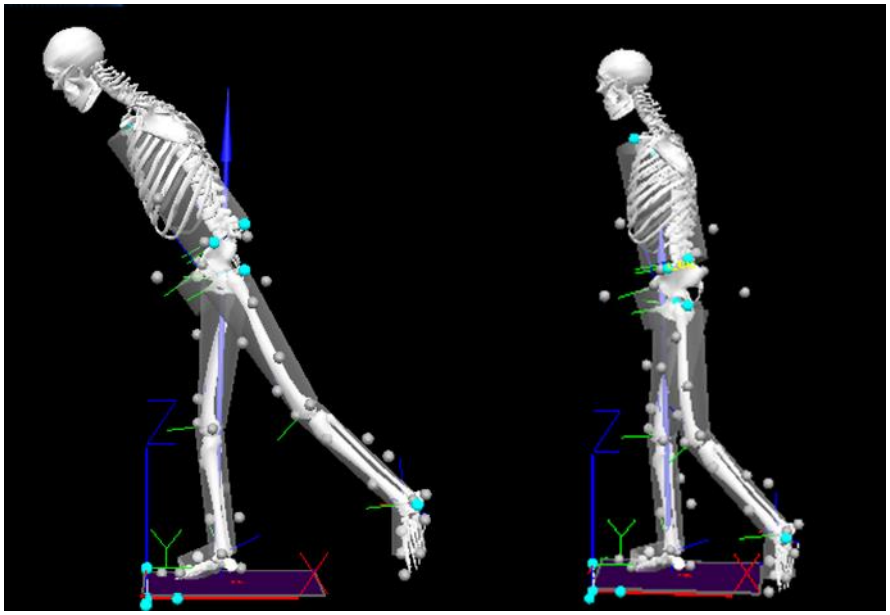

Figure 6-25 Visual 3D avatars of two different volunteers at the end of step up activity.

The accuracy determined in Chapter 5 using dynamic tests assumed that the knee remained in the field of view. When performing the biplane fluoroscopy it was found that due to the limiting field of view the volunteer's knee was moving out of the field of view.

The fluoroscopy equipment is built with an automatic exposure control. This changes the voltage of the X-ray generated based on what is in the centre of the field of view. The voltage of an X-ray determines how far the X-ray can penetrate. Therefore if the knee moves out of the centre of the field of view it automatically decreases the voltage as it has less to penetrate and the exposure control adjusts accordingly (Geise 2001). This means that the X-ray

has less penetration and if the knee is imaged at the edge of the field of view making the bone difficult to visualise (Figure 6-26). This decreases the accuracy of the MBIR further as the edges of the bones can't be determined. This could further explain the variety in the kinematics.

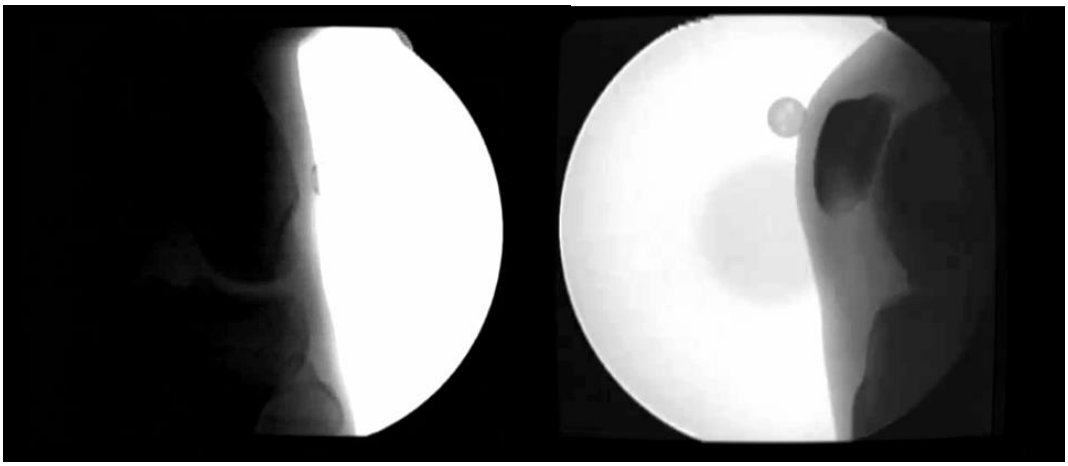

Figure 6-26 Example biplane images of healthy volunteer with knee out of field of view in both C-arms. The intensity has been increased to try and visualise the bone edges but it is difficult to determine suitable bone positions.

Due to the problems faced in this healthy volunteer study with the clinical C-arms and the hardware limitations, the conclusion is that this system is not suitable for use with patient volunteer studies.

6.6 Summary

During this study significant improvements have been made to the MBIR protocol allowing combined biplane fluoroscopy and motion analysis to be performed on a healthy pilot study. Updates to imaging protocols have allowed the inclusion of cartilage models to be combined with fluoroscopy data to better inform contact point estimates.

It was found during this study and the previous study presented in Chapter 5 that the refurbished C-arm systems used to perform biplane fluoroscopy have significant hardware limitations. They have provided the opportunity to develop the MBIR protocol further but have been deemed unsuitable for any future patient volunteer studies. Despite this, the study presented here has aided in

determining the specification for the requirements for a future bespoke system and the MBIR protocol developed here will form the groundwork for analysing any future data.

Chapter 7 Conclusions and Future Work

7.1 Conclusions

The studies presented in this thesis have contributed to the development of a combined motion capture and biplane fluoroscopy protocol and MBIR protocols to look at in-vivo knee kinematics.

Throughout the different studies, improvements and additions have been made to existing data collection and data processing protocols. Single-plane fluoroscopy protocols have been updated and applied to a unique patient population and address clinically led hypothesis. A validation protocol was defined to examine the errors associated with generating 3D bone models and using MBIR to calculate skeletal kinematics.

A biplane fluoroscopy and combined motion capture system was commissioned and an updated MBIR protocol was performed to investigate in-vivo kinematics of the knee on a healthy cohort.

Summary conclusions for each of the objectives defined in Chapter 1 are addressed below.

Objective 1: To assess the current single plane protocols performed at Cardiff University and determine essential required improvements.

A large, multi-factor retrospective study was performed on a unique patient cohort who had surgically mal-aligned Total Knee Replacements (TKR). The study focused on the methods for processing marker based motion capture and single plane fluoroscopy data collected for this group of patients. The Model Based Image Registration (MBIR) protocol was applied for this TKR cohort and it was also improved to work with new software and analysis techniques. Output data was analysed for knee kinematics and loading during level gait recorded using motion capture, and knee kinematics resulting from the single plane fluoroscopy and MBIR for a step up and step down activity. Hip-Knee-Ankle (HKA) alignment measurements taken from long leg X-rays, and implant component alignment measurements taken from low dose Computed Tomography (CT) scans of the patients. They provided clinically relevant comparators and allowed three clinically relevant hypothesis to be tested.

Hypothesis 1 - Frontal plane alignment of the knee, quantified using static clinical measures, influences knee joint kinematics and loading significantly when measured using marker based motion analysis.

Patients with valgus frontal plane alignment, quantified using HKA, were found to have a significantly reduced flexion ROM during gait. Patients with varus frontal plane alignment, quantified using HKA, had significantly increased peak adduction moments.

Hypothesis 2 – Frontal plane alignment of the knee, quantified using static clinical measures, influences knee joint kinematics significantly during a step up and step down activity when measured using MBIR and single plane fluoroscopy.

No significant differences were found for any of the patient groups across varus, neutral and valgus HKA alignment.

Hypothesis 3 – Surgical measures relating to implant alignment have a significant impact on in-vivo joint kinematics and Centre of Rotation during a step up and step down activity when measured using MBIR and single plane fluoroscopy.

Increased posterior Tibial Slope angle was found to have a significant negative relationship with joint compression in relation to the distance between the femoral and tibial components. This suggests a potential reduction in the flexion gap as the tibial slope angle increases.

A study was also performed to examine a combined motion capture and single plane fluoroscopy protocol using MR defined bone models. The findings showed that there were significant technical challenges that must be addressed. Resulting recommendations were provided to perform single plane studies and inform research groups on best practice.

Objective 2: To determine the main potential sources of errors associated with the MBIR protocol

From single plane fluoroscopy studies it was found that the main potential sources of errors associated with the protocol were: (i) synchronisation of

motion capture and fluoroscopy data collection; (ii) positioning of the motion capture cameras leading to incorrect 3D tracking of retro-reflective marker data and marker (data) drop-out and (iii) determining the Anatomical Coordinate System (ACS) of the bone models when registering bone models derived from low resolution scans together.

The main potential errors found to be associated with determining in-vivo kinematics were: (i) accurate and repeatable segmentation of the MRI scans to produce derived bone models and (ii) model based image registration processing.

These were highlighted as errors to be further investigated and are described and quantitative in the proceeding Chapters.

Objective 3: Create a standardised validation protocol for determining the errors and accuracy associated with the MBIR method for use in present and future system and protocol development at Cardiff University.

A validation protocol was developed to examine the accuracy of MR segmentation using a combination of Computed Tomography (CT) and Structured White Light (SL) scanning techniques. Since working with cadaveric specimens was not possible at Cardiff, ovine femora and tibiae were imaged using MR and CT. They were then dissected and SL scanned to generate a reference model. The MR and CT images were segmented and a comparison was performed between the three different models (MR, CT and SL). When compared with the CT bone models, it was found that MRI derived ovine femora models had a RMS error of 0.799 ±0.102 mm (mean±stdev) and the tibiae models had a RMS error of 0.806±0.106 mm (mean±stdev). This error was acceptable as it was found to be of the same magnitude as the slice thickness for the MR scan sequence and is discussed in the next sections in relation to the errors associated with MBIR using the C-arms. This is the first study to investigate the accuracy associated with generating bone models using a 3T MR scanner. It has provided detailed instructions to enable this

process to be repeated by other researchers and groups and for use with future alternative MR imaging sequences.

A study was performed to develop a standardised validation protocol for MBIR processing using two second hand C-arms (Siremobil). A series of experiments were performed to investigate the errors associated with using this equipment to measured kinematics when subjects perform a step up and down activity. The approach compared MBIR, bead MBIR and marker based motion capture using a Bland-Altman analysis was performed. The bead MBIR (based on RSA techniques) was investigated as a reference method. When compared to a data obtained using a 'ground truth' x-y two-axis linear stage, a mean difference in the resulting displacement data of under 0.2 mm was found between the two methods.

Static and dynamic experiments were performed using Sawbones models. A cluster of three metal beads covered in retro-reflective tape were rigidly attached to the models. This enabled recording of motion capture data when using the three different methods (MBIR, bead MBIR, marker based motion capture) to quantify the joint kinematics. A linear actuator was used to apply three different dynamic velocities to the bone model to simulate joint function.

The results revealed that, when calculating joint kinematics for static positions, the largest absolute difference found for joint rotation was associated with calculating the frontal plane angle (1.80°±1.58) and for joint translations, it was the anterior-posterior translations (2.92mm±2.74), when comparing MBIR and bead MBIR methods.

These differences were found to further increase when considering dynamic joint movements. In particular for the highest velocity, where the largest absolute difference was found when calculating the flexion angle (4.82° ± 3.60) and anterior-posterior translation (3.20 mm ± 1.83) when comparing bead MBIR to motion capture (considered in this case to be the independent measure due to the blur observed in the C-arm images).

To account for the errors introduced when using MR scans to produce bone models and also related to the overlying soft tissue, an ovine specimen was tested and the same static and dynamic movements performed. The

differences in the calculated kinematics found for the dynamic movements were less than those found for the Sawbones models. This was discussed in relation to the increased constraint in the ovine specimen due to the presence of ligaments and other soft tissue structures.

This was the first ovine study to investigate MBIR kinematics accuracy when using biplane fluoroscopy and to investigate the errors associated with MR segmentation to generate bone models. The validation protocol presented here provides an alternative for research groups who do not have access to cadaveric specimens. The errors were found to be significantly larger when calculating the MBIR kinematics compared to those associated with MR segmentation methods. This was understood to be related to the technical limitations of the c-arms rather than the MBIR processing.

These results suggest that the errors associated with the use of MR rather than CT for the creation of bone models do not contribute significantly to the cumulative errors in the MBIR protocol.

Since the errors were underestimated when considering static movements alone or dynamic activities performed at slower speeds, this study has demonstrated the importance of performing validation experiments that effectively represent the activity under examination and the movement velocity at which subjects would perform the activity.

Objective 4: To establish a combined biplane fluoroscopy and motion analysis system in the new Musculoskeletal Biomechanics Research Facility (MSKBRF) at Cardiff University

A Fluoroscopy Laboratory, fully lead lined, RPA approved, and large enough to allow synchronised Biplane Fluoroscopy, marker based motion capture, force plate and EMG analysis for human walking studies was established and commissioned at Cardiff University as part of the new Musculoskeletal Biomechanics Research Facility (MSKBRF). The initial biplane fluoroscopy system was developed based on two refurbished mobile C-arms. Protocols were developed to define the optimum orientation of the C-arm equipment relative to a laboratory coordinate system defined when using marker based

motion capture cameras for applications involving imaging of human knees, in-vivo.

A custom trigger was also developed to synchronise the two C-arm systems with the motion capture equipment. Because the equipment was set up in the new Fluoroscopy Laboratory the position of motion capture cameras were optimised to allow full coverage of movements and improved data collection protocols.

Further, a new suite of musculoskeletal MR imaging sequences was developed to allow improved image segmentation, structural analysis and identification of osteoarthritis imaging markers such as bone marrow lesions, for use in future multi factor studies. Image segmentation techniques were improved to allow the incorporation of cartilage in subsequent calculations that estimate joint contact positions during recorded activities. These improvements addressed several associated errors defined in Objective 2. This is only facility of its kind in the UK and using articular cartilage models from MRI introduces new opportunities for joint contact studies in the furture.

Objective 5: To perform a pilot study using the new MBIR protocol and establish this as a future comparator for future patient studies

A pilot study was performed involving five healthy volunteers to assess whether the new MBIR protocol could be applied practically. Subject specific 3D cartilage and bone models were created using new MR imaging protocols and updated segmentation methods described in the previous Objectives.

Synchronised biplane fluoroscopy and marker based motion capture was performed during a step up and down activity. This is the first time that biplane fluoroscopy combined with motion capture has been used to calculate in-vivo kinematics of the knee in the UK.

The results from the fluoroscopy study revealed a large amount of variability between subjects. This was suggested to be related to limitations in the old C-arm system which limited the ability for volunteers to perform the activity in a natural and consistent way. During the data processing, it was found that, due to the small size of the image intensifier (230mm) and the large pulse width (40ms), the recorded data was challenging to use when performing MBIR

processing. Because of this and the other errors calculated in Objective 3, it was decided that the C-arm system would not be suitable for future patient volunteer studies.

Despite these limitations, this study was not carried out in vain. The protocols developed and the extensive new information and understanding gained in the application of MBIR and biplane fluoroscopy has provided a valuable foundation for future work. This knowledge and expertise has contributed to the development of the requirements for, and an understanding of the limitations related to, a bespoke biplane X-ray system currently under design and construction. This new system, to be installed in late 2018 in the MSKBRF at Cardiff will be unique in the UK and possibly in the world.

7.2 Future Work

Despite the new and novel contributions made from the studies described in this thesis, there is much to do to further develop these techniques and established an automated, validated protocol for the dynamic bi-plane X-ray system that is synchronised with all of the usual measurements associated with gold standard human motion capture. Based on the knowledge gained to date, the following describes a series of further studies that will provide further confidence in the efficacy and accuracy of the techniques and technology that will be applied to measure human movement at the MSKBRF, Cardiff University

7.2.1 Determine the errors using the new MRI imaging protocols

Investigate the errors using the new 3T Magnetom Prisma (Siemens, Germany) MR sequences defined in Chapter 6. The protocol defined in Chapter 4 could be used to assess which sequence is the most suitable for segmenting accurate MR derived bone model.

7.2.2 Apply protocols to calculate TKR in-vivo kinematics

Adapting the biplane MBIR protocols to calculate TKR in-vivo kinematics and undertake the validation protocols to calculate the associated errors.

7.2.3 Investigations into new Software approaches

Since this work has been carried out a collaboration between C-motion and Cardiff University has been developed to investigate using their new Dynamic Stereo X-ray Suite (DSX, C-Motion, USA) with the existing protocols. Work has been carried out to adapt MR derived bone models to create a digitally reconstructed radiographs to then be aligned with the x-ray image, an example of which is shown in Figure 7-1. This allows further automation within the MBIR and direct integration into the Visual3D software.

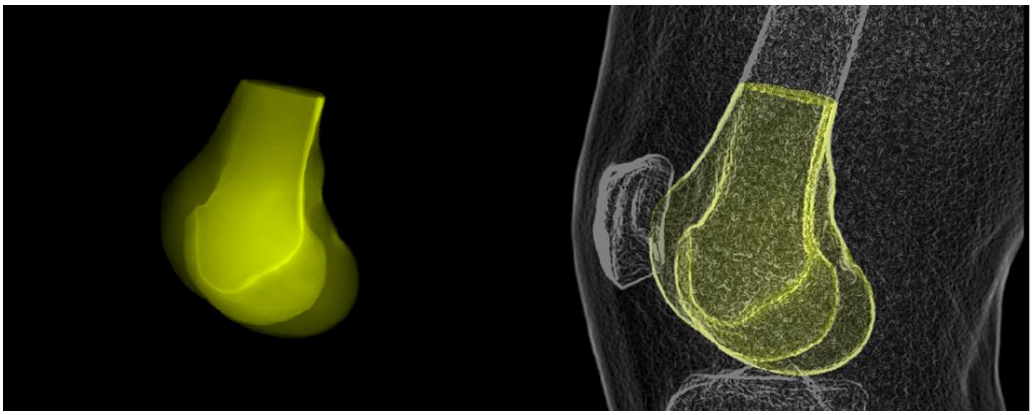

Figure 7-1 Example image of MRI derived bone model converted into a DRR and subsequently aligned with X-ray image

7.2.4 Bespoke X-ray System

To address some of the limitations described in Chapter 6 during the Biplane Fluoroscopy pilot study, new equipment was purchased as part of an internal funding opportunity. This equipment includes new flat panel image detectors (CXDI-50RF, Canon, Japan) and separate x-ray tube and generator. This has been set up as a bespoke single plane system at Cardiff to collect pilot data on subjects with healthy, intact, or implanted knees (Figure 7-1)**.**

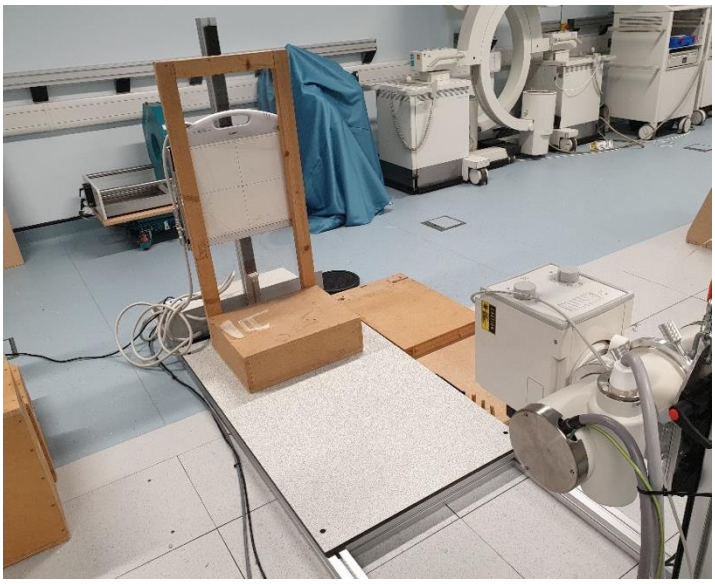

Figure 7-2 Bespoke single plane flat panel x-ray system

The bespoke system uses pulsed X-ray exposure to record dynamic activities. The X-ray generator allows complete control of X-ray tube current, the kV and the pulse width. The flat panel system can perform at up to 20 FPS at 305 x 305 mm FOV. Although this limits the activities to simpler dynamic tasks (step up, lunge etc), the images captured during dynamic activities have no blur and show good contrast of the different structures (Figure 7-3).

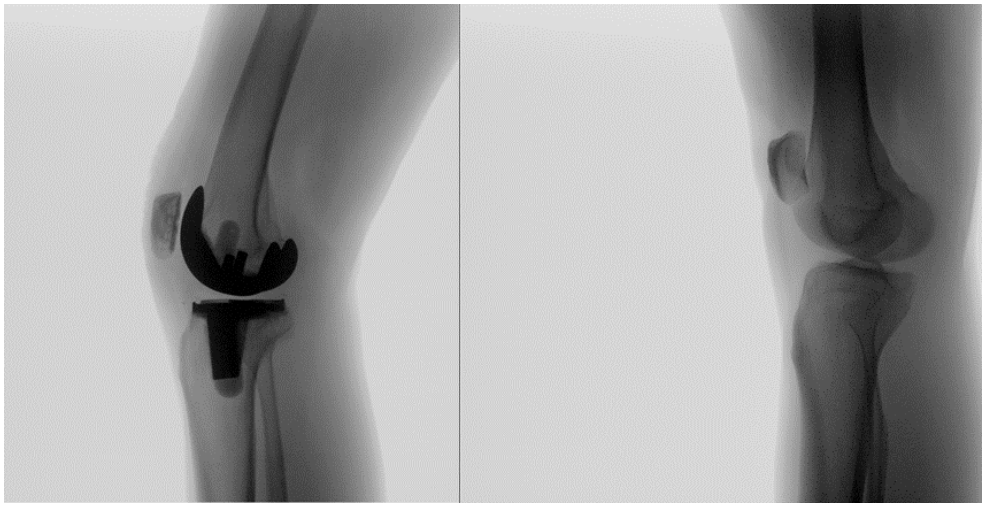

Figure 7-3 Example X-ray images taken from the bespoke system showing the superior image quality over the other systems used in this study

This equipment forms the basis of the new bespoke, biplane X-ray system being developed and installed at Cardiff University.

As part of the Welsh Government funding provide to design and build the MSKBRF, one of the unique selling points was the new bespoke biplane X-ray system. Electron-X, an industrial X-ray company based in the UK, was awarded the contract to work with Cardiff University to design and build the system. The author was employed as a research associate to be Project Manager on this project and was involved at all stages in the specification, design, manufacture and commissioning. A detailed design was finalised at the beginning of July 2018, with planned installation and commissioning by beginning of December 2018. Due to intellectual property rights the detailed design cannot be disclosed in this thesis however the initial specification that the design was based on is shown in section 7.2.2.1 below. A computer model demonstrating how the final system will look is shown in Figure 7-4. MBIR protocols defined in this thesis will be applied to this new system and will form the foundation for future studies.

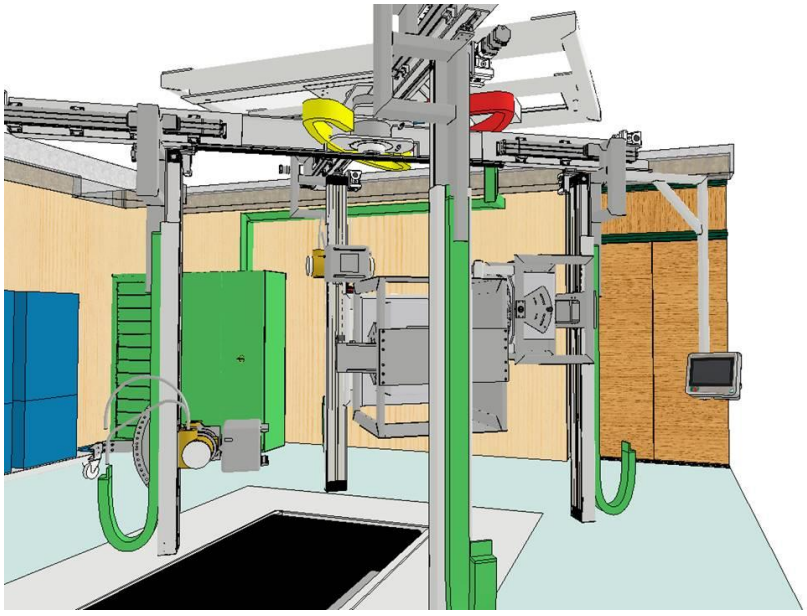

Figure 7-4 Bespoke Biplane X-ray system being developed at Cardiff University allowing numerous configurations to perform high-speed biplane X-ray and Fluoroscopy for a number of different human joints.

7.2.4.1 Bespoke Biplane X-ray Initial Specification

1. Capture synchronised bi-plane pulsed X-ray/fluoroscopy of a human joint (e.g. Knee, ankle, shoulder, elbow, and wrist) during a range of

daily activities e.g. the knee during stepping up onto a step or walking over a force plate.

2. Ability of time synchronised pulsed capture frame rates of over 100 fps and fluoroscopy up to 1000 fps.
3. To be able to interchange imaging detector between flat panel detector and image intensifier with high-speed cameras.
4. Field of view size of the order of 16" (to be advised on options).
5. Control over pulse width to minimise blurring between frames.
6. Control over the brightness and contrast of the images captured.
7. High quality images required - contrast needs to ensure defined edges of imaged moving bones and implants so that they are able to use them for image registration purposes.
8. Minimise dose to patient
9. Ability to synchronise the fluoroscopy capture with our motion capture cameras, force plates and EMG equipment.
10. The system must be moveable.
    a. Translate along the length of the room to work in different stations. There will be a row of force plates to look at gait, squats, stair climbing, seated activities, and at the far end of the room there will be a treadmill, where we would look at either knee, ankle, feet etc. during gait.
    b. It should rotate to allow joints to be viewed from different angles depending on the joint under investigation and activity e.g. view knee from front to back or side to side.
    c. The height should be adjustable — allow assessment of a range of joints at different heights
    d. The distance between source and detector should be adjustable - guidance will be needed to determine optimum range to maximise image quality (source-detector distance has been recommended in literature to be 160-220 cm).
    e. The angle between the 2 X-ray systems should be adjustable e.g. for many applications, ideally 90 degrees between them is

optimum but we may need to adjust this to allow more room for patients to move their limbs

11. Must save all synchronised images and be date and time stamped such that they can be read in sequence.
12. Be flexible so that one or both fluoroscopy systems can be used for image capture.
13. Information on system delays and how accurate the synchronisation is.
14. Controls to position the equipment (within lab)
15. Controls for start/stop (within control room).
16. Contain emergency stop within control room, and an emergency stop that the patient can press in the lab.

References

Acker, S. et al. 2011. Accuracy of single-plane fluoroscopy in determining relative position and orientation of total knee replacement components. *Journal of Biomechanics* 44(4), pp. 784–787. Available at: http://dx.doi.org/10.1016/j.jbiomech.2010.10.033.

Ackland, D.C. et al. 2011. Future trends in the use of X-ray fluoroscopy for the measurement and modelling of joint motion. *Proceedings of the Institution of Mechanical Engineers, Part H: Journal of Engineering in Medicine* 225(12), pp. 1136–1148. Available at: http://www.scopus.com/inward/record.url?eid=2-s2.0-84862694813&partnerID=tZOtx3y1.

Aglietti, P. and Buzzi, R. 1988. Posteriorly stabilised total-condylar knee replacement. Three to eight years' follow-up of 85 knees. *The Journal of bone and joint surgery. British volume* 70(2), pp. 211–6. Available at: http://www.ncbi.nlm.nih.gov/pubmed/3346290.

Allen, M. et al. 1998. The Surgical Anatomy of the Stifle Joint in Sheep. *Vertinary Surgery* 27, pp. 596–605.

Anderst, W. et al. 2009. Validation of three-dimensional model-based tibio-femoral tracking during running. *Medical Engineering and Physics* 31(1), pp. 10–16. doi: 10.1016/j.medengphy.2008.03.003.

Anderst, W. et al. 2011. Validation of a Non-Invasive Technique to Precisely Measure In Vivo Three-Dimensional Cervical Spine Movement. *Spine* 36(6), pp. 997–1003. doi: 10.1016/j.biotechadv.2011.08.021.Secreted.

Andriacchi, T.P. 1994. Dynamics of knee malalignment. *The Orthopedic clinics of North America* 25(3), p. 395—403. Available at: http://europepmc.org/abstract/MED/8028883.

Arthritis Research UK 2013. *Osteoarthritis in general practice*.

Back, D.L. et al. 2001. The Kinemax total knee arthroplasty. *The Journal of Bone and Joint Surgery* 83(3), pp. 359–363. Available at: http://www.bjj.boneandjoint.org.uk/cgi/doi/10.1302/0301-620X.83B3.11006.

Balter, S. 1999. X-ray Image Intensifier. *Catheterization and Cardiovascular Interventions* 46, pp. 238–244.

Banks, S. a. 1992. *Model Based 3D Kinematic Estimation From 2D Persperctive Silhouettes, Application With Total Knee Prostheses*. Massachusetts Institute of Technology.

Banks, S. a and Hodge, W. a 1996. Accurate measurement of three dimensional knee replacement kinematics using single-plane flouroscopy. *IEEE Transactions on Biomedical Engineering* 46(6), pp. 638–649.

Banks, S. a and Hodge, W.A. 2004. Implant design affects knee arthroplasty kinematics during stair-stepping. *Clinical orthopaedics and related research* (426), pp. 187–193. doi: 10.1097/01.blo.0000138956.04316.ac.

Banks, S.A. et al. 2005. Comparing in vivo kinematics of unicondylar and bi-unicondylar knee replacements. *Knee Surgery, Sports Traumatology, Arthroscopy* 13(7), pp. 551–556. doi: 10.1007/s00167-004-0565-x.

Barker, T.M. et al. 1994. Accuracy of stereolithographic models of human anatomy. *Australasian radiology.* 38(2), pp. 106–111. doi: 10.1111/j.1440-1673.1994.tb00146.x.

Barré, A. and Aminian, K. 2018. Error performances of a model-based biplane fluoroscopic system for tracking knee prosthesis during treadmill gait task. *Medical and Biological Engineering and Computing* 56(2), pp. 307–316. doi: 10.1007/s11517-017-1680-4.

Basad, E. et al. 2010. Matrix-induced autologous chondrocyte implantation versus microfracture in the treatment of cartilage defects of the knee: A 2-year randomised study. *Knee Surgery, Sports Traumatology, Arthroscopy* 18(4), pp. 519–527. doi: 10.1007/s00167-009-1028-1.

Bäthis, H. et al. 2004. Alignment in total knee arthroplasty. *The Journal of Bone and Joint Surgery* 86(5), pp. 682–687. Available at: http://www.bjj.boneandjoint.org.uk/cgi/doi/10.1302/0301-620X.86B5.14927.

Baudet, A. et al. 2014. Cross-Talk Correction Method for Knee Kinematics in Gait Analysis Using Principal Component Analysis (PCA): A New Proposal. *PLoS ONE* 9(7), p. e102098. Available at:

http://dx.plos.org/10.1371/journal.pone.0102098.

Bellamy, N. et al. 1988. Validation study of WOMAC: A health status instrument for measuring clinically important patient relevant outcomes to antirheumatic drug therapy in patients with osteoarthritis of the hip or knee. *Journal of Rheumatology* 15(12), pp. 1833–1840. Available at: https://www.scopus.com/inward/record.uri?eid=2-s2.0-0024268463&partnerID=40&md5=fbb901b0fe6613d2f9fbec650ef08dca.

Benoit, D.L. et al. 2006. Effect of skin movement artifact on knee kinematics during gait and cutting motions measured in vivo. *Gait and Posture* 24, pp. 152–164. doi: 10.1016/j.gaitpost.2005.04.012.

Berger, A. 2002. How does it work? Magnetic resonance imaging. *Bmj* 324, p. 35. doi: 10.1136/bmj.312.7025.247.

Bertec Corporation 2012. Bertec Force Plates. (September). Available at: https://bertec.com/uploads/pdfs/manuals/Force Plate Manual.pdf.

Biggs, P.R. 2016. Classification of Biomechanical Changes in Gait Following Total Knee Replacement: An Objective, Multi-feature Analysis. (December)

Bland, J.M. and Altman, D.G. 1986. Statistical Methods for Assessing Agreement Between Two Methods of Clinical Measurement. *Lancet* 327, pp. 307–310. Available at: http://www.sciencedirect.com/science/article/pii/S0140673686908378.

Bland, J.M. and Altman, D.G. 1991. Measuring agreement in method comparison studies. *Statistical Methods in Medical Research* 8, pp. 135–160. Available at: http://www.sciencedirect.com/science/article/pii/S0140673686908378.

Bland, J.M. and Altman, D.G. 2007. Agreement between methods of measurement with multiple observations per individual. *Journal of Biopharmaceutical Statistics* 17(4), pp. 571–582. doi: 10.1080/10543400701329422.

Board, T.N. and Javed, A. 2003. Patellar resurfacing in total knee arthroplasty. *J Bone Joint Surg Am* 85–A(12), p. 2483–4; author reply 2484.

Bonner, T.J. et al. 2011. The effect of post-operative mechanical axis alignment on the survival of primary total knee replacements after a follow-up of 15 years. *The Journal of bone and joint surgery. British volume* 93(9), pp. 1217–1222. doi: 10.1302/0301-620X.93B9.26573.

Bourne, R.B. et al. 2010. Patient satisfaction after total knee arthroplasty: Who is satisfied and who is not? *Clinical Orthopaedics and Related Research* 468(1), pp. 57–63. doi: 10.1007/s11999-009-1119-9.

Bragdon, C.R. et al. 2002. Experimental assessment of precision and accuracy of radiostereometric analysis for the determination of polyethylene wear in a total hip replacement model. *Journal of Orthopaedic Research* 20(4), pp. 688–695. doi: 10.1016/S0736-0266(01)00171-1.

Bragdon, C.R. et al. 2004. Comparison of two digital radiostereometric analysis methods in the determination of femoral head penetration in a total hip replacement phantom. *Journal of orthopaedic research : official publication of the Orthopaedic Research Society* 22(3), pp. 659–64. Available at: http://www.ncbi.nlm.nih.gov/pubmed/15099649.

Brainerd, E.L. et al. 2010. X-ray reconstruction of moving morphology (XROMM): precision, accuracy and applications in comparative biomechanics research. *Journal of Experimental Zoology Part A: Ecological Genetics and Physiology* 9999A(May 2009), p. n/a-n/a. Available at: http://doi.wiley.com/10.1002/jez.589.

Breighner, R.E. et al. 2018. Technical Developments: Zero Echo Time Imaging of the Shoulder: Enhanced Osseous Detail by Using MR Imaging. *Radiology* 286(3), pp. 960–966. doi: 10.1148/radiol.2017170906.

Brittberg, M. et al. 1994. Treatment Of Deep Cartilage Defects In The Knee With Autologous Chondrocyte Transplantation. *The New England journal of medicine* 10(14), pp. 1268–1292. doi: 10.1056/NEJM199410273311701.

Van den Broeck, J. et al. 2014. Segmentation accuracy of long bones. *Medical Engineering and Physics* 36(7), pp. 949–953. Available at: http://dx.doi.org/10.1016/j.medengphy.2014.03.016.

Brown, R.W. 2014. *Magnetic Resonance Imaging*. Second edi. Hoboken, New

Jersey : John Wiley & Sons, Inc.,.

Bücking, T.M. et al. 2017. From medical imaging data to 3D printed anatomical models. *PLoS ONE* 12(5), pp. 1–10. doi: 10.1371/journal.pone.0178540.

Bushong, S. 2012. *Radiologic Science for Technologists: Physics, Biology and Protection*. 10th ed. Texas: Elsevier.

Buttgereit, F. et al. 2015. Non-surgical management of knee osteoarthritis: Where are we now and where do we need to go? *RMD Open* 1(1), pp. 1–4. doi: 10.1136/rmdopen-2014-000027.

Calvet, J. et al. 2016. High prevalence of cardiovascular co-morbidities in patients with symptomatic knee or hand osteoarthritis. *Scandinavian Journal of Rheumatology* 45(1), pp. 41–44. Available at: http://dx.doi.org/10.3109/03009742.2015.1054875.

Campbell, K.J. et al. 2016. Normative rearfoot motion during barefoot and shod walking using biplane fluoroscopy. *Knee Surgery, Sports Traumatology, Arthroscopy* 24(4), pp. 1402–1408. doi: 10.1007/s00167-014-3084-4.

Cappozzo, A. et al. 1996. Position and orientation in space of bones during movement: Experimental artefacts. *Clinical Biomechanics* 11, pp. 90–100. doi: 10.1016/0268-0033(95)00046-1.

Cappozzo, A. et al. 2005. Human movement analysis using stereophotogrammetry. Part 1: Theoretical background. *Gait and Posture* 21(2), pp. 186–196. doi: 10.1016/j.gaitpost.2004.01.010.

Castellano, J. and Webb, S. 2012. X-Ray Transmission Computed Tomography. In: Flower, M. ed. *Webb's Physics of Medical Imaging*., pp. 97–153.

Chambers, A.W. et al. 2016. Effect of Posterior Tibial Slope on Flexion and Anterior-Posterior Tibial Translation in Posterior Cruciate-Retaining Total Knee Arthroplasty. *Journal of Arthroplasty* 31(1), pp. 103–106. Available at: http://dx.doi.org/10.1016/j.arth.2015.08.027.

Chang, E.Y. et al. 2015. Quantitative bi-component T2* Analysis of histologically normal achilles tendons. *Muscles, Ligaments and Tendons*

Journal 5(2), pp. 58–62. doi: 10.11138/mltj/2015.5.2.058.

Chauhan, S.K. et al. 2004. Computer-assisted total knee replacement. A controlled cadaver study using a multi-parameter quantitative CT assessment of alignment (the Perth CT Protocol). *The Journal of Bone and Joint Surgery* 86(6), pp. 818–823. Available at: http://www.bjj.boneandjoint.org.uk/cgi/doi/10.1302/0301-620X.86B6.15456.

Chiari, L. et al. 2005. Human movement analysis using stereophotogrammetry. Part 2: Instrumental errors. *Gait and Posture* 21(2), pp. 197–211. doi: 10.1016/j.gaitpost.2004.04.004.

Cobb, J.P. et al. 2008. The anatomical tibial axis: RELIABLE ROTATIONAL ORIENTATION IN KNEE REPLACEMENT. *Journal of Bone and Joint Surgery - British Volume* 90–B(8), pp. 1032–1038. Available at: http://www.bjj.boneandjoint.org.uk/cgi/doi/10.1302/0301-620X.90B8.19905.

Collier, M.B. et al. 2007. Factors Associated with the Loss of Thickness of Polyethylene Tibial Bearings After Knee Arthroplasty. *The Journal of Bone and Joint Surgery (American)* 89(6), pp. 1306–1314. Available at: http://jbjs.org/cgi/doi/10.2106/JBJS.F.00667.

Cooke, T.D. V et al. 2007. Frontal plane knee alignment: A call for standardized measurement. *Journal of Rheumatology* 34(9), pp. 1796–1801. doi: 0315162X-34-1796 [pii].

Della Croce, U. et al. 2005. Human movement analysis using stereophotogrammetry Part 4: Assessment of anatomical landmark misplacement and its effects on joint kinematics. *Gait and Posture* 21(2), pp. 226–237. doi: 10.1016/j.gaitpost.2004.05.003.

Cross, J.A. et al. 2017. Biplane fluoroscopy for hindfoot motion analysis during gait: A model-based evaluation. *Medical Engineering and Physics* 43, pp. 118–123. doi: 10.1016/j.medengphy.2017.02.009.

Cross, M. et al. 2014. The global burden of hip and knee osteoarthritis: Estimates from the Global Burden of Disease 2010 study. *Annals of the Rheumatic Diseases* 73(7), pp. 1323–1330. doi: 10.1136/annrheumdis-2013-204763.

Czurda, T. et al. 2010. The association between component malalignment and post-operative pain following navigation-assisted total knee arthroplasty: Results of a cohort/nested case-control study. *Knee Surgery, Sports Traumatology, Arthroscopy* 18(7), pp. 863–869. doi: 10.1007/s00167-009-0990-y.

D'Lima, D.D. et al. 2001. Polyethylene wear and variations in knee kinematics. *Clinical orthopaedics and related research* (392), pp. 124–130.

Dale, B.M. 2015. *MRI : basic principles and applications*. Fifth edit.

Dawson, J. et al. 1998a. Questionnaire on the Perceptions of Patients about Total Knee Replacement. *The Journal of Bone and Joint Surgery. British Volume* 80(1), pp. 63–69. doi: http://dx.doi.org/10.1302/0301-620X.80B1.7859.

Dawson, J. et al. 1998b. Questionnaire on the Perceptions of Patients about Total Knee Replacement. *The Journal of Bone and Joint Surgery. British Volume* 80(1), pp. 63–69. Available at: http://www.ncbi.nlm.nih.gov/entrez/query.fcgi?cmd=Retrieve&db=PubMed&dopt=Citation&list_uids=9460955.

Defrate, L.E. et al. 2004. In vivo tibiofemoral contact analysis using 3D MRI-based knee models. *Journal of Biomechanics* 37, pp. 1499–1504. doi: 10.1016/j.jbiomech.2004.01.012.

Defrate, L.E. et al. 2006. The 6 degrees of freedom kinematics of the knee after anterior cruciate ligament deficiency: an in vivo imaging analysis. *The American journal of sports medicine* 34(8), pp. 1240–1246. doi: 10.1177/0363546506287299.

Demehri, S. et al. 2014. Imaging Characteristics of Contralateral Asymptomatic Patellofemoral Joints in Patients with Unilateral Instability. *Radiology* 273(3), pp. 821–830. Available at: http://pubs.rsna.org/doi/10.1148/radiol.14140295.

DeVries, N. a. et al. 2008. Validation of phalanx bone three-dimensional surface segmentation from computed tomography images using laser scanning. *Skeletal Radiology* 37, pp. 35–42. doi: 10.1007/s00256-007-0386-

3.

Doran, S.J. and Leach, M.O. 2012. Spatially Localised Magnetic Resonance. In: Flower, M. A. ed. *Webb's Physics of Medical Imaging*. Second. Taylor & Francis Group, pp. 489–611. Available at: https://aapm.onlinelibrary.wiley.com/doi/abs/10.1118/1.4818282.

Dossett, H.G. et al. 2012. Kinematically Versus Mechanically Aligned Total Knee Arthroplasty. *Orthopedics* , pp. 160–169. Available at: http://www.slackinc.com/doi/resolver.asp?doi=10.3928/01477447-20120123-04.

Dragoo, J.L. et al. 2010. Mechanics of the anterior interval of the knee using open dynamic MRI. *Clinical Biomechanics* 25(5), pp. 433–437. Available at: http://dx.doi.org/10.1016/j.clinbiomech.2010.01.011.

Driban, J.B. et al. 2010. Is osteoarthritis a heterogeneous disease that can be stratified into subsets? *Clinical Rheumatology* 29(2), pp. 123–131. doi: 10.1007/s10067-009-1301-1.

Duda, R.O. and Hart, P.E. 1972. Use of the Hough transformation to detect lines and curves in pictures. *Communications of the ACM* 15(1), pp. 11–15. Available at: http://portal.acm.org/citation.cfm?doid=361237.361242.

Van Dyck, P. et al. 2015. Morphological MR imaging of the articular cartilage of the knee at 3 T—comparison of standard and novel 3D sequences. *Insights into Imaging* 6(3), pp. 285–293. doi: 10.1007/s13244-015-0405-1.

Eckstein, F. et al. 2006. Double echo steady state magnetic resonance imaging of knee articular cartilage at 3 Tesla: A pilot study for the Osteoarthritis Initiative. *Annals of the Rheumatic Diseases* 65(4), pp. 433–441. doi: 10.1136/ard.2005.039370.

Ellingson, A.M. et al. 2017. Characterizing Fluoroscopy Based Kinematic Accuracy as a Function of Pulse Width and Velocity. *Journal of Biomechanics* 49(15), pp. 3741–3745. doi: 10.1016/j.jbiomech.2016.09.044.Characterizing.

Fang, D.M. et al. 2009. Coronal Alignment in Total Knee Arthroplasty. Just How Important is it? *Journal of Arthroplasty* 24(6 SUPPL.), pp. 39–43. Available at: http://dx.doi.org/10.1016/j.arth.2009.04.034.

Fantozzi, S. et al. 2003. Fluroscopic and gait analysis of the functional performance in stair ascent of total knee replacement designs. *Gait and Posture* 17, pp. 225–234. doi: 10.1016/S0966-6362(02)00096-6.

Faulkner, K. 2012. Physics for diagnostic radiology. 3rd edition. *The British Journal of Radiology* 85(1011), p. 290. doi: 10.1259/bjr/89098047.

Fernandez, J.W. et al. 2008. Integrating modelling, motion capture and x-ray fluoroscopy to investigate patellofemoral function during dynamic activity. *Computer Methods in Biomechanics and Biomedical Engineering* 11(1), pp. 41–53. doi: 10.1080/10255840701551046.

Fiacchi, F. et al. 2014. In vivo kinematics of medial unicompartmental osteoarthritic knees during activities of daily living. *Knee* 21(S1), pp. S10–S14. Available at: http://dx.doi.org/10.1016/S0968-0160(14)50003-8.

Fiorentino, N.M. et al. 2017. Soft tissue artifact causes significant errors in the calculation of joint angles and range of motion at the hip. *Gait and Posture* 55(March), pp. 184–190. Available at: http://dx.doi.org/10.1016/j.gaitpost.2017.03.033.

Fletcher, J. 2016. *Validation of a multiplanar x- ray fluoroscopy system looking at knee osteoarthritis*. Cardiff University.

Fong, J.W.-Y. et al. 2011. Validation and Precision of Model-Based Radiostereometric Analysis (MBRSA) for Total Ankle Arthroplasty. *Foot & Ankle International* 32(12), pp. 1155–1163. Available at: http://journals.sagepub.com/doi/10.3113/FAI.2011.1155.

Freeman, M.A.R. and Pinskerova, V. 2005. The movement of the normal tibio-femoral joint. *Journal of Biomechanics* 38(2), pp. 197–208. doi: 10.1016/j.jbiomech.2004.02.006.

Fregly, B.J. et al. 2005. Theoretical accuracy of model-based shape matching for measuring natural knee kinematics with single-plane fluoroscopy. *Journal of biomechanical engineering* 127(4), pp. 692–699. doi: 10.1115/1.1933949.

Garling, E.H. et al. 2007. Soft-tissue artefact assessment during step-up using fluoroscopy and skin-mounted markers. *Journal of Biomechanics* 40(SUPPL. 1), pp. S18–S24. Available at:

http://www.embase.com/search/results?subaction=viewrecord&from=export&id=L46873581%0Ahttp://dx.doi.org/10.1016/j.jbiomech.2007.03.003.

GBD 2013. *WHO methods and data sources for global burden of disease estimates 2000-2011*.

Geise, R.A. 2001. Fluoroscopy : Recording of Fluoroscopic Images and Automatic Exposure Control. *Radiographics : a review publication of the Radiological Society of North America, Inc* (21), pp. 227–236.

Gelaude, F. et al. 2008. Accuracy assessment of CT-based outer surface femur meshes. *Computer Aided Surgery* 13(4), pp. 188–199. doi: 10.1080/10929080802195783.

Geng, J. 2011. Structured-light 3D surface imaging: a tutorial. *Advances in Optics and Photonics* 3(2), p. 128. Available at: https://www.osapublishing.org/abstract.cfm?URI=aop-3-2-128.

Giavarina, D. 2015. Understanding Bland Altman analysis. *Biochemia Medica* 25(2), pp. 141–151. doi: 10.11613/BM.2015.015.

Gilbert, J.W. et al. 2011. Guidance of magnetic resonance imaging and placement of skin-marker localization devices. *J Neurosurg Sci* 55(2), pp. 85–88.

Giphart, J.E. et al. 2012. Accuracy of a contour-based biplane fluoroscopy technique for tracking knee joint kinematics of different speeds. *Journal of Biomechanics* 45(16), pp. 2935–2938. Available at: http://dx.doi.org/10.1016/j.jbiomech.2012.08.045.

Goldberg, S. et al. 2009. In situ calibration and motion capture transformation. *Journal of Applied Biomechanics* 25, pp. 401–406.

Gray, H. et al. 2016. Measurement of 3D Dynamic Joint Motion Using Biplane Videoradiography. In: Muller, B. and Wolf, S. I. eds. *Handbook of Human Motion*. Springer International Publishing AG, pp. 102–113. Available at: http://link.springer.com/10.1007/978-3-319-30808-1_154-1.

Green, G. et al. 2002. The Effects of Varus Tibial Alignment on Proximal Tibial Surface Strain in Total Knee Arthroplasty: The Posteromedial Hot Spot. *The*

Journal of arthroplasty 17(8), pp. 1033–1039.

Grieco, T.F. et al. 2017. In Vivo Kinematic Comparison of a Bicruciate Stabilized Total Knee Arthroplasty and the Normal Knee Using Fluoroscopy. *Journal of Arthroplasty* 33(2), pp. 565–571. Available at: https://doi.org/10.1016/j.arth.2017.09.035.

Grood, E.S. and Suntay, W.J. 1983. A Joint Coordinate System for the Clinical Description of Three-Dimensional Motions: Application to the Knee. *Journal of Biomechanical Engineering* 105(2), p. 136. Available at: http://biomechanical.asmedigitalcollection.asme.org/article.aspx?articleid=1396188.

Guan, S. et al. 2016. Mobile biplane X-Ray imaging system for measuring 3D dynamic joint motion during overground gait. *IEEE Transactions on Medical Imaging* 35(1), pp. 326–336. doi: 10.1109/TMI.2015.2473168.

Hallén, L.G. and Lindahl, O. 1966. The " Screw-Home " Movement in the Knee-Joint. 37(1), pp. 97–106. doi: 10.3109/17453676608989407.

Hamai, S. et al. 2009. Knee kinematics in medial osteoarthritis during in vivo weight-bearing activities. *Journal of Orthopaedic Research* 27(12), pp. 1555–1561. doi: 10.1002/jor.20928.

Hamai, S. et al. 2013. In vivo healthy knee kinematics during dynamic full flexion. *BioMed Research International* 2013. doi: 10.1155/2013/717546.

Hangody, L. et al. 2001. Mosaicplasty for the Treatment of Articular Defects of the Knee and Ankle. *Clinical Orthopaedics and Related Research*® 391. Available at: https://journals.lww.com/clinorthop/Fulltext/2001/10001/Mosaicplasty_for_the_Treatment_of_Articular.30.aspx.

Hangody, L. and Kárpáti, Z. 1994. New possibilities in the management of severe circumscribed cartilage damage in the knee. *Magyar traumatologia, ortopedia, kezsebeszet, plasztikai sebeszet* 37(3), p. 237—243. Available at: http://europepmc.org/abstract/MED/7920908.

Hargreaves, B. et al. 2011. Metal-induced artifacts in MRI. *AJR, American journal of roentgenology.* 197(3)

Harman, M.K. et al. 2012. Prosthesis alignment affects axial rotation motion after total knee replacement: a prospective in vivo study combining computed tomography and fluoroscopic evaluations. *BMC Musculoskelet Disord* 13, p. 206. Available at: http://www.ncbi.nlm.nih.gov/pubmed/23088451.

Harrington, M.E. et al. 2007. Prediction of the hip joint centre in adults, children, and patients with cerebral palsy based on magnetic resonance imaging. *Journal of Biomechanics* 40(3), pp. 595–602. doi: 10.1016/j.jbiomech.2006.02.003.

Haug, L. et al. 2017. Dynamic MRI Assessment of Normal Knee Kinematics. *Journal of Clinical and Experimental Orthopaedics* 3(3), pp. 1–6. doi: 10.21767/2471-8416.100041.

Health and Safety *The Ionising Radiation (Medical Exposure) Regulations 2017*. United Kingdom. Available at: http://www.legislation.gov.uk/uksi/2017/1322/pdfs/uksi_20171322_en.pdf.

Health and Safety *The Ionising Radiations Regulations 2017*. United Kingdom. Available at: http://www.legislation.gov.uk/uksi/2017/1075/pdfs/uksi_20171075_en.pdf.

Health in Wales 2004. Press release from Wales NHS: ‘Second offer scheme helping to cut waiting lists, says Jane Hutt’. Available at: http://www.wales.nhs.uk/document/33746 [Accessed: 20 October 2016].

Hickey, B. a et al. 2012. Review of Kinemax total knee replacements performed at the NHS treatment centre, Weston-Super-Mare: five-year results. *The Journal of bone and joint surgery. British volume* 94(4), pp. 510–6. Available at: http://www.ncbi.nlm.nih.gov/pubmed/22434468.

Hilding, M.B. et al. 1996. Knee joint loading and tibial component loosening. RSA and gait analysis in 45 osteoarthritic patients before and after TKA. *The Journal of bone and joint surgery. British volume* 78(1), pp. 66–73.

Hirokawa, S. et al. 2008. A 3D kinematic estimation of knee prosthesis using X-ray projection images: Clinical assessment of the improved algorithm for fluoroscopy images. *Medical and Biological Engineering and Computing* 46(12), pp. 1253–1262. doi: 10.1007/s11517-008-0398-8.

Holden, J.P. et al. 2003. A proposed test to support the clinical movement analysis laboratory accreditation process. *Gait and Posture* 17(3), pp. 205–213. doi: 10.1016/S0966-6362(02)00088-7.

Holst, G. 1998. *CCD Arrays, Cameras and Displays*. 2nd ed. SPIE - The International Society for Optical Engineering. doi: 10.1037/023990.

Howell, S.M. et al. 2013. Does a kinematically aligned total knee arthroplasty restore function without failure regardless of alignment category? Knee. *Clinical Orthopaedics and Related Research* 471(3), pp. 1000–1007. doi: 10.1007/s11999-012-2613-z.

Hunt, M.A. et al. 2006. Associations among knee adduction moment, frontal plane ground reaction force, and lever arm during walking in patients with knee osteoarthritis. *Journal of Biomechanics* 39(12), pp. 2213–2220. doi: 10.1016/j.jbiomech.2005.07.002.

Ide, Y. et al. 2015. Anatomical examination of the fibula: Digital imaging study for osseointegrated implant installation. *Journal of Otolaryngology - Head and Neck Surgery* 44(February), pp. 1–8. doi: 10.1186/s40463-015-0055-9.

In, Y. et al. 2009. Factors Affecting Flexion Gap Tightness in Cruciate-Retaining Total Knee Arthroplasty. *Journal of Arthroplasty* 24(2), pp. 317–321. Available at: http://dx.doi.org/10.1016/j.arth.2007.10.022.

Ioppolo, J. et al. 2007. Validation of a low-dose hybrid RSA and fluoroscopy technique: Determination of accuracy, bias and precision. *Journal of Biomechanics* 40(3), pp. 686–692. doi: 10.1016/j.jbiomech.2006.01.012.

Irrgang, J.J. et al. 1998. Development of a patient-reported measure of function of the knee. *The Journal of bone and joint surgery. American volume* 80(8), pp. 1132–45. Available at: http://www.ncbi.nlm.nih.gov/pubmed/9730122.

Isherwood, I. 2005. Sir Godfrey Hounsfield. *Radiology* 234(3), pp. 975–976.

Ivester, J.C. et al. 2015. A Reconfigurable High-Speed Stereo-Radiography System for Sub-Millimeter Measurement of In Vivo Joint Kinematics. *Journal of Medical Devices* 9(4), p. 041009. Available at: http://medicaldevices.asmedigitalcollection.asme.org/article.aspx?doi=10.111

5/1.4030778.

Jacobs, C.A. and Christensen, C.P. 2009. Correlations between knee society function scores and functional force measures. *Clinical Orthopaedics and Related Research* 467(9), pp. 2414–2419. doi: 10.1007/s11999-009-0811-0.

Jenny, J.Y. et al. 2005. Consistency of implantation of a total knee arthroplasty with a non-image-based navigation system: A case-control study of 235 cases compared with 235 conventionally implanted prostheses. *Journal of Arthroplasty* 20(7), pp. 832–839. doi: 10.1016/j.arth.2005.02.002.

Johal, P. et al. 2005. Tibio-femoral movement in the living knee. A study of weight bearing and non-weight bearing knee kinematics using 'interventional' MRI. *Journal of Biomechanics* 38(2), pp. 269–276. doi: 10.1016/j.jbiomech.2004.02.008.

Jones, L. 2004. *The Development Of A Novel Method For The Classification Of Osteoarthritic And Normal Knee Function*. Cardiff University.

Kadam, U.T. et al. 2004. Clinical comorbidity in patients with osteoarthritis: A case-control study of general practice consumers in England and Wales. *Annals of the Rheumatic Diseases* 63(4), pp. 408–414. doi: 10.1136/ard.2003.007526.

Kaiser, J. et al. 2016. Accuracy of model-based tracking of knee kinematics and cartilage contact measured by dynamic volumetric MRI. *Medical Engineering and Physics* 38(10), pp. 1131–1135. Available at: http://dx.doi.org/10.1016/j.medengphy.2016.06.016.

Kanisawa, I. et al. 2003. Weight-bearing knee kinematics in subjects with two types of anterior cruciate ligament reconstructions. *Knee Surgery, Sports Traumatology, Arthroscopy* (11), pp. 16–22. doi: 10.1007/s00167-002-0330-y.

Kansara, D. and Markel, D. 2006. The effect of posterior tibial slope on knee stability after Ortholoc total knee arthroplasty. *The Journal of arthroplasty* 21(6), pp. 809–813. doi: 10.1016/S0883-5403(88)80009-3.

Kaptein, B.L. et al. 2011. A comparison of calibration methods for stereo fluoroscopic imaging systems. *Journal of Biomechanics* 44(13), pp. 2511–2515. Available at: http://dx.doi.org/10.1016/j.jbiomech.2011.07.001.

Karrholm, J. et al. 2006. The History and Future of Radiostereometric Analysis. *Clinical Orthopaedics and Related Research* 448(448), pp. 10–21. Available at: http://content.wkhealth.com/linkback/openurl?sid=WKPTLP:landingpage&an=00003086-200607000-00003.

Karsdal, M.A. et al. 2016. Disease-modifying treatments for osteoarthritis (DMOADs) of the knee and hip: lessons learned from failures and opportunities for the future. *Osteoarthritis and Cartilage* 24(12), pp. 2013–2021. Available at: http://dx.doi.org/10.1016/j.joca.2016.07.017.

Kedgley, A.E. et al. 2012. Image intensifier distortion correction for fluoroscopic RSA: The need for independent accuracy assessment. *Journal of Applied Clinical Medical Physics* 13(1), pp. 197–204. doi: 10.1120/jacmp.v13i1.3441.

Kempshall, P.J. et al. 2009. Review of Kinemax knee arthroplasty performed at the NHS Treatment Centre, Weston-Super-Mare. *The Journal of bone and joint surgery. British volume* 91, pp. 229–233. doi: 10.1302/0301-620X.94B4.27978.

Khan, S.S. et al. 2017. Effects of Toe-out and Toe-in gait with varying walking speeds on knee adduction moment and mechanical work done-A pilot study. *IFMBE Proceedings* 58, pp. 106–110. Available at: http://dx.doi.org/10.1016/j.gaitpost.2017.01.022.

Kim, J.H. et al. 2017. Survival of opening versus closing wedge high tibial osteotomy: A meta-Analysis. *Scientific Reports* 7(1), pp. 1–7. Available at: http://dx.doi.org/10.1038/s41598-017-07856-8.

Kim, Y.H. et al. 2014. The relationship between the survival of total knee arthroplasty and postoperative coronal, sagittal and rotational alignment of knee prosthesis. *International Orthopaedics* 38(2), pp. 379–385. doi: 10.1007/s00264-013-2097-9.

King, L.K. et al. 2013. Obesity & osteoarthritis. *The Indian journal of medical research.* 138, pp. 185–193.

Kinney, A.L. et al. 2013. Update on Grand Challenge Competition to Predict

in Vivo Knee Loads. *Journal of Biomechanical Engineering* 135(2), p. 021012. Available at: http://biomechanical.asmedigitalcollection.asme.org/article.aspx?doi=10.1115/1.4023255.

Knörlein, B.J. et al. 2016. Validation of XMALab software for marker-based XROMM. *The Journal of Experimental Biology* 219(23), pp. 3701–3711. Available at: http://jeb.biologists.org/lookup/doi/10.1242/jeb.145383.

Knuth, D.E. 1998. *The art of computer programming. Vol.3, Sorting and searching*. 2nd ed. Boston, MA: Addison-Wesley.

Koff, M.F. et al. 2014. Ultrashort echo imaging of cyclically loaded rabbit patellar tendon. *Journal of Biomechanics* 47(13), pp. 3428–3432. doi: 10.1016/j.jbiomech.2014.08.018.

Komistek, R.D. et al. 2003. In vivo fluoroscopic analysis of the normal human knee. *Clinical orthopaedics and related research* (410), pp. 69–81. doi: 10.1097/01.blo.0000062384.79828.3b.

Komistek, R.D. and Dennis, D.A. 2003. In Vivo Fluoroscopic Analysis of the Normal Human Knee. (410), pp. 69–81. doi: 10.1097/01.blo.0000062384.79828.3b.

Koo, S. et al. 2009. Accuracy of 3D Cartilage Models Generated From MR Images is Dependent on Cartilage Thickness: Laser Scanner Based Validation of In Vivo Cartilage. *Journal of biomechanical engineering* 131(12), pp. 997–1003. doi: 10.1016/j.biotechadv.2011.08.021.Secreted.

Koo, S. and Andriacchi, T.P. 2008. The knee joint center of rotation is predominantly on the lateral side during normal walking. *Journal of Biomechanics* 41(6), pp. 1269–1273. doi: 10.1016/j.jbiomech.2008.01.013.

Koshino, T. et al. 2003. Regeneration of degenerated articular cartilage in OA knee after high tibial osteotomy. *Arthroscopy: The Journal of Arthroscopic & Related Surgery* 19(6), pp. 229–236. doi: 10.1016/S0749-8063(03)00534-6.

Kozanek, M. et al. 2009. Tibiofemoral kinematics and condylar motion during the stance phase of gait. *Journal of Biomechanics* 42(12), pp. 1877–1884. Available at: http://dx.doi.org/10.1016/j.jbiomech.2009.05.003.

Kraus, V.B. et al. 2015. Call for standardized definitions of osteoarthritis and risk stratification for clinical trials and clinical use. *Osteoarthritis and Cartilage* 23(8), pp. 1233–1241. doi: 10.1016/j.joca.2015.03.036.

Kwong, Y. et al. 2015. Four-dimensional computed tomography (4DCT): A review of the current status and applications. *Journal of Medical Imaging and Radiation Oncology* 59(5), pp. 545–554. doi: 10.1111/1754-9485.12326.

Lafortune, M.A. et al. 1992. Three-dimensional kinematics of the human knee during walking. *Journal of Biomechanics* 25(4), pp. 347–357. doi: 10.1016/0021-9290(92)90254-X.

Lane, N.E. et al. 2011. OARSI-FDA initiative: Defining the disease state of osteoarthritis. *Osteoarthritis and Cartilage* 19(5), pp. 478–482. Available at: http://dx.doi.org/10.1016/j.joca.2010.09.013.

Leardini, A. et al. 2005. Advanced multimodal visualisation of clinical gait and fluoroscopy analyses in the assessment of total knee replacement. *Computer Methods and Programs in Biomedicine* 79(3), pp. 227–240. doi: 10.1016/j.cmpb.2005.04.007.

Leardini, A. et al. 2005. Human movement analysis using stereophotogrammetry Part 3. Soft tissue artifact assessment and compensation. *Gait and Posture* 21(2), pp. 212–225. doi: 10.1016/j.gaitpost.2004.05.002.

Lee, D.C. and Byun, S.J. 2012. High Tibial Osteotomy. 24(2), pp. 61–69.

Lee, Y.S. et al. 2008. Anatomical evaluation of CT-MRI combined femoral model. *Biomedical engineering online* 7, p. 6. doi: 10.1186/1475-925X-7-6.

Li, G. et al. 2005. In vivo articular cartilage contact kinematics of the knee: An investigation using dual-orthogonal fluoroscopy and magnetic resonance image-based computer models. *American Journal of Sports Medicine* 33(1), pp. 102–107. doi: 10.1177/0363546504265577.

Li, G. 2008. Response to the Letter to the Editor-Comments on ‘Validation of a non-invasive fluoroscopic imaging technique for the measurement of dynamic knee motion’. *Journal of Biomechanics* 41(15), pp. 3292–3293. doi: 10.1016/j.jbiomech.2008.08.029.

Li, G. et al. 2008. Validation of a non-invasive fluoroscopic imaging technique for the measurement of dynamic knee joint motion. *Journal of Biomechanics* 41(7), pp. 1616–1622. doi: 10.1016/j.jbiomech.2008.01.034.

Li, X. et al. 2009. Prospective comparison of 3D FIESTA versus fat-suppressed 3D SPGR MRI in evaluating knee cartilage lesions. *Clinical Radiology* 64(10), pp. 1000–1008. Available at: http://dx.doi.org/10.1016/j.crad.2009.07.008.

Lin, C.C. et al. 2014. Comparisons of surface vs. volumetric model-based registration methods using single-plane vs. bi-plane fluoroscopy in measuring spinal kinematics. *Medical Engineering and Physics* 36(2), pp. 267–274. Available at: http://dx.doi.org/10.1016/j.medengphy.2013.08.011.

Lin, C.C. et al. 2016. Effects of soft tissue artifacts on differentiating kinematic differences between natural and replaced knee joints during functional activity. *Gait and Posture* 46, pp. 154–160. Available at: http://dx.doi.org/10.1016/j.gaitpost.2016.03.006.

Lin, H. et al. 2013. In-vitro validation of a non-invasive dual fluoroscopic imaging technique for measurement of the hip kinematics. *Medical Engineering and Physics* 35(3), pp. 411–416. Available at: http://dx.doi.org/10.1016/j.medengphy.2012.10.004.

List, R. et al. 2017. A moving fluoroscope to capture tibiofemoral kinematics during complete cycles of free level and downhill walking as well as stair descent. *Plos One* 12, p. e0185952. doi: 10.1371/journal.pone.0185952.

Liu, F. et al. 2010. In vivo tibiofemoral cartilage deformation during the stance phase of gait. *Journal of Biomechanics* 43(4), pp. 658–665. Available at: http://dx.doi.org/10.1016/j.jbiomech.2009.10.028.

Loeser, R. 2011. Aging and Osteoarthritis. *Curr Opin Rheumatol* 23(5), pp. 492–496. doi: 10.1097/BOR.0b013e3283494005.Aging.

Lu, T.W. et al. 2008. In vivo three-dimensional kinematics of the normal knee during active extension under unloaded and loaded conditions using single-plane fluoroscopy. *Medical Engineering and Physics* 30(8), pp. 1004–1012. doi: 10.1016/j.medengphy.2008.03.001.

Mahfouz, M.R. et al. 2003. A Robust Method for Registration of Three-Dimensional Knee Implant Models to Two-Dimensional Fluoroscopy Images. *IEEE* 22(12), pp. 1–14.

Mann, R.W. and Berryman, H.E. 2012. A Method for Defleshing Human Remains Using Household Bleach. *Journal of Forensic Sciences* 57(2), pp. 440–442. doi: 10.1111/j.1556-4029.2011.01987.x.

Maquet, P. 1976. Valgus osteotomy for osteoarthritis of the knee. *Clinical orthopaedics and related research* (120), pp. 143–148.

March, L. et al. 2016. *Osteoarthritis: A serious disease*. Available at: https://www.oarsi.org/sites/default/files/docs/2016/oarsi_white_paper_oa_serious_disease_121416_1.pdf.

Matsuda, S. et al. 1999. The effect of varus tilt on contact stresses in total knee arthroplasty: a biomechanical study. *Orthopedics* 22(3), pp. 303–307.

Matsui, Y. et al. 2005. Rotational Deformity in Varus Osteoarthritis of the Knee. *Clinical* 433, pp. 147–151. doi: 10.1097/01.blo.0000150465.29883.83.

McClelland, J.A. et al. 2007. Gait analysis of patients following total knee replacement: A systematic review. *Knee* 14(4), pp. 253–263. doi: 10.1016/j.knee.2007.04.003.

McCollough, C. 1997. X-ray Production. *Imaging & Therapeutic Technology* 17(4), pp. 967–984.

McCoy, A.M. 2015. Animal Models of Osteoarthritis: Comparisons and Key Considerations. *Veterinary Pathology* 52(5), pp. 803–818. doi: 10.1177/0300985815588611.

McGonagle, D. et al. 2010. The anatomical basis for a novel classification of osteoarthritis and allied disorders. *Journal of Anatomy* 216(3), pp. 279–291. doi: 10.1111/j.1469-7580.2009.01186.x.

Metcalfe, A.J. et al. 2017. Abnormal loading and functional deficits are present in both limbs before and after unilateral knee arthroplasty. *Gait and Posture* 55(February 2016), pp. 109–115. Available at: http://dx.doi.org/10.1016/j.gaitpost.2017.04.008.

Miller, E.J. et al. 2014. Tibiofemoral alignment in posterior stabilized total knee arthroplasty: Static alignment does not predict dynamic tibial plateau loading. *Journal of Orthopaedic Research* 32(8), pp. 1068–1074. doi: 10.1002/jor.22644.

Miranda, D.L. et al. 2010. Automatic determination of anatomical coordinate systems for three-dimensional bone models of the isolated human knee. *Journal of Biomechanics* 43(8), pp. 1623–1626. Available at: http://dx.doi.org/10.1016/j.jbiomech.2010.01.036.

Miranda, D.L. et al. 2013. Kinematic differences between optical motion capture and biplanar videoradiography during a jump-cut maneuver. *Journal of Biomechanics* 46(3), pp. 567–573. Available at: http://dx.doi.org/10.1016/j.jbiomech.2012.09.023.

Mitchell, E.L. and Furey, P. 2011. Prevention of radiation injury from medical imaging. *Journal of Vascular Surgery* 53(1 SUPPL.), p. 22S–27S. Available at: http://dx.doi.org/10.1016/j.jvs.2010.05.139.

Mizner, R.L. et al. 2011. Measuring Functional Improvement After Total Knee Arthroplasty Requires Both Performance-Based and Patient-Report Assessments. A Longitudinal Analysis of Outcomes. *Journal of Arthroplasty* 26(5), pp. 728–737. Available at: http://dx.doi.org/10.1016/j.arth.2010.06.004.

Moro-oka, T. et al. 2007. Can Magnetic Resonance Imaging-Derived Bone Models Be Used for Accurate Mortion Measurement with Single-Plane Three-Dimensional Shape Registration? *Journal of Orthopaedic Research* 11(7), pp. 867–872. doi: 10.1002/jor.

Moro-Oka, T.A. et al. 2008. Dynamic activity dependence of in vivo normal knee kinematics. *Journal of Orthopaedic Research* 26(4), pp. 428–434. doi: 10.1002/jor.20488.

Moseley, J.B. et al. 2002. A Controlled Trial of Arthroscopic Surgery for Osteoarthritis of the Knee. *New England Journal of Medicine* 347(2), pp. 81–88. Available at: http://www.nejm.org/doi/abs/10.1056/NEJMoa013259.

Mould, R.F. 1995. The early history of x-ray diagnosis with emphasis on the contributions of physics 1895-1915. *Physics in Medicine and Biology* 40(11),

pp. 1741–1787. doi: 10.1088/0031-9155/40/11/001.

Mu, S. 2007. Jointtrack: an Open-Source, Easily Expandable Program for Skeletal Kinematic Measurement Using Model-Image Registration. 53, pp. 1689–1699. doi: 10.1017/CBO9781107415324.004.

Mu, S. 2010. *Skeletal Kinematic Measurement Using Model-Image Registration and Mechanical constraints*. University of Florida.

Myers, C. a. et al. 2012. In Vivo Tibiofemoral Kinematics During 4 Functional Tasks of Increasing Demand Using Biplane Fluoroscopy. *The American Journal of Sports Medicine* 40(1), pp. 170–178. doi: 10.1177/0363546511423746.

Naili, J.E. et al. 2017. Deficits in functional performance and gait one year after total knee arthroplasty despite improved self-reported function. *Knee Surgery, Sports Traumatology, Arthroscopy* 25(11), pp. 3378–3386. doi: 10.1007/s00167-016-4234-7.

National Joint Registry 2018. *15th Annual Report 2018*.

National Joint Registry for England Wales and Northern Ireland 2016. *NJR 13th Annual Report*. Available at: www.njrreports.org.uk.

Neubert, A. et al. 2017. Comparison of 3D bone models of the knee joint derived from CT and 3T MR imaging. *European Journal of Radiology* 93(September 2016), pp. 178–184. doi: 10.1016/j.ejrad.2017.05.042.

NICE 2014. *Osteoarthritis : care and management*. Available at: https://www.nice.org.uk/guidance/cg177.

Nickoloff, E.L. 2011. Physics of flat-panel fluoroscopy systems: Survey of modern fluoroscopy imaging: flat-panel detectors versus image intensifiers and more. *Radiographics : a review publication of the Radiological Society of North America, Inc* 31(2), pp. 591–602. Available at: http://www.ncbi.nlm.nih.gov/pubmed/21415199.

Ogilvie-Harris, D.J. and Fitsialos, D.P. 1991. Arthroscopic management of the degenerative knee. *Arthroscopy : the journal of arthroscopic & related surgery.* 7(2), pp. 151–157. doi: 10.1016/0749-8063(91)90101-3.

Okazaki, K. et al. 2014. Influence of the posterior tibial slope on the flexion gap in total knee arthroplasty. *Knee* 21(4), pp. 806–809. Available at: http://dx.doi.org/10.1016/j.knee.2014.02.019.

Önsten, I. et al. 2001. Accuracy and precision of radiostereometric analysis in the measurement of THR femoral component translations: Human and canine in vitro models. *Journal of Orthopaedic Research* 19(6), pp. 1162–1167. doi: 10.1016/S0736-0266(01)00039-0.

Pal, N.R. and Pal, S.K. 1993. A review on image segmentation techniques. *Pattern Recognition* 26(9), pp. 1277–1294. Available at: http://www.sciencedirect.com/science/article/pii/0031320393901 35J.

Pang, C.H. et al. 2009. Comparison of total knee arthroplasty using computer-assisted navigation versus conventional guiding systems: a prospective study. *Journal of orthopaedic surgery (Hong Kong)* 17(2), pp. 170–173.

Patel, V. V. et al. 2004. A three-dimensional MRI analysis of knee kinematics. *Journal of Orthopaedic Research* 22, pp. 283–292. doi: 10.1016/j.orthres.2003.08.015.

Peterfy, C.G. et al. 2004. Whole-organ magnetic resonance imaging score (WORMS) of the knee in osteoarthritis. *Osteoarthritis and Cartilage* 12(3), pp. 177–190. doi: 10.1016/j.joca.2003.11.003.

Pick, J. et al. 1941. Measurements on the human femur - I. Lengths, diameters and angles. *Quarterly Bulletin of the Northwestern University Medical School* 15(4), pp. 281–290. Available at: http://www.ncbi.nlm.nih.gov/pmc/articles/PMC3802358/.

Pitcairn, S. et al. 2018. In vivo validation of patellofemoral kinematics during overground gait and stair ascent. *Gait and Posture* 64(March), pp. 191–197. Available at: https://doi.org/10.1016/j.gaitpost.2018.06.028.

Piva, S.R. et al. 2015. Links Between Osteoarthritis and Diabetes. *Clinics in geriatric medicine.* 31(1), pp. 67–87.

Powers, C. et al. 1998. Quantification of Patellar Tracking Using Kinematic MRI. *JMRI* 8, pp. 724–732. doi: 10.1002/jmri.1880080332.

Pridie, K.H. 1959. A method of resurfacing osteoarthritic knee joints. In: *Proceedings of the British Orthopaedic Association. J. Bone and Joint Surg*., pp. 618–619.

Proffen, B.L. et al. 2012. A comparative anatomical study of the human knee and six animal species. *The Knee* 19(4), pp. 493–499. Available at: http://dx.doi.org/10.1016/j.knee.2011.07.005.

Public Health England 2011. Ionising radiation: dose comparisons. Available at: https://www.gov.uk/government/publications/ionising-radiation-dose-comparisons/ionising-radiation-dose-comparisons [Accessed: 15 October 2018].

Puenpatom, R.A. and Victor, T.W. 2009. Increased prevalence of metabolic syndrome in individuals with osteoarthritis: An analysis of NHANES III data. *Postgraduate Medicine* 121(6), pp. 9–20. doi: 10.3810/pgm.2009.11.2073.

Ramsey, D.K. and Wretenberg, P.F. 1999. Biomechanics of the knee: Methodological considerations in the in vivo kinematic analysis of the tibiofemoral and patellofemoral joint. *Clinical Biomechanics* 14(9), pp. 595–611. doi: 10.1016/S0268-0033(99)00015-7.

Rathnayaka, K. 2011. *3D Reconstruction of Long Bones Utilising Magnetic Resonance Imaging (MRI)*. Queensland University of Technology.

Rathnayaka, K. et al. 2012. Quantification of the accuracy of MRI generated 3D models of long bones compared to CT generated 3D models. *Medical Engineering and Physics* 34(3), pp. 357–363. Available at: http://dx.doi.org/10.1016/j.medengphy.2011.07.027.

Reinschmidt, C. et al. 1997. Tibiofemoral and tibiocalcaneal motion during walking: External vs. Skeletal markers. *Gait and Posture* 6(2), pp. 98–109. doi: 10.1016/S0966-6362(97)01110-7.

Rhudy, M. et al. 2009. Microphone Array Analysis Methods Using Cross-Correlations. In: *ASME 2009 International Mechanical Engineering Congress and Exposition*., pp. 281–288.

Ritter, M.A. et al. 1994. Postoperative alignment of total knee replacement. Its effect on survival. *Clinical orthopaedics and related research* (299), pp. 153–

156.

Rizon, M. et al. 2005. Object Detection using Circular Hough Transform. *American Journal of Applied Sciences* 2(12), pp. 1606–1609. Available at: http://medcontent.metapress.com/index/A65RM03P4874243N.pdf.

Robbins, S.M.K. and Maly, M.R. 2009. The effect of gait speed on the knee adduction moment depends on waveform summary measures. *Gait and Posture* 30(4), pp. 543–546. doi: 10.1016/j.gaitpost.2009.08.236.

Rocchini, C. et al. 2001. A low cost 3D scanner based on structured light. *Computer Graphics Forum* 20(3), pp. 299–308. Available at: http://doi.wiley.com/10.1111/1467-8659.00522.

Ronn, K. et al. 2011. Current Surgical Treatment of Knee Osteoarthritis. *Arthritis* , pp. 1–9. doi: 10.1155/2011/454873.

Roos, E.M. et al. 1998. Knee Injury and Osteoarthritis Outcome Score (KOOS)—Development of a Self-Administered Outcome Measure. *Journal of Orthopaedic & Sports Physical Therapy* 28(2), pp. 88–96. Available at: http://www.jospt.org/doi/10.2519/jospt.1998.28.2.88.

Van Rossom, S. et al. 2018. Subjects with medial and lateral tibiofemoral articular cartilage defects do not alter compartmental loading during walking. *Clinical Biomechanics* 60(October), pp. 149–156. Available at: http://www.ncbi.nlm.nih.gov/pubmed/30366244%0Ahttps://linkinghub.elsevier.com/retrieve/pii/S0268003318303620.

Rudin, S. et al. 1991. Accurate characterization of image intensifier distortion. *Medical physics.* 18(6), pp. 1145–1151.

Ryd, L. et al. 2000. Methods for determining the accuracy of radiostereometric analysis (RSA). *Acta Orthopaedica Scandinavica* 71(4), pp. 403–408. Available at: http://www.tandfonline.com/doi/full/10.1080/000164700317393420.

Salvi, J. et al. 2004. Pattern codification strategies in structured light systems. *Pattern Recognition* 37(4), pp. 827–849. doi: 10.1016/j.patcog.2003.10.002.

Saris, D. et al. 2014. Matrix-Applied Characterized Autologous Cultured

Chondrocytes Versus Microfracture. *The American Journal of Sports Medicine* 42(6), pp. 1384–1394. Available at: http://journals.sagepub.com/doi/10.1177/0363546514528093.

Scarvell, J.M. et al. 2010. New registration algorithm for determining 3D knee kinematics using CT and single-plane fluoroscopy with improved out-of-plane translation accuracy. *Journal of Orthopaedic Research* 28(3), pp. 334–340. doi: 10.1002/jor.21003.

Schneider, C.A. et al. 2012. NIH Image to ImageJ: 25 years of image analysis. *Nature Methods* 9(7), pp. 671–675. Available at: http://dx.doi.org/10.1038/nmeth.2089.

Schueler, B. a 2000. The AAPM / RSNA Physics Tutorial for Residents Fluoroscopic Imaging 1. *RadioGraphics* 20(5), pp. 1115–1126. Available at: http://radiographics.rsna.org/content/19/5/1289.full.

Schueler, B.A. 2000. Tutorial - General Overview of Fluoroscopic Imaging. *Radiographics* , pp. 1115–1126.

Selvik, G. 1989. Roentgen stereophotogrammetry. A method for the study of the kinematics of the skeletal system. *Acta Orthop Scand Suppl.* 232, pp. 1–51.

Semelka, R.C. et al. 2007. Imaging strategies to reduce the risk of radiation in CT studies, including selective substitution with MRI. *Journal of Magnetic Resonance Imaging* 25(5), pp. 900–909. doi: 10.1002/jmri.20895.

Seo, S.-S. et al. 2016. Complications and Short-Term Outcomes of Medial Opening Wedge High Tibial Osteotomy Using a Locking Plate for Medial Osteoarthritis of the Knee. *Knee Surgery & Related Research* 28(4), pp. 289–296. Available at: http://www.jksrr.org/journal/view.html?doi=10.5792/ksrr.16.028.

Sharma, L. et al. 2001. Functional Decline in Knee Osteoarthritis The Role of Knee Alignment in Disease Progression and The Role of Knee Alignment in Disease Progression and Functional Decline in Knee Osteoarthritis. *Jama* 2862862188(2), pp. 188–195. Available at: http://jama.ama-assn.org/cgi/content/full/286/2/188%5Cnhttp://jama.ama-

assn.org/cgi/content/full/jama;286/7/792%5Cnhttp://pubs.ama-assn.org/misc/permissions.dtl%5Cnhttp://jama.com/subscribe%5Cnhttp://jamaarchives.com/alerts%5Cnwww.jama.com.

Sheehan, F.T. et al. 1997. Using cine phase contrast magnetic resonance imaging to non-invasively study in vivo knee dynamics. *Journal of Biomechanics* 31(1), pp. 21–26. doi: 10.1016/S0021-9290(97)00109-7.

Shefelbine, S. et al. 2006. MRI Analysis of In Vivo Meniscal and Tibiofemoral Kinematics in ACL-Deficient and Normal Knees. *Journal of Orthopaedic Research* 24(6), pp. 1208–17. doi: 10.1002/jor.

Shimmin, A. et al. 2015. The Knee Fluoroscopic motion study con fi rming the stability of a medial pivot design total knee arthroplasty. *The Knee* 22(6), pp. 522–526. Available at: http://dx.doi.org/10.1016/j.knee.2014.11.011.

Siemieniuk, R.A.C. et al. 2017. Arthroscopic surgery for degenerative knee arthritis and meniscal tears: a clinical practice guideline. *BMJ* 357, p. j1982. Available at: http://www.bmj.com/content/357/bmj.j1982.abstract.

Sikorski, J.M. 2008. Alignment in total knee replacement. *J Bone Joint Surg Br* 90(9), pp. 1121–1127. Available at: http://www.ncbi.nlm.nih.gov/pubmed/18757949.

Sint Jan, S. Van et al. 2006. Low-dose computed tomography: A solution for in vivo medical imaging and accurate patient-specific 3D bone modeling? *Clinical Biomechanics* 21(9), pp. 992–998. doi: 10.1016/j.clinbiomech.2006.05.007.

Sneag, D.B. et al. 2015. Quantitative Ultrashort Echo Time Magnetic Resonance Imaging Evaluation of Postoperative Menisci: a Pilot Study. *HSS journal : the musculoskeletal journal of Hospital for Special Surgery* 11(2), pp. 123–9. Available at: http://www.ncbi.nlm.nih.gov/pubmed/26140031.

Solomon, L.B. et al. 2010. The accuracy and precision of radiostereometric analysis in monitoring tibial plateau fractures. *Acta Orthopaedica* 81(4), pp. 487–494. doi: 10.3109/17453674.2010.487930.

Stagni, R. et al. 2005. Quantification of soft tissue artefact in motion analysis by combining 3D fluoroscopy and stereophotogrammetry: A study on two

subjects. *Clinical Biomechanics* 20(3), pp. 320–329. doi: 10.1016/j.clinbiomech.2004.11.012.

Stagni, R. et al. 2010. Can Patellar Tendon Angle reveal sagittal kinematics in total knee arthroplasty? *Knee Surgery, Sports Traumatology, Arthroscopy* 18(7), pp. 949–954. doi: 10.1007/s00167-010-1075-7.

Stanhope, S.J. et al. 1990. Kinematic-based technique for event time determination during gait. *Medical & Biological Engineering & Computing* 28(4), pp. 355–360. doi: 10.1007/BF02446154.

Stratford, P.W. and Kennedy, D.M. 2006. Performance measures were necessary to obtain a complete picture of osteoarthritic patients. *Journal of Clinical Epidemiology* 59(2), pp. 160–167. doi: 10.1016/j.jclinepi.2005.07.012.

Stroud Larreal, L.A. 2011. *In vivo measurement and objective classification of healthy, injured and pathological shoulder complex function*. Cardiff University. Available at: http://ezproxy.ithaca.edu:2048/login?url=https://search.proquest.com/docview/1221967871?accountid=11644%0Ahttp://ithaca-primo.hosted.exlibrisgroup.com/openurl/01ITHACACOL/01ITHACACOL_SP?sid/primo.exlibrisgroup.com-proquest&rft.genre=dissertations+%26+thes.

Sullivan, L.M. and Romney, C.P. 1999. Cleaning and Preserving Animal Skulls. *University of Arizona Cooperative Extension Publication* , pp. 1–4.

Tanamas, S. et al. 2009. Does knee malalignment increase the risk of development and progression of knee osteoarthritis? A systematic review. *Arthritis Care and Research* 61(4), pp. 459–467. doi: 10.1002/art.24336.

Tang, T.S.Y. et al. 2004. Accurate assessment of patellar tracking using fiducial and intensity-based fluoroscopic techniques. *Medical Image Analysis* 8(3), pp. 343–351. doi: 10.1016/j.media.2004.06.011.

Tapper, J.E. et al. 2004. In vivo measurement of the dynamic 3-D kinematics of the ovine stifle joint. *Journal of biomechanical engineering* 126(2), pp. 301–305. doi: 10.1115/1.1695576.

Tashman, S. et al. 2004. Abnormal rotational knee motion during running after anterior cruciate ligament reconstruction. *American Journal of Sports Medicine*

32(4), pp. 975–983. doi: 10.1177/0363546503261709.

Tashman, S. 2008. Comments on ‘validation of a non-invasive fluoroscopic imaging technique for the measurement of dynamic knee joint motion’. *Journal of Biomechanics* 41(15), pp. 3290–3291. doi: 10.1016/j.jbiomech.2008.07.038.

Tashman, S. and Anderst, W. 2003a. In-vivo measurement of dynamic joint motion using high speed biplane radiography and CT: application to canine ACL deficiency. *Journal of biomechanical engineering* 125(2), pp. 238–245. doi: 10.1115/1.1559896.

Tashman, S. and Anderst, W. 2003b. In-Vivo Measurement of Dynamic Joint Motion Using High Speed Biplane Radiography and CT: Application to Canine ACL Deficiency. *Journal of Biomechanical Engineering* 125(2), p. 238. Available at: http://biomechanical.asmedigitalcollection.asme.org/article.aspx?articleid=1409893.

Telfer, S. et al. 2017. Factors influencing knee adduction moment measurement: A systematic review and meta-regression analysis. *Gait & Posture* 58(April), pp. 333–339. Available at: http://linkinghub.elsevier.com/retrieve/pii/S0966636217308792.

Tersi, L. et al. 2013. In vitro quantification of the performance of model-based mono-planar and bi-planar fluoroscopy for 3D joint kinematics estimation. *Medical and Biological Engineering and Computing* 51(3), pp. 257–265. doi: 10.1007/s11517-012-0987-4.

Toft, B. 2011. *Independent review of the orthopaedic knee surgery undertaken by visiting Scandinavian Consultant Orthopaedic Surgeons at the Weston NHS Treatment Centre for comparison with the findings of the British Orthopaedic Association with respect to the same coho*.

Torry, M.R. et al. 2011. Knee kinematic profiles during drop landings: A biplane fluoroscopy study. *Medicine and Science in Sports and Exercise* 43, pp. 533–541. doi: 10.1249/MSS.0b013e3181f1e491.

Tsai, T.Y. et al. 2011. Effects of soft tissue artifacts on the calculated

kinematics and kinetics of the knee during stair-ascent. *Journal of Biomechanics* 44(6), pp. 1182–1188. Available at: http://dx.doi.org/10.1016/j.jbiomech.2011.01.009.

Tuominen, U. et al. 2007. The effect of co-morbidities on health-related quality of life in patients placed on the waiting list for total joint replacement. *Health and Quality of Life Outcomes* 5, pp. 1–6. doi: 10.1186/1477-7525-5-16.

Tupling, S.J. and Pierrynowski, M.R. 1987. Use of cardan angles to locate rigid bodies in three-dimensional space. *Medical & Biological Engineering & Computing* 25(5), pp. 527–532. doi: 10.1007/BF02441745.

Valstar, E.R. et al. 2005. Guidelines for standardization of radiostereometry (RSA) of implants. *Acta Orthopaedica* 76(4), pp. 563–572. doi: 10.1080/17453670510041574.

Vandekerckhove, P.J. et al. 2016. The current role of coronal plane alignment in Total Knee Arthroplasty in a preoperative varus aligned population: An evidence based review. *Acta Orthopaedica Belgica* 82(1), pp. 129–142.

Vandekerckhove, P.J.T.K. et al. 2017a. The Impact of Coronal Plane Alignment on Polyethylene Wear and Damage in Total Knee Arthroplasty: A Retrieval Study. *Journal of Arthroplasty* 32(6), pp. 2012–2016. doi: 10.1016/j.arth.2016.12.048.

Vandekerckhove, P.J.T.K. et al. 2017b. The Impact of Coronal Plane Alignment on Polyethylene Wear and Damage in Total Knee Arthroplasty: A Retrieval Study. *Journal of Arthroplasty* 32(6), pp. 2012–2016. Available at: http://dx.doi.org/10.1016/j.arth.2016.12.048.

Vandeweerd, J.M. et al. 2013. Magnetic resonance imaging (MRI) anatomy of the ovine stifle. *Veterinary Surgery* 42(5), pp. 551–558. doi: 10.1111/j.1532-950X.2013.12026.x.

Varadarajan, K.M. et al. 2008. In vivo contact kinematics and contact forces of the knee after total knee arthroplasty during dynamic weight-bearing activities. *Journal of Biomechanics* 41(10), pp. 2159–2168. doi: 10.1016/j.jbiomech.2008.04.021.

Varadarajan, K.M. et al. 2010. Relationship between three-dimensional

geometry of the trochlear groove and in vivo patellar tracking during weight-bearing knee flexion. *Journal of biomechanical engineering* 132(6), p. 061008. doi: 10.1115/1.4001360.

Vedi, V. et al. 1999. Meniscal movement. An in-vivo study using dynamic MRI. *The Journal of bone and joint surgery. British volume* 81(1), pp. 37–41. doi: 10.1302/0301-620X.81B1.8928.

Victor, J. and Premanathan, A. 2013. Virtual 3D planning and patient specific surgical guides for osteotomies around the knee: a feasibility and proof-of-concept study. *The bone & joint journal* 95 B(11 Suppl A), pp. 153–158. doi: 10.1302/0301-620X.95B11.32950.

Wassilew, G.I. et al. 2013. Real time visualization of femoroacetabular impingement and subluxation using 320-slice computed tomography. *Journal of Orthopaedic Research* 31(2), pp. 275–281. doi: 10.1002/jor.22224.

Watanabe, T. et al. 2012. Clinical Biomechanics Matched comparison of kinematics in knees with mild and severe varus deformity using fi xed- and mobile-bearing total knee arthroplasty. *JCLB* 27(9), pp. 924–928. Available at: http://dx.doi.org/10.1016/j.clinbiomech.2012.07.005.

Watanabe, T. et al. 2013. Knee Kinematics in Anterior Cruciate Ligament-Substituting Arthroplasty With or Without the Posterior Cruciate Ligament. *Journal of Arthroplasty* 28(4), pp. 548–552. Available at: http://dx.doi.org/10.1016/j.arth.2012.06.030.

Watling, D. 2014. *Development of novel methodologies to quantify, analyse and classify in-vivo knee function affected by aging, osteoarthritis and total knee replacement*. Cardiff University. Available at: https://www.lib.uwo.ca/cgi-bin/ezpauthn.cgi?url=http://search.proquest.com/docview/1775429412?accountid=15115%5Cnhttp://vr2pk9sx9w.search.serialssolutions.com/?ctx_ver=Z39.88-2004&ctx_enc=info:ofi/enc:UTF-8&rfr_id=info:sid/ProQuest+Dissertations+%26+These.

Werner, F.W. et al. 2005. The effect of valgus/varus malalignment on load distribution in total knee replacements. *Journal of Biomechanics* 38(2), pp. 349–355. doi: 10.1016/j.jbiomech.2004.02.024.

Whatling, G.M. 2009. *A Contribution To the Clinical Validation of a Generic Method for the Classification of Osteoarthritic and Non- Pathological Knee Function*. Cardiff.

Whelton, C. et al. 2017. Combined effect of toe out gait and high tibial osteotomy on knee adduction moment in patients with varus knee deformity. *Clinical Biomechanics* 43, pp. 109–114. Available at: http://dx.doi.org/10.1016/j.clinbiomech.2017.02.009.

White, D. et al. 2008. Accuracy of MRI vs CT imaging with particular reference to patient specific templates for total knee replacement surgery. *The International Journal of Medical Robotics and Computer Assisted Surgery* 4(3), pp. 224–231. Available at: http://doi.wiley.com/10.1002/rcs.201.

Wright, R.J. et al. 2004. Patient-Reported Outcome and Survivorship After Kinemax Total Knee Arthroplasty. *The Journal of Bone and Joint Surgery-American Volume* 86(11), pp. 2464–2470. Available at: http://content.wkhealth.com/linkback/openurl?sid=WKPTLP:landingpage&an=00004623-200411000-00016.

Wu, G. et al. 2002. ISB recommendation on definitions of joint coordinate system of various joints for the reporting of human joint motion—part I: ankle, hip, and spine. *Journal of biomechanics* 35(4), pp. 543–548. Available at: http://www.sciencedirect.com/science/article/pii/S0021929001002226.

Wylde, V. et al. 2007. Total knee replacement: Is it really an effective procedure for all? *Knee* 14(6), pp. 417–423. doi: 10.1016/j.knee.2007.06.001.

Yang, C. et al. 2018. Kinematics and arthrokinematics in the chronic ACL-deficient knee are altered even in the absence of instability symptoms. *Knee Surgery, Sports Traumatology, Arthroscopy* 26(5), pp. 1406–1413. Available at: http://dx.doi.org/10.1007/s00167-017-4780-7.

You, B.M. et al. 2001. In vivo measurement of 3-D skeletal kinematics from sequences of biplane radiographs: Application to knee kinematics. *IEEE Transactions on Medical Imaging* 20(6), pp. 514–525. doi: 10.1109/42.929617.

Zatsiorsky, V.M. and Zaciorskij, V.M. 2002. *Kinetics of human motion*. Human Kinetics.

Zhao, K. et al. 2015. A Technique for Quantifying Wrist Motion Using Four-Dimensional Computed Tomography: Approach and Validation. *Journal of Biomechanical Engineering* 137(7), p. 074501. Available at: http://biomechanical.asmedigitalcollection.asme.org/article.aspx?doi=10.1115/1.4030405.

APPENDIX A Questionnaires

A.1 Knee Outcome Survey (KOS)

KNEE OUTCOME SURVEY
Activities of Daily Living Scale

SYMPTOMS:

1. **To what degree does pain in your knee affect your daily activity level?**

L	R	
☐	☐	I never have pain in my knee.
☐	☐	I have pain in my knee, but it does not affect my daily activity.
☐	☐	Pain affects my activity slightly.
☐	☐	Pain affects my activity moderately.
☐	☐	Pain affects my activity severely.
☐	☐	Pain in my knee prevents me from performing all daily activities.

2. **To what degree does grinding or grating of your knee affect your daily activity level?**

L	R	
☐	☐	I never have grinding or grating in my knee.
☐	☐	I have grinding or grating in my knee, but it does not affect my daily activity.
☐	☐	Grinding or grating affects my activity slightly.
☐	☐	Grinding or grating affects my activity moderately.
☐	☐	Grinding or grating affects my activity severely.
☐	☐	Grinding or grating in my knee prevents me from performing all daily activities.

3. **To what degree does stiffness in your knee affect your daily activity level?**

L	R	
☐	☐	I never have stiffness in my knee.
☐	☐	I have stiffness in my knee, but it does not affect my daily activity.
☐	☐	Stiffness affects my activity slightly.
☐	☐	Stiffness affects my activity moderately.
☐	☐	Stiffness affects my activity severely.
☐	☐	Stiffness in my knee prevents me from performing all daily activities.

Subject: ID: Date:

4. **To what degree does swelling in your knee affect your daily activity level?**

L	R	
☐	☐	I never have swelling in my knee.
☐	☐	I have swelling in my knee, but it does not affect my daily activity.
☐	☐	Swelling affects my activity slightly.
☐	☐	Swelling affects my activity moderately.
☐	☐	Swelling affects my activity severely.
☐	☐	Swelling in my knee prevents me from performing all daily activities.

5. **To what degree does slipping of your knee affect your daily activity level?**

L	R	
☐	☐	I never have slipping of my knee.
☐	☐	I have slipping in my knee, but it does not affect my daily activity.
☐	☐	Slipping affects my activity slightly.
☐	☐	Slipping affects my activity moderately.
☐	☐	Slipping affects my activity severely.
☐	☐	Slipping of my knee prevents me from performing all daily activities.

6. **To what degree does buckling of your knee affect your daily activity level?**

L	R	
☐	☐	I never have buckling of my knee.
☐	☐	I have buckling of my knee, but it does not affect my daily activity.
☐	☐	Buckling affects my activity slightly.
☐	☐	Buckling affects my activity moderately.
☐	☐	Buckling affects my activity severely.
☐	☐	Buckling of my knee prevents me from performing all daily activities.

7. **To what degree does weakness or lack of strength of your leg affect your daily activity level?**

L	R	
☐	☐	My leg never feels weak.
☐	☐	My leg feels weak, but it does not affect my daily activity.

Subject: ID: Date:

☐☐ Weakness affects my activity slightly.
☐☐ Weakness affects my activity moderately.
☐☐ Weakness affects my activity severely.
☐☐ Weakness of my leg prevents me from performing all daily activities.

FUNCTIONAL DISABILITY WITH ACTIVITIES OF DAILY LIVING:

8. How does your knee affect your ability to walk?

L R

☐☐ My knee does not affect my ability to walk.
☐☐ I have pain in my knee when walking, but it does not affect my ability to walk.
☐☐ My knee prevents me from walking more than 1 mile.
☐☐ My knee prevents me from walking more than 1/2 mile.
☐☐ My knee prevents me from walking more than 1 block.
☐☐ My knee prevents me from walking.

9. Because of your knee, do you walk with crutches or a cane?

L R

☐☐ I can walk without crutches or a cane.
☐☐ My knee causes me to walk with 1 crutch or a cane.
☐☐ My knee causes me to walk with 2 crutches.
☐☐ Because of my knee, I cannot walk even with crutches.

10. Does your knee cause you to limp when you walk?

L R

☐☐ I can walk without a limp.
☐☐ Sometimes my knee causes me to walk with a limp.
☐☐ Because of my knee, I cannot walk without a limp.

11. How does your knee affect your ability to go up stairs?

L R

☐☐ My knee does not affect my ability to go up stairs.

Subject: ID: Date:

☐☐ I have pain in my knee when going up stairs, but it does not limit my ability to go up stairs.
☐☐ I am able to go up stairs normally, but I need to rely on use of a railing.
☐☐ I am able to go up stairs one step at a time with use of a railing.
☐☐ I have to use crutches or a cane to go up stairs.
☐☐ I cannot go up stairs.

12. How does your knee affect your ability to go down stairs?

L R

☐☐ My knee does not affect my ability to go down stairs.
☐☐ I have pain in my knee when going down stairs, but it does not limit my ability to go down stairs.
☐☐ I am able to go down stairs normally, but I need to rely on use of a railing.
☐☐ I am able to go down stairs one step at a time with use of a railing.
☐☐ I have to use crutches or a cane to go down stairs.
☐☐ I cannot go down stairs.

13. How does your knee affect your ability to stand?

L R

☐☐ My knee does not affect my ability to stand, I can stand for unlimited amounts of time.
☐☐ I have pain in my knee when standing, but it does not limit my ability to stand.
☐☐ Because of my knee I cannot stand for more than 1 hour.
☐☐ Because of my knee I cannot stand for more than 1/2 hour.
☐☐ Because of my knee I cannot stand for more than 10 minutes.
☐☐ I cannot stand because of my knee.

14. How does your knee affect your ability to kneel on the front of your knee?

L R

☐☐ My knee does not affect my ability to kneel on the front of my knee. I can kneel for unlimited amounts of time.
☐☐ I have pain when kneeling on the front of my knee, but it does not limit my ability to kneel.
☐☐ I cannot kneel on the front of my knee for more than 1 hour.

Subject: ID: Date:

☐☐ I cannot kneel on the front of my knee for more than 1/2 hour.
☐☐ I cannot kneel on the front of my knee for more than 10 minutes.
☐☐ I cannot kneel on the front of my knee.

15. How does your knee affect your ability to squat?

L R

☐☐ My knee does not affect my ability to squat, I can squat all the way down.
☐☐ I have pain in my knee when squatting, but I can still squat all the way down.
☐☐ I cannot squat more than3/4 of the way down.
☐☐ I cannot squat more than 1/2 of the way down.
☐☐ I cannot squat more than 1/4 of the way down.
☐☐ I cannot squat because of my knee.

16. How does your knee affect your ability to sit with your knee bent?

L R

☐☐ My knee does not affect my ability to sit with my knee bent, I can sit for unlimited amounts of time.
☐☐ I have pain in my knee when sitting with my knee bent, but it does not limit my ability to sit.
☐☐ I cannot sit with my knee bent for more than 1 hour.
☐☐ I cannot sit with my knee bent for more than 1/2 hour.
☐☐ I cannot sit with my knee bent for more than 10 minutes.
☐☐ I cannot sit with my knee bent.

17. How does your knee affect your ability to rise from a chair?

L R

☐☐ My knee does not affect my ability to rise from a chair.
☐☐ I have pain when rising from a seated position, but it does not affect my ability to rise from a seated position.
☐☐ Because of my knee I can only rise from a chair if I use my hands and arms to

Subject: ID: Date:

assist.

☐☐ Because of my knee I cannot rise from a chair.

A.2 Knee Injury and Osteoarthritis Outcome Score (KOOS)

KOOS KNEE SURVEY

Today's date: _____/_____/_____ Date of birth: _____/_____/_____

Name: _____

INSTRUCTIONS: This survey asks for your view about your knee. This information will help us keep track of how you feel about your knee and how well you are able to perform your usual activities.
Answer every question by ticking the appropriate box, only one box for each question. If you are unsure about how to answer a question, please give the best answer you can.

Symptoms
These questions should be answered thinking of your knee symptoms during the **last week**.

S1. Do you have swelling in your knee?

Never	Rarely	Sometimes	Often	Always
☐	☐	☐	☐	☐

S2. Do you feel grinding, hear clicking or any other type of noise when your knee moves?

Never	Rarely	Sometimes	Often	Always
☐	☐	☐	☐	☐

S3. Does your knee catch or hang up when moving?

Never	Rarely	Sometimes	Often	Always
☐	☐	☐	☐	☐

S4. Can you straighten your knee fully?

Always	Often	Sometimes	Rarely	Never
☐	☐	☐	☐	☐

S5. Can you bend your knee fully?

Always	Often	Sometimes	Rarely	Never
☐	☐	☐	☐	☐

Stiffness
The following questions concern the amount of joint stiffness you have experienced during the **last week** in your knee. Stiffness is a sensation of restriction or slowness in the ease with which you move your knee joint.

S6. How severe is your knee joint stiffness after first wakening in the morning?

None	Mild	Moderate	Severe	Extreme
☐	☐	☐	☐	☐

S7. How severe is your knee stiffness after sitting, lying or resting **later in the day**?

None	Mild	Moderate	Severe	Extreme
☐	☐	☐	☐	☐

Pain

P1. How often do you experience knee pain?

Never	Monthly	Weekly	Daily	Always
☐	☐	☐	☐	☐

What amount of knee pain have you experienced the **last week** during the following activities?

P2. Twisting/pivoting on your knee

None	Mild	Moderate	Severe	Extreme
☐	☐	☐	☐	☐

P3. Straightening knee fully

None	Mild	Moderate	Severe	Extreme
☐	☐	☐	☐	☐

P4. Bending knee fully

None	Mild	Moderate	Severe	Extreme
☐	☐	☐	☐	☐

P5. Walking on flat surface

None	Mild	Moderate	Severe	Extreme
☐	☐	☐	☐	☐

P6. Going up or down stairs

None	Mild	Moderate	Severe	Extreme
☐	☐	☐	☐	☐

P7. At night while in bed

None	Mild	Moderate	Severe	Extreme
☐	☐	☐	☐	☐

P8. Sitting or lying

None	Mild	Moderate	Severe	Extreme
☐	☐	☐	☐	☐

P9. Standing upright

None	Mild	Moderate	Severe	Extreme
☐	☐	☐	☐	☐

Function, daily living

The following questions concern your physical function. By this we mean your ability to move around and to look after yourself. For each of the following activities please indicate the degree of difficulty you have experienced in the **last week** due to your knee.

A1. Descending stairs

None	Mild	Moderate	Severe	Extreme
☐	☐	☐	☐	☐

A2. Ascending stairs

None	Mild	Moderate	Severe	Extreme
☐	☐	☐	☐	☐

For each of the following activities please indicate the degree of difficulty you have experienced in the **last week** due to your knee.

A3. Rising from sitting

None	Mild	Moderate	Severe	Extreme
☐	☐	☐	☐	☐

A4. Standing

None	Mild	Moderate	Severe	Extreme
☐	☐	☐	☐	☐

A5. Bending to floor/pick up an object

None	Mild	Moderate	Severe	Extreme
☐	☐	☐	☐	☐

A6. Walking on flat surface

None	Mild	Moderate	Severe	Extreme
☐	☐	☐	☐	☐

A7. Getting in/out of car

None	Mild	Moderate	Severe	Extreme
☐	☐	☐	☐	☐

A8. Going shopping

None	Mild	Moderate	Severe	Extreme
☐	☐	☐	☐	☐

A9. Putting on socks/stockings

None	Mild	Moderate	Severe	Extreme
☐	☐	☐	☐	☐

A10. Rising from bed

None	Mild	Moderate	Severe	Extreme
☐	☐	☐	☐	☐

A11. Taking off socks/stockings

None	Mild	Moderate	Severe	Extreme
☐	☐	☐	☐	☐

A12. Lying in bed (turning over, maintaining knee position)

None	Mild	Moderate	Severe	Extreme
☐	☐	☐	☐	☐

A13. Getting in/out of bath

None	Mild	Moderate	Severe	Extreme
☐	☐	☐	☐	☐

A14. Sitting

None	Mild	Moderate	Severe	Extreme
☐	☐	☐	☐	☐

A15. Getting on/off toilet

None	Mild	Moderate	Severe	Extreme
☐	☐	☐	☐	☐

For each of the following activities please indicate the degree of difficulty you have experienced in the **last week** due to your knee.

A16. Heavy domestic duties (moving heavy boxes, scrubbing floors, etc)

None	Mild	Moderate	Severe	Extreme
☐	☐	☐	☐	☐

A17. Light domestic duties (cooking, dusting, etc)

None	Mild	Moderate	Severe	Extreme
☐	☐	☐	☐	☐

Function, sports and recreational activities

The following questions concern your physical function when being active on a higher level. The questions should be answered thinking of what degree of difficulty you have experienced during the **last week** due to your knee.

SP1. Squatting

None	Mild	Moderate	Severe	Extreme
☐	☐	☐	☐	☐

SP2. Running

None	Mild	Moderate	Severe	Extreme
☐	☐	☐	☐	☐

SP3. Jumping

None	Mild	Moderate	Severe	Extreme
☐	☐	☐	☐	☐

SP4. Twisting/pivoting on your injured knee

None	Mild	Moderate	Severe	Extreme
☐	☐	☐	☐	☐

SP5. Kneeling

None	Mild	Moderate	Severe	Extreme
☐	☐	☐	☐	☐

Quality of Life

Q1. How often are you aware of your knee problem?

Never	Monthly	Weekly	Daily	Constantly
☐	☐	☐	☐	☐

Q2. Have you modified your life style to avoid potentially damaging activities to your knee?

Not at all	Mildly	Moderately	Severely	Totally
☐	☐	☐	☐	☐

Q3. How much are you troubled with lack of confidence in your knee?

Not at all	Mildly	Moderately	Severely	Extremely
☐	☐	☐	☐	☐

Q4. In general, how much difficulty do you have with your knee?

None	Mild	Moderate	Severe	Extreme
☐	☐	☐	☐	☐

Thank you very much for completing all the questions in this questionnaire.

A.3 Oxford Knee Score (OKS)

The Oxford Knee Score

During the past four weeks:

1. **How would you describe the pain you usually have from your knee**

L	R	
☐	☐	None
☐	☐	Very mild
☐	☐	Mild
☐	☐	Moderate
☐	☐	Severe

2. **Have you had any trouble with washing and drying yourself (all over) because of your knee?**

L	R	
☐	☐	No trouble at all
☐	☐	Very little trouble
☐	☐	Moderate trouble
☐	☐	Extreme difficulty
☐	☐	Impossible to do

3. **Have you had any trouble getting in and out of a car or using public transport because of your knee? (whichever you tend to use)**

L	R	
☐	☐	No trouble at all
☐	☐	Very little trouble
☐	☐	Moderate trouble
☐	☐	Extreme difficulty
☐	☐	Impossible to do

4. **For how long have you been able to walk before the pain from your knee becomes severe? (with or without a stick)**

L	R	
☐	☐	No Pain/ > 30min
☐	☐	16 to 30 min
☐	☐	5 to 15 min
☐	☐	Around the house only
☐	☐	Not at all – severe on walking

5. **After a meal (sat at table), how painful has it been for you to stand up from a chair because of your knee?**

L	R	
☐	☐	Not at all painful
☐	☐	Slightly painful
☐	☐	Moderately painful
☐	☐	Very painful
☐	☐	Unbearable

6. **Have you been limping when walking, because of your knee?**

L	R	
☐	☐	Rarely/never
☐	☐	Sometimes or just at first
☐	☐	Often, not just at first
☐	☐	Most of the time
☐	☐	All of the time

7. **Could you kneel down and get up again afterwards?**

L	R	
☐	☐	Yes, easily
☐	☐	With a little difficulty
☐	☐	With moderate difficulty
☐	☐	With extreme difficulty
☐	☐	No, impossible

8. **Have you been troubled by pain from your knee in bed at night?**

L	R	
☐	☐	No nights
☐	☐	Only 1 or 2 nights
☐	☐	Some nights
☐	☐	Most nights
☐	☐	Every night

9. **How much has pain from your knee interfered with your usual work (including housework)**

L	R	
☐	☐	Not at all
☐	☐	A little bit
☐	☐	Moderately
☐	☐	Greatly
☐	☐	Totally

10. **Have you felt that your knee might suddenly "give way" or let you down?**

L	R	
☐	☐	Rarely/never
☐	☐	Sometimes or just at first
☐	☐	Often, not just at first
☐	☐	Most of the time
☐	☐	All of the time

11. **Could you do the household shopping on your own?**

L	R	
☐	☐	Yes, easily
☐	☐	With little difficulty
☐	☐	With moderate difficulty
☐	☐	With extreme difficulty
☐	☐	No, impossible

12. **Could you walk down a flight of stairs?**

L	R	
☐	☐	Yes, easily
☐	☐	With little difficulty
☐	☐	With moderate difficulty
☐	☐	With extreme difficulty
☐	☐	No, impossible

A.4 The Western Ontario and Mc Master Universities Osteoarthritis Index (WOMAC)

The Western Ontario and McMaster Universities Osteoarthritis Index (WOMAC)

Name:_____ Date:_____

Instructions: Please rate the activities in each category according to the following scale of difficulty: 0 = None, 1 = Slight, 2 = Moderate, 3 = Very, 4 = Extremely

Circle **one number** for each activity

Pain	1. Walking	0 1 2 3 4
	2. Stair Climbing	0 1 2 3 4
	3. Nocturnal	0 1 2 3 4
	4. Rest	0 1 2 3 4
	5. Weight bearing	0 1 2 3 4
Stiffness	1. Morning stiffness	0 1 2 3 4
	2. Stiffness occurring later in the day	0 1 2 3 4
Physical Function	1. Descending stairs	0 1 2 3 4
	2. Ascending stairs	0 1 2 3 4
	3. Rising from sitting	0 1 2 3 4
	4. Standing	0 1 2 3 4
	5. Bending to floor	0 1 2 3 4
	6. Walking on flat surface	0 1 2 3 4
	7. Getting in / out of car	0 1 2 3 4
	8. Going shopping	0 1 2 3 4
	9. Putting on socks	0 1 2 3 4
	10. Lying in bed	0 1 2 3 4
	11. Taking off socks	0 1 2 3 4
	12. Rising from bed	0 1 2 3 4
	13. Getting in/out of bath	0 1 2 3 4
	14. Sitting	0 1 2 3 4
	15. Getting on/off toilet	0 1 2 3 4
	16. Heavy domestic duties	0 1 2 3 4
	17. Light domestic duties	0 1 2 3 4

Total Score: _____ / 96 = _____%

Comments / Interpretation (to be completed by therapist only):

APPENDIX B MBIR Protocol for TKR's

B.1 Joint Track Protocol

B.1.1 Fluoroscopy Image Formatting

1. Import fluoroscopy images into ImageJ. Select the convert images to 8-bit Greyscale and Sort Numbers Numerically from the options.
2. If the images were reversed during image acquisition go to Image, Rotate and select Flip horizontally.
3. Save as an Image sequence with tagged image file format (TIFF).

B.1.2 Image Calibration

1. Open MATLAB (Version 2013) and browse for the directory where Xcal.m is located and run.
2. Select Open Image from the File Menu and locate the calibration image.
3. Press the button 'Find all dots'. This highlights all the ball bearings in the calibration image.
4. Change minimum circle radius and radius range if not all the dots are found and then try again.
5. If required add or delete dots by clicking on the image and selecting the a or d key (a = add, d=delete). Added dots appear as red crosses on the calibration frame (Figure B-1).

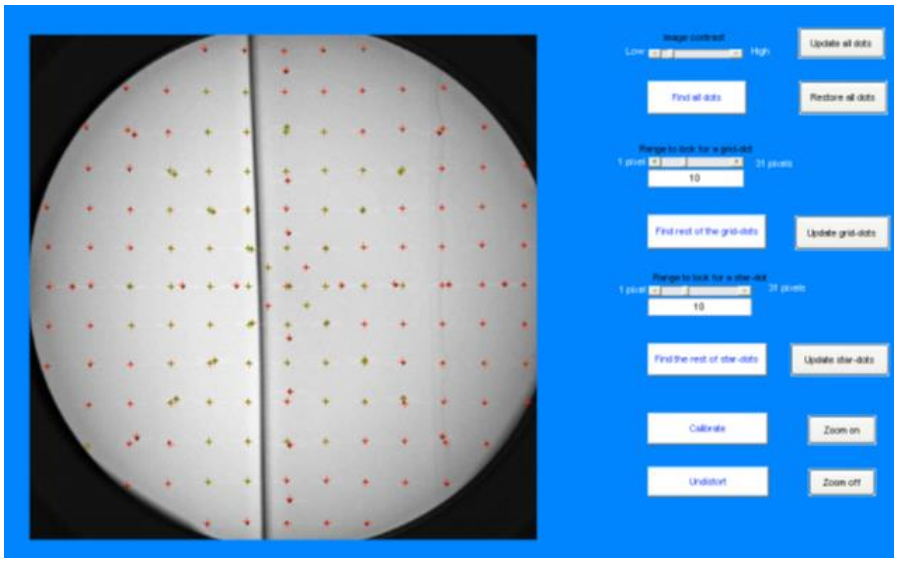

Figure B-1 Calibration frame with added dots

6. To sort the grid coordinates from all the other dots click on the central grid dot, the dot above center and then the dot to the right of center.

Press the button 'Find rest of the grid-dots' and two screens will appear. One showing the grid dots and another with all the dots in the image. Delete any excess dots.

7. Press 'Update grid-dots' and the position of the ball bearing belonging to the square grid should be visible on a plot.
8. To sort out the star coordinates from all dots found press 'Restore all dots' then select the dot to the right of the central star dot, the dot to the left of the central star dot and then on the central dot. Press 'Update star dots' and the position of the ball bearings that belong to the star grid should appear as a plot (Figure B-2).

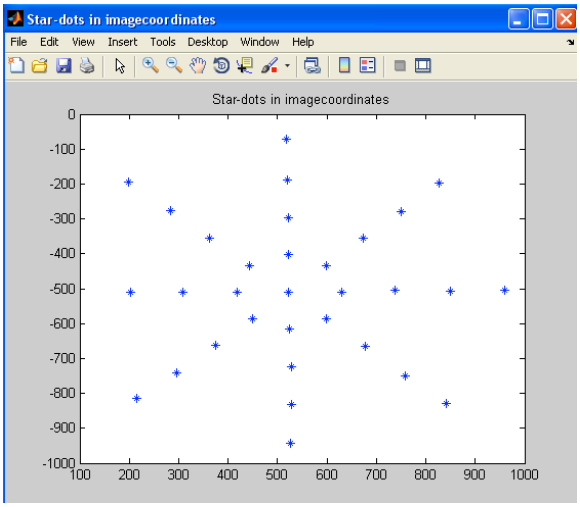

Figure B-2 Image coordinate of the star grid on the calibration frame

9. Press 'Calibrate' and the results should appear in the Matlab prompt and are saved in an m-file called image name.m
10. To save the distortion parameters in order to undistort other images using the calibration results. Select File, Save data, Distortion correction Parameters.
11. Press 'Undistort' and the undistorted image is saved as 'name of the original image_undist.tif'
12. To select all the motion images, go to File/'Undistort after calibration' and select the required images. Next select the corresponding file containing the saved distortion parameters and the undistorted images are saved in the path as the distorted images.

B.1.3 Joint Track Calibration

1. Open Matlab , set the Current directory as the Joint Track calibration folder and run m2cal.m program.
2. Select the .m filed that was created in Xcal and several calibration options should appear in the Matlab prompt (Figure B-3).

```
What unit are you using?
  1/Enter = mm, 2 = cm, 3 = inch.
  For other units, please input its scale relative to mm (e.g. 25.4 = inch):
   1
Did you crop the images after distortion correction?
  1 = yes, 0/Enter = no : 0
```

Figure B-3 Joint Track calibration options

3. Select units as mm and that the images were not cropped after distortion correction.
4. The calibration file is saved as JTcalibration.cal file and is imported into JointTrack during the One Button Load.

B.2 Rhinoceros Preparation

Rhinoceros is the program used to identify correct axis alignment and origin location.

- X axis is dependent for left and right – forwards and backwards respectively
- Y axis (green) is always vertical
- Z axis is always medically aligned

Correct axis alignment (right & left femoral components) can be seen in Figure B-4 & Figure B-5. Likewise the axis convention applies to Tibial components and the correct axial alignment can be seen in Figure B-6 & Figure B-7.

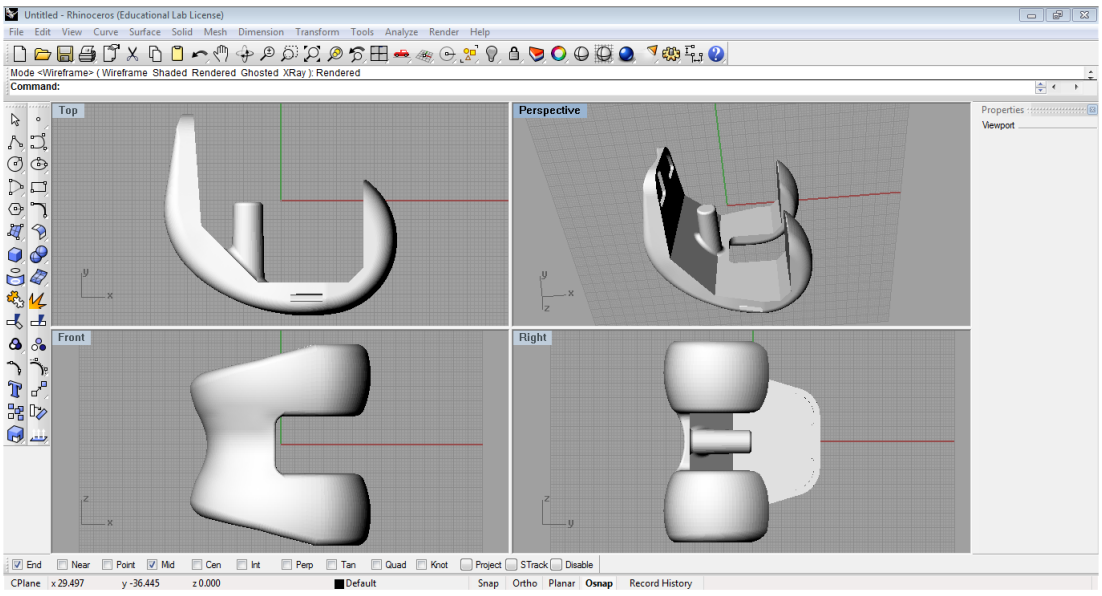

Figure B-4 - Axis alignment for right femoral component

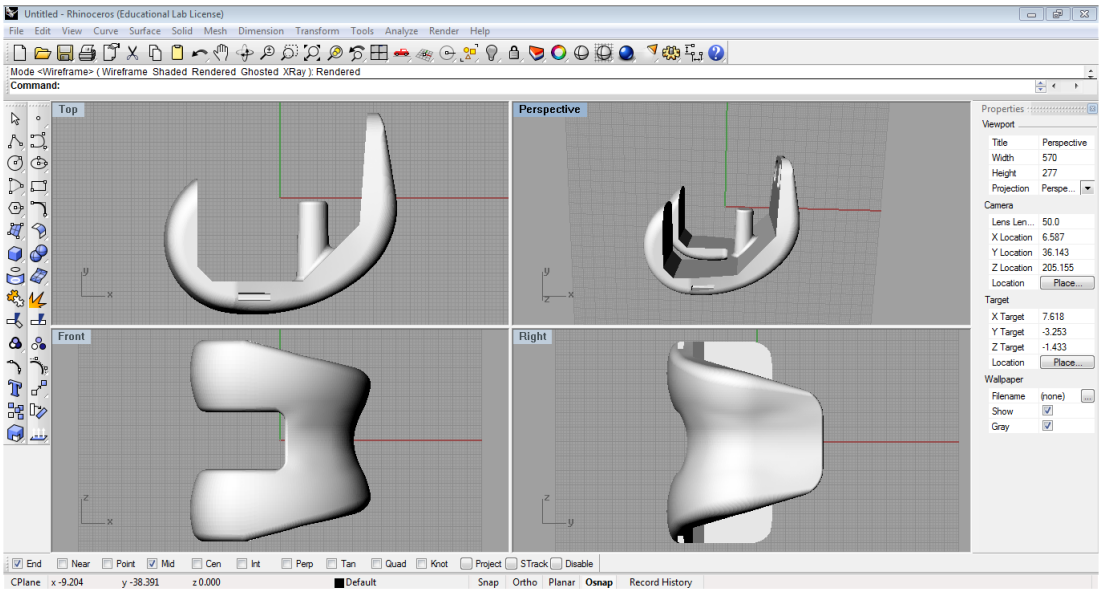

Figure B-5 - Axis alignment for left femoral component

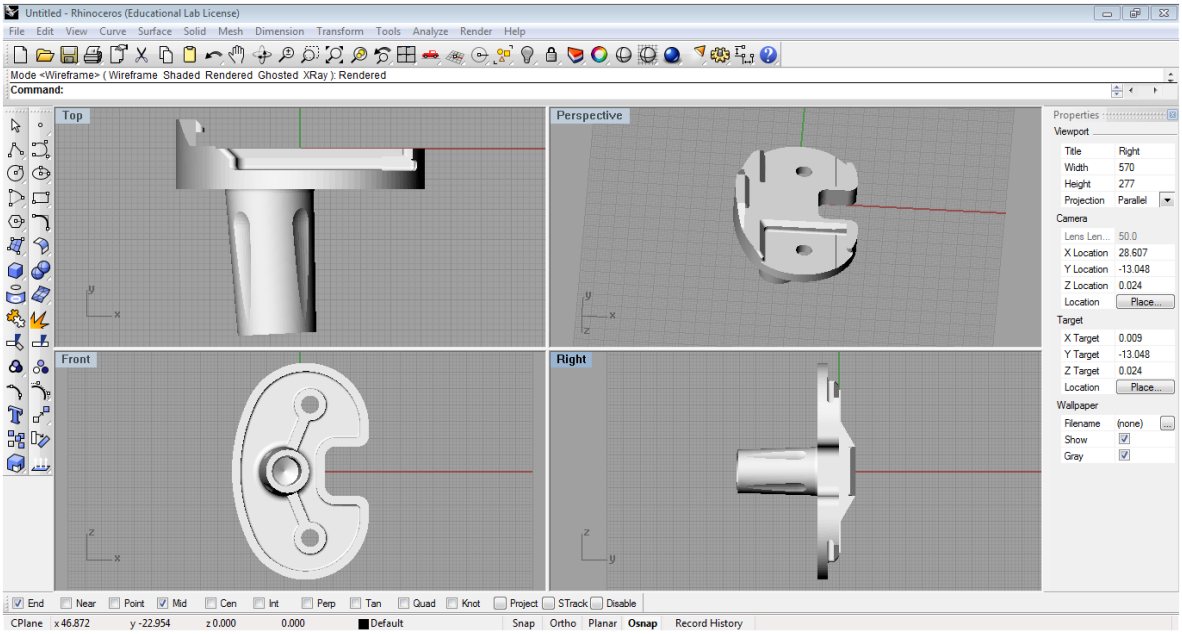

Figure B-6- Axis alignment for right Tibial component

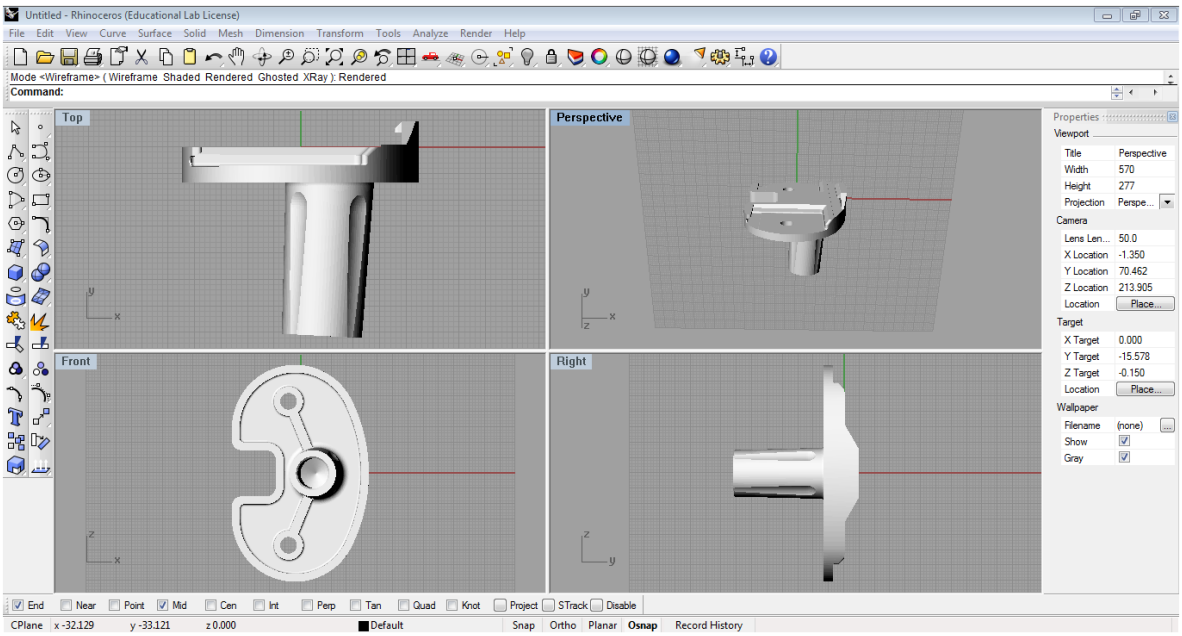

Figure B-7 Axis alignment for left Tibial Component

B.3 Origin Adjustment

Once the models have had axial alignment checked the next step is to ensure that the origin is located at the Banks point.

B.3.1 Step-by-step to locate origin at Banks point - Femur

1. The first step is to locate the topmost point of the condyle (the back of the CAD mode) and draw a line using the "polyline" function from this point to the corresponding point on the front of the CAD model, as shown in Figure B-8.
2. This line is 2R and it must be ensured that all image snap options are unselected to ensure that this line remains central to the model. Select the line and navigate to "Analyze > Length" to measure the length of 2R. In this case 2R = 52.321mm which means that R = 26.1605mm.

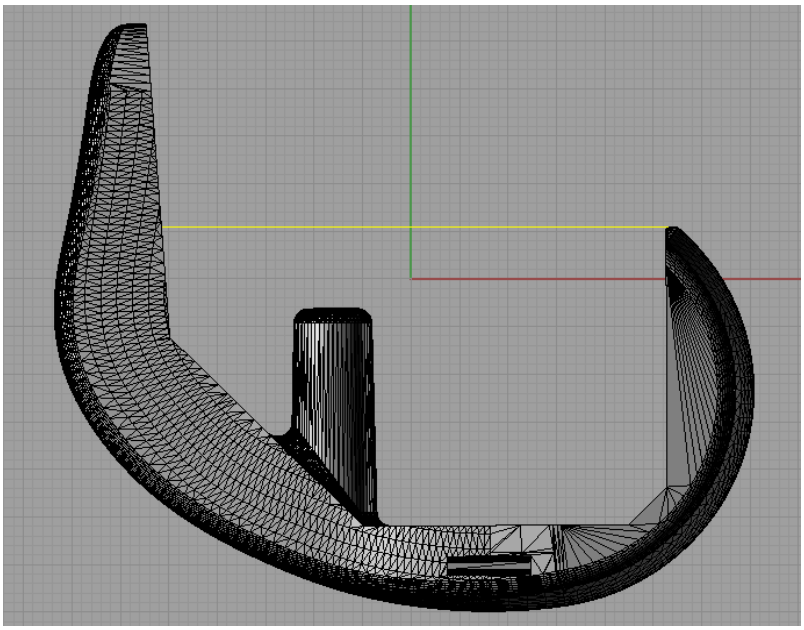

Figure B-8 Identifying and drawing the line 2R

3. Enable the mid-point & end point snap function (Figure B-9) from the bottommost toolbar and locate the midpoint of 2R using Linear Dimension to the left of the question mark (Figure B-10).

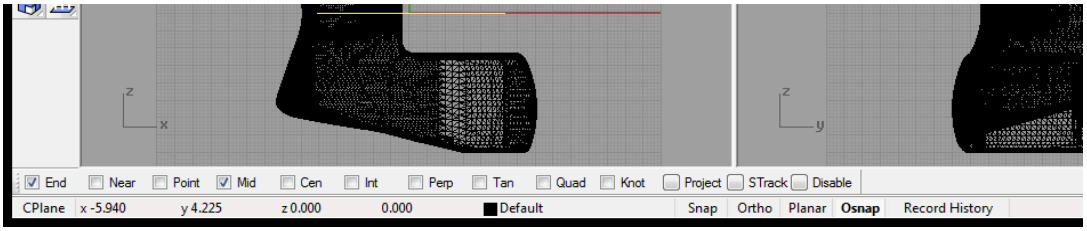

Figure B-9 Enabling mid/end point snap functions

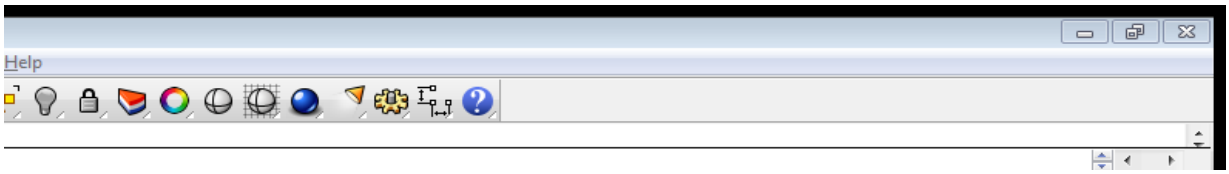

Figure B-10 Selecting Linear Dimension tool

4. Drag a linear dimension line from the midpoint of line 2R to the bottom of the inside of the femoral component as seen in Figure B-11. The distance as shown is 31.36mm.

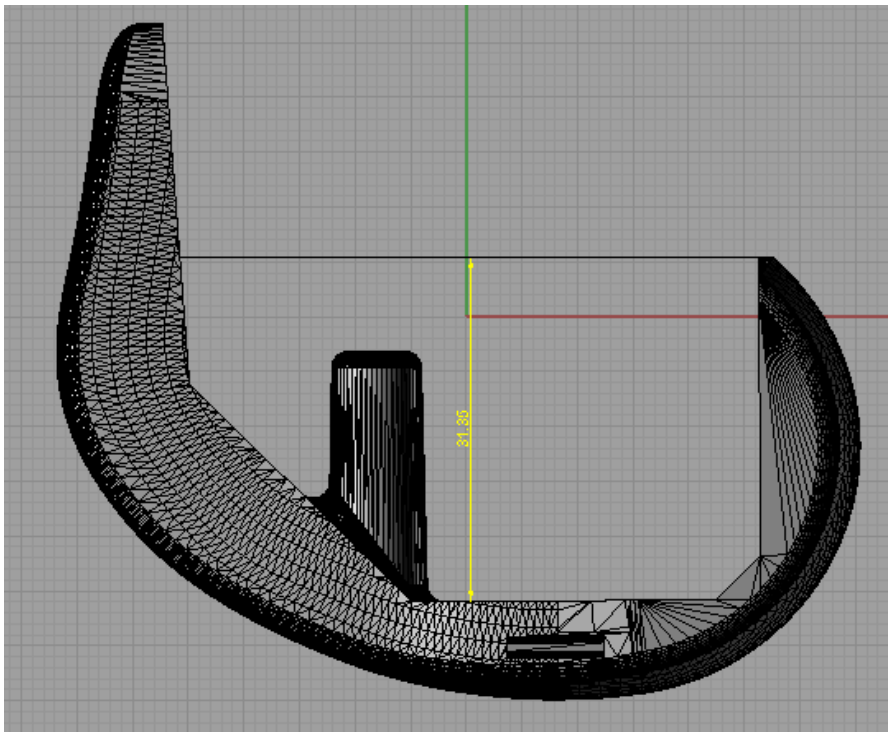

Figure B-11 Calculating the distance between the midpoint of 2R and the bottom of the inside of the component

5. Using this vale it is now possible to calculate the amount by which the components origin needs to be transformed by. This vertical length (31.36mm) minus R results in a value of 5.1895mm. Now select the linear line and press delete to remove it.
6. The next step is to locate the midpoint of 2R again and draw a line of length 5.1895mm vertically downwards as seen in Figure B-12.

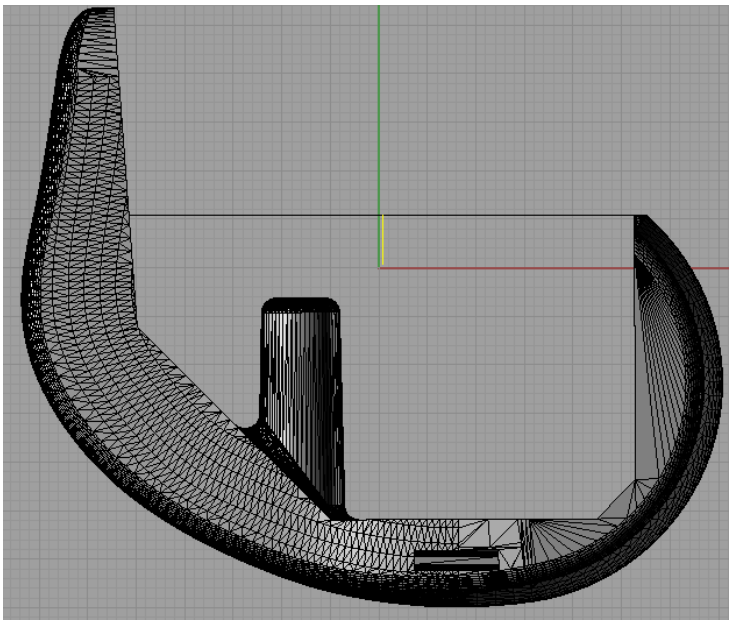

Figure B-12 Vertical line of length 5.1895mm drawn from the midpoint of 2R

7. Navigate and select the point function from the main toolbar and select the end of the new vertical line to place a terminating point. Following this delete any remaining lines, leaving just the Banks Point as shown in Figure B-13.

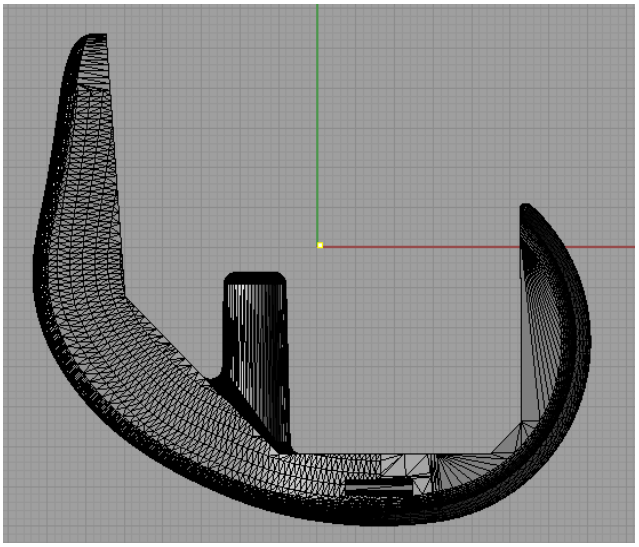

Figure B-13 Banks point located and marked

8. Take note of the x,y & z coordinates of the Banks point.
9. Select both the model and the banks point and navigate to Transform>move and input the banks point coordinates then press enter and input the values 0,0,0 to set the new origin of the model to the banks point.
10. Select the banks point and press delete
11. Navigate to File>Export Selected and click on the model and press enter.

12. Save file as chosen name and as a .STL file type and select binary when prompted. This will save the adjusted file in a compressed and easily accessible file format for the next stages.

B.3.2 Step by Step to locate origin at banks point - Tibia

1. After opening the corresponding tibia model ensure that the snap functions are disabled as in the femoral section. Then maximise the Front View port and plot a straight line from left most point of one condyle to the other, as shown in Figure B-14.

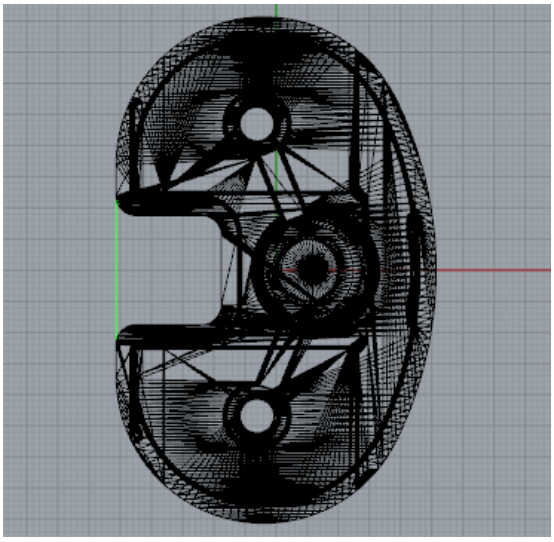

Figure B-14 - Support Line created in step 1

2. Next plot a straight line from the topmost point to the bottom most point as shown by the yellow line in Figure B-15. Navigate to analyse> Length and note the length of the line.

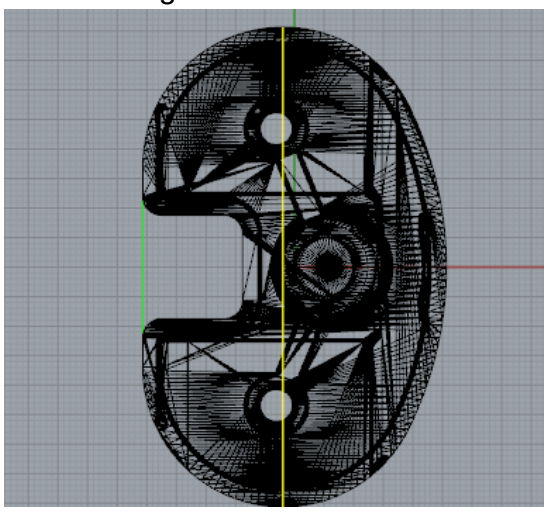

Figure B-15 - Max Vertical length line created in step 2

3. Now plot a line from the right most edge of the model to the line created in step one, again navigate to analyse>length and note the horizontal length of the tibia. Figure B-16 shows an example of this line.

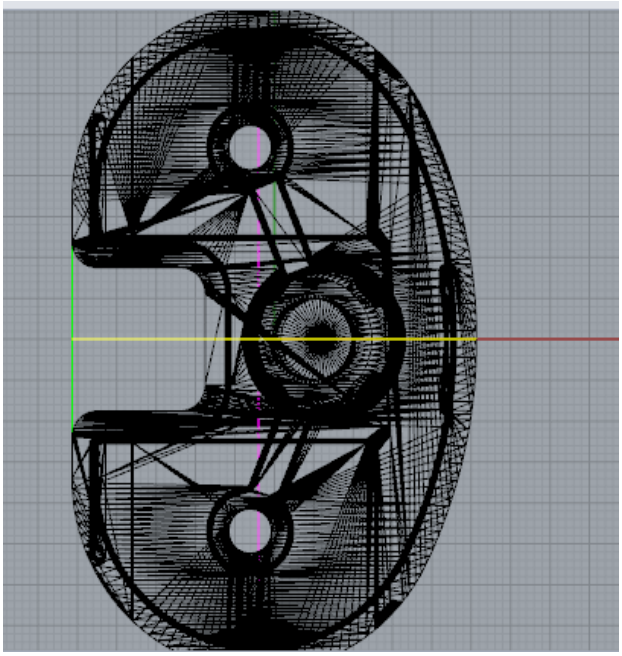

Figure B-16 - Intersecting max horizontal line created in step 3

4. Select the single point tool and create a point where the vertical and horizontal lines intersect. This is the banks point of the tibia model. Delete any lines created and take not of the newly created points coordinates
5. Select both the model and the banks point and navigate to Transform>move and input the banks point coordinates then press enter and input the values 0,0,0 to set the new origin of the model to the banks point.
6. Select the banks point and press delete
7. Navigate to File>Export Selected and click on the model and press enter.

B.4 Matching Procedure in Joint Track

1. Open JointTrack for 3D to 2D image registration (if you get an error message, close all the windows and try again)
2. Select thethe following in order
    a. JT calibration fill
    b. Fluoroscopic images
    c. Femur and Tibia component models

3. There are three main views for displaying the models 3D, Edge and Shadow. It is recommended to use Edge for the model.
4. The fluoroscopy image can be viewed in three display modes Intensity, Edge and Hybrid.).
5. Use the Upper and Lower intensity bound to adjust the intensity settings and adjust the aperture and thresholds to adjust the edge detection to aid with the image registration. It recommended that the bounds be reversed to make matching slightly easier – upper: 75-100 lower: 0
6. Controls for translating and rotating models are as follow:
   Arrow keys = in-plane translation
   Ctrl + arrow keys = rotation about model's x/y axis
   Ctrl + Shift + Left/Right = rotation about model's z axis
   Shift + Up/Down = out-of-plane translation
   Shift + Left/Right = in-plane spin
   +/- = increase/decrease the step size of motion
7. Match the femur first. The Femur is asymmetric proximally and the tibia is symmetric down its midline. By matching the femur first it is easier to see if the pose of the knee is physiologically possible.
8. When moving on to the next image select 'Copy previous' to copy the kinematics from the previous frame. Thus allowing you to do small adjustments rather than starting the registration from the beginning for each image.
9. Once manual matching has been carried out on all the images select 'Config Registration' and the optimization settings should appear. The settings shouldn't need to be adjusted.
10. Once the settings have been set select 'Optimize Whole Sequence' and the algorithm should make some slight adjustments to your matching. Check to see if all the images have been correctly matched afterwards.
11. Select 'Save All Kinematics' for each model kinematics to be saved as .jts files.

APPENDIX C ACS protocol for MRI derived bone models

C.1 Axis Preparation Femur and Tibia

Rhinoceros is the program used to identify correct axis alignment and origin location.

- X axis is dependent for left and right – forwards and backwards respectively
- Y axis (green) is always vertical
- Z axis is always medially aligned

Correct axis alignment (right & left femur bone models) can be seen in Figure C-1 & Figure C-2. Likewise the axis convention applies to Tibia bone models and the correct axial alignment can be seen in Figure C-3 & Figure C-4.

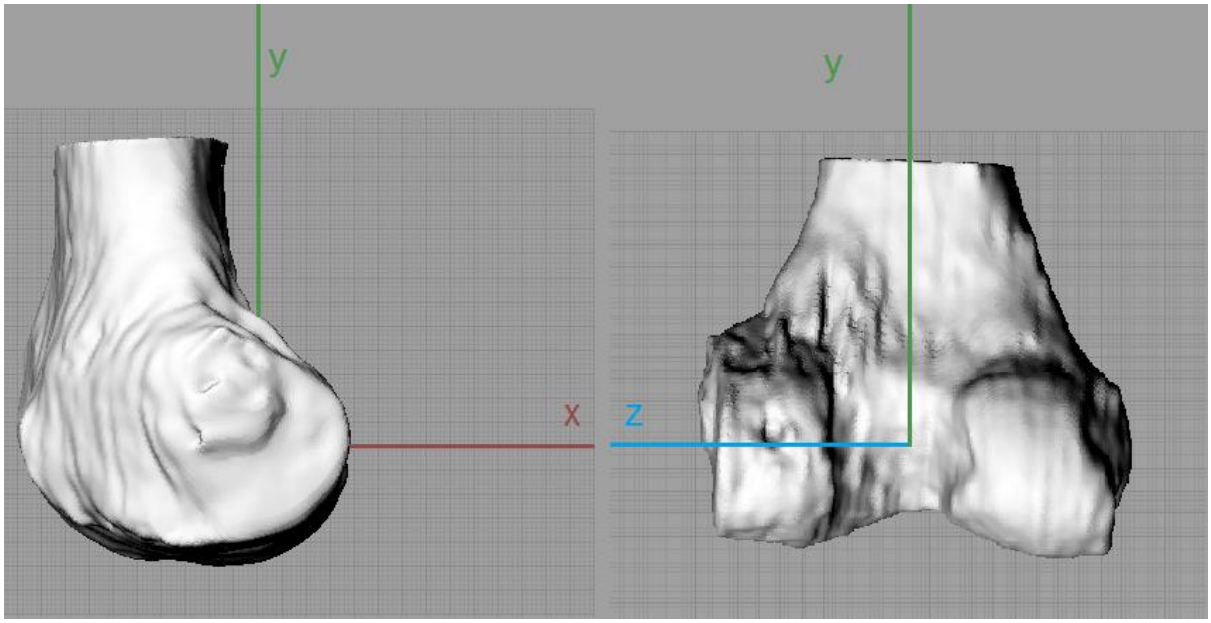

Figure C-1 - Axis alignment for right femur

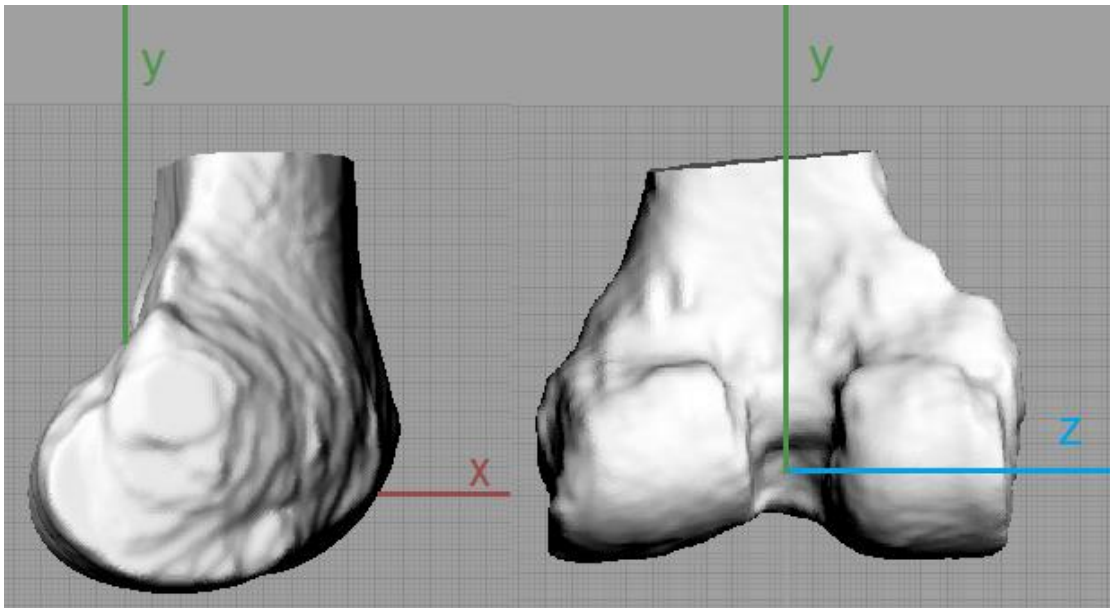

Figure C-2 - Axis alignment for left femur

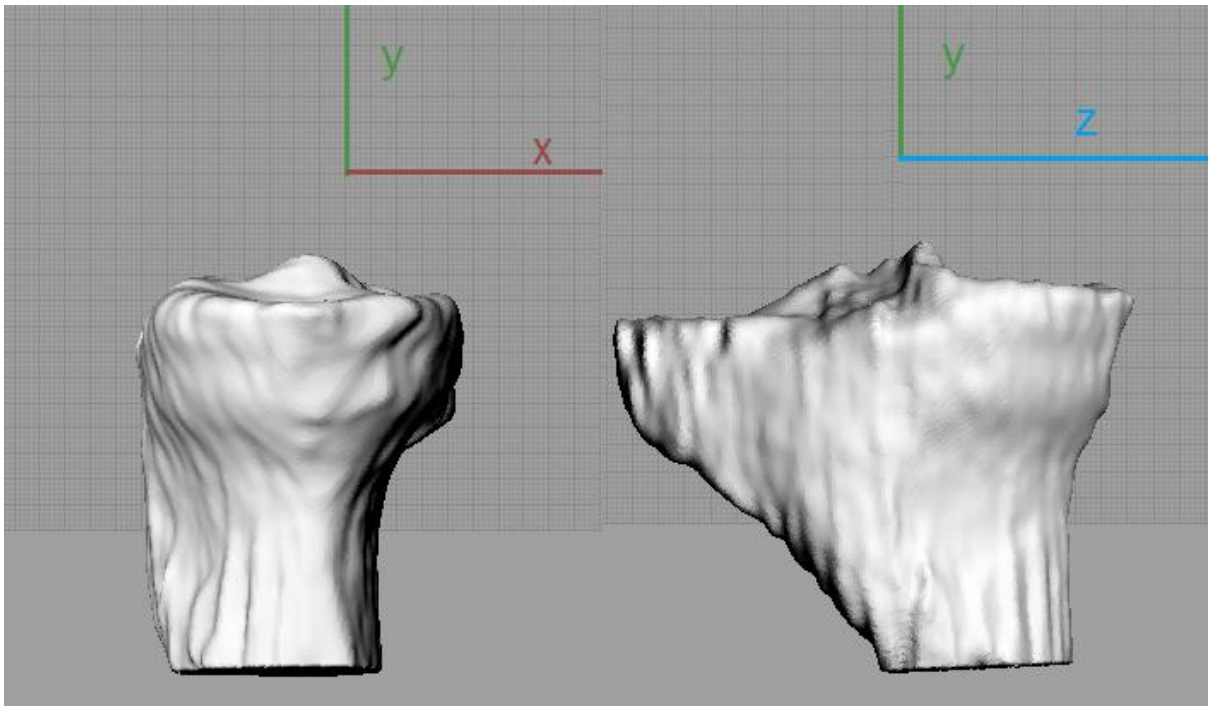

Figure C-3- Axis alignment for right tibia

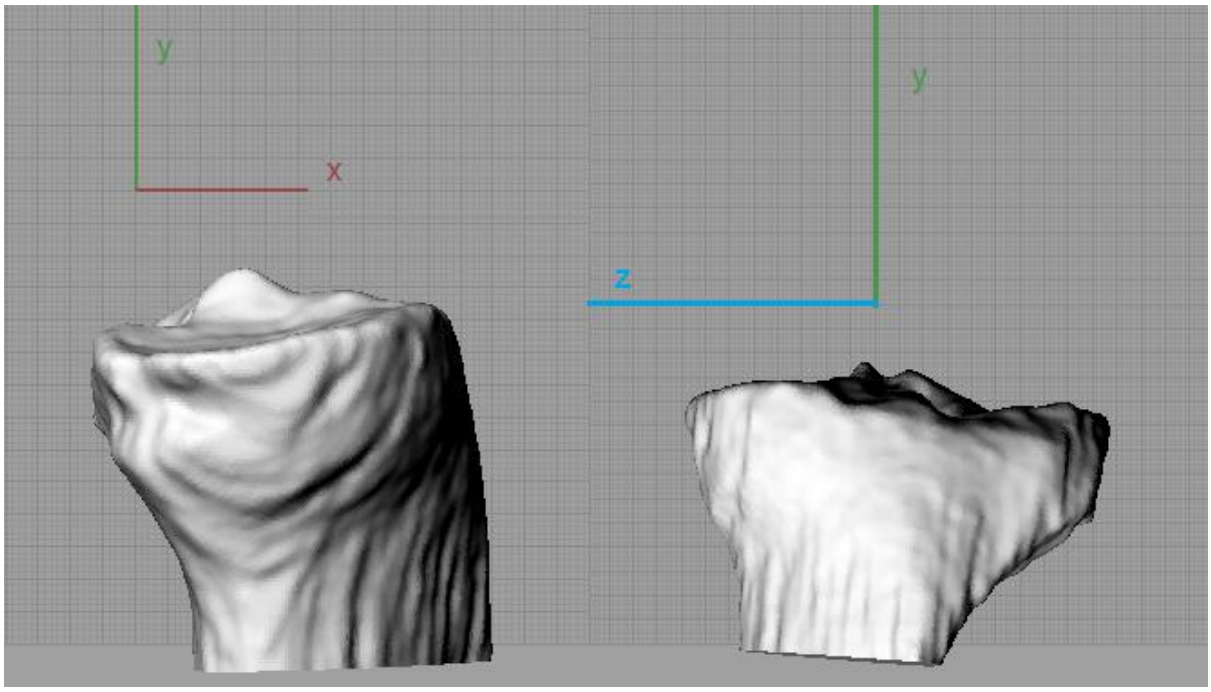

Figure C-4 Axis alignment for left Tibia

C.2 Creating full leg bone model

1. Import coarse full leg bone models into Rhino 4
2. If segmented on Scanip 6.0+ they should already register to each other as a coordinate system is applied by the software (Figure C-5)

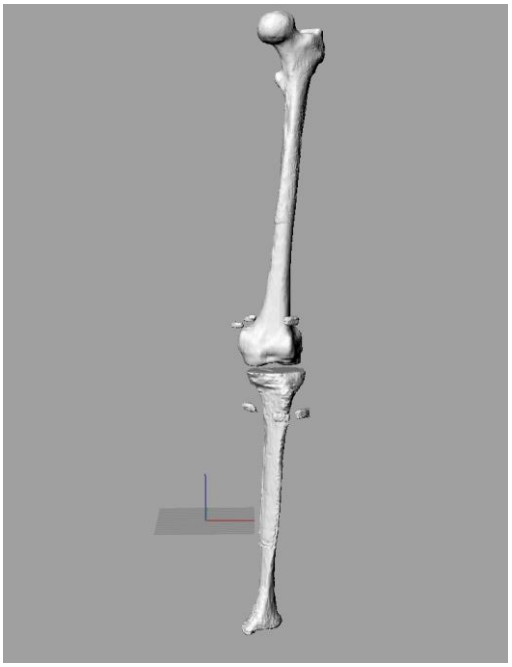

Figure C-5 Imported coarse full leg model

3. If coarse models do not look correctly aligned use the models of the MRI markers to translate and rotate the models to the correct alignment.
4. Import high resolution extension unloaded models
5. Using the MRI markers as a guide rotate and translate the high resolution model to match the full leg model
6. The Nudge tool can be used to provide very small translations (Tools - Options - Modelling Aids)

Once correctly aligned an anatomical coordinate system needs to be applied to the high res femur, tibia and patella models.

C.2.1 Femoral Anatomical Coordinate System (ACS): Defining the origin

Using a method described by (Moro-oka, et al., 2007) the origin of the Femoral ACS can be defined by using points from the model.

1. To define the mediolateral (Z) axis carefully fit cylinders (Solid-Cylinder) to both femoral condyles (Figure C-6). The Z-axis is the vector formed between the centres of the cylinders on the femoral condyles.
2. When creating the cylinders use the distance tool (Analyze-Distance) to find out the length of the individual femoral condyles.
3. Using the Volume centroid command (Analyze-Mass Properties-Volume Centroid) determine the coordinates for both cylinders
4. Using the matlab script femuracs.m input the coordinates of the volume centroid for both condyles

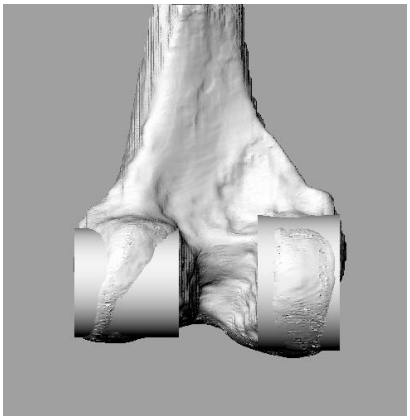

Figure C-6 Cylinders attached to femoral condyles

The origin of the coordinate system is found by taking the midpoint between the cylinders.

5. The matlab script will provide a coordinate for the origin, create a point within rhino to represent this position (Curve-Point object-Single point). Make sure to input the coordinate in this format e.g. w1.000,2.000,3.000 (x,y,z)
6. Group all the models in the workspace together using the group tool in rhino
7. Using the move tool (Transform-Move) input the coordinate where the origin was found to be as the point to move from and translate the model to the origin of the world coordinate system in Rhino.
8. This will position the origin of the Femur ACS in the same position as the world coordinate system (Figure C-7)

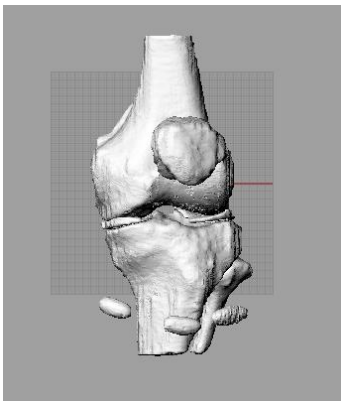

Figure C-7 Models translated to the origin of the world coordinates

C.2.2 Femoral Anatomical Coordinate System (ACS): Aligning the axes

The next stage is to rotate the model to the correct axis alignment by calculating the vectors that form the proximal/distal (Y) axis and the anteroposterior (X) axis. This is done by using the method described by Moro-oka, et al. (2007).

1. Fit a sphere carefully to the femoral head (Figure C-8)
2. Calculate the volume centroid to determine the centre of the sphere

A vector is formed between the origin and the centre of the sphere. To define the Y axis it is necessary to find the vector perpendicular to the Z axis and that is in the plane intersecting the femoral head with the Y axis. This is done be taking the cross product of the vector from the origin to the centre of the femoral head with the Z axis. This vector follows the direction of the Y axis. To find the anteroposterior (X) axis take the cross product of the Y and Z axis.

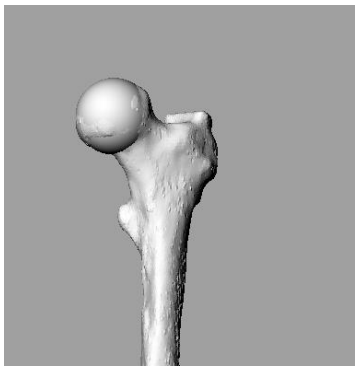

Figure C-8 Sphere carefully fitted to Femoral head

3. Calculate the new coordinates for femoral condyles cylinders
4. Input the coordinates of the cylinders and femoral head into the Matlab script femuracs.m to calculate the Y axis vector
5. The code will output two unit vectors in the direction of the Y axis and X-axis.
6. The next step is to create polylines in the direction of each axis starting from the origin (Figure C-9). This helps to visualise orientating the axes and to act as guidelines.

Figure C-9 Polylines representing the axes

7. Next rotate the femur model from the origin so that the axes guidelines match with the world coordinates.

C.2.3 Tibial Anatomical Coordinate System (ACS): Defining the Proximal/Distal axis

The proximal/distal (y) axis for the tibia is defined as being perpendicular to the axis intersecting the ankle centre (Moro-oka et al., 2007).

1. To define the ankle centre a cylinder is carefully fitted to the malleolus (Figure C-10)
2. Using the Volume centroid command (Analyze-Mass Properties-Volume Centroid) determine the coordinates for the centre of the ankle

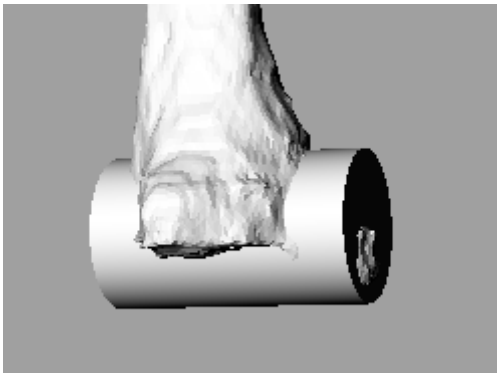

Figure C-10 Cylinder carefully fitted to Mallelous

3. Calculate the new coordinates of the condyle cylinders post femur orientation. Input coordinates of cylinders and ankle.
4. The Code calculates a unit vector in the direction of the tibial x-axis and y axis.
5. Create polylines to visualise the vectors (Figure C-11). Using the rotate command (transform-rotate) set the centre of rotation to be the origin of the world coordinate system (0,0,0) and rotate the model until the polylines align with the correct axis.

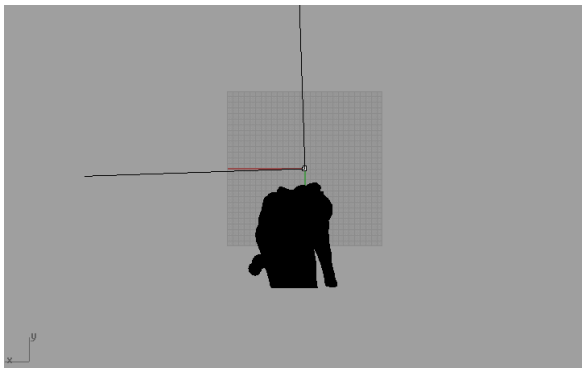

Figure C-11 Polylines used to visualise axes for tibial coordinate system

6. Once all the axes are correctly aligned export the individual models (Bones, Cartilage etc) as binary stereolithography (.stl) files.

APPENDIX D Standard Operating Protocol for Dissection of Ovine Hind Limb

At all times lab coat and gloves should be worn. When using scalpels chain mail glove must be worn and lab coat sleeves must cover the arms.

1. Place foil on the area of desk designated for animal dissection, along with disposable scalpels.
2. If specimen is from abattoir prepare a container of tepid soapy water (Teepol), place limb into container and scrub away faeces and other debris using a brush.
3. Place onto layers of Torq roll to absorb excess water prior to dissection.
4. Transfer the cleaned limb to the foiled area.
5. Carefully remove the skin and flesh using a disposable blade on an appropriate sized handle. Tissue must be removed by cutting away from the direction of the user's body.
6. Using a disposable scalpel, open up the stifle joint to expose the tibia and femur (Figure D-1a).
7. Carefully remove tendons and ligaments that are holding tibia and femur together and separate femur from tibia exposing the menisci (Figure D-1 B).

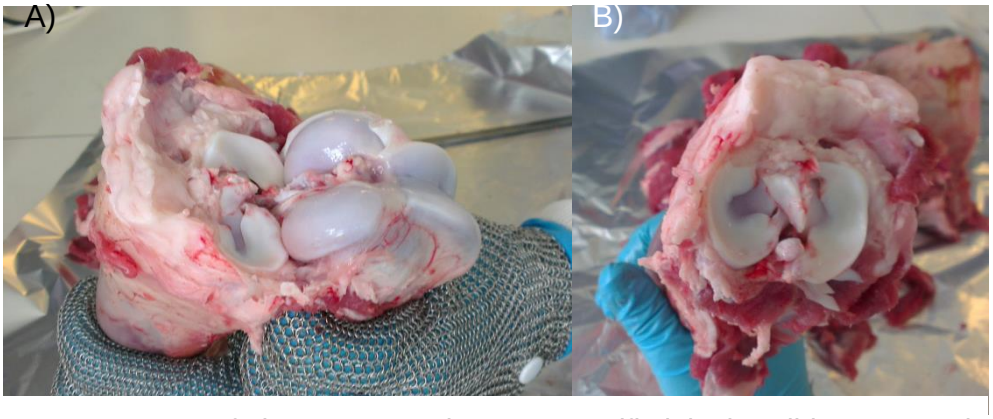

Figure D-1a - Soft tissue removed to expose stifle joint b - Tibia separated from Femur and exposed menisci

Once separated carefully remove the rest of the flesh and soft tissue for both femur and tibia.

8. Once complete wrap bones up tissue and place into cold storage.
9. Carefully remove the disposable blades from the metal handles and place in the designated sharps bin in the dissection area.
10. Disinfect the blade handles, cleaning brush etc. in a solution of water and Trigene (detergent).
11. Dispose of the skin and remains of the limb in a yellow waste bin; disposing of foil and soiled tissue in the some bin.
12. Fill out a waste disposal form taking note of the barcode on the yellow waste box and submit for incineration.

APPENDIX E Bland-Altman Plots from Chapter 5

E.1 Phantom Static Plots

E.1.1 Flexion Extension Angle

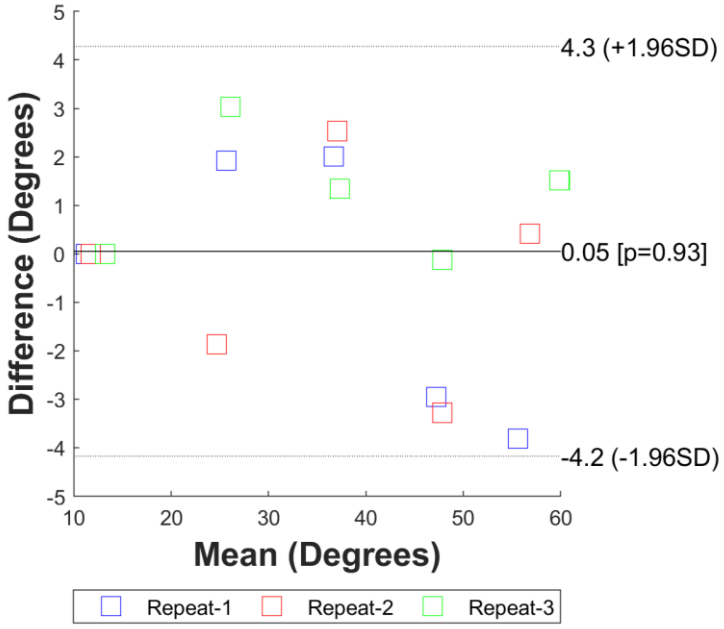

Figure E-1 Bland-Altman plot comparing bead MBIR and MBIR derived flexion-extension angle kinematics during a static task.

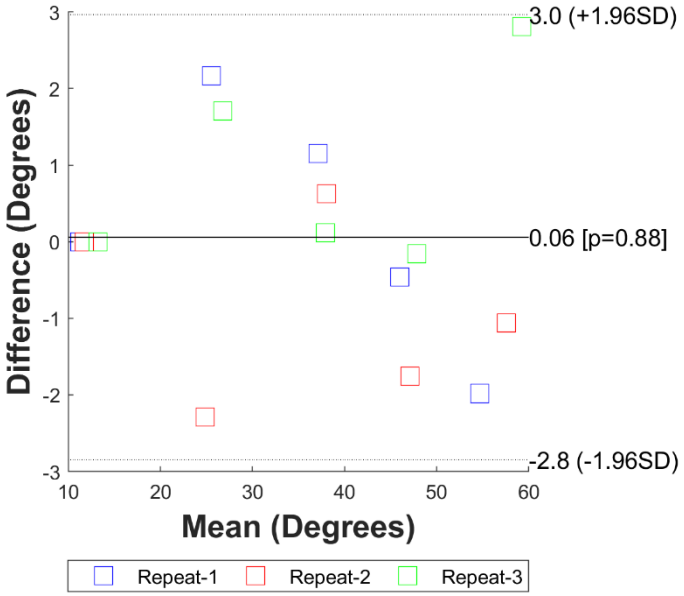

Figure E-2 Bland-Altman plot comparing motion capture and MBIR derived flexion-extension angle kinematics during a static task.

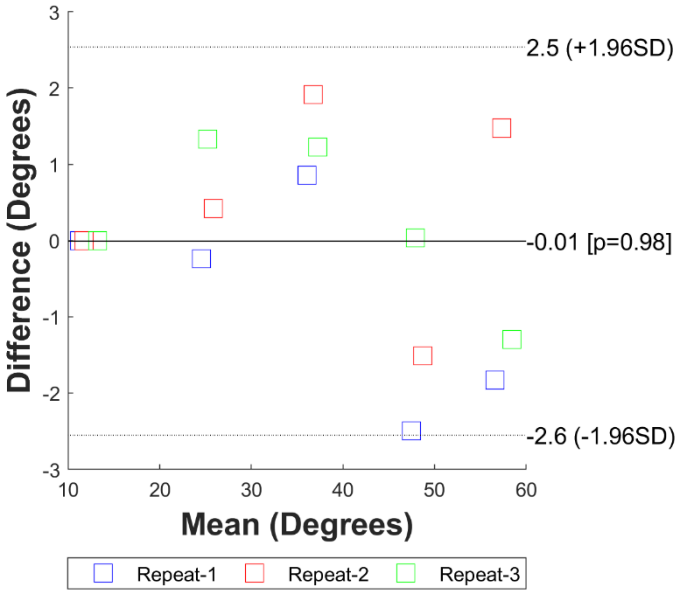

Figure E-3 Bland-Altman plot comparing motion capture and bead MBIR derived flexion-extension angle kinematics during a static task.

E.1.2 Abduction-Adduction Angle

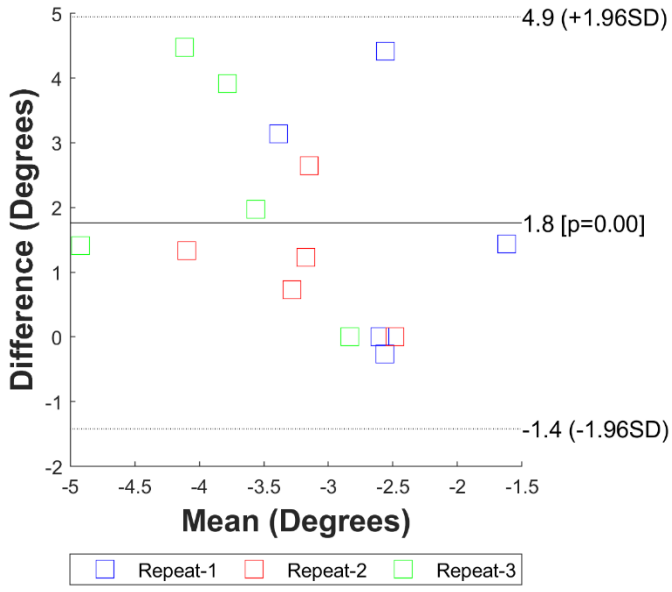

Figure E-4 Bland-Altman plot comparing bead MBIR and MBIR derived abduction-adduction angle kinematics during a static task.

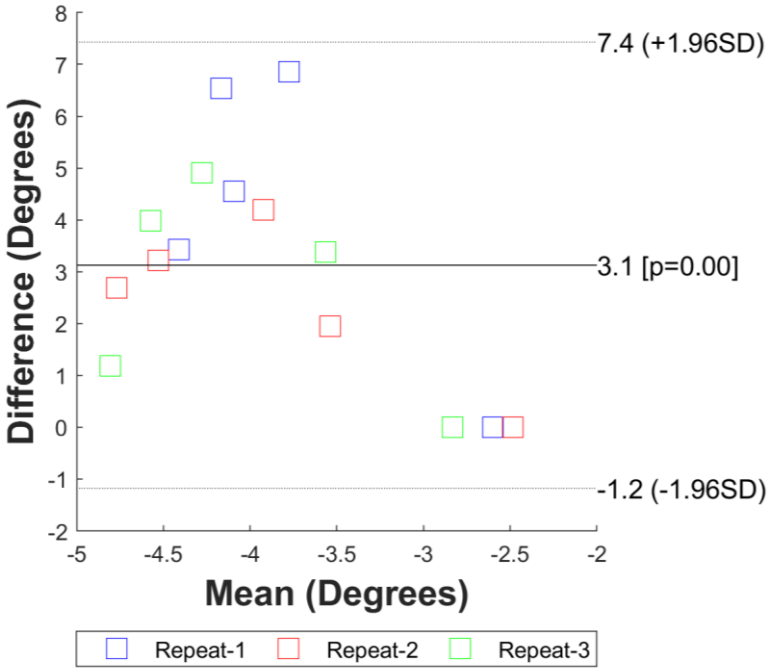

Figure E-5 Bland-Altman plot comparing motion capture and MBIR derived abduction-adduction angle kinematics during a static task.

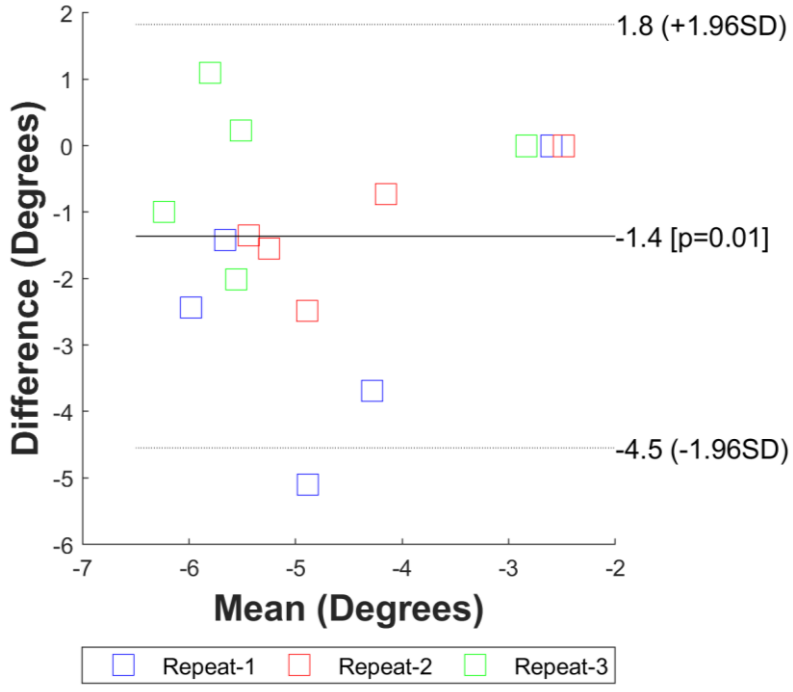

Figure E-6 Bland-Altman plot comparing motion capture and bead MBIR derived abduction-adduction angle kinematics during a static task.

E.1.3 Internal-External Rotation

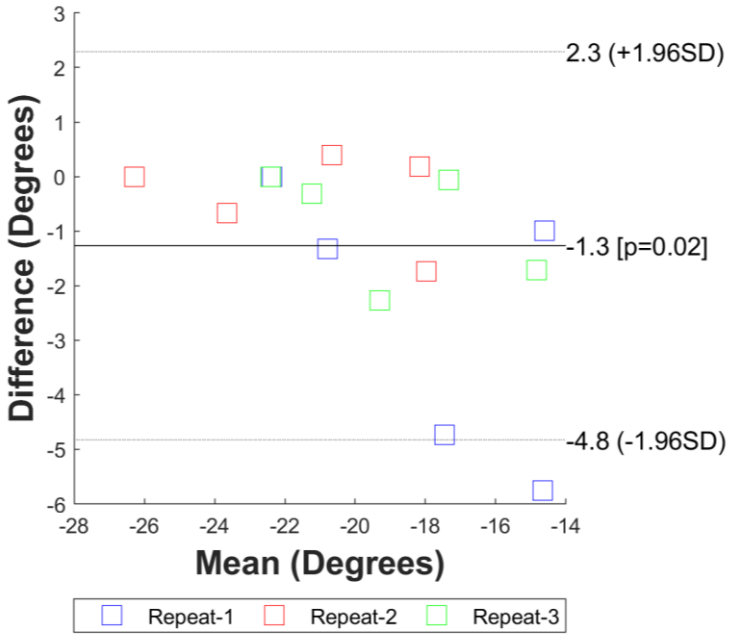

Figure E-7 Bland-Altman plot comparing bead MBIR and MBIR derived internal-external rotation angle kinematics during a static task.

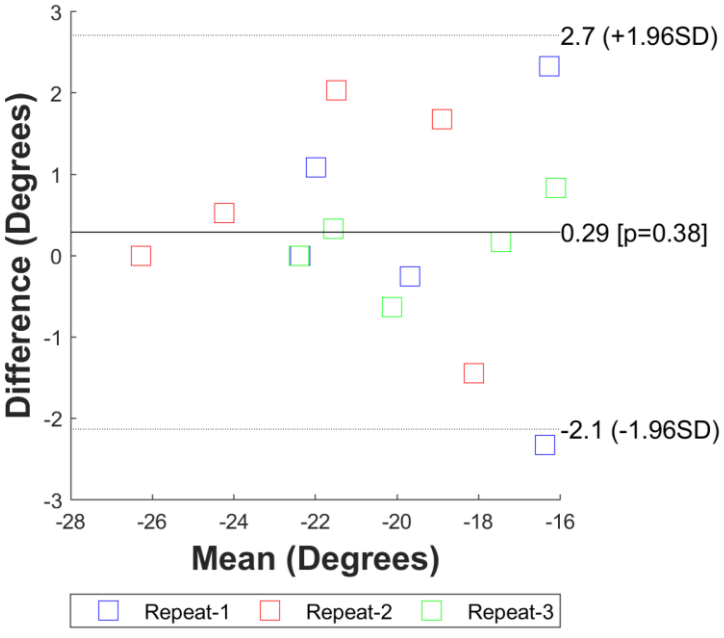

Figure E-8 Bland-Altman plot comparing motion capture and MBIR derived internal-external rotation angle kinematics during a static task.

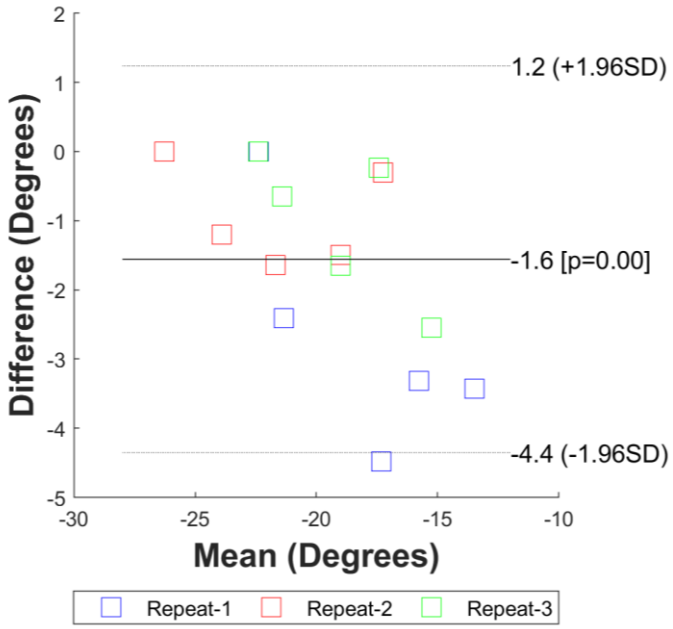

Figure E-9 Bland-Altman plot comparing motion capture and bead MBIR derived internal-external rotation angle kinematics during a static task.

E.1.4 Anterior-Posterior Translation

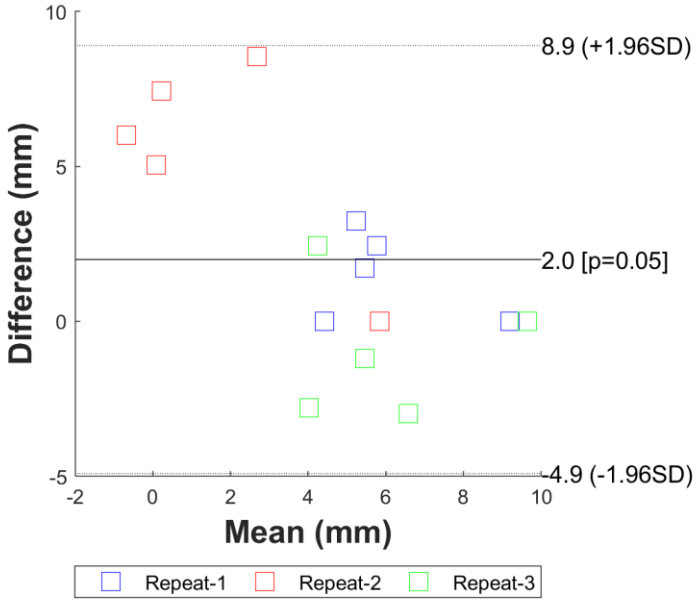

Figure E-10 Bland-Altman plot comparing bead MBIR and MBIR derived anterior-posterior translation kinematics during a static task.

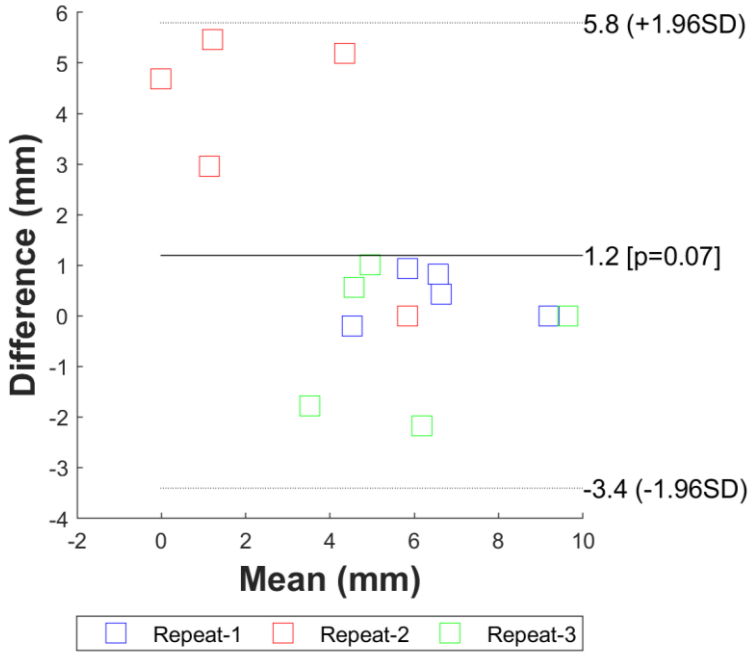

Figure E-11 Bland-Altman plot comparing motion capture and MBIR derived anterior-posterior translation kinematics during a static task.

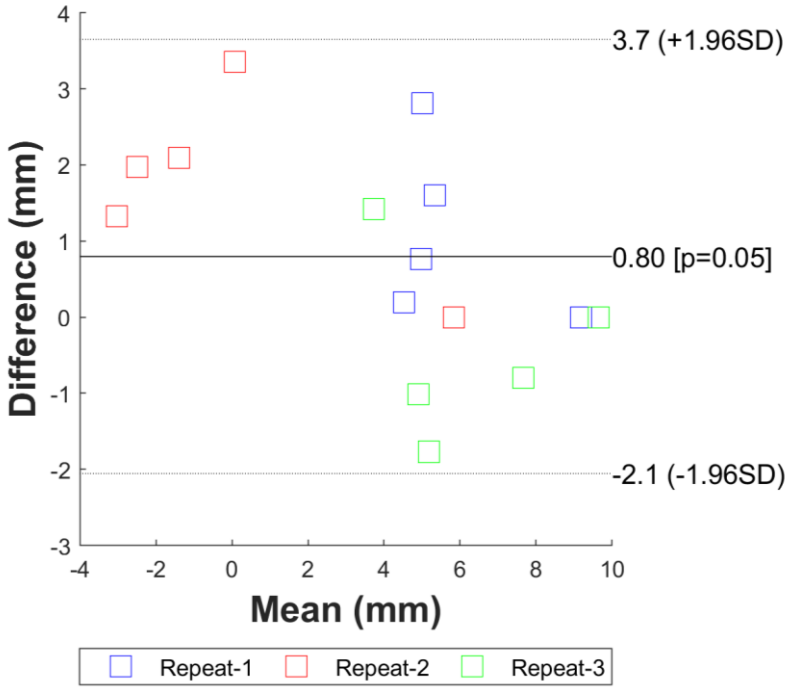

Figure E-12 Bland-Altman plot comparing motion capture and bead MBIR derived anterior-posterior translation kinematics during a static task.

E.1.5 Superior-Inferior Translation

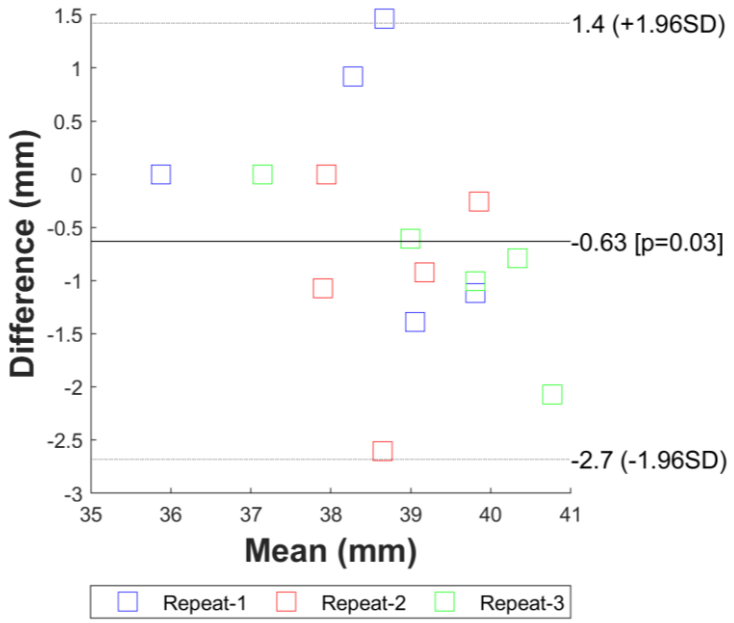

Figure E-13 Bland-Altman plot comparing bead MBIR and MBIR derived superior-inferior translation kinematics during a static task.

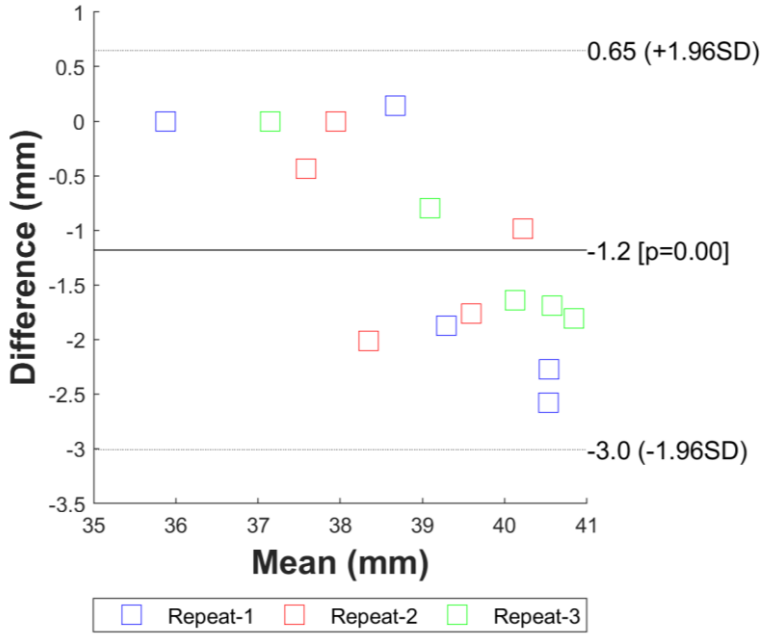

Figure E-14 Bland-Altman plot comparing motion capture and MBIR derived superior-inferior translation kinematics during a static task.

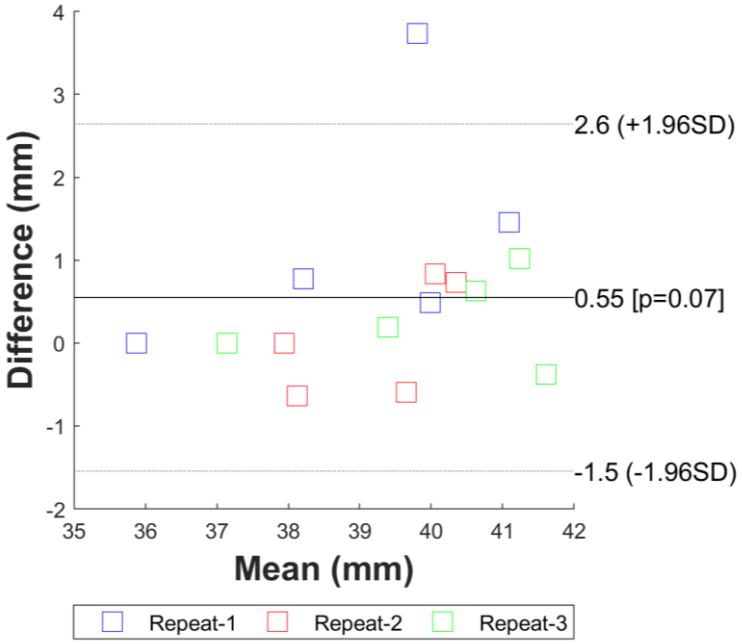

Figure E-15 Bland-Altman plot comparing motion capture and bead MBIR derived superior-inferior translation kinematics during a static task.

E.1.6 Medial-Lateral Translation

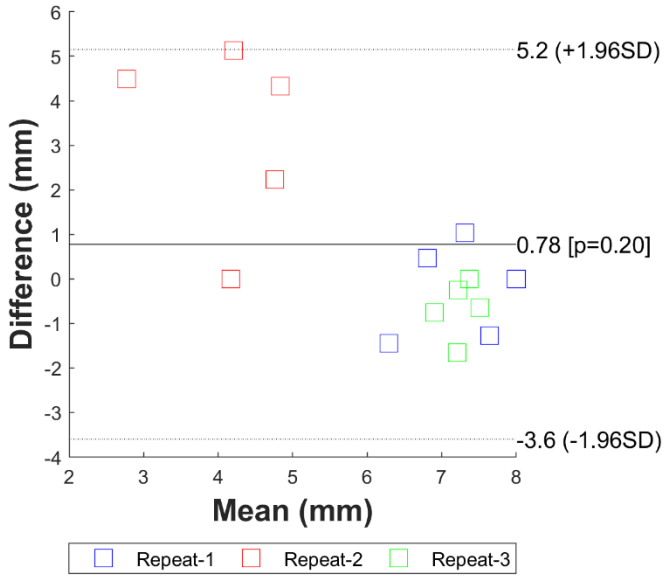

Figure E-16 Bland-Altman plot comparing bead MBIR and MBIR derived medial-lateral translation kinematics during a static task.

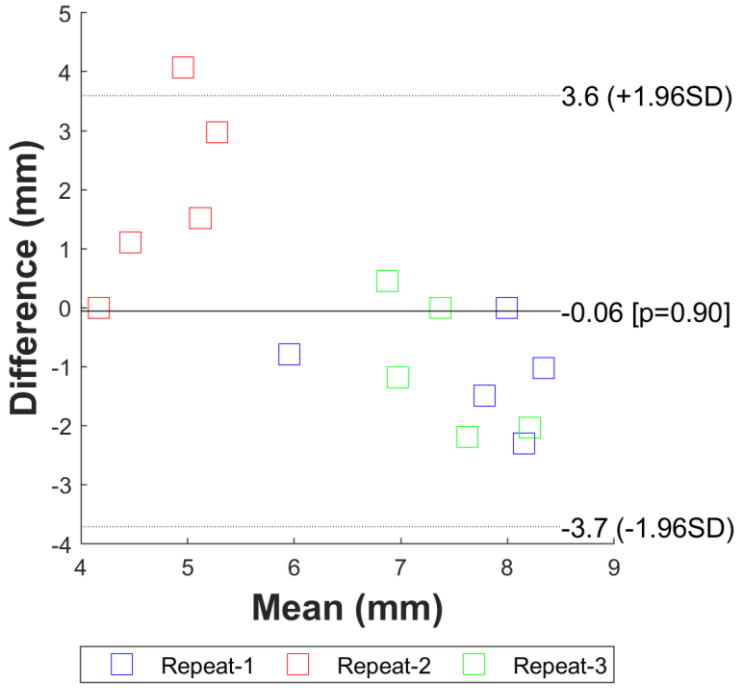

Figure E-17 Bland-Altman plot comparing motion capture and MBIR derived medial-lateral translation kinematics during a static task.

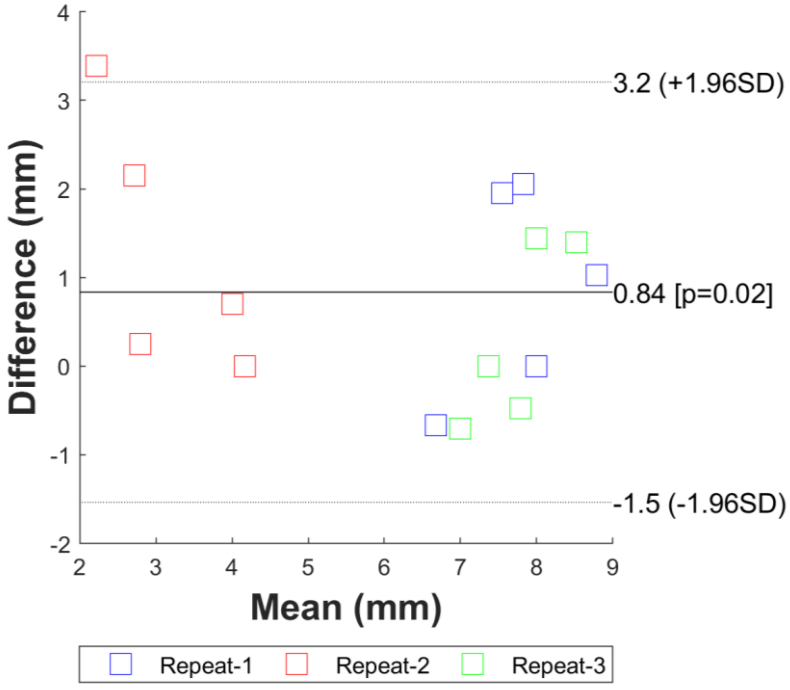

Figure E-18 Bland-Altman plot comparing motion capture and bead MBIR derived medial-lateral translation kinematics during a static task.

E.2 Phantom Slow Dynamic Task

E.2.1 Flexion Extension Angle

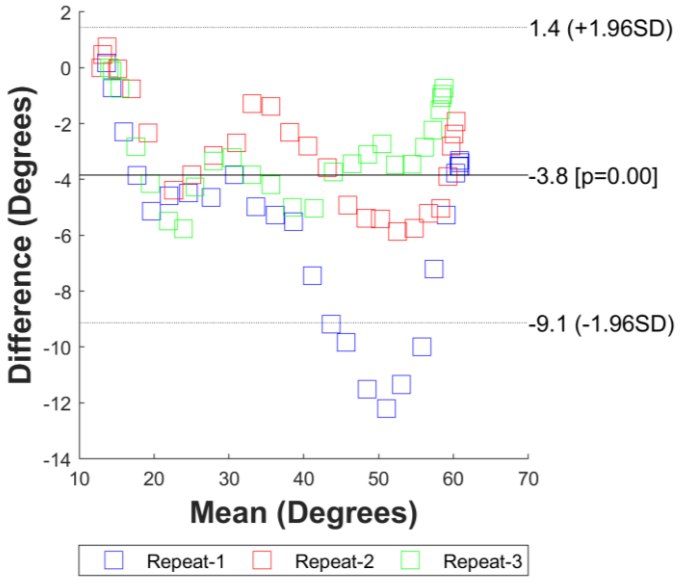

Figure E-19 Bland-Altman plot comparing bead MBIR and MBIR derived flexion-extension angle kinematics during a slow dynamic task.

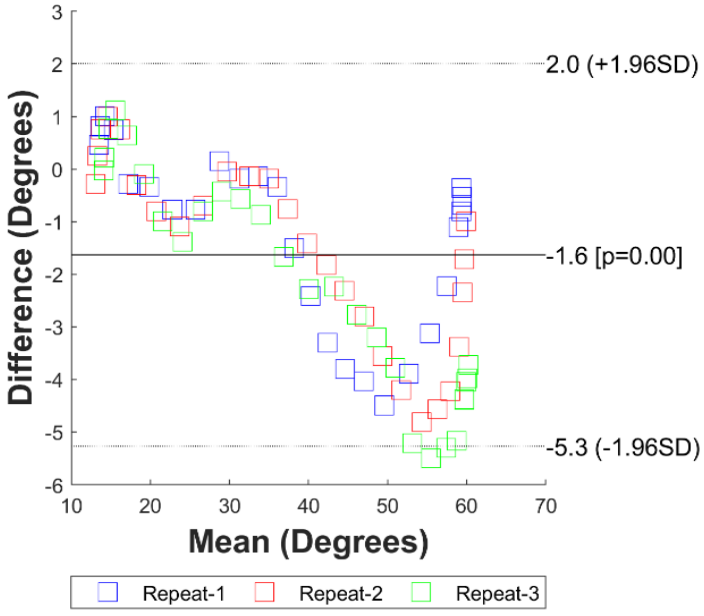

Figure E-20 Bland-Altman plot comparing motion capture and MBIR derived flexion-extension angle kinematics during a slow dynamic task.

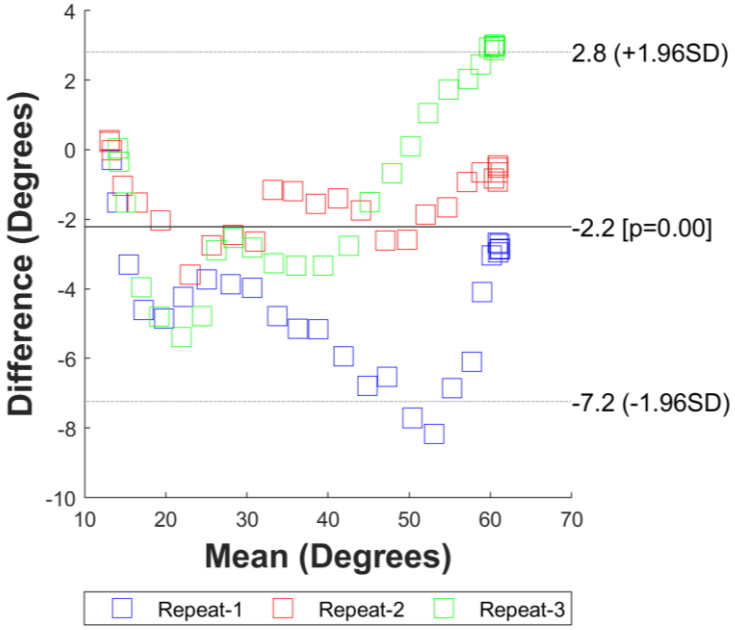

Figure E-21 Bland-Altman plot comparing motion capture and bead MBIR derived flexion-extension angle kinematics during a slow dynamic task.

E.2.2 Abduction-Adduction Angle

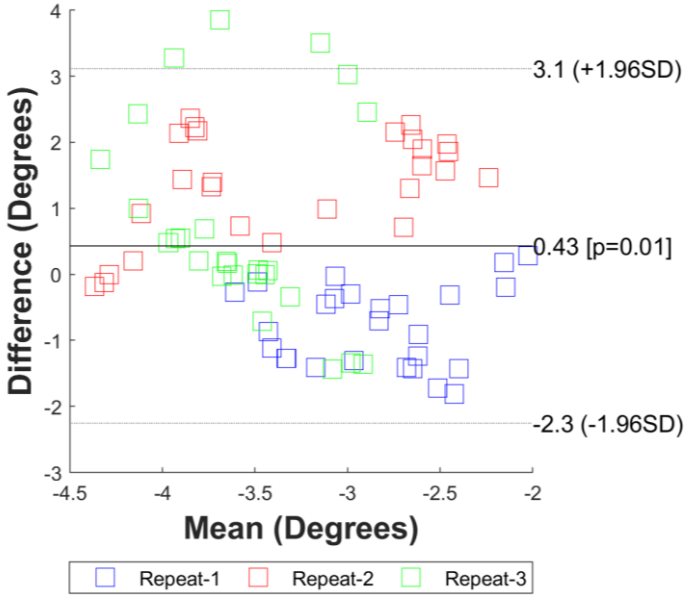

Figure E-22 Bland-Altman plot comparing bead MBIR and MBIR derived abduction-adduction angle kinematics during a slow dynamic task.

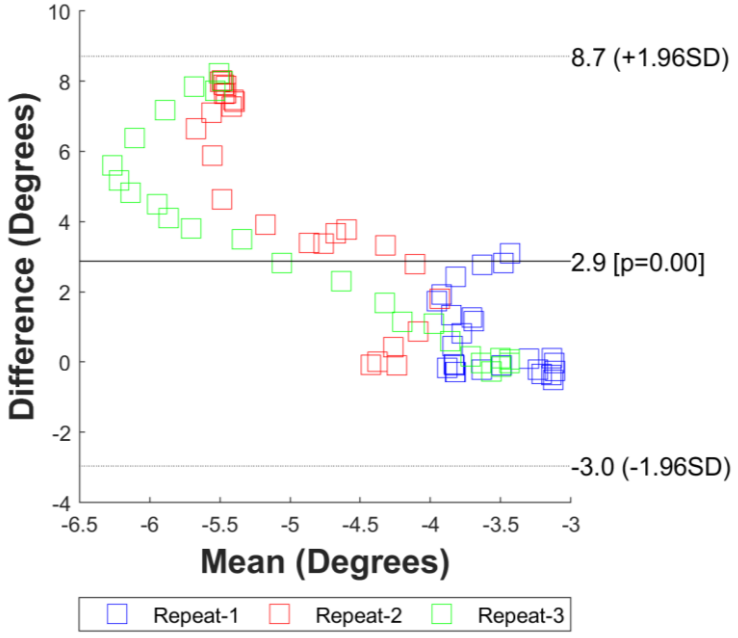

Figure E-23 Bland-Altman plot comparing motion capture and MBIR derived abduction-adduction angle kinematics during a slow dynamic task.

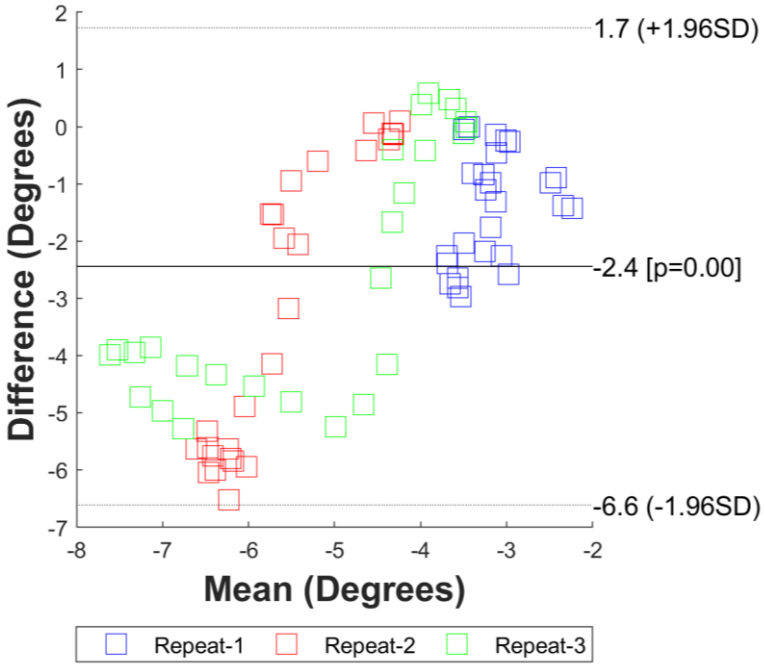

Figure E-24 Bland-Altman plot comparing motion capture and bead MBIR derived abduction-adduction angle kinematics during a slow dynamic task.

E.2.3 Internal-External Rotation

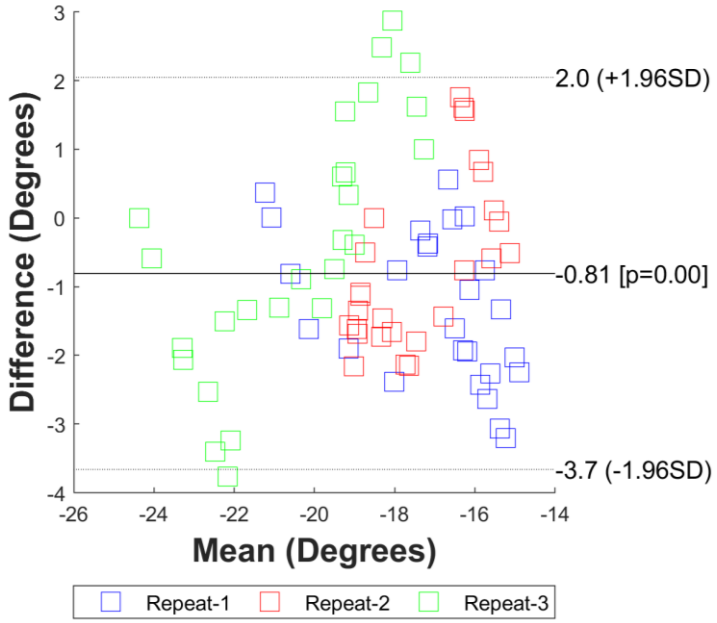

Figure E-25 Bland-Altman plot comparing bead MBIR and MBIR derived internal-external rotation angle kinematics during a slow dynamic task.

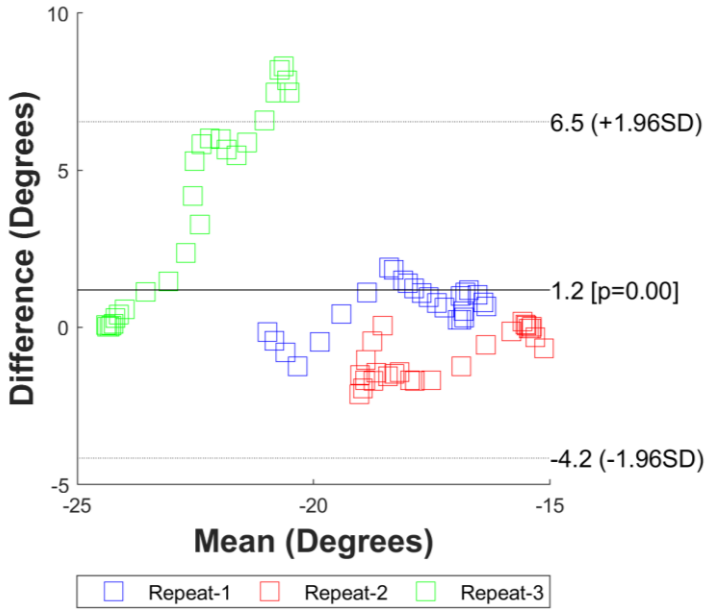

Figure E-26 Bland-Altman plot comparing motion capture and MBIR derived internal-external rotation angle kinematics during a slow dynamic task.

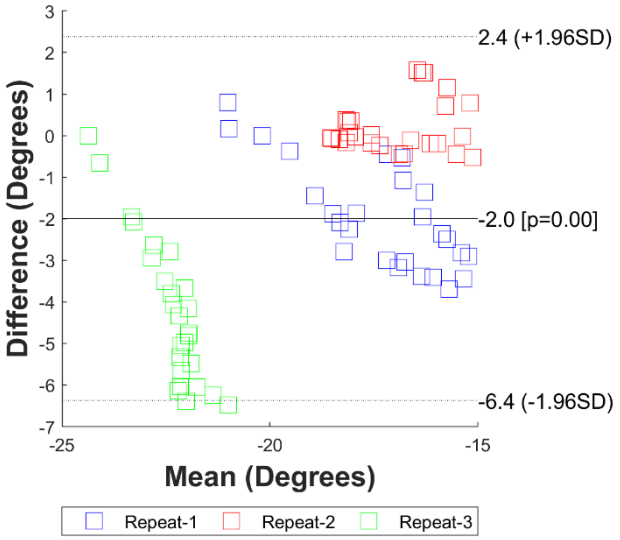

Figure E-27 Bland-Altman plot comparing motion capture and bead MBIR derived internal-external rotation angle kinematics during a slow dynamic task.

E.2.4 Anterior-Posterior Translation

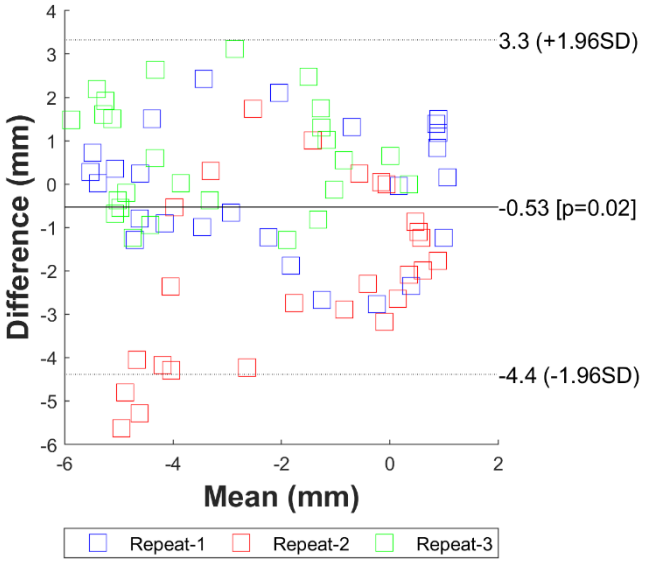

Figure E-28 Bland-Altman plot comparing bead MBIR and MBIR derived anterior-posterior translation kinematics during a slow dynamic task.

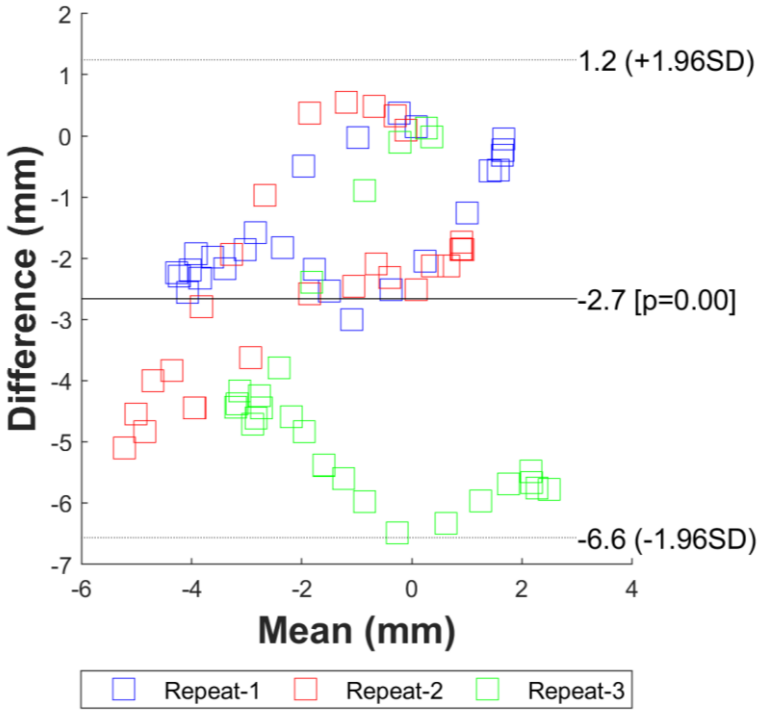

Figure E-29 Bland-Altman plot comparing motion capture and MBIR derived anterior-posterior translation kinematics during a slow dynamic task.

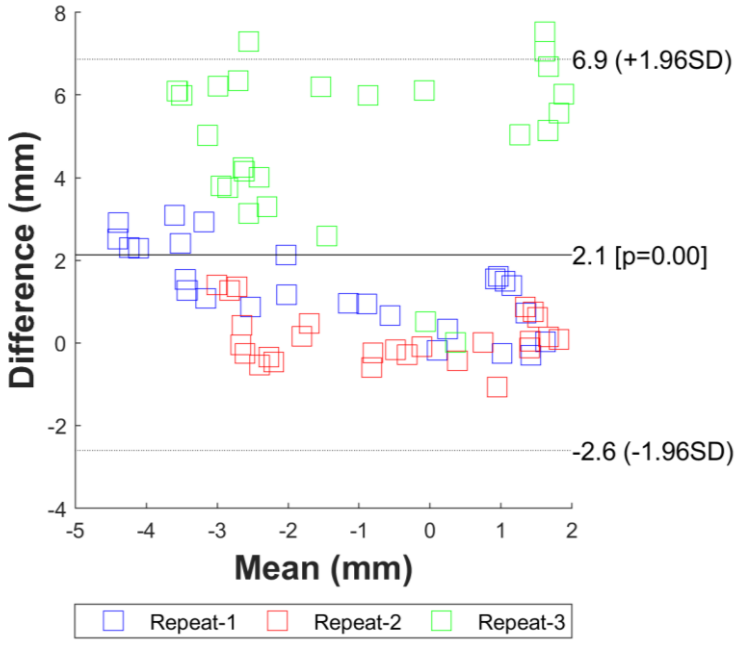

Figure E-30 Bland-Altman plot comparing motion capture and bead MBIR derived anterior-posterior translation kinematics during a slow dynamic task.

E.2.5 Superior-Inferior Translation

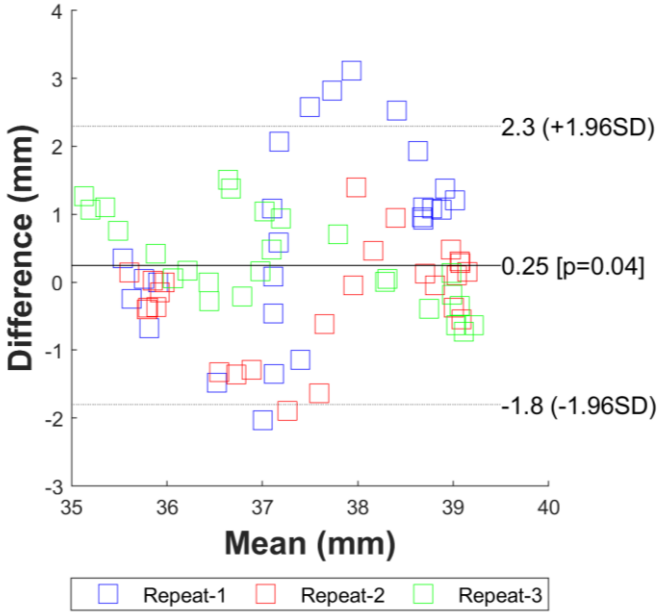

Figure E-31 Bland-Altman plot comparing bead MBIR and MBIR derived superior-inferior translation kinematics during a slow dynamic task.

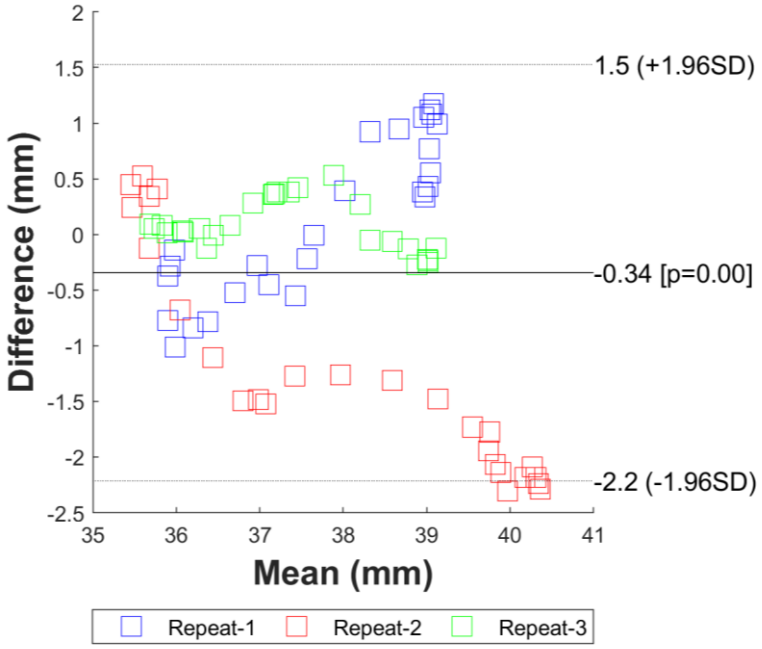

Figure E-32 Bland-Altman plot comparing motion capture and MBIR derived superior-inferior translation kinematics during a slow dynamic task.

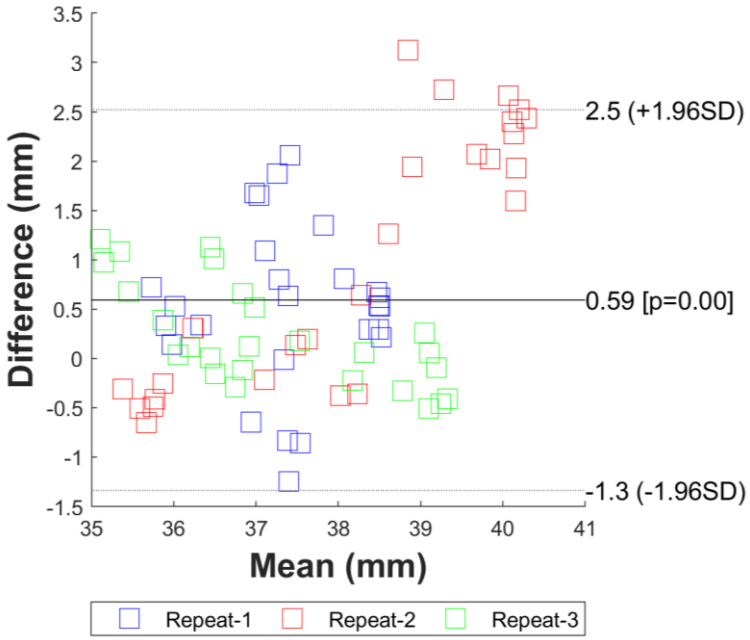

Figure E-33 Bland-Altman plot comparing motion capture and bead MBIR derived superior-inferior translation kinematics during a slow dynamic task.

E.2.6 Medial-Lateral Translation

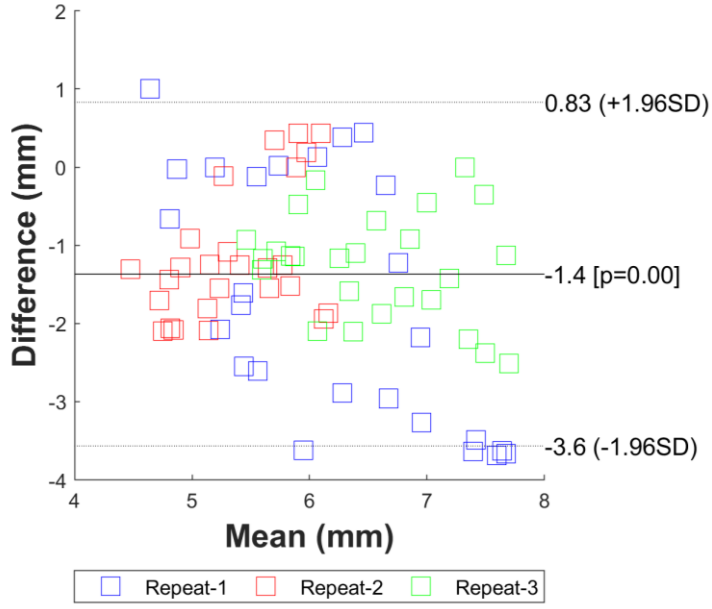

Figure E-34 Bland-Altman plot comparing bead MBIR and MBIR derived medial-lateral translation kinematics during a slow dynamic task.

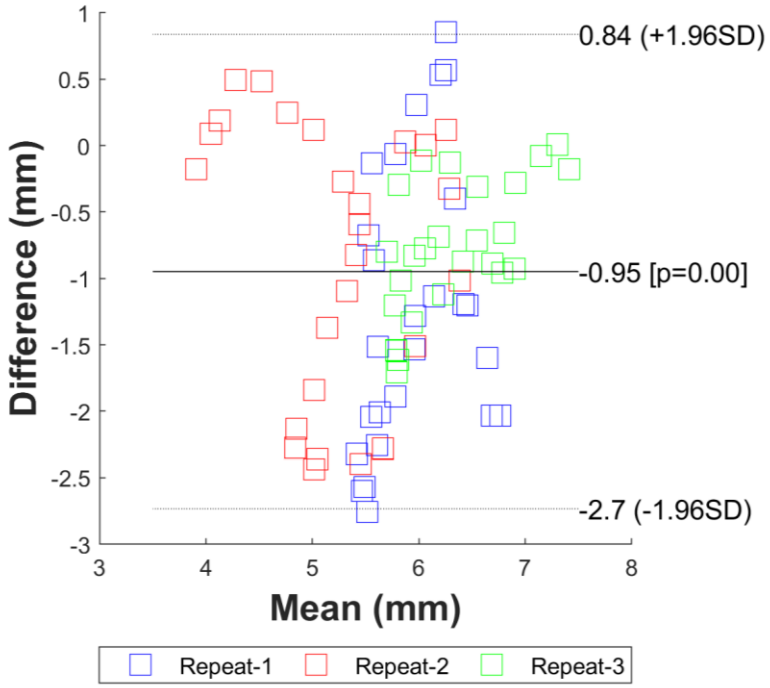

Figure E-35 Bland-Altman plot comparing motion capture and MBIR derived medial-lateral translation kinematics during a slow dynamic task.

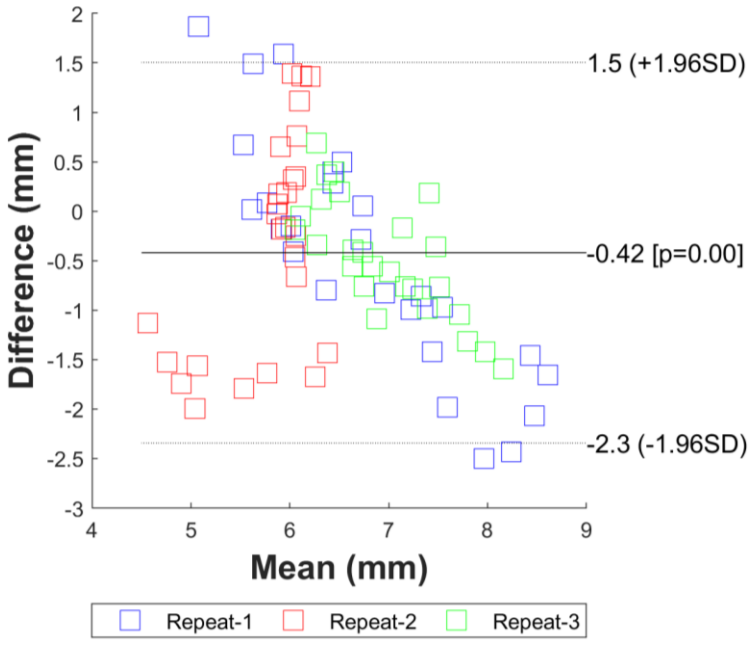

Figure E-36 Bland-Altman plot comparing motion capture and bead MBIR derived medial-lateral translation kinematics during a slow dynamic task.

E.3 Phantom Medium Dynamic Task

E.3.1 Flexion-Extension Angle

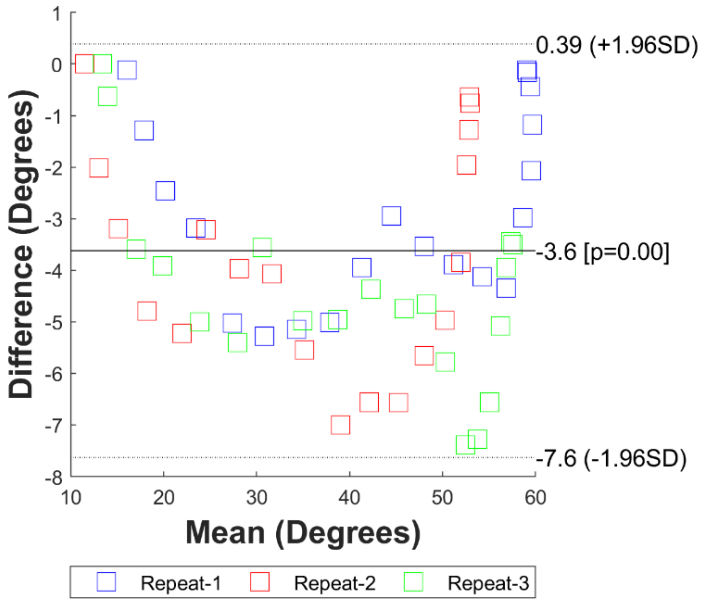

Figure E-37 Bland-Altman plot comparing bead MBIR and MBIR derived flexion-extension angle kinematics during a medium dynamic task.

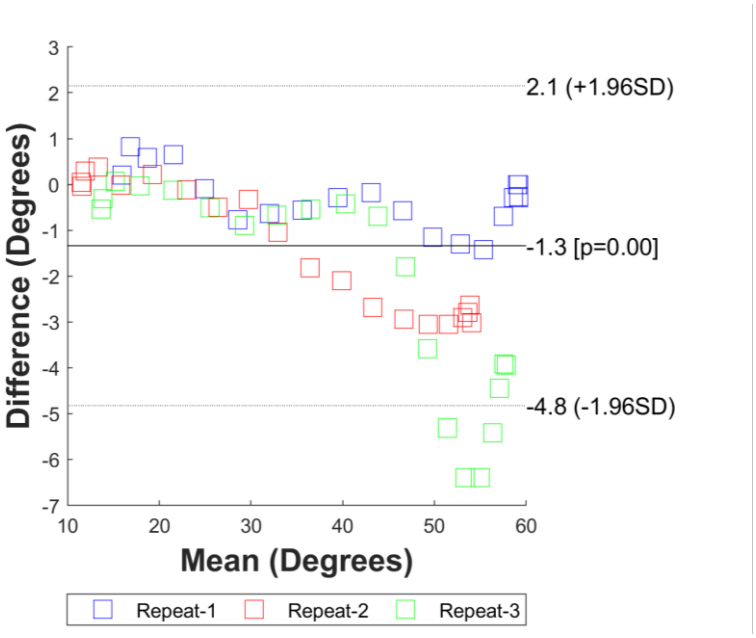

Figure E-38 Bland-Altman plot comparing motion capture and MBIR derived flexion-extension angle kinematics during a medium dynamic task.

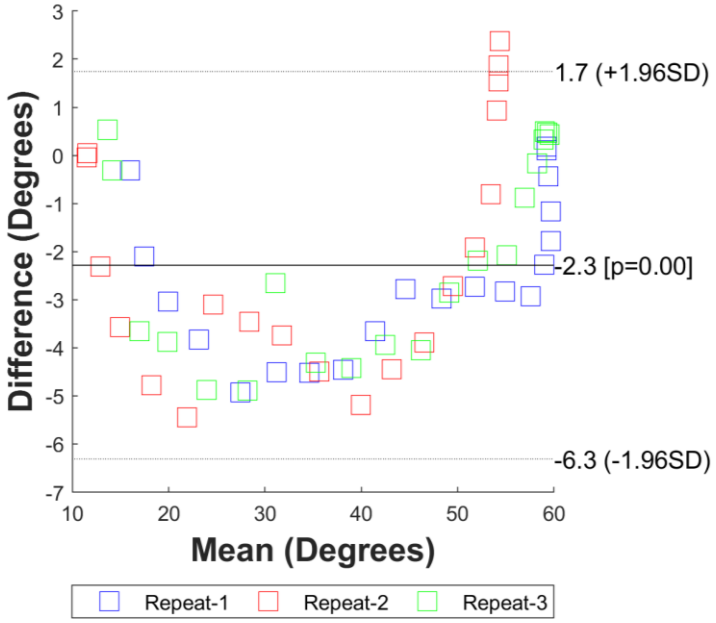

Figure E-39 Bland-Altman plot comparing motion capture and bead MBIR derived flexion-extension angle kinematics during a medium dynamic task.

E.3.2 Abduction-Adduction Angle

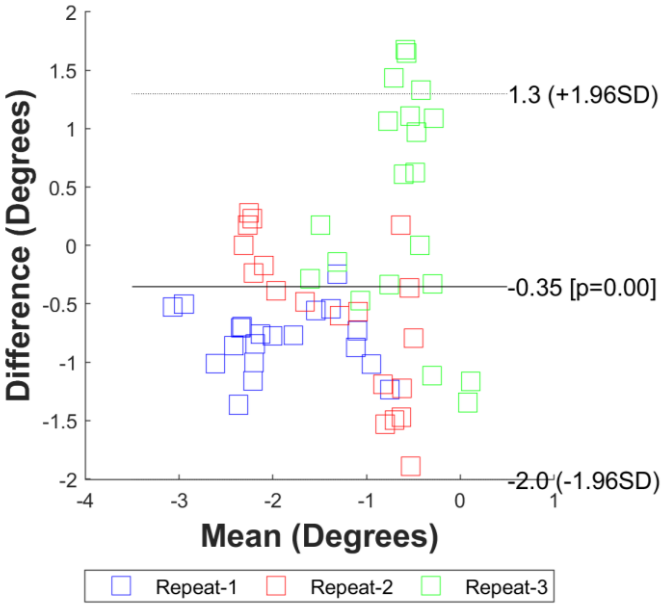

Figure E-40 Bland-Altman plot comparing bead MBIR and MBIR derived abduction-adduction angle kinematics during a medium dynamic task.

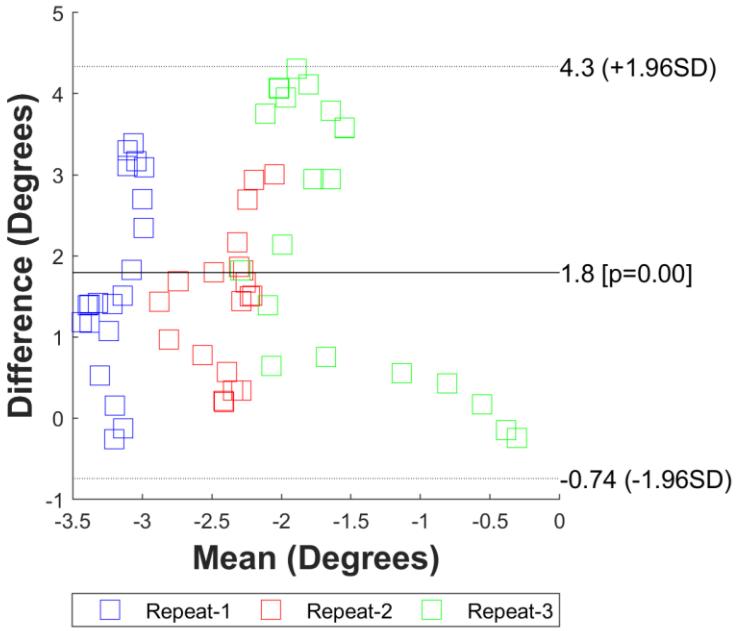

Figure E-41 Bland-Altman plot comparing motion capture and MBIR derived abduction-adduction angle kinematics during a medium dynamic task.

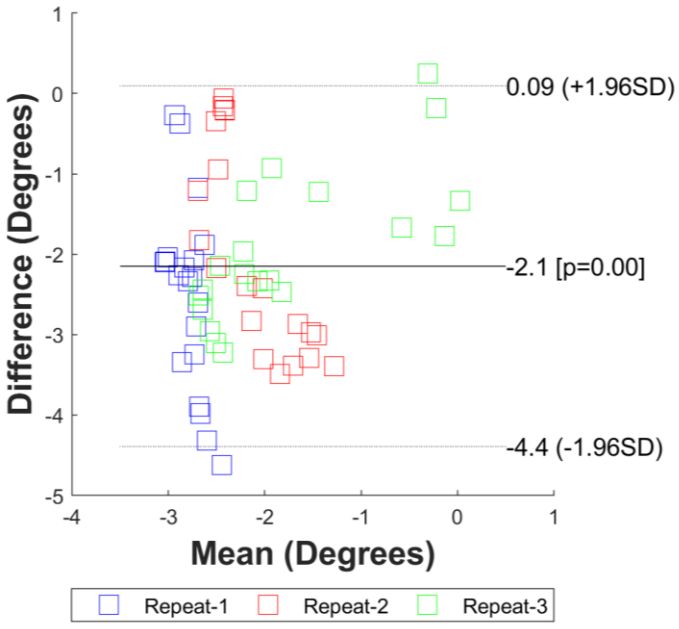

Figure E-42 Bland-Altman plot comparing motion capture and bead MBIR derived abduction-adduction angle kinematics during a medium dynamic task.

E.3.3 Internal-External Rotation

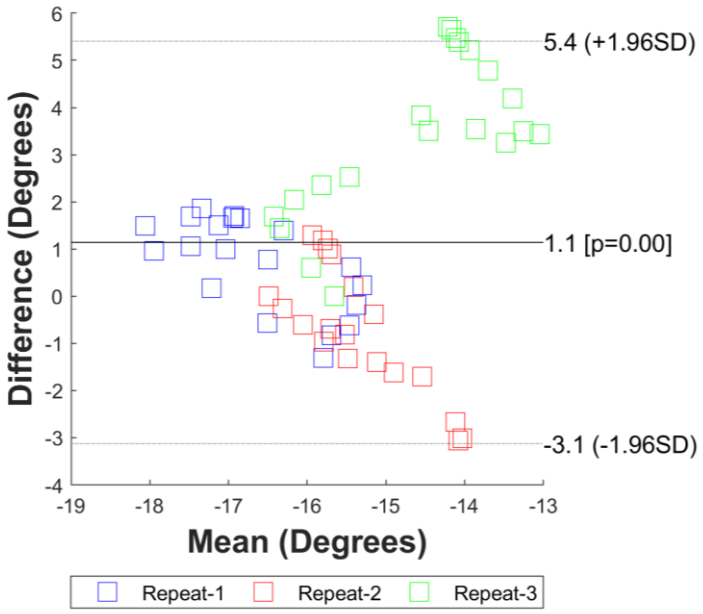

Figure E-43 Bland-Altman plot comparing bead MBIR and MBIR derived internal-external rotation angle kinematics during a medium dynamic task.

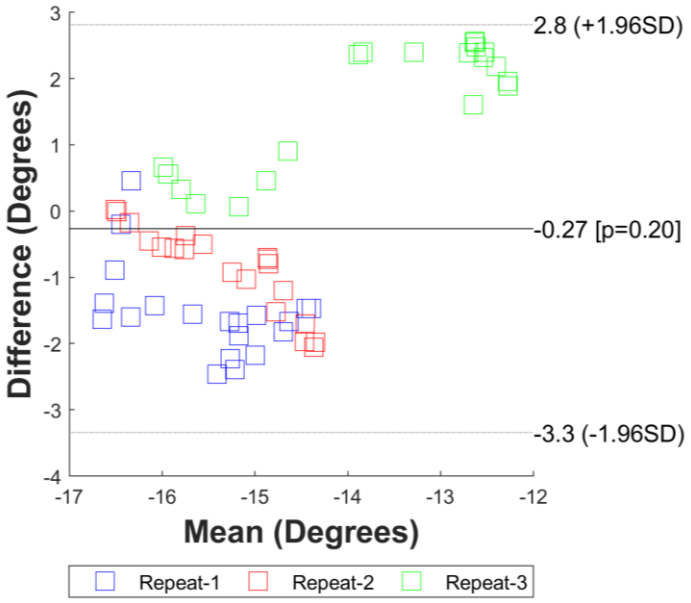

Figure E-44 Bland-Altman plot comparing motion capture and MBIR derived internal-external rotation angle kinematics during a medium dynamic task.

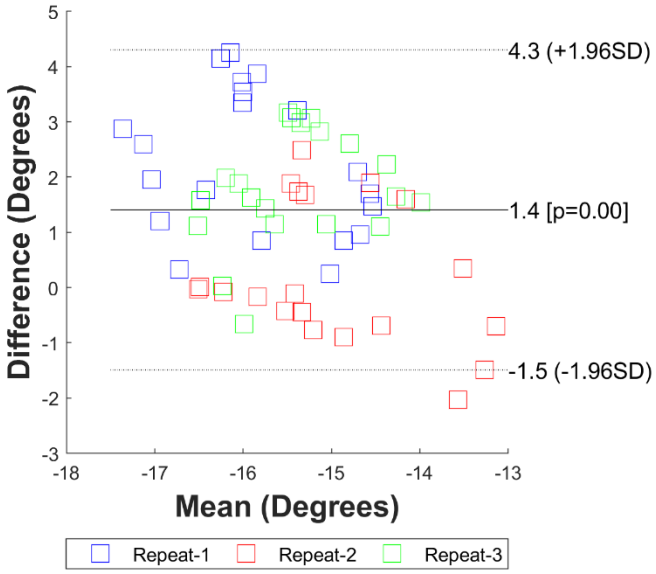

Figure E-45 Bland-Altman plot comparing motion capture and bead MBIR derived internal-external rotation angle kinematics during a medium dynamic task.

E.3.4 Anterior-Posterior Translation

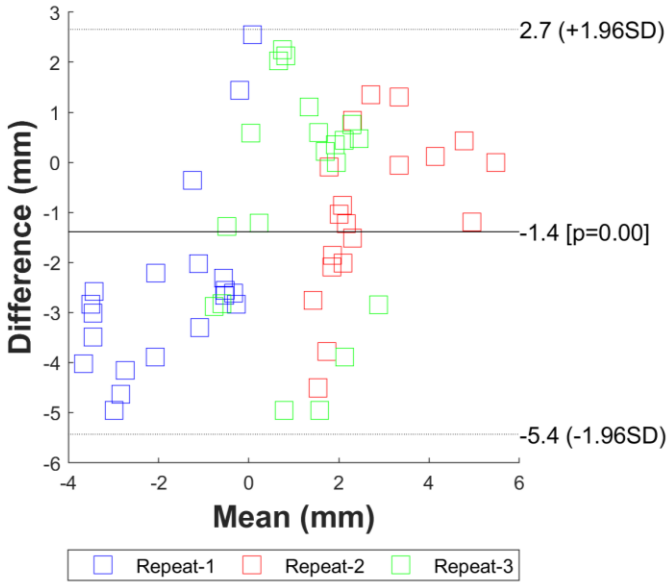

Figure E-46 Bland-Altman plot comparing bead MBIR and MBIR derived anterior-posterior translation kinematics during a medium dynamic task.

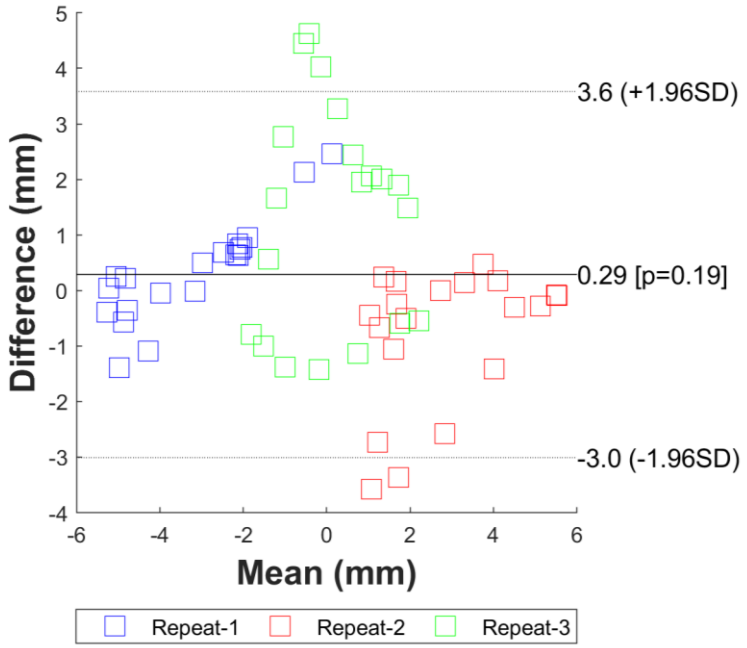

Figure E-47 Bland-Altman plot comparing motion capture and MBIR derived anterior-posterior translation kinematics during a medium dynamic task.

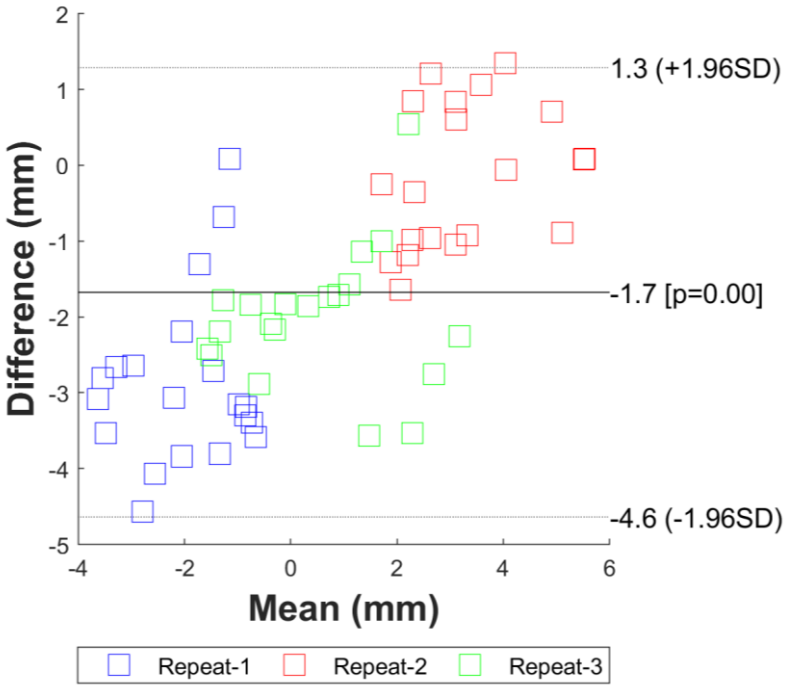

Figure E-48 Bland-Altman plot comparing motion capture and bead MBIR derived anterior-posterior translation kinematics during a medium dynamic task.

E.3.5 Superior-Inferior Translation

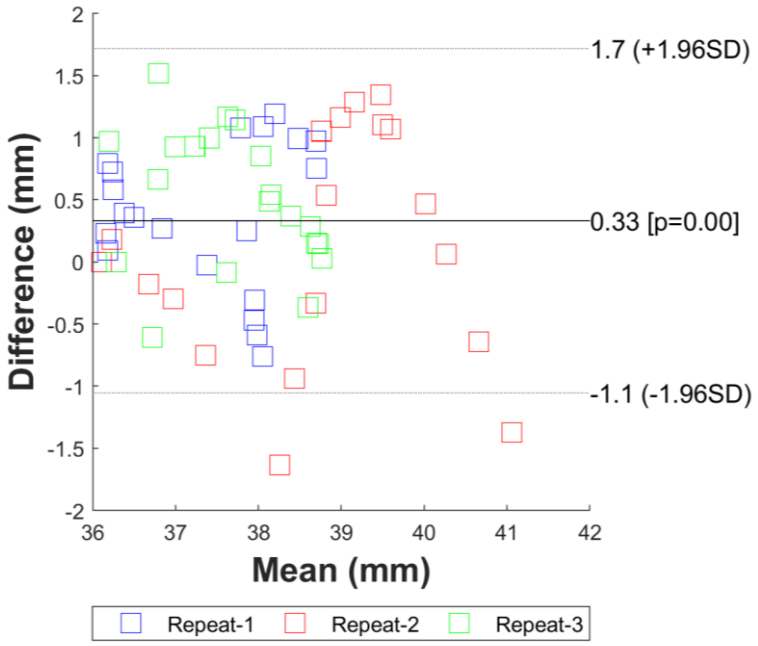

Figure E-49 Bland-Altman plot comparing bead MBIR and MBIR derived superior-inferior translation kinematics during a medium dynamic task.

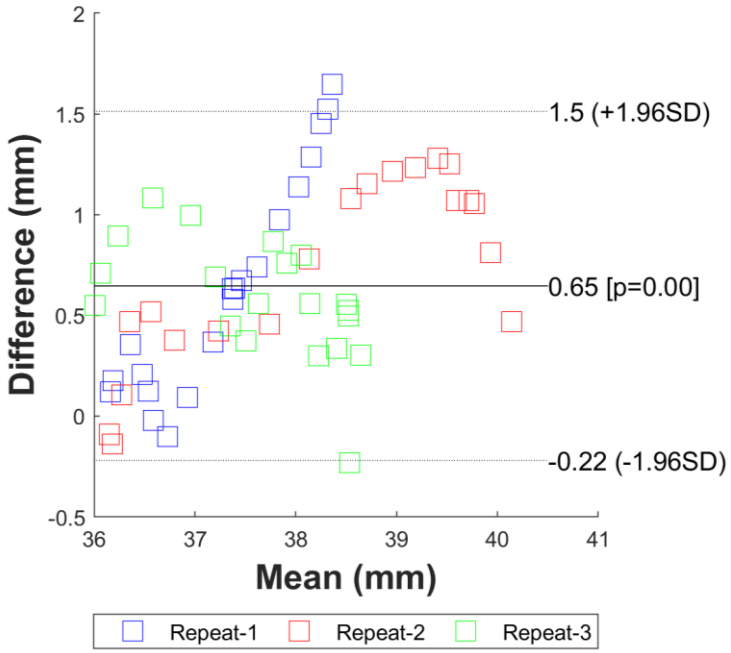

Figure E-50 Bland-Altman plot comparing motion capture and MBIR derived superior-inferior translation kinematics during a medium dynamic task.

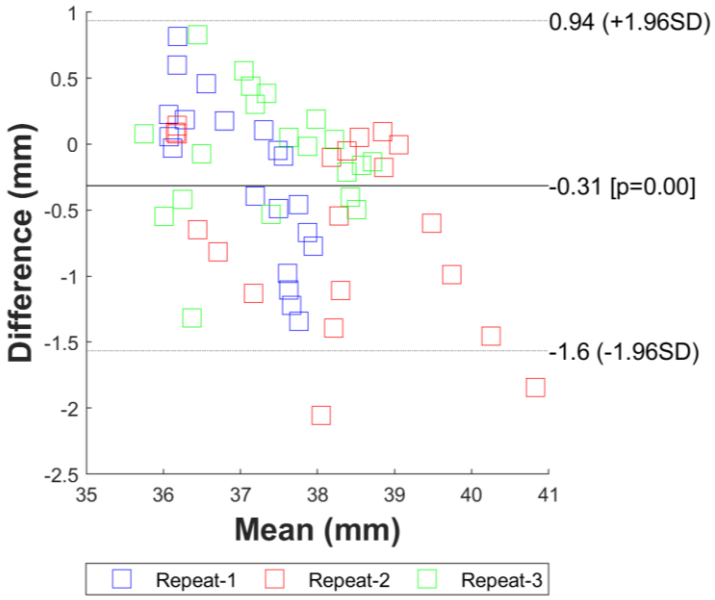

Figure E-51 Bland-Altman plot comparing motion capture and bead MBIR derived superior-inferior translation kinematics during a medium dynamic task.

E.3.6 Medial-Lateral Translation

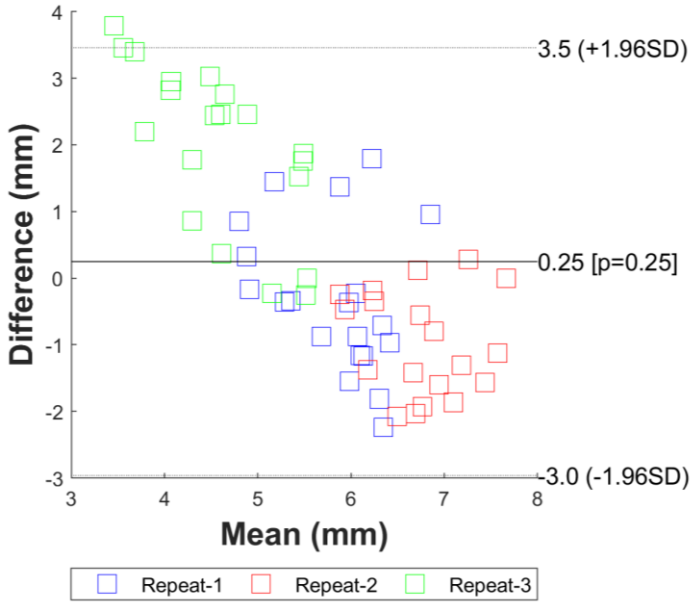

Figure E-52 Bland-Altman plot comparing bead MBIR and MBIR derived medial-lateral translation kinematics during a medium dynamic task.

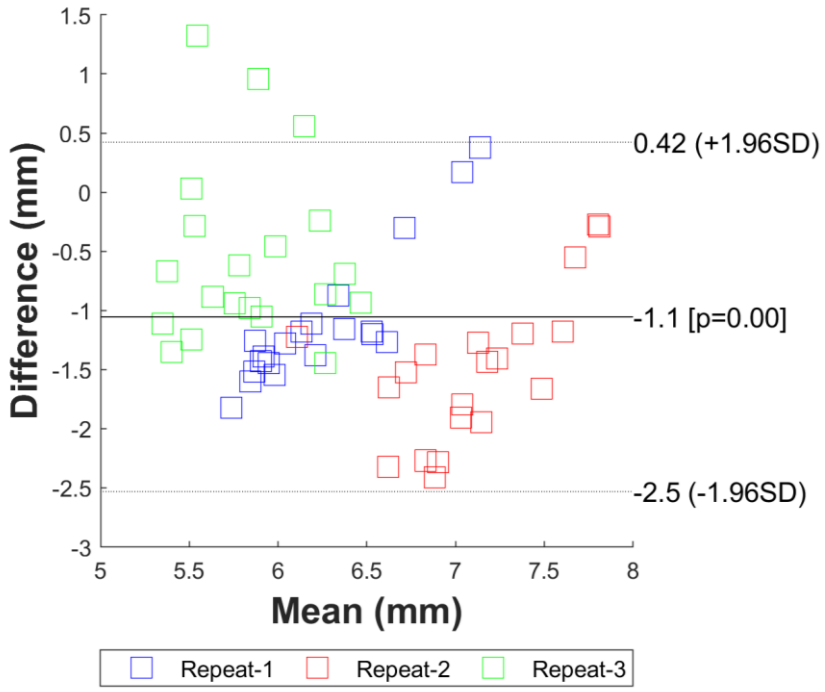

Figure E-53 Bland-Altman plot comparing motion capture and MBIR derived medial-lateral translation kinematics during a medium dynamic task.

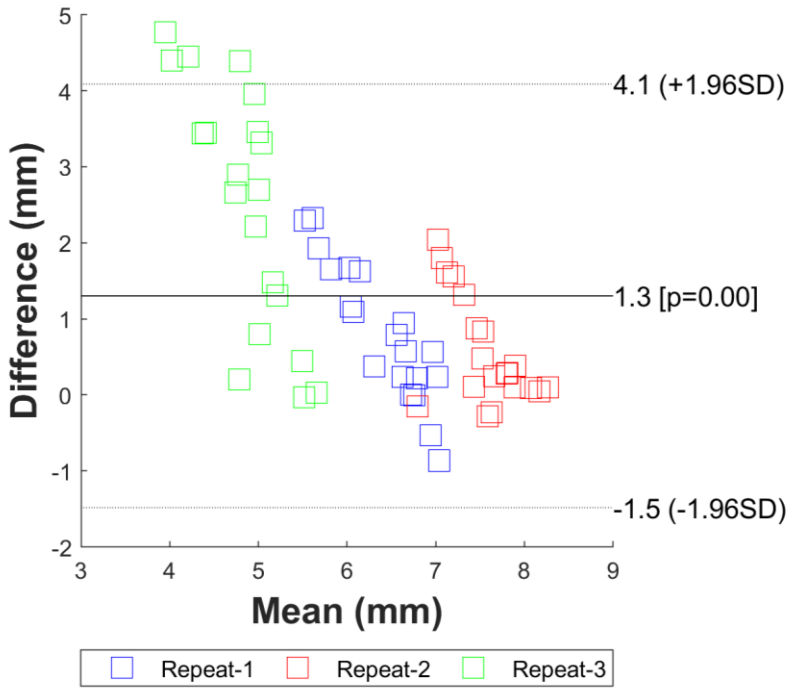

Figure E-54 Bland-Altman plot comparing motion capture and bead MBIR derived medial-lateral translation kinematics during a medium dynamic task.

E.4 Phantom Fast Dynamic Task

E.4.1 Flexion Extension Angle

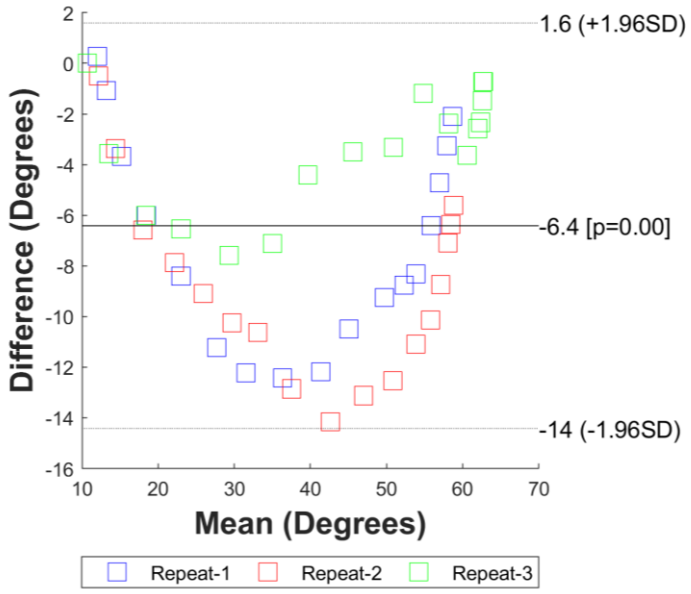

Figure E-55 Bland-Altman plot comparing bead MBIR and MBIR derived flexion-extension angle kinematics during a fast dynamic task.

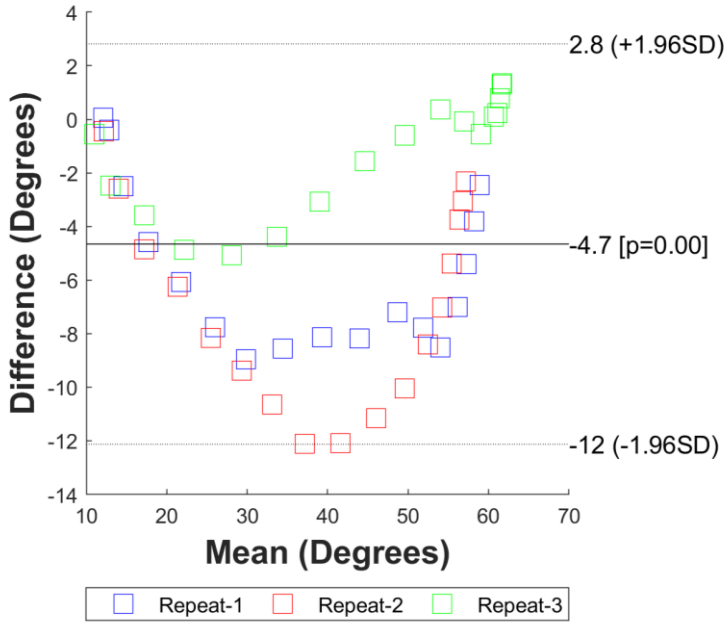

Figure E-56 Bland-Altman plot comparing motion capture and MBIR derived flexion-extension angle kinematics during a fast dynamic task.

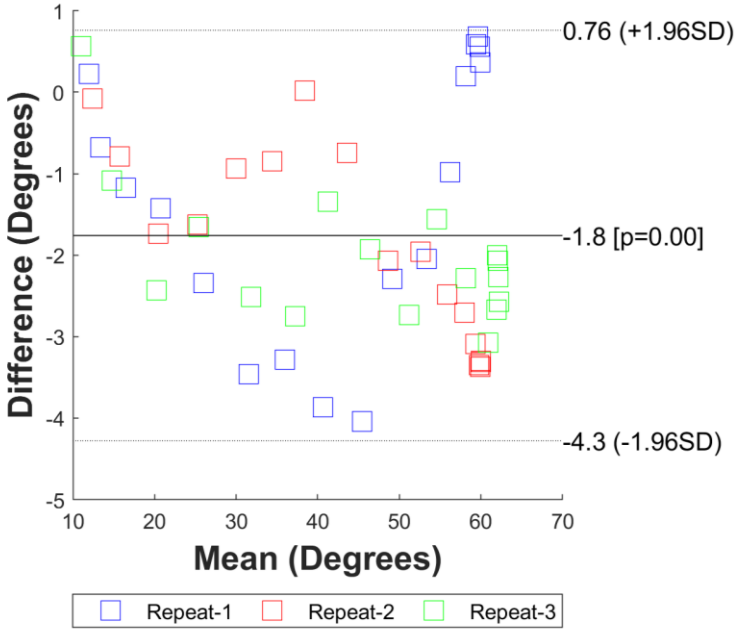

Figure E-57 Bland-Altman plot comparing motion capture and bead MBIR derived flexion-extension angle kinematics during a fast dynamic task.

E.4.2 Abduction-Adduction Angle

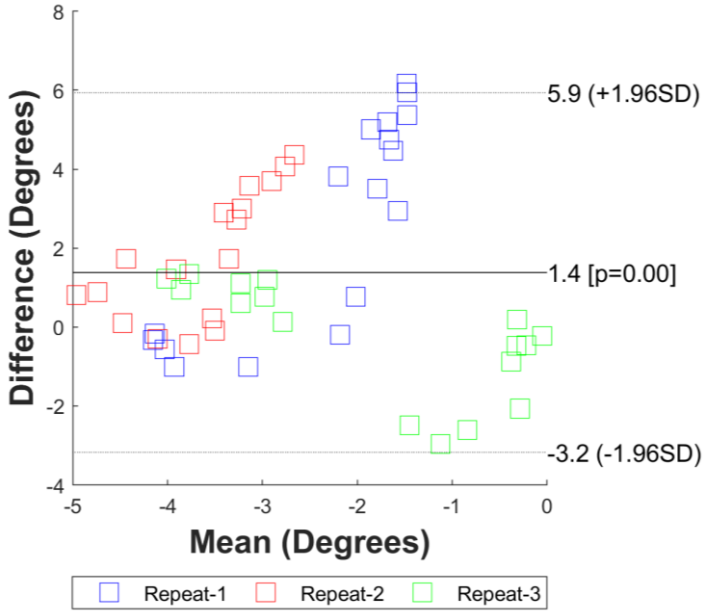

Figure E-58 Bland-Altman plot comparing bead MBIR and MBIR derived abduction-adduction angle kinematics during a fast dynamic task.

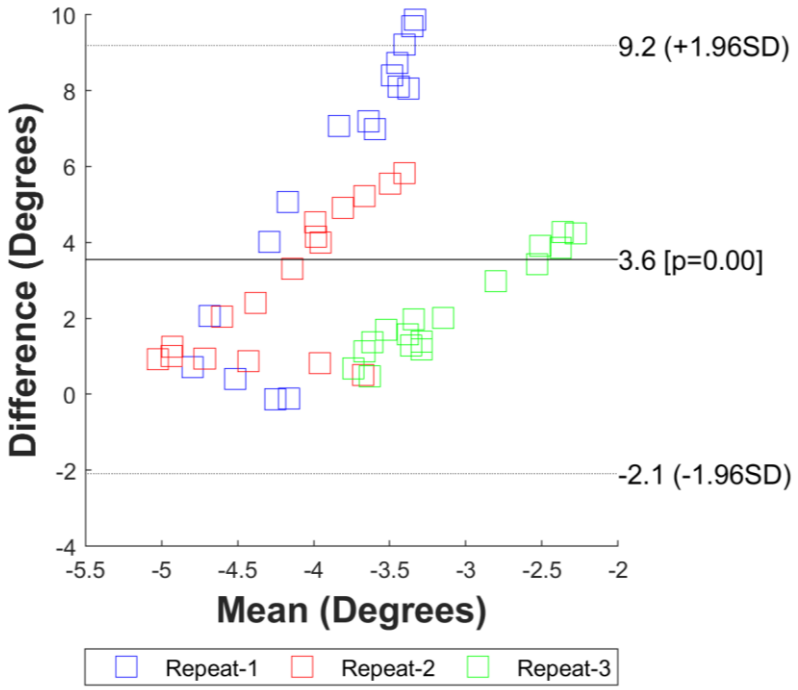

Figure E-59 Bland-Altman plot comparing motion capture and MBIR derived abduction-adduction angle kinematics during a fast dynamic task.

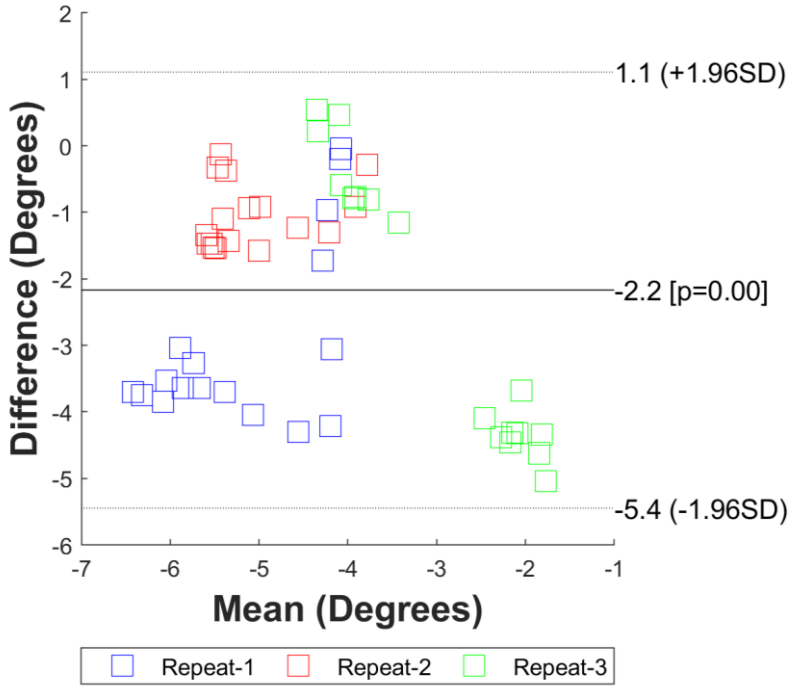

Figure E-60 Bland-Altman plot comparing motion capture and bead MBIR derived abduction-adduction angle kinematics during a fast dynamic task.

E.4.3 Internal-External Rotation

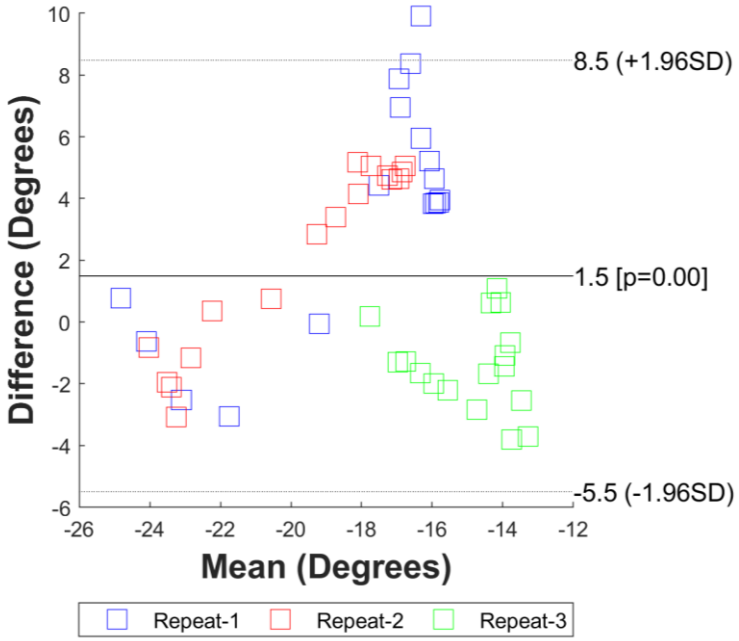

Figure E-61 Bland-Altman plot comparing bead MBIR and MBIR derived internal-external rotation angle kinematics during a fast dynamic task.

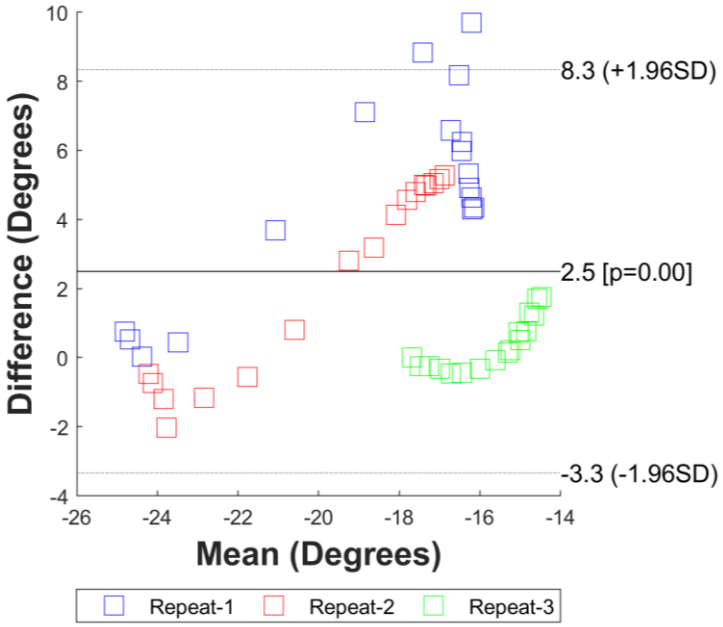

Figure E-62 Bland-Altman plot comparing motion capture and MBIR derived internal-external rotation angle kinematics during a fast dynamic task.

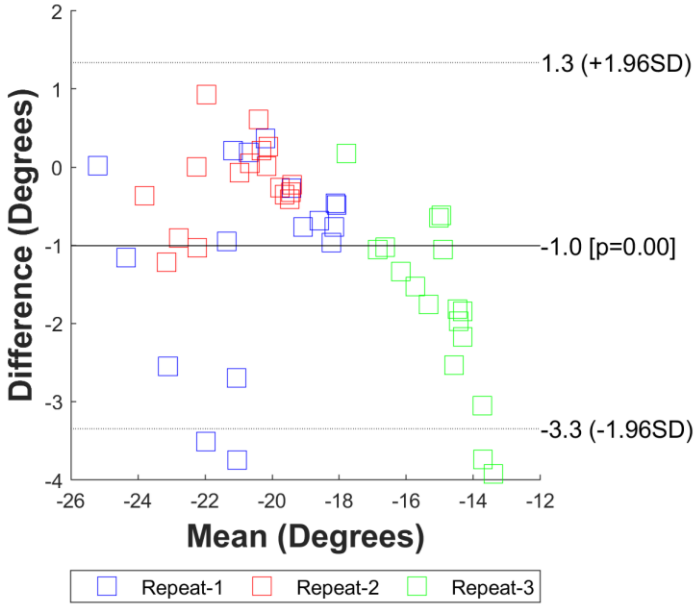

Figure E-63 Bland-Altman plot comparing motion capture and bead MBIR derived internal-external rotation angle kinematics during a fast dynamic task.

E.4.4 Anterior-Posterior Translation

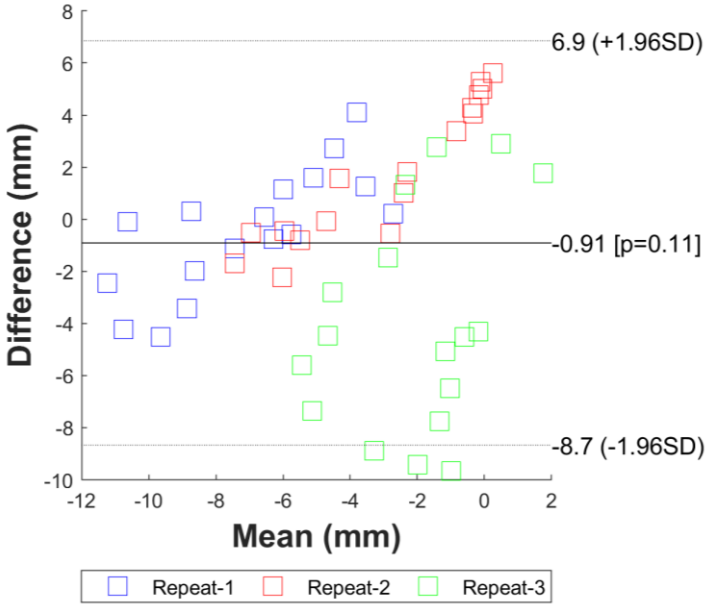

Figure E-64 Bland-Altman plot comparing bead MBIR and MBIR derived anterior-posterior translation kinematics during a fast dynamic task.

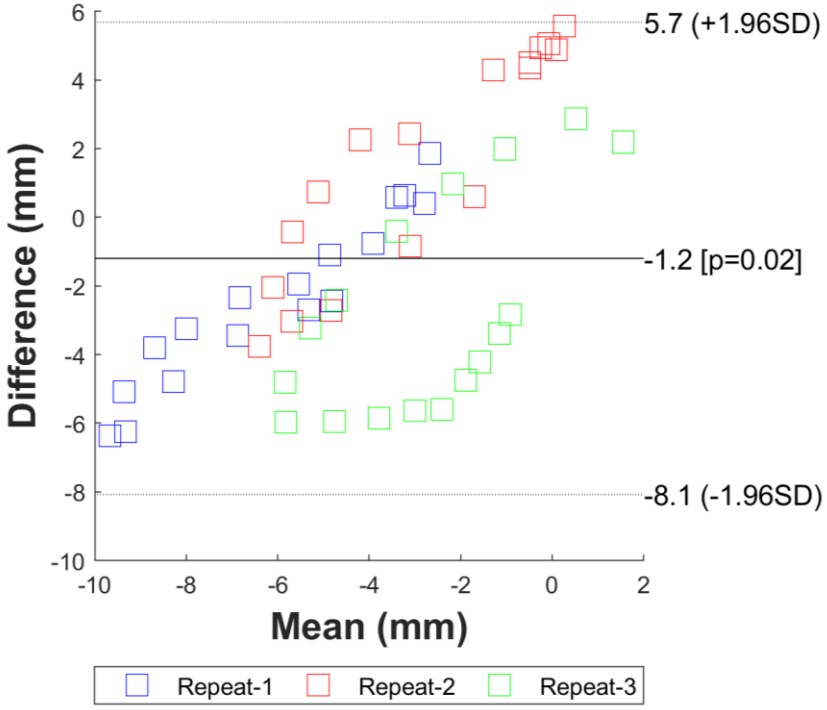

Figure E-65 Bland-Altman plot comparing motion capture and MBIR derived anterior-posterior translation kinematics during a fast dynamic task.

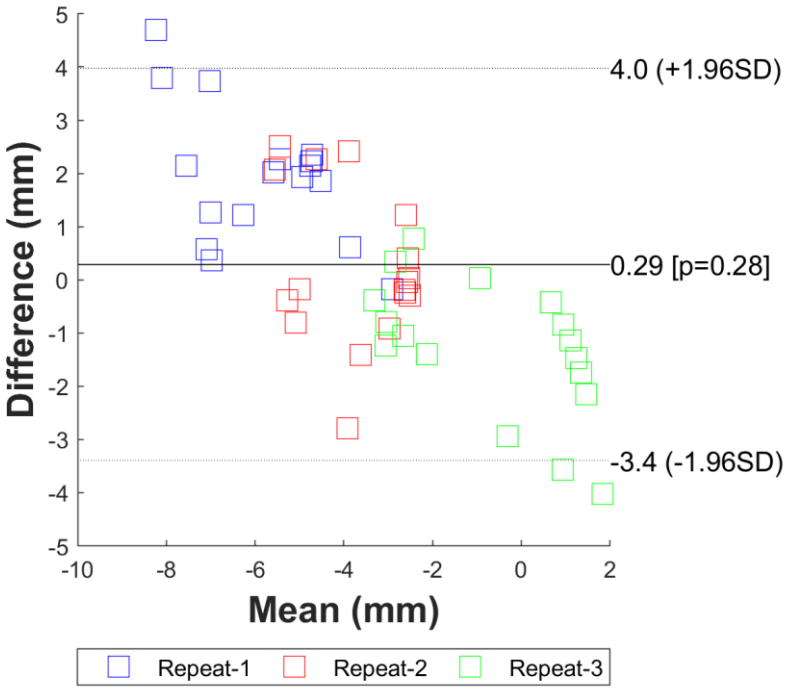

Figure E-66 Bland-Altman plot comparing motion capture and bead MBIR derived anterior-posterior translation kinematics during a fast dynamic task.

E.4.5 Superior-Inferior Translation

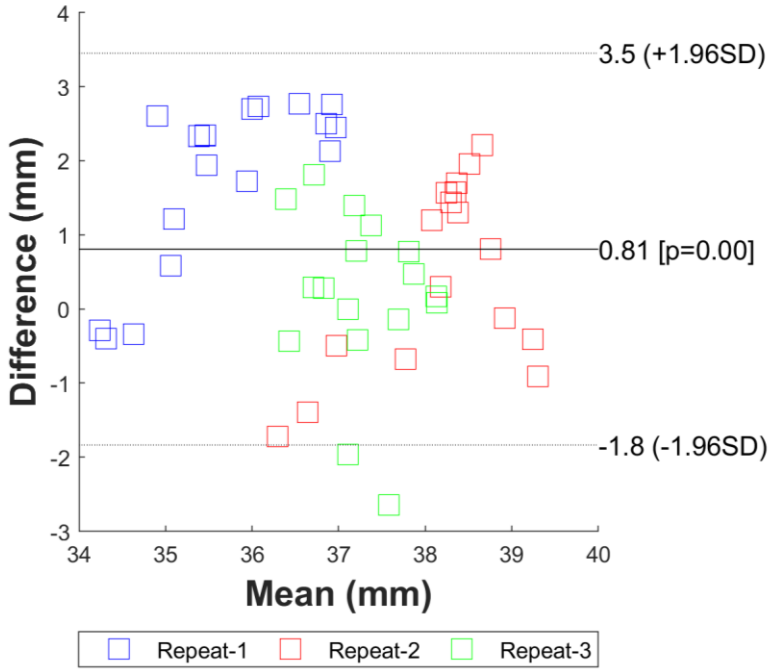

Figure E-67 Bland-Altman plot comparing bead MBIR and MBIR derived superior-inferior translation kinematics during a fast dynamic task.

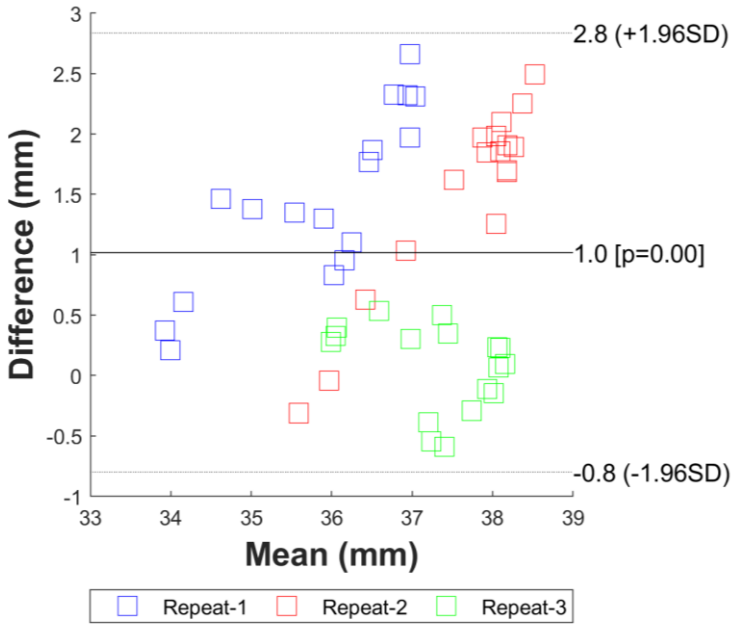

Figure E-68 Bland-Altman plot comparing motion capture and MBIR derived superior-inferior translation kinematics during a fast dynamic task.

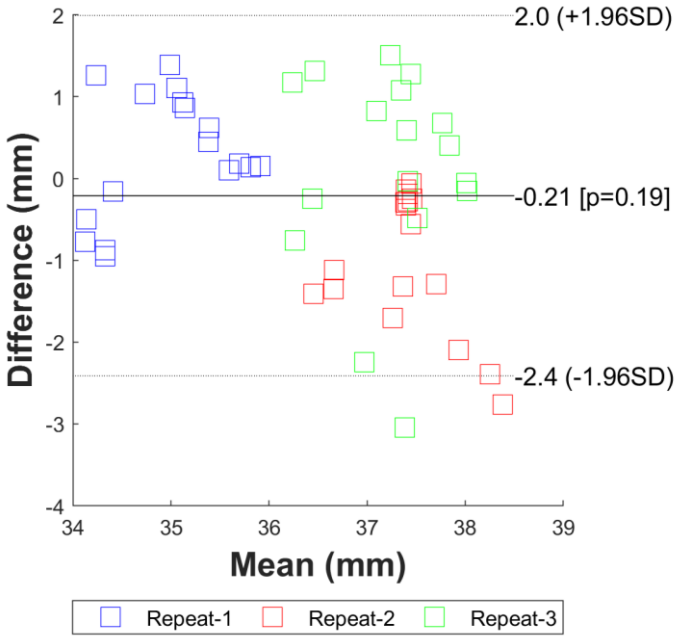

Figure E-69 Bland-Altman plot comparing motion capture and bead MBIR derived superior-inferior translation kinematics during a fast dynamic task.

E.4.6 Medial-Lateral Translation

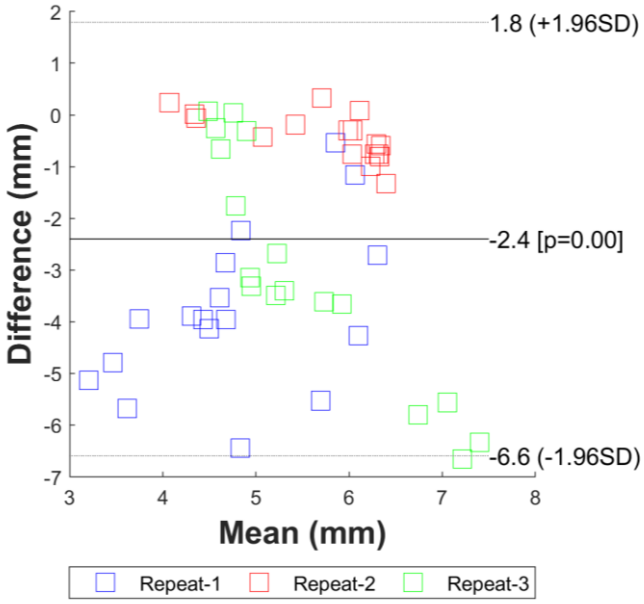

Figure E-70 Bland-Altman plot comparing bead MBIR and MBIR derived medial-lateral translation kinematics during a fast dynamic task.

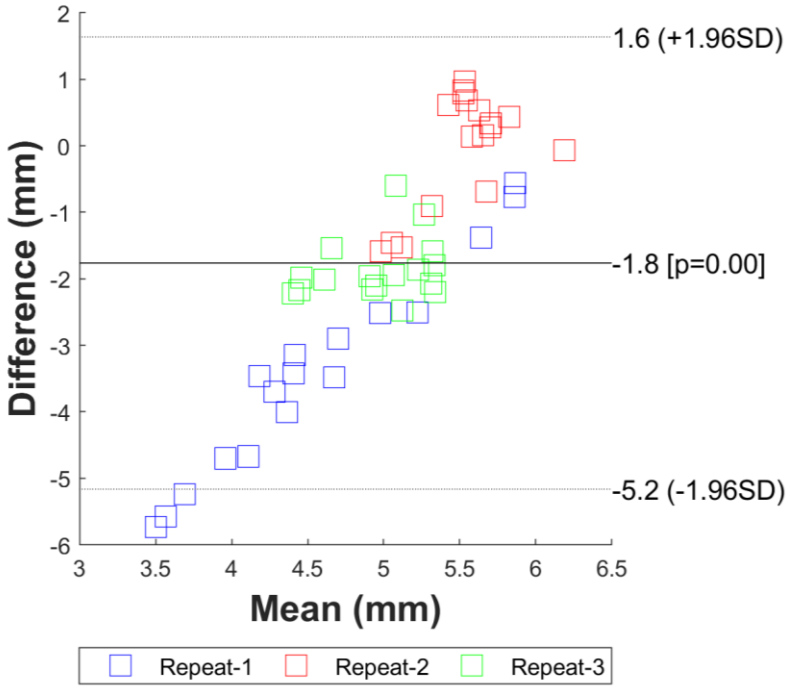

Figure E-71 Bland-Altman plot comparing motion capture and MBIR derived medial-lateral translation kinematics during a fast dynamic task.

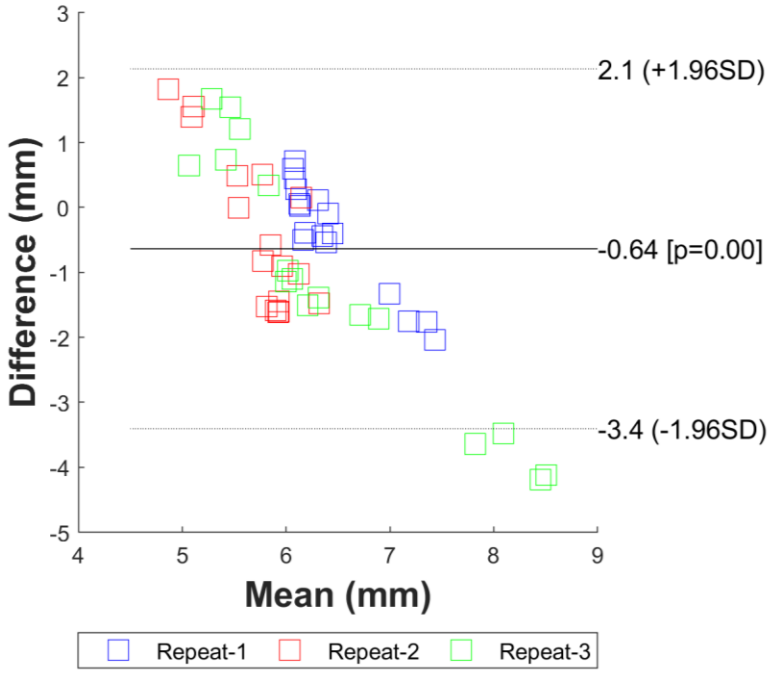

Figure E-72 Bland-Altman plot comparing motion capture and bead MBIR derived medial-lateral translation kinematics during a fast dynamic task.

E.5 Ovine Experiments

E.5.1 Static Task Plots

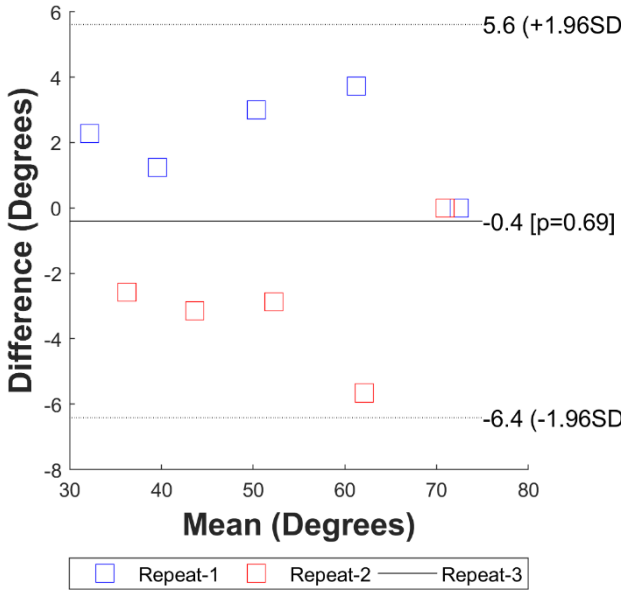

Figure E-73 Bland-Altman plot comparing motion capture and MBIR derived flexion extension angle kinematics during a static task.

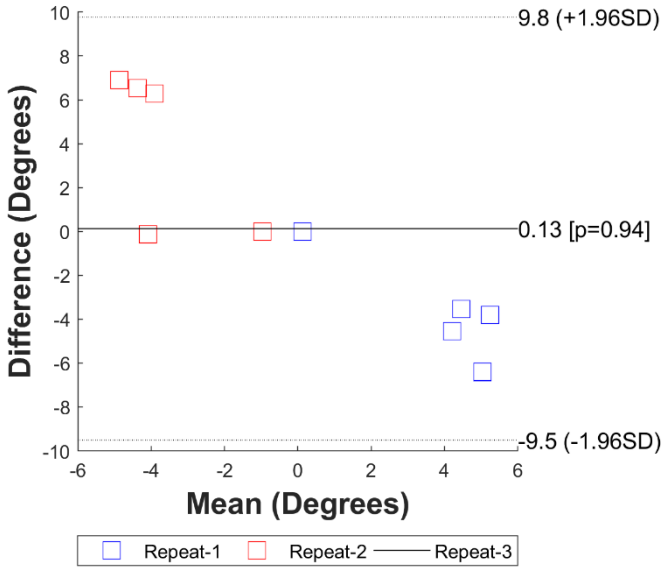

Figure E-74 Bland-Altman plot comparing motion capture and MBIR derived abduction-adduction angle kinematics during a static task.

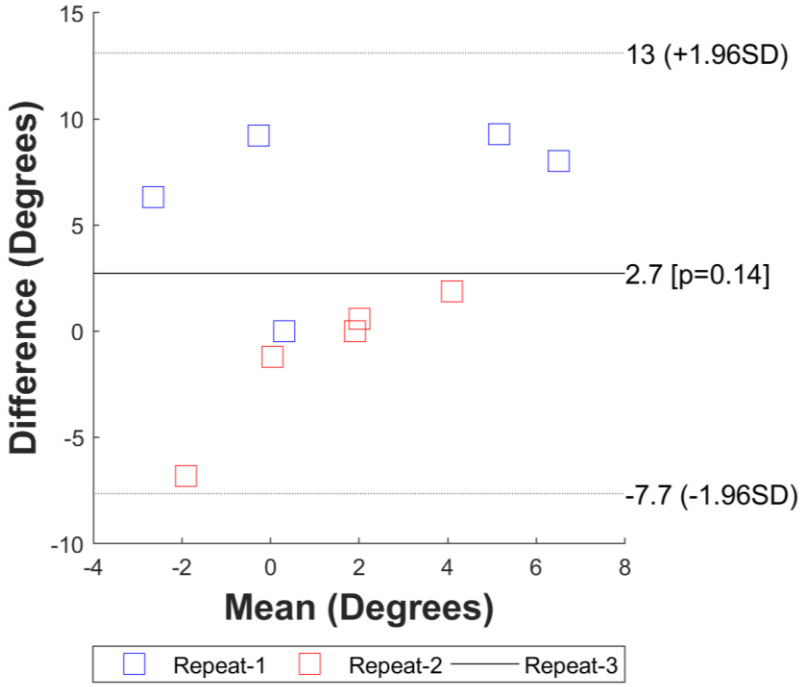

Figure E-75 Bland-Altman plot comparing motion capture and MBIR derived internal external rotation angle kinematics during a static task.

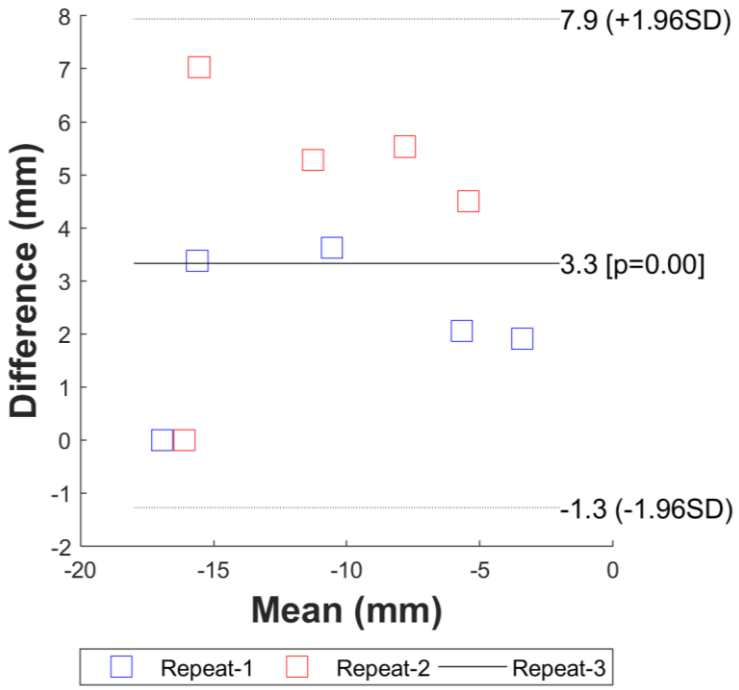

Figure E-76 Bland-Altman plot comparing motion capture and MBIR derived anterior-posterior translation kinematics during a static task.

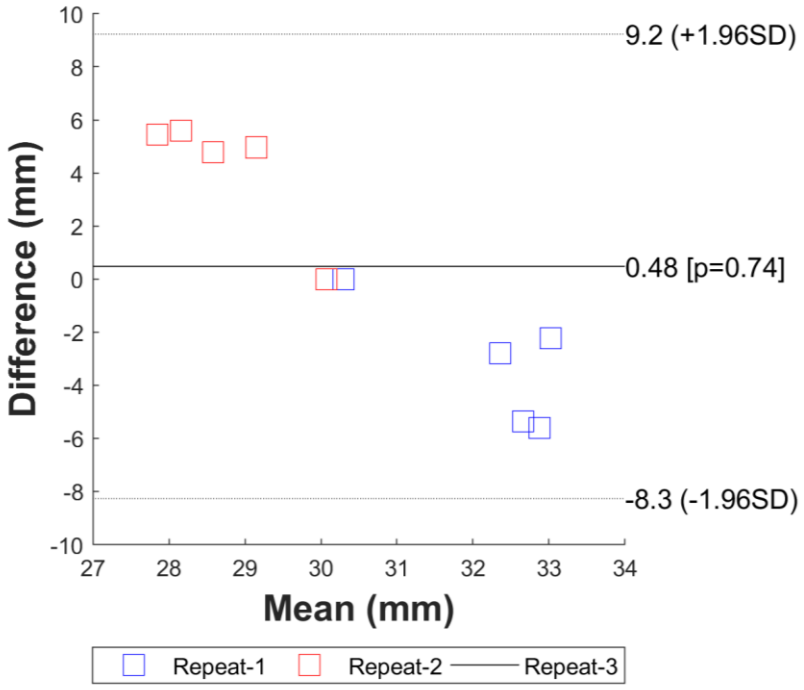

Figure E-77 Bland-Altman plot comparing motion capture and MBIR derived superior- inferior translation kinematics during a static task.

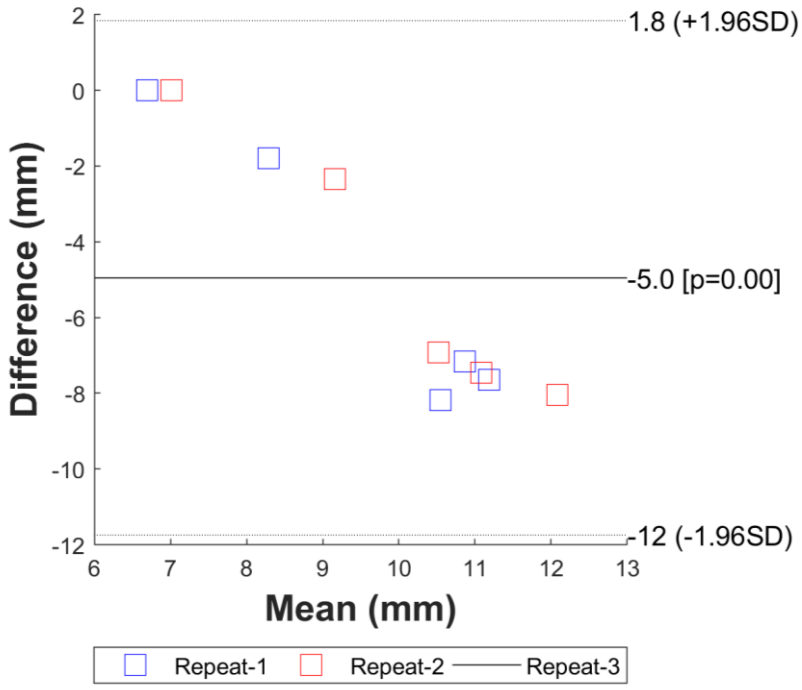

Figure E-78 Bland-Altman plot comparing motion capture and MBIR derived medial-lateral translation kinematics during a static task.

E.5.1 Dynamic Task Plots

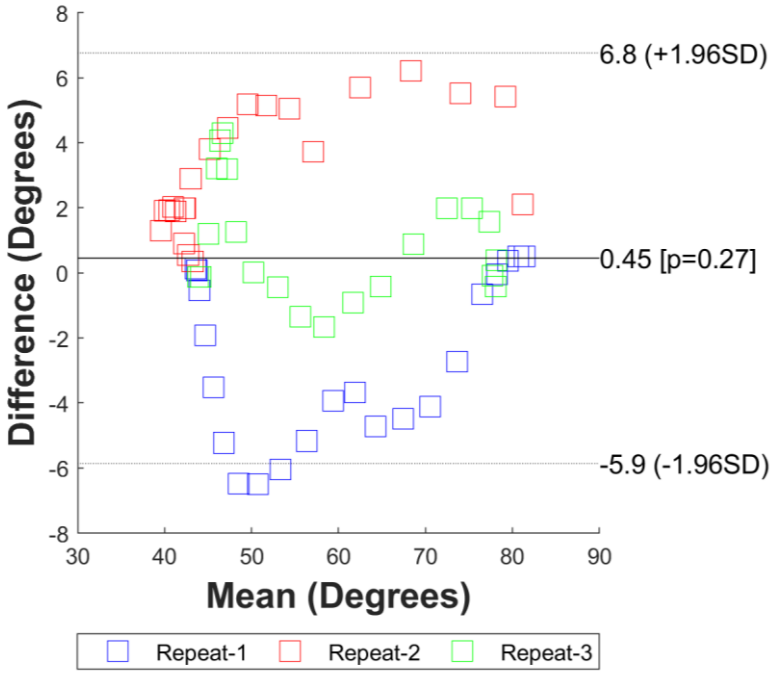

Figure E-79 Bland-Altman plot comparing motion capture and MBIR derived flexion extension angle kinematics during a dynamic task.

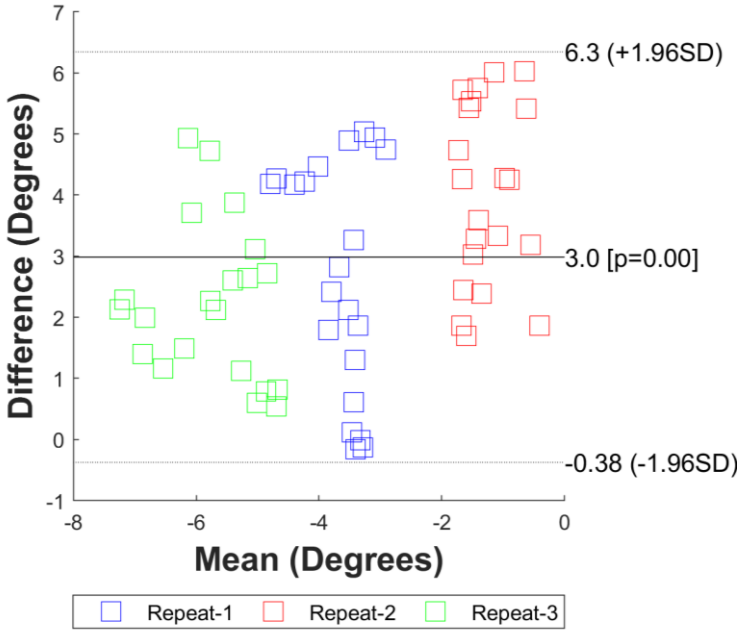

Figure E-80 Bland-Altman plot comparing motion capture and MBIR derived abduction-adduction angle kinematics during a dynamic task.

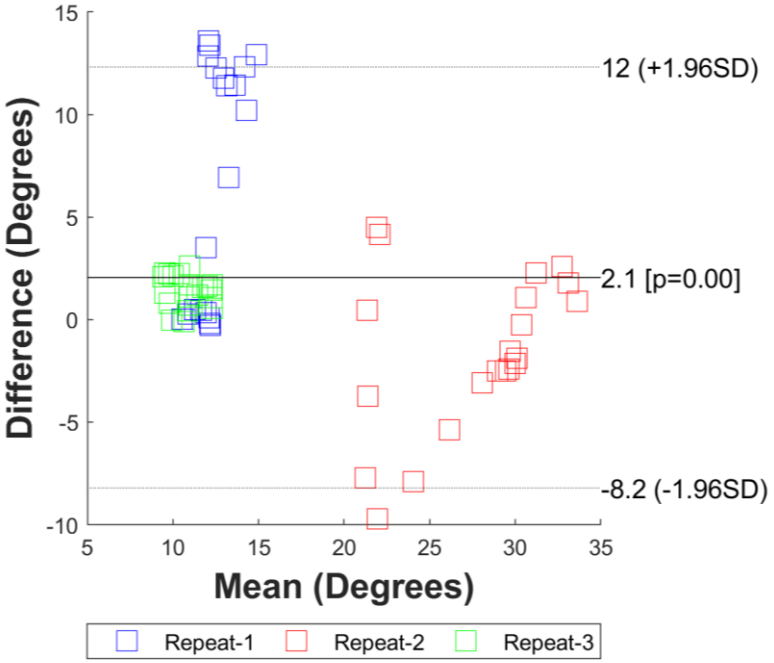

Figure E-81 Bland-Altman plot comparing motion capture and MBIR derived internal external rotation angle kinematics during a dynamic task.

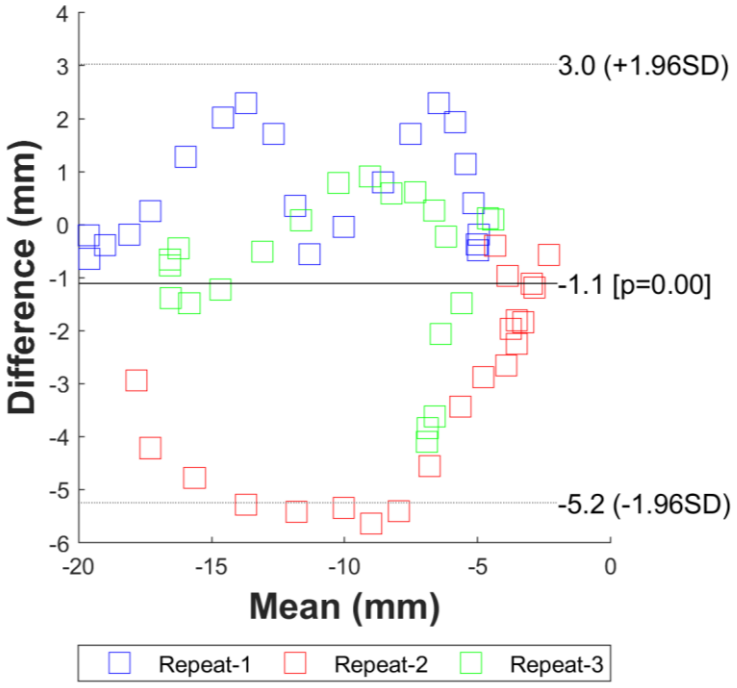

Figure E-82 Bland-Altman plot comparing motion capture and MBIR derived anterior-posterior translation kinematics during a dynamic task.

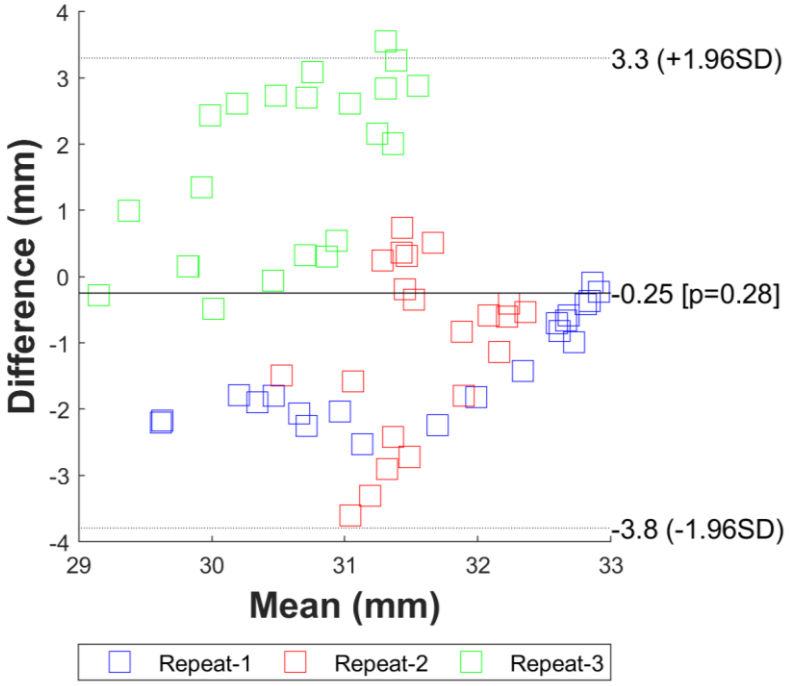

Figure E-83 Bland-Altman plot comparing motion capture and MBIR derived superior- inferior translation kinematics during a dynamic task.

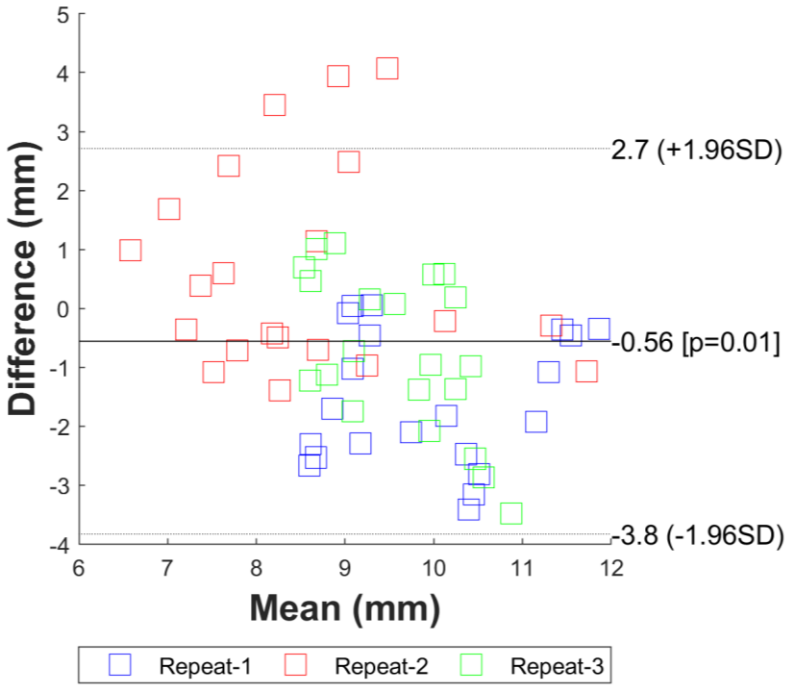

Figure E-84 Bland-Altman plot comparing motion capture and MBIR derived medial-lateral translation kinematics during a dynamic task.

APPENDIX F Standard Operating Procedure for the Operation of the Two Mobile Fluoroscopy C-arms

F.1 Background

The School of Engineering collects radiographic data on healthy volunteers and patients with joint pathology for research purposes. Some of this data is collected as part of interdisciplinary research project within the Arthritis Research UK Biomechanics and Bioengineering Centre. This data may be used for research, education and training.

F.2 Purpose

The purpose of this Standard Operating Procedure (SOP) is to ensure that staff involved in the collection of radiographic data and hence the use of ionising radiation fully understand the procedure for safely operating the two Siemens Siremobil 2000 C-Arms.

F.3 Responsible Personnel

This SOP applies to all **Cardiff University, Cardiff and Vale UHB and Health and Care Research Wales Staff and students** responsible for the operation of the two mobile fluoroscopy c-arms.

The Radiation Protection Supervisor for the lab is responsible for defining SOP, updating it, dissemination to all Centre staff, monitoring adherence and reporting.

Principal Investigators/Research Supervisors are responsible for ensuring that this SOP is correctly applied in the conduct of research and each researcher also has individual responsibility for applying this SOP when required to do so.

Individual Members of Staff are responsible for ensuring that this SOP is correctly applied when imaging patients.

F.4 Imaging policy

When carrying out a fluoroscopic procedure on a human subject it is the policy of ENGIN to ensure the following:

- All fluoroscopic examinations should be conducted as rapidly as possible
- The image intensifier should be positioned as close to the patient as possible
- During fluoroscopy, placing the hands in the direct x-ray beam should be carefully avoided.

F.5 Equipment Set up

For data collection using only one mobile C-arm, fluoroscopy unit 1 labelled “Bill” will be used.

Steps must be followed in the exact order

1. Turn on the C1 X-ray Safety interface located in the control room (T0.16) by rotating the red control clockwise to the on position. Emergency alarm will sound and is deactivated by turning the emergency alarm reset key clockwise. This initialises the green X-ray ready lights.
2. Ensure all other motion capture and corresponding equipment is set up and the C-Arms are correctly positioned around the stairs as stated below (**Figure F-1**):-
    A. Fluoroscopy Unit 1 (Ben)
        i. Length – 20 cm (Figure F-2)
        ii. Angle – 120° (Figure F-3)
    B. Fluoroscopy Unit 2 (Bill)
        i. Length – 16 cm (Figure F-4)
        ii. Angle - 60° (**Figure F-5**)

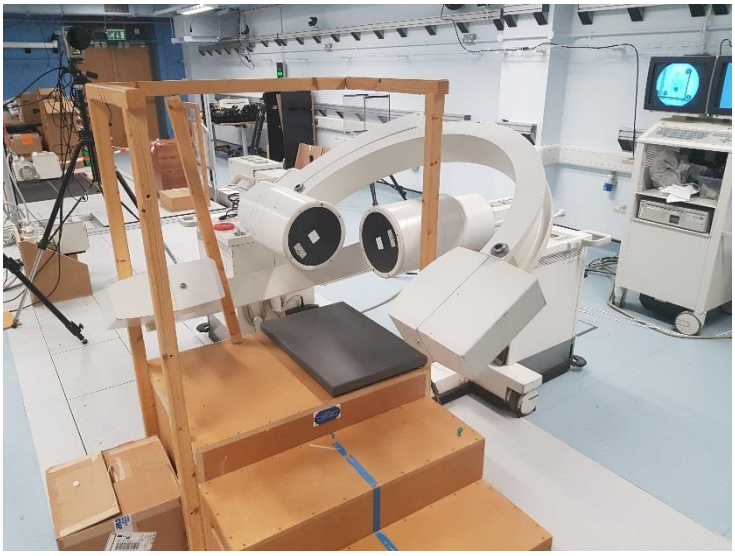

Figure F-1 Fluoroscopy C-Arm Arrangement

3. Remove the key for the mobile C-arm from the locked key safe in T0.16.
4. Insert the key into the C-arm interface panel and rotate clockwise.
5. When the system is on it automatically defaults to continuous fluoroscopy. The settings should be changed as following:
    i. Program name: Knee 1
    ii. Dose rate: 0.22 uGy/s
    iii. Characteristic SIREMATIC curve: 3ma Ramped

F.6 Biomechanical and Fluoroscopy Data collection

Prior to exposure of volunteer switch the C1 Xray Safety interface to 'Patient mode'. This can only be performed by or under the supervision of the local RPS. Position the volunteer in the field of view of Bill and Ben and adjust the height such that the knee is in the centre of the field of view.

F.7 Initiating the exposure:

1. Position the subject within the field of view
2. Press the enable X-ray button (**Figure F-6**) and wait 5 secs till the yellow imminent light remains constant
3. Press the Operator Presence Control (OPC) (**Figure F-7**) switch down to the halfway position.
    i. This initialises the red warning light located in several locations around T0.15, one next to the viewing window in the control room and one outside T0.15 door
4. Wait one second for the kV to stabilise.
5. Fully depress the OPC switch. This will initialise
    i. Motion capture data acquisition
    i. Force plate data acquisition
    ii. EMG data acquisition
    iii. Digital capture of analogue fluoroscopy video output

F.8 During the exposure:

1. Remain inside T0.16 at all times
2. Visually ensure the subject remains within the field of view of the C-arm on the duplicate monitor.
3. Ensure no other part of the subject enters the field of view other than that defined in the protocol
4. Ensure the effective dose rate does not exceed the maximum denoted by the RPA. This can be found in the SOP's folder.
5. Ensure all non-fluoroscopic equipment is operating correctly

Maximum total combined time for exposure to a participant is 60 secs: operator to make note of each exposure time and whether one or both c-arms used.

F.9 Terminating the exposure:

1. Release the OPC switch half way and then fully press the switch once more and then release fully. This will terminate:
    ii. Fluoroscopy exposure
    iii. Digital capture of analogue fluoroscopy video output
    iv. Force plate data acquisition
    v. EMG data acquisition
    vi. Motion capture data acquisition

After any exposure of a volunteer record the kV and the time exposed in the fluoroscopy database from the outputs on Bill and Ben.

F.10 Emergency Safety Precautions

The Emergency stop should be used if x-rays are emitted when not intended i.e. where safety features fail or emission fails to terminate or if a patient collapses on the equipment.

F.11 Emergency termination of exposure

- The initial Emergency stop for the fluoroscopy exposure is the Operator Presence Control switch
- If that fails, then there are red Emergency Stop buttons (**Figure F-8**) in the control room and in several locations in T0.15 (Directly below the warning lights), this will disconnect the power and turn on an alarm in the control room.
- If the unit cannot be shut down using the red Emergency Stop buttons then this can be done by using the C1 X-ray Safety interface (**Figure F-9**) located in the control room (T0.16) and rotating the red control anti clockwise to the off position

F.12 Emergency contingency arrangements

- In a medical emergency, contact the nearest first aider or ambulance if required (Tel: 999) or security (Tel:4444)
- If a person enters the room when the system is in use, the unit will automatically have stopped due to safety interlocks in the door and will not fire until the door is closed. The person will be told to enter into the control room T0.16.
- Should monitoring equipment or other indicator warn of an unsafe condition (e.g. a high ambient dose rate, unintended or continued emission, activation of relevant warning signs or alarms, etc.) retreat from the immediate area of the source of radiation to a place of safety e.g. in the control room (T0.16). If only the participant is located in T0.15 then the operator can inform the patient to exit the lab via the intercom in the control room (T0.16).
- If an external hazard to other persons persists, warn others in the vicinity to stay in the control room.
- Should fire alarms sound or a fire occurs remain calm, power down the equipment, remove operation keys, and escort any patients, volunteers, visitors with you out of the facility. Action to take and evacuation should be in accordance with local fire policy (information provided on the wall and during lab induction).
- Report incidents and accidents, safety concerns, obstinacy in compliance with local rules or verbal instruction, to the RPS, who is required to report in turn to the RPA. There are HSE, Health

Inspectorate Wales and MHRA reporting requirements required in some cases this will be advised by the RPA**.**

- If the equipment is not working correctly for any reason attach a warning notice on the control console in accordance with requirements in Section 8 of the Local Rules. If the system is damaged, this must be checked by the RPS at Velindre NHS Trust before further use.

F.13 Maintenance

- Clean unit by wiping with a mild disinfectant and soft cloth.
- Unit is visually inspected by the operator every time before exposure
- Unit is functionally tested by RPS every month
- Unit is calibrated every year.
- Any malfunction should be reported to RPS
- Any additional maintenance/service should be performed by authorized personnel and unit re-certified in writing.

F.14 C-Arm Set up and Equipment Images

Figure F-2 Ben Length at 20 cm

Figure F-3 Ben C-Arm Rotated to 120°

Figure F-4 Bill at Length 16cm

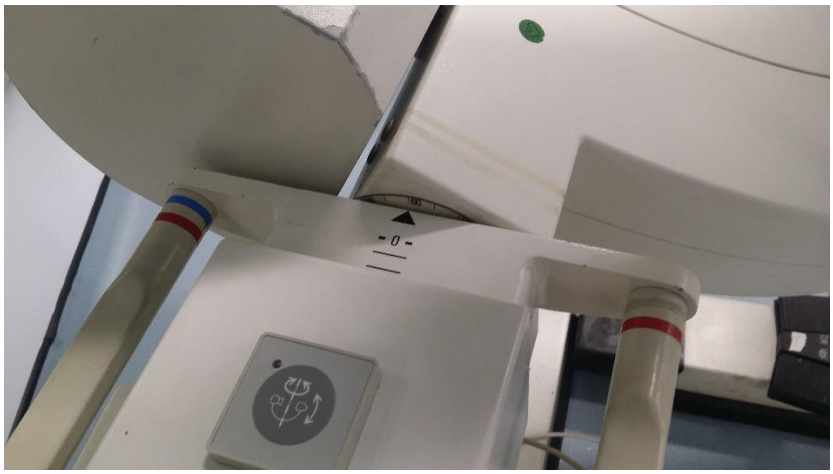

Figure F-5 Bill C-Arm rotated to 60°

Figure F-6 Enable X-Rays Button

Figure F-7 Operator Present Control switch

Figure F-8 Emergency Stop Switch

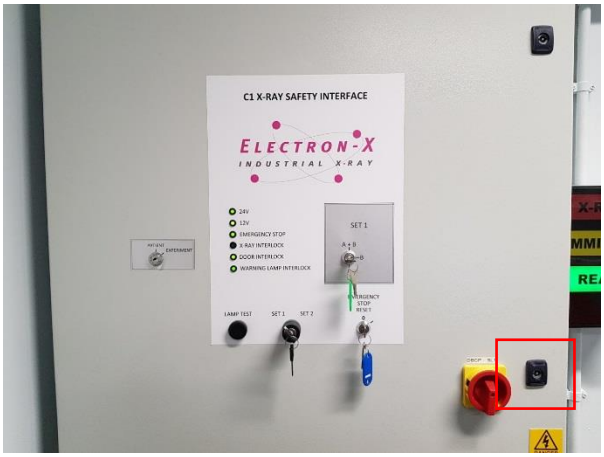

Figure F-9 C1 X-Ray Safety interface

APPENDIX G Research Trial Radiation Dose and Risk Assessment

Radiation Protection Service

Department of Medical Physics & Clinical Engineering,
Velindre Hospital, Cardiff, CF14 2TL

02920 316 268
VCC.RadiationEthicsReviews@wales.nhs.uk

File Ref: \\RQFH5SRVFILE001.CYMRU.NHS.UK\Radprot\Ionising Radiation\Ethics\2018 Trials\Knee Study\Knee Study (Generic) MPE Review.Docx

Research Trial Radiation Dose and Risk Assessment
Lead Medical Physics Expert (MPE) Review

Title:	Knee Study (Generic)
IRAS No:	N/A
Protocol Version:	N/A
Lead Site:	University of Cardiff, Engineering Department, Biomechanical musculoskeletal research facility.
Trial Phase:	N/A
Circulation:	David Williams

1. Background

The University of Wales Engineering Department wishes to conduct research trials involving medical radiation exposures. This review has been undertaken as the Medical Physics Expert component of the radiation review of the research proposal. The dose and risk assessment information will be inserted into the relevant sections of the IRAS form (Section A22 and Part B Section 3) or local Cardiff University documentation as required. Advice regarding the Participant Information Sheet is provided in section 5 of this review.

This review is a generic review for all research trials at the centre involving biplane fluoroscopic imaging of the knees utilising the 'Bill' and 'Ben' Siremobil 2000 c-arms. The research trials involve imaging of the knee joint with the volunteer undertaking prescribed knee joint movements.

2. IRAS Form: Section A22: Potential Risks

No IRAS form available for review.

3. IRAS Form: Part B: Section 3

Does the study involve exposure to radioactive materials? (if 'Yes' answer A & C)	Yes		No	✓
Does the study involve other diagnostic or therapeutic ionising radiation? (if 'Yes' answer B & C)	Yes	✓	No	

A. Radioactive Materials

A1. Details of radioactive materials

Type of investigation/therapy:			
Radionuclide:			
Chemical form:			
Proposed Activity:			
Route of administration:			
Number of administrations per participant:			
Effective dose or target tissue dose per administration:			

A2. Details of study participants

Radiation Protection Service

Department of Medical Physics & Clinical Engineering,
Velindre Hospital, Cardiff, CF14 2TL

02920 316 268
VCC.RadiationEthicsReviews@wales.nhs.uk

File Ref: \\RQFH5SRVFILE001.CYMRU.NHS.UK\Radprot\Ionising Radiation\Ethics\2018 Trials\Knee Study\Knee Study (Generic) MPE Review.Docx

Canolfan Ganser Felindre Velindre Cancer Centre

RPS Cardiff Ysbyty Felindre, Caerdydd

Will any of the study participants be patients?					Yes		No	✓
Will any of the study participants be healthy volunteers?					Yes	✓	No	
Number (whole study)	Age Range	Sex	Clinical Condition	Total effective or target tissue dose per individual				

A3. What steps will you take to exclude women who are pregnant or who could become pregnant during the study?

Screening at recruitment of volunteers.

A4. ARSAC research certificate

Not applicable as no radioactive materials involved.

B. Other Ionising Radiation

B1. Details of other ionising radiation

Procedure	Number of procedures	Estimated procedure dose (mSv)
Biplane fluoroscopic imaging of the knees	1 minute 5 minutes 10 minutes	0.0026 0.013 0.026
Total Research Protocol Dose (mSv):	**Dependent on total screening time**	

C. Dose and risk assessment

This study requires exposures to ionising radiation. Participants, all of whom are healthy volunteers, will undergo fluoroscopic x-ray imaging of the knees.

The whole body effective dose received by the participant as a result of participation in this trial is dependent on the total screening time – 0.0026mSv per minute of screening. This dose was calculated based on phantom measurements carried out in 2015, with the doses adjusted based on the increase in patient entrance dose measurements at the last annual RPS Cardiff testing.

Ionising radiation can cause cancer which manifests itself after many years or decades. Assuming individuals are of average age and otherwise in good health, the lifetime risk of (fatal) cancer induction is 5% per Sv (ICRP 103). Therefore, the risk from exposure to ionising radiation for such individuals participating in this trial would be:

For 1 minute screening: 1 in 7.7 million
For 5 minutes screening: 1 in 1.5 million
For 10 minute screening: 1 in 770000

For comparison, the natural lifetime cancer incidence in the general population is about 50%. This risk places the trial into Category I of the ICRP 62 categories of risks associated with radiation exposure (for a total screening time less than 40 minutes). This level of radiation dose is equivalent to approximately the following exposure to the average natural background radiation in the United Kingdom:

Radiation Protection Service

Department of Medical Physics & Clinical Engineering,
Velindre Hospital, Cardiff, CF14 2TL

02920 316 268
VCC.RadiationEthicsReviews@wales.nhs.uk

File Ref: \\RQFH5SRVFILE001.CYMRU.NHS.UK\Radprot\Ionising Radiation\Ethics\2018 Trials\Knee Study\Knee Study (Generic) MPE Review.Docx

Canolfan Ganser Felindre Velindre Cancer Centre

RPS Cardiff
Ysbyty Felindre, Caerdydd

For 1 minute screening: ½ a day
For 5 minutes screening: 2 days
For 10 minute screening: 4½ days

No provision is made in this assessment for any projections that need to be repeated for technical reasons or any further radiological investigations that might be required, which would increase the total radiation dose.

4. Review of Participant Information Sheet (PIS)	
PIS Document Reviewed:	**None**

Patient information sheets for individual trials must be submitted for MPE review before commencement of each trial.

The PIS must:

- State that all exposures to ionising radiation are to healthy volunteers only and form no part of any routine clinical care.
- Specify the type and number of exposures
- Specify and quantify the risk of cancer induction (e.g. '*Exposure to ionising radiation will increase your risk of cancer induction, by taking part in this trial your additional risk of cancer induction will be 1 in 1.5 million*'

It is also recommended that the following statement is included: '*We are all at risk of developing cancer during our lifetime. The normal risk is that this will happen to about 50% of people at some point in their life. Taking part in this study will add only a very small chance of this happening to you.*'

5. Other Comments

This is a generic risk assessment. The dose and risk for any individual trial will depend on the total screening time. Details and PIS for individual trials should be submitted for MPE review.

Assessor Name	Assessor Signature	Assessor Designation	Assessment Date
Samantha Nicholson	S Nicholson	Clinical Scientist	22nd May 2018
MPE Name	**MPE Signature**	**Designation**	**MPE Signature Date**
Arnold Rust	A. J. Rust	Head of Radiation Protection Service	30th May 2018

APPENDIX H Healthy Volunteer Biplane Fluoroscopy Consent Form

HEALTHY VOLUNTEER INFORMATION SHEET

Assessment of knee function in healthy volunteers using fluoroscopic imaging techniques

Part 1

You are being invited to take part in a research study with Cardiff University's Musculoskeletal Biomechanics Research Facility (MSKBRF). Before you decide, it is important for you to understand why the research is being done and what it will involve. Please take time to read the following information carefully and discuss it with others if you wish. One of our team will go through the information sheet with you. Ask us if there is anything that is not clear or if you would like more information. Take time to decide whether or not you wish to participate. Part 1 tells you about the purpose of this study and what will happen to you if you take part. Part 2 gives you more detailed information about the conduct of the study.

What is the purpose of this study?

This research is part of a series of studies being conducted by the MSKBRF, which use an interlinking approach to investigate the effects of disease, injury and/or any related treatment on the biomechanics of the joint compared to healthy joints. This part of the research involves assessing movement by using special imaging techniques of the knee.

Measurement of knee movement is essential for the understanding and evaluation of the function of the knee. The purpose of this study is to use a mathematical tool developed in a previous study to examine the differences

between normal, arthritic and knee replacement/surgical intervention knees. We will also look at the design of replacement knee joints (and some other operations) and look at how their function compares to normal knees.

The close relationship between orthopaedic surgeons, physiotherapists, scientists and engineers in this study will hopefully allow us to develop new methods of diagnosing knee problems, to improve the way decisions are made about treatment and to help improve the design of knee replacements in the future.

With improved clinical assessment for this common disease, surgical input to relieve the painful and functionally disabling symptoms could be more effectively tailored to suit patients.

Why have I been asked to take part in this study?

You have been asked to take part in this study as it will allow us to gain further insight into the nature of movements of people with a normal knee which is helpful when developing treatments for people with knee problems. It additionally helps with us calculating any errors with our motion analysis techniques.

Do I have to take part?

It is up to you to whether or not to take part. If you do decide to take part you will be given this information sheet to keep and after you have had enough time to read through it, be asked to sign a consent form. If you decide to take part, you are still free to withdraw at any time or without giving a reason. However, any data that we may have collected up to the point of withdrawal will be kept for analysis.

What will happen if I agree to take part?

You will be asked to attend one session at the Cardiff School of Engineering, lasting approximately 2 hours. All participants will be sent a map.

Data will be kept securely for a minimum of 15 years from the end of the study in accordance with good research practice and data protection regulations imposed by Cardiff University in accordance with the Data Protection Act 1998. All data obtained during the study will remain confidential. Access to data will only be available to the investigators attached to the Musculoskeletal Biomechanics Research Facility at Cardiff University.

If new information becomes available, we may invite you to take part in a follow-up study in the future, please indicate on the consent sheet if you do not mind us contacting you.

What will I have to do?

At the beginning of your visit, we will explain the full study to you and ask for your consent, bearing in mind that you are free to withdraw at any time.

As part of the assessment, you will have to remove your trousers or skirt, we ask you to bring a pair of shorts to wear. You will have very light plastic

markers placed onto the surface of your legs and held in place with non-stick tape or bandages. You will be asked to perform a series of movements so that recordings can then be made to track the movement of the markers. Small, lightweight sensors may also be attached to the skin to record body movements.

You may be asked to wear a lead-rubber apron for protection you will be asked to perform simple knee movements in a set pattern of bending and straightening. This will be recorded for a maximum period of 300 seconds using low-dosage fluoroscopic X-ray equipment.

Throughout the session, your knee movements will be recorded using standard audio-visual equipment. These recordings will be used for data verification. All data files, including audio-visual files will be stored in encrypted folders on Cardiff University password protected computers. Full participant anonymity will be ensured in all video content used in presentations/publications if you consent for us to use your data in this way, with identifiable features digitally masked when needed.

Regular rest and toilet breaks will be provided as often as you need them to ensure maximum comfort.

After attendance at the session you will be reimbursed for reasonable travel expenses.

Are there any risks in participating in this study?

Before participating you should consider if this will affect any insurance you have and seek advice if necessary.

If you take part in this study you will have one X-ray fluoroscopic procedure. This procedure uses ionising radiation to form images of your knee which will be used for medical research. Ionising radiation can cause cell damage that may, after many years or decades, turn cancerous.

We are all at risk of developing cancer during our lifetime. The normal risk is that this will happen to about 50% of people at some point in their life. Taking part in this study will add only a very small chance of this happening to you.

While the intended exposure is very low, there is a very small chance it may affect an embryo or foetus. Pregnant women must not, therefore, take part in this study; neither should women who plan to become pregnant during the study. If there is any chance that you could be pregnant, you will not be able to participate in this study. Confirmation as to whether you could be pregnant will be required on the day of each data collection. Any woman who finds that she has become pregnant while taking part in this study should immediately inform the researcher or her GP.

What are the benefits of taking part?

We hope to be able to better understand how disease and injury affect the motion of the knee. There is no intended clinical benefit to the participant from taking part in the study. It is hoped that the information that we get from this study will help us to treat future patients with joint problems more effectively.

If the information in Part 1 has interested you and you are considering participation, please read the additional information in Part 2 before making a decision.

HEALTHY VOLUNTEER INFORMATION SHEET

Assessment of knee function in healthy volunteers using fluoroscopic imaging techniques

Part 2

What if new information becomes available?

Occasionally during the course of a research project, new information may become available about the investigation being carried out. If this happens, a member of the research team will contact you to inform you about it and discuss with you whether you would like to continue in the study. If, after considering the new information, you decide to withdraw from the study, it will not affect your legal rights. If you are happy to continue, you will be asked to sign an updated information sheet and consent form which contains the updated information. .

What will happen if I do not want to carry on with this research?

If you decide you would like to withdraw from the study, we will erase all identifiable material. However, any information collected up to that point will be kept and used unless you tell us that you would like your information removed from the project.

What if something goes wrong?

In the rare circumstance that you are harmed by taking part in this research project, there are no special compensation arrangements. If you are harmed

due to someone's negligence, then you may have ground for legal action, but you may have to pay for it. Regardless of this, if you wish to complain, or have any concerns about any aspect of the way you have been approached or treated during the course of this study, please contact a member of our team the details of which are in the "What if I wish to lodge a complaint?" section below.

Will my taking part in this study be kept confidential?

Once you have consented to take part in the study, you will be assigned a unique identifier which will linked to your details and will also allow us to track you through the appropriate and relevant arms of the study. All information which is collected about you during the course of the research will be kept strictly confidential. We may share the data we collect with researchers at other institutions including Universities and commercial research organisations, in the UK and aboard. However, any information that leaves the Centre will be anonymised. It will have your name and address removed so that you cannot be recognised from it. In any sort of report we might publish, we will not include information that will make it possible for other people to know your name or identify you in any way. You will simply be referred to by your gender, age, the affected joint and possibly some characteristic such as left or right handedness. If you join the study, some parts of your records and the data collected for the study may be looked at by authorised persons from the University for the purposes of monitoring and auditing. We may share information (including related medical findings such as radiological images) with external collaborators but all this information will contain no identifiable information about you.

Will my GP be informed of my involvement in this study?

We do not routinely send a letter to the GP to inform them of your participation in this research. However, with your permission we may contact your GP before getting in touch with you in the future to ensure it is suitable for us to do so. For this reason we ask you to bring details (name, address and telephone number) of the GP with whom you are registered.

What will happen to the results of the research?

We hope to publish the results of this study in a scientific journal. We may also present the results at a scientific conference or a seminar in a university. We may also publish results on our website. We would be happy to discuss the results of the study with you and send you a copy of the published results. It will not be possible to identify you or images of your joint in any report or publication.

Who is organising and funding the research?

Research staff at the MSKBRF at Cardiff University are carrying out the study.

What if I wish to lodge a complaint?

If you wish to make a complaint regarding the way you were approached or treated during the trial, please contact the MSKBRF Coordinator on Telephone: 029225 10238 Email: SawleL1@cardiff.ac.uk.

Contact for further information

Musculoskeletal Biomechanics Research Facility

Cardiff School of Engineering

Cardiff University

Cardiff

CF10 3AA

Tel: 029225 10238

Email: SawleL1@cardiff.ac.uk or Williamsd37@cardiff.ac.uk

This completes Part 2. Thank you for reading this information sheet.

If you agree to take part in this study you will be given a copy of the information sheet and a signed consent form to keep.

VOLUNTEER CONSENT FORM

Assessment of knee function in healthy volunteers using fluoroscopic imaging techniques

Study Number:

Volunteer Identification Number for this research:

You DO NOT have to sign this document. Please DO NOT sign this document unless you fully understand it. If there is ANYTHING which you do not understand please do not hesitate to ask for a full explanation.

To confirm agreement with each of the statements below, please initial each box and amend as necessary:

1. I confirm that I have read and understand the information sheet dated 05 July 2017 (version 1) for the above study and have had the opportunity to ask questions. ☐

2. I understand that my participation in the study is voluntary and that I am free to withdraw at any time, without giving any reason, and without my legal rights being affected but any data collected up to the point of my withdrawal will be retained. ☐

3. I understand that my details will be linked to a unique identifier to allow you to

follow me through course of the study ☐

4. You may / may not (please delete as appropriate) contact me in the future to ask if I would be interested in participating in a follow up or future research project/survey. ☐

5. I do / do not (please delete as appropriate) agree for you to share my anonymised data with external collaborators in the UK and abroad, including commercial companies. ☐

6. I agree to my GP being contacted ☐

7. (Women only)I confirm that to the best of my knowledge I am not currently pregnant but will inform the researchers if my circumstances change and I become pregnant during the course of the study. ☐

8. I agree to take part in the above study. ☐

Name of Volunteer: _____

(Please print)

Signature: _____ Date:_____

I confirm that I have fully explained the experimental protocol and purpose of the study.

Name of Researcher:_____

Signature: _____ Date:_____

Name of person taking consent: _____

(If different from researcher)

Signature: _____ Date:_____

GP Details

GP Name:

GP Address:

GP Telephone Number:

APPENDIX I Healthy Volunteer Motion Analysis Results from Chapter 6

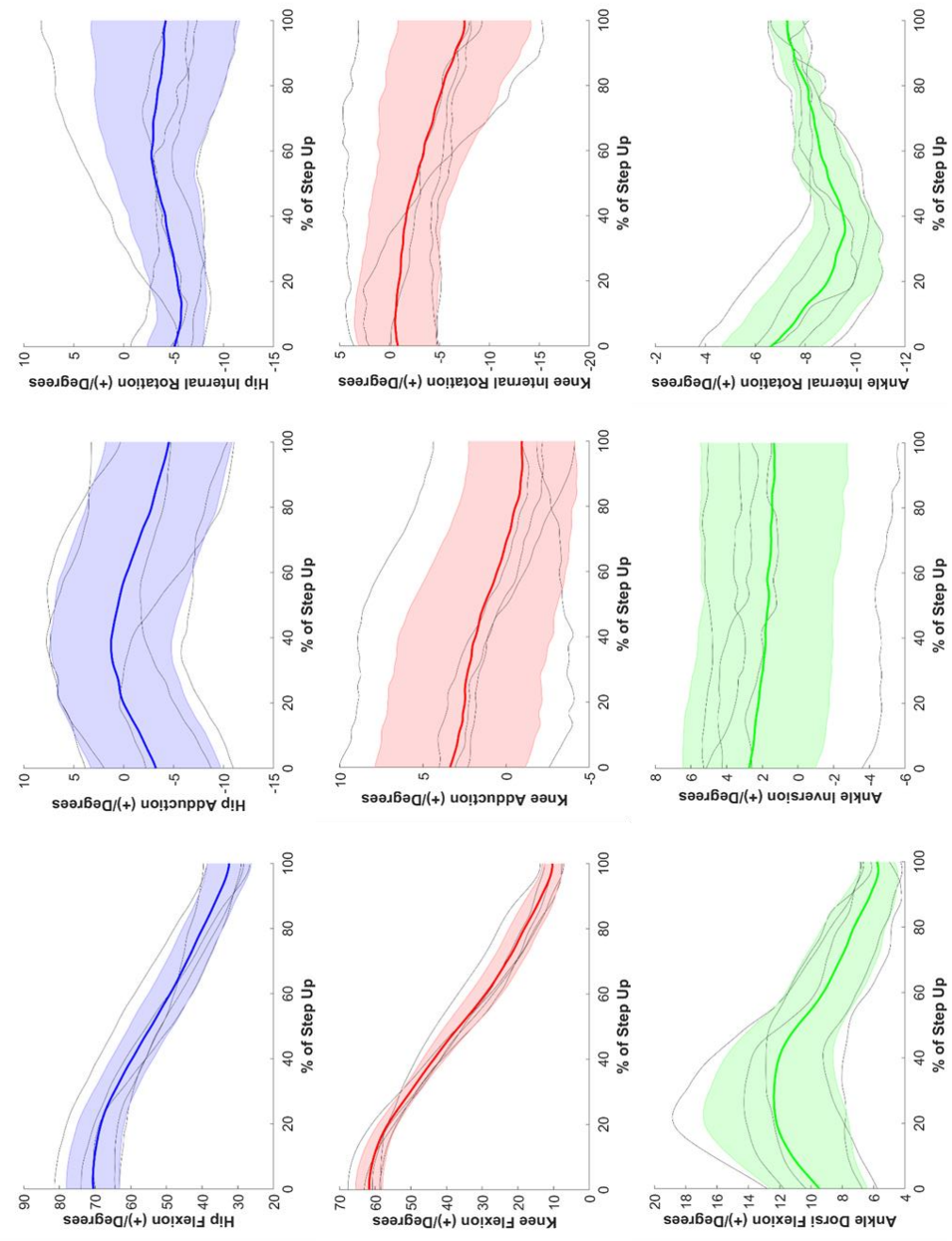

Figure I-1 X, Y, Z, Rotation angles calculated from motion capture for hip (blue), knee (red) and ankle (green) during step up

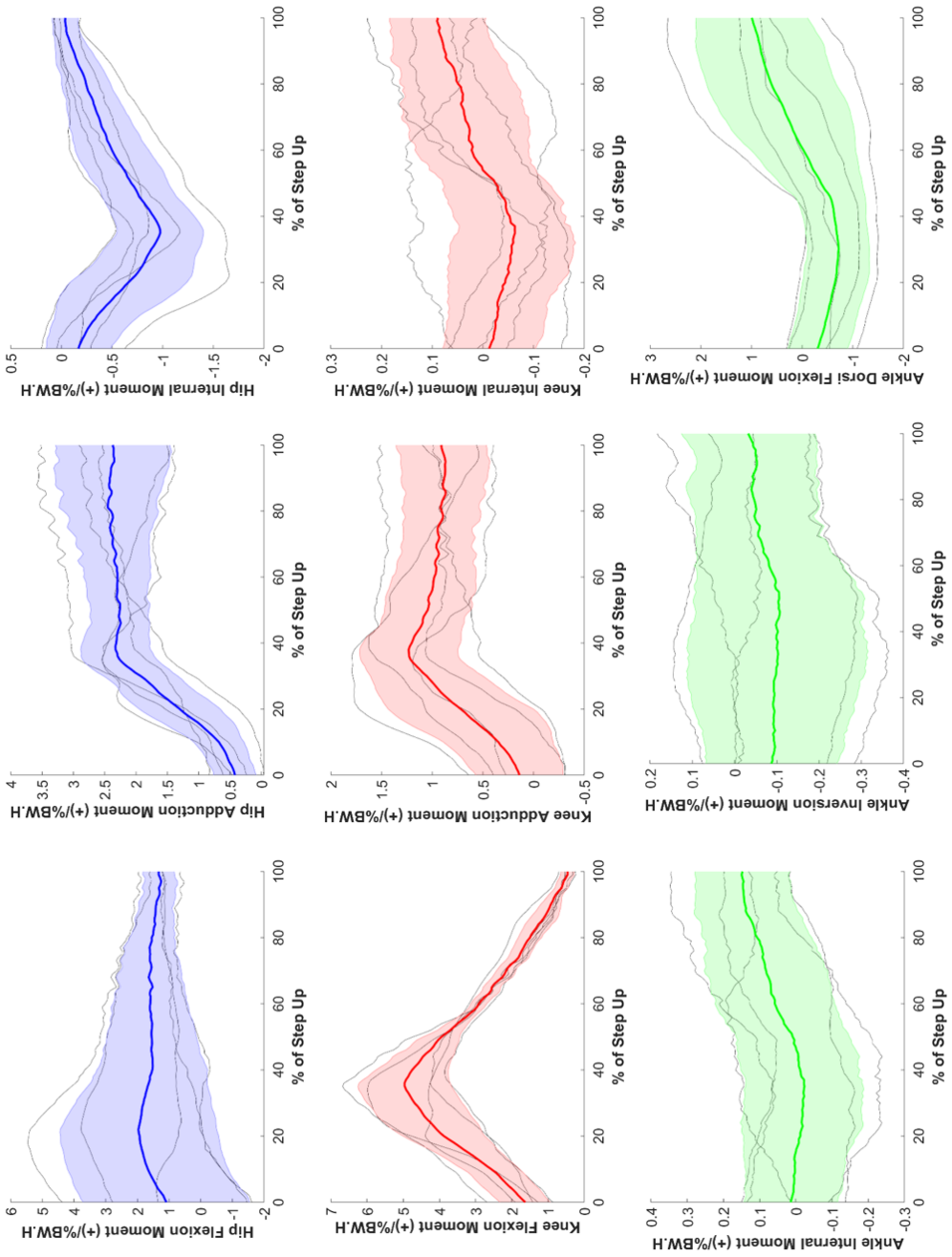

Figure I-2 X, Y, Z, moments calculated from motion capture for hip (blue), knee (red) and ankle (green) during step up

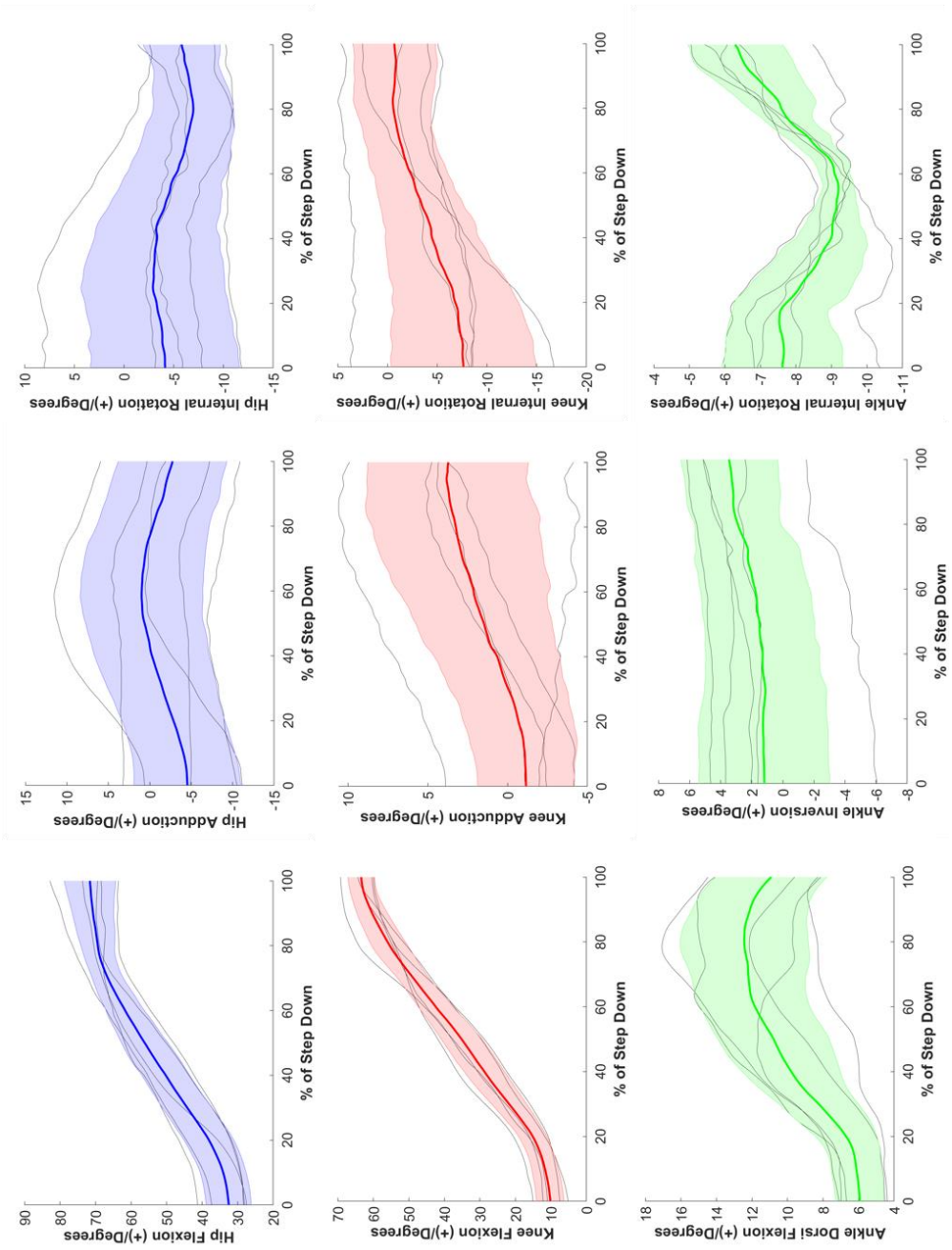

Figure I-3 X, Y, Z, Rotation angles calculated from motion capture for hip (blue), knee (red) and ankle (green) during step down

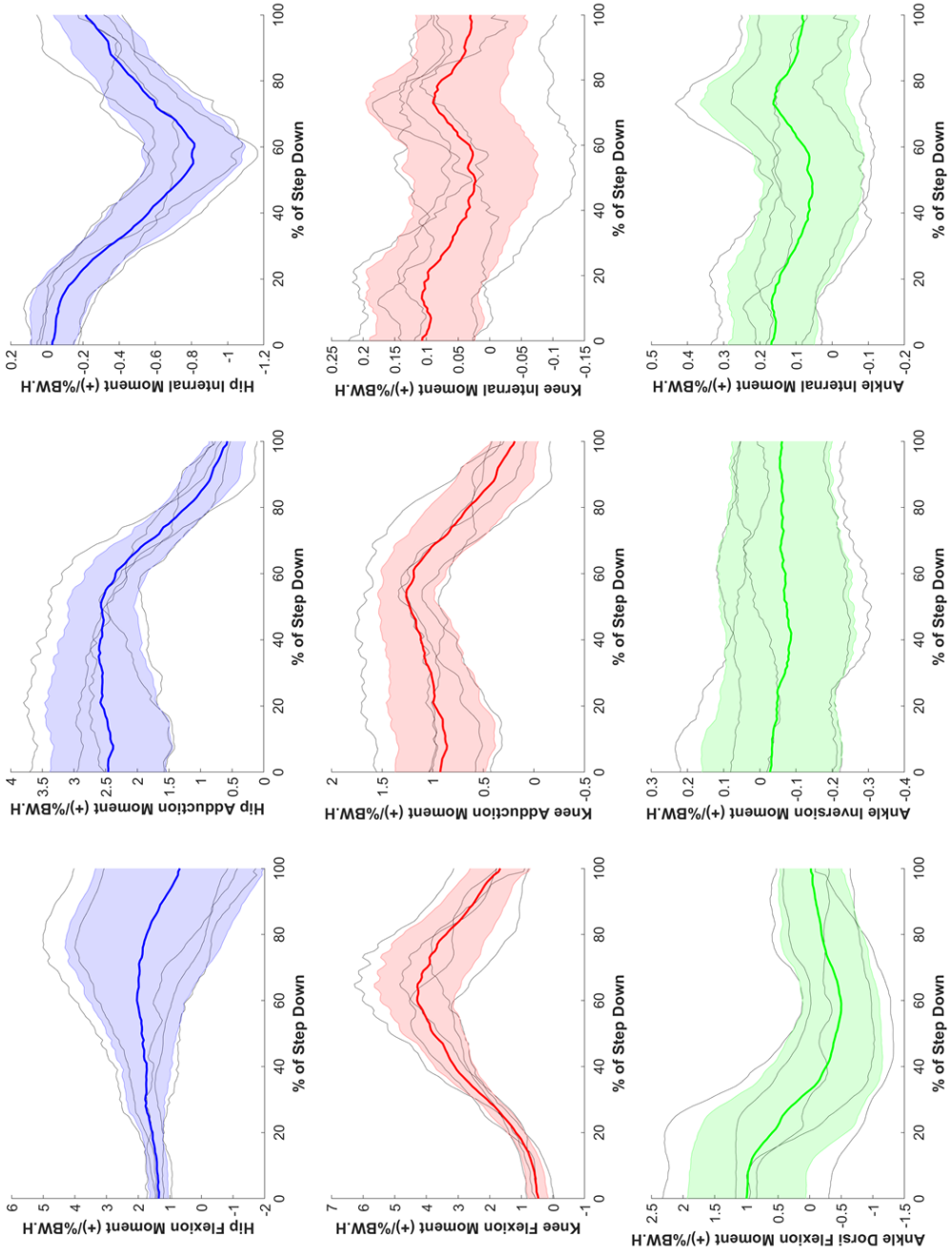

Figure I-4 X, Y, Z, moments calculated from motion capture for hip (blue), knee (red) and ankle (green) during step down